JAEA-Conf 2015-003
INDC(JPN)-201
DOI:10.11484/jaea-conf-2015-003

JAEA-Conf

Proceedings of the 2014 Symposium on Nuclear Data November 27-28, 2014, Conference Hall, Hokkaido University, Sapporo, Japan

(Eds.) Masayuki AIKAWA, Osamu IWAMOTO, Shuichiro EBATA, Satoshi KUNIEDA
Shoji NAKAMURA and Hiroyuki KOURA

Nuclear Data and Reactor Engineering Division
Nuclear Science and Engineering Center
Sector of Nuclear Science Research

March 2016

Japan Atomic Energy Agency

日本原子力研究開発機構

本レポートは国立研究開発法人日本原子力研究開発機構が不定期に発行する成果報告書です。
本レポートの入手並びに著作権利用に関するお問い合わせは、下記あてにお問い合わせ下さい。
なお、本レポートの全文は日本原子力研究開発機構ホームページ（http://www.jaea.go.jp）
より発信されています。

国立研究開発法人日本原子力研究開発機構 研究連携成果展開部 研究成果管理課
〒319-1195 茨城県那珂郡東海村大字白方 2 番地4
電話 029-282-6387, Fax 029-282-5920, E-mail:ird-support@jaea.go.jp

This report is issued irregularly by Japan Atomic Energy Agency.
Inquiries about availability and/or copyright of this report should be addressed to
Institutional Repository Section,
Intellectual Resources Management and R&D Collaboration Department,
Japan Atomic Energy Agency.
2-4 Shirakata, Tokai-mura, Naka-gun, Ibaraki-ken 319-1195 Japan
Tel +81-29-282-6387, Fax +81-29-282-5920, E-mail:ird-support@jaea.go.jp

JAEA-Conf 2015-003
INDC(JPN)-201

Proceedings of the 2014 Symposium on Nuclear Data November 27-28, 2014, Conference Hall, Hokkaido University, Sapporo, Japan

(Eds.) Masayuki AIKAWA*, Osamu IWAMOTO, Shuichiro EBATA*
Satoshi KUNIEDA, Shoji NAKAMURA and Hiroyuki KOURA+

Nuclear Data and Reactor Engneering Division,
Nuclear Science and Engineering Center, Sector of Nuclear Science Research,
Japan Atomic Energy Agency
Tokai-mura, Naka-gun, Ibaraki-ken

(Received December 24 , 2015)

The 2014 Symposium on Nuclear Data was held at Conference Hall, Hokkaido University, on November 27 and 28, 2014. The symposium was organized by the Nuclear Data Division of the Atomic Energy Society of Japan, Hokkaido Branch of the Atomic Energy Society of Japan, and Nuclear Reaction Data Centre, Faculty of Science, Hokkaido University in cooperation with Nuclear Science and Engineering Center of Japan Atomic Energy Agency(JAEA). In the symposium, there were two tutorials, “Cross section measurement strategy for long lived fission product” and “Physics and Nuclear Data in Radiation Therapy” and four sessions, “A Neutron TOF Measurement Instrument desired by Nuclear Data Community”, “Recent Topics”, “Application of Nuclear Data”, and “Nuclear Theory and Nuclear Data”. In addition, recent research progress on experiments, evaluation, benchmark and application was presented in a poster session. Among 88 participants, all presentations and following discussions were very active and fruitful. This report consists of total 62 papers including 2 tutorials, 16 oral and 44 poster presentations.

Keywords: Nuclear Data Symposium 2014, JENDL-4.0, Experiments, Nuclear Theory, Nuclear Data Evaluation, Benchmark, Nuclear Data Applications

---

+Advanced Science Research Center
*Faculty of Science, Hokkaido University

Organizers: M. Aikawa (Hokkaido U., Chair), O. Iwamoto (JAEA, Vice-Chair), N. Yamano (Univ. of Fukui), T. Yoshii (TEPSYS), K. Nakajima (Kyoto U.), I. Murata (Osaka U.), J. Hori (Kyoto U.), T. Hazama (JAEA), S. Kunieda (JAEA), H. Koura (JAEA), S. Chiba (Tokyo Tech.), S. Nakamura (JAEA), K. Kino (Hokkaido U.), G. Chiba (Hokkaido U.)

JAEA-Conf 2015-003
INDC(JPN)-201

2014 年度核データ研究会プロシーディングス
2014 年 11 月 27 日～ 28 日、
北海道大学学術交流会館、北海道札幌市

日本原子力研究開発機構 原子力科学研究部門
原子力基礎工学研究センター
核工学・炉工学ディビション

（編）合川　正幸 *、岩本　修、江幡　修一郎 *、
國枝　賢、中村　詔司、小浦　寛之 +

（2015 年 12 月 24 日受理）

2014 年度核データ研究会は、2014 年 11 月 27 日～ 28 日に、北海道札幌市の北海道大学学術交流会館にて開催された。本研究会は、日本原子力学会核データ部会、日本原子力学会北海道支部、北海道大学大学院理学研究院原子核反応データベース研究開発センターが主催、日本原子力研究開発機構原子力基礎工学研究センターが共催した。今回、チュートリアルとして「長寿命核分裂生成物の核変換データとその戦略」、「がん放射線治療に必要な物理と核データ」の 2 件を、講演・議論のセッションとして「核データコミュニティーが望む中性子飛行時間法測定装置」、「最近のトピックス」、「核データの利用」、「核理論と核データ」の 4 件を企画・実施した。さらに、ポスターセッションでは、実験、評価、ベンチマーク、応用など、幅広い研究内容について発表が行われた。参加者総数は 88 名で、それぞれの口頭発表及びポスター発表では活発な質疑応答が行われた。本報告書は、本研究会におけるチュートリアル 2 件、口頭発表 16 件、ポスター 44 件の論文をまとめている。

+ 先端基礎研究センター
* 北海道大学大学院理学研究院

Contents

Papers presented at a Poster session

目 次

1 Program of 2014 Symposium on Nuclear Data

Date : November 27(Thu)13:00 – 28(Fri) 17:00, 2014
Venue : Hokkaido University Conference Hall (N8W5, Kita-ku, Sapporo 060-0808, Japan)
Host : Nuclear Data Division, Atomic Energy Society of Japan; Hokkaido Branch, Atomic Energy Society of Japan; Nuclear Research Data Centre, Faculty of Science, Hokkaido University
Co-host :Nuclear Science and Engineering Center of Japan Atomic Energy Agency

November 27 (Thu), at Room No.1

12:00 - 13:00 Registration

13:00 - 13:15 Opening Session

13:15 – 14:35
Session 1: A Neutron TOF Measurement Instrument desired by Nuclear Data Community
【Chair:M. Igashira (Tokyo Tech.)】

1.1 Nuclear Data Measurement s at ANNRI [15] A.Kimura(JAEA)
1.2 Neutron Energy Resolution at ANNRI [15] K. Kino (Hokkaido U.)
1.3 Development of NaI(Tl) Detectors at ANNRI [15] T. Katabuchi (Tokyo Tech.)
1.4 Activation Analysis at ANNRI [15] Y. Toh (JAEA)
1.5 Free Discussion [20]

14:35 – 15:00 Conference Photo and Coffee Break [25]

15:00 – 17:00 **Poster presentation** (Lobby)

17:10 – 19:00 Social Gathering (Room No.2)

November 28 (Fri), at Room No.1
9:00 – 10:20
Session 2: Recent Topics 【Chair: S. Chiba (Tokyo Tech.)】

2.1 Final Report of Advisory Subcommittee on Development of JENDL
- Guideline for Developing Next JENDL [30] G. Chiba (Hokkaido U.)
2.2 Toward the advancement of nuclear data in the resonance region [30] S. Kunieda (JAEA)
2.3 International Collaboration of Hokkaido University Nuclear Reaction Data Center [20]
M. Aikawa (Hokkaido U.)

10:20 – 10:35 Coffee Break [15]

10:35 – 11:55
Session 3: Application of Nuclear Data 【Chair: K. Suyama (JAEA)】

3.1 Development of multi-group neutron activation cross-section library for decommissioning of nuclear facilities [20] K. Okumura (JAEA)

3.2 Uncertainty quantification of core characteristics parameter based on covariance data of evaluated nuclear data library [20] T. Endo (Nagoya U.)
3.3 Design studies for a small accelerator-based Be(p,n) neutron source for boron neutron capture therapies [20] F. Hiraga (Hokkaido U.)
3.4 Elemental analysis by neutron resonance transmission method [20] H. Hasemi(Hokkaido U.)

11:55 – 13:00 Lunch [65]

13:00 – 14:00 【Chair: Y. Watanabe (Kyushu U.)】
Tutorial 1: Cross Section measurement strategy for long lived fission product in RIBF / In beam gamma spectroscopy in RIBF [60] He Wang (RIKEN)

14:00 – 14:15 Coffee Break [15]

14:15 – 15:15 【Chair: A. Makinaga (Kyushu U.)】
Tutorial 2: Physics and Nuclear Data in Radiation Therapy [60] C. Kurokawa (Juntendo U.)

15:15 – 15:30 Coffee Break [15]

15:30 – 16:45
Session 4:Nuclear Theory and Nuclear Data 【Chair: S. Ebata (JAEA)】
4.1 Clustering phenomena studied by Antisymmetrized Molecular Dynamics [25] M. Kimura (Hokkaido U.)
4.2 Fission process of low excited nuclei with Langevin approach [25] Y. Aritomo (Tokyo Tech.)
4.3 Present status of fission research based on TDDFT [25] Y. Iwata (U. Tokyo)

16:45 – 17:00 Closing Address
Poster Awards
Closing Address

Poster Presentation

Date : November 27 (Thu), 15:00 – 17:00

1. Photodisintegration Cross Section of the ^{9}Be(1/2+) state in the Complex Scaling Method
   K. Kato (Hokkaido U.)
2. Effect of stripping reaction on calculation of deuteron-induced activation cross sections
   S. Nakayama (Kyushu U.)
3. Cold neutron total cross-section and its application to materials science H. Sato (Hokkaido U.)
4. Search for neutron resonances of ^{106}Pd S. Nakamura (JAEA)
5. Evaluation of Gamma-ray Strength Function based on Measured Neutron Capture Gamma-ray Spectra N. Iwamoto (JAEA)
6. JENDL/HE-2007 benchmark test with iron shielding experiment at JAEA/TIARA
   C. Konno (JAEA)
7. Problems in FENDL-3.0 C. Konno (JAEA)
8. New Nuclear Data Group Constant Sets for Fusion Reactor Nuclear Analyses based on FENDL-2.1 C. Konno (JAEA)
9. Measurements of gamma-ray emission probabilities of minor actinides K. Terada (JAEA)
10. Compilation for Chart of the Nuclides 2014: a comprehensive decay data H. Koura (JAEA)
11. Sensitivity of Delayed Neutron to Fission Yields and Beta-Decay Half-Lives F. Minato (JAEA)
12. Measurements of gamma-ray production cross sections and yields from carbon induced by 500 MeV/u iron beam Y. Imahayashi (Kyushu U.)
13. Measurements of cross sections for production of light nuclides by 120 GeV and 400 MeV proton bombardment of Ni, Y, Tb, Au S. Okumura (Kyoto U.)
14. Supplemental Integral Experiment for Benchmarking Nuclear Data Libraries on Copper with D-T Neutron Source at JAEA/FNS S. Kwon (JAEA)
15. Integral Test of JENDL Dosimetry File 99 with a Graphite Experiment at JAEA/FNS
    M. Ohta (JAEA)
16. Integral Experiment on Molybdenum with DT Neutrons at JAEA/FNS M. Ohta (JAEA)
17. Nuclear data evaluation of the ^{7}Li(p,xn) reaction for incident energies from 7 to 200MeV
    Y. Matsumoto (Kyushu U.)
18. Investigation of Variable Neutron Field for Accurate Determination of Thermal Neutron Capture Cross Section at KURRI-LINAC T. Yagi (Kyoto U.)
19. Composite source system to measure a neutron and x-ray imaging at Hokkaido University
    K.Y. Hara (Hokkaido U.)
20. Neutron Intensity Monitor with Isomer Production Reaction for p-Li Neutrons
    Y. Ootani (Osaka U.)
21. Systematic study of fission modes by a dynamical model based on Langevin equation
    D. Hosoda (Tokyo Tech)
22. Simple phase-space-population control method for Monte-Carlo particle transport calculation
    S. Tamaki (Osaka U.)
23. Thick-target yields on radioactive targets estimated by inverse kinematics S. Imai (Hokkaido U.)
24. Measurement of Neutron-Capture Cross Section of ^{120}Sn with the array of Ge Spectrometer at J-PARC/MLF/ANNRI A. Kimura (JAEA)
25. ^{243}Am neutron-induced capture cross section measurement with a large coverage HPGe detector at ANNRI/J-PARC L.S. Leong (JAEA)
26. Evaluation of Delayed Neutron Data of the Photo-Fission T. Murata

27 Nuclear data for shielding design on International Linear Collider T. Sanami (KEK)

28. Verification of the Cd-ratio method in ^{241}Am using JENDL-4.0 K. Mizuyama (JAEA)
29. A Burnup Calculation for Creation of Palladium by Nuclear Transmutation
A. Terashima (Tokyo Tech)
30. Cross Talk Experiment of Array-type CdTe Detector for BNCT-SPECT M. Manabe (Osaka U.)
31. Measurement of double differential cross sections of light ion emission in interaction of 430 MeV/u carbon with carbon T. Kajimoto (Hiroshima U.)
32. The container picture with two-alpha correlation for the ground state of ^{12}C
B. Zhou (Hokkaido U.)
33. Prediction Calculation of Criticality at KUCA Solid Moderator Core for Integral Validation of MA nuclear data T. Sano (Kyoto U.)
34. A new EXFOR editor system: Java version of HENDEL A. Sarsembayeva (Hokkaido U.)
35. Calculation of the scattering cross section for ^{6}Li+n and ^{7}Li+n reactions
D. Ichinkhorloo (Hokkaido U.)
36. Nuclear Data Sensitivity Analysis for Isotopic Generation Using JEFF-3.1.1 and -3.2
Y. Kawamoto (Hokkaido U.)
37. Measurement of neutron yield by foils activation unfolding method for medical radioisotopes production using accelerator neutrons T. Kawagoe (Kyushu U.)
38. R&D of the heat measurement method for accurate determination of amount of minor actinides samples for accuracy improvement of neutron nuclear data T. Nakao (JAEA)
39. Evaluation of the photoabsorption cross section of three-nucleon systems R. Sekine (Hokkaido U.)
40. Validation of CBZ Code System for Decay Heat Analysis T. Kajihara (Hokkaido U.)
41. Evaluation of neutron nuclear data on krypton isotopes M.M. Rashid (Kyushu U.)
42. Dipole strength in ^{80}Se (γ,γ') below the neutron-separation energy A. Makinaga (Hokkaido U.)
43. Photo-activation experiment on ^{197}Au A. Makinaga (Hokkaido U.)
44. Development of Digitization Software GSYS for NRDF/EXFOR compilation
R. Suzuki (Hokkaido U.)

2 Current activities for nuclear data measurements at ANNRI

A.Kimura[1)], H.Harada[1)], S.Nakamura[1)], Y.Toh[1)], M.Igashira[2)], T.Katabuchi[2)],
M.Mizumoto[2)], J.Hori[3)], K.Kino[4)]

1) Japan Atomic Energy Agency
Nuclear Science and Engineering Center, Japan Atomic Energy Agency
2-4 Shirakata Shirane, Tokai, Naka, Ibaraki 319-1195, Japan
kimura.atsushi04@jaea.go.jp
2) Research Laboratory for Nuclear Reactors, Tokyo Institute of Technology
3) Research Reactor Institute, Kyoto University
4) Faculty of Engineering, Hokkaido University

In order to obtain accurate neutron-capture cross sections for minor actinides (MAs) and long-lived fission products (LLFPs), an experimental instrument named "Accurate Neutron-Nucleus Reaction measurement Instrument (ANNRI)" has been constructed in the Materials and Life science experimental Facility at the Japan Proton Accelerator Research Complex. Measurements of neutron-capture cross sections not only for MAs and LLFPs but also for stable isotopes have been started. In this paper, a brief view, measurement activities and results are presented.

1. Introduction

Accurate data of neutron-capture cross sections are important in detailed engineering designs and safety evaluations of innovative nuclear reactor systems.[1],[2] Especially, neutron-capture cross sections of minor actinides (MAs) and long-lived fission products (LLFPs) are strongly required for an evaluation and transmutation of radioactive waste and a design of various innovative reactor systems. However, accurate measurements of these cross sections are very difficult due to high radioactivity. To overcome this difficulty, the Accurate Neutron-Nucleus Reaction measurement Instrument (ANNRI) has been constructed by the collaboration of Hokkaido University, Tokyo Institute of Technology and JAEA. The. ANNRI is located on the Beam Line No. 04 of the materials and life science experimental facility (MLF) in the Japan Proton Accelerator Research Complex (J-PARC). Measurements of neutron-capture cross sections not only for MAs and LLFPs but also for stable isotopes have been started. In this paper, a brief view, measurement activities and an example of measured result are presented.

2. A brief view of ANNRI

2.1 ANNRI Beam Line

ANNRI is located on the Beam Line No. 04 of the MLF in the J-PARC. **Figure 1** shows the structure of ANNRI. The ANNRI uses neutrons from a coupled moderator (with a 140 mm diameter and 120 mm height) that provides the most intense neutron beam among the moderators at JSNS[3]. The neutron beam goes through collimators and a beam duct to reach the sample positions. The neutron beam goes through a T0 chopper, a neutron filter, a double disk chopper, and a rotary collimator and two experimental areas, and then is dumped into a beam stopper. Two detector systems are installed in the ANNRI. An array of large germanium (Ge) detectors is installed at the flight length of 21.5m. The other one is a NaI spectrometer located at a flight-length of 27.9 m. Using the array of germanium (Ge) detectors, prompt γ-ray spectra are obtained. And using the NaI spectrometer, a reliable analysis is possible by the established pulse-height weighting technique.[4]

Due to the safety regulations at the MLF, unsealed samples and nuclear fuel samples cannot be handled. Only sealed RI samples can be measured in the ANNRI.

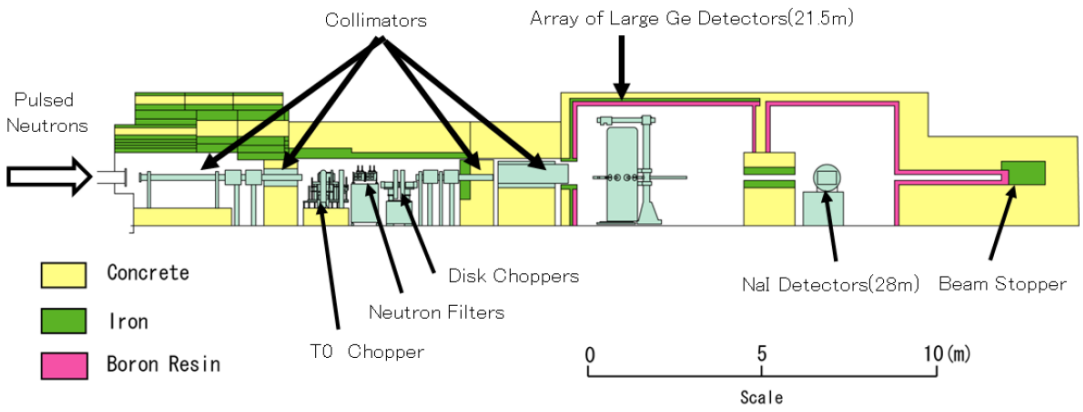

Fig. 1 A schematic view of ANNRI. There are two detector systems in ANNRI. The array of large germanium (Ge) detectors is the main detector of ANNRI and located at a flight-length of 21.5 m. A NaI spectrometer located at a flight-length of 27.9 m.

2.2 Characteristics of the neutron beam at ANNRI

The neutron intensity at the 21.5-m sample position of the ANNRI under a 17.5-kW operation is compared with those of DANCE at LANSCE and n TOF at CERN in **Fig.2**.[5] Current proton beam power generating spallation neutrons is 500 kW. The deduced present neutron intensity and the expected neutron intensity under the future 1-MW operation are also shown in Fig. 2. As seen from Fig. 2, the present and future neutron intensities of ANNRI are much higher than those of the other facilities by about one order of magnitude.

The energy resolution of the neutron beam at the 21.5-m sample position depends on the

moderator system and the proton-beam operation of MLF. The proton beam usually consists of two bunches with a distance of 600 ns. The width of each bunch increases up to 185 ns depending on an incident proton beam power to MLF. [3] The simulated resolution function at the moderator surface are shown in **Fig.3 (a)** and **(b)** [6]. Figs. 3 (a) and (b) are the results for the single- and double-bunch modes, respectively. As shown in Fig. 3, in the case of double-bunch modes, the resonances split into two peaks on the TOF spectra in the neutron energy range above 100 eV.

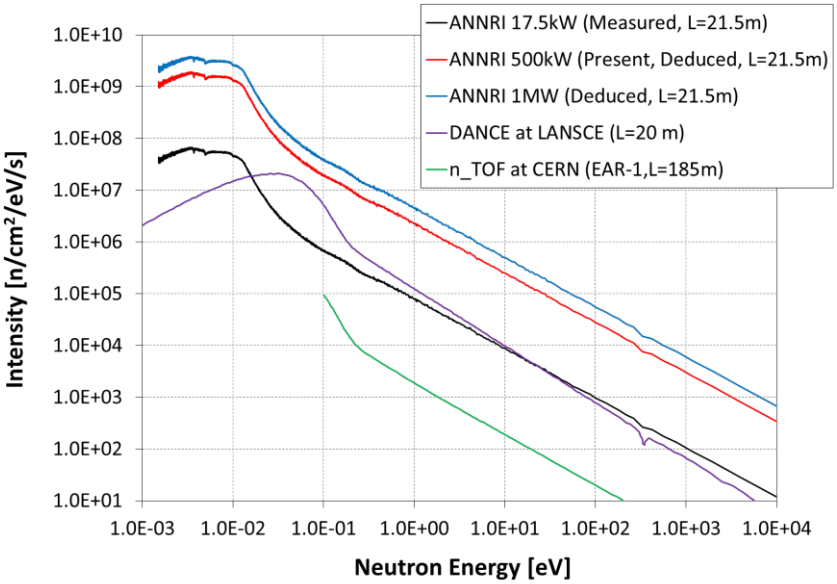

Fig. 2. Neutron intensities per second at the 21.5-m sample position of ANNRI under 17.5-kW operation comparison to those of DANCE at LANSCE, and n TOF at CERN [5]. The deduced present neutron intensity under 500-kW operation and the expected neutron intensity under the future 1-MW operation are also shown.

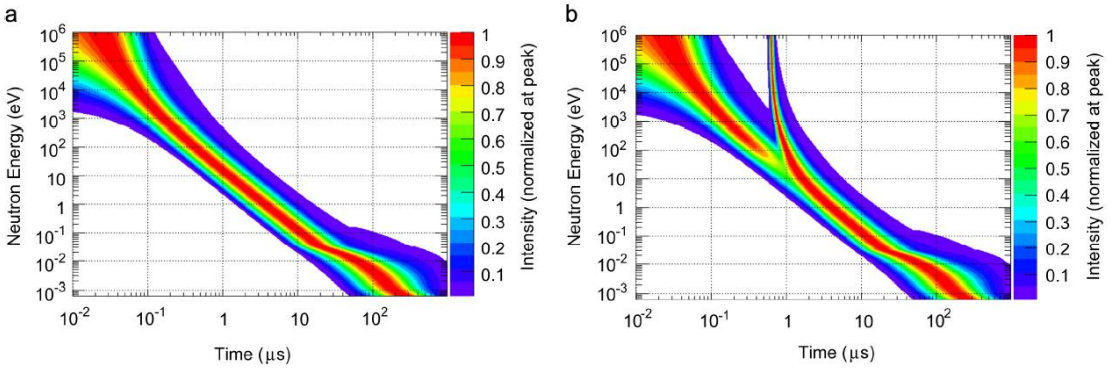

Fig.3 Two-dimensional plots of the time and energy of neutrons at the moderator surface [6]. The time structure are the results for "single-" and "double-bunch mode", respectively.

2.3 The array of large germanium (Ge) detectors

The array of Ge detectors is composed of two cluster-Ge detectors, eight coaxial-Ge detectors and anti-coincidence shields around each Ge detector as seen in **Fig.4**[7]. Each cluster Ge detector consists of seven Ge crystals. The positions of the cluster Ge detectors were arranged so that the distance between the front surface of each detector and the center of the sample position was 125 mm. ^{6}LiF tiles with 10 mm thickness and ^{6}LiH powder with a total thickness of 40 mm (sealed in aluminum cases) were also placed in front of each Ge detector. The peak efficiency of the spectrometer is 2.28 ± 0.11 % for 1.33 MeV γ rays[7]. Typical energy resolutions (FWHM) for 1.33-MeV γ-rays are 5.5 keV (beam-on) and 2.4 keV (beam-off).

A high count rate and high resolution DAQ, based on a digital data processing technique, was developed[8],[9]. In the data acquisition, γ-ray pulse heights, TOFs were recorded together with detector IDs by the DAQ (list mode).

The advantage of the Ge array is its excellent energy resolution, and γ rays from impurities in the objective sample can be discriminated by analyzing γ-ray spectra.

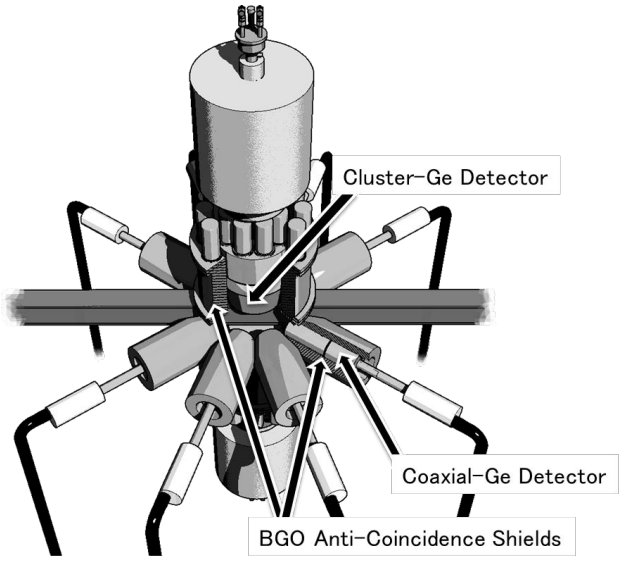

Fig.4 Layout of the array of Ge detectors. The array is composed of two cluster-Ge detectors, eight coaxial-Ge detectors and anti-coincidence shields around each Ge

2.4 NaI(Tl) spectrometer

The NaI(Tl) spectrometer is composed of two anti-Compton NaI(Tl) scintillators with neutron and γ-ray shields, as shown in **Fig. 5** [10]. The cylindrical NaI(Tl) scintillators are located at 90 degree and 125 degree with respect to the neutron-beam line, respectively. If necessary, the detector 125 degree is used in order to reduce the effects of angular distributions of capture rays from resonances with $l > 0$.

The measurement using the NaI(Tl) spectrometer has two objectives. One is to perform the

complementary measurement to that using the Ge array. By comparing the results from the two measurements for the same sample with each other, the validation of both measurements can be performed. The other is to extend the upper limit of neutron energy region in the measurement.

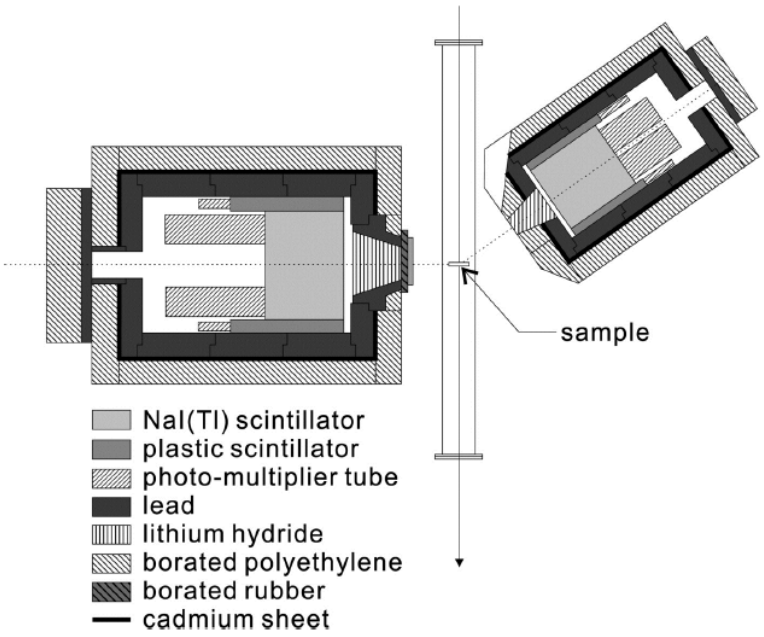

Fig.5. NaI(Tl) spectrometer installed at the flight length of 28-m. The spectrometer is composed of two anti-Compton NaI(Tl) detectors with neutron and gamma-ray shields.

3. Current activities and future plans for nuclear data measurements

Table. 1 Current status and future plans for neutron-capture cross-section measurements.

	Analysis was finished.	A part of results were reported.	Already Measured	Future Plan
MA	^{237}Np[11] ^{241}Am[12] $^{244, 246}$Cm[13]		^{243}Am	^{241,243}Am (New Sample)
LLFP		^{93}Zr ^{99}Tc ^{107}Pd	^{129}I	$^{135, 137}$Cs
Stable Isotopes		$^{74, 77}$Se, $^{90, 91}$Zr $^{112, 118}$Sn $^{105, 106, 108}$Pd	^{54}Fe, ^{61}Ni, ^{76,78}Se,^{127}I $^{117, 119, 120, 122}$Sn	$^{58, 60, 62}$Ni, ^{80}Se $^{115, 116}$Sn, ^{133}Cs $^{155, 157}$Gd

Current status and future plans for neutron-capture cross-section measurements are listed in Table 1. Currently, analyses for ^{244}Cm, ^{246}Cm, ^{241}Am, and ^{237}Np have been finished,

analyses for ^{129}I, ^{107}Pd, ^{99}Tc, ^{93}Zr and some stable isotopes are in progress.

4.Summary

Accurate Neutron-Nucleus Reaction measurement Instrument (ANNRI) has been constructed at the Beam Line No. 04 of the MLF in J-PARC. Measurements of neutron-capture cross sections not only for MAs and LLFPs but also for stable isotopes have been started. Not only nuclear data measurements but also nuclear astrophysics research and quantitative analysis are done in ANNRI.

References

[1]M. Salvatores, *et al.*, OECD/NEA Report NEA No. 6410, (2008).
[2]T. Sugawara, *et al.*, J. Nucl. Sci. Technol. **47**, (2010) 521.
[3]F. Maekawa, *et al.*, *Nucl. Instrum. Methods. Phys. Res. A*, **620** (2010), pp. 159 -165.
[4]S. Mizuno, *et al.*, *J. Nucl. Sci. Technol.*, **36** 493 (1999).
[5]K. Kino *et al.*, *Nucl. Instrum. Methods. Phys. Res. A* **626,** 58 (2011).
[6]K. Kino *et al.*, *Nucl. Instrum. Methods. Phys. Res. A* **736,** 66 (2014).
[7]T. Kin, *et al.*, *the 2009 NSS-MIC Conf. Rec.*, Orland USA, Oct. 25-31, 2009 (2009), pp. 1194 -1197.
[8]A. Kimura, *et al.*, *Int. Conf. on ND 2004*, Santa Fe, USA, Sept. 27 - Oct. 1 2004, *AIP Conference Proceedings*, 769 (2005), pp. 792-795.
[9]A. Kimura, *et al.*, *NSS-MIC 2008*, Dresden, Germany, Oct.19-25 2008 (2009), pp. 2107-2111
[10]M. Igashira, *et al.*, *Nuclear Data Sheets.*, **118**, (2014) 72.
[11]K. Hirose, *et al.*, *J. Nucl. Sci. Technol.*, **50**, (2013) 188.
[12]H. Harada, *et al.*, *Nuclear Data Sheets.*, **119**, (2014) 61.
[13]A. Kimura, *et al.*, *J. Nucl. Sci. Technol.*, **49**, (2012) 708.

3 Neutron Energy Resolution at ANNRI

Koichi KINO[a], Michihiro FURUSAKA[a], Fujio HIRAGA[a], Takashi KAMIYAMA[a],
Yoshiaki KIYANAGI[a,b], Atsushi KIMURA[c], Hideo HARADA[c],
Shyoji NAKAMURA[c], Yosuke TOH[c], Masayuki IGASHIRA[d], Tatsuya KATABUCHI[d],
Motoharu MIZUMOTO[d], Jun-ichi HORI[e]
[a]Faculty of Engineering, Hokkaido University
Kita-13, Nishi-8, Kita-ku, Sapporo 060-8628, Japan
[b]Graduate school of Engineering, Nagoya University
Furo-cho, Chikusa-ku, Nagoya 464-8603, Japan
[c]Japan Atomic Energy Agency
2-4 Shirakata Shirane, Tokai, Ibaraki 319-1195, Japan
[d]Research Laboratory for Nuclear Reactors, Tokyo Institute of Technology
O-okayama, Meguro-ku, Tokyo 152-8550, Japan
[e]Research Reactor Institute, Kyoto University
2-1010, Asashiro Nishi, Kumatori, Osaka 590-0494, Japan
e-mail: k-kino@eng.hokudai.ac.jp

To understand the neutron energy resolution is important for precise analysis of the nuclear resonances at the pulsed neutron-beam induced experiments. The neutron energy resolution is analyzed by simulation calculation and experiments for the Accurate Neutron-Nucleus Reaction measurement Instrument (ANNRI) at the Japan proton accelerator research complex. The simulation calculation provides the time and energy resolutions in the neutron energy range from the thermal energy to 1 MeV. It shows that the neutron pulse splits at the energy above about 10 eV for the double-bunch mode. However, the energy resolution is less than about 1% below 100 eV. The experiments are performed at the thermal and epithermal energies. Both experimental results show agreements of the neutron pulse shape with the simulation prediction. These agreements indicate the proper behavior of the neutron source and ANNRI, and reliability of the simulation calculation.

1. Introduction

One of ANNRI's missions is the measurement of the neutron capture cross sections especially to obtain the resonance parameters. The resonance shape on the neutron energy spectrum is distorted by the finite energy resolution of the pulsed neutron beam at ANNRI. Therefore, the energy resolution has to be

understood for precise analysis of the resonances. The neutron energy is calculated by the time of flight at ANNRI. Therefore, the neutron energy resolution is related to the time resolution. The origins of the time resolution are mainly the time structure of the incident proton beam to the mercury target of the Japan Spallation Neutron Source (JSNS) and the time uncertainty due to the neutron slowing-down process in the liquid hydrogen moderator of the JSNS.

To understand the neutron pulse, we used the simulation calculation and experiments. They have both advantage and disadvantage. The simulation calculation can predict the pulse at arbitrary neutron energy. However, the simulation result depends on the actual system of the JSNS and ANNRI. On the other hand, the experimental result is reliable, although only the discrete energies are available. Therefore, these methods are the complementary relation.

2. Analyses and Discussions

2.1 Simulation

The simulation calculation was performed using the JSNS model and the Monte-Carlo code PHITS[1]. The proton beam of 3 GeV without the time structure was induced to the mercury target of the JSNS. A tally of 10×10 cm^2 was set at the moderator surface and the neutrons traveling to the ANNRI beamline were recorded. The detail is described in the reference[2]. The pulses at many energy values were fitted by the model function proposed by Ikeda and Carpenter [3],

$$\psi(v,t)=\int dt'\phi(v,t')\left[(1-R)\delta(t-t')+R\beta\theta(t-t')\exp(-\beta(t-t'))\right]$$

$$=\frac{\alpha}{2}\left\{(1-R)(\alpha t)^2e^{-\alpha t}+2R\frac{\alpha^2\beta}{(\alpha-\beta)^3}\left[e^{-\beta t}-e^{-\alpha t}(1+(\alpha-\beta)t+\frac{1}{2}(\alpha-\beta)^2t^2)\right]\right\}. \quad (t>0) \quad (1)$$

Here, $\phi(v,t')$ describes the neutron flux for the slowing-down process in an infinite hydrogenous medium. The velocity of neutrons is v. The important fitting parameters are α, β, and R. Eq. (1) consists of two physical terms. One is the slowing-down term and the other is the storage term. These are $1-R$ and R in the ratio ($0\le R\le1$) of the total intensity, respectively. The decay constants of the former and latter are α and β, respectively. The pulse shape was obtained as a function of the neutron energy using these parameters.

Figure 1 shows the obtained neutron pulse at the neutron energy range from the thermal energy to 1 MeV. The pulse width becomes broader as the neutron energy decreases because the number of

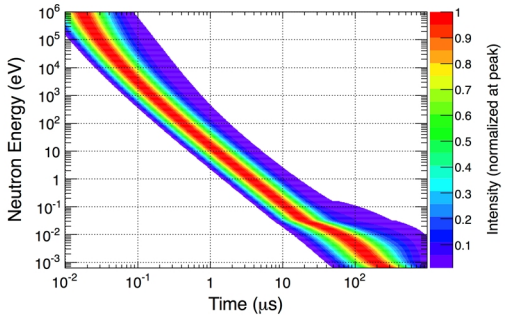

Fig. 1. Two-dimensional plot of the time and energy of neutrons at the moderator surface. The time structure of the proton beam is not convoluted. The intensity is normalized at the pulse peak. This plot is drawn at 1/100th of the intensity of the peak. [2]

collisions between neutron and hydrogen increases in the moderator. The JSNS is typically operated at the double-bunch mode where the proton beam consists of the two bunches with the time distance of 599 ns. At the experiment of this paper, the width (FWHM) of each bunch was 60 ns.

The time structure of the proton beam was convoluted to the neutron pulse shown in Fig. 1. The obtained relations of the time and energy for the single- and double-bunch modes are shown in Fig. 2. The time distribution is almost the same as that of Fig. 1 in the thermal neutron energy. However, the time widths are wider than that of Fig. 1 as the energy increases due to the finite time width of the proton beam. Furthermore, the pulse splits above about 10 eV for the double-bunch mode.

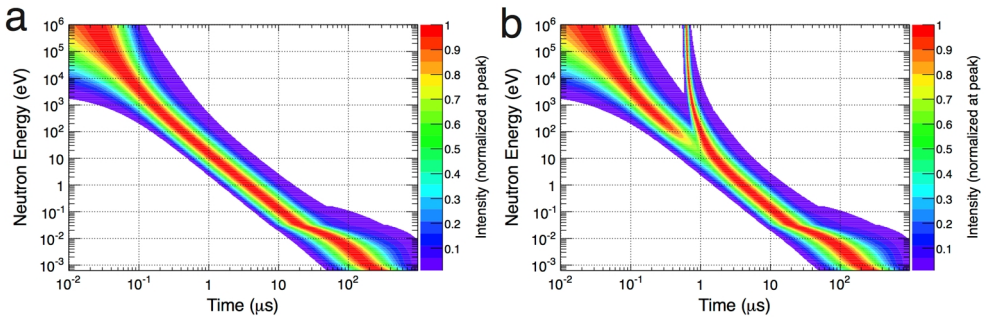

Fig. 2. Two-dimensional plots of the time and energy of neutrons at the moderator surface. The time structure of the proton beam is taken into account. Figures a and b are the results for the single- and double-bunch modes, respectively.[2]

Figure 3 shows the FWHM values for the time structure as a function of the neutron energy. They are the same for both the single- and double-bunch modes in the thermal neutron energy since the slowing down process is dominant compared to the proton time structure. As the energy increases, the FWHM values reaches to the proton time structures. The neutron energy resolution based on the result in Fig. 3 is shown in Fig. 4. It is less than about 1% below about 100 eV for the both bunch-modes. However, the energy resolution deteriorates drastically for the double-bunch mode above about 100 eV.

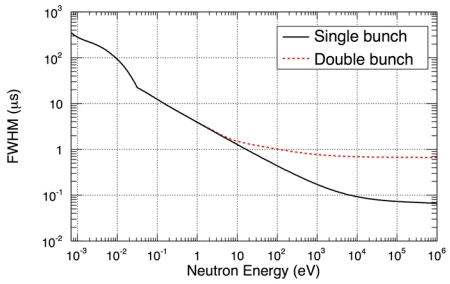

Fig. 3. The FWHM values for the time structure by the simulation as a function of neutron energy. The solid and dashed lines represent the single- and double-bunch modes, respectively.[2]

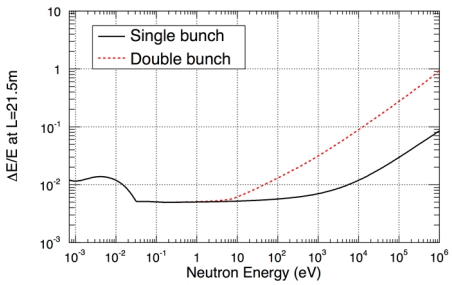

Fig. 4. Neutron energy resolution at 21.5 m from the moderator based on the simulation. The solid and dashed lines represent the single- and double-bunch modes, respectively.[2]

2.2 Experiment

We obtained neutron pulses experimentally at the thermal and epithermal neutron energies. At the thermal energy, a mica sample was set in the beamline of ANNRI at a distance of 28.8 m from the neutron

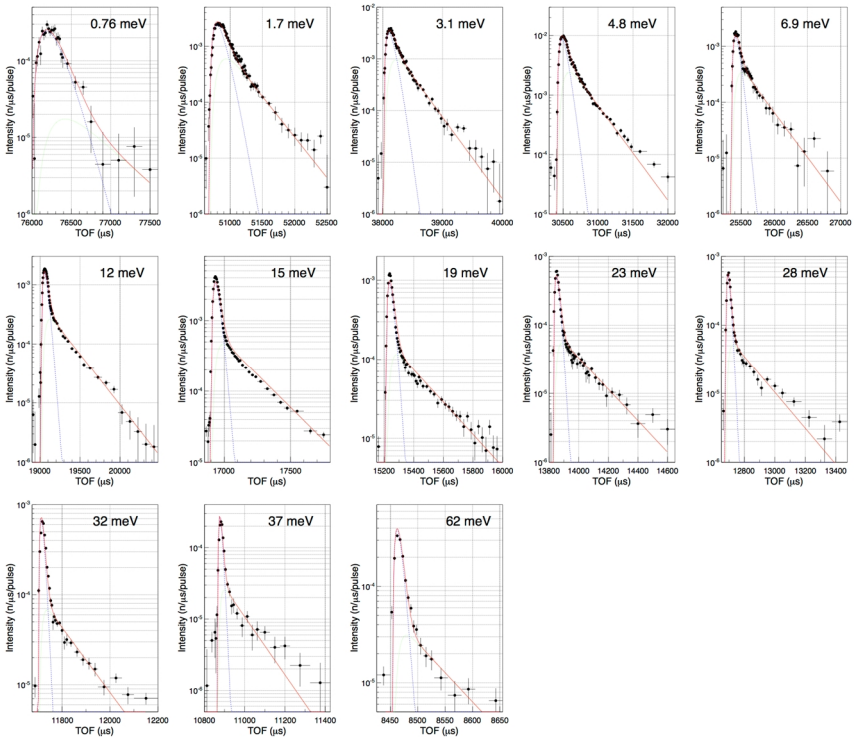

Fig. 5. Comparison of measured diffractions (data points) with the time structures obtained by the simulation (solid lines). The value indicated in each figure corresponds to the neutron energy of the diffraction. The dashed and dotted lines are the slowing-down and storage terms in Eq. (1), respectively.[2]

source. A He-3 neutron detector was set at an angle of 162 degree with respect to the downstream of the beamline and observed diffraction neutrons by the mica sample. Figure 5 shows the diffraction peaks and red curves are the simulation predictions. The measurement and simulation are in agreement very well. Measured diffraction peaks were fitted by Eq. (1) and parameters were obtained as shown in Fig. 6. All the parameters are in agreement with the simulation predictions as expected from Fig. 5.

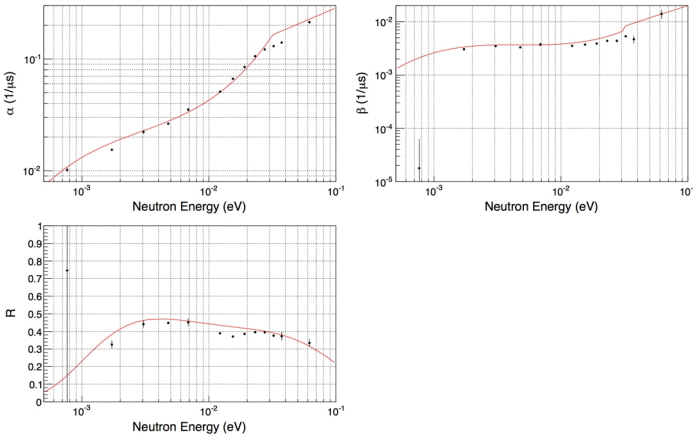

Fig. 6. Comparison of parameters α, β, and R in the thermal neutron region. The lines and data points are the simulation and measurement data, respectively.[2]

At the epithermal energy, we utilized the neutron capture resonances for Ta-181 nuclei. A tantalum foil was set in the beamline of ANNRI at 29.54 m from the neutron source. The prompt gamma rays following the neutron capture reaction were detected by a plastic scintillation detector and the time of flight of

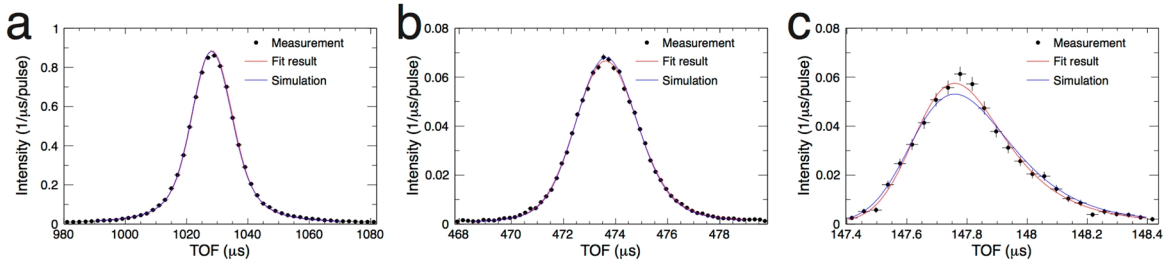

Fig. 7. Examples of fits of the measured TOF spectra in the epithermal neutron energy region. Figures a, b, and c show the resonances with energies of 4.28, 20.29, and 208.48 eV, respectively. Resonance curves are also evident, which are calculated using the parameters obtained by the simulation.[2]

neutrons was recorded. The operation mode of JSNS at the experiment was the single bunch. Figure 7 shows examples of analyzed resonances. The 17 resonances were fitted by the function, which was obtained by the convolution of the intrinsic resonance shape expressed by the single-level Breit−Wigner, the neutron pulse expressed by Eq. (1), the time structure of the proton beam, and the Doppler effect of Ta-181 nuclei. Figure 8 shows the comparison of fit parameters in Eq. (1) between the measurement and simulation. The absolute value and dependence on the neutron energy are in agreement.

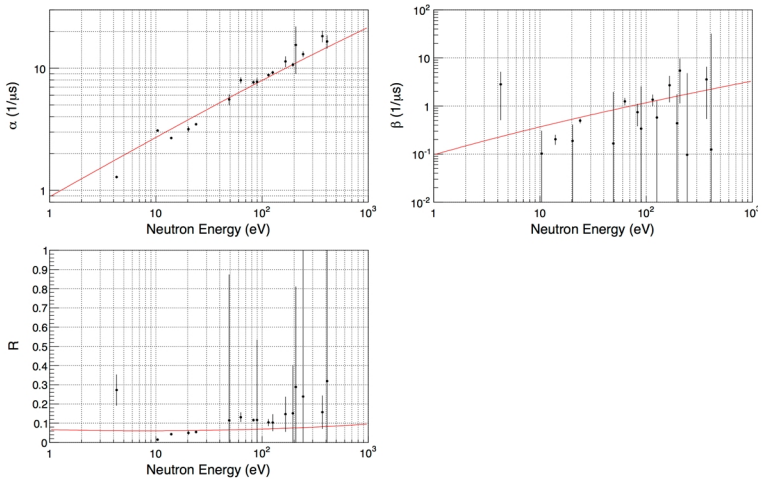

Fig. 8. Comparison of parameters α, β, and R in the epithermal neutron region. The lines and data points are the simulation and measurement data, respectively. [2]

2.3 Neutron time and energy resolution

Figure 9 shows the FWHM of the neutron pulse between the simulation and measurements. Both are in agreement in the wide energy range. Furthermore, Figures 6 and 8 show that the pulse shapes including two components in Eq. (1) are in agreement between the simulation and measurements. These results imply that the JSNS and ANNRI work properly and the simulation calculation is reliable.

3. Conclusions

We performed the simulation and measurements of neutron pulses of the pulsed neutron beam at ANNRI. They showed good agreement in the width and parameters of the model function, which implies the reliability of the simulation calculation. For the more precise understanding of the neutron pulse, which can be applied to the quantitative nuclear-data analysis, the analysis of the neutron capture reaction data for Au is on going using the REFIT (Multilevel Resonance Parameter Least Square Fit of Neutron Transmission, Capture, Fission & Self Indication Data) code[4,5].

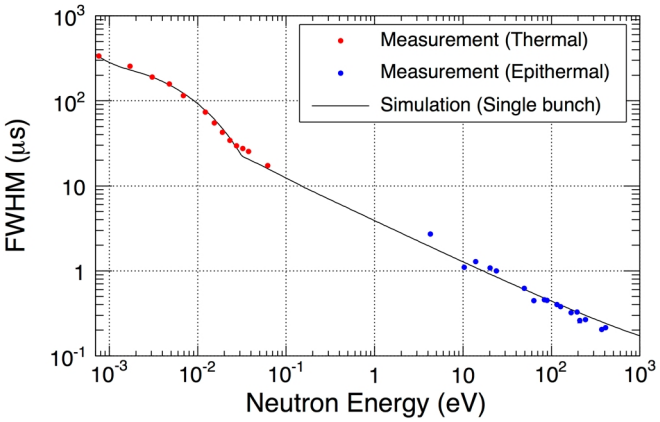

Fig. 9. Comparison between the simulation and measurements of the FWHM values of the time structures of neutron pulses for single-pulse mode.[2]

Acknowledgements

The present study is the result of "Study on nuclear data by using a high intensity pulsed neutron source for advanced nuclear system" entrusted to Hokkaido University by the Ministry of Education, Culture, Sports, Science, and Technology of Japan (MEXT). This work was supported by JSPS KAKENHI Grant no. 22226016.

References

[1] K. Niita, N. Matsuda, Y. Iwamoto, H. Iwase, T. Sato, H. Nakashima, Y. Sakamoto and L. Sihver: PHITS: "Particle and Heavy Ion Transport code System", Version 2.23, JAEA-Data/Code 2010-022 (2010)189.

[2] K. Kino *et al.*: Nucl. Instr. and Meth. Phys. Res. A**736** (2014) 66.

[3] S. Ikeda and J. M. Carpenter: Nucl. Instr. and Meth. A **239**, (1985) 536.

[4] M.C. Moxon, J.B. Brisland: "GEEL REFIT, A least squares fitting program for resonance analysis of neutron transmission and capture data computer code", AEA-InTec-0630, AEA Technology, October (2008).

[5] P. Schillebeeckx, B. Becker, Y. Danon, K. Guber, H. Harada, J. Heyse, A.R. Junghans, S. Kopecky, C. Massimi, M.C. Moxon, N. Otuka, I. Sirakov and K. Volev: Nuclear Data Sheets **113**, (2012) 3054.

4 Development of NaI(Tl) Detectors at ANNRI

Tatsuya KATABUCHI[1)]*, Hideo HARADA[2)], Jun-ich HORI[3)], Masayuki IGASHIRA[1)], Atsushi KIMURA[2)], Motoharu MIZUMOTO[1)], Shoji NAKAMURA[2)], Taro NAKAO[2)], Kazushi TERADA[2)]

1) Research Laboratory for Nuclear Reactors, Tokyo Institute of Technology,
2-12-1 Ookayama, Meguro-ku, Tokyo 152-8550, Japan
2) Japan Atomic Energy Agency
2-4 Shirakata Shirane, Tokai, Ibaraki 319-1195, Japan
3) Research Reactor Institute, Kyoto University
2-1010, Asashiro Nishi, Kumatori-cho, Sennan-gun, Osaka 590-0494, Japan
*e-mail: buchi@nr.titech.ac.jp

NaI(Tl) detectors have been used for neutron capture cross section measurement at the Japan Proton Accelerator Research Complex. Recent progress and ongoing development of the NaI(Tl) detectors are overviewed.

1. Introduction

Neutron capture cross section measurements have been conducted with the Accurate Neutron Nucleus Reaction Measurement Instrument (ANNRI) [1-4] at the Materials and Life Science Facility of the Japan Proton Accelerator Research Complex (J-PARC). Accurate neutron capture cross section data are required in many fields such as nuclear engineering, astrophysics and fundamental nuclear physics. A spallation neutron source of J-PARC produces intense pulsed neutron beams [5], which allow us to perform new experiments, improving neutron nuclear data or completely new measurements for radioactive samples that could not be measured before [6-7]. ANNRI was designed for neutron nuclear data measurements. Two different types of γ-ray detectors have been installed in ANNRI. One is a large Ge detector array [8-9], which allows for high energy resolution γ-ray spectroscopy in the neutron capture reaction. The other is NaI(Tl) scintillation detectors, which have faster detector response than a Ge semiconductor detector. The two detector system complement each other. Neutron capture cross section measurement using Ge detectors in a spallation neutron facility is new challenge. The Ge detector array gives us detailed information on a

γ-ray spectrum in decay from a neutron capture state. On the other hand, an NaI(Tl) detector has a poorer γ-ray energy resolution but a pulse height weighting technique with an NaI(Tl) detector is well-established for neutron capture cross section measurement. Comparing experimental results independently made with the two detector systems, reliable cross section data can be provided. Moreover, faster detector response of the NaI(Tl) detectors facilitates measurements in the high energy region where the Ge detector array cannot work well due to its slow response. This short report gives the recent progress and ongoing development of the NaI(Tl) detectors.

2. ANNRI NaI(Tl) detectors

The NaI(Tl) detectors are located at a flight path length of 27.9 m from the spallation neutron source. The detector setup is illustrated in Fig. 1. The two differently sized detectors were placed at angles of 90° and 125° with respect to the neutron beam axis. The NaI(Tl) crystal size of the 90° detector is 330 mm diameter x 203 mm long. The 125° detector crystal is 203 mm diameter x 203 mm long. The 90° detector was designed to provide a large detection efficiency because of closer geometry to the sample position with a larger detector volume than the 125° detector. The 125° detector is for measurement at the special angle of 125°, where the angular dependent term of the dominant *E1* and *M1* γ-ray transitions vanishes. Both the 90° and 125° detectors are inserted into annular plastic scintillation detectors to suppress cosmic-ray background by anti-coincidence detection. Shielding of the detectors were made with several shielding materials: lead, cadmium, borated polyethylene, borated rubber and isotopically enriched Lithium-6 hydride.

Several upgrades of the neutron beam collimation system and additional shielding to reduce background neutrons and γ-rays have been done. Figure 2 shows comparison of pulse-height spectra of blank runs made at three different times from June of 2009 to April of 2013. Major upgrades of the neutron collimator and shielding have been made between the times. The pulse-height spectra are normalized to the proton beam power and the number of proton pulses for comparison. The observed events were caused by background neutrons and γ-rays. As seen in Fig. 2, the background events were successfully reduced by two order of magnitudes.

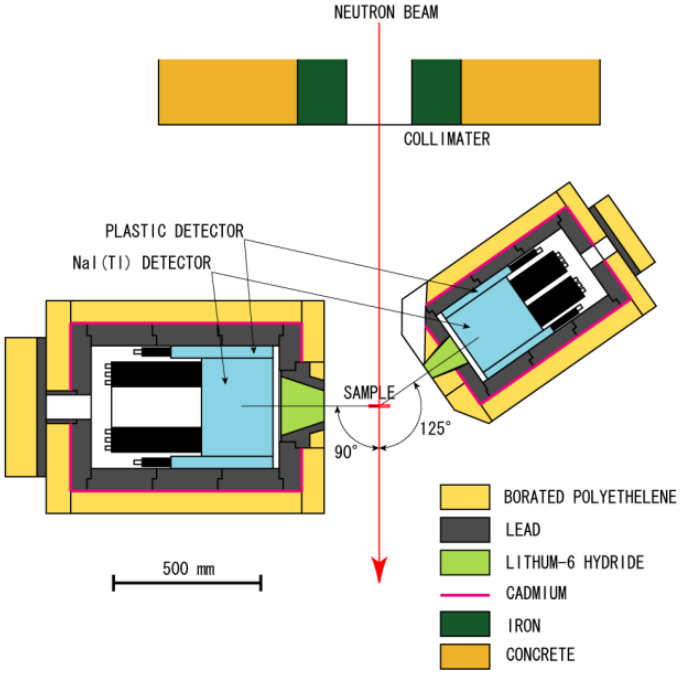

Fig. 1. NaI(Tl) detectors of ANNRI.

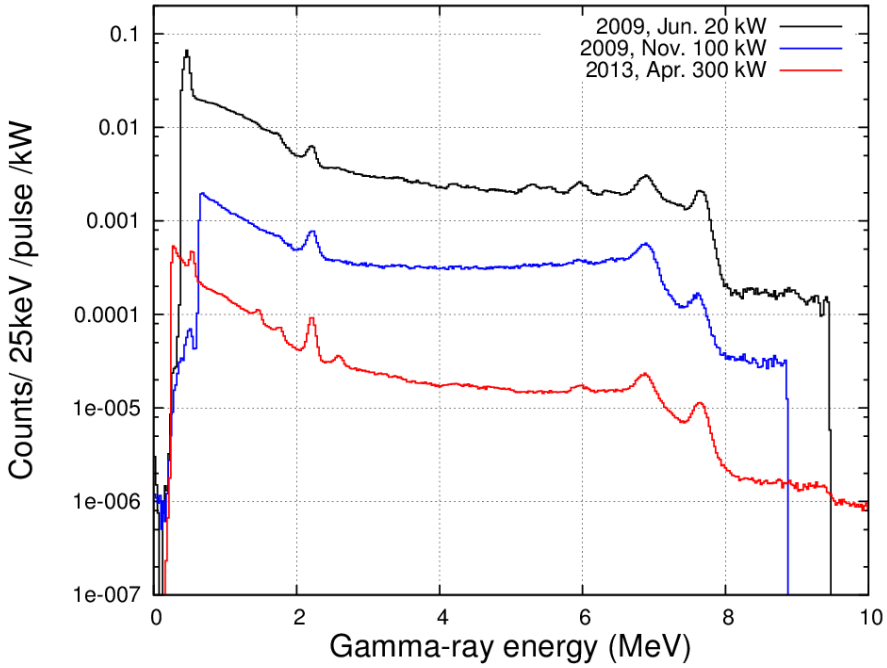

Fig. 2. Pulse-height spectra of blank runs measured at different times. The spectra are normalized to the proton beam power and the number of the incident proton pulses.

Another technological development was achieved for signal processing and data acquisition. The gamma flash emitted at the beginning of time-of-flight cycle saturates traditional pulse height analysis system consisting of analog amplifiers and peak-hold

analog-to-digital convertor. Our previous experiments showed that the baseline of the output signal of the analog modules were distorted for more than 10 μs, sometimes reaching 300 μs. Pulse height analysis cannot be made correctly during the baseline distortion. The traditional system could not be used in the high energy region above 30 keV. To avoid the problem, we have developed a new signal processing method based on pulse-width analysis [10]. In this method, instead of measuring the pulse height, the pulse width of the anode output signal from the NaI(Tl) detector is measured with a high-speed time digitizer, FAST Com Tec MCS6. Analog modules were completely removed. This makes the system more robust to the gamma flash. We tested the method using γ-rays from standard γ-ray sources and neutron-induced reactions. Pulse-height spectra were successfully reconstructed from pulse-width spectra using an experimentally determined conversion curve.

Neutron capture cross section measurements for many samples using the NaI(Tl) detectors have been done or are ongoing. Some of the results were already published. For example, the capture cross section of ^{237}Np, one of the important minor actinides for nuclear transmutation, was measured [11]. A long-lived fission product ^{107}Pd was also measured from 10 meV to 100 keV [12].

3. Ongoing development

A technological challenge is still ongoing for the ANNRI NaI(Tl) detectors. In a project "*Research and Development for accuracy improvement of neutron nuclear data on minor actinides*", we are trying to extend the high energy limit of the NaI(Tl) detector system. The current high energy limit is around 100 keV. We are upgrading the system to reach 300 keV. First, the time-digitizer MCS6 for pulse-width analysis was replaced with a higher upgraded version FAST Com Tec MPA4T. Second, additional shielding for scattered neutrons from a sample was designed and will be installed in early 2015. Actual cross section measurement is planned to start in 2015.

4. Summary

In this report, recent progress and ongoing development of the ANNRI NaI(Tl) detectors were overviewed. The neutron collimation system and the radiation shielding have been upgraded, thereby considerably reducing background events. A new signal processing method based on pulse width analysis was developed to overcome the challenges caused by the gamma flash. In an ongoing project, further development is underway to extend the high energy limit of measurement.

Acknowledgements

This work was supported by JSPS KAKENHI Grant number 22226016. Present study includes the result of "Research and Development for accuracy improvement of neutron nuclear data on minor actinides" entrusted to the Japan Atomic Energy Agency by the Ministry of Education, Culture, Sports, Science and Technology of Japan (MEXT).

References

[1] M. Igashira *et al*., Nuclear Data Study at J-PARC BL04, Nuclear Instruments and Methods in Physics Research A 600, 332-334 (2009).

[2] Y. Kiyanagi *et al*., The 'Study on Nuclear Data by Using a High Intensity Pulsed Neutron Source for Advanced Nuclear System' Nuclear Data Project and the Characteristics of the Neutron Beam Line for the Capture Cross Section Experiments at J-PARC, Journal of Korean Physical Society, 59, 1781-1784 (2011).

[3] K. Kino *et al.*, Measurement of Energy Spectra and Spatial Distributions of Neutron Beams Provided by the ANNRI Beamline for Capture Cross-Section Measurements at the J-PARC/MLF, Nuclear Instruments and Methods in Physics Research A 626-627, 58-66 (2011).

[4] K. Kino *et al.*, Energy resolution of pulsed neutron beam provided by the ANNRI beamline at the J-PARC/MLF, Nuclear Instruments and Methods in Physics Research A 736, 66-74 (2014).

[5] F. Maekawa *et al*., First Neutron Production Utilizing J-PARC Pulsed Spallation Neutron Source JSNS and Neutron Performance Demonstrated, Nuclear Instruments and Methods in Physics Research A 620, 159-165 (2010).

[6] S. Goko *et al*., Measurement of Neutron Capture Cross Section Ratios of ^{244}Cm Resonances Using NNRI, Journal of Nuclear Science and Technology 47, 1097-1100 (2010).

[7] A. Kimura *et al*., Neutron-Capture Cross-Sections of ^{244}Cm and ^{246}Cm Measured with an Array of Large Germanium Detectors in the ANNRI at J-PARC/MLF, Journal of Nuclear Science and Technology 49, 708-724 (2012).

[8] H. Harada *et al*., Study of Neutron Capture Reactions Using the 4π Ge Spectrometer, Journal of the Korean Physical Society, 59, 1547-1552 (2011).

[9] T. Kin *et al*., The "4π Ge Spectrometer" for Measurements of Neutron Capture Cross Section by the TOF Method at the J-PARC/MLF/ANNRI, Journal of the Korean Physical Society, 59, 1769-1772 (2011).

[10] T. Katabuchi *et al.*, Nuclear Instruments and Methods in Physics Research Section A, 764, 369-377 (2014).

[11] K. Hirose *et al*., Cross-Section Measurement of ^{237}Np(n,γ) from 10 meV to 1 keV at

Japan Proton Accelerator Research Complex, Journal of Nuclear Science and Technology 50, 188-200 (2013).

[12] K. Terada *et al.*; Progress in Nuclear Energy, **82**, 118-121(2015).

5 Activation Analysis at ANNRI

Yosuke Toh[*1], Mitsuru Ebihara[2], Atsushi Kimura[1], Shoji Nakamura[1], Hideo Harada[1], Minghui Huang[1]

[1] Nuclear Science and Engineering Center, Japan Atomic Energy Agency
Shirakata-Shirane 2-4, Tokai-mura, Naka-gun, Ibaraki-ken 319-1195 Japan

[2] Graduate School of Science and Engineering, Tokyo Metropolitan University
Minami-Osawa 1-1, Hachioji-shi, Tokyo, 192-0397 Japan

[*] E-mail: toh.yosuke@jaea.go.jp

The Accurate Neutron-Nucleus Reaction Measurement Instrument (ANNRI) has been proposed and designed for activation analysis (PGA), nuclear data measurements, and nuclear astrophysics. We have developed new non-destructive elemental analysis (TOF-PGA) which combines PGA with time-of-flight technique at ANNRI. It allows us to obtain the results from both methods at the same time. Moreover, significant synergy has been achieved. Specifically, it will be used to quantify elemental concentrations in the sample that neither of these methods can be applied.

1. Introduction

Prompt gamma-ray analysis (PGA) is well known as a rapid and non-destructive analytical method which is used for trace and major multi-elemental analysis in many fields, especially geochemistry, cosmochemistry, environmental science and industrial applications [1-3]. PGA has an advantage of being able to detect light elements, such as hydrogen and boron as well as heavy elements. The time-of-flight (TOF) technique is a general method for determining the kinetic energy of a traveling neutron, by measuring the arriving time from a pulsed neutron source to a sample position. Neutron capture cross sections for most of nuclides are strongly dependent on the neutron energy, and have sharp resonance peaks at neutron energies where the sum of a neutron kinetic energy and neutron separation energy is equal to the one of levels in the compound nucleus. Neutron resonance capture analysis is an analytical method which uses the energy of the resonance and the resonance peak area (counts) to identify and quantify, respectively, with TOF technique [4,5]. The Accurate Neutron-Nucleus Reaction Measurement Instrument (ANNRI) has been designed and developed for activation analysis (PGA), nuclear data measurements, and nuclear astrophysics (Fig. 1) [6]. For improvements of the accuracy, selectivity and sensitivity, we have developed an analytical technique

which combines PGA with TOF technique (TOF-PGA) at ANNRI [7]. In this work, we will give an

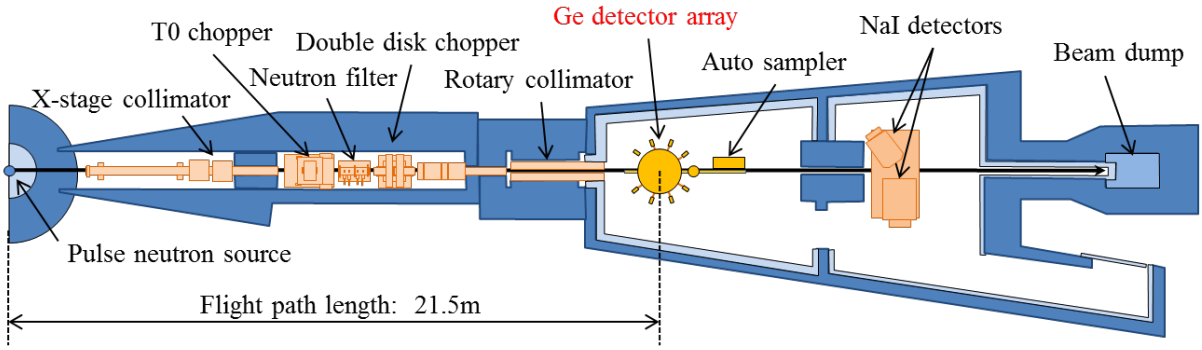

Fig. 1 The accurate neutron-nucleus reaction measurement instrument (ANNRI).

overview of some recent progress of TOF-PGA, and discuss similarities and differences between nuclear data and activation analysis measurements at ANNRI.

2. Prompt gamma-ray analysis and nuclear data measurements at ANNRI

ANNRI is located at the beamline No. 04 at J-PARC MLF. MLF is high intensive pulsed neutron facility, which operates at approximately 300 kW proton beam power, and the proton beam will be increased up to 1 MW in the near future. The Ge detectors, which are combination of two cluster-Ge and eight coaxial-Ge detectors, and BGO anti-Compton shields surrounding these Ge detectors, are installed at the flight path length of 21.5 m in ANNRI (Fig.1). Each cluster-Ge detector consists of seven individually encapsulated Ge detectors. The absolute photopeak efficiency of the Ge array for 1.3 MeV gamma rays is approximately 3.6 %. Two cluster-Ge detectors with BGO shields were used in the present experiment.

Prompt gamma-rays produced in a neutron capture reaction are detected by gamma-ray detectors in both PGA and nuclear data measurements. The number of prompt gamma-rays is directly proportional to a neutron capture cross section and a weight of sample. In PGA, the weight of sample is treated as unknown parameters. On the other hand, the neutron capture cross section is determined in the nuclear data measurement. Therefore, these are technically regarded as same measurements. In contrast, there is an important difference between PGA and nuclear data measurements. Namely, in the nuclear data measurements, the sample highly enriched in the desired isotope or at least with as low impurity contents as possible is used. In contrast, the sample in PGA is often a complex mixture. Therefore, spectrum analysis for the nuclear data measurements is generally simpler than the analysis for the PGA measurements where the sample contains many elements. In this sense, the intrinsic merit of the measurement by ANNRI is to be first recognized in elemental analysis.

3. New method for multi-elemental analysis at J-PARC MLF ANNRI

The energy of the neutron capture resonance has no relation to the energies of prompt gamma rays

emitted in the neutron capture reaction. Therefore PGA and TOF methods have different sensitivity for individual elements. For improvements of the accuracy, selectivity and sensitivity, we have developed a novel technique which combines prompt gamma-ray analysis with time-of-flight technique (TOF-PGA) and gamma-ray coincidence technique (TOF-MPGA) by using an intense pulsed neutron beam at J-PARC MLF ANNRI [7] (Fig. 2). The combined method allows us to obtain results from both PGA and TOF methods at the same time. Moreover, there is a possibility that TOF-PGA and TOF-MPGA methods may be used to determine element concentrations in the sample that neither PGA nor TOF methods can be applied.

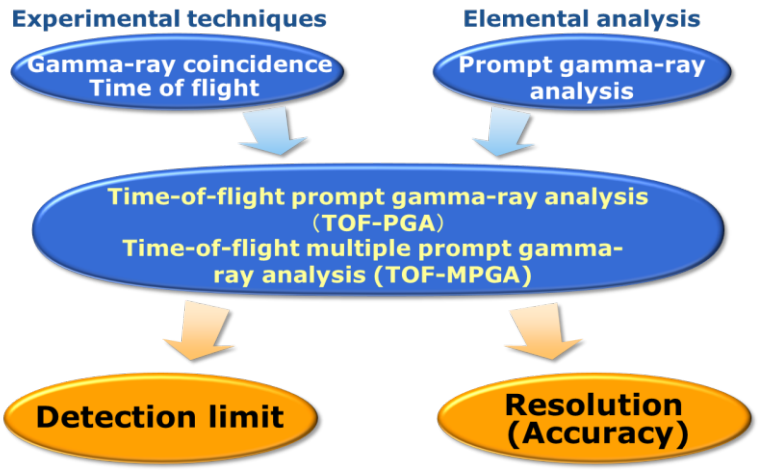

Fig. 2 New method for multi-elemental analysis.

4. The mixed sample measurements and results

We demonstrate how the new technique can be a useful tool for the mixed sample that contains Ag, Au, Co and Ta [7]. These elements are commonly used as standard samples or notch filter [8,9], which is an established technique for background gamma-rays estimation and energy calibration of neutron. Pure samples of these elements provide the isolated peaks on the PGA and TOF spectra. Thus, these are typically easy to quantify by PGA and TOF for a sample that contains only a single element. In contrast, severe peak overlaps in both PGA and TOF spectra are inevitable when the mixed sample that contains Ag, Au, Cd, Co and Ta is measured. Therefore, it is difficult to obtain accurate and reliable results for Co in the mixed sample by PGA and TOF methods.

The TOF-PGA spectrum has three dimensions and plots the energy of the gamma-ray on the X axis, the time-of-flight on the Y axis, and the number of counts on the Z axis. Figure 3b shows the background-subtracted PGA spectra gated on the neutron capture resonance peak of Co (130 eV). In the conventional PGA spectrum, most of the prompt gamma rays from Co overlap with the gamma rays from other elements and/or background gamma rays. In contrast, significant improvements in SNR for Co peaks have been achieved in the gated PGA spectrum of TOF-PGA spectrum.

The neutron resonance peak of Co (Co-59) in the conventional TOF spectrum mainly overlaps that of Ta because the width of Co peak is broad. The background-subtracted TOF spectrum gated on the gamma-ray peak (229.7 keV) in the TOF-PGA spectrum is shown in Figure 3c. The gated TOF spectrum is plotted on a logarithmic TOF axis. The overlapping has also been eliminated from the Co peak in the spectrum (Fig. 3c). The most of overlapping gamma-ray events appear in

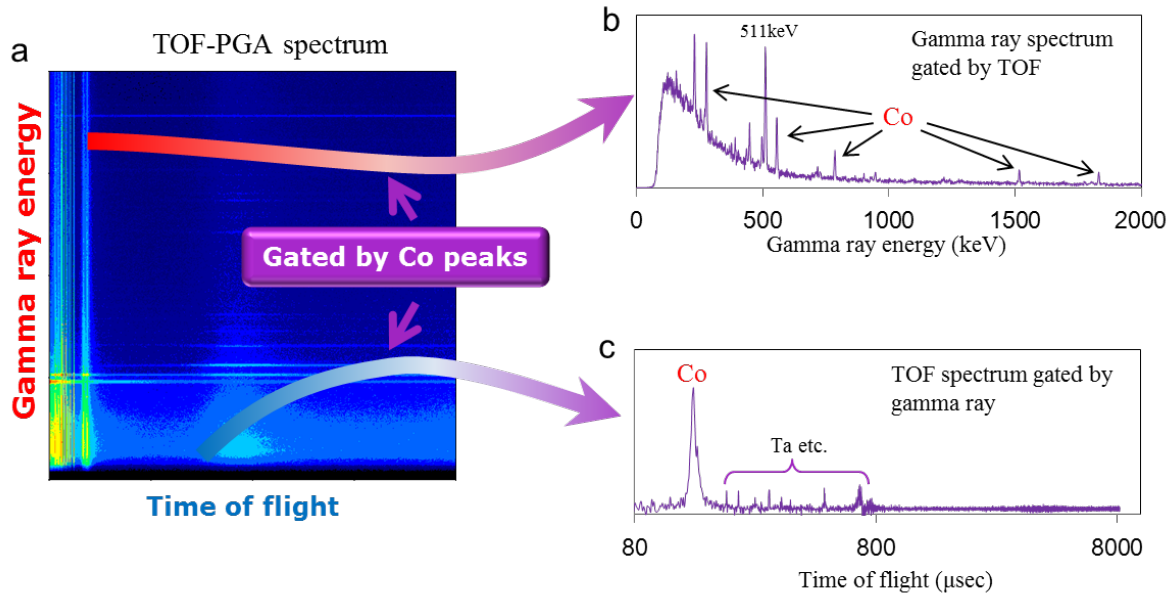

Fig. 3 TOF-PGA spectrum and the gated spectra of the mixed sample.

different points on the gated TOF spectrum because the most of resonance peak energies of Co are different from these of the other elements. As a consequence, TOF-PGA allows to eliminate or at least to greatly suppress those of the other elements in Co peak, and can accurately quantify Co even with the presence of these elements.

5. Conclusions

PGA and nuclear data measurements are technically regarded as same measurements. In contrast, there is an important difference between PGA and nuclear data measurements. In nuclear data measurements, pure elemental sample can be used. On the other hand, the most of samples for PGA have rather complex elemental composition. We have developed the non-destructive analytical method which combines PGA and TOF by using an intense pulsed neutron beam at J-PARC MLF ANNRI. In the analysis of the new method, PGA, TOF, TOF-PGA, MPGA and TOF-MPGA spectra are available. TOF-PGA allows us to eliminate or at least to greatly suppress the contamination from the other elements or the neutron shields of Ge detectors, etc. in the Co peak. We show that the developed method allows significant improvements in the background subtracted gated spectra of TOF-PGA spectrum for the mixed sample. These will provide correspondingly more accurate results. Finally, TOF-PGA and TOF-MPGA will be irreplaceable tools for many fields, such as cosmochemistry, geochemistry, environmental science, and archaeology, because the specimen can be reused, as it is, after the measurement, and the reliable and valid results will be obtained.

Acknowledgements

The author would like to express our sincere gratitude to the accelerator staff of J-PARC for

providing the pulsed neutron beam. This work was supported in part by Grants-in-Aid for Scientific Research (25246038).

References

[1] R. Paul, Analysit, 122, p.35 (1997).
[2] M. P. Failey *et. al.*, Anal. Chem., 51, 2209 (1979).
[3] Rossbach, M. Anal. Chem., 63, 2156 (1991).
[4] H. Postma *et. al.*, J. Radioanal. Nucl. Chem., 248, p.115 (2001).
[5] H. Postma *et. al.*, J. Radioanal. Nucl. Chem., 271, 95 (2007).
[6] H. Harada *et al.,* J. Korean Phys. Soc., 59, p. 1547 (2011).
[7] Y. Toh *et al.*, Anal. Chem., 86, 12030 (2014).
[8] V. R. Skoy *et al.,* Nucl. Instr. Meth. Phys. Res. B267, 2351 (2009).
[9] W. Ratynski and F. Käppeler, Phys. Rev. C 37, 595 (1988)

This is a blank page.

6 Final Report of Advisory Subcommittee on Development of JENDL — Guideline for Developing Next JENDL

Go CHIBA
Graduate School of Engineering, Hokkaido University, Sapporo, Hokkaido, 060-8628
e-mail: go_chiba@eng.hokudai.ac.jp

An advisory subcommittee on development of JENDL was established in 2013 to discuss future development of JENDL among experts on nuclear data experiments, evaluations and applications. This paper is a summary of a final report which was submitted to the JENDL committee on March in 2014[1].

In order to utilize achievements of research and developments on the nuclear data field for the public and society, development of evaluated nuclear data libraries (or files) is essential. Japanese Evaluated Nuclear Data Library, JENDL, has played an important role as a bridge between the nuclear data research and the real world in Japan. There have been forty years since the release of the first version of JENDL, JENDL-1. During this period application fields of JENDL have been extended from fast neutron fission reactors to thermal neutron fission reactors, fusion reactors and accelerators. Also, various kinds of nuclear data, such as secondary gamma-ray production data, double-differential cross section data, covariance data, and so on, have been requested by users' community.

Fission reactor application

As described above, nuclear data files have been developed mainly for fission reactor applications so far. In fast reactor core design activities in Japan, Japanese own nuclear data files have been desired by domestic users, so JENDL has been a standard nuclear data library in this field. On the other hand, in thermal reactor core design activities in Japan, domestic industries have utilized packages consisting of nuclear data and reactor core calculation codes developed in foreign countries, so JENDL has not been utilized as frequently as fast reactor design. Recently, however, JENDL-based application libraries have been implemented to reactor core design codes of some domestic plant vendors and nuclear fuel production companies. JENDL has been utilized also for crosscheck in safety regulations, so nowadays the role of JENDL in thermal reactor core design becomes much more important than that in the past.

After the release of JENDL-3.2 in 1994, a special committee was established in 1997 to have discussions on the development of the next version of JENDL: JENDL-3.3. This committee proposed to reach the goal of the nuclear data research for fission reactor

applications with JENDL-3.3. In other words, JENDL-3.3 was expected to satisfy all the requirements from users of fission reactor applications. Actually, some engineering corrections/adjustments had been required when ones use evaluated nuclear data files for fission reactor core design calculations since every nuclear data files have their own non-negligible biases. If such a nuclear data file, that is applicable to fission reactor core calculations without any corrections, is realized, ambiguity due to the engineering corrections can be eliminated, and accountability would significantly increase. JENDL-3.3 was released in 2002 with the target mentioned above, but unfortunately, accuracy requirements are not satisfied and engineering corrections are still required when ones use JENDL-3.3.

In nuclear data evaluations for modern nuclear data files, such as the latest version of JENDL, JENDL-4.0, feedbacks from integral testing of nuclear data have been taken into consideration keeping consistency with differential measurement data and nuclear reaction model. Performance of JENDL-4.0 for fission reactor core parameter prediction has been significantly improved in comparison with JENDL-3.3. However, fission reactor core parameter prediction still has some problems and ambiguities even with JENDL-4.0, so we cannot say that nuclear data researches have reached their goals in fission reactors applications.

One of other features of the modern nuclear data files is that they contain a large amount of covariance data for nuclear data. Especially in the fast reactor applications, covariance data are evaluated for almost all the required nuclear data in JENDL-4.0. It has been pointed out that, however, some of them be revised to improve their reliability. In thermal reactor applications, there is a possibility that uncertainty estimations for reactor core design calculations become mandatory in safety regulation procedures, so covariance data for both fast and thermal reactor applications are required and further improvement in their quality is quite important in future libraries.

Other application fields in nuclear engineering

Not only reactor core designs and operations but also so-called backend fields, such as management of nuclear fuels, reactor decommissioning and nuclear waste disposal, are also application fields of nuclear data. Many nuclear power plants will experience 40-year operations within upcoming 10 years, so most of them will be decommissioned in near future. Nuclear data files having high accuracy, reliability and accountability are essential to evaluate accurately radioactivity inventories of power plants and to carry out plant decommissioning safely and cheaply. We would suggest that a radioactivity inventory evaluation procedure consisting of numerical tools and nuclear data, that will be established through the plant decommissioning in Japan, can be a global standard in future.

Some of technologies, which are measures for Fukushima-Daiichi nuclear power plants accident, such as detection of fissile materials and estimation of system subcriticality require further development of the relevant nuclear data. JENDL has to respond to these requirements.

Fusion reactor application

The fusion reactor field has been one of major application fields of JENDL since the release of JENDL-3 in 1989. JENDL has supplied high-quality data to this field through JENDL Fusion File in 1996, JENDL-3.2, JENDL-3.3 and JENDL/HE-2007. As the results, many JENDL evaluations have been adopted to the Fusion Evaluated Nuclear Data Library FENDL-3.0 library of International Atomic Energy Agency. Even with JENDL-4.0, however, some integral measurement data relevant to fusion reactor applications (FNS and OKTAVIAN) are not well reproduced, so reevaluations and revisions of some nuclear data are required. Fortunately the detailed information on these integral data can be shared by Japanese nuclear data community, so efficient use of these data, i.e., reevaluation of the relevant nuclear data and integral testing with well-established numerical calculation method against these integral data, would contribute to increase the presence of JENDL and Japanese nuclear data community in the fusion reactor field.

Medical and accelerators applications

Nuclear data have been just recently utilized in other application fields such as medical applications and accelerator designs. Historically shielding and radiation dose/inventory calculations have been based on the empirical formula. However, increases of accelerator power and requirements for high accuracy of dose calculations motivate to particle transport calculation-based evaluations, which utilize nuclear data and event generators. Although constructions of accelerators with various kinds of particles with different energy/strength are now planned, a nuclear data set which can cover all the ranges for design of these accelerators does not exist. While JENDL has responded to part of such requirements by providing special-purpose files so far, we would suggest that JENDL can be a standard data set in these engineering fields by covering wider ranges of data in future.

New trends in evaluated nuclear data files developments

During forty years since the release of JENDL-1, styles of research and development of nuclear data files have drastically changed due to the significant advancements on information and computer technologies. The typical procedure of nuclear data-related technology development, which consists of nuclear data measurements, integral experiments, collections of differential measurement data, development of nuclear reaction models, nuclear data evaluations, validation through integral experiments and production of evaluated nuclear data files, will drastically change within upcoming ten years. While an evaluated nuclear data file has been developed by each country/district historically, the TENDL library is developed by NRG-Petten, just one research organization. TENDL is also unique since it chooses a nuclear data set which shows the best performance in integral data testing among a huge number of nuclear data sets which are generated randomly within nuclear data uncertainties. Although we cannot judge whether this approach is reasonable or not at

present, it is apparent that manners of evaluated nuclear data files development are changing now. GND, a new-style nuclear data infrastructure which overcomes problems in the conventional ENDF format, and the CIELO project, the world-wide nuclear data evaluation project, should be referred also.

In the final report we mention future perspectives of the JENDL development based on just an extrapolation from our experiences, and an unexpected drastic technical breakthrough is not considered. Our recommendations are the best just among those from our experiences and knowledge. We also would point out that it is the most important for each researcher or engineer in the nuclear data field not to be satisfied with the present technology, to try to generate new findings and to develop a novel technology. These are quite important under the present situation that the number of nuclear data-related researchers/engineers is decreasing. Actually, it is not easy, but we are hoping that JENDL will be invaluable flag for all the nuclear data-related engineers/researchers in future as well as in the past.

References

[1] G. Chiba, O. Iwamoto (Ed.), Final Report of Advisory Subcommittee on Development of JENDL —Guideline for Developing Next JENDL—, JAEA-Review 2014-046. [in Japanese]

Appendix Members of the advisory subcommittee on development of JENDL

Go Chiba (Hokkaido Univ., Chair), Mikio Tokashiki (Nuclear Fuel Industry), Naoki Sugimura (Nuclear Engineering Ltd.), Ken-ichi Tanaka (Japan Atomic Power Company), Yasushi Nauchi (Central Research Institute of Electric Power Industory), Toshiya Sanami (KEK), Nobuhiro Shigyo (Kyushu Univ.), Tatsuya Katabuchi (Tokyo Institute of Technology), Taira Hazama, Kazufumi Tsujimoto, Chikara Konno, Osamu Iwamoto (JAEA), Nobuyuki Iwamoto, Satoshi Kunieda (JAEA, observers)

7 Toward advancement of nuclear data research in the resonance region

S. Kunieda, K. Shibata and T. Fukahori
Japan Atomic Energy Agency, Tokai-mura, Naka-gun, Ibaraki 319-1195, Japan

T. Kawano, M. Paris and G. Hale
Los Alamos National Laboratory, Los Alamos, New Mexico 87545, USA

A consistent cross-section evaluation could be made in the resonance energy region through the R-matrix analysis which is rigorous and straightforward to the quantum mechanical reaction theory. This paper shortly review the present status of our R-matrix code together with preliminary results of the p+^{7}Li cross-section analysis. We also present evidence of the unitarity constraint from the theory, which could be a powerful tool to understand the source of differences among experimental data.

1. Introduction

The resonant peaks are observed in the nuclear reaction cross-sections over the low-energy range where the level structure of compound systems mirrors their unique characters. Since it is difficult to understand explicit natures of excited states only by the structure theories at this moment, experimental cross-sections are essential for the nuclear data evaluation. Once we measured cross-sections, a consistent evaluation may be performed through the R-matrix analysis which is rigorous and straightforward to the quantum mechanical reaction theory.

The light-system should be an accessible research-object since the number of resonance peaks appeared in the cross-sections is virtually limited. Also, it is substantially because that the radiative capture cross-section is so small that we may eliminate a number of photon channels. Indeed, the R-matrix theory had already been applied to the cross-sections evaluation in IAEA standard [1] for light-nuclei. A number of the analysis had also been reported to study the nature of nucleosynthesis in the astrophysics.

We are developing a Multi-channel R-matrix code which is based on the Wigner-Eisenbuds formalism [2]. It is designed to calculate/analyze cross sections not only for the neutron but also the charged-particle reactions, where all the model parameters can be explicitly channel-dependent. Recently, the code had been updated to calculate the elastic-scattering differential cross-sections for charged-particles. We are also including the photon channels based on the Reich-Moore approximation [3]. The code also has a capability of parameter search based on the Bayes' theorem with several options, where both the theoretical and experimental parameters could be searched for. In this paper, we briefly report the status of the code development. The preliminary analysis for p+^{7}Li cross-sections is also presented. Finally, let us review a physical constraint from the theory which could be a powerful tool to understand the source of differences among experimental data.

2. Status of the Code development

We are developing a Multi-channel R-matrix code AMUR [4] which is based on the Wigner-Eisenbuds formalism [2]. It already has been designed for the

evaluation of neutron cross-sections (except for radiative capture cross-sections) as we reported on ^{17}O system [4]. However, it was not allowed for the evaluation of charged-particle cross-section because the Coulomb scattering process was missing. Since the charged-particle reaction is getting more attention in the medical applications and astrophysics, we calculate the total scattering-amplitude by following Lane and Thomas [5] as follows.

$$A_{\alpha' s' \nu', \alpha s \nu}(\Omega_{\alpha'}) = \frac{\sqrt{\pi}}{k_\alpha}\left\{ -C_{\alpha'}(\theta_{\alpha'})\delta_{\alpha' s' \nu', \alpha s \nu} + i\sum_{l' m l}\sqrt{2l+1} \times \left[e^{2i\omega_{\alpha' l}}\delta_{\alpha' s' l' \nu' m', \alpha s l \nu 0} - U_{\alpha' s' l' \nu' m', \alpha s l \nu 0} \right] Y_m^{(l)}(\Omega_{\alpha'}) \right\}$$

The symbol $C_\alpha(\theta_{\alpha'})$ stands for the Coulomb-amplitude while the other terms express nuclear-scattering amplitude (notations of the equation above are the same as in Ref. [5]). Now, elastic-scattering differential cross-sections can be calculated by considering the interference in-between the nuclear- and Coulomb-scattering amplitudes.

We also added the other functions as follows.

1. Consideration of the excited states of residual nuclei to calculate cross-sections such as (n,n$_1$), (n,n$_2$), …, (p,p$_1$), (p,p$_2$), …, (p,n$_1$), (p,n$_2$), … and so on.
2. The function to generate an ENDF-format file both for neutron and charged-particle cross-sections.

3. Preliminary Analysis for p+^{7}Li Reaction

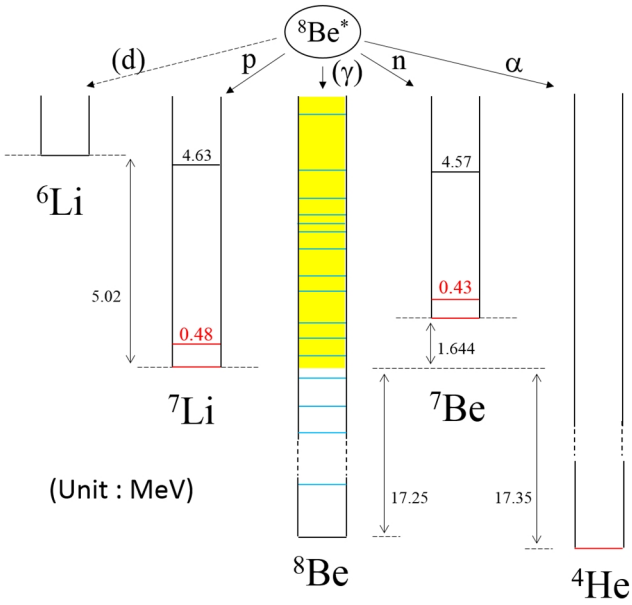

Fig. 1 : Schematic chart of decay process from ^{8}Be* system

One of our challenges is to perform the evaluation of p+^{7}Li cross-sections through R-matrix analysis in the resonance region. It is because the ^{7}Li(p,n) reaction is one

of the promising candidates for neutron source in practical applications such as in Boron Neutron Capture Therapy (BNCT). Figure 1 shows the schematic chart of decay processes from the ^{8}Be* system in a lower energy region. In this analysis, we analyzed experimental data of ^{7}Li(p,p$_0$)^{7}Li$_{g.s.}$, ^{7}Li(p,p$_1$)^{7}Li$_{(ex=0.48\ MeV)}$, ^{7}Li(p,n$_0$)^{7}Be$_{g.s.}$, ^{7}Li(p,n$_1$)^{7}Be$_{(ex=0.43\ MeV)}$ and ^{7}Li(p,α)^{4}He cross-sections. The R-matrix parameters, e.g., the reduced-width amplitudes $\gamma_{cc'}$, are deduced for each explicit-channel by fitting to those measured cross-sections simultaneously with a reasonable boundary condition. In this preliminary analysis, energy eigenvalues of ^{8}Be* are fixed to those taken from ENSDF while the distant (pseudo) levels are additionally considered as a source of the background.

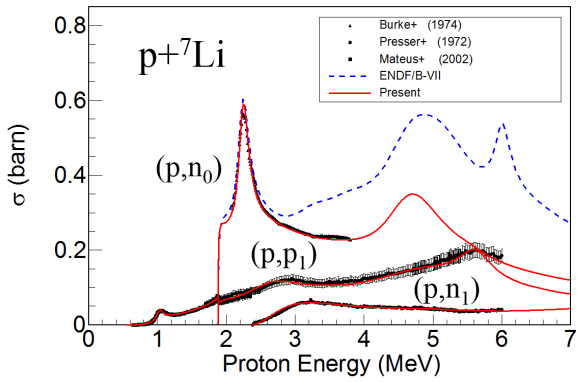

Fig. 2 : R-matrix fits to experimental ^{7}Li(p,n$_0$), (p,n$_1$ and (p,p$_1$) cross-sections.

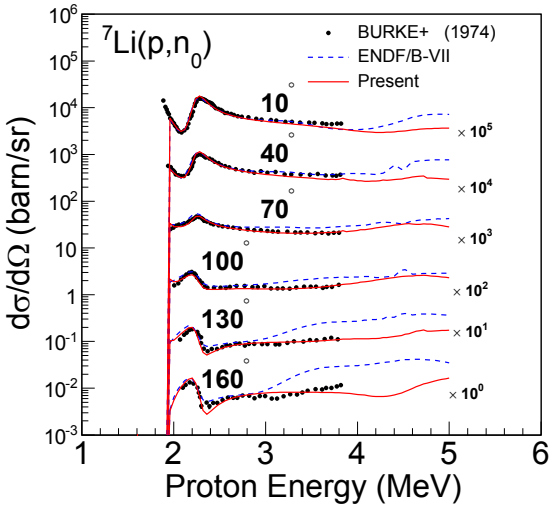

Fig. 3 : R-matrix fits to experimental ^{7}Li(p,n$_0$), differential cross-sections.

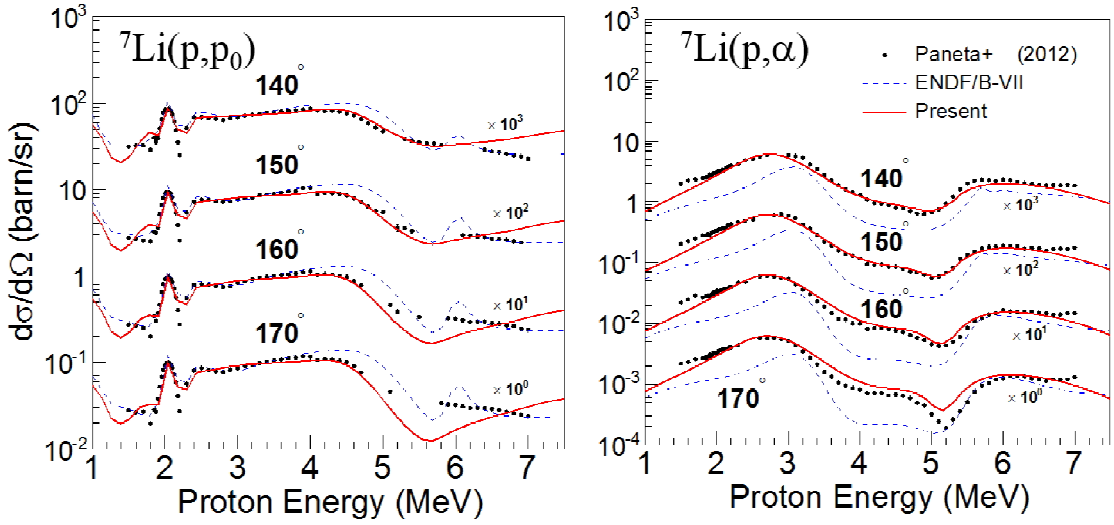

Fig. 4 : R-matrix fits to experimental ^{7}Li(p,p$_0$) and (p,α) differential cross-sections.

Figure 2 illustrates calculated/evaluated cross-sections for ^{7}Li(p,p$_1$)^{7}Li, ^{7}Li(p,n$_0$)^{7}Be and ^{7}Li(p,n$_1$)^{7}Be reactions together with experimental data [6,7,8]. We successfully fitted those measured cross-sections while ENDF/B-VII.(0,1) [9] overestimates the experimental ^{7}Li(p,n$_0$)^{7}Be cross-sections above 3 MeV. Also, ^{7}Li(p,p$_1$)^{7}Li and ^{7}Li(p,n$_1$)^{7}Be cross-sections are missing in ENDF/B-VII. Reasonable fits were also obtained for differential cross-sections, simultaneously. For example, differential cross-sections of the ^{7}Li(p,n$_0$)^{7}Be reaction are plotted in Fig. 3 for each angle together with experimental data of Burke et al. [6]. Figure 4 shows results for differential cross-sections of ^{7}Li(p,n$_0$)^{7}Be and ^{7}Li(p,α)^{4}He reactions compared with experimental data of Peneta et al. [10]. Those results are not yet satisfactory because there are still disagreements below 2 MeV and around 5 MeV in ^{7}Li(p,p$_0$)^{7}Li reaction while ENDF/B-VII shows more reasonable fits. Source of those disagreements are probably due to an inappropriate sign of the reduced-width amplitude which is adversely affected by the Coulomb-scattering amplitude.

4. Toward Unitarity Constraint Analysis

There remains differences among measured data more or less, which makes the present cross-section evaluation still uncertain. One of the typical example is the systematic uncertainty resulting from the data normalization. For instance, ~3% difference is observed between the experimental ^{16}O(n,tot) cross-sections of Schrack et al. [11] and Cierjacks et al. [12] as shown in Fig. 5. This problem could be solved by introducing re-normalization parameter N for each measurement in the R-matrix analysis since the collision matrix calculated from the theory is the unitary.

Figure 6-(a) illustrates calculated n+^{16}O total cross-sections up to 5.2 MeV with all the experimental data taken from EXFOR [13] where dashed-curve shows contribution only from $J^{\pi}=3/2^{+}$. In Fig. 6-(b), we plot sensitivity of the cross-sections to the reduced width amplitude for the first resonance appearing in $J^{\pi}=3/2^{+}$. It should be noted that sensitivity curve is very unique, in which the value is strongly reduced around the peak position of the resonance. This is consequence of the unitarity in the collision matrix, which gives a large constraint to the R-matrix analysis.

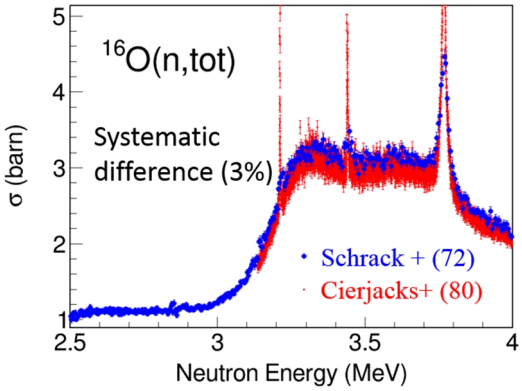

Fig. 5 : Example systematic difference in-between measurements

Indeed, in our preliminary analysis [15], we obtained $N = 0.999 \pm 0.14\%$ and $1.046 \pm 0.16\%$ for Schrack et al. and Cierjacks et al., respectively. This suggests there could be a normalization problem in experimental data of Cierjacks et al.

5. Summary and Outlook

The R-matrix could be a powerful tool in the cross-section evaluation in the resonance region. Recently, the Coulomb-scattering amplitude was incorporated in

AMUR, which enables us to make evaluation for incident charged-particles. We are also including the Reich-Moore approximation to calculate radiative capture cross-sections. One of the great nature in the theory is the unitarity constraint which is expected to reduce the uncertainty of evaluated cross-sections.

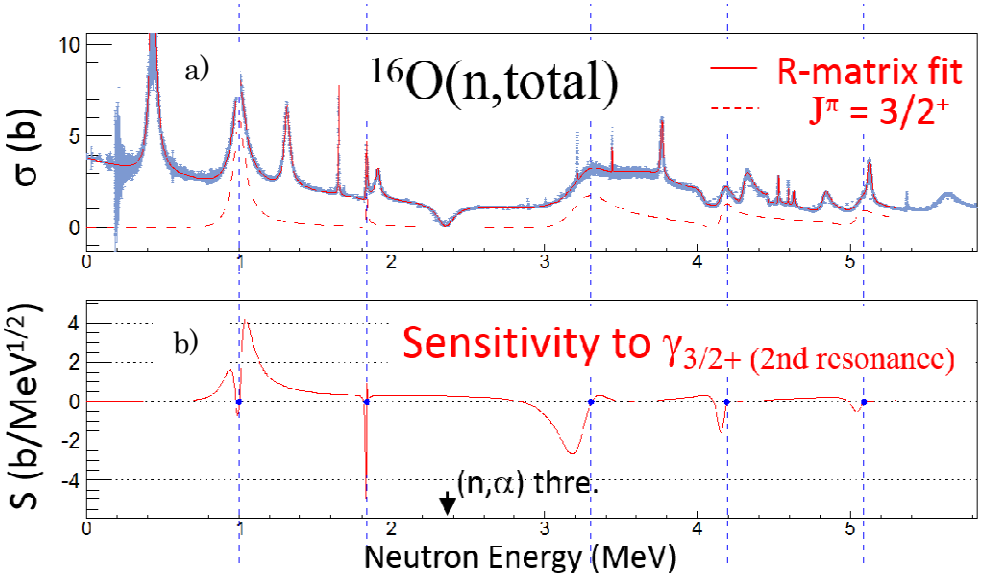

Fig. 6 : (upper panel) Calculated n+^{16}O total cross-sections up to 5.2 MeV with all the experimental data taken from EXFOR where dashed-curve shows contribution only from $J^{\pi}=3/2^{+}$. (lower panel) Sensitivity of the cross-sections to reduced width amplitude for the first resonance appearing in $J^{\pi}=3/2^{+}$.

Reference

1. A. D. Carlson et al., “International Evaluation of Neutron Cross Section Standards”, Nucl. Data Sheets 110, 3215 (2009).
2. E. P. Wigner and L. Eisenbud, “Higher Angular Momenta and Long Range Interaction in Resonance Reactions”, Phys. Rev. 72, 29 (1947).
3. C. W. Reich and M. S. Moore, “Multilevel Formula for the Fission Process”, Phys. Rev. 111, 929 (1958).
4. S. Kunieda et al., “R-matrix Analysis for n+^{16}O Cross-sections up to E_n=6.0 MeV with Covariances”, Nucl. Data Sheets 118, 250 (2014).
5. A. M. Lane and R. G. Thomas, “R-Matrix Theory of Nuclear Reactions”, Rev. Mod. Phys. 30, 257 (1958).
6. C. A. Burke, M. T. Lunnon and H. W. Lefevre, "^{7}Li(p,n)^{7}Be angular distribution to Ep=3.8 MeV", Phys. Rev. C10, 1299 (1974).
7. G. Presser and R. Bass, “Reactions ^{7}Li+n, ^{7}Li+p and excited states of the A = 8 system”, Nucl. Phys. A182, 321 (1972).
8. R. Mateus, A. P. Jesus, B. Braizinha, J. Cruz, J. V. Pinto, J. P. Ribeiro, “Proton-induced gamma-ray analysis of lithium in thick samples”, Nucl. Instr. and Meth. B190, 117 (2002).
9. M. B. Chadwick et al, “ENDF/B-VII.1 Nuclear Data for Science and Technology: Cross

Sections, Covariances, Fission Product Yields and Decay", Nucl. Data Sheets 112, 2887 (2011).
10. V. Paneta, A. Kafkarkou, M. Kokkoris, A. Lagoyannis, "", Nucl. Instr. and Meth. B288, 53 (2012).
11. R. A. Schrack, R. B. Schwartz and H. T. Heaton, Bulletin of the American Physical Society 17, 555 (1972).
12. S. Cierjacks, F. Hinterberger, G. Schmalz, D. Erbe, P. V. Rossen, and B. Leugers, Nucl. Instr. Meth., 169, 185-198 (1980).
13. Otuka et al., "Towards a More Complete and Accurate Experimental Nuclear Reaction Data Library (EXFOR): International Collaboration Between Nuclear Reaction Data Centres (NRDC)", Nucl. Data Sheets 120, 272 (2014).

8 International Collaboration of Hokkaido University Nuclear Reaction Data Centre

Masayuki Aikawa[1], Shuichiro Ebata[2], Naoya Furutachi[1], Dagvadorj Ichinkhorloo[2], Shotaro Imai[2], Kiyoshi Katō[1], Aiganym Sarsembayeva[2], Bo Zhou[2], Naohiko Otuka[3]

[1] Faculty of Science, Hokkaido University, Sapporo 060-0810, Japan

[2] Meme Media Laboratory, Hokkaido University, Sapporo 060-8628, Japan

[3] Nuclear Data Section, International Atomic Energy Agency, A-1400 Vienna, Austria

e-mail: aikawa@sci.hokudai.ac.jp

The Hokkaido University Nuclear Reaction Data Centre (JCPRG) cooperates in nuclear data compilation and researches with foreign institutes. In this report, we present such cooperative activities with the International Network of Nuclear Reaction Data Centres (NRDC), institutes among Asian countries, and the Institute of Nuclear Research of the Hungarian Academy of Sciences (ATOMKI), respectively.

Nuclear data are available for many application fields, such as nuclear engineering and medicine. For such fields, many kinds of nuclear reaction data are obtained experimentally in institutes worldwide. The nuclear reaction experiments sometimes require high investment and resources. The nuclear data, therefore, must be stored in a database and opened to the public, free of charge. One such database is the EXFOR (EXchange FORmat) database maintained by the International Network of Nuclear Reaction Data Centres (NRDC) coordinated by the International Atomic Energy Agency (IAEA) [1, 2].

The Hokkaido University Nuclear Reaction Data Centre (JCPRG) is a member of the NRDC. JCPRG compiles charged-particle and photon induced nuclear reaction data obtained in Japanese institutes (Fig. 1). Papers to be compiled into the EXFOR database are surveyed in peer-reviewed journals. JCPRG performs such surveys of papers in addition to the NRDC survey. If papers are found, we assign entry numbers with E, J, and K which are charged-particle, meson, and photon induced reactions, respectively. We also maintain entries with R, which was compiled by RIKEN group, a former member of the NRDC. JCPRG contributes about 10 percent of the data on charged-particle nuclear reactions in the EXFOR database.

In the NRDC, there are four institutes located in Asia. Recently, Central Asian Nuclear Reaction Database (CANRDB) jointly consisting of institutes in Kazakhstan and Uzbekistan started to compile

nuclear reaction data obtained in their own countries. Thus, nuclear data activities in Asia are quickly increasing. Under such situation, we contributed to promote the activities under the support of the 'R&D' Platform Formation of Nuclear Reaction Data in Asian Countries (2010-2013), the Asia-Africa Science Platform Program, the Japan Society for the Promotion of Science (JSPS) from April 2010 to March 2013. Since 2010, annual workshops, referred to as the Asian Nuclear Reaction Database Development Workshop, were held. The workshops were devoted to sharing information about their activities, to strengthen collaboration among the NRDC members in Asia and to promote the dissemination and improvement of data compilation techniques [3].

One of the research topics in JCPRG is related to nuclear medicine. To obtain and evaluate nuclear data for medicine, we are supported by the JSPS Bilateral Program "Measurement and Evaluation of Important Nuclear Data for Diagnosis and Therapy Treatments" for two years from Apr. 2014. The program is in collaboration with the Institute of Nuclear Research of the Hungarian Academy of Sciences (ATOMKI), which is also a member of the NRDC. In Apr. 2014, we performed an experiment at ATOMKI to obtain the cross section of ^{100}Mo(p,2n)^{99m}Tc reaction [4].

JCPRG energetically cooperates in and promotes nuclear data activities with foreign institutes. In this report, we briefly introduce the activities with the International Network of Nuclear Reaction Data Centres (NRDC), institutes among Asian countries, and the Institute of Nuclear Research of the Hungarian Academy of Sciences (ATOMKI), respectively.

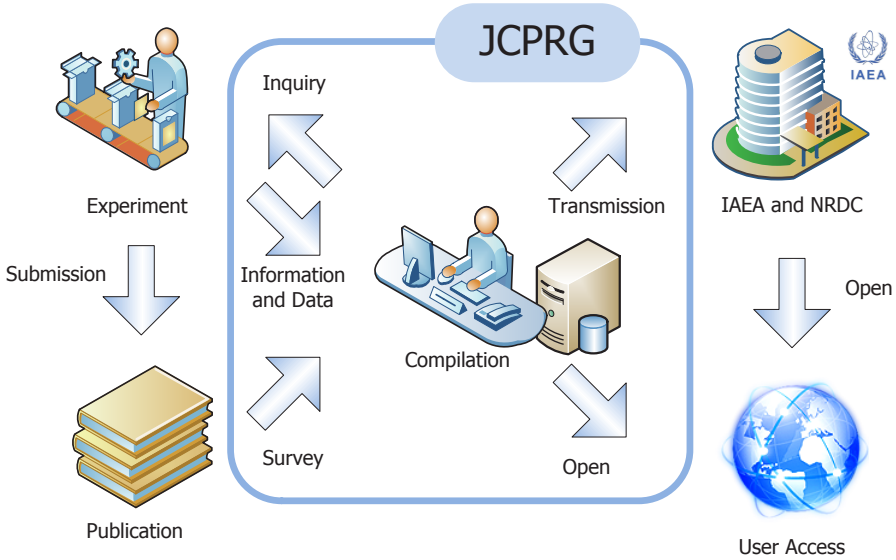

Figure 1: Compilation procedure

Acknowledgement

The authors are grateful for the support of JSPS Grant-in-Aid for Publication of Scientific Research Results (No. 257005) and the support of JSPS and HAS under the Japan - Hungary Research Cooperative Program.

References

[1] Otuka N, Dupont E, Semkova V, Pritychenko B, Blokhin AI, Aikawa M, Babykina S, Bossant M, Chen G, Dunaeva S, Forrest RA, Fukahori T, Furutachi N, Ganesan S, Ge Z, Gritzay OO, Herman M, Hlavac S, Kato K, Lalremruata B, Lee YO, Makinaga A, Matsumoto K, Mikhaylyukova M, Pikulina G, Pronyaev VG, Saxena A, Schwerer O, Simakov SP, Soppera N, Suzuki R, Takacs S, Tao X, Taova S, Tarkanyi F, Varlamov VV, Wang J, Yang SC, Zerkin V, Zhuang Y. Towards a More Complete and Accurate Experimental Nuclear Reaction Data Library (EXFOR): International Collaboration Between Nuclear Reaction Data Centres (NRDC), Nucl. Data Sheets 2014;120:272-276.

[2] Otuka N, Dupont E. Summary Report of the Technical Meeting on International Network of Nuclear Reaction Data Centres, INDC(NDS) 2014;661:1-50.

[3] Aikawa M, Ebata S, Furutachi N, Ichinkhorloo D, Katō K, Makinaga A, Devi V, Odsuren M, Otsuka N, Takibayeva M, Tsubakihara K. International and Asian Collaboration on Nuclear Data, Proceedings of the Fourth Asian Nuclear Reaction Database Development Workshop, INDC(KAS) 2013;001:54-55.

[4] Takács S, Hermanne A, Ditrói F, Tárkányi F, Aikawa M. Reexamination of cross sections of the ^{100}Mo(p,2n)^{99}mTc reaction, Nucl. Instrum. Methods in Phys. Res. B 2015;347:26-38.

This is a blank page.

9 Development of multi-group neutron activation cross-section library for decommissioning of nuclear facilities

Keisuke OKUMURA*, Kensuke KOJIMA
Nuclear Science and Engineering Center, Japan Atomic Energy Agency
Tokai-mura, Naka-gun, Ibaraki-ken 319-1195 Japan
Ken-ichi TANAKA †
The Japan Atomic Power Company, Mitoshiro-cho, Kanda, Chiyoda-ku, Tokyo, 101-0053, Japan

A new multi-group neutron activation cross-section library (MAXS2015) was developed based on the nuclear data libraries JENDL-4.0 and JEFF-3.0/A to apply it to the activation calculations for the decommissioning of nuclear facilities.

1. Introduction

The reliable prediction of radionuclide inventory generated in the decommissioning of nuclear facilities is important in making and optimizing the decommissioning strategy [1]. In the activation calculation for the planning, we have to pay much attention to the activation of many impurities in the structured materials irradiated in various neutron spectra depending on their positions and materials. Therefore, accurate activation cross-section data are necessary for many nuclides and reactions. A new multi-group neutron activation cross-section library (MAXS2015) was developed based on the recent nuclear data libraries JENDL-4.0 [2] and JEFF-3.0/A [3] to apply it to the activation calculations for the decommissioning of nuclear facilities.

2. Procedure to generate MAXS2015

Since most of activated nuclides in structured materials are originated in additives or impurities, all of the group-wise cross-sections of MAXS2015 were produced in the conditions of the infinite dilution at the temperature of 300K by using NJOY2012 [4]. The energy group structure of MAXS2015 is the same as that of VITAMIN-B6[5] with 199-group structure which consists of 163 groups for the fast energy region (19.64 MeV～3.9279 eV) and 36 groups for the thermal energy region (3.9279 eV ～10^{-5} eV). The thermal energy region is often treated as a condensed-group in shielding calculations. However, the multi-group treatment in the thermal energy region is important for the activation calculation of some nuclear facilities, because fast leakage neutrons may be moderated by water in outer concrete structures where the activation is mainly caused in the thermal energy region and it strongly depends on the thermal flux spectrum.

* Corresponding author, E-mail: okumura.keisuke@jaea.go.jp
† Present address : The Institute of Applied Energy, 1-14-2 Nishi-Shinbashi, Minato-ku, Tokyo, 105-0003, Japan, and Tokyo Institute of Technology, 2-12-N1-9 Ookayama, Meguro-ku, Tokyo 152-8550, Japan

A weighting function equipped in NJOY2012 (IWT=11 in GROUPR: VITAMIN-E weight function) was employed to produce the multi-group cross-sections. A room temperature of 300 K was assumed here, but the temperature is not effective for resonance integrals of all nuclides in the infinite dilution condition. Although the temperature generally affects the shape of the neutron spectrum in the thermal energy region, i.e. Maxwellian distribution, it will not have much influence on results of activation calculations, because the activation calculation is performed with the one-group condensed cross-sections using a realistic neutron spectrum supplied by a user and cross-sections of MAXS2015 with sufficiently fine energy group structure.

MAXS2015 covers most of activation cross-sections necessary for decommissioning of nuclear facilities in which the maximum neutron energy is less than or equal to 19.64 MeV. The number of neutron induced reaction types is 25 at a maximum. They are MT=16, 17, 18, 22, 24, 25, 28, 29, 30, 32, 33, 34, 37, 41, 51, 102, 103, 104, 105, 106, 107, 108, 111, 112, and 113, in accordance with the integer (MT) in the ENDF-6 format [6]. The cross-section data for MAXS2015 were first taken from JENDL-4.0 including updated data as of 13 Aug. 2013[7], for 404 nuclides, as far as the data had been evaluated in JENDL-4.0 except for He-4 and C-nat.. For the other data, they were filled with the data taken from JEFF-3.0/A. Finally, MAX2015 provides cross-section data for 9504 reactions (the total numbers of MTs) of 779 nuclides.

The multi-group isomeric ratio of each reaction of each nuclide was also compiled from the data of MF9 or MF10 of the evaluated nuclear data libraries. Since MF9 or MF10 data are evaluated only for ^{209}Bi(n,γ), ^{241}Am (n,γ), and ^{237}Np(n,2n) in JENDL-4.0, the other isomeric ratios of MAXS2015 are based on JEFF-3.0/A. The multi-group isomeric ratio $I_{x,g}^{i\to j_n}$ of MAXS2015 is defined as

$$I_{x,g}^{i\to j_n} = \sigma_{x,g}^{i\to j_n} / \sigma_{x,g}^{i} \quad , \tag{1}$$

where x: reaction type, g: energy group, i :nuclide index, j_n : the n-th isomer (e.g. n=0,1,2: ground state, 1st meta-stable, 2nd meta-stable) of the nuclide j generated from nuclide i by reaction x, $\sigma_{x,g}^{i\to j_n}$: partial microscopic cross-section to generate the isomer j_n, $\sigma_{x,g}^{i}$: usual microscopic cross-section for the reaction x of nuclide i. $I_{x,g}^{i\to j_n}$ is directly given by using the data of MF9 if it is evaluated. If not, $I_{x,g}^{i\to j_n}$ is calculated by Eq.(1) by using the data of MF10. When both data of MF9 and MF10 are not evaluated in JENDL-4.0 and JEFF-3.0/A, it is assumed that no meta-stable isomer is generated by reaction x of nuclide i (i.e. $I_{x,g}^{i\to j_0} = 1.0$).

When a neutron spectrum φ_g is given by a user, one-group isomeric ratio $\langle I_x^{i\to j_n}\rangle$, which is used in most of irradiation calculation codes, can be given by Eq.(2).

$$\langle I_x^{i\to j_n}\rangle = \sum_g \left(\sigma_{x,g}^{i\to j_n}\varphi_g\right) \Big/ \sum_g \left(\sigma_{x,g}^{i}\varphi_g\right) \tag{2}$$

3. Format of MAXS2015

In MAXS2015, the data of multi-group cross-sections and of the multi-group isomeric ratios are given by two text files for each nuclide. They are with file names of *ZZmmmn*.maxs-xs (nuclide-wise cross-section file) and *ZZmmmn*.maxs-isom (nuclide-wise isomeric ratio file), respectively. In the file name, '*ZZmmm*[*n*]' denotes a nuclide; 'ZZ' is a chemical symbol of the nuclide (e.g. Fe), '*mmm*' is a three-digit number to denote mass number (e.g. 054), and '*n*' is a character to denote the meta-stable level ('m': 1st meta-stable, 'n': 2nd meta-stable) and it is omitted for the ground state (e.g. *ZZmmmn*='Fe054' for ^{54}Fe).

Figure 1 shows the data format of a nuclide-wise cross-section file (e.g. Fe054.maxs). The data of each file consist of the header part and the cross-section data table. In the header part, the nuclide name, the number of energy groups, reaction types whose cross-sections are stored, etc. are written. Although the background cross-section and temperature are specified in the header part, they are not essential for users, because the MAXS2015 library is generated in the infinitely dilution condition, as mentioned above. These two parameters are prepared for the convenience of an advanced user who wants to use the effective cross-sections depending on two arbitrary parameters by replacing the original cross-section table with his own one.

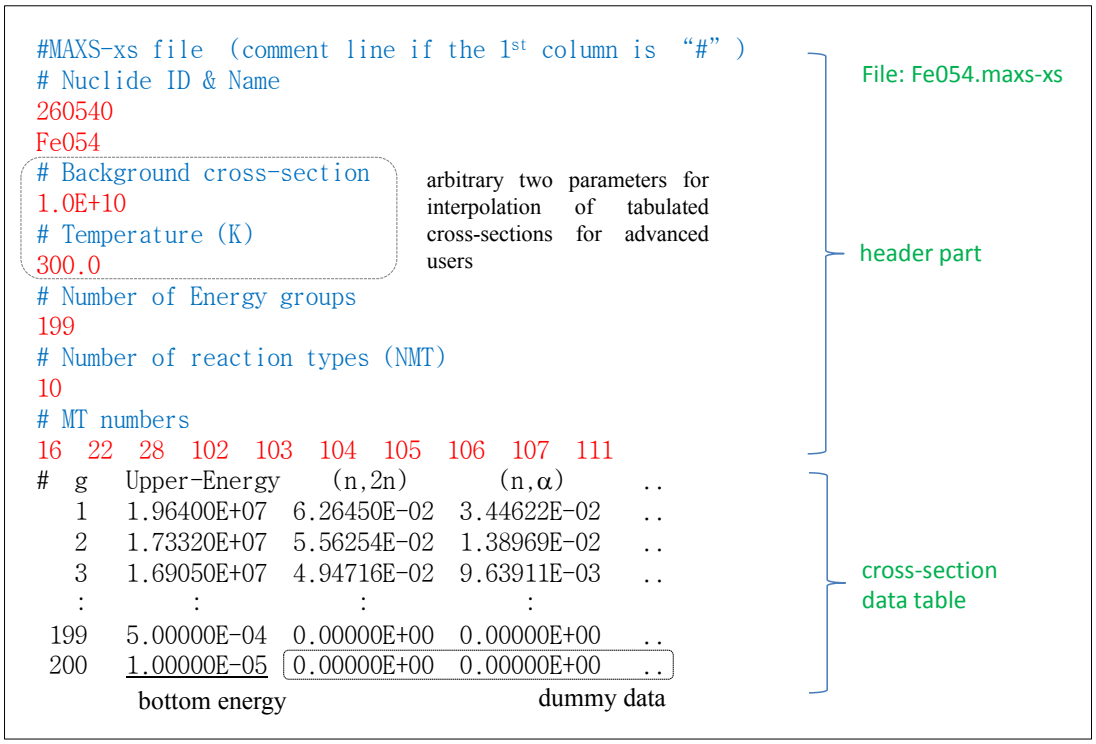

Fig. 1 Data format of a nuclide-wise cross-section file

Figure 2 shows the data format of a nuclide-wise isomeric ratio file (e.g. Fe054.maxs-isom). The data of each file consist of the header part, a data block of the energy group structure, and one or more data block(s) of isomeric ratio. The data block of isomeric ratio is repeated as many times as the number of

reaction types (NMT) in the header part. The reaction type of the isomeric ratio is specified at the top of each data block by MT number (e.g. 16 for (n,2n)), symbol to denote emission particles (e.g. '2n'), and residual nuclide (e.g. 'Fe053').

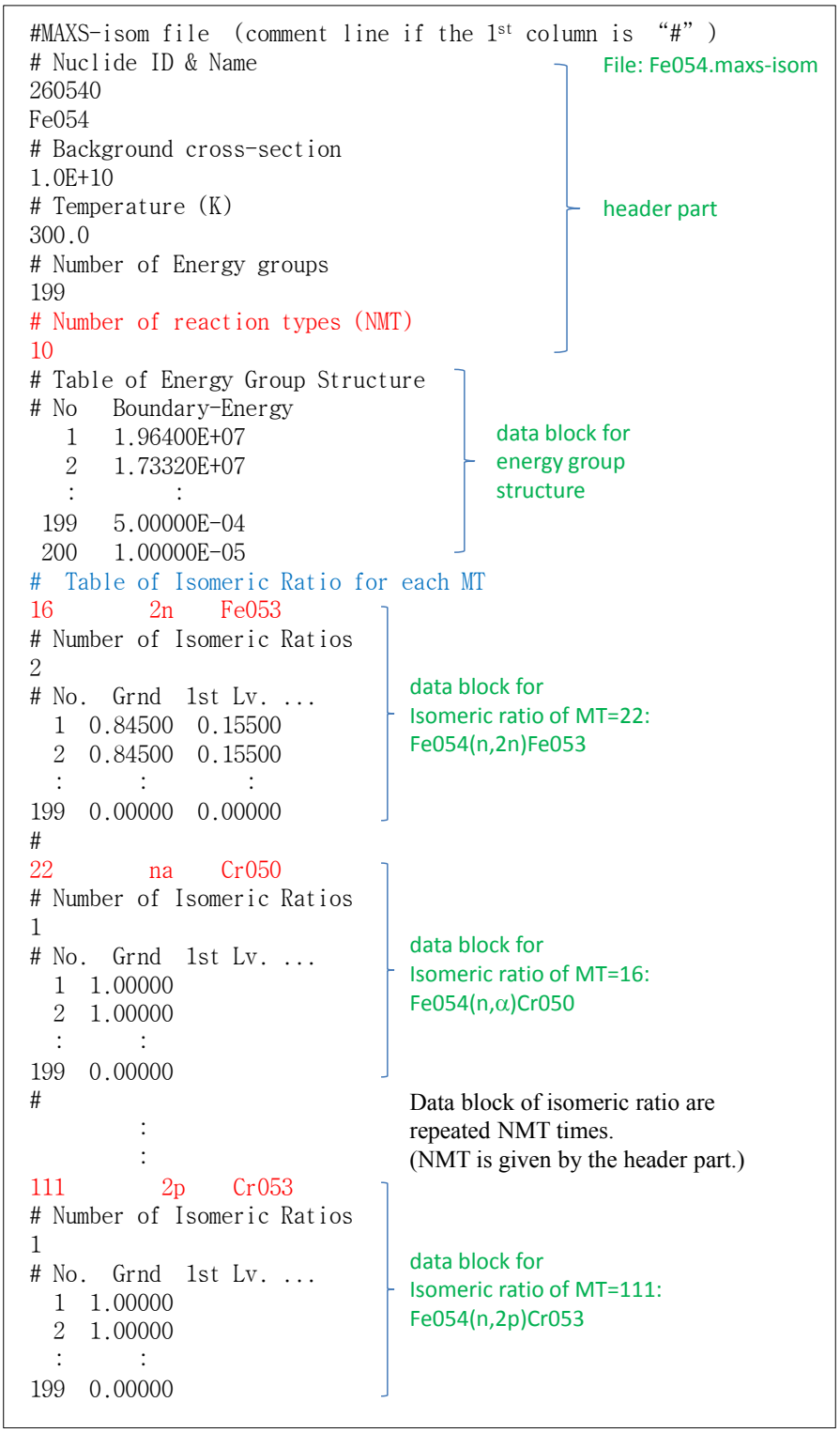

Fig. 2 Data format of a nuclide-wise isomeric ratio file

4. Auxiliary codes

The following two auxiliary codes are equipped with MAXS2015 for convenience of users.

- CONV_EGROUP

The energy group structure of the neutron spectrum to be used for one-group energy condensation is not always the same as that of MAXS2015. The CONV_ EGROUP code converts the neutron spectrum provided by a user to a new spectrum with the energy group structure of MAXS2015. Optionally, when the number of thermal energy groups is only one, it can be changed to the multi-thermal groups by assuming a Maxwellian distribution.

- MAXS2ORLIB

By using this auxiliary code and a neutron spectrum provided by a user, a new one-group cross-section library for the ORIGEN2[8] can be generated from MAXS2015. The one-group cross-sections of (n,*f*), (n,γ), (n,p), (n,α), (n,2n), (n,3n) in ORLIBJ40 are replaced with the one-group cross-sections generated from MAXS2015 and user's neutron spectrum.

5. Summary

A Multi-group activation cross-section library (MAXS2015) has been developed based on JENDL-4.0 and JEFF-3.0/A for radioactivity inventory calculation to optimize decommissioning strategy. MAXS2015 provides cross-section for 9504 reactions of 779 nuclides in 199-group energy structure.

References

[1] K. Tanaka, H. Ichige, H. Tanabe, "Radiological Characterization for Samll Type Light Water Reactor," Proc. of 19th Int. Conf. on Nuclear Engineering, Chiba, Japan, May 16-19 2011, Paper-ID: ICONE19-43234, (2011).

[2] K. Shibata, O. Iwamoto, T. Nakagawa, *et al*., "JENDL-4.0: A New Library for Nuclear Science and Engineering", J. Nucl. Sci. Technol. 48[1], 1 (2011).

[3] J-Ch. Sublet, A. J. Koning, R.A. Forrest, J. Kopecky, "The JEFF-3.0/A Neutron Activation File - EAF-2003 into ENDF-6 format -," JEFDOC-982, OECD/NEA (2003).

[4] R. E. MacFarlane, D. W. Muir, R. M. Boicourt, A. C. Kahler, "The NJOY Nuclear Data Processing System, Version 2012," LA-UR-12-27079, Los Alamos National Laboratory (2012).

[5] J. E. White, *et al*., "Production and Testing of the Revised VITAMIN-B6 Fine-Group and the BUGLE-96 Broad-Group Neutron/Photon Cross-Section Libraries Derived from ENDF/B-VI.3 Nuclear Data," NUREG/CR-6214, Rev. 1, U.S. Nuclear Regulatory Commission (2000).

[6] Cross Section Evaluation Working Group, "ENDF-6 Formats Manual, Data Formats and Procedures for the Evaluated Nuclear Data Files," ENDF-102 (BNL-90365-2009 Rev.2), National Nuclear Data Center (2012).

[7] JAEA Nuclear Data Center, "JENDL-4.0 updated files (JENDL-4.0u) and JENDL-4.0 Plus files," available from http://wwwndc.jaea.go.jp/jendl/j40/update/ (accessed 2015-7-14).

[8] A.G. Croff: "ORIGEN2: A Versatile Computer Code for Calculating the Nuclide Compositions and Characteristics of Nuclear Materials," Nucl. Technol. 62, 335 (1983).

This is a blank page.

10 Uncertainty Quantification of Core Characteristics Parameter Based on Covariance Data of Evaluated Nuclear Data Library

Tomohiro Endo, Kuniharu Kinoshita, Tomoaki Watanabe, Akio Yamamoto
Department of Materials, Physics and Energy Engineering, Nagoya University
Furo-cho, Chikusa-ku, Nagoya-shi, 464-8603, Japan
e-mail: t-endo@nucl.nagoya-u.ac.jp

In the present paper, uncertainty quantification (UQ) due to covariance data of evaluated nuclear data library will be presented, especially for the light water reactor (LWR) core analysis. In order to perform the practical UQ for the LWR, the random sampling (RS) method is applied instead of the "Sandwich formula" using sensitivity coefficients. As an example of the RS-based UQ, we will discuss uncertainties of assembly power distributions of BWR, compared with that of PWR. Through this comparison, it is confirmed that the uncertainties of assembly power distributions of BWR are significantly smaller than that of PWR under operating condition, because of the strong void feedback effect in the BWR core.

1. Introduction

Safety of nuclear reactor is ensured by a core analysis which numerically predicts core characteristics parameters. In this context, the accuracy and precision of core analysis are crucial to the reactor safety. Note that numerical results of core analysis have uncertainties due to various factors, *e.g.*, analytical modeling errors and uncertainties of input parameters. Among of these factors, uncertainties of microscopic cross-section data, *i.e.*, the covariance data of evaluated nuclear data library, could be a major factor. The uncertainty quantification (UQ) due to the covariance of nuclear data has been mainly studied in the field of the fast reactor core analysis [1]. In the case of light water reactor (LWR) core analysis, a complicated two-step calculation scheme (lattice physics calculation followed by core calculation) is commonly adapted [2,3], furthermore burnup and thermal-hydraulic feedback effects cause non-linear effects on the UQ; thus the UQ for the LWR core analysis is one of the challenging issues. One of the methodologies for the UQ is so-called "Sandwich formula", where uncertainties can be estimated on the basis of the linear approximation using the sensitivity coefficients of microscopic cross-sections for core characteristics parameters. If we try to apply the Sandwich formula for the UQ in the LWR core analysis, there are two difficulties; one is enormous amount of microscopic cross-section data and another is various types of target core characteristics parameters. Because of the enormous number of microscopic cross-section data, the direct forward calculation requires huge computational time to evaluate the sensitivity coefficients. On

the other hand, the adjoint calculation can be utilized to efficiently estimate sensitivity coefficients for criticality, reactivity worth, and reaction-rate ratios. However, if the burnup and thermal-hydraulic feedback effects are treated, it requires troublesome adjoint calculations; furthermore the calculation cost of adjoint approach increases in proportion to the number of target core characteristics parameters.

In order to device the practical UQ for the LWR, we focus on the random sampling (RS) method [4-6]. In the present paper, the overview of the UQ based on the RS method will be briefly explained. After that, the numerical examples of the UQ for typical LWR core analyses will be presented.

2. Uncertainty Quantification Using Random Sampling Method

In this section, the RS method for LWR core analysis is briefly explained in the case of UQ due to the covariance data of microscopic cross-section data. The procedures are as follows:

1. First of all, the covariance matrix for multi energy-group microscopic cross-section of each nuclide is generated using the NJOY code [7].
2. Several hundreds of microscopic cross-section libraries $\vec{\sigma}_i$ used in a lattice physics code are generated using multivariate normal random numbers with the covariance matrix of nuclear data:

$$\vec{\sigma}_i = \vec{\mu} + \mathbf{A}\vec{z}_i \quad (i = 1,2,\dots,N), \tag{1}$$

where $\vec{\mu}$ corresponds mean values of microscopic cross-section libraries; $\mathbf{A}$ is a square root matrix of the covariance matrix of nuclear data and can be numerically calculated using the singular value decomposition[4]; $\vec{z}_i$ is a column vector whose elements are standard normal random numbers and are independent of each other; and N is the number of random-sampling microscopic cross-section libraries.

3. For each of perturbed libraries $\vec{\sigma}_i$, forward calculations using a lattice physics code are carried out to evaluate a macroscopic cross-section table $\vec{X}_i$ for a core analysis code.
4. By the subsequent core analysis with each cross-section table $\vec{X}_i$, the corresponding core characteristics parameters $\vec{R}_i$ are evaluated. The vector $\vec{R}_i$ consists of criticality, reactivity worth (*e.g.*, control rod worth, Doppler and void coefficients), power peaking factors, assembly burnup, and so on.
5. Consequently, uncertainties of core characteristics parameters $\vec{R}$ due to the covariance data of nuclear data can be quantified through the following statistical procedure for the set of core analysis results:

$$\mathrm{cov}(\vec{R},\vec{R}) = \frac{1}{N-1}\sum_{i=1}^{N}\left\{\vec{R}_i - \left(\frac{1}{N}\sum_{i=1}^{N}\vec{R}_i\right)\right\}\left\{\vec{R}_i - \left(\frac{1}{N}\sum_{i=1}^{N}\vec{R}_i\right)\right\}^T, \tag{2}$$

where $\mathrm{cov}(\vec{R},\vec{R})$ is the covariance matrix of core characteristics parameters $\vec{R}$; and the superscript T means the transposed vector. The square-root of each diagonal element of $\mathrm{cov}(\vec{R},\vec{R})$ correspond to the standard deviation, *i.e.*, the 1σ uncertainty due to the covariance data of nuclear data. Non-diagonal elements of $\mathrm{cov}(\vec{R},\vec{R})$ represent the correlation among different core characteristics parameters.

As shown in the above-mentioned procedure, statistical errors are inevitably involved in the uncertainties estimated by the RS method. Through our previous researches, the bootstrap method [8,9] is applicable to reasonably estimate the statistical errors (*e.g.*, standard deviations or confidence intervals) of the RS-based uncertainties, without the assumption of normal distribution for target core characteristic parameter [10].

3. Numerical Examples of Uncertainties in Typical LWR Core Analyses

For examples of the UQ using the RS method, typical BWR and PWR core analyses were carried out using the covariance data of JENDL-4.0(u) [11,12] for ^{234}U, ^{235}U, ^{238}U, ^{237}Np, ^{238}Pu-^{242}Pu, ^{241}Am-^{243}Am, and ^{242}Cm-^{246}Cm, which are major contributors for uncertainties of core characteristics in the LWR core analysis. In the present UQ, capture, fission, elastic microscopic cross-section and number of neutrons emitted per fission (ν) were randomly sampled. As an efficient random sampling strategy, the Latin Hypercube Sampling (LHS) method were utilized in the sampling process based on Eq. (1) [13]. The total number of sampling libraries $\vec{\sigma}_i$ is 300; thereby relative statistical errors (1σ) of estimated uncertainties are ~4%, which can be roughly estimated by $1/\sqrt{2(N-1)}$ on the basis of the statistical property of χ^2-distribution if the frequency distribution of target core parameter follows a normal distribution.

The detail of numerical results and discussion will be reported in a scientific paper in the near future. In the present paper, we focus on the uncertainty of assembly power distribution in the BWR core, compared with that of PWR core. Figure 1 shows the relative uncertainty (which is defined by the ratio of standard deviation to mean) of assembly power distributions for octant BWR and PWR cores at the beginning of cycle (BOC). Note that the relative uncertainties of assembly power distributions tend to decreases, as the cycle burnup increases though detail results are not presented in this paper.

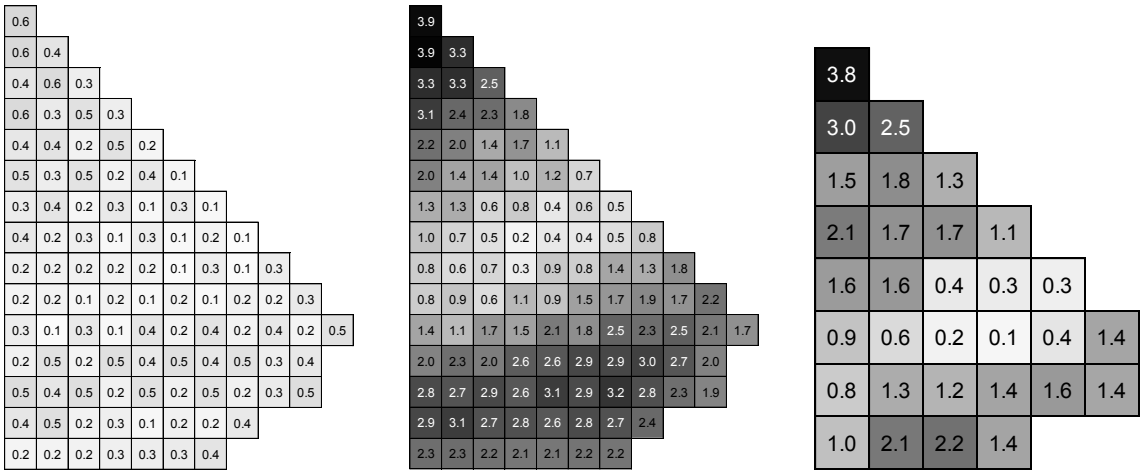

a) BWR/hot full power condition b) BWR/cold condition c) PWR/hot full power condition

Fig. 1 Relative uncertainties [%] of assembly power distribution of octant cores at the beginning of cycle

Interestingly, numerical results clarify that the uncertainties of assembly power distribution in the BWR (Fig. 1-a) are significantly smaller than those in the PWR (Fig. 1-c) under the operating condition (hot full power condition). It is noted that, in the case of BWR at the cold condition (Fig. 1-b), where the assembly power distribution is unaffected by the void feedback effect, then the uncertainties of BWR are comparable to that of PWR. This results suggest that the strong void feedback effect in the BWR tends to prevent large variations of assembly power due to the perturbation of cross-section data; consequently the assembly power distribution of BWR are more robust for uncertainties of cross-section data under the hot full power condition. In addition, it is interesting to note that the uncertainties of assembly power distributions tend to be small in the intermediate region between the center and the periphery, in both BWR and PWR cores. The perturbation due to uncertainty of cross-section results in excitation of spatial higher modes of neutron flux. In general, a core loading pattern in typical LWR has quadrant or octant symmetry; thereby the excitation of higher modes related to the azimuth angle direction could be suppressed, in other words, the higher order modes related to the radial direction (Bessel function-like modes) are more likely to be excited [14]. Consequently, the symmetrical loading pattern of LWR results in “in-out” power tilt due to the covariance data of nuclear data. That is why the uncertainties of assembly power distributions are small at the core middle region, which corresponds to the nodal point of higher mode related to the radial direction.

4. Conclusion

The RS-based UQ technique is one of the practical and efficient approaches to evaluate uncertainties of core characteristics parameters, especially for the LWR core analysis which treat burnup and thermal-hydraulic feedback effects with the two-step (lattice/core) calculation scheme. As a further research, we have been investigating the applicability of the RS method to the cross-section adjustment technique [15] and the bias factor method [16] for the LWR core analysis, in order to reduce the bias and the uncertainty in the LWR core analysis.

Acknowledgements

We sincerely appreciate Nuclear Fuel Industries, Ltd. for the technical supports for the use of randomly-sampled microscopic cross section libraries. This work was supported in part by JSPS KAKENHI, Grant-in-Aid for Scientific Research (C) (24561040).

References

[1] Sugino K, Ishikawa M Numata K, et al.: “Development of a standard data base for FBR core design (XIV) - Analyses of extensive FBR core characteristics based on JENDL-4.0,” JAEA-Research 2012-013, (2012), 411p.

[2] CASMO-4 A Fuel Assembly Burn-up Program. User's manual. Waltham (MA): Studsvik Scandpower Inc; 2009 (SSP-09/443-U Rev 0).

[3] SIMULATE-3 advanced three-dimensional two-group reactor analysis code. Waltham (MA): Studsvik Scandpower Inc; 2009 (SSP-09/447-U Rev 0).

[4] Kato S, Endo T, Yamamoto A, et al. Random sampling based cross-section adjustment technique for LWR core analysis. Paper presented at: 2013 International Congress on Advances in Nuclear Power Plants (ICAPP'13); 2013 Apr 14-18; Jeju Island, Korea.

[5] Watanabe T, Endo T, Yamamoto A, et al. Uncertainty and correlation estimation of reload safety parameters of PWR using random sampling method. Trans. Am. Nucl. 2013;109:1365-1368.

[6] Kinoshita K, Yamamoto A, Endo T, et al. Uncertainty quantification of BWR core characteristics using Latin hypercube sampling method. Paper presented at: PHYSOR2014; 2014 Sep. 28-Oct. 2; Kyoto, Japan.

[7] Macfarlane RE, Muir DW. The NJOY nuclear data processing system version 91. Los Alamos (NM): Los Alamos National Laboratory; 1994 (LA-12740-M).

[8] Efron B. Bootstrap methods: another look at the Jackknife. Ann Stat. 1979;7:1-26.

[9] Efron B. Better bootstrap confidence intervals. J Am Stat Assoc. 1987;82:171-185.

[10] Endo T, Watanabe T, Yamamoto A. Confidence interval estimation by bootstrap method for uncertainty quantification using random sampling method. J. Nucl. Sci. Technol. 2015;52:993-999.

[11] Shibata K, Iwamoto O, Nakagawa T, et al. JENDL-4.0: a new library for nuclear science and engineering. J. Nucl. Sci. Technol. 2011;48:1-30.

[12] JENDL-4.0u [Internet]. Japan: Japan Atomic Energy Agency; 2012 Sep 14; [cited 2014 Dec 31]. Available from: http://wwwndc.jaea.go.jp/jendl/j40/update/

[13] Kinoshita K, Yamamoto A, Endo T, et al. Uncertainty quantification of neutronics characteristics using Latin hypercube sampling method. Paper presented at: PHYSOR2014; 2014 Sep. 28-Oct. 2; Kyoto, Japan.

[14] Endo T, Ohori K, Yamamoto A. Application of the robust design concept for fuel loading pattern. J .Nucl. Sci. Technol. 2011;48:1077-1086.

[15] Watanabe T, Endo T, Yamamoto A, et al. Cross section adjustment method based on random sampling technique. J. Nucl. Sci. Technol. 2014;51:590-599.

[16] Endo T, Yamamoto A, Watanabe T. Bias factor method using random sampling technique. J. Nucl. Sci. Technol. [to be published].

This is a blank page.

11 Design Studies for a Small Accelerator-based Be (p, n) Neutron Source for Boron Neutron Capture Therapy

Fujio HIRAGA, Yusuke TAKIZAWA, Ryuichi INOUE and Yoshiaki KIYANAGI

Graduate school of engineering, Hokkaido University
Kita-13, Nishi-8, Kita-ku, Sapporo 060-8628, Japan
e-mail: hiraga@eng.hokudai.ac.jp

Abstract

A calculation model of the Be (p, n) neutron source for the BNCT, which is driven by an 8 MeV accelerator in a proton beam of 10 mA current, was designed to intensify the neutron beam at a treatment position, to maximize the efficiency of treatment for tumors, and to ensure the safety of treatment. With this calculation model, the residual radioactivity that is induced in the various components of neutron source was estimated, and a way to drop the residual radioactivity as well as a possibility of a reduction in radioactive waste was discussed.

Introduction

The boron neutron capture therapy (BNCT), which selectively irradiates tumor cells that have taken up a sufficient amount of ^{10}B, is considered to be effective in treatments for tumors. The BNCT has been performed in research reactor sites; however, high thermal output and huge radioactive waste from research reactors will cost to maintain these facilities. The BNCT will be therefore performed in hospital sites if accelerator-based compact neutron sources that generate sufficient neutron beam at a treatment position are available.

Small accelerators that generate a beam of protons with energy less than 10 MeV have a merit of easy construction of accelerators. In this energy, the yield of neutron by ^{7}Li (p, n) reactions is higher than that of Be (p, n) reactions, but there is a merit of the Be target that is much easier than the Li target to make and handle. Moreover, the neutrons from the Be (p, n) reactions by protons with energies around 10 MeV should be effective in easy maintenance in hospital sites, since the neutrons with energies less than 10 MeV should have the advantage of lower neutron-induced radioactivity than neutrons having higher energies.

The present study is aimed at designing a Be (p, n) neutron source driven by a 8 MeV accelerator in a proton beam of 10 mA current. Here, we examined the material and the dimensions of Be target to intensify the neutron beam at a treatment position. Moreover, the dimensions of a moderator system as well as a collimator were examined to maximize the efficiency of treatment for tumors, and to ensure the safety of

treatment. With this calculation model, the residual radioactivity that is induced in the various components of neutron source was estimated, and the dose rate of photons around the Be target or at the treatment position as a function of the cooling time was examined. Finally, we investigated a way to drop the residual radioactivity of the Be target and discussed a reduction in radioactive waste that is indispensable for the use of this system in hospital sites.

Calculation model and methods

Figure 1 shows the calculation model of the Be (p, n) neutron source. The Be foil has a neutron yield of 1.03 x 10^{14} [1/sec]. The Cu base of Be target, which includes a 0.3 cm-thick water zone for coolant, has high heat conductivity, and the effects of the thickness of the Cu base on the intensity of neutron beam at a treatment position were examined; a 0.05 cm-thick foil of Ta or Nb or Pd or Ti was set between the Be foil and the Cu base to avoid the blistering of Cu base. The Fe filter was used to reduce the fast neutrons from radiation from the Be target; the MgF_2 moderator and the Cd shield for thermal neutrons were used to make a proper spectrum of neutron beam at the treatment position; the effects of the thicknesses of Fe filter and MgF_2 moderator on properties of neutron beam were examined; here, the diameter of 50 cm of Fe filter and MgF_2 moderator was used, since preliminary calculations showed that this diameter of Fe filter and MgF_2 moderator were sufficient to produce epithermal neutrons. The Bi shield for photons was used to reduce photons from the neutron beam. The collimator, which is made with polyethylene including LiF, was used to drop the radiation exposure to the organs around the object for the treatment, and the effects of the thickness and the aperture of collimator on properties of neutron beam were examined. The Pb shield was used to reduce the dose rate of photons around the treatment position. The Be target, Fe filter and MgF_2 moderator were enclosed in the Pb reflector.

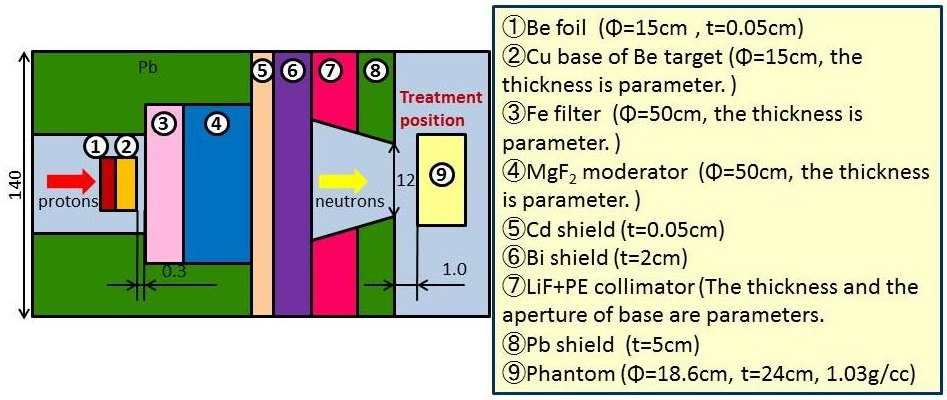

Fig.1 Calculation model of Be (p, n) neutron source

Here, the neutron flux and photon flux in free air around the treatment position were calculated by MCNPX [1]; the neutron dose and photon dose were estimated using kerma coefficients for soft tissue. Moreover, the residual radioactivity that is induced in the components of neutron source was estimated by using DCHAI-SP 2001 [2]. Further, the RBE dose in a phantom that was placed on the treatment position

was calculated by the sum of boron dose, neutron dose and photon dose [3]; here, the ^{10}B concentrations for tumor and normal tissue of 30 ppm and 10 ppm were assumed. **Figure 2** shows an example of calculated RBE dose for tumor or normal tissue as a function of the depth in a phantom. Here, we must limit the maximum of the RBE dose for normal tissue to 10 [Gy-eq] to ensure the safety of treatment; a higher value for the maximum of the RBE dose for tumor is more effective in treatments for tumors. The dose ratio in a phantom, which is defined by the ratio of the maximum of RBE dose of tumor tissue to the maximum of RBE dose of normal tissue, therefore dominates the efficiency of treatments for tumors and a higher value of the dose ratio in a phantom is desired.

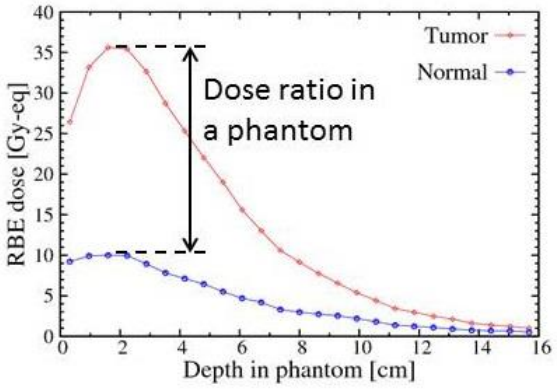

Fig.2 Calculated RBE dose for tumor or normal tissue as a function of the depth in a phantom

We designed the neutron source to obtain the following properties of neutron beam which are necessary for the BNCT: (a) the epithermal neutron flux in free air at a treatment position is more than 1.5 x 10^9 [1/cm^2/sec] to reduce the time of treatment per patient, (b) the dose ratio in a phantom that is noted above is more than three to obtain a higher efficiency of treatment for tumors, (c) the ratio between the total neutron current and the total neutron flux (J/φ) in free air at a treatment position is more than 0.7 to limit divergence of the neutron beam and reduce undesired irradiation of other tissues, and (d) the dose of neutrons on the Pb shield at a distance of 25 cm from the neutron beam axis is less than 1 % of the value at the neutron beam axis to drop the radiation exposure to the organs around the object for the treatment. Here, the properties of (a) and (c) match the desired neutron beam parameters for the BNCT shown by IAEA [4], and the properties of (b) and (d) meet a medical criterion[5] that is adopted in Japan.

Results and discussions

1. Material and thickness of the base of Be target

With changing the thickness of the Cu base of Be target, the total neutron flux in free air at the treatment position was calculated. The cases where the base of Be target is made with graphite or beryllium oxide were calculated for comparison, since graphite has a lower cross section of neutrons and beryllium oxide has a higher strength. **Figure 3** shows the dependence of total neutron flux at the treatment position on the thickness of base of Be target. Here, the thicknesses of Fe filter and MgF_2 moderator were set at 11

cm and 30 cm, and the curve showing Be + Nb + Cu is almost identical to that of Be + Pd + Cu. When the thickness of the Cu base increased by 1 mm, the reduction of the total neutron flux was estimated at 0.6 [%/mm], which was smaller than those for graphite (0.8 [%/mm]) and beryllium oxide (1.1 [%/mm]). Moreover, the total neutron flux for the BeO base was 3 % smaller than that for the Cu base. These results showed that the thin Cu base, which can bare the thermal stress in the Be target, should be used. We therefore assumed that we use a copper can of 15 cm diameter and 0.7 cm thickness having a 0.3 cm-thick water layer for coolant as the base of Be target.

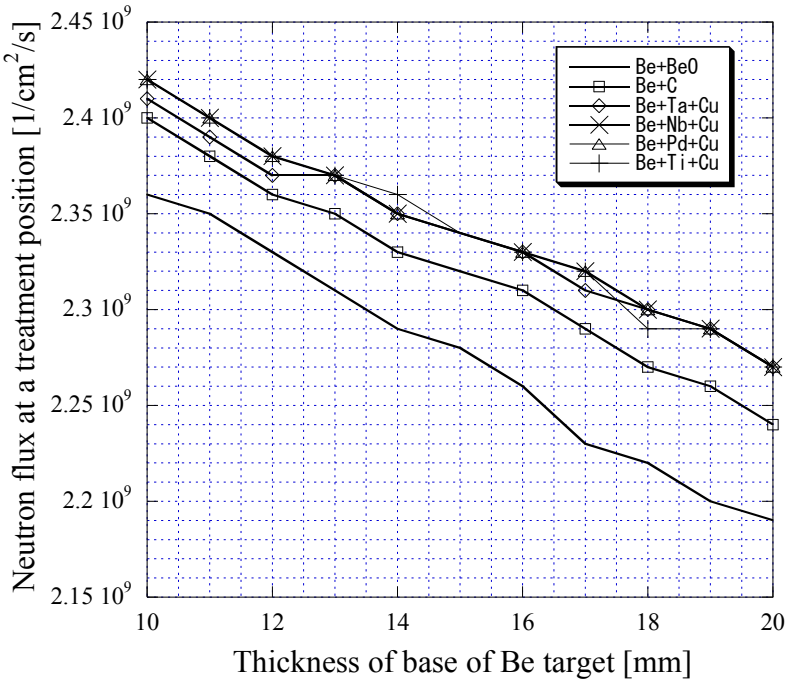

Fig.3 Dependence of total neutron flux at the treatment position on the thickness of base of Be target

2. Thickness and aperture of collimator

With changing the thickness and aperture of collimator, properties of neutron beam were examined about the cases with or without the phantom at the treatment position. Here, a cylindrical aperture was used in these calculations, and the thicknesses of Fe filter and MgF_2 moderator were set at 15 cm and 31 cm, respectively. The dependence of properties of neutron beam on the thickness of collimator having an aperture of 12 cm was summarized in **Table 1**. With the increase in the thickness of collimator, the dose ratio in a phantom hardly changes except for the drop at the thickness of 15 cm but the epithermal neutron flux in free air at the treatment position decreases. Moreover, calculation results about the dose distribution of neutrons on the Pb shield showed that the neutron dose at a distance of 25 cm from the beam axis was less than 1 % of the value at the beam axis when the thickness of collimator exceeds 16 cm. We therefore decided that we use the thickness of collimator of 16 cm.

Table 1 Dependence of properties of neutron beam on thickness of collimator having an aperture of 12 cm

Thickness of collimator [cm]	Dose ratio in a phantom	Epithermal neutron flux at a treatment position [1/cm^2/sec]
10	3.56	7.70 x 10^8
15	3.46	4.69 x 10^8
16	3.58	4.64 x 10^8
17	3.59	4.24 x 10^8

The dependence of properties of neutron beam on the aperture of collimator having a thickness of 16 cm is summarized in **Table 2**. The dose ratio in a phantom has a maximum at the aperture of about 30 cm, and this is explained by calculation results that the dose of fast neutrons in free air at the treatment position increases when the aperture increases beyond 30 cm and consequently causes the increases in the RBE dose of normal tissue but brings about small changes in the RBE dose of tumor tissue. Further, the J/φ at the treatment position becomes less than 0.7 when the aperture exceeds 40 cm. These results showed that we should use the aperture of base of collimator around 30 cm.

Table 2 Dependence of properties of neutron beam on aperture of collimator having a thickness of 16 cm

Aperture of collimator [cm]	Dose ratio in a phantom	Epithermal neutron flux [1/cm^2/sec]	J/φ
20	3.53	9.82 x 10^8	0.78
24	3.54	1.26 x 10^9	0.76
28	3.57	1.52 x 10^9	0.74
32	3.55	1.74 x 10^9	0.72
36	3.50	1.95 x 10^9	0.71
40	3.48	2.12 x 10^9	0.69
44	3.33	2.25 x 10^9	0.68

3. Thicknesses of Fe filter and MgF_2 moderator

By repeated calculations with changing the thicknesses of Fe filter and MgF_2 moderator, we obtained the properties of neutron beam necessary for the BNCT. Here, we examined the cases where the collimator has the aperture of base of 28 cm or 32 cm; the thickness of 16 cm and the aperture of top of 12 cm of the collimator were used. **Table 3** summarizes the difference in the properties of neutron beam between the cases that the aperture of base of collimator is 28cm or 32 cm. The epithermal neutron flux and the J/φ in free air at the treatment position for the aperture of base of 28 cm are almost identical to those of the aperture of base of 32 cm; however, the dose ratio in a phantom for the aperture of base of 32 cm is higher than that of the aperture of base of 28 cm. These results show that we should use the thicknesses of 15 cm and 33 cm for the Fe filter and MgF_2 moderator as well as the aperture of base of 32 cm for the collimator.

Table 3 Difference in properties of neutron beam between cases that the aperture of base of collimator is 28cm or 32 cm

Aperture of base [cm]	Moderator thickness [cm]	Filter thickness [cm]	Dose ratio in a phantom	Epithermal neutron flux [1/cm^2/sec]	J/φ
28	31	15	3.57	1.52 x 10^9	0.74
32	33	15	3.64	1.52 x 10^9	0.72

4. Residual radioactivity that is induced in the components of neutron source

The dose rate of photons near the Be target, which has a 0.7 cm-thick can for the Cu base with a 0.05 cm-thick foil to avoid the blistering of copper, was calculated as a function of the cooling time. The dose rate of photons at the treatment position as a function of the cooling time was also examined. Here, we set the condition of calculations at two hours irradiation per day for 250 days operation of an 8 MeV accelerator in a proton beam of 10mA current.

It turned out that the anti-blistering foil of Ta, in which the atoms of ^{182}Ta are induced, should not be used since the dose rate of photons near the Be target after a cooling time of 10 days is still high, 3 mSv/hr, and is attributable to ^{182}Ta; however, the dose rate near the Be target at 10 days were low, 100μSv/hr, for the cases of the anti-blistering foils of Nb or Pd or Ti. It also turned out that radioactive elements having long lifetime are hardly generated in the massive components such as the Fe filter and MgF_2 moderator and Pb reflector, and the dose rate of photons at the treatment position after a cooling time of 24 hours becomes low, 1 μSv/hr. This result indicates that there is a merit of a reduction in radioactive waste that is indispensable for the use of this system in hospital sites.

Conclusions

We designed a calculation model of Be (p, n) neutron source that is driven by an 8 MeV accelerator in a proton beam of 10 mA current. To intensify the neutron beam at a treatment position, the thin copper base of Be target, which can bare the thermal stress in the Be target, should be used. To maximize the efficiency of treatments for tumors and to ensure the safety of treatment, we should use the thicknesses of 15 cm and 33 cm for the Fe filter and MgF_2 moderator as well as the aperture of base of 32 cm and the thickness of 16 cm for the collimator. To drop the residual radioactivity that is induced in the Be target, the anti-blistering foil of Ta, in which ^{182}Ta nucleuses are induced, should not be used. Further, calculation results indicated that there is a merit of a reduction in radioactive waste that is indispensable for the use of this system in hospital sites.

References

1. D. B. Pelowitz, MCNPX User's Manual Version 2.6.0. LA-CP-07-1473 (2008).
2. T. Kai et al., "DCHAI-SP 2001: High Energy Particle Induced Radioactivity Calculation Code",

JAERI-Data/Code 2001-016 (2001), 82p.

3. R. Inoue et al., “Optimum design of a moderator system based on dose calculation for an accelerator driven Boron Neutron Capture Therapy”, Appl. Radiat. Isot., 88, 225 (2014).
4. Current Status of Neutron Capture Therapy, IAEA-TECDOC-1223 (2001).
5. H. Tanaka et al., “Improvement of dose distribution in phantom by using epithermal neutron source based on the Be(p,n) reaction using a 30 MeV proton cyclotron accelerator”, Appl. Radiat. Isot., 67, 258 (2009).

This is a blank page.

12 Elemental analysis by neutron resonance transmission method

Hiroyuki HASEMI[a], Masahide HARADA[b], Tetsuya KAI[b], Motoki OOI[b], Koichi KINO[a],
Takashi KAMIYAMA[a], Yoshiaki KIYANAGI[c]
[a]Graduate School of Engineering, Hokkaido University
Kita-13, Nishi-8, Kita-ku, Sapporo 060-8628, Japan
[b]J-PARC Center, Japan Atomic Energy Agency
2-4 Shirakata-shirane, Tokai-mura, Naka-gun, Ibaraki 319-1195, Japan
[c]Graduate School of Engineering, Nagoya University
Furo-cho, Chikusa-ku, Nagoya 464-8603, Japan
e-mail: hasemi@eng.hokudai.ac.jp

Using the neutron resonance transmission (NRT) method that measures neutron transmission spectrum by a time-of-flight (TOF) method, we can observe the neutron resonance spectrum. By analyzing the resonance dips appearing in the transmission spectrum, atomic densities in a sample and local temperatures which depend on the Doppler broadening due to atomic thermal motion can be estimated non-destructively. Presently, the elemental analysis/imaging using the NRT method has been studying at the NOBORU instrument installed in J-PARC/MLF/BL10. In order to perform the NRT analysis/imaging quantitatively, we developed the analysis system for NRT firstly and then performed some NRT experiments at NOBORU.

1. Introduction

Neutron resonance transmission (NRT) is the method that observes the neutron resonance reaction by measurement of neutron transmission spectrum using time-of-flight (TOF) method. Since the transmission factor is proportional to the atomic density in a sample, we can non-destructively estimate the density by analyzing the transmission dips due to the neutron resonance reaction. In addition, we can investigate local temperatures by analyzing the Doppler broadening due to atomic thermal motion. Atomic density and temperature imaging can be achieved by NRT combined with two-dimensional neutron detector. We have attempted to perform NRT analysis and imaging for industrial products in the energy region between 1 eV and a few eV at the NeutrOn Beam-line for Observation and Research Use (NOBORU) [1,2] instrument installed at beam line 10 (BL10) at the Materials and Life Science Experimental Facility (MLF) at Japan Proton Accelerator Research Complex (J-PARC).

The observed resonance dips are expressed by the convolution of the theoretical transmission and the

pulse function (i.e., the emission time distribution from a moderator). Therefore, the pulse function should be reproduced at arbitrary neutron energies in order to analyze resonance dips quantitatively. We have developed the pulse function expressing the neutron pulse shapes of the NOBORU by the Monte Carlo simulation, and found that the Cole-Windsor function [3] was the best function expressing the simulated pulse [4]. In order to analyze the transmission dips considering the pulse function, we applied the function to the REFIT (Multilevel Resonance Parameter Least Square Fit of Neutron Transmission, Capture, Fission & Self Indication Data) code [5,6].

In order to evaluate the quality of our NRT analysis system, we measured the transmission spectra of several samples at the NOBORU and analyzed these using the revised REFIT code. The atomic densities of sample element, tantalum, silver and copper were estimated by fitting the experimental obtained resonance dips.

2. Resonance shape analysis system

The REFIT code can be used to deduce resonance parameters from the experimental spectra. This code performs convolution of the pulse function with theoretical transmission. The observed transmission spectrum $T_{obs}(t)$ is expressed as

$$T_{obs}(t) = \int_0^\infty R(t,E)\exp[-\sigma(E)d]dE, \quad (1)$$

where $R(t,E)$ is the pulse function, $\sigma(E)$ is the total cross section and d is atomic density. This code is applicable to evaluate atomic density from transmission spectrum. Since the code have not been implemented the dedicated function for the NOBORU, we have rewritten the subroutines of the code to calculate the transmission spectrum considering the pulse function.

The time structure of proton pulses from J-PARC synchrotron accelerator consists of double bunches with a separation of 0.6 μs. In the case of decoupled moderator at J-PARC, the effect of the double pulse on the pulse function begins to appear above 10 eV [7], the time structure of double bunches should be considered for the resonance analysis. Therefore, we obtained the time structure of the proton pulse from J-PARC 3 GeV synchrotron by the current transformer installed in the 3 GeV proton transport facility. We can reproduce the transmission spectrum accounting for the pulse function and the double pulse by the REFIT code because the REFIT code can treat the time structure of the proton as a table of data point of time versus amplitude.

Using the revised REFIT code, we were able to analyze the transmission spectra in the energy region between 1 eV and 10 keV at the NOBORU.

3. Experiments

In order to evaluate the quality of the analysis using the revised REFIT code, we carried out NRT experiments for several elements at the NOBORU. As test samples, 10 μm-thick Ta foil and 1 mm-thick Ag plates and 1 mm-thick Cu plates were chosen. The Ta foil and the Ag plates were used for analysis of the

resonances up to several hundred eV. On the other hand, the Cu plates were used in the energy range from several hundred eV to a few keV. We measured NRT of the Ta foil at a J-PARC beam power of 200 kW, and that of the Ag and the Cu plates at that of 300 kW.

A Gas Electron Multiplier (GEM) developed by High Energy Accelerator Research Organization (KEK) [8] was used as a neutron detector in both experiments. Since the GEM detector has low gamma-ray efficiency and high time resolution, it is suitable for the NRT measurement. The time bin width was 150 ns for Ta, 100 ns for Ag and 40 ns for Cu.

The schematic layout of the experiments is shown in figure 1. For the experiment of Ta, the detector position was 14.19 m from the moderator, and the sample was located immediately in front of the detector. For the experiment of Ag and Cu, the detector position was 13.99 m, and the distance between the sample and the detector was 20 cm. The Rotary Collimator (RC) installed in BL10 was used for beam collimating to avoid counting loss, and the size of RC was “small” in all experiments. In addition, in order to cut the frame-overlap neutrons, a Cd filter was located upstream of the samples.

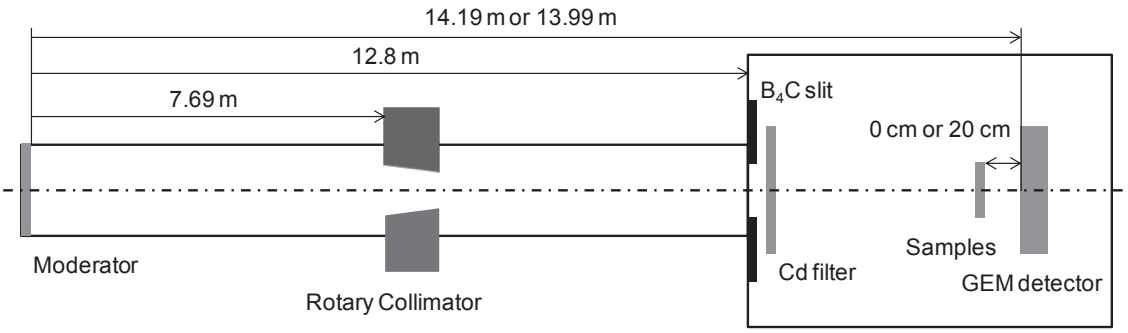

Fig. 1. Schematic layout of the experiments for NRT measurements at the NOBORU.

4. Results and discussion

4.1. Evaluation of atomic densities of Ta and Ag

Using the revised REFIT code, we carried out fitting calculations on the transmission dips due to the Ta foil and the Ag plate. The resonance parameters listed in the evaluated nuclear data library, JENDL-4.0 [9], were used for calculation of resonance cross section. The free gas model was used to calculate the Doppler broadening, and the sample temperatures were 300 K. In this work, only uncertainties due to counting statistics were considered.

Figure 2 shows the measured resonance dips due to the 4.28 eV resonance of ^{181}Ta and the 133.9 eV resonance of ^{109}Ag with fitted curves calculated by the REFIT. The estimated atomic area density of the Ta foil was $(5.44 \pm 0.13) \times 10^{-5}$ atoms/barn from fitting to the 4.28 eV resonance dip (actual density of the Ta foil was 5.48×10^{-5} atoms/barn). We could estimate the atomic density within an error of 1% in the case of analysis for the resonance dips of the Ta foil. The estimated atomic area density of the Ag plate was $(5.54 \pm 0.10) \times 10^{-3}$ atoms/barn from fitting to the 133.9 eV resonance dip (actual density of the Ag plate was 5.81×10^{-3} atoms/barn). For the 133.9 eV resonance, although we could reproduce the shape of resonance dip,

the density of the sample was underestimated by 4.6%. Since the impact of the pulse function was predominant above 100 eV [4], this underestimation may have been caused by the deviation of the pulse function due to the fluctuation of the width of proton pulse from 3 GeV synchrotron.

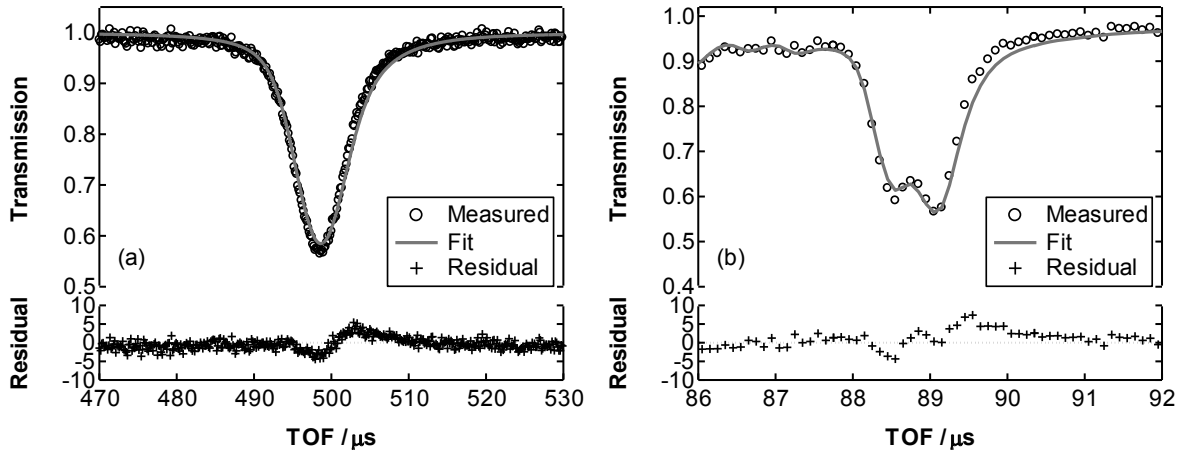

Fig. 2. Measured resonance dips due to (a) the 4.28 eV resonance of ^{181}Ta and (b) the 133.9 eV resonance of ^{109}Ag with fitted curves [4].

4.2. Evaluation of atomic density of Cu

We carried out the fitting to the resonance dips due to the Cu plate using the revised REFIT with the JENDL-4.0. However, the resonance dips calculated by the resonance parameters of JENDL-4.0 were not adopted by the experimental obtained dips. Therefore, we tried to calculate the dips using the resonance parameters reported by Weigmann and Winter [10]. Table 1 show the resonance parameters, the neutron width Γ_n and the radiation width Γ_γ, of Cu listed in the JENDL-4.0 and reported by Weigmann and Winter. Here, the resonance energies, E_R, in the JENDL-4.0 were used. The radiation width of Wigmann and Winter were adopted by that of the JENDL-4.0 except for the 230 eV resonance. In particular, the neutron widths of the 579 eV resonance differ from each other.

Figure 3 shows the resonance dips due the 579 eV resonance calculated by the parameters of JENDL-4.0 and that of Weigmann and Winter. In this calculation, atomic density was fixed. The calculated dip using the parameters of Weigmann and Winter was adopted by the experimental obtained dip. Therefore, in this work, we used the parameters of Cu reported by Weigmann and Winter.

Figure 4 shows the measured resonance dips due to the Cu plate with fitted curves calculated by the REFIT. We could fit the resonance dips broadened by the double bunched proton beam. The estimated atomic area density of the Cu plate was $(8.05 \pm 0.29) \times 10^{-3}$ atoms/barn from fitting to the 230 eV resonance dip and $(8.09 \pm 0.13) \times 10^{-3}$ atoms/barn from fitting to the 579 eV resonance dip (actual density of the Cu plate was 8.41×10^{-3} atoms/barn). As is the case in the fitting to the 133.9 eV resonance dip of the Ag plate, the density of the sample was also underestimated by about 5%. The main reason of these underestimations above 100 eV may have been the fluctuation of the proton pulse.

Table 1. Resonance parameters of Cu.

Isotope	E_R [eV]	JENDL-4.0 [9]		Weigmann and Winter [10]	
		Γ_n [eV]	Γ_γ [eV]	Γ_n [eV]	Γ_γ [eV]
^{65}Cu	230	0.01776	0.245	0.0178	0.24
^{63}Cu	579	0.59	0.485	0.86	0.485
^{63}Cu	2038	42.6666	0.5	43.5	0.57
^{65}Cu	2529	17.6	0.36	16.8	0.36
^{63}Cu	2642	5.28	0.58	4.5	0.58

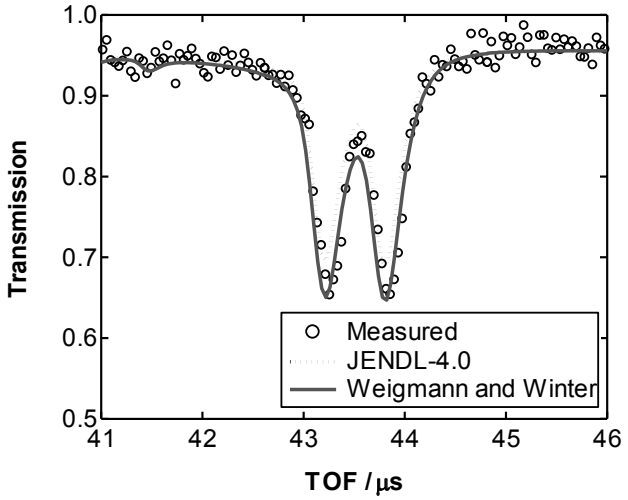

Fig. 3. Comparison of calculated resonance dips due to the 579 eV resonance of ^{63}Cu.

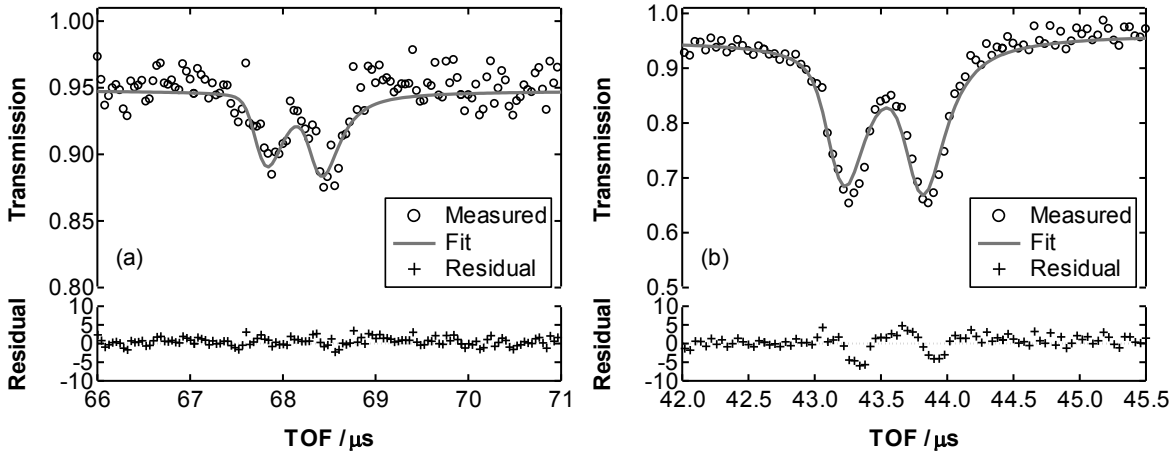

Fig. 4. Measured resonance dips due to the Cu plate with fitted curves. (a) is 230 eV resonance of ^{65}Cu [4] and (b) is 579 eV resonance of ^{63}Cu.

5. Conclusions

In order to perform quantitative NRT analysis/imaging, we have developed the resonance shape analysis system based on the REFIT code and carried out some NRT experiments at the NOBORU in J-PARC/MLF/BL10. The resonance dips due to Ta, Ag and Cu were obtained and analyzed by the revised REFIT code. We found that the resonance parameters of Cu reported by Weigmann and Winter were adopted by the experimental obtained data. We could estimate the atomic area densities within an error of about 1% at the energy region of 1 eV to 100 eV. On the other hand, above 100 eV, the densities were underestimated by about 5%. Since the impact of the pulse function was predominant at this energy region, the main reason of the underestimation was possibly the fluctuation of the proton pulse width.

Acknowledgements

The authors would like to acknowledge Dr. Kenichi Oikawa, Dr. Takenao Shinohara and Dr. Mariko Segawa in J-PARC Center for their help during the experiments at NOBORU and Prof. Shoji Uno in KEK for his cooperation with our use of the GEM detector.

This work was supported by a Grant-in-Aid for Scientific Research (S) from the Japan Society for the Promotion of Science (No. 23226018).

References

[1] K. Oikawa, F. Maekawa, M. Harada, T. Kai, S. Meigo, Y. Kasugai, M. Ooi, K. Sakai, M. Teshigawara, S. Hasegawa, M. Futakawa, Y. Ikeda, N. Watanabe: Nucl. Instr. and Meth. A **589**, (2008) 310.

[2] F. Maekawa, K. Oikawa, M. Harada, T. Kai, S. Meigo, Y. Kasugai, M. Ooi, K. Sakai, M. Teshigawara, S. Hasegawa, M. Futakawa, Y. Ikeda, N. Watanabe: Nucl. Instr. and Meth. A **600**, (2009) 335.

[3] F. Izumi, H. Asano, H. Murata and N. Watanabe: J. Appl. Cryst. **20**, (1987) 411.

[4] H. Hasemi, M. Harada, T. Kai, T. Shinohara, M. Ooi, H. Sato, K. Kino, M. Segawa, T. Kamiyama, Y. Kiyanagi: Nucl. Instr. and Meth. A **773** (2015) 137.

[5] M.C. Moxon, J.B. Brisland: "GEEL REFIT, A least squares fitting program for resonance analysis of neutron transmission and capture data computer code", AEA-InTec-0630, AEA Technology, October (2008).

[6] P. Schillebeeckx, B. Becker, Y. Danon, K. Guber, H. Harada, J. Heyse, A.R. Junghans, S. Kopecky, C. Massimi, M.C. Moxon, N. Otuka, I. Sirakov and K. Volev: Nuclear Data Sheets **113**, (2012) 3054.

[7] M. Harada, N. Watanabe, F. Maekawa and M. Futakawa: Nucl. Instr. and Meth. A **597**, (2008) 242.

[8] S. Uno, T. Uchida, M. Sekimoto, T. Murakami, K. Miyama, M. Shoji, E. Nakano and T. Koike: Physics Procedia **37**, (2012) 600.

[9] K. Shibata, O. Iwamoto, T. Nakagawa, N. Iwamoto, A. Ichihara, S. Kunieda, S. Chiba, K. Furutaka, N. Otuka, T. Ohsawa, T. Murata, H. Matsunobu, A. Zukeran, S. Kamada and J. Katakura: J. Nucl. Sci. Technol. **48**(1), (2011) 1.

[10] H. Weigmann and J. Winter: Zeitschrift für Physik **213**, (1968) 411.

13 In-beam gamma-ray spectroscopy and cross section measurement strategy for long-lived fission products at RIBF

He WANG
RIKEN Nishina Center, 2-1 Hirosawa, Wako, Saitama 351-0198, Japan
e-mail: wanghe@ribf.riken.jp

In-beam γ-ray spectroscopy is a powerful tool to study the properties of nuclei. It has been widely used to investigate the structure in very exotic nuclei at the Radioactive Isotope Beam Factory (RIBF) using the in-flight BigRIPS fragment separator and the ZeroDegree spectrometer as well as the γ-ray detection array DALI2. The first 2^+ excited state in the neutron-rich ^{136}Sn was identified via this technique. This energy is higher than the ones for heavier even-even N = 86 isotones reflecting the Z = 50 magicity. It is similar to the first 2^+ excited state in ^{134}Sn, which may suggest that the seniority scheme holds also for ^{136}Sn. For the tin isotopes, it was found that the 2^+ excitation energies beyond N = 82 are lower than those values in between the two doubly magic nuclei ^{100}Sn and ^{132}Sn.

Aiming at studying the nuclear transmutation for the long-lived fission products, cross section measurements of ^{90}Sr and ^{137}Cs have been performed at RIBF.

1. In-beam γ-ray spectroscopy at RIBF

In-beam γ-ray spectroscopy experiments cover many topics, such as the collective nuclear excitation modes, deformation of the nuclear shapes, and the shell evolution in the nuclei located far from the line of β stability. Indeed, the knowledge of nuclear shell evolution towards both proton and neutron drip-lines has been extended by the in-beam γ-ray spectroscopy research at the Radioactive Isotope Beam Factory (RIBF) [1] by studying some of the most basic properties of exotic nuclei. For instance, the energies of the first 2^+ excited states in even–even nuclei, the transition probabilities from the 2_1^+ state to the ground state, and the energy ratios between the first 2^+ and 4^+ states yield direct signatures for shell evolution.

Using the combination of BigRIPS/ZeroDegree [2] and the DALI2 γ-ray spectrometer [3], several regions in the nuclear chart have been explored via the in-beam γ-ray spectroscopy technique. The known examples are the N = 20 and N = 28 shell quenching in very neutron-rich Ne [4] and Si [5] isotopes, respectively, a new nuclear magic number N = 34 [6] in ^{54}Ca, and

nuclear structure around doubly magic nucleus ^{132}Sn [7].

In-beam γ-ray spectroscopy of ^{136}Sn

Motivation

The properties of nuclei in the vicinity of ^{132}Sn (Z = 50, N = 82) have been in focus for decades, as it is doubly magic while lying far away from the line of β stability. It thus provides an opportunity to investigate possible modifications in the shell structure toward the neutron-drip line [8]. In addition, tin has a long isotopic chain, which enables benchmark studies for the change of nuclear properties in a wide range.

However, at present experimental knowledge for the tin isotopes heavier than ^{132}Sn is very limited. In this study, the first spectroscopic information for ^{136}Sn was obtained by measuring its 2_1^+ state via the in-beam γ-ray spectroscopy technique.

Experiment setup

The experiment was performed at RIBF [1] operated by the RIKEN Nishina Center and the Center for Nuclear Study, the University of Tokyo. The secondary beams including ^{137}Sb were produced by an in-flight fission reaction of a ^{238}U primary beam incident on a tungsten target. Secondary cocktail beams were selected and purified in the first stage of the BigRIPS fragment separator [2]. A wedge-shaped aluminum energy degrader with thickness of 0.8 g/cm^2 was located at the dispersive focus to separate the unwanted fission products. Another 0.4 g/cm^2 thick wedge-shaped degrader was used in the second stage of BigRIPS for a further purification. The fission products were identified event-by-event via the ΔE-$B\rho$-TOF method as described in Ref. [9] using similar beam-line diagnostic detectors.

The secondary beams were incident on a 6 mm thick ^{9}Be target for the secondary reaction. The ^{136}Sn isotopes were produced via the one-proton removal from ^{137}Sb. In the middle of the target, the average energy of ^{137}Sb was about 240 MeV/nucleon. Reaction residues were delivered into the ZeroDegree spectrometer [2] for particle identification using again the ΔE-$B\rho$-TOF method. In addition, a $LaBr_3$(Ce) scintillator located at the final focus of the ZeroDegree spectrometer was used for a total kinetic energy measurement for the charge states identification.

The γ-rays emitted from the decaying excited states were detected by the DALI2 spectrometer, which surrounded the secondary target. The DALI2 spectrometer is based on large-volume NaI(Tl) scintillators arranged in a high solid-angle covering geometry. The energy resolution and full energy peak efficiency for the present DALI2 configuration of 186 crystals are 9% (FWHM) and 22%, respectively, for the 0.662 MeV γ-rays from a stationary ^{137}Cs source. The detailed information for DALI2 is given in Ref. [3].

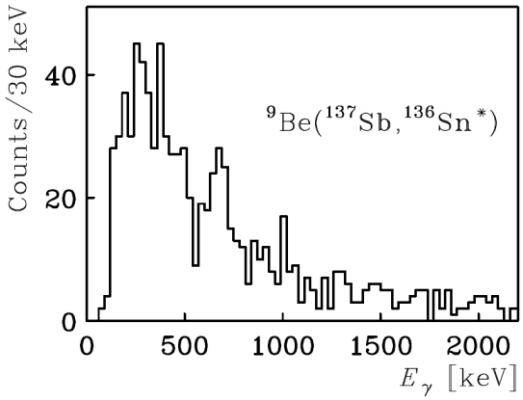

Fig. 1 Doppler-shift corrected γ-ray spectrum in coincidence with ^{136}Sn detected in ZeroDegree following the one-proton removal reaction.

Results and discussion

The Doppler-shift corrected γ-ray energy spectrum in coincidence with ^{136}Sn produced via the one-proton knockout reaction from ^{137}Sb is shown in Fig. 1. The transition was observed at 682(13) keV, which was assigned to the γ-ray decay from the first 2^+ state to the ground state.

Figure 2 (a) displays the 2_1^+ excitation energies for the even-even N = 86 isotones as a function of the proton number. The 2_1^+ state in ^{136}Sn is much higher than those for the neighboring nuclei, indicating the presence of the Z = 50 magicity in the N = 86 isotones.

The experimental $E_x(2_1^+)$ systematics for the even-even Sn isotopes is shown in Fig. 2 (b). The newly measured $E_x(2_1^+)$ value for ^{136}Sn is close to the one for ^{134}Sn. The constant $E_x(2_1^+)$ values at ^{134}Sn and ^{136}Sn reflect the characteristic of the seniority scheme. This is similar to the lighter Sn isotopes, where the first 2^+ excited states stay almost constant in a wide range. The constancy of the 2_1^+ state in the semi-magic isotopes can be understood by a dominance of the seniority v = 2 configuration [10]. The similar $E_x(2_1^+)$ values for ^{134}Sn and ^{136}Sn may suggest that the seniority scheme holds also for the tin isotopic chain beyond N = 82 up to N = 86.

Another interesting feature of the $E_x(2_1^+)$ systematics along the tin isotopes is its asymmetric behavior below and above N = 82. The 2_1^+ excitation energies in ^{134}Sn and ^{136}Sn are about 500 keV lower than those values for the lighter isotopes with N < 82. The asymmetric pattern for the $E_x(2_1^+)$ systematics might be due to a reduction of the pairing energy in the N > 82 region, because the 2_1^+ excitation energy is determined mostly by the strength of the pairing under the seniority scheme. Indeed, a quenching in the pairing gap is suggested from an observation of the decrease of the odd-even-mass-staggering in the Sn isotopes across N = 82 in the recent mass measurement [11].

A comparison of our experimental finding with mean-field calculations is displayed in Fig. 2

(b). The QRPA calculation [12] with the Skyrme force Sly4 shows a good agreement with the lighter Sn isotopes, however does not reproduce the asymmetry. The relativistic QRPA (RQRPA) calculation using the NL3 effective interaction and Gogny's paring forces (D1S) [13] overestimates the $E_x(2_1^+)$ values toward $N = 82$, although it shows an asymmetric pattern around $N = 82$. It seems that the two features cannot be reproduced at the same time by these calculations.

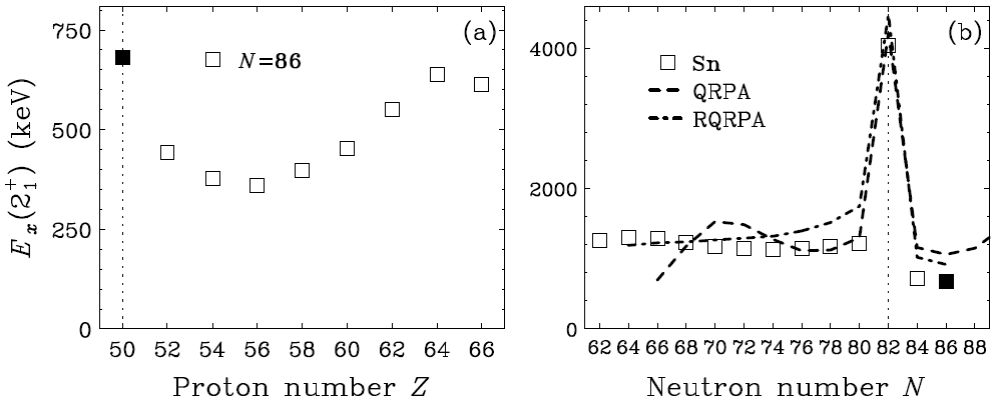

Fig. 2 Systematics of the first 2^+ excitation energies for (a) the even-even $N = 86$ isotones and (b) even-even Sn isotopes. The filled symbols are obtained in the present work and other data are taken from Ref. [14]. In Panel (b), the mean-field calculations using QRPA (dashed) [12] and RQRPA (dot-dashed) [13] for the Sn isotopes are displayed for comparison. The error bars are smaller than the symbol sizes and vertical dotted lines indicate the magic numbers in both panels.

Summary

In summary, the in-beam γ-ray spectroscopy at RIBF has been widely applied to study the structure of the exotic nuclei. For the first time, the first 2^+ excited state in the semi-magic nucleus ^{136}Sn was determined via this technique in coincidence with one proton removal from ^{137}Sb. The $E_x(2_1^+)$ value in ^{136}Sn is much higher than the neighboring $N = 86$ isotones reflecting the $Z = 50$ magicity. The similar 2_1^+ excitation energies in ^{134}Sn and ^{136}Sn suggest that the seniority scheme holds up to $N = 86$. The asymmetric pattern in the $E_x(2_1^+)$ systematics in the tin isotopes above and below $N = 82$ might be due to the quenching of the pairing gap. The mean-field calculations cannot reproduce the $E_x(2_1^+)$ constancy and the asymmetry in the Sn isotope at the same time.

2. Cross section measurement strategy for long-lived fission products

Nuclear power has become a modern energy source since the middle of the twentieth century. Nuclear safety and security are matters of concern in the entire world. One of the major issues in the world is the treatment on the radioactive waste produced from the nuclear power plant. There are two main types of long-lived radioactive wastes from the fission reaction, one is long-lived fission products (FP), and the other is minor actinides (MA).

In order to minimize the radioactivities, it has been suggested to transmute these long-lived radioactive wastes into the stable or short-lived nuclei via nuclear reactions. The MA transmutation has been promoted by some facilities, such as the accelerator-driven system at JAEA [15]. In contrast, the study on FP is very limited, although they have long half lives and high level radioactivities [16]. Aiming at investigating the transmutation on the long-live fission products, cross section measurements for ^{90}Sr and ^{137}Cs have been performed at RIBF. The data analysis is now ongoing.

References

[1] H. Okuno, N. Fukunishi, and O. Kamigaito: Prog. Theor. Exp. Phys. 2012, 03C002 (2012).
[2] T. Kubo *et al*., Prog. Theor. Exp. Phys. 2012, 03C003 (2012).
[3] S. Takeuchi *et al*., Nucl. Instr. Methods. A 763, 596 (2014).
[4] P. Doornenbal *et al*., Phys. Rev. Lett., 111, 212502 (2013).
[5] S. Takeuchi *et al*., Phys. Rev. Lett., 109, 182501 (2012).
[6] D. Steppenbeck *et al*., Nature (London), 502, 207 (2013).
[7] H. Wang *et al*., Prog. Theor. Exp. Phys., 2014, 023D02 (2014).
[8] J. Dobaczewski *et al*., Phys. Rev. C 53, 2809 (1996).
[9] N. Fukuda *et al*., Nucl. Instr. Methods. B 317, 323 (2013).
[10] R. Casten and B. Sherrill, Prog. Part. Nucl. Phys. 45, S171 (2000).
[11] J. Hakala *et al*., Phys. Rev. Lett. 109, 032501 (2012).
[12] J. Terasaki and J. Engel, Phys. Rev. C 74, 044301 (2006).
[13] A. Ansari, Phys. Lett. B 623, 37 (2005).
[14] NNDC, http://www.nndc.bnl.gov
[15] J. Nucl. Sci. Technol. 44, 483 (2007).
[16] W. S. Yang *et al*., Nucl. Sci. Eng. 146, 291 (2004).

This is a blank page.

14 Physics and Nuclear Data in Radiation Therapy

Chie Kurokawa
Department of Radiation Oncology, Graduate School of Medicine, Juntendo University,
2-1-1 Hongo, Bunkyo-ku, Tokyo, 113-8421, Japan,
e-mail: ckuroka@juntendo.ac.jp

Cancer patients can receive more sophisticated radiation therapy technology and enjoy a better quality of life. To assess the benefit of these therapies, it is important to evaluate the dose to patient with high accuracy (< 5%). Nuclear data is necessary for the evaluation. The role of nuclear data not only in particle therapy but in photon therapy is briefly discussed.

1. Introduction

Along with surgery and chemotherapy, radiation therapy is one of the important methods of cancer treatment, which delivers high doses to kill cancer cells and stop them from spreading. Radiation therapy can improve quality of life (QOL) since it can preserve organ function. It is used to treat localized solid tumors, such as cancers of the skin, prostate, brain, breast, cervix, etc., and can also be used to treat leukemia and lymphoma. The radiation types are external from accelerators, or internal from radioactive substances that a physician places inside patient's body. In US and Europe, more than 60% of cancer patients receive radiation therapy at some stage during the course of their illness. Although in Japan only about 25% of all cancer patients receive it, the number is expected to increase due to the increase in incidence of certain cancers, such as prostate, lung and breast, for which radiation therapy are effective.

Since radiation therapy can damage normal cells as well as cancer cells, treatment must be carefully planned to minimize side effects. From physicist point of view, accurate estimation of prescribed dose to patient is quite important for success of treatment. ICRU report recommends that the dose errors should be maintained within acceptable level (5%) [1]. In order to manage dose errors, it is necessary to understand the factors of errors and their magnitude. Nuclear data especially relevant for medical application, such as microscopic cross-sections for neutron and proton interaction with elements (H, C, N, and O for tissue

elements, and Pb and W for accelerator components), is important to dosimetry and it is one of the errors in patient dose.

In this report, the roles of nuclear data in radiation therapy, both of photon and particle therapies, are reviewed.

2. Impact of nuclear data on radiation therapy

2.1 Photon therapy

External radiation therapy involves the use of electrons, X-rays, high-energy γ-rays or hadrons (neutrons, protons, and heavy ions such as ^{12}C) and most patients receive photon therapy. In spite of clinically useful photon beam, LINACs produce secondary particles such as neutrons from the giant dipole resonance reactions, (γ, n), when the incident photon energy is above the threshold energy of the (γ, n) reaction. This threshold depends on the atomic number of the target and is around 8 MeV for high atomic numbers (7.42 MeV for tungsten). The energy and angular distributions of the emitted neutrons are necessary for radiation transport and radiation shielding calculations. Zanini et al. evaluates neutron fluence to patients in 18 MV photon beam by using Monte Carlo simulation [2]. Table 1 shows the calculated neutron production in the components of LINAC head. In their study, it is evaluated the photoneutron energy spectra at patient plane. They concluded that most photoneutrons are produced at energies around 200 – 700 keV where the biological effectiveness is high (Radiation weighting factor is around 20 [3]). For advanced techniques of radiation therapy, such as Intensity Modulated Radiation Therapy (IMRT), it is considered that neutron contribution can increase due to increase in the amount of radiation comparing to conventional treatment technique. Howell et al. showed that IMRT treatment plan resulted in a higher neutron fluence and higher dose equivalent (IMRT: neutron ambient dose equivalent is 300 mSv for 45 Gy, Conventional plan : neutron ambient dose equivalent is 105 mSv for 45 Gy) [4]. The neutron contribution is non-negligible and could represent a late risk for surrounding healthy tissues. However, these undesired doses due to neutrons are not taken into account when the dose calculation is performed by treatment planning systems. Detailed studies are necessary for accurate evaluation of patient's dose in future. For that purpose, the precise nuclear data are necessary and play a significant role.

Component	Clinical configuration[1]
Target (W)	15.2%
Primary Collimator (W)	44.3%
Flattening Filter (Fe)	8.9%
Jaws (W)	30.7%
Muli-Leaf Collimator (W)	0.6%
Minor components	0.3%

Table 1. Calculated neutron production in photon collisions with components of LINAC head. ([1] In this configuration, the direct photon beam impinges on the jaws and then on the MLC shaping the photon field.)

2.2 Particle therapy

As for the particle therapy, the major advantage is the capability to treat deep-lying tumors, close to critical structures. This is possible mainly due to the high selectivity of the Bragg-peak. Therefore, it is critical to evaluate the position of Bragg-peak with high accuracy in order to deliver safe treatment. As an example of dose distribution for proton therapy, Figure1 shows patch field technique [5]. In this technique, the field combinations consisting of multiple fields of proton beam are used such that its distal edge (patch beam) abuts to the lateral edge of the other field (thru beam). This technique enables to deliver high dose to target volume while minimizing dose to normal structures close to the target. As shown in patch field technique, it should be noted that a range error of Bragg-peak can cause a portion of a tumor not receiving enough dose, or over dose to the normal tissue. Uncertainties including the range error in proton therapy are from several sources and error in nuclear reaction cross sections is one of the sources. In proton therapy, cross sections are needed for the formation of neutrons and γ-rays, and to some extent secondary charged particles. This information is required to calculate the radiation transport and radiation dose deposited in patient. Data of cross sections used in proton therapy are already available and play an important role to reduce the calculation time. However, they do not cover whole the energy range used in proton therapy facilities (0-250 MeV) and do not include all nuclei existing in the human body.

It is shown that well-evaluated nuclear data are also important in proton therapy PET-imaging [6]. In this method, the actual dose to patient is verified via the PET imaging where the positron-annihilation γ-rays following the decay of the proton-induced positron emitters, such as ^{11}C, ^{13}N and ^{15}O, are detected. Various groups have investigated the possibility and accuracy of proton therapy monitoring by PET imaging [7-10]. It is discussed that the accuracy of the dose verification by PET imaging is limited by several factors. One of

the factors is the accuracy of the measured cross sections for the relevant nuclear reaction channels. Table 2 lists the major nuclear reaction channels for proton-induced positron emitter productions [11]. However, the current available data do not cover the set of reaction data for all the nuclei of interest up to 250 MeV.

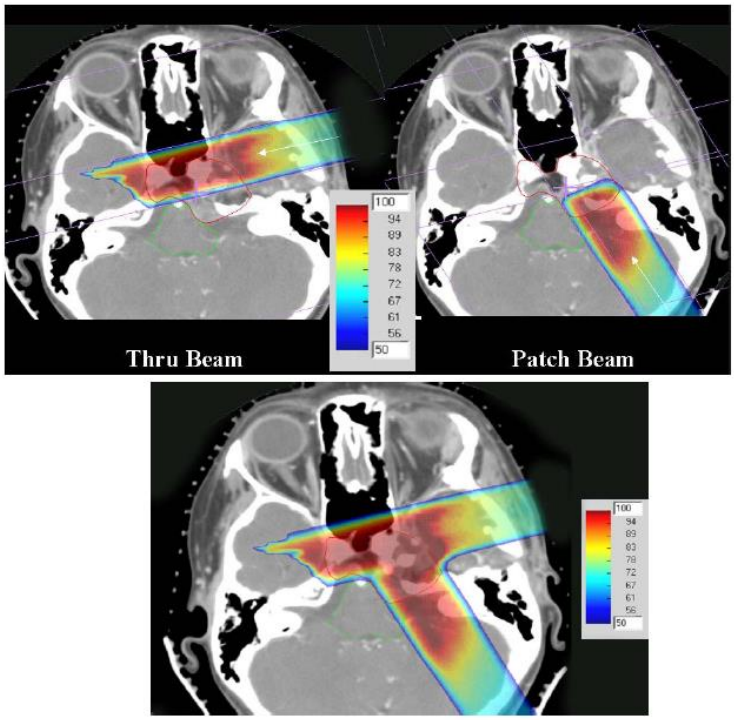

Figure 1. Patch-field technique used in treatment of the target while avoiding the brainstem [5]. The lower panel shows the dose distribution of combined thru/patch field.

Nuclear Reactions	Threshold Energy [MeV]	Half-life Time [min.]	Positron Max. Energy [MeV]
^{16}O (p, pn) ^{15}O	16.79	2.037	1.72
^{16}O (p, 2p2n) ^{13}N	5.66	9.965	1.19
^{14}N (p, pn) ^{13}N	11.44	9.965	1.19
^{12}C (p, pn) ^{11}C	20.61	20.39	0.96
^{14}N (p, 2p2n) ^{11}C	3.22	20.39	0.96
^{16}O (p, 3p3n) ^{11}C	27.5	20.39	0.96

Table 2. Relevant positron-emitter production reactions for PET imaging in proton therapy [11]. (p, 2p2n), (p, 3p3n) are inclusive of (p, α), (p, αpn), respectively. The threshold energies in the table refer to (p, α) and (p, αpn).

Summary

Radiation therapy is a treatment that can cure cancer preserving organ functions. In order to maximize tumor control while minimizing risk to normal tissue, the process of radiotherapy becomes complex and involves understanding of the principles of physics, radiobiology, radiation safety, dosimetry, etc.. In order to assess the benefit of radiation therapy, the important role of medical physicists is to maintain the dose errors within acceptable level (5%). Nuclear data plays an important role in dose evaluation both for the photon and particle therapies and thus it is necessary to study how the errors impact on patient dose.

References

[1] Determination of Absorbed Dose in a Patient Irradiated by Beams of X or Gamma Rays in Radiotherapy Procedures. International Commission on Radiation Units and Measurements (ICRU) Report 24: ICRU; 1976.

[2] Zanini A, Durisi E, Fasolo F, Ongaro C, Visca L, Nastasi U, Burn KW, Scielzo G, O Adler J, Annand JRM and Rosner G. Monte Carlo simulation of the photoneutron field in linac radiotherapy treatments with different collimation systems. Phys Med Biol. 2004 Jan;49:571-582.

[3] The 2007 Recommendations of the International Commission on Radiological Protection. International Commission on Radiological Protection (ICRP) Publication 103: ICRP; 2007.

[4] Howell RM, Ferenci MS, Hertel NE, Fullelton GD. Investigation of secondary neutron dose for 18 MV dynamic MLC IMRT delivery. Med Phys. 2005 Mar;32:786-793.

[5] Paganetti H, Bortfeld T. Proton Beam Radiotherapy – The State of the Art.: The American Association of Physicists in Medicine (AAPM) 47th Annual Meeting; 2005 July 24-28; Washington, US.

[6] Seravalli E, Robert C, Bauer J, Stichelbaut F, Kurz C, Smeets J, Van Ngoc Ty C, Schaart DR, Buvat I, Parodi K. Monte Carlo calculations of positron emitter yields in proton radiotherapy. Phys Med Biol. 2012 Mar;57:1659-1673.

[7] Enghardt W, Debus J, Haberer T, Hasch BG, Hinz R, Jäkel O, Krämer M, Lauckner K, Pawelke J, Pönisch F. Positron emission tomography for quality assurance of cancer therapy with light ion beams. Nucl Phys. 1999 July;A654:1047c-1050c.

[8] Parodi K, Enghardt W. Potential application of PET in quality assurance of proton therapy. Phys Med Biol. 2000 Nov;45:N151-6.

[9] Oelfke U, Lam GK, Atkins MS. Proton dose monitoring with PET: qualitative studies in Lucite. Phys Med Biol. 1996 Jan;41:177-96.

[10] Nishio T, Ogino T, Nomura K, Uchida H. Dose-volume delivery guided proton therapy using beam on-line PET system. Med Phys. 2006 Nov;33:4190-7.

[11] Beebe-Wang J, Vaska P, Dilmanian FA, Peggs SG, Schlyer DJ. Simulation of Proton Therapy Treatment Verification via PET Imaging of Induced Positron-Emitters. IEEE Nuclear Science Symposium/Medical Imaging Conference; 2003 Oct.19-25; Portland, US.

15 Clustering phenomena studied by Antisymmetrized Molecular Dynamics

Masaaki Kimura
Graduate School of Science, Hokkaido University, Sapporo 060-0810, Japan
e-mail: masaaki@nucl.sci.hokudai.ac.jp

The theoretical framework of antisymmetrized molecular dynamics (AMD) is explained and the illustrative examples of applications to the nuclear reaction and structure problems are introduced. In the application to the multifragmentation phenomena in heavy-ion collision, by taking into account the branch and coalescence of nucleon wave packets, time-dependent version of AMD successfully describes the yields of fragment nuclei populated in the heavy-ion reaction. The time-independent version of AMD is applied to the nuclear structure problems. We focus on the cluster states in the highly excited states of N=Z nuclei, in particular those of ^{24}Mg.

1. Introduction

Clustering phenomena where groups of nucleons (clusters of nucleons) are formed in the nuclear system are unique and fascinating phenomena in nuclear many body problem. Nucleus is a self-bound system formed by attractive nuclear force, and hence, the spatial correlations between nucleons can be rather strong. As a result, the assembling and disassembling of nucleons occur in various ways. Furthermore, the saturation of binding energy and nucleon density in a nuclear system implies that the assembling and disassembling of nucleons can take place with a small input of excitation energy. Thus, clustering manifests itself in many aspects of nuclear many-body dynamics. A typical example of nuclear clustering is multifragmentation phenomena in heavy-ion reaction, where hot compound nucleus formed by collision is spatially expanded and disintegrated into many fragments of nuclei. Another example is the cluster structure of the excited states of finite nucleus which is known to exist in the vicinity of the threshold energies which decompose the system into clusters. In the cluster states, the system is decomposed into several clusters and nucleons are well confined within each cluster.

The ordinary mean-field approaches are inadequate to describe clustering phenomena, because the spatially localized correlations between nucleons which are essential for clustering are not properly taken into account. The theoretical model of antisymmetrized molecular dynamics [1-4] has been one of the powerful models to describe clustering phenomena. It was first proposed in the studies of heavy-ion collisions [5,6]. It describes nuclear many-body systems by antisymmetrized products of Gaussian wave packets of nucleons and incorporates quantum effects and nucleon–nucleon collisions. AMD has also proved to be a powerful tool for nuclear structure study [7,8]. All centers of the Gaussian packets are independently treated as variational parameters in the AMD framework, and it is possible to describe the formation of various clusters as well as the

independent-particle motion in a mean field without *a priori* assumptions. Thus, AMD has been applied to investigate various phenomena in nuclear structure and reactions. In this contribution, we will explain theoretical framework of AMD and introduce applications to nuclear reaction and structure problems

2. Theoretical framework of antisymmetrized molecular dynamics

We briefly review the formulation of AMD. For a detailed formulation of the AMD method, the reader is directed to references [1-4]. The wave function of AMD (Φ_{AMD}) describing A-nucleon system is represented by a Slater determinant of single particle wave packets (φ_{i}) that describe nucleons,

$$\Phi_{\mathrm{AMD}} = \frac{1}{\sqrt{A!}}\det\{\varphi_1, \dots, \varphi_A\}, \tag{1}$$

$$\varphi_{\mathrm{i}}(r_j) = \exp\left(-\nu\left(r_j - \frac{Z_i}{\sqrt{\nu}}\right)^2 + \frac{1}{2}Z_i^2\right) \otimes (\alpha_i\chi_{\uparrow} + \beta_i\chi_{\downarrow}) \otimes (proton\ or\ neutron), \tag{2}$$

where the spatial part of the single particle wave packet is parametrized by a complex numbered 3-dimensional vector Z_{i} whose real and imaginary parts, roughly speaking, correspond to the position and momentum of a nucleon. The direction of nucleon spin is parametrized by α_{i} and β_{i}. From the time-dependent variational principle, the equation-of-motion of those parameters for given Hamiltonian $\hat{H}$ reads,

$$i\hbar\sum_{j\rho} C_{i\sigma j\rho}\frac{dX_{j\sigma}}{dt} = \frac{\partial H}{\partial X^*_{i\sigma}}, \quad X \in \{Z_1, \dots, Z_A, \alpha_1, \dots, \alpha_A, \beta_1, \dots, \beta_N\} \tag{3}$$

$$C_{i\sigma j\rho} = \frac{\partial^2}{\partial X^*_{i\sigma}\partial X_{j\rho}}\log\langle\Phi_{AMD}(X)|\Phi_{AMD}(X)\rangle, \quad H(X^*, X) = \frac{\langle\Phi_{AMD}(X)\left|\hat{H}\right|\Phi_{AMD}(X)\rangle}{\langle\Phi_{AMD}(X)|\Phi_{AMD}(X)\rangle} \tag{4}$$

According to this equation of motion Eq. (3), the parameters Z, α, β are evolved and the time evolution of the system during the nucleus-nucleus collisions is described. It is easy to prove that if we change the time t into imaginary number, the energy of the system described by Eq.(3) decreases. Using this property, the wave function with minimum energy (the ground state) is calculated for nuclear structure study. Typical form of the Hamiltonian used in AMD studies is given as,

$$\hat{H} = \sum_i \hat{t}_i - \hat{t}_g + \sum_{ij}\hat{v}_{NN}(r_i - r_j) + \sum_{ij\in proton}\hat{v}_{Coul}(r_i - r_j) \tag{5}$$

where $\hat{t}_i$ and $\hat{t}_g$ represent the kinetic energies of nucleons and the center-of-mass. $\hat{v}_{NN}$ and $\hat{v}_{Coul}$ represent nucleon-nucleon interaction and Coulomb interaction, respectively. For $\hat{v}_{NN}$, effective interactions such as Volkov, Gogny and Skyrme forces are often used. Additional terms in the equation-of-motion and calculational procedures to restore broken symmetries are introduced, and we shall explain them below.

3. Application to nuclear reaction problem – multifragmentation in heavy-ion reaction –

To describe the nucleon-nucleon correlation during the nucleus-nucleus collision, three additional terms are introduced to the equation-of-motion,

$$(6) \qquad i\hbar \sum_{j\rho} C_{i\sigma j\rho} \frac{dX_{j\sigma}}{dt} = \frac{\partial H}{\partial X^{*}_{i\sigma}} + (NN\ collision\ term) + \Delta Z_i(t) + \mu(Z_i, H)$$

The second term of rhs (*NN collision term*) describes two nucleon collisions. When two nucleons are close to each other, the momenta of nucleons are stochastically interchanged according to the energy-dependent in-medium cross section. This collision effect is treated with the "physical nucleon coordinate" to take the Pauli blocking effect into account. The third term $\Delta Z_i(t)$ symbolically denotes the stochastic wave packet splitting. During the collision, in a short time scale, nucleons propagate in the mean-field of other nucleons. However, after some period, the single nucleon wave function will be split into several wave packets (quantum branching) due to the correlation lost. This quantum branching is approximately described by the splitting of Gaussian wave packet. As a result, a single AMD wave function for the initial state is fragmented into many Slater determinants and the system is described by a superposition of them after the reaction process. The last term $\mu(Z_i, H)$ is a dissipation term required from the quantum branching. Since the quantum branching process treated approximately as mentioned above does not necessarily guarantee the energy conservation, we add this term to compensate it.

As an example of reaction study by AMD, we here introduce that reported in the reference [9]. Figure 1 shows the density distribution of ^{40}Ca+^{40}Ca collisions for two different events. It can be confirmed that owing to the two nucleon collisions and quantum branching, the system is fragmented into many clusters after the collision time. It is also noted that owing to the stochastic effects and branching, even if we started from a single initial state, many different the final wave functions are obtained as shown in Fig. 1. As a result, the observed fragment yields are reasonably reproduced as shown in Fig. 2. Based on such calculations, equation of state of nuclear matter and nuclear liquid-gas phase transition have been discussed intensively.

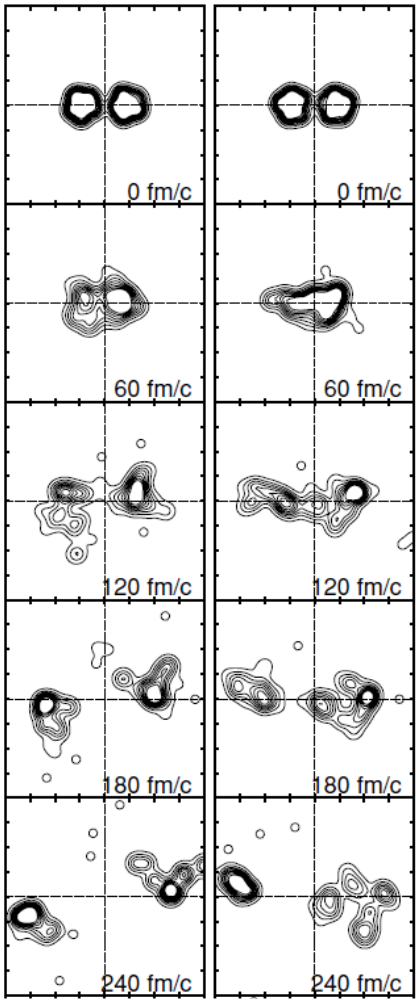

Fig. 1: density distribution of ^{40}Ca+^{40}Ca central collision at 35 MeV/nucleon from t = 0 to 300 fm/c for two different events. Taken from Ref. [9]

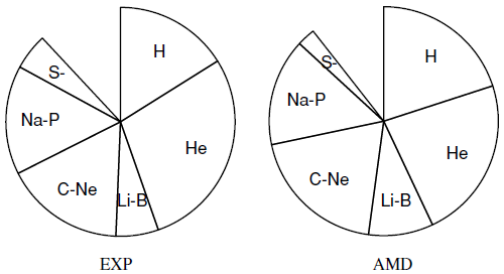

Fig. 2: yield ratio of the charged fragments at the final state of the reaction 40Ca+40Ca at 35 MeV/ nucleon. Taken from Ref. [9]

4. Application to nuclear structure problem – nuclear clustering –

In the case of the structure study, we perform the energy minimization by setting the time in Eq. (3) to imaginary number. Adding to this, since the nucleus is an isolated system, the parity and rotational symmetry that are broken in Eq. (1) must be restored. For this purpose, we perform the parity and angular momentum projections. Namely, the wave functions below are used as the model wave function instead of Eq. (1).

(7) $\Phi^{\pm}_{AMD} = \dfrac{1 \pm P_x}{2}\Phi_{\mathrm{AMD}}$, parity projection (parity symmetry)

(8) $\Phi^{J\pm}_{AMD} = \dfrac{2J+1}{8\pi^2}\int d\Omega\, D^{J*}_{MK}(\Omega)\, R(\Omega)\, \Phi_{AMD}$, angular momentum projection (rotational symmetry)

where, P_x and $R(\Omega)$ represent the parity and rotation operators. $D^{J}_{MK}(\Omega)$ is so-called Wigner function and the integration over three Euler angles $\int \mathrm{d}\Omega$ is performed numerically. The parity projection is performed before the energy minimization, but the angular projection before the energy variation is only possible for the light mass systems, because it demands much CPU time. Furthermore, the wave function given by Eq. (8) are superposed to take into account the beyond-mean-field effects such as configuration mixing, shape fluctuation and the mixing of different cluster configurations,

(9) $\Psi_\alpha = \sum_i C_{i\alpha}\Phi^{J\pm}_{\mathrm{AMD}}(i)$,

where the unknown coefficients and eigen energies are determined by solving the Hill-Wheeler equation,

(10) $\sum_{ij} H_{ij}C_{i\alpha} = E_\alpha \sum_{ij} N_{ij}C_{i\alpha}$, $H_{ij} = \langle\Phi^{J\pm}_{\mathrm{AMD}}(i)|\hat{H}|\Phi^{J\pm}_{\mathrm{AMD}}(j)\rangle$, $N_{ij} = \langle\Phi^{J\pm}_{\mathrm{AMD}}(i)|\hat{H}|\Phi^{J\pm}_{\mathrm{AMD}}(j)\rangle$.

Usually, the basis wave functions $\Phi^{J\pm}_{\mathrm{AMD}}(i)$ are generated by imposing the constraints on the energy variation. Owing to the rapidly developing computational power, today it is possible to superpose more than 500 basis wave function in these days.

As an example of the structure study, we report the recent result obtained for the clustering in ^{24}Mg. As well known, various kinds of cluster states can appear in this nucleus, such as ^{12}C+^{12}C of astrophysical interest and very exotic 2α+^{16}O and 6α gas-like states. However, due to the experimental difficulties, very little is known for those clusters. Recently, it was suggested that isoscalar monopole transition strength is a good probe for nuclear clustering. To deal with the various cluster states, we have introduced the constraint on the quantum number of the harmonic oscillator to describe high excited states. Figure 3 shows the examples of the resultant wave functions obtained by the energy minimization with the constraint. As we can see, many different cluster states such as ^{20}Ne+α, ^{12}C+^{12}C and 6α are obtained without

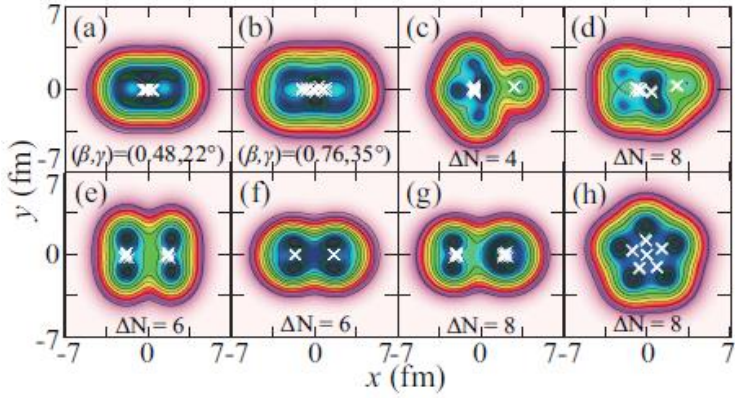

Fig 3: Density profile of ^{24}Mg with various cluster structure.

any a priori assumption on nuclear structure. Those wave functions obtained by the energy minimization are superposed to describe the eigenstates of the Hamiltonian. From thus-obtained wave function, we have calculated the strength function of the isoscalar monopole transition as shown in Fig. 4. Here we confirmed that several cluster states appear as the strong peaks in the strength function. For example, the strong peak located at 15.3 MeV in the excitation energy of ^{24}Mg corresponds to the 0_8^+ state which has the ^{12}C+^{12}C cluster structure. This state is dominantly described by the cluster wave functions illustrated in Fig.3 panels (e), (f) and (g). Since this strength function is already measured at the Osaka University, we expect that the detailed comparison between the theory and experiment will reveal the cluster states of ^{24}Mg.

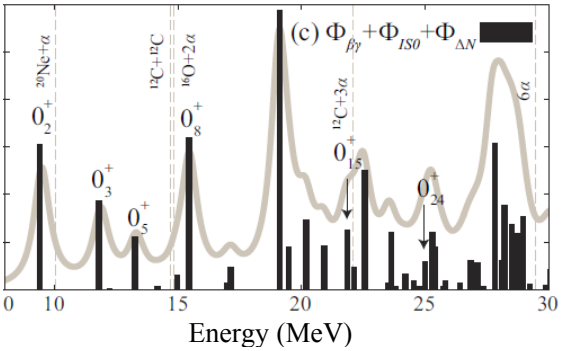

Fig. 4: Isoscalar monopole transition strength of ^{24}Mg

5. Summary

In summary, we have briefly reviewed the theoretical framework of antisymmetrized molecular dynamics and introduced its applications to the nuclear reaction and structure problems. In the nuclear system, the coexistence of the mean-field and cluster aspects brings a rich variety of phenomena, and AMD is one of the very powerful theoretical framework to describe both aspects in reaction and structure problems. Since the computational power is rapidly increasing in these days, it is now possible to perform very sophisticated and accurate reaction and structure calculations with AMD. This development will make it possible to use AMD not only for the fundamental physics studies but also for applications for industrial and medical purposes.

References

[1] Y. Kanada-En'yo, M. Kimura, and H. Horiuchi, C. R. Physique, 4, 497 (2003).

[2] A. Ono and H. Horiuchi, Prog. Part. Nucl. Phys. 53, 501 (2004).

[3] Y. Kanada-En'yo and M. Kimura, Lecture notes in Physics, 818, 129 (2010).

[4] Y. Kanada-En'yo, M. Kimura and A. Ono, Porg. Theor. Exp. Phys. 2012, 01A202 (2012).

[5] A. Ono, H. Horiuchi, T. Maruyama, and A. Ohnishi, Phys. Rev. Lett. 68, 2898 (1992).

[6] A. Ono, H. Horiuchi, T. Maruyama, and A. Ohnishi, Prog. Theor. Phys. 87, 1185 (1992).

[7] Y. Kanada-Enyo and H. Horiuchi, Prog. Theor. Phys. 93, 115 (1995).

[8] Y. Kanada-Enyo, H. Horiuchi, and A. Ono, Phys. Rev. C, 52, 628 (1995).

[9] T.Furuta and A.Ono, Phys. Rev. C 79, 014608 (2009)

This is a blank page.

16 Fission process of low excited nuclei with Langevin approach

Y. Aritomo[1], D. Hosoda[1], S. Chiba[1], F.A. Ivanyuk[1,2]

[1]*Research Laboratory for Nuclear Reactors, Tokyo Institute of Technology, Tokyo, Japan*
[2]*Institute for Nuclear Research, Kiev, Ukraine*

Contact e-mail : aritomo@ele.kindai.ac.jp

Abstract

Fission fragment mass distributions from the fission of U and Pu isotopes at low excitation energies are studied using a dynamical model based on the fluctuation-dissipation theorem formulated as Langevin equations. The present calculations reproduced the overall trend of the asymmetric mass distribution without parameter adjustment using the Langevin approach. It was found that the shell effect of the potential-energy landscape has a dominant role in determining the mass distribution, although it is rather insensitive to the strength of dissipation. Nevertheless, it is essential to include the effect of dissipation, since it has a crucial role in giving "fluctuation" to Langevin trajectories as well as for explaining the multiplicities of pre-scission neutrons as the excitation energy increases. Therefore, the present approach can serve as a basis for more refined analysis.

1 Introduction

The discovery of nuclear fission [1, 2] opened an important chapter not only in the study of nuclear physics but also in the technology of energy supply. Since the nuclear power plant accident at Fukushima in March 2011, further understanding of the fission process has been to required to quantitatively predict the amounts of heavy elements and radioactive fission products remaining as "debris" and the amount of melted spent nuclear fuel still present in the remains of the power plant. Moreover, such information is also important for improving the safety of planned nuclear power plants world wide. Therefore, further study of the nuclear fission process is necessary.

The mass-asymmetric fission remained a puzzle as far as nuclei were described in the analogy with the liquid drop. The origin of the asymmetry in the mass distribution of fission fragments (MDFFs) nowadays is related to the shell structure of the fissioning nucleus. Many theoretical dynamical models have been applied to nuclear fission at low excitations in an attempt to explain its mechanism. In order to investigate the time evolution of the nuclear shape during the fission process a dynamical approach using the Langevin equation can be used. These past investigations focused on systems having high excitation energy. The calculations resulted in a symmetric mass distribution of MDFFs, in good agreement with experimental data at high excitation energies. The MDFF reflects the properties of the potential energy surface in the liquid drop model. In contract, the dynamical calculation using Langevin equations has been seldom applied to the fission process at low excitation energies, owing to difficulties in obtaining the shell correction energy of configurations in the multi-dimensional space of collective coordinates, as well as the huge computation time. However, the computation time has recently been dramatically reduced with the recent advances in computer technologies and the utilization of parallel computing. Moreover, we can calculate the shell correction energy at each configuration using the two-center shell model.

In this paper, we propose the possibility of dynamically calculating the fission process at a low excitation energy using Langevin equations, taking into account the shell effects, pairing effects, dissipation and fluctuation. Using this model, we calculate the MDFFs of $n+^{235}$U, $n+^{233}$U,

and n+^{239}Pu at a low excitation energy and compare them with experimental data, and obtain the independent fission yield. Using this approach, we can investigate the fission mechanism, including the origin of mass-asymmetric fission.

The paper is organized as follows. In Sec. 2, we detail the framework of the model. In Sec. 3, we show the results for MDFFs at the excitation energy $E^* = 20$ MeV. The independent fission yield of n+^{233}U at $E^* = 20$ MeV is presented in Sec. 4. In Sec. 5, we present a summary of this study and further discussion.

2 Model

We use the fluctuation-dissipation model and employ Langevin equations [3] to investigate the dynamics of the fission process. The nuclear shape is defined by the two-center parametrization [4, 5], which has three deformation parameters, z_0, δ, and α to serve as collective coordinates: z_0 is the distance between two potential centers, while $\alpha = (A_1 - A_2)/(A_1 + A_2)$ is the mass asymmetry of the two fragments, where A_1 and A_2 denote the mass numbers of heavy and light fragments. The symbol δ denotes the deformation of the fragments. The detail of the definition is explained in Ref [3]. We assume in this work that each fragment has the same deformation. This constraint should be relaxed in the future work since the deformations of the heavy and light fragments in the fission of U region are known to be different from each other. In order to reduce the computational time, we employ the coordinate z defined as $z = z_0/(R_{CN}B)$, where R_{CN} denotes the radius of a spherical compound nucleus and B is defined as $B = (3 + \delta)/(3 - 2\delta)$. We use the neck parameter $\epsilon = 0.35$. The three collective coordinates may be abbreviated as q, $q = \{z, \delta, \alpha\}$. The potential energy is defined as a sum of the liquid-drop part $V_{\rm LD}$ and a microscopic part $E^0_{\rm shell}$ [3].

The multidimensional Langevin equations [3] are given as

$$\begin{aligned}
\frac{dq_i}{dt} &= \left(m^{-1}\right)_{ij} p_j, \\
\frac{dp_i}{dt} &= -\frac{\partial V}{\partial q_i} - \frac{1}{2}\frac{\partial}{\partial q_i}\left(m^{-1}\right)_{jk} p_j p_k - \gamma_{ij}\left(m^{-1}\right)_{jk} p_k + g_{ij} R_j(t),
\end{aligned} \tag{1}$$

where $i = \{z, \delta, \alpha\}$ and $p_i = m_{ij} dq_j/dt$ is a momentum conjugate to coordinate q_i. The summation is performed over repeated indices. In the Langevin equation, m_{ij} and γ_{ij} are the shape-dependent collective inertia and the friction tensors, respectively. The wall-and-window one-body dissipation is adopted for the friction tensor. A hydrodynamical inertia tensor is adopted with the Werner-Wheeler approximation for the velocity field. The normalized random force $R_i(t)$ is assumed to be that of white noise, *i.e.*, $\langle R_i(t)\rangle$=0 and $\langle R_i(t_1)R_j(t_2)\rangle = 2\delta_{ij}\delta(t_1 - t_2)$. The strength of the random force g_{ij} is given by Einstein relation $\gamma_{ij}T = \sum_k g_{ij}g_{jk}$. T is the nuclear temperature. The fission events are determined in our model calculation by identifying the different trajectories in the deformation space. We consider the neutron emission in our calculation. However, we only take into account the decrease in the excitation energy of the system by neutron emission, not the change in the potential energy surface, as our first step.

3 Mass distribution of fission fragments

A sample trajectory is projected onto the z-α plane (a) and the z-δ plane (b) in Fig. 1. The trajectory starts at $z = 0.65$, $\delta = 0.2$ and $\alpha = 0.0$ at $E^* = 20$ MeV, corresponding to the second

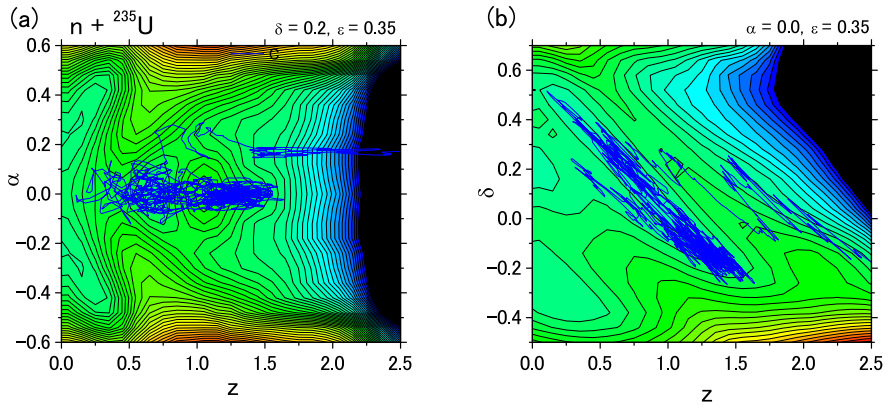

Figure 1: Sample trajectory of $V_{\rm LD} + E^0_{\rm shell}$ for n+^{235}U projected onto the z-α plane at $\delta = 0.2$ (a) and the z-δ plane at $\alpha = 0.0$ (b). The trajectory starts at $z = 0.65$, $\delta = 0.2$, and $\alpha = 0.0$, at $E^* = 20$ MeV, corresponding to the second minimum of the potential energy surface, to reduce the calculation time.

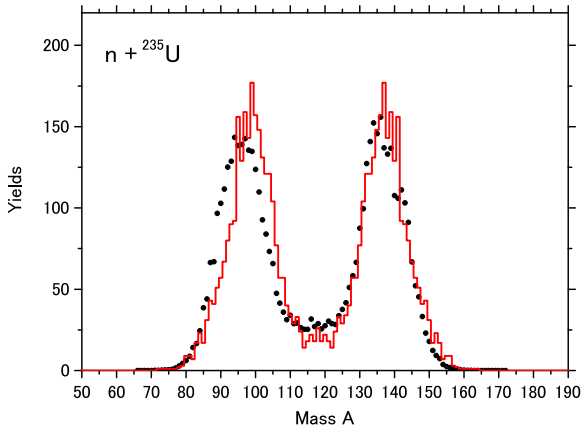

Figure 2: Mass distribution of fission fragments of n+^{235}U at $E^* = 20$ MeV. Calculation and experimental data are denoted by histogram and circles, respectively.

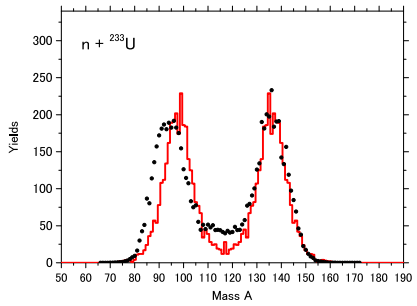

Figure 3: Mass distribution of fission fragments of n+^{233}U at $E^* = 20$ MeV. Calculation and experimental data are denoted by histogram and circles, respectively.

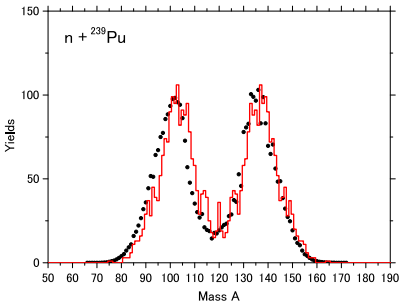

Figure 4: Mass distribution of fission fragments of n+^{239}Pu at $E^* = 20$ MeV. Calculation and experimental data are denoted by histogram and circles, respectively

minimum of the potential energy surface, to reduce the calculation time. Indeed, the MDFFs thus obtained were equivalent to those starting from the ground state, namely, $z = 0.0$, $\delta = 0.2$, and $\alpha = 0.0$. The trajectory remains around the pocket located at $\{z, \delta, \alpha\} \sim \{1.35, -0.2, 0.0\}$ with thermal fluctuations. Then, it escapes from the second minimum and moves along the valley corresponding to $A \sim 140$. Fission from a compound nucleus is defined as the case that a trajectory overcomes the scission point on the potential energy surface. We define the scission point as the configuration in which the neck radius becomes zero.

Figure 2 shows the calculated MDFFs for n+^{235}U in the form of a histogram, together with the corresponding experimental data (dots) for neutron-induced fission leading to the same compound nuclei at $E^* = 20$ MeV, respectively. The dots were taken from JENDL Fission Yield Data File [6] to represent the experimental data concisely. In the present calculation, we prepared 10,000 trajectories, which is equivalent to the number of trajectories of fission normalized by the total number of fission events in the experimental data. For these nuclei, the present approach yields results consistent with the measured data without any adjustment of the parameters in the Langevin calculation, showing the predictive power of the present model. The widths and positions of the peaks are reproduced with high accuracy. We consider that the trajectories move along the fission valley corresponding to $A \sim 140$ ($\alpha \sim 0.18$) in Fig. 1(a). However, the peak position of the light fragments in the calculation is located at a few mass units lower than the experimental data. This discrepancy is partly caused by the changes in the mass numbers of fissioning nuclei upon the emission of neutrons from fragments, which is not included in our model.

We also calculate the MDFFs of n+^{233}U and n+^{239}Pu at $E^* = 20$ MeV, which are shown in Figs. 3 and 4 together with the corresponding experimental data. The results are obtained using the same parameters as these in the calculation for n+^{235}U. The results quantitatively agree with the experimental data, and the tendency of the difference between the calculated results and experimental data is similar to the case of n+^{235}U. We calculate the average total kinetic energy of the fission fragments $\langle TKE \rangle$ of n+^{235}U at $E^* = 20$ MeV. We obtain $\langle TKE \rangle = 171.8$ MeV, which is consistent with the experimental data [7].

4 Independent fission yield

Using our dynamical model, we estimate the independent protons and neutrons fission yield. To describe properly the yield of different isotopes of a given element, one needs to consider separately neutron and proton transfer. We extend our model and introduce the neutron and proton asymmetries instead of the mass asymmetry as

$$\alpha_N = \frac{2N - N_{CN}}{N_{CN}}, \tag{2}$$

$$\alpha_Z = \frac{2Z - Z_{CN}}{Z_{CN}}, \tag{3}$$

where N and Z are the neutron and proton numbers in one of the fragments. N_{CN} and Z_{CN} refer to the compound nucleus. For the neutron and proton asymmetries, the inertia-free Langevin type equation is applied as

$$\begin{aligned} \frac{d\alpha_N}{dt} &= \frac{2}{N_{CN}} D_N^{(1)}(\alpha_N) + \frac{2}{N_{CN}} \sqrt{D_N^{(2)}}\Gamma(t), \\ \frac{d\alpha_Z}{dt} &= \frac{2}{Z_{CN}} D_Z^{(1)}(\alpha_Z) + \frac{2}{Z_{CN}} \sqrt{D_Z^{(2)}}\Gamma(t), \end{aligned} \tag{4}$$

where $\Gamma(t)$ is the normalized random variable with Gaussian distribution, and $D^{(1)}, D^{(2)}$ are the transport coefficients. The detail is explained in Ref [8]. Figure 5 shows the charge distribution of the lighter fission fragments of n+^{233}U at $E^* = 20$ MeV. The experimental data and calculation are denoted by the dashed and solid lines, respectively. Because the value of the proton transfer rate is not known, the results are presented for the several proton transfer rates λ_Z^0 [8]. The calculation with $\lambda_Z^0 = 1.0 \times 10^{22}$ s^{-1} shows a good agreement with the experimental data. The independent fission yield of n+^{233}U at $E^* = 20$ MeV is presented in Fig. 6. Here, we use $\lambda_Z^0 = \lambda_N^0 = 1.0 \times 10^{22}$ s^{-1}. To obtain more aciculate results, we need to increase the number of trials in the Langevin calculation.

5 Summary

In this study, we investigated the fission process for excitation energy 20 MeV using Langevin equations. We calculated the MDFF of n+^{235}U, n+^{233}U, and n+^{239}Pu, and the results indicate mass-asymmetric fission, in good agreement with the experimental data, without any parameter adjustment. This is the first time that the MDFF has been obtained by a Langevin calculation while incorporating the shell effect and compared with experimental data. In the present model, we used three collective variables to describe the shape of the nuclear fission. We discussed the origin of the mass-asymmetric fission by analyzing sample trajectories. This analysis allowed us to directly observe the time evolution of the dynamical process.

In the future, we plan to improve the model to decrease the differences between the calculated MDFF and the experimental data. We must increase the number of variables, at least by introducing independent deformation parameters for each fragment. Moreover, the change in the potential energy owing to neutron emission from the fissioning system as well as from fission fragments should be included in the model.

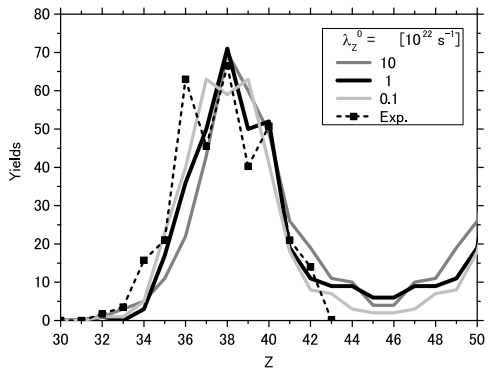

Figure 5: Charge distribution of the lighter fission fragments of n+^{233}U at $E^* = 20$ MeV for each proton transfer rates λ_Z^0.

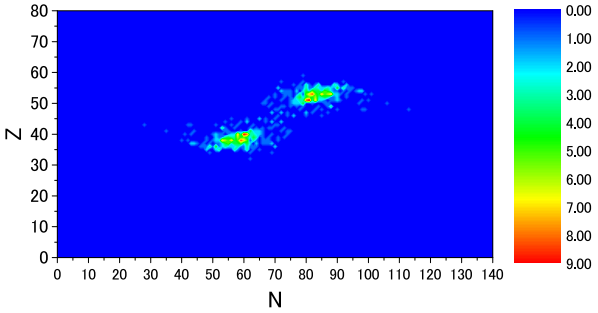

Figure 6: Independent fission yield of n+^{233}U at $E^* = 20$ MeV with $\lambda_Z^0 = 1.0 \times 10^{22}$ s^{-1}.

Present study is the results of "Comprehensive study of delayed-neutron yields for accurate evaluation of kinetics of high-burn up reactors" entrusted to Tokyo Institute of Technology by the Ministry of Education, Culture, Sports, Science and Technology of Japan (MEXT).

References

[1] O. Hahn and F. Straßmann, Naturwissenschaften **27**, 11 (1939).

[2] L. Meitner and O.R. Frisch, Nature (London) **143**, 239 (1939).

[3] Y. Aritomo and M. Ohta, Nucl. Phys. A **744**, 3 (2004).

[4] J. Maruhn and W. Greiner, Z. Phys. **251**, 431 (1972).

[5] K. Sato, A. Iwamoto, K. Harada, S. Yamaji, and S. Yoshida, Z. Phys. A **288**, 383 (1978).

[6] J. Katakura, "*JENDL FP Decay Data File 2011 and Fission Yields Data File 2011*, JAEA-Data/Code 2011-025 (2012), 73p.

[7] R. Vandenbosh and J.R. Huizenga, *Nuclear Fission*, Academic Press, New York and London (1973).

[8] V. Zagrebaev and W. Greiner, Phys. Rev. Lett. **101**, 122701 (2008); V. Zagrebaev and W. Greiner, Phys. Rev. C **78**, 034610 (2008); V. Zagrebaev and W. Greiner, J. Phys. G **35**, 125103 (2008).

17 Present Status of Fission Research Based on TDDFT

Yoritaka Iwata

Center for Nuclear Study, The University of Tokyo, Hongo 7-3-1, 113-0033 Tokyo, Japan

E-mail: iwata@cns.s.u-tokyo.ac.jp

Fission resulting from collision of atomic nuclei is systematically investigated based on time-dependent density functional calculations. Time-dependent density functional theory (TDDFT) is a framework, which enables us to treat quantum many-body dynamics with nucleon degrees of freedom. In this article a theoretical framework called "Composite-Nucleus Constrained TDDFT" is introduced, and charge equilibrium hypothesis for collision fission dynamics is examined.

1 Introduction

Fission of the nucleus is important to many processes. For instance fission should play an important role in superheavy synthesis, as well as many astrophysical phenomena. As for the researches based on the TDDFT, there are several developments in the fission research recently (for example, see [1, 2, 3, 4]).

Let us imagine the collision between nuclei. We use a terminology collision-fission to denote the fission resulting from collision. Fusion-fission and quasi-fission are the main components of the collision-fission. There are several stages in nuclear collisions depending on the time-scales [5]. At the early stage there is a contact between the two nuclei, and the quite rapid processes ($\sim 10^{-22}$s) such as the fast charge equilibration follows [6, 7]. At the intermediate stage ($\sim 10^{-21}$s) composite nucleus is formed, and the collective oscillation such as giant resonance follows. Sometimes after a sufficient time ($> 10^{-20}$s), fission appears.

We present a formalism called "Composite-Nucleus Constrained TDDFT" to investigate the collision-fission dynamics. In this article we mostly focus on the examination of charge equilibrium hypothesis of the collision-fission dynamics. Collision-fission dynamics of a composite nucleus Thorium 240 is systematically investigated based on time-dependent density functional calculations employing SV-bas interaction parameter set [8].

2 Fission after collision

2.1 Charge equilibrium hypothesis

A hypothesis, in which fission fragments produced from collision-fission have almost the same Z/N-ratio to the composite nucleus, is assumed in phenomenological treatments of studying the

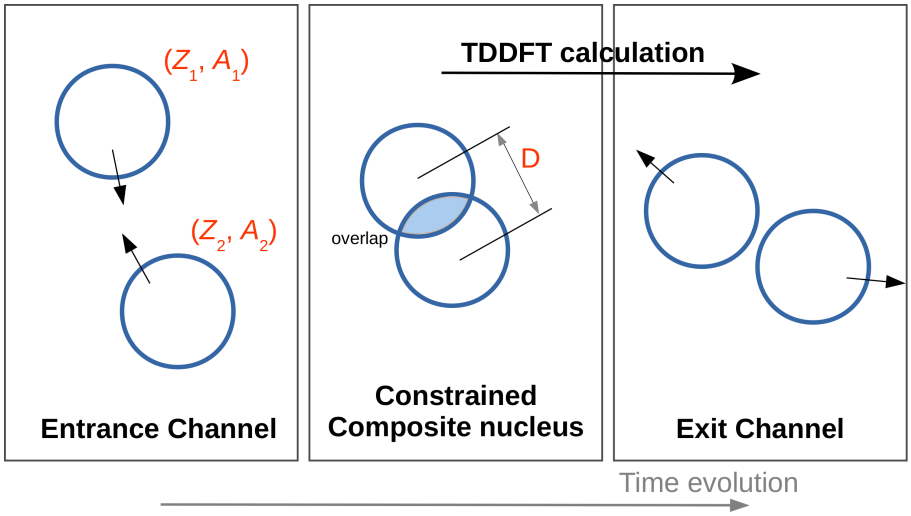

Figure 1: (Color online) Illustration of "Composite-Nucleus Constrained TDDFT". Only the proton and mass numbers of colliding nuclei are given for the entrance channel (i.e., Z_1, Z_2, A_1 and A_2 in the left panel). The two nuclei in the entrance channel might have relative velocity (shown as the arrows), but the velocities in the entrance channel are free parameters in this formalism. There is a constraint on the composite nucleus in which the distance between the two center of mass is given (center panel). The relative velocity of the two nuclei is set to exactly equal to zero for the composite nucleus, and they might have a certain overlap. This constrained composite nucleus is the initial state of the TDDFT calculations. The details of the exit channel such as the kind of emitted nuclei and the relative velocity between the nuclei are determined by the TDDFT calculations. The conditions for the calculations are shown in red character.

collision-fission events (for the charge equilibration dynamics in collision-fission events, see [9, 10, 11]). The reason is that quantum mechanical time-evolution including the nucleon degrees of freedom is desired to determine the time evolution of charge distribution. In this case $Z/N = 90/150 = 0.60$ for the initial nucleus, and the point is to examine whether the Z/N-ratio of fission product is close to 0.60 or not.

2.2 Composite-nucleus constrained TDDFT

For a given energy and a given impact parameter, long-lived composite nuclei with certain excitation energies (compared to the ground state) are possible to be produced. Let us take a composite nucleus of mass number A and proton number Z. Consider binary collision-fission (Fig. 1):

$$ {}^{A_1}Z_1 + {}^{A_2}Z_2 \rightarrow {}^{A}Z \rightarrow {}^{A'_1}Z'_1 + {}^{A'_2}Z'_2 $$

where $A = A' = A_1 + A_2 = A'_1 + A'_2 = 240$ and $Z = Z_1 + Z_2 = Z'_1 + Z'_2 = 90$. First, choose the combination of the two nuclei at the entrance channel (A_i and Z_i) to determine the heavy-ion

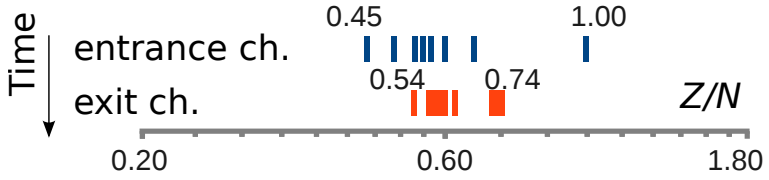

Figure 2: (Color online) Z/N-ratio is plotted for entrance and exit channels (blue and red bars, respectively). The logarithmic scale is adopted for the horizontal axis. Duration time from the entrance to exit channels is roughly equal to 10^{-20}s. The charge equilibrium corresponds to $Z/N = 90/150 = 0.60$ in this case. The maximal and minimal Z/N values are also shown for reference.

reaction being considered ($i = 1, 2$); six cases are taken as $(Z_1, A_1) = (10, 20)$, $(20, 40)$, $(30, 60)$, $(30, 80)$, $(40, 80)$, and $(40, 100)$. Those states are obtained by the static density functional calculations. Second, two states are put at a distance D =13.125 fm without giving any velocities to the center of mass (center panel of Fig. 1), where the diameter ($= 2R$) of $A = 240$ nucleus is roughly equal to 14.9 fm (cf. $R = 1.2A^{1/3}$). This corresponds to the constraint on the composite nucleus. Third, the initial many-body wave function of the TDDFT calculations that is eventually given as an orthogonalized single Slater determinant is given. In fact a single Slater determinant consisting of two single wave functions of two different nuclei (two different Slater determinants) are orthogonalized before starting TDDFT calculations (cf. the Gram-Schmidt orthogonalization method), since the two single wave functions should have overlap. The initial many-body wave function physically simulates the excited composite nucleus in which the relative velocity of the original colliding nuclei is equal to zero. Forth, the TDDFT calculation is carried out to see whether the fission appears or not and to see whether the fission fragments are in charge equilibrium or not.

In this formalism two physical quantities are constrained: the shortest distance of the two colliding nuclei (i.e., distance of the closest approach) and the kind of colliding nuclei at the entrance channel. The most significant assumption included in this formalism is that no change is assumed to happen to the two colliding nuclei at the very early stage before the two colliding nuclei reach the shortest distance. This formalism is originally proposed by Refs. [12]. Certain difficulty in the standard TDDFT approach is expected to be overcome; indeed, the constrained composite nuclei sometimes hold the localization effect (e.g. clustering effect), which can be lost in the mean-field type calculations such as the standard TDDFT.

2.3 TDDFT Results

The smaller one of the final products are $(Z, A - Z) = (7.6, 10.5)$, $(18.0, 24.6)$, $(24.5, 34.3)$, $(30, 50)$, $(34.9, 47.4)$ and $(38.2, 61.3)$, which are produced from $(Z', A' - Z') = (10, 10)$, $(20, 20)$, $(30, 30)$, $(30, 50)$, $(40, 40)$, and $(40, 60)$, respectively. One case results in fusion, and the others in binary fission. Among five binary-fission cases, the masses of the lighter fragment decrease for three cases, which is pronounced to be a specific feature with the fragmentation arising from lowly-excited composite nuclei [13].

Figure 2 shows Z/N-ratios of the fragments for the entrance and exit channels. This figure corresponds to a

one-dimensional dynamical system projected in terms of a physical quantity Z/N in which the charge equilibrium ($Z/N = 0.60$) plays a role of attractor. Indeed the Z/N-range of the distribution becomes smaller from $0.55(= 1.00 - 0.45)$ to $0.20(= 0.74 - 0.54)$. Consequently it is confirmed in this specific setting that the charge equilibrium hypothesis is satisfied rather well.

3 Concluding remark

Charge equilibration hypothesis has been examined by means of a microscopic TDDFT framework, and this hypothesis has been confirmed to be satisfied well. Alrhough, as for the TDDFT calculations, the charge equilibration dynamics was examined with nonzero initial relative-velocities, it is carried out with zero initial relative-velocities (i.e., zero TDDFT-initial velocities). Despite researchers believed the possibility of the non-negligible effects of relative velocity on the charge equilibration in old times, the present results suggest that such an effect is quite small.

Acknowlegements

This work, which is based on the collaboration with Dr. Sophie Heinz (GSI Helmholtz Center for heavy-ion research) and Prof. Satoshi Chiba (Tokyo institute of technology), was supported by Research Laboratory for Nuclear Reactors, Tokyo Institute of Technology. The author is grateful to the financial support by MEXT SPIRE and JICFuS.

References

[1] A. Wakhle, C. Simenel, D. J. Hinde, M. Dasgupta, M. Evers, D. H. Luong, R. du Rietz and E. Williams, Phys. Rev. Lett. **113** (2014) 182502.

[2] V.E. Oberacker, A. S. Umar and C. Simenel, Phys. Rev. **C 90** (2014) 054605.

[3] C. Simenel and A. S. Umar, Phys. Rev. **C 89** (2014) 031601(R).

[4] G. Scamps, C. Simenel and D. Lacroix, arXiv:1501.03592.

[5] Y. Iwata, J. Phys.: Conf. Ser. 445 (2013) 012017.

[6] Y.Iwata, T. Otsuka, J. A. Maruhn and N. Itagaki, Phys. Rev. Lett. **104** (2010) 252501.

[7] Y. Iwata, J. Mod. Phys. **3** (2012) 476.

[8] P. Klüpfel, P.-G. Reinhard, T. J. Bürvenich and J. A. Maruhn, Phys. Rev. **C 79** (2009) 034310.

[9] A. C. Wahl, Atomic data and Nuclear Data Tables **39** (1988) 1.

[10] I. Nishinaka, H. Nakahara and Y. Nagame, Eur. Phys. J. **A 33** (2007) 213.

[11] I. Nishinaka, M. Tanikawa, Y. Nagame and H. Nakahara, Eur. Phys. J. **A 47** (2011) 9.

[12] Y.Iwata and S. Heinz, J. Phys. Conf. Ser. 420 (2013) 012012; CERN Proceedings 002 (2012) 241; "Exotic Nuclei, EXON-2012", World Scientific (2013) 153.

[13] Y. Iwata, T. Otsuka, J. A. Maruhn and N. Itagaki, Nucl. Phys. **A 836** (2010) 108.

This is a blank page.

18 Photodisintegration Cross Section of the ^{9}Be(1/2$^+$) State in the Complex Scaling Method

Myagmarjav Odsuren[1], Yuma Kikuchi[2], Takayuki Myo[3,4], Masayuki Aikawa[5] and Kiyoshi Katō[5],
[1]School of Engineering and Applied Sciences, National University of Mongolia, Ulaanbaatar 210646, Mongolia
[2]RIKEN Nishina Center, Wako, 351-0198, Japan
[3]General Education, Faculty of Engineering, Osaka Institute of Technology, Osaka 535-8585, Japan
[4]Research Center for Nuclear Physics (RCNP), Osaka University, Ibaraki 567-0047, Japan
[5]Nuclear Reaction Data Centre, Faculty of Science, Hokkaido University, Sapporo 060-0810, Japan
e-mail: kato@nucl.sci.hokudai.ac.jp

Abstract: We investigate the photodisintegration cross section for the ^{9}Be(1/2$^+$) state, which is important to realize the properties of the unbound 1/2$^+$ state of ^{9}Be. The recent experimental data are discussed to be explained by an α+α+n model. In order to calculate the photodisintegration cross section into α+α+n three-body final states, the complex scaling method is used.

1. Introduction

The complex scaling method (CSM) [1-3] is a well-established technique in wide areas of physics especially in areas of resonance studies in nuclear physics. At the beginning, its advantage was mainly explained by the superior description of the resonance states of composite systems. Nowadays, it is successfully utilized for getting information of unbound and scattering states.

We apply the CSM to an α+α+n three-cluster model to understand the structure and (γ,n) reaction for low-lying states in ^{9}Be. For the purpose of this work we investigate the unbound nature of the 1/2$^+$ state of ^{9}Be and study the $E1$ transition between the excited 1/2$^+$ and ground 3/2$^-$ states. In this study, we discuss the recent experimental data [4] of the photodisintegration cross section and structure of the 1/2$^+$ state in the ^{9}Be system. The results provide us an interesting suggestion of the virtual state property of the 1/2$^+$ state.

2. Method

The Schrodinger equation is solved by utilizing the orthogonality condition model for the α+α+n (^{9}Be) three-body system as following

$$\widehat{H}\Psi_J^{\upsilon} = E^{\upsilon}\Psi_J^{\upsilon}, \quad (1)$$

where J is the total spin of the α+α+n system and υ is the state index. The Hamiltonian of the three-body system for ^{9}Be is given as

$$\widehat{H} = \sum_{i=1}^{3} t_i - T_{c.m.} + \sum_{i=1}^{2} V_{\alpha n}(\xi_i) + V_{\alpha\alpha} + V_3 + V_{PF}, \quad (2)$$

where t_i and $T_{c.m.}$ are kinetic energy operators for each particle and the center-of-mass of the system, respectively. Here $V_{\alpha n}(\xi_i)$ and $V_{\alpha\alpha}$ are potentials of subsystems for α–n and α–α, respectively. Where ξ_i

is the relative coordinate between *i*-th α–particle and neutron. We here employ the KKNN [5] and, the folding [6] potentials for $V_{\alpha n}$ and $V_{\alpha\alpha}$, respectively. In the Hamiltonian, we use the Pauli-potential V_{PF} to take into account of the Pauli-principle between clusters. The explicit form of V_{PF} is given as

$$V_{PF} = V_F^0 |\Phi_{PF}\rangle\langle\Phi_{PF}|, \tag{3}$$

where the Φ_{PF} is the harmonic oscillator wave functions of the Pauli-forbidden states and the V_F^0 is the potential strength. In this calculation, $V_F^0 = 10^6$ MeV is used.

The three-body potential V_3 is explicitly given by the following one-range Gaussian form with the strength v_{3b}

$$V_3 = v_{3b}\, e^{-\mu\rho^2}, \tag{4}$$

where ρ is the hyper-radius of the α+α+*n* system.

In this study, the properties of the unbound state of ^{9}Be(1/2$^+$) is studied by using the CSM. From Eq.(1), the complex-scaled Schrodinger equation can be rewritten as

$$\widehat{H}^\theta \Psi_J^\upsilon(\theta) = E_\upsilon^\theta \Psi_J^\upsilon(\theta), \tag{5}$$

where $\widehat{H}^\theta$ and $\Psi_J^\upsilon(\theta)$ are the complex-scaled Hamiltonian and wave function, respectively, which are commonly transformed by using the scaling angle θ. Solving the eigenvalue problem of Eq. (5), we obtain the energy eigenvalues and eigenstates (their biorthogonal states) of the complex-scaled Hamiltonian $\widehat{H}^\theta$ as $\{E_\upsilon^\theta\}$ and $\{\Psi_J^\upsilon(\theta)\}$ $\left(\widetilde{\Psi}_J^\upsilon(\theta)\right)$, respectively. In the CSM, all energy eigenvalues of unbound states are obtained as complex numbers. Resonances are separated from the 2θ-lines, and their energy eigenvalues are independent of the scaling angle θ. The eigenvalues of resonance states are found as $E_\upsilon^\theta = E_\upsilon^r - i\Gamma_\upsilon/2$, where E_υ^r and Γ_υ are resonance energies and decay widths of the resonant states, respectively.

By using the basis function expansion, the eigen-function $\Psi_J^\upsilon(\theta)$ for the state υ with the total spin J can be expressed as

$$\Psi_J^\upsilon(\theta) = \sum_{\beta=1}^N c_\beta^\upsilon(\theta)\psi_\beta^J, \tag{6}$$

where ψ_β^J is the basis function for three-body states of ^{9}Be and given as

$$\psi_\beta^J = \left[\left[\phi_{l_\beta}^{i_\beta}(\vec{r}_1^c) \otimes \phi_{\lambda_\beta}^{j_\beta}(\vec{r}_2^c)\right]_{L_\beta} \otimes \chi_{1/2}^\sigma\right]_J. \tag{7}$$

The index β represents a set of $\{c, i, l, j, \lambda, L\}$ where $c = 1$ and 2 specifies a channel of *(*α+α*)+n* and *(*α+*n)+*α, respectively. The orbital angular momenta l and λ are corresponding to the relative motion for the two Jacobi coordinates of $\vec{r}_1$ and $\vec{r}_2$, respectively, in the channel c. Furthermore, L is the total orbital angular momentum. The indices i and j are to distinguish the radial basis functions. We use the Gaussian expansion method [7] to describe the radial component of the wave function. Each relative basis is described as

$$\phi_l^k(\vec{r}) = N_l^k r^l exp\left(-\frac{a_k}{2}r^2\right) Y_l(\hat{r}), \tag{8}$$

where the width of Gaussian basis is taken as

$$a_k = a_0 \eta^{k-1} \tag{9}$$

with the first term a_0 and common ratio η in the geometric progression.

The photodisintegration cross section is calculated in terms of the multipole response and is expressed as

$$\sigma_{E\lambda}^{\gamma}(E_\gamma) = \frac{(2\pi)^2(\lambda+1)}{\lambda[(2\lambda+1)!!]^2}\left(\frac{E_\gamma}{\hbar c}\right)^{2\lambda-1}\frac{dB(E\lambda,E_\gamma)}{dE_\gamma}, \tag{10}$$

where E_γ is the incident photon energy and $B(E\lambda)$ is the electric transition strength with the rank λ. We here calculate the photodisintegration cross section from the ground $3/2^-$ state to $1/2^+$ states in ^{9}Be through the *E1* transition the *^{9}Be(γ,n)^{8}Be* cross section is given as

$$\sigma_{E1}^{\gamma}(E_\gamma) = \frac{16\pi^3}{9\hbar c}E_\gamma\frac{dB(E1,E_\gamma)}{dE_\gamma}. \tag{11}$$

3. Results and Discussion

The CSM has been utilized to investigate ^{9}Be($1/2^+$) state [8, 9]. But in the previous works, the $3/2^-$ ground state of ^{9}Be is calculated as 2.16 MeV from the α+α+*n* threshold without three-body potential. The KKNN [5] and folding [6] potentials are effective potentials for (α,*n*) and (α,α), respectively, which reproduce well the experimental data in the low energy region and it is widely applied in the analysis of two- or three-body systems. We introduce a repulsive three-body potential with v_{3b}=6.57 MeV and $\mu = 0.1$ fm^{-2} in Eq. (4) to reproduce the experimental binding energy of the ground state as 1.574 MeV measured from the three-body threshold [10]. Figure 1 displays an example of the eigenvalue distribution of ^{9}Be($1/2^+$) for the attractive V_3 with v_{3b}=-17 MeV and θ=15^0. This result is obtained by diagonalization of the complex scaled Hamiltonian.

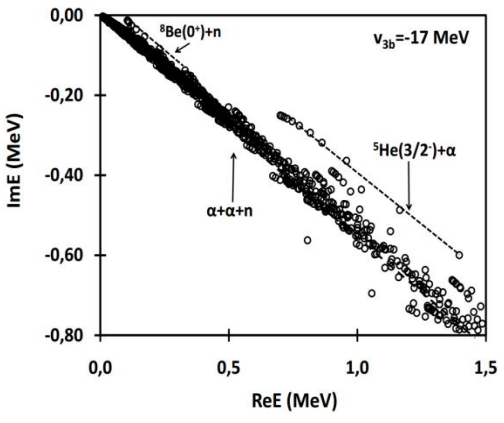

Fig. 1. The energy eigenvalue distribution of ^{9}Be($1/2^+$) in the complex-scaled α+α+n model with θ=15^0.

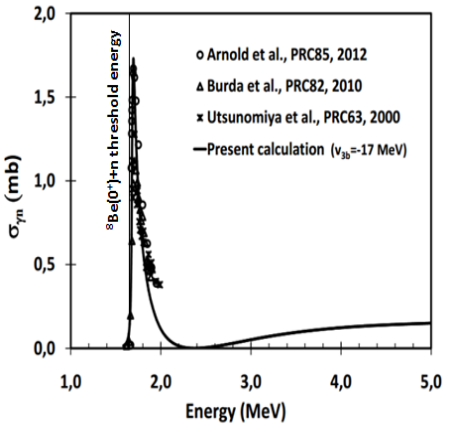

Fig. 2. The ^{9}Be(γ,n)^{8}Be cross section as a function of excitation energy. The experimental data are taken from Refs. [4, 11-12]

All solutions for continuum states are shown by open circles which lie on three 2θ lines starting from the α+α+n three-body threshold and, ^{8}Be(0^{+})+n and ^{5}He($3/2^{-}$)+α two-body thresholds. From Fig.1 we can see there is no resonance pole in the low excitation energy region by the present calculation.

To solve resonance of larger widths, it is necessary to calculate by employing large values of θ. However, in the present α+α+n calculations, it is difficult to keep the numerical accuracy for a θ-value larger than 15^{0}. Therefore, here, we cannot discuss resonances of $\Gamma > 2E_r/\sqrt{3}$ and virtual state. To overcome this problem, we investigate the *E1* transition strength. When such broad resonances and virtual state exist, it is expected that peaks appear in the E1 transition strength even if they are calculated with a small value of θ.

From this result, it is shown that there is calculated no cross section in energies below the ^{8}Be+(0^{+})+n threshold. The sharp peak of the cross section, furthermore, indicates that if this peak is caused by a resonance, its width is smaller than 0.2 MeV. However, our eigenvalue solutions of the CMS Schrodinger equation indicate that there is not such a sharp resonance. To solve this problem, we investigate the properties of the *E1* strength peak in more detail.

We first check the *E1* strength applying wide range values (from 30 MeV to -30 MeV) of the v_{3b} strength and we look for the appropriate v_{3b} strength for the $1/2^{+}$ state. Then, we calculate the photodisintegration cross section using the *E1* transition strength with v_{3b}=-17 MeV. Comparing the calculated photodisintegration cross section of the $1/2^{+}$ state with the recent new experiment [4], we find that v_{3b} =-17 MeV gives a good agreement as shown in Fig. 2.

Using classified eigenvalues into two- and three-body continuum states which are shown in Fig. 1, we investigate the detailed structures of the *E1* transition strength calculated with different v_{3b} strengths. The results of the *E1* transition strength distributions are shown in Figs. 3, 4, 5 and 6. From Figs. 3 and 4, we can see the contributions of the decomposed transition strengths for v_{3b}= 0 and -17 MeV have a dominant component of the ^{8}Be+(0^{+})+n continua. But the α+α+n three-body and ^{5}He($3/2^{-}$)+α two-body continuum states do not contribute strongly. Although they are not presented in figures, we obtained that the decomposed transition strengths also have a dominant component of the ^{8}Be+(0^{+})+n continua for the three-body strength v_{3b} from -16 to -10 MeV.

In Figs. 5 and 6, the contributions of the decomposed transition strengths are shown for v_{3b}=20 and -25 MeV, which correspond to repulsive and attractive cases, respectively. The results of calculated transition strengths are quite different from those shown for v_{3b}=-17 MeV. In Fig. 5, the total transition strength is small and shows a broad peak. This small and broad peak behavior is similar with the v_{3b}=0 case shown in Fig. 3. It should be noticed that the total transition strengths are small and broad for v_{3b}>=0.

On the other hand, we show the results of the transition strengths for an attractive three-body potential (v_{3b}=-25 MeV), in Fig. 6. It is confirmed that the bound state of $1/2^{+}$ is obtained for v_{3b}=-26 MeV.

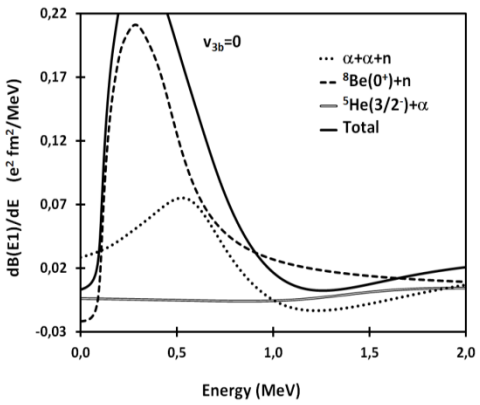

Fig. 3. Decomposed E1 transition strength distributions at v_{3b}=0.

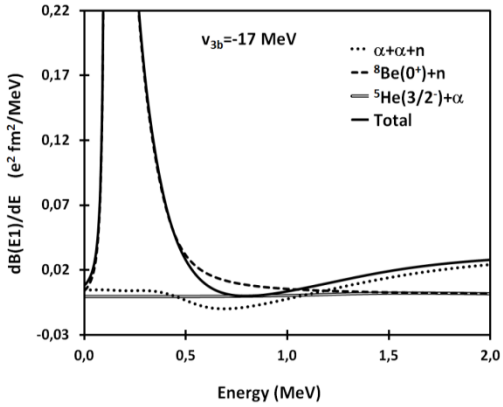

Fig. 4. Decomposed E1 transition strength distributions at v_{3b}=-17 MeV.

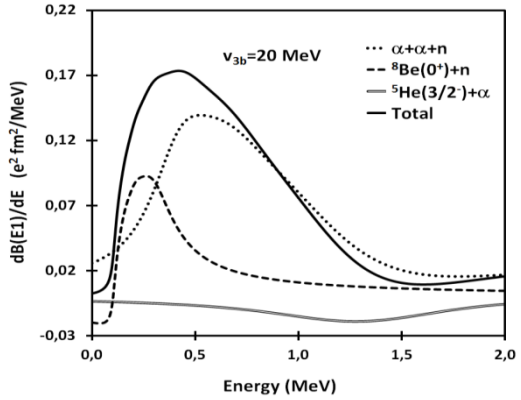

Fig. 5. Decomposed *E1* transition strength distributions at v_{3b}=20 MeV.

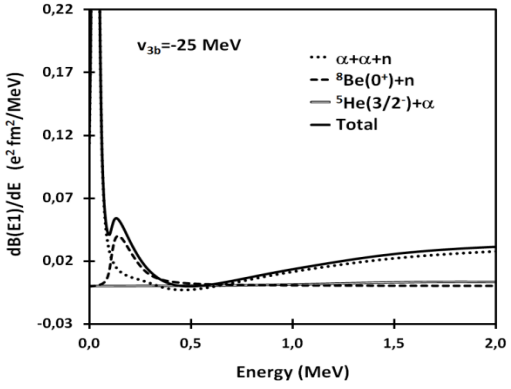

Fig. 6. Decomposed *E1* transition strength distributions at v_{3b}=-25 MeV.

We can see that very sharp peak of the total transition strength in the low-energy (0-0.1 MeV) range. From Figs. 5 and 6, we also understand that the α+α+n three-body continuum states give a rather large contribution to the total transition strength. However, other components of ^{5}He(3/2$^-$)+α and ^{8}Be(0$^+$)+n two-body continuum states give a small contribution in the total transition strength. It is interesting that the peak energies of the transition strengths shift in the low energy range.

By changing v_{3b} strength, the different contributions are obtained for the total transition strength. From the results, we can see how the three-body potential changes the shape of the total transition strength and then which component gives the main contribution and makes a large enhancement at low energies in the total transition strength. We also investigate which eigenstates of continuum solutions makes a peak of the *E1* transition strength.

4. Summary

The objective of this work is to discuss the photodisintegration cross section of the $1/2^+$ state of ^{9}Be system in the framework of the CSM by applying three-body potential. To understand the origin of the calculated cross section, each component of the *E1* transition strength is calculated and investigated contributions to the total cross section.

From the results of the decomposition of the *E1* transition strengths, we can see that the ^{8}Be(0^+)+n two-body continuum is dominant when we apply v_{3b}=0 or -17 MeV but other contributions are small, where the v_{3b} case reproduces the observed cross section. For the v_{3b}=20 or -25 MeV, the α+α+n three-body continuum states give a strong contribution in the total transition strength.

It was noticed that the ^{5}He($3/2^-$)+α two-body continuum states give a very small contribution in the total transition strength at different v_{3b} strengths.

Acknowledgement

The numerical calculations were done with use of computing system of the Nuclear Research Center, National University of Mongolia and Theoretical Nuclear Physics Laboratory, Hokkaido University. One of the authors, K.K., is thankful for the support from a Grant-in Aid Scientic Research (No. 25400241) of the Ministry of Education, Science and Culture, Japan.

Reference

[1]. Y. K. Ho, Phys. Rep.99, 1 (1983)

[2]. S. Aoyama, T. Myo, K. Katō, K. Ikeda, Prog. Theor.Phys. 116, 1 (2006)

[3]. T. Myo, Y. Kikuchi, H. Masui, K. Katō, Prog. Part. Nucl. Phys. 79, 1 (2014)

[4]. C.W. Arnold, T.B. Clegg, C. Iliadis, H.J. Karwowski, G.C. Rich, J.R. Tompkins, C.R. Howell, Phys. Rev. C85, 044605 (2012)

[5]. H. Kanada, T. Kaneko, S. Nagata, M. Nomoto, Prog.Theor. Phys. 61, 1327 (1979).

[6]. C. Kurokawa and K. Katō, Nucl. Phys. A 738, 455 (2004)

[7]. E. Hiyama, Y. Kino, M. Kamimura, Prog. Part. Nucl. Phys. 51, 223 (2003).

[8]. K. Arai, P. Descouvemont, D. Baye, W. N. Catford, Phys. Rev. C 68, 014310 (2003).

[9]. M. Kato, Master Thesis in Hokkaido University (March, 2012) and private communication.

[10]. F. Ajzenberg-Selove, Nucl. Phys. A 490, 1 (1988).

[11]. O. Burda, P. von Neumsnn-Cosel, A. Richter, C. Forssen, B.A. van Overstraeten Brow, Phys. Rev. C82, 015808 (2010)

[12]. H. Utsunomiya, Y. Yonezawa, H. Akimune, T. Yamagata, M. Ohta, M. Fujishiro, H. Toyokawa, H. Ohgaki, Phys. Rev. C63, 018801 (2000)

19 Effect of stripping reaction on calculation of deuteron-induced activation cross sections

Shinsuke NAKAYAMA and Yukinobu WATANABE*

Department of Advanced Energy Engineering Science, Kyushu University
6-1, Kasuga-kouen, Kasuga-shi, Fukuoka 816-8580, Japan
*E-mail: watanabe@aees.kyushu-u.ac.jp

A computer code system for model calculations of deuteron-induced reactions is applied to analyses of deuteron-induced activation cross sections. In the code system, several calculation codes are combined in order to describe the direct processes such as elastic breakup and stripping reactions properly. The calculation using the code system reproduces the experimental activation cross sections from the ^{27}Al(d,p)^{28}Al and ^{45}Sc(d,p)^{46}Sc reactions in the incident energy range from the threshold to 50 MeV very well. From the results of analyses, the importance of stripping reactions in evaluation of deuteron-induced activation cross sections is shown.

1. Introduction

In recent years, intensive neutron sources using a deuteron accelerator have been proposed for various applications involved with not only international scientific projects such as International Fusion Materials Irradiation Facility (IFMIF) [1] and Neutron For Science (NFS) in SPIRAL2 [2], but also medical applications such as Boron Neutron Capture Therapy (BNCT) [3] and production of radioisotopes for Positron Emission Tomography (PET) [4]. In these facilities, the (d,xn) reaction on light nuclei (Li, Be, C, etc.) is considered as a promising reaction to generate intensive neutron beams. In addition, deuteron accelerator components consist of various structure materials including Fe, Cr, Ni, etc. as well as target materials. Thus, comprehensive and accurate nuclear data of deuteron-induced reactions over wide ranges of target mass number and incident deuteron energy are indispensable for accurate estimation of neutron yields, induced radioactivity, and so on. However, currently available experimental data of deuteron-induced reactions are not necessarily enough to meet the requirement. In such the case, theoretical model calculations play an important role in nuclear data evaluation.

2. Integrated code system for deuteron-induced reactions

Under these circumstances, we have been developing an integrated code system dedicated for deuteron nuclear data evaluation [5, 6]. In the code system, several calculation codes are combined in order to describe the direct processes properly. Elastic breakup and stripping reactions to continuum are calculated using the codes based on the Continuum-Discretized Coupled-Channels (CDCC) theory

[7] and the Glauber model [8], respectively. In addition, the DWUCK4 [9], which is the calculation code based on conventional zero-range Distorted Wave Born Approximation (DWBA), is used to calculate stripping reactions to bound states in the residual nuclei. Finally, statistical decay components from compound nuclei are calculated using the Hauser-Feshbach and the exciton models implemented in the CCONE code [10] which was successfully applied to nuclear data evaluation for JENDL-4.0 [11].

For nuclear design of neutron sources, double-differential cross sections (DDXs) for (*d*,*xn*) reactions are critically important. However, experimental data of DDXs for (*d*,*xn*) reactions are lack over wide ranges of target mass number and incident energy. On the other hand, experimental data of DDXs for (*d*,*xp*) reactions do exist. In our previous works [6, 12], therefore, we have compared the calculation results with experimental data about DDXs for (*d*,*xp*) reactions instead of (*d*,*xn*) reactions in order to validate the employed physical models. As the result of analysis, the calculation reproduced DDXs for (*d*,*xp*) reaction on ^{12}C, ^{27}Al and ^{58}Ni in the incident energy ranges up to 100MeV.

Moreover, we have extracted neutron spectroscopic factors (SFs) for the (*d*,*p*) reactions on ^{12}C, ^{27}Al, ^{40}Ca, and ^{58}Ni for incident deuteron energies up to 100 MeV by DWBA analyses and investigated the incident energy dependence of extracted spectroscopic factors in Ref [12]. Consequently, the energy dependence was found to be similar regardless of target nuclei and the empirical expression to represent the energy dependence was implemented in the integrated code system. The calculations with the code system reproduced successfully the experimental activation cross sections from the ^{27}Al(*d*,*p*)^{28}Al reactions at incident energies from the threshold to 20 MeV.

In the present work, we analyze the activation cross sections from the ^{45}Sc(*d*,*p*)^{46}Sc reaction along with that from the ^{27}Al(*d*,*p*)^{28}Al reaction. Since the experimental ^{45}Sc(*d*,*p*)^{46}Sc cross sections exist in the wide incident energy range from the threshold to 50 MeV [13, 14], these data are favorable for further validation of the code system and the empirical expression for SFs implemented in it.

3. DWBA analysis

Before analyzing activation cross sections, we extract the SF which is necessary to determine the absolute values of DWBA calculations. The DWBA differential cross section for the (*d*,*p*) transition to bound state *i* is given by

$$\frac{d\sigma_{bound,i}^{DWBA}}{d\Omega}(E_d) = \frac{D_0^2}{10^4}\frac{2J_i+1}{2J_A+1}\frac{S_i}{2j+1}\frac{d\sigma_{bound,i}^{DWUCK4}}{d\Omega}(E_d), \quad (1)$$

where E_d is the incident deuteron energy, D_0 is a constant used in zero-range approximation and a value of $D_0^2 = 1.50\times10^4$, J_A and J_i are the spins of target nucleus and *i*-th state of residual nucleus, respectively, S_i is the SF for each state, j is the spin of transferred neutron, and $d\sigma_{bound,i}^{DWUCK4}/d\Omega$ is the differential cross section calculated with the DWUCK4 code. The S_i is extracted by fitting the

calculated DWBA cross section to the corresponding experimental one in the small angular region where the neutron stripping process is dominant. In the DWUCK4 calculation, the finite range correction factor is set to be 0.75, and the nonlocality parameters are set to be 0.54 for deuteron and 0.85 for proton, respectively. In addition, global optical potentials (OPs) of Koning and Delaroche (KD) [15] are employed for proton. The adiabatic potential based on nucleon OPs of KD is used for deuteron [16]. The Woods-Saxon shape with fixed radius r_0 = 1.25 fm and diffuseness parameter a = 0.65 fm is assumed for neutron binding potential. No spin-orbit coupling is considered.

Figure 1 shows comparisons of experimental and calculated differential cross sections for (d,p) reactions on ^{27}Al at 6 MeV [17] and ^{45}Sc at 12 MeV [18] where the experimental differential cross sections for as many final states as possible are available. In the present work, we define these incident energies as E_0 and the number of final states at E_0 as I_0. Although I_0 = 35 and 140 final states of ^{28}Al and ^{46}Sc are taken into consideration respectively, the results for some cases are shown in the figure. The calculations show good agreement with the experimental data at small angles. The SF values extracted here are used in calculations of activation cross sections in the next section.

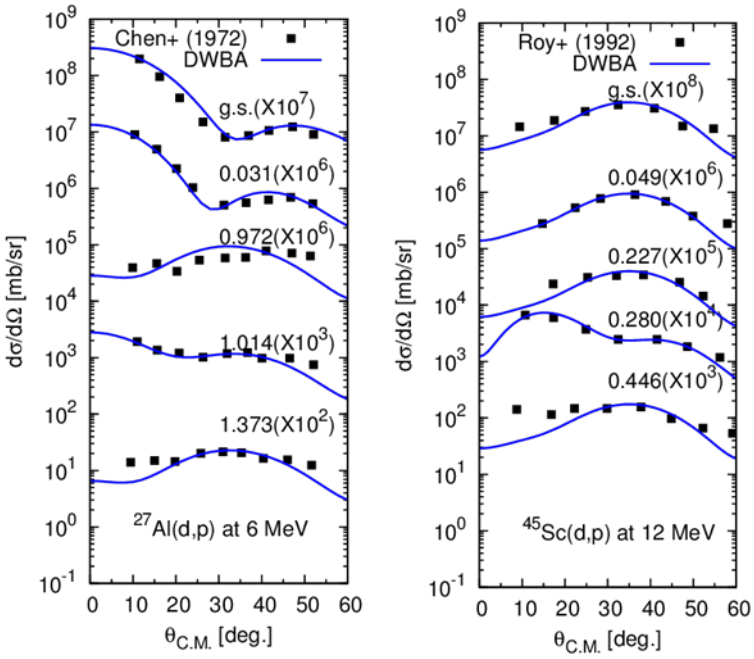

Fig. 1 Calculated and experimental differential cross sections for (d,p) reactions.

4. Activation cross sections

In the calculation code system, the production cross section of the residual nucleus Y from an X(d,p)Y reaction is expressed as follows [6]:

$$\sigma_{\mathrm{Y}} = \sigma_{\mathrm{Y}}^{STR} + \sigma_{\mathrm{Y}}^{SD}, \tag{2}$$

where $\sigma_{\mathrm{Y}}^{STR}$ and σ_{Y}^{SD} correspond to the production cross section of Y for neutron stripping reaction

and statistical decay, respectively. In the code system, all of the neutron stripping reactions to the *i*-th bound state up to I_0 are considered. Thus, neutron stripping reaction components are calculated by summation of angle-integrated DWBA differential cross sections up to I_0 as follows:

$$\sigma_{\mathrm{Y}}^{STR} = \sum_{i}^{I_0} \int \frac{d\sigma_{bound,i}^{DWBA}}{d\Omega} d\Omega . \tag{3}$$

The contribution from the statistical decay process is calculated using the Glauber model [8] and the CCONE code [10]. In general, three different types of compound nuclei can be formed in the case of deuteron-induced reactions. However, since Y is not formed by the proton absorption on X, σ_{Y}^{SD} at E_d is given by summation of two components:

$$\sigma_{\mathrm{Y}}^{SD} = R_d \sigma_Y^d + R_n \sigma_{\mathrm{Y}}^n , \tag{4}$$

where σ_{Y}^d, and σ_{Y}^n are production cross sections of Y from deuteron and neutron-induced reactions on X calculated with the CCONE code, respectively; R_d and R_n are the formation fractions calculated by the Glauber model. In the present code system, we use the Glauber model with the trajectory modification [19] to calculate each formation fraction because the eikonal approximation in the Glauber model gets worse at low incident energies below 20 MeV. In Ref. [19], it is found that the Glauber model with trajectory modification reproduces experimental data of total reaction cross sections even at low incident energies.

In the Glauber model, the nucleon OPs of target nucleus are necessary as input data. In the present work, we use KD OPs [15] at half of the incident deuteron energy both for proton and neutron. In addition, the OPs used in the CCONE code are the global nucleon OPs of KD [15] for proton and neutron and the adiabatic OP [16] for deuteron. Default values in the CCONE code are used for other physical parameters such as level density parameters. The SF values necessary in DWBA calculations are given by Eqs. (5) and (6) [12] in which $F_{k,i}$ is determined at E_0 so that $S_{k,i}(E_0)$ is equal to the SF value extracted from DWBA analysis in Sec. 3.

$$S_{\text{C-12,1}}(E_d) = -2.18\times10^{-6} E_d^3 + 3.19\times10^{-4} E_d^2 - 1.56\times10^{-2} E_d + 8.20\times10^{-1} \tag{5}$$

$$S_{k,i}(E_d) = F_{k,i} S_{\text{C-12,1}}(E_d) \tag{6}$$

Figure 2 shows the comparisons between the calculated and experimental activation cross sections from the ^{27}Al(*d*,*p*)^{28}Al and ^{45}Sc(*d*,*p*)^{46}Sc reactions, respectively. The experimental data are taken from Refs. [15, 16, 20]. The sum of the statistical decay components σ_{Y}^{SD} and the contribution from neutron stripping to bound states $\sigma_{\mathrm{Y}}^{STR}$ reproduce the experimental data in the wide incident energy region up to 50 MeV fairly well. As shown in Fig. 2, the components of stripping reactions to

bounds states in the residual nuclei have a large contribution in the calculation of the activation cross sections for both the (*d*,*p*) reactions.

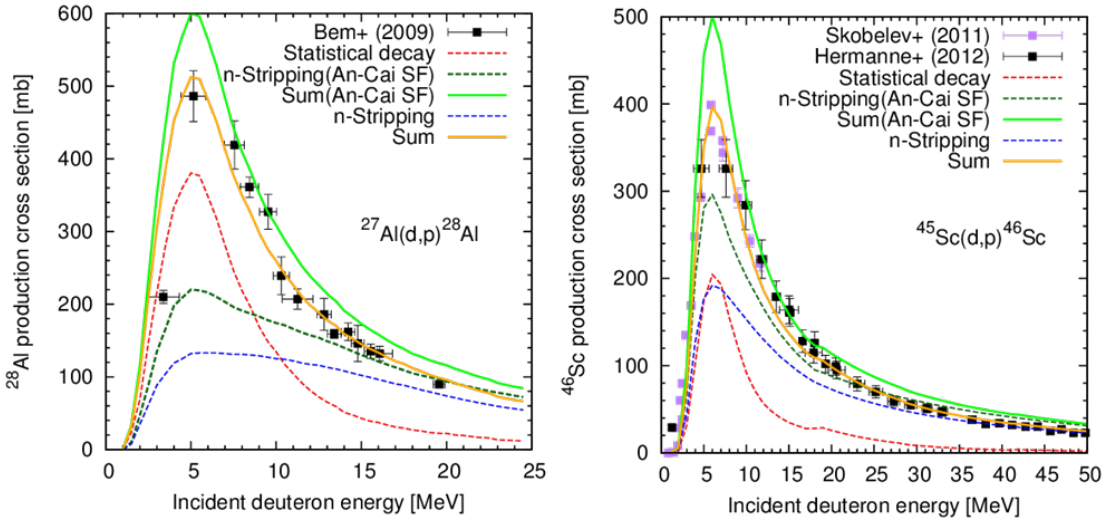

Fig.2 Calculated and experimental activation cross section from (*d*,*p*) reactions.

Let us discuss the importance of SF values. In "An-Cai SF" cases in Fig. 2, the SF values extracted from the DWBA analysis using the global deuteron OP of An and Cai [21] as deuteron OPs are used and the calculation results overestimate the experimental data. From these results, we can conclude that it is not appropriate to use the SF values derived from different analysis conditions. As in this work, we should extract the SF values directly from experimental data instead of the SF values cited in the literatures if the conditions in DWBA calculations, such as OPs, are different.

5. Conclusions

The calculation using our code system reproduced measured activation cross sections from the ^{27}Al(*d*,*p*)^{28}Al and ^{45}Sc(*d*,*p*)^{46}Sc reactions at incident energies from threshold to 50 MeV fairly well. The analysis results demonstrated that it is of importance to consider the stripping reaction to bound states appropriately. When one performs DWBA calculation for the stripping reaction, one should extract the spectroscopic factor (SF) directly from experimental data instead of the SF values cited in the literatures, in the case where the input parameters used in DWBA calculations, such as optical potentials, are different from those used in the literatures.

Acknowledgments

The authors wish to thank K. Ogata, T. Matsumoto and S. Hashimoto for fruitful discussion and comments on DWBA analyses. This work was supported by Grant-in-Aid for The Japan Society for the Promotion of Science (JSPS) Fellows Grant Number 26・1995.

References

[1] Moeslang A, Heinzel V, Matsui H, Sugimoto M. Fusion Eng. Des. 2006; 81:863-871.

[2] Fadil M, Rannou B, the SPIRAL2 project team. Nucl. Instr. Meth. B 2008; 266:4318-4321.

[3] Agosteo S, Curzio G, d'Errico F, Nath R, Tinti R. Nucl. Instr. Meth. A 2002; 476:106-112.

[4] Kin T, Nagai Y, Iwamoto N, Minato F, Iwamoto O, Hatsukawa Y, Segawa M, Harada H, Konno C, Ochiai K, Takakura K. J. Phys. Soc. Jpn. 2013; 82:034201.

[5] Nakayama S, Araki S, Watanabe Y, Iwamoto O, Ye T, Ogata K. Nuclear Data Sheets 2014; 118:305-307.

[6] Nakayama S, Araki S, Watanabe Y, Iwamoto O, Ye T, Ogata K. Energy Procedia 2015; 71:219-227.

[7] Yahiro M, Ogata K, Matsumoto T, Minomo K. Prog. Theor. Exp. Phys. 2012; 2012:01A206.

[8] Ye T, Hashimoto S, Watanabe Y, Ogata K, Yahiro M. Phys. Rev. C 2011; 84:054606.

[9] Kunz PD. computer code DWUCK4. 1974, *http://spot.colorado.edu/~kunz/*.

[10] Iwamoto O. J. Nucl. Sci. Technol. 2007; 44:687-697.

[11] Shibata K, Iwamoto O, Nakagawa T, Iwamoto N, Ichihara A, Kunieda S, Chiba S, Furutaka K, Otuka N, Ohsawa T, Murata T, Matsunobu H, Zukeran A, Kamada S, Katakura. J. Nucl. Sci. Technol. 2011; 48:1-30.

[12] Nakayama S, Watanabe Y. J. Nucl. Sci. Technol. 2015; 53:89-101.

[13] Hermanne A, Adam Rebeles A, Tarkanyi F, Takacs S, Takacs MP, Csikai J, Ignatyuk A. Nucl. Inst. Meth. B 2012; 270:106-115.

[14] Skobelev NK, Kulko AA, Kroha V, Burjan V, Hons Z, Daniel AV, Demekhina NA, Kalpakchieva R, Kugler A, Mrazek J, Penionzhkevich Yu E, Piskor S, Simeckova E, Voskoboynik EI. J. Phys. G Nucl. Part. Phys. 2011; 38:035106.

[15] Koning AJ, Delaroche JP. Nucl. Phys. A 2003; 713:231-310.

[16] Madland DG. Proc. Specialists' Meeting on Preequilibrium Nuclear Reactions; 1988 Feb 10-12; Semmering (Austria). pp.103-110.

[17] Chen S, Rapaport J, Enge H, Buechner WW. Nucl. Phys. A 1972; 197:97-105.

[18] Roy JN, Majumder AR, Sen Gupta HM. Phys. Rev. C 192; 46:144-157.

[19] Ye T, Watanabe Y. Nucl. Data Sheets 2014; 118:308-311.

[20] Bem P, Simeckova E, Honusek M, Fischer U, Simakov SP, Forrest RA, Avrigeanu M, Obreja AC, Roman FL, Avrigeanu V. Phys. Rev. C 2009; 79:044610.

[21] An H, Cai C. Phys. Rev. C 2006; 73:054605.

20 Cold neutron total cross-section and its application to materials science

Hirotaka Sato[1], Yoshinori Shiota[2], Takenao Shinohara[3], Takashi Kamiyama[1], Masato Ohnuma[1], Michihiro Furusaka[1] and Yoshiaki Kiyanagi[2]

[1]Faculty of Engineering, Hokkaido University, Kita-13 Nishi-8, Kita-ku, Sapporo 060-8628, Japan

[2]Graduate School of Engineering, Nagoya University, Furo-cho, Chikusa-ku, Nagoya 464-8603, Japan

[3]J-PARC Center, Japan Atomic Energy Agency (JAEA), 2-4 Shirakata-shirane, Tokai, Naka, Ibaraki 319-1195, Japan

E-mail: h.sato@eng.hokudai.ac.jp

Abstract

Neutron-nucleus total cross-section at the energy region of thermal/cold neutrons consists of not only 1/v absorption cross-section but also coherent/incoherent elastic scattering and inelastic scattering cross-sections. Coherent elastic scattering is caused by diffraction phenomenon (so-called Bragg scattering) of neutrons from nuclei in a crystalline material, which is Bragg-edge transmission cross-section indicating properties of crystal structure and crystalline microstructure of a material [1]. Total cross-section at such energy region can be calculated for various nuclides/elements from databases of nucleus and crystal [2]. Furthermore, for evaluation of engineering materials in actual use, we developed the cold neutron total cross-section analysis software "RITS" [3]. Owing to the RITS code combined with an energy-resolved neutron transmission imaging experiment using the pulsed neutron TOF spectroscopy, a large area/volume mapping of crystallographic information became feasible. In the presentation, we introduce the activities on materials science by using the cold neutron total cross-section analysis, and also discuss some issues on the calculation procedure of cold neutron total cross-section.

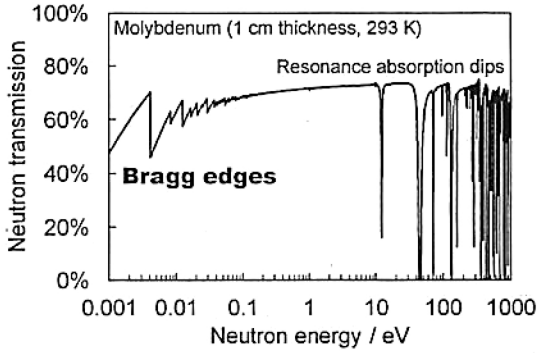

Figure: Bragg-edge neutron transmission caused by coherent elastic scattering (so-called Bragg scattering or diffraction) in a polycrystalline material.

References

[1] E. Fermi, W. J. Sturm and R. G. Sachs, Phys. Rev. **71** (1947) 589-594.

[2] F. Kropff and J. R. Granada, *CRIPO: A fast computer code for the evaluation of σ_T in polycrystalline materials*, Unpublished Report CAB-1977, Institute Balseiro, Bariloche (1977).

[3] H. Sato, T. Kamiyama and Y. Kiyanagi, Mater. Trans. **52** (2011) 1294-1302.

This is a blank page.

21 Search for neutron resonances of ^{106}Pd

Shoji Nakamura*[1)], Atsushi Kimura[1)], Yosuke Toh[1)], Hideo Harada[1)],
Tatsuya Katabuchi[2)], M.Mizumoto[2)], Masayuki Igashira[2)], Jun-ichi Hori[3)], Koichi Kino[4)]

1) Japan Atomic Energy Agency, 2-4 Shirakata, Tokai-mura, Naka-gun, Ibaraki 319-1195, Japan
2) Research Laboratory for Nuclear Reactors, Tokyo Institute of Technology, O-okayama, Meguro, Tokyo 152-8550, Japan
3) Research Reactor Institute, Kyoto University, 2-1010 Asashiro Nishi, Kumatori-cho, Sennan-gun, Osaka 590-0494, Japan
4) Faculty of Engineering, Hokkaido University, Kita 13, Nishi 8, Kita-ku, Sapporo, 060-8628, Japan
*E-mail: shoji.nakamura@jaea.go.jp

Measurements of neutron capture cross sections with a Time-Of-Flight (TOF) method have been performed vigorously at the Accurate Neutron-Nucleus Reaction measurement Instrument (ANNRI) in the Materials and Life Science Experimental Facility (MLF) of J-PARC. In a series of the measurements, we found that there were many miss-assignments for resonance peaks even in stable isotopes. When resonance data of ^{106}Pd were examined, there were discrepancies between JENDL-3.3 and ENDF/B-VII.0. In JENDL-3.3, the weak resonances at 63, 146 and 156 eV were not adopted for ^{106}Pd, and afterwards these resonances were adopted in JENDL-4.0. Then, this work was aimed to search the resonances of ^{106}Pd and confirm the existence of them by using the ANNRI.

1. Introduction

There is a concern to reduce the influence for environment by radioactive wastes caused from nuclear spent fuels. The radioactive wastes are long lived fission products (LLFPs) and Minor Actinides (MAs). The transmutation is one of candidates to reduce amount of LLFPs and MAs. When the transmutation method by using neutrons is thought, accurate data of neutron capture cross-sections should be needed for objective LLFPs and MAs. This is why we have measured neutron capture cross-sections of LLFPs and MAs with a Time-Of –Flight (TOF) method by using the Accurate Neutron-Nucleus Reaction measurement Instrument (ANNRI) installed in the Materials and Life Science Experimental Facility (MLF) of J-PARC[1-7]. In a series of the measurements of LLFPs, for example ^{107}Pd[5], it was found that some resonances due to impurities in the Pd sample were miss-assigned. Then, it is easily imaged that there would be any miss-assigned resonances for other Pd isotopes. For ^{106}Pd nuclide among them isotopes, **Figure 1** plotted the evaluated neutron capture cross sections sited in JENDL-3.3[8] and ENDF/B-VII.0[9]. The 63, 146 and 156-eV resonances marked with a circle in the figure are not

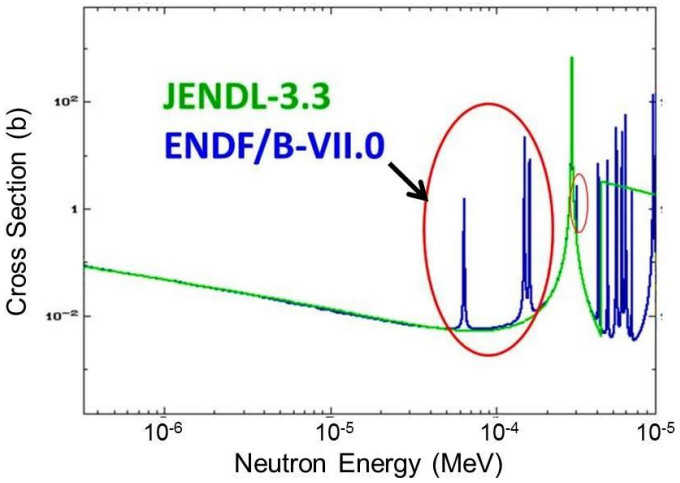

Figure 1 Comparison of cross-section data from JENDL-3.3 to those from ENDF/B-VII.0

adopted in JENDL-3.3, but in ENDF/B-VII.0. In the later revision, those resonances are adopted in JENDL-4.0[10]. The resonance data by Crawford *et al.*[11] might be adopted in the libraries, but anyway, it should be need to confirm whether or not those resonances belong to ^{106}Pd. Then, this study is aimed to confirm those resonances experimentally with the ANNRI.

2. Experiments

The experiments were carried out with the Ge detector of ANNRI. Our Ge spectrometer as shown in **Figure 2** has two cluster Ge detectors, eight coaxial-Ge detectors, and Compton suppressing BGO detectors. Its energy resolutions for 1.33-MeV γ-ray s are 5.8 keV in on-beam and 2.4 keV in off- beam conditions. Its peak efficiency for 1.33-MeV γ-ray is 3.64±0.11%[12]. A high purity ^{106}Pd metal powder was used, and its weight was 34.7mg. Its isotopic abundances are summarized in **Table 1**. The ^{106}Pd sample was wrapped with a FEP film. The measurements were performed for 134 hours in total. The beam power was 300 kW. To reduce neutron scattering by air, the air in the beam duct is replaced with Helium gas.

Figure 2 Ge spectrometer installed with the ANNRI

Table 1 Isotopic abundance of the ^{106}Pd sample

Isotopes	102	104	105	106	108	110
Sample(%)	＜0.02	0.14	3.17	95.56±0.15	0.66	0.07
Natural(%)	1.02	11.14	22.33	27.33	26.46	11.72

An example of the prompt gamma r-ray spectrum is shown in **Figure 3**. The prompt gamma rays due to capture reaction of ^{106}Pd were clearly observed at gamma-ray energies of 115 keV and around 300 keV. **Table 2** listed the information of prompt gamma rays [13] emitted via neutron capture of ^{106}Pd.

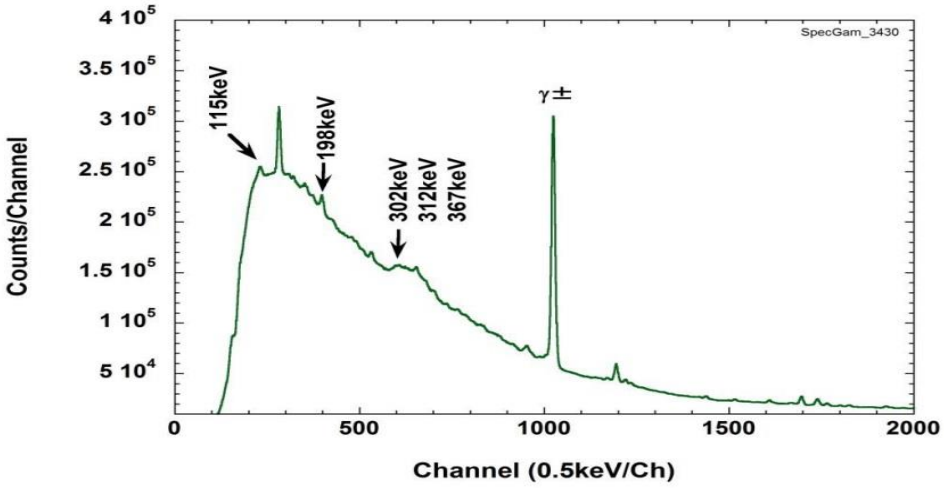

Figure 3 An example of prompt gamma-ray spectrum measured with the ^{106}Pd sample

One finds that an overlap of gamma-rays from 266 to 367 keV in Table 2 is observed around 600 channels in Fig.3. These gamma rays originated to ^{106}Pd were used for analyses.

For the time calibration, a Au foil (6mmϕ × 10mm^{t}) was used, and measured it for 1.8 hours. The time calibration was performed with the known resonance energies of Au from 4.9-eV up to 1 keV.

While the energy calibration for the Ge detector, a pellet of NaCl (500mg) was used, and measured for 2.4 hours. Prompt gamma-rays via neutron captures of ^{35}Cl, ^{37}Cl and ^{14}N were used to calibrate energies from 511 keV up to about 10 MeV. The time and energy calibrations are shown in **Figure 4** and **5**, respectively.

Table 2 Prompt gamma rays emitted via neutron capture of ^{106}Pd

Eγ (keV)	Δ Eγ (keV)	Δ Iγ/Iγ(max) (%)
80.10	0.30	
102.40	0.50	
115.86	0.07	100.00
198.70	0.50	20.00
266.10	0.20	
277.58	0.20	40.00
288.28	0.20	20.00
302.54	0.06	100.00
312.0	0.11	40.00
321.84	0.20	60.00
357.84	0.20	20.00
367.31	0.20	60.00
381.81	0.11	
392.41	0.15	60.00
471.29	0.15	40.00
554.40	0.30	
670.10	0.12	60.00

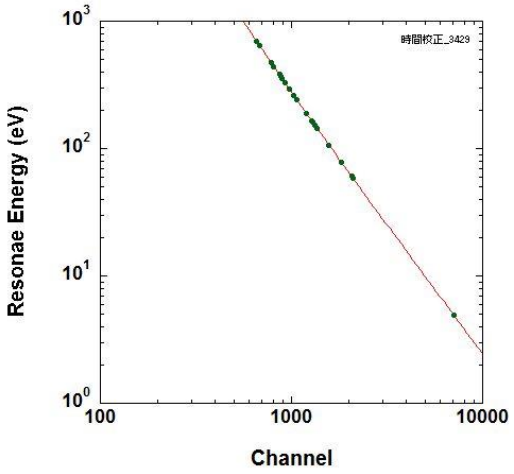

Figure 4 Time correction curve from 4.9eV to 1 keV with resonances of Gold

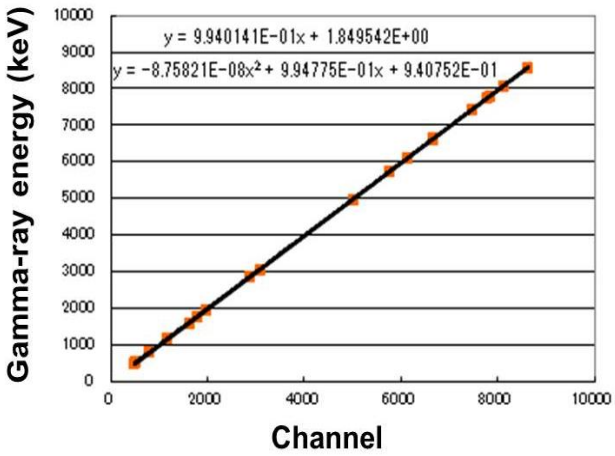

Figure 5 An example of gamma-ray energy calibration curve from 511 keV to 9 MeV

3. Analysis and Discussions

An example of TOF spectrum of ^{106}Pd is given in **Figure 6**. Energies for resonance peaks are written in the Figure by using the time correction curve. The resonances due to ^{106}Pd are observed at the neutron energies of 63, 146, 156 and 281 keV. The dips behind the resonances at 33 and 281 eV were caused by the high counting rates due to the large resonance capture reaction. The resonance peaks due to ^{105}Pd and ^{108}Pd are also observed because of their relatively large neuron capture cross-sections, even though their abundances are small as listed in Table 1. Since many peaks are observed, it is necessary to eliminate resonances due to Pd isotopes and impurities and to extract resonances due to ^{106}Pd.

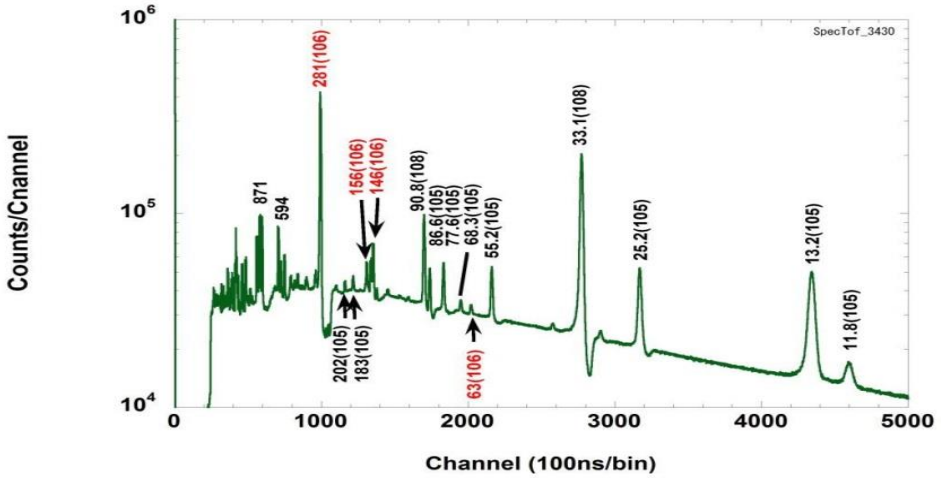

Figure 6 An example of TOF spectrum obtained by the ^{106}Pd sample

The ANNRI has an advantage to get the two dimensional data of the information for pulse height and TOF. Then, by gating at 281-eV resonance of ^{106}Pd, the gamma-ray spectrum was extracted as shown in **Figure 7**. One finds almost gamma-rays peaks listed in Table 2, however the 198-keV gamma ray was not observed against the first expectation because of its emission probability. The gamma rays are obviously observed at the energies of 330, 348, 415 keV and so on, though they are not reported as ^{106}Pd capture gamma rays. It is probably that they are unreported prompt gamma rays. But, more measurements and detailed confirmation should be needed about that.

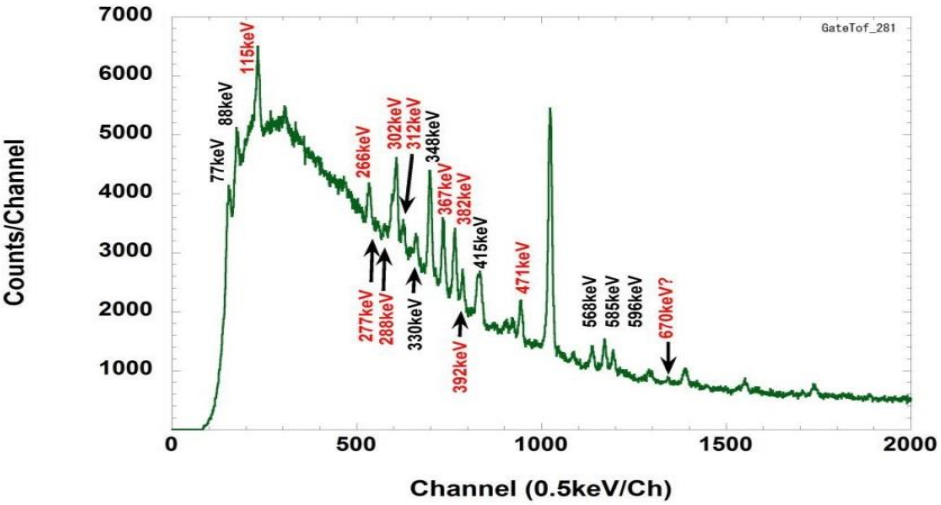

Figure 7 An example of gamma-ray spectrum obtained by gating at the 281-eV resonance

From the result of Fig.7, the overlap around 300 keV in Fig.3 is due to gamma rays emitted from the neutron capture of ^{106}Pd. In this time, a TOF spectrum was extracted by gating around 300 keV in the gamma-ray spectrum of Fig.3. A gated TOF spectrum is shown in **Figure 8**. The 33- and 90-eV resonance peaks are also extracted in Fig.8, because ^{105}Pd and ^{108}Pd also emit about 300 keV prompt gamma rays via neutron capture reaction. The 63-eVresonance was not observed because of the lack of statics due to its small neutron capture cross-section as about 1 (b). On the contrary, the 146- and 156-eV resonances are observed.

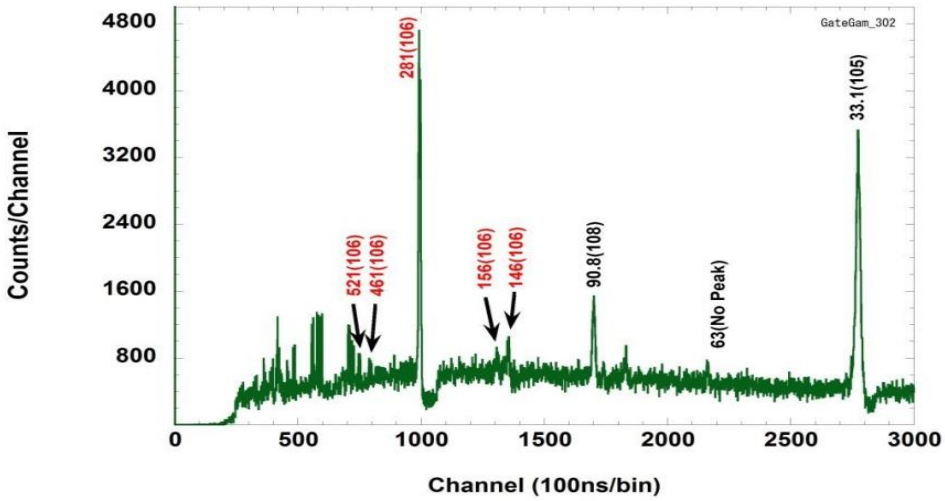

Figure 8 A TOF Spectrum obtained by gating the gamma-ray spectrum of ^{106}Pd at the gamma-ray energy around 300 keV

In next time, a gate was imposed at 115-keV gamma ray in Fig.3 in order to check whether or not the resonances were surely due to ^{106}Pd. An example of the obtained gated TOF spectrum is given in **Figure 9**. The resonance peaks were observed at the neutron energy of 146 and 156 eV in the gated TOF spectrum.

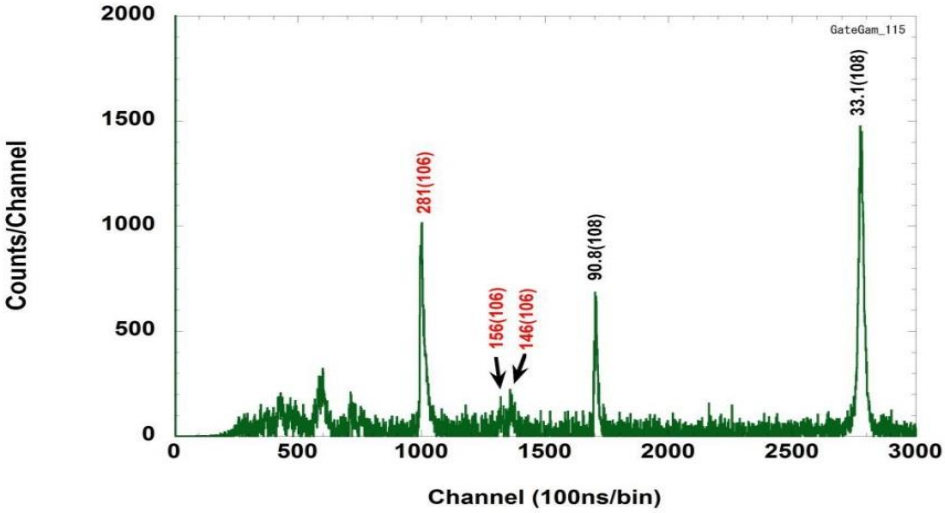

Figure 9 A TOF Spectrum obtained by gating the gamma-ray spectrum of ^{106}Pd at the gamma-ray energy of 115 keV

From these results, it concludes that the 146- and 156-eV resonances are due to ^{106}Pd, and correctly adapted in both of JENDL-4.0 and ENDF/B-VII.0.

4. Conclusion

Measurements of ^{106}Pd were performed by the Ge spectrometer installed at ANNRI in MLF of J-PARC to confirm whether or not the reported resonances are due to ^{106}Pd. In the TOF spectrum, the 63, 146, 156, and 281-eV resonances were clearly observed. By gating at the prompt γ-rays emitted from the ^{106}Pd neutron capture, TOF spectra were extracted and examined. As the result, it was confirmed that the 146 and 156-eV resonances are surely originated from ^{106}Pd capture reaction. The most prominent resonance at 281 eV was also due to ^{106}Pd. However, further experiment and analysis should be necessary for other weak resonances.

Acknowledgment

The authors would like to appreciate the accelerator staff of J-PARC for their operation of the accelerator. This work is supported by JSPS KAKENHI (22226016).

References

[1] A.Kimura *et al*., *J. Nucl. Sci. Technol.*, **49**, 708-724 (2012).
[2] K.Hirose *et al*., *J. Nucl. Sci. Technol.*, **50**, 188-200 (2013).
[3]H.Harada *et al*., *International Conference on Nuclear Data For Science and Technology (ND2013), New York NY USA*, March 4-8, 2013, *Nuclear Data Sheets*, **119**,61-64 (2014).
[4]K. Hirose *et al*., *International Conference on Nuclear Data For Science and Technology (ND2013), New York NY USA*, March 4-8, 2013, *Nuclear Data Sheets,* **119**,48-51 (2014).
[5]S.Nakamura *et al*., *International Conference on Nuclear Data for Science and Technology (ND2013), New York NY USA*, March 4-8, 2013, *Nuclear Data Sheets*, **119**,143-146 (2014).
[6]J.Hori *et al*., *International Conference on Nuclear Data For Science and Technology (ND2013), New York NY USA*, March 4-8, 2013, *Nuclear Data Sheets*, **119**,128-131 (2014).
[7]K.Kino *et al*., *International Conference on Nuclear Data for Science and Technology (ND2013), New York NY USA*, March 4-8, 2013, *Nuclear Data Sheets*, **119**,140-142 (2014).
[8]K.Shibata *et al*.,"Japanese Evaluated Nuclear Data Library Version 3 Revision-3: JENDL-3.3" , *J. Nucl. Sci. Technol*. **39**, 1125 (2002).
[9]M.B.Chadwick *et al.,* "ENDF/B-VII.0: Next Generation Evaluated Nuclear Data Library for Nuclear Science and Technology", *Nuclear Data Sheets*, **107**(12), 2931 (2006)
[10] K.Shibata *et al*., "JENDL-4.0: A New Library for Nuclear Science and Engineering," *J.Nucl.Sci. Technol*. **48**(1), 1-30 (2011).
[11]B.E.Crawford *et al*., *Physical Review* C, **58**(2), 729 (1998).
[12] T.Kin *et al., the 2009 NSS-MIC Conf. Rec.*, N24-2, (2009).
[13]National Nuclear Data Center, http://www.nndc.bnl.gov/capgam/

22 Evaluation of Gamma-ray Strength Function based on Measured Neutron Capture Gamma-ray Spectra

Nobuyuki Iwamoto
Nuclear Data Center, Nuclear Science and Engineering Center,
Japan Atomic Energy Agency, Tokai, Ibaraki 319-1195, Japan
e-mail: iwamoto.nobuyuki@jaea.go.jp

We systematically tested the predictive capability of capture gamma-ray spectra and capture cross sections by using nuclear reaction model code CCONE with several types of E1 gamma-ray strength function, in comparison with experimental data of nuclides from Fe to Au. It is found that the simplified modified Lorentzian model better predicts the experimental data. In addition, the enhancement factor of enhanced generalized Lorentzian model was evaluated, in the case of using the Fermi-gas model of Mengoni-Nakajima formulation for nuclear level density. This revised model shows high reproducibility especially for capture cross sections.

1 Introduction

Gamma-ray strength function (GSF) is one of the important ingredients to describe gamma-ray emissions in nuclear reaction. In order to fix the GSF, it is valuable to measure photoabsorption cross sections and neutron capture gamma-ray spectra. The latter has been systematically measured at Tokyo Institute of Technology (Tokyo Tech), where the capture cross sections have also been derived in the 10-100 keV and around 550 keV neutron energy regions.

In this work the capture gamma-ray spectra and cross sections of 40 nuclides from Fe to Au were calculated by nuclear reaction model code CCONE [1]. This code takes into account proposed various types of GSF (e.g., standard Lorentzian (SLO), enhanced generalized Lorentzian (EGLO), and modified Lorentzian (MLO) models [2]). We evaluated the validity of calculated capture gamma-ray spectra and also cross sections on the basis of different GSF models, comparing them with the experimental data measured at Tokyo Tech.

2 Calculations

The coupled channels (CC) optical models were used with the potential form [3]. The global parameters of optical model potential were taken from Kunieda *et al.* [4]. Coupled levels were chosen in the ground-state band from Evaluated Nuclear Structure Data File (ENSDF) [5]. Deformation parameters were taken from RIPL-3 database [2]. They were interpolated by using the values of neighboring nuclides if not available. The total, reaction, and shape elastic scattering cross sections and inelastic scattering information from CC calculations, together with neutron transmission coefficients, were applied to the Hauser-Feshbach statistical model calculations.

The statistical model with width fluctuation correction [6, 7] is incorporated in CCONE. There are two important ingredients in calculating the de-excitation process by gamma-ray emissions. One is the nuclear level density, and the other is the GSF. Information of nuclear levels such as excitation energy, spin-parity and gamma-ray transition rates between levels were taken from RIPL-3. The level density above adopted discrete levels was prescribed by Gilbert and Cameron formalism [8]. The formulation of level density parameter in Fermi-gas model was adopted with an odd-even effect [9]. The gamma-ray transitions were considered for E1, M1 and E2 ones. E1 component has a larger contribution than M1 and E2 ones. Hence, several models for E1 GSF have been proposed. Especially three types described below were selected for comparisons in this work.

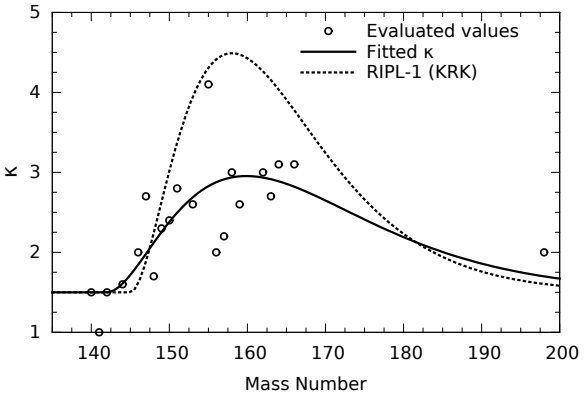

Figure 1: The evaluated values and fitted curve of κ

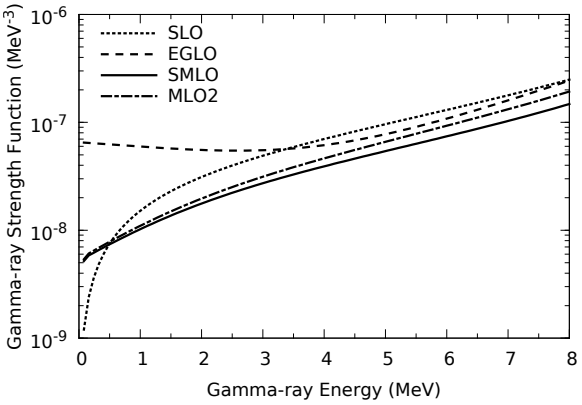

Figure 2: Gamma-ray strength functions of SLO, EGLO, SMLO and MLO2 models for ^{162}Dy

The SLO model has been widely applied to the calculation of capture cross section. The formulation with three parameters (resonance energy E_r, energy independent resonance width Γ_r, and peak cross section σ_r) is presented as follows:

$$f(\epsilon_\gamma) = C\sigma_r\Gamma_r \frac{\epsilon_\gamma \Gamma_r}{(\epsilon_\gamma^2 - E_r^2)^2 + (\epsilon_\gamma \Gamma_r)^2} \quad (\mathrm{MeV}^{-3}), \tag{1}$$

where the constant value $C = 8.674 \times 10^{-8}$ in units of MeV for energy and width, and of mb for cross section, ϵ_γ is the γ-ray energy.

The EGLO model has energy and temperature dependent collisional width Γ_k and a term which corrects the behavior of SLO form close to $\epsilon_\gamma = 0$. The form is described as follows:

$$f(\epsilon_\gamma) = C\sigma_r\Gamma_r \left[\frac{\epsilon_\gamma \Gamma_k(\epsilon_\gamma, T_f)}{(\epsilon_\gamma^2 - E_r^2)^2 + (\epsilon_\gamma \Gamma_k(\epsilon_\gamma, T_f))^2} + 0.7 \frac{\Gamma_k(\epsilon_\gamma = 0, T_f)}{E_r^3} \right] \quad (\mathrm{MeV}^{-3}), \tag{2}$$

$$\Gamma_k(\epsilon_\gamma, T_f) = \mathcal{K}(\epsilon_\gamma) \frac{\Gamma_r}{E_r^2} [\epsilon_\gamma^2 + (2\pi T_f)^2], \quad \mathcal{K}(\epsilon_\gamma) = \kappa + (1-\kappa)\frac{\epsilon_\gamma - \epsilon_0}{E_r - \epsilon_0}, \tag{3}$$

$$\kappa = \begin{cases} 1.5 & \text{if } A < 145, \\ 1.5 + 0.131(A-145)^2 \exp(-0.154(A-145)) & \text{if } A \geq 145, \end{cases} \tag{4}$$

where T_f is the temperature at the final state, the reference energy $\epsilon_0 = 4.5$, A is the mass number. The empirical expression of κ in Eq. (4) was extracted from calculations with level density provided by Kataria *et al.* [10]. In contrast, another type of level density formula was adopted in this work. Therefore, the factor κ was required to be re-evaluated under the present assumptions, in order to obtain better agreement with experimental data. The open circles in **Figure 1** show the evaluated values of κ which was fixed to reproduce experimental data of capture cross section (measured at Tokyo Tech) for nuclei with $A \sim$ 140-200. The dotted line represents the empirical expression of Eq. (4). The overestimation of capture cross sections is obviously seen at $A =$ 150-170 if using the present set of level density and EGLO type GSF with κ of Eq. (4). The evaluated κ was fitted with the same functional form as Eq. (4). The present expression was obtained as follows:

$$\kappa = \begin{cases} 1.5 & \text{if } A < 142, \\ 1.5 + 0.0337(A-142)^2 \exp(-0.112(A-142)) & \text{if } A \geq 142, \end{cases} \tag{5}$$

which is depicted by solid line in Figure 1. Hereafter, the calculated results with Eq. (5) are referred to as EGLO-rev model.

The MLO model is based on the expression for gamma width averaged on microcanonical ensemble of initial states [11]. This form is expressed as follows:

$$f(\epsilon_\gamma) = C\sigma_r\Gamma_r\mathcal{L}(\epsilon_\gamma, T_f)\left[\frac{\epsilon_\gamma\Gamma_m(\epsilon_\gamma, T_f)}{(\epsilon_\gamma^2 - E_r^2)^2 + (\epsilon_\gamma\Gamma_m(\epsilon_\gamma, T_f))^2}\right] \quad (\mathrm{MeV}^{-3}), \tag{6}$$

$$\mathcal{L}(\epsilon_\gamma, T_f) = \frac{1}{1 - \exp(-\epsilon_\gamma/T_f)}, \tag{7}$$

where scaling factor $\mathcal{L}(\epsilon_\gamma, T_f)$ is the correction term for heated nuclei, Γ_m is the width as a function of ϵ_γ and T_f. The MLO model has variants with different physical bases of the width Γ_m. In this paper the results with MLO2 and simplified MLO (SMLO) models are only presented because capture gamma-ray spectra were almost identical to those with other variants. It should be noted that the different variants give different capture cross sections.

The energy and temperature dependent width in the MLO2 model has two independent dissipation sources (i.e., collision and fragmentation) expressed as

$$\Gamma_m(\epsilon_\gamma, T_f) = \frac{\hbar}{\tau_c(\epsilon_\gamma, T_f)} + k_s(\epsilon_\gamma)\Gamma_w, \quad \frac{\hbar}{\tau_c(\epsilon_\gamma, T_f)} = b(\epsilon_\gamma + U), \tag{8}$$

where τ_c is the collisional relaxation time of the collective motion in a Fermi system, $\Gamma_w = 32.846/A^{1/3}$ (MeV) which approximates the fragmentation component, k_s is the energy dependent scaling factor, b is the constant, U is the excitation energy related to T_f. The width of SMLO model is simply proportional to the initial energy as $a_s(\epsilon_\gamma + U)$, where $a_s = \Gamma_r/E_r$.

The values of parameters E_r, Γ_r and σ_r were taken from the systematics of RIPL-2 [12]. No extra contributions such as pygmy dipole resonances usually appearing around 6 MeV were taken into consideration. The M1 and E2 GSFs were described in the forms of Kopecky and Uhl [13].

3 Comparison Results

The calculated results in set of capture gamma-ray spectra and cross sections are shown for representative four nuclides, ^{78}Se, ^{91}Zr, ^{161}Dy and ^{197}Au.

One prominent feature exists for the capture gamma-ray spectra in comparison between EGLO(-rev) and the other models. The spectral shape of EGLO model are softer than those of the others. This is attributed to the behavior of GSF in low γ-ray energy region. The contribution of GSF to the low energy part of spectrum is larger in the EGLO model, compared to those in the others. The SLO model and MLO variants make identical spectra. This is because the shapes of GSF are similar each other in the energy region of 1-8 MeV as seen in **Figure 2**. In this paper, the spectra of EGLO(-rev) and SMLO models are only presented for definitive comparisons.

In the case of ^{78}Se the gamma-ray spectra based on the EGLO model at 58 and 550 keV neutrons well explain the data measured at Tokyo Tech [14] at 15-100 keV and around 550 keV neutrons, respectively, in **Figure 3**. The other models predict spectra rather hard. As a result, the contribution of direct transitions from capture state to discrete ones becomes large. On the other hand, **Figure 4** shows that the EGLO model provides cross sections marginally consistent with the measured data. The shaded areas classified with dark and light colors show the difference from the cross section with EGLO-rev model, which is the same as the EGLO model in this case, by 20 and 50%, respectively, for eye-guide. It is found that the SLO model predicts the cross section much larger than those of the others. The SMLO model better explains the measured cross sections.

Figure 5 represents that the present results with all the GSF models for ^{91}Zr are in good agreement with the measured data [15] of capture gamma-ray spectra at 15-100 keV (on average 48 keV) and 550 keV neutron energies. Especially, the primary transitions from capture state to low excited ones are well reproduced in the case of 15-100 keV neutrons. The measured

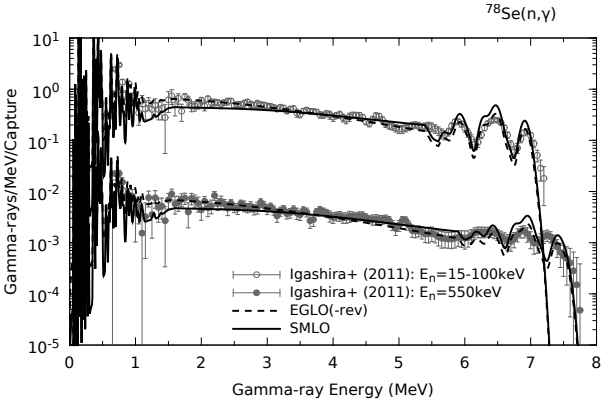

Figure 3: Capture gamma-ray spectra of ^{78}Se

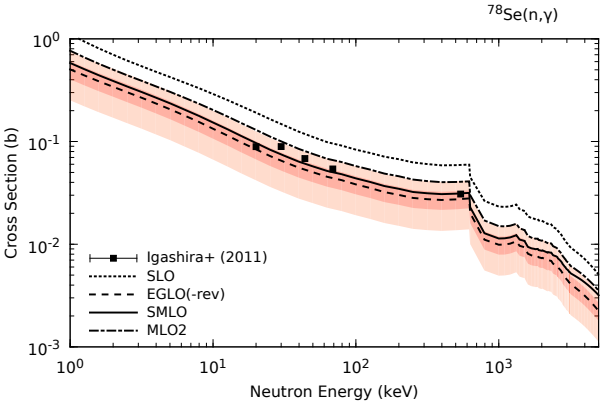

Figure 4: Capture cross sections of ^{78}Se

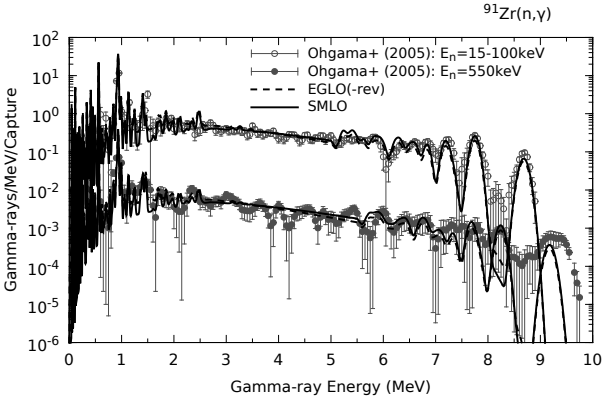

Figure 5: Capture gamma-ray spectra of ^{91}Zr

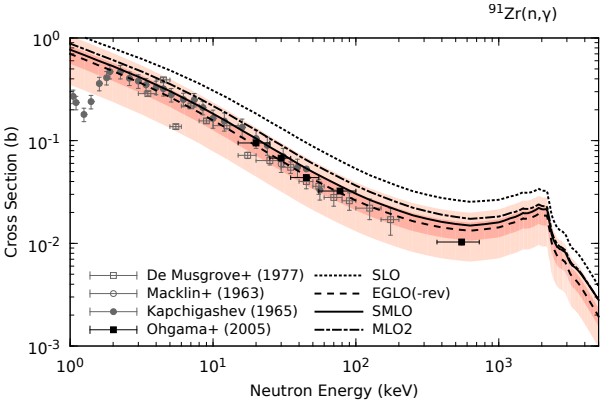

Figure 6: Capture cross sections of ^{91}Zr

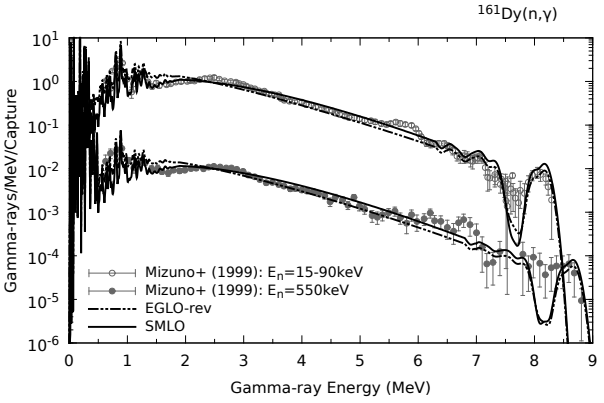

Figure 7: Capture gamma-ray spectra of ^{161}Dy

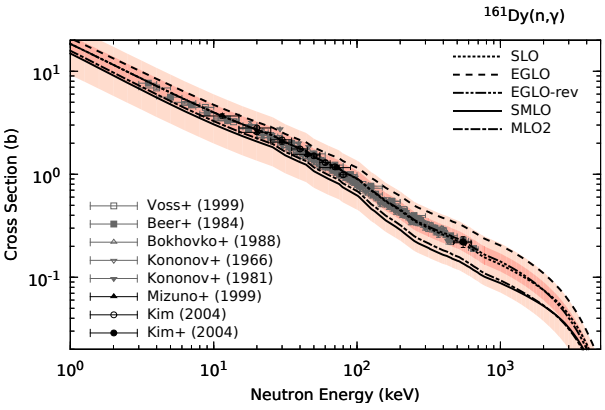

Figure 8: Capture cross sections of ^{161}Dy

spectrum at 550 keV neutrons has a little bit high energy tail above the maximum transition energy (∼9.2 MeV from capture state to the ground one). Incident neutron spectrum with a wide FWHM (180 keV) might be responsible for that. The EGLO and SMLO models well reproduce the cross section data of Ohgama *et al.* [15], which are consistent with those of other measurements, as shown in **Figure 6**.

All gamma-ray spectra of ^{161}Dy calculated by applying the GSF models are in agreement with the measured data [16] at the neutron energies of 15-90 keV (on average 47 keV) and 550 keV in **Figure 7**. The SLO, SMLO and MLO2 models reasonably explain the spectra around 2 MeV. This is due to weaker decay strength, compared to those at higher γ-ray energies. **Figure 8** illustrates that the present result with the fitted κ value (i.e., EGLO-rev model) well reproduce

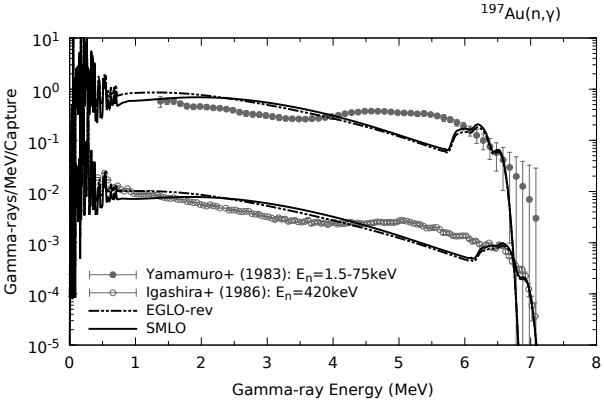

Figure 9: Capture gamma-ray spectra of ^{197}Au

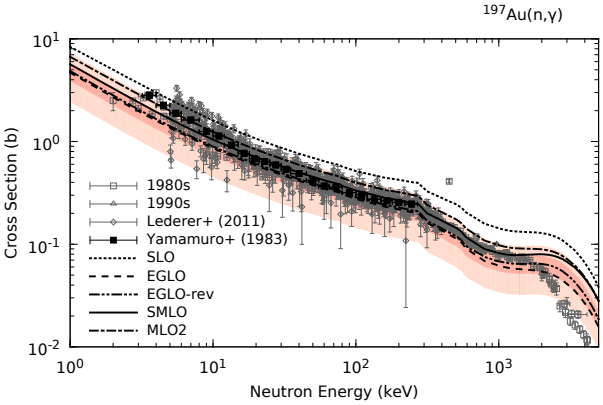

Figure 10: Capture cross sections of ^{197}Au

the cross sections measured by Mizuno *et al*. [16] at Tokyo Tech, which show a good match with other experimental data. In contrast, the result with the original EGLO model overestimates those measured data by 20-50%. It should be noted that the SMLO and MLO2 models provide smaller cross sections in the region of deformed nuclides.

The experimental capture gamma-ray spectra of ^{197}Au have an extremely different shape from spectra of other nuclides as seen in **Figure 9**. There is a large and broad bump around 5.5 MeV. The present calculations at 40 and 420 keV neutrons cannot give valid results in comparisons with the data of Yamamuro et al. [17] and Igashira *et al*. [18] at the neutron energies of 1.5-75 and 420 keV, respectively. The (d, p) experiment also obtained a huge bump-like feature around 5.5-6 MeV [19]. These results suggested that a strong pygmy-like contribution to GSF should be included at around 5.5 MeV. Nevertheless, the cross section derived with the EGLO-rev model is slightly smaller than the data of Yamamuro *et al*. and others in **Figure 10**, but still reasonable.

4 Conclusion

The predictive capability of calculated capture gamma-ray spectra and capture cross sections was systematically investigated by using different types of E1 GSF such as SLO, EGLO, SMLO and MLO2 models in the nuclear reaction model code CCONE. The present results for 40 nuclides from Fe to Au were compared with the data measured at Tokyo Tech, supplemented with other data available.

The original expression of enhancement factor κ in the EGLO model leads to an overestimation of the cross sections in the present set of GSF and nuclear level density. Therefore, the factor κ was re-evaluated in the case of using the Fermi-gas model of Mengoni-Nakajima formulation for level density.

It is found that the SLO, SMLO and MLO2 models have almost identical spectra. Nevertheless, the cross sections are different due to the different magnitudes of GSF below the neutron binding energy (i.e., about 8 MeV). The SMLO model has a fine performance to predict the spectra and cross sections within the present comparisons. The EGLO-rev model also shows high reproducibility especially for capture cross sections.

Acknowledgments

This work was supported by JSPS KAKENHI Grant Number 22226016.

References

[1] Iwamoto O. Development of a Comprehensive Code for Nuclear Data Evaluation, CCONE, and Validation Using Neutron-Induced Cross Sections for Uranium Isotopes. J. Nucl. Sci.,

Technol. 2007;44:687-697.

[2] Capote R, Herman M, Oblozinsky P, Young PG, Goriely S, Belgya T, Ignatyuk AV, Koning AJ, Hilaire S, Plujko VA, Avrigeanu M, Bersillon O, Chadwick MB, Fukahori T, Ge Z, Han Y, Kailas S, Kopecky J, Maslov VM, Reffo G, Sin M, Soukhovitskii ESh, Talou P. RIPL - Reference Input Parameter Library for Calculation of Nuclear Reactions and Nuclear Data Evaluations. Nucl. Data Sheets. 2009;110:3107-3214.

[3] Soukhovitski ESh, Chiba S, Iwamoto O, Shibata K, Fukahori T, Morogovskij GB. Programs OPTMAN and SHEMMAN Version 8 (2004): JAERI-Data/Code 2005-002, 2006, 78p.

[4] Kunieda S, Chiba S, Shibata K, Ichihara A, Sukhovitskii ESh. Coupled-channels Optical Model Analyses of Nucleon-induced Reactions for Medium and Heavy Nuclei in the Energy Region from 1keV to 200 MeV. J. Nucl. Sci. Technol. 2007;44:838-852.

[5] Evaluated Nuclear Structure Data File. Available from http://www.nndc.bnl.gov/ensdf/.

[6] Gruppelaar H, Reffo G. Some Properties of the Width Fluctuation Factor. Nucl. Sci. Eng. 1977;62:756-763.

[7] Moldauer PA. Statistics and the average cross section. Nucl. Phys. 1980;A344:185-195.

[8] Gilbert A, Cameron AGW. A Composite nuclear-level density formula with shell corrections. Can. J. Phys. 1965;43:1446-1496.

[9] Mengoni A, Nakajima Y. Fermi-Gas Model Parametrization of Nuclear Level Density. J. Nucl. Sci. Technol. 1994;31:151-162.

[10] Kataria SK, Ramamurthy VS, Kapoor SS. Semiempirical nuclear level density formula with shell effects. Phys. Rev. 1978;C18:549-563.

[11] Plujko VA, Ezhov SN, Kavatsyuk MO, Grebenyuk AA, Yermolenko RV. Testing and Improvements of Gamma-Ray Strength Functions for Nuclear Model Calculations. J. Nucl. Sci. Technol. 2002;Suppl. 2:811-814.

[12] Belgya T, Bersillon O, Capote R, Fukahori T, Zhigang G, Goriely S, Herman M, Ignatyuk AV, Kailas S, Koning A, Oblozinsky P, Plujko V, Young P. Handbook for calculations of nuclear reaction data, RIPL-2. IAEA-TECDOC-1506 (IAEA, Vienna, 2006). Available online at http://www-nds.iaea.org/RIPL-2/.

[13] Kopecky J, Uhl M. Test of gamma-ray strength functions in nuclear reaction model calculations. Phys. Rev. 1990;C41:1941-1955.

[14] Igashira M, Kamada S, Katabuchi T, Mizumoto M. Systematic Study on KeV-Neutron Capture Reaction of Se Isotopes. J. Korean Phys. Soc. 2011;59,1665-1669.

[15] Ohgama K, Igashira M, Ohsaki T. Measurement of keV-Neutron Capture Cross Sections and Capture Gamma-Ray Spectra of ^{91,92}Zr. J. Nucl. Sci. Technol. 2005;42:333-340.

[16] Mizuno S, Igashira M, Masuda K. Measurements of keV-Neutron Capture Cross Sections and Capture Gamma-Ray Spectra of ^{161,162,163}Dy. J. Nucl. Sci. Technol. 1999;36:493-507.

[17] Yamamuro N, Igashira M, Sekiya T, Shirayanagi H. KeV-Neutron Capture in Cesium-133, Gold-197 and Tantalum-181. J. Nucl. Sci. Technol. 1983;20:797-811.

[18] Igashira M, Kitazawa H, Shimizu M, Komano H, Yamamuro N. Systematics of the pygmy resonance in keV neutron capture gamma-ray spectra of nuclei with N=82-126. Nucl. Phys. 1986:A457;301-316.

[19] Giacoppo F, Bello F, Bernstein LA, Bleuel D, Firestone RB, Görgen A, Guttormsen M, Hagen TW, Klintefjord M, Koehler PE, Larsen AC, Nyhus HT, Renstrøsm T, Sahin E, Siem S, Tornyi T. EPJ Web of Conferences 2014;66:02041.

23 JENDL/HE-2007 Benchmark Test with Iron Shielding Experiment at JAEA/TIARA

Chikara Konno, Masayuki Ohta, Saerom Kwon, Kentaro Ochiai, and Satoshi Sato

Sector of Fusion Research and Development, Japan Atomic Energy Agency
Tokai-mura, Naka-gun, Ibaraki-ken 319-1195 Japan
e-mail : konno.chikara@jaea.go.jp

At the last nuclear data symposium we pointed out that calculation result with JENDL/HE-2007 underestimated the measured neutron spectra more than that with FENDL-3.0 in the iron experiment with 65 MeV neutrons at TIARA in JAEA. In this study we investigated reasons of this underestimation in detail. As a result, we specified that the slightly larger non-elastic scattering cross section data of ^{56}Fe in JENDL/HE-2007 around 65 MeV caused the underestimation. Additionally it was found out that the elastic scattering cross section data of ^{56}Fe in FENDL-3.0 around 40 MeV were too large, which caused more underestimation for the measured data than that with JENDL/HE-2007 in the iron experiment with 40 MeV neutrons at TIARA in JAEA. The non-elastic scattering data around 65 MeV of ^{56}Fe in JENDL/HE-2007 and the elastic scattering data around 40 MeV of ^{56}Fe in FENDL-3.0 should be revised based on this study.

1. Introduction

At the last nuclear data symposium [1] we presented the analyses of the iron and concrete shielding experiments [2] with 40 and 65 MeV neutrons at TIARA in JAEA in order to validate FENDL-3.0 [3]. We also used JENDL/HE-2007 [4] for comparison and pointed out that the calculation result with JENDL/HE-2007 slightly underestimated the measured neutron flux of 60-70 MeV and calculated one with FENDL-3.0 in the iron experiment with 65 MeV neutrons as shown in Fig. 1. Now we study reasons of this underestimation in

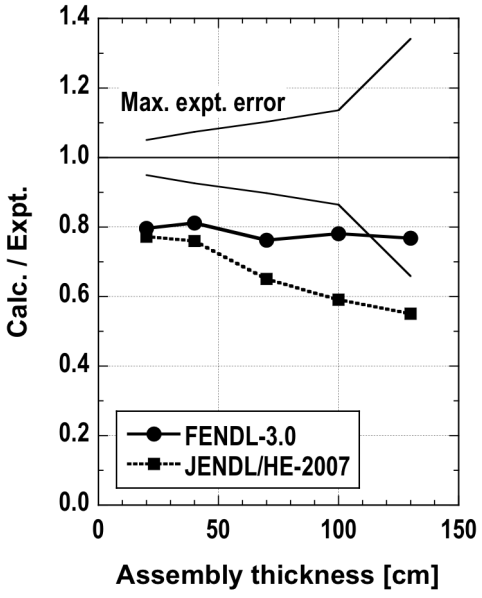

Fig. 1 Ratio for calculated peak neutron flux of 60-70 MeV to experimental one.

detail.

2. TIARA iron shielding experiments and analysis method

In the TIARA iron shielding experiments, quasi-mono energetic 40 or 65 MeV neutrons were generated by bombarding 43 or 68 MeV proton to a ^{7}Li target and collimated ones were injected to an iron test shield of 1.2 m x 1.2 m as shown in Fig. 2. Only the collimated neutron beam and iron test shield with an additional iron shield were modeled in the analysis as shown in Fig. 3. The measured source neutron spectrum was used as the source neutron in the analysis. The neutron spectra above 10 MeV just behind the test shield on beam axis measured with a BC501A scintillation detector were compared with the calculated ones.

The Monte Carlo code MCNP5-1.40 [5] and the ACE files of FENDL-3.0 [6] and JENDL/HE-2007 [7] supplied from IAEA Nuclear Data Section and Japan Atomic Energy Agency, respectively, were used in the analysis. The source of FENDL-3.0 is the followings, 1) ^{54}Fe, ^{57}Fe : ENDF/B-VII.0 [8], 2) ^{56}Fe, ^{58}Fe : JEFF-3.1.1 [9] (<20MeV) + TENDL-2011 [10] (>20MeV). The nuclear data processing code NJOY99.364 [11] with a patch [7] for JENDL/HE-2007 was used to process a temporary nuclear data file for specifying reasons of the underestimation.

We focused on the ^{56}Fe data because the abundance of ^{56}Fe is 91.754 % and compared the cross section data of ^{56}Fe in FENDL-3.0 and JENDL/HE-2007. Figure 4 shows the elastic and non-elastic scattering cross section data. The elastic scattering cross section data in FENDL-3.0 are almost the same as those in JENDL/HE-2007 around 65 MeV, while the non-elastic scattering cross section data in JENDL/HE-2007 are by 4 % larger than those in FENDL-3.0. It seems that the larger non-elastic scattering cross section data of ^{56}Fe in JENDL/HE-2007 cause the underestimation in the calculation result with JENDL/HE-2007. In

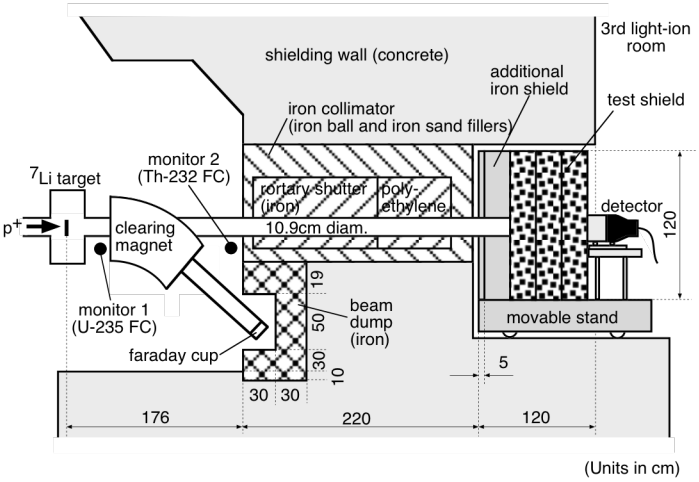

Fig. 2 Experimental configuration.

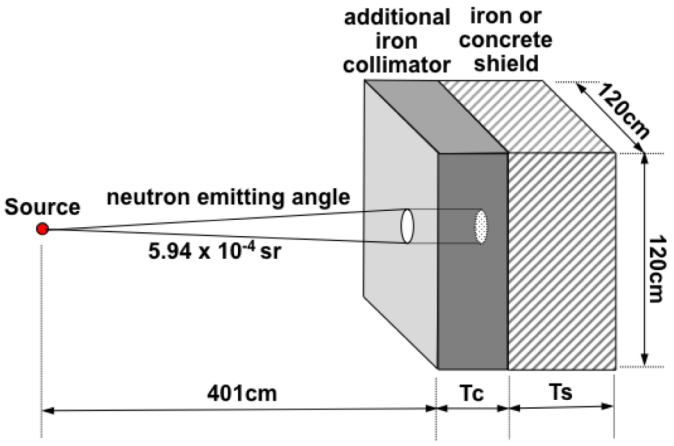

Fig. 3 Calculation model.

order to confirm this presumption, we generated two temporary ^{56}Fe files, where the elastic

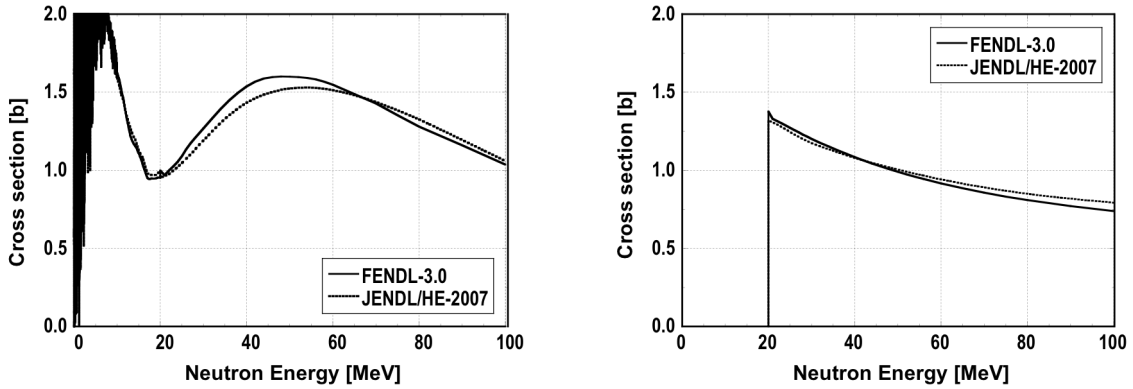

(a) Elastic scattering (b) Non-elastic scattering

Fig. 4 Cross section data of ^{56}Fe.

scattering data in the whole energy (JENDL/HE-2007 test1) and the non-elastic scattering data above 20 MeV (JENDL/HE-2007 test2) of ^{56}Fe in JENDL/HE-2007 were replaced with those in FENDL-3.0, respectively and processed them with NJOY99.363 patched for JENDL/HE-2007. We carried out two calculations with JENDL/HE-2007 test1 and JENDL/HE-2007 test2.

3. Results and discussion

Figure 5 shows the ratios for the calculated neutron fluxes to the experimental ones in the iron shielding experiment with 65 MeV neutrons. It is found out that the underestimation in the calculation result with the original JENDL/HE-2007 is resolved in that with JENDL/HE-2007 test2. On the other hand, the calculation result with JENDL/HE-2007 test1 is almost the same as that with the original JENDL/HE-2007 because the difference of the elastic scattering data around 65 MeV of ^{56}Fe is very small between in FENDL-3.0 and JENDL/HE-2007. It is concluded that the non-elastic scattering data around 65 MeV of ^{56}Fe in FENDL-3.0 are better than those in JENDL/HE-2007, which leads to the better agreement between the measured and calculated results in FENDL-3.0.

Figures 6 shows the ratios for the calculated neutron fluxes to the experimental ones in the iron shielding experiment with 40 MeV neutrons. Differently from Fig. 5, the calculation result with JENDL/HE-2007 test2 is almost the same as that with the original JENDL/HE-2007 because the difference of the non-elastic scattering data around 40 MeV of ^{56}Fe is very small between in FENDL-3.0 and JENDL/HE-2007. On the other hand, the calculated neutron flux of 30 - 40 MeV with JENDL/HE-2007 test1 is similar with that with FENDL-3.0. It is considered that the elastic scattering cross section data around 40 MeV of ^{56}Fe in JENDL/HE-2007 are better than those in FENDL-3.0 because the calculation result with JENDL/HE-2007 agrees with the measured one better that that with FENDL-3.0 in the

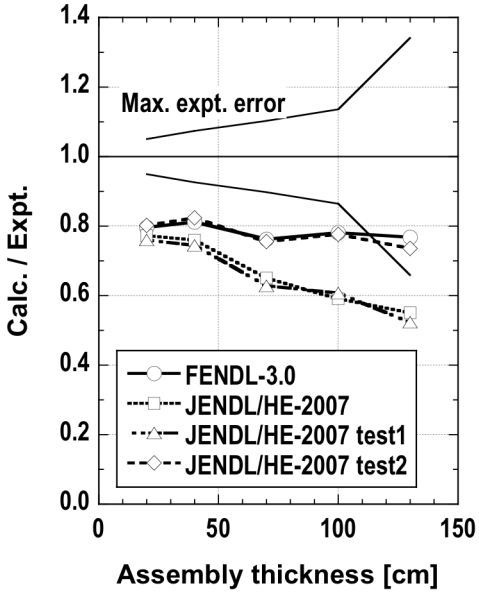

(a) Peak neutron flux (60 - 70 MeV)

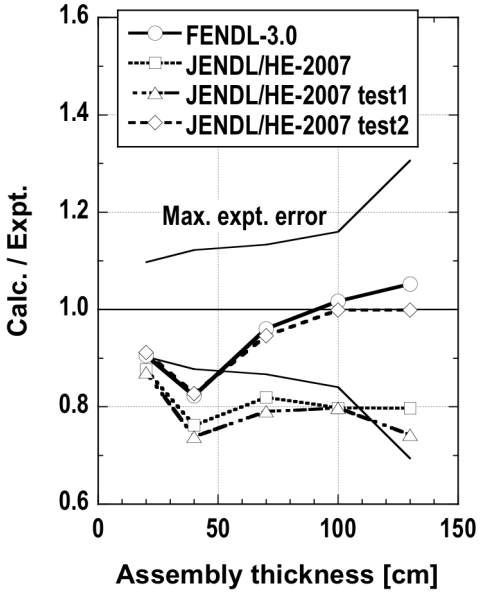

(b) Continuum neutron flux (10 - 60 MeV)

Fig. 5 Ratio of calculated neutron flux to experimental one in iron shielding experiment with 65 MeV neutrons.

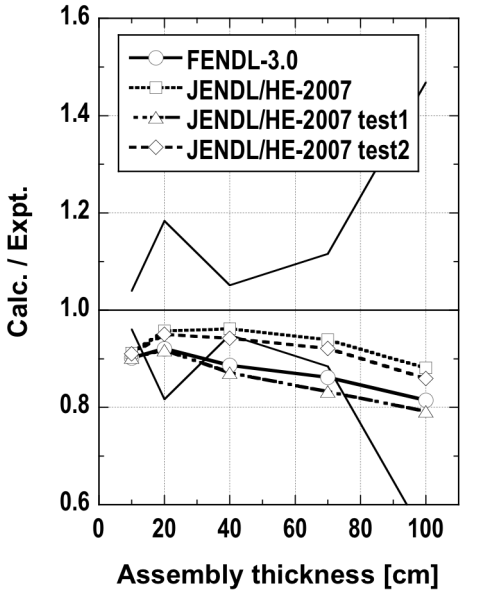

(a) Peak neutron flux (35 - 45 MeV)

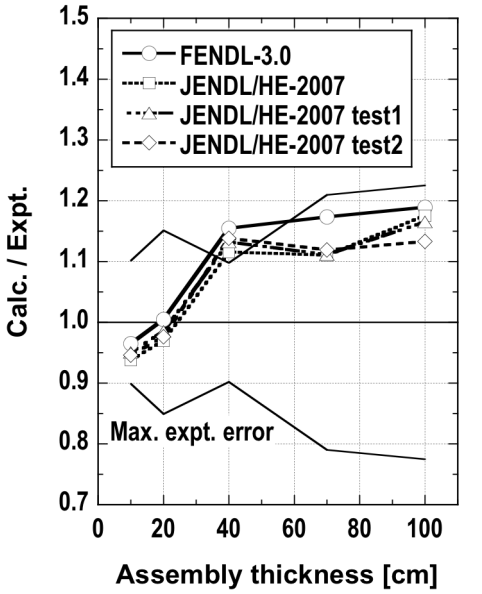

(b) Continuum neutron flux (10 - 35 MeV)

Fig. 6 Ratio of calculated neutron flux to experimental one in iron shielding experiment with 40 MeV neutrons.

iron shielding experiment with 40 MeV neutrons.

Finally the non-elastic scattering data around 65 MeV of ^{56}Fe in JENDL/HE-2007 and the elastic scattering data around 40 MeV of ^{56}Fe in FENDL-3.0 should be revised based on this study.

4. Summary

We analyzed the iron shielding experiment with 65 MeV neutrons at JAEA/TIARA by directly modifying cross section data in order to investigate reasons why the calculation result with JENDL/HE-2007 underestimated the measured neutron fluxes more than that with FENDL-3.0. As a result, it was specified that the slightly larger non-elastic scattering cross section data of ^{56}Fe in JENDL/HE-2007 caused the underestimation in the calculation result with JENDL/HE-2007. We also analyzed the iron shielding experiment with 40 MeV neutrons at JAEA/TIARA by using the same method. It was found out that the elastic scattering cross section data around 40 MeV of ^{56}Fe in FENDL-3.0 were too large. It is necessary to revise the ^{56}Fe data in JENDL/HE-2007 and FENDL-3.0 based on this study.

References

[1] Konno C, Ohta M, Asahara H, Ochiai K, Sato S. FENDL-3.0 benchmark test with shielding experiments at JAEA/TIARA. Proceedings of the 2013 Symposium on Nuclear Data, JAEA-Conf 2014-002, pp.160-166(2014).

[2] Nakane Y, Hayashi K, Sakamoto Y, Yoshizawa N, Nakao N, Ban S, Hirayama H, Uwamino Y, Shin K, Nakamura T. Neutron transmission benchmark problems for iron and concrete shields in low, intermediate and high energy proton accelerator facilities. JAERI-Data/Code 96-029, 1996, 80p.

[3] Forrest RA, Capote N, Otsuka N, Kawano T, Koning AJ, Kunieda S, Sublet J-Ch, Watanabe Y. FENDL-3 Library – Summary documentation. INDC(NDS)-0628. Austria: International Atomic Energy Agency; 2012.

[4] Available from : http://wwwndc.jaea.go.jp/ftpnd/jendl/jendl-he-2007.html

[5] X-5 Monte Carlo Team. MCNP - A General Monte Carlo N-Particle Transport Code, Version 5. LA-UR-03-1987. USA: Los Alamos National Laboratory; 2005.

[6] Aldama DL, Noy RC. FENDL-3 : Processing the evaluated nuclear data library for fusion applications. INDC(NDS)-0611. Austria: International Atomic Energy Agency; 2011.

[7] Sasa T, Sugawara T, Kosako K, Fukahori T. Continuous Energy Cross Section Library for MCNP/MCNPX Based on JENDL High Energy File 2007 -FXJH7-. JAEA-Data/Code 2008-022 , 2008, 18p.

[8] Chadwick MB, Herman M, Oblozinsky P, Dunn ME, Danon Y, Kahler AC, Smith DL, Pritychenko B, Arbanas G, Arcilla R, Brewer R, Brown DA, Capote R, Carlson AD, Cho YS, Derrien H, Guber K, Hale GM, Hoblit S, Holloway S, Johnson TD, Kawano T, Kiedrowski BC, Kim H, Kunieda S, Larson NM, Leal L, Lestone JP, Little RC, McCutchan EA, MacFarlane RE, MacInnes M, Mattoon CM, McKnight RD, Mughabghab SF, Nobre GPA, Palmiotti G, Palumbo A, Pigni MT, Pronyaev VG, Sayer RO, Sonzogni AA, Summers NC, Talou P, Thompson IJ, Trkov A, Vogt RL, van der

Marck SC, Wallner A, White MC, Wiarda D, Young PG. ENDF/B-VII.1 Nuclear Data for Science and Technology: Cross Sections, Covariances, Fission Product Yields and Decay Data. Nucl Data Sheets. 2011;112:2887–2996.

[9] Santamarina A, Bernard D, Blaise P, Coste M, Courcelle A, Huynh TD, Jouanne C, Leconte P, Litaize O, Mengelle S, Noguère G, Ruggiéri J-M, Sérot O, Tommasi J, Vaglio C, Vidal J-F. The JEFF-3.1.1 Nuclear Data Library. JEFF Report 22. Paris (France): OECD Nuclear Energy Agency; 2009.

[10] Available from : ftp://ftp.nrg.eu/pub/www/talys/tendl2011/tendl2011.html/

[11] MacFarlane RE, Muir DW. The NJOY Nuclear Data Processing System, Version 91. LA-12740-M. USA: Los Alamos National Laboratory; 1994.

24 Problems on FENDL-3.0

Chikara Konno, Masayuki Ohta, Saerom Kwon, Kentaro Ochiai, and Satoshi Sato

Sector of Fusion Research and Development, Japan Atomic Energy Agency
Tokai-mura, Naka-gun, Ibaraki-ken 319-1195 Japan
e-mail : konno.chikara@jaea.go.jp

We had carried out the benchmark tests of the general-purpose data library for neutron-induced reactions in FENDL-3.0 with the integral experiments at JAEA/FNS, JAEA/TIARA and Osaka Univ./OKTAVIAN. We had also tested the MATXS files of FENDL-3.0 with a simple calculation model and compared KERMA and DPA data included in the ACE and MATXS files of FENDL-3.0 with those in other nuclear data libraries. Through this study we found out the following problems in FENDL-3.0; 1) The ^{16}O data above 20 MeV in FENDL-3.0 are not correct, 2) The most MATXS files in FENDL-3.0 have no energy-angular distribution data for the non-elastic scattering reaction, 3) Some of the KERMA and DPA data included in the ACE and MATXS files of FENDL-3.0 are not correct. These problems should be revised.

1. Introduction

A new version of Fusion Evaluated Nuclear Data Library (FENDL), FENDL-3.0 [1] was released from IAEA in 2012. FENDL-3.0 has the following features; 1) extension of the neutron energy range of neutron-induced reactions from 20 MeV to more than 60 MeV, 2) activation data libraries for proton- and deuteron-induced reactions up to more than 60 MeV. We had carried out the benchmark tests of the general-purpose data library for neutron-induced reactions in FENDL-3.0 with the integral experiments at JAEA/FNS, JAEA/TIARA and OKTAVIAN [2-4]. We had also tested the MATXS files of FENDL-3.0 with a simple calculation model and compared KERMA and DPA data included in the ACE and MATXS files of FENDL-3.0 with those in other nuclear data libraries. Here we introduce problems in FENDL-3.0 found out in our study.

2. Problem 1 : ^{16}O data above 20 MeV

At the last symposium [3] and the Symposium on Fusion Technology in 2014 [4] we analyzed the iron and concrete shielding experiments [5] with 40 and 65 MeV neutrons at

TIARA in JAEA in order to validate to FENDL-3.0 with JENDL/HE-2007. It was pointed out that the calculations with FENDL-3.0 overestimated the measured ones for the concrete experiment more for the thicker assemblies as shown in Fig. 1, while they agreed with the measured ones for the iron experiment well. It was also specified that the ^{16}O data (the larger elastic scattering and smaller non-elastic scattering cross section data than those in JENDL/HE-2007 as shown in Fig. 2) above 20 MeV caused the drastic overestimation of measured neutron fluxes above 10 MeV in the concrete shielding experiment. The ^{16}O data above 20 MeV in FENDL-3.0 should be replaced with those in JENDL/HE-2007.

3. Problem 2 : MATXS files above 20 MeV

We tested the MATXS files [6] of FENDL-3.0 with a simple model calculation. The model of this calculation test was a natural iron sphere of 1 m in radius with an isotropic neutron source of 50 MeV (49 - 50 MeV, which is the sixth group of the MATXS files in

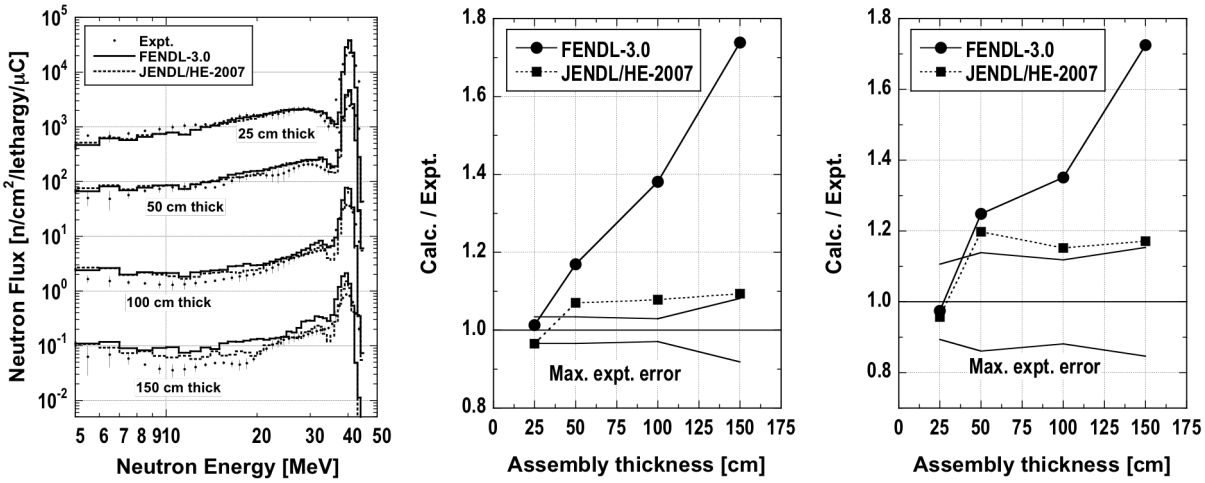

(a) Neutron spectra (b) C/E for peak neutrons (35-45MeV) (c) C/E for continuum neutrons (10-35MeV)

Fig. 1 Typical results for concrete experiment with 40 MeV neutrons.

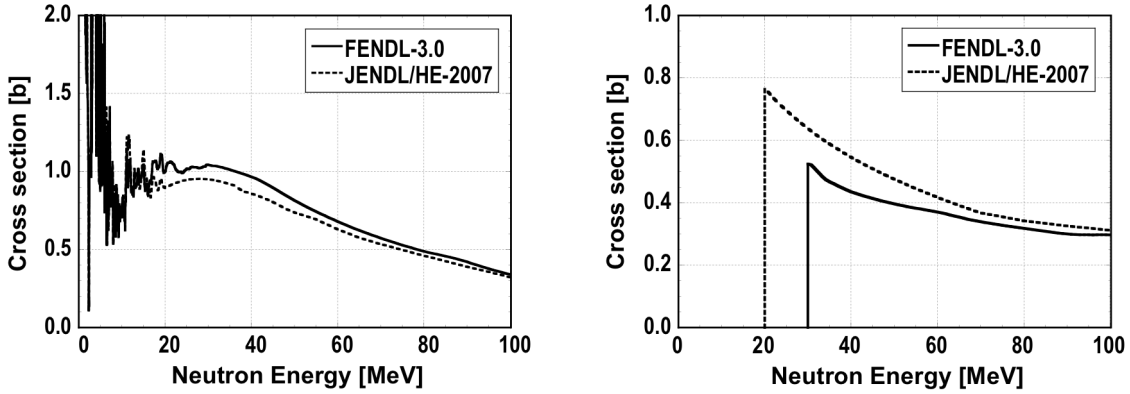

(a) Elastic scattering (b) Non-elastic scattering

Fig. 2 Cross section of ^{16}O.

FENDL-3.0) in the center. Neutron spectra inside the sphere were calculated by using the Sn code ANISN [7] with a multigroup library, which was generated from the MATXS files in FENDL-3.0 with the TRANSX code [8], and the Monte Carlo code MCNP5-1.40 [9] with the ACE files [6] of FENDL-3.0. Figure 3 (a) shows the calculated neutron spectra at the distance of 40 cm from the center of the iron sphere. The neutron spectrum with ANISN is very different from that with MCNP. After checking the MATXS file of FENDL-3.0 in detail, we found out that the MTAXS files for iron isotopes in FENDL-3.0 had no energy-angular distribution data for the non-elastic scattering reaction above 20 MeV. We adequately re-generated the MTAXS files for iron isotopes in FENDL-3.0 with the NJOY code [10]. By using the re-generated MATXS files, the difference between the neutron spectra with ANISN and MCNP became very small as shown in Fig. 3 (b). It is noted that not only the MATXS files for iron isotopes but also most of the MATXS files in FENDL-3.0 have the same problem. Most of the MATXS files in FENDL-3.0 should be re-generated with the NJOY code adequately.

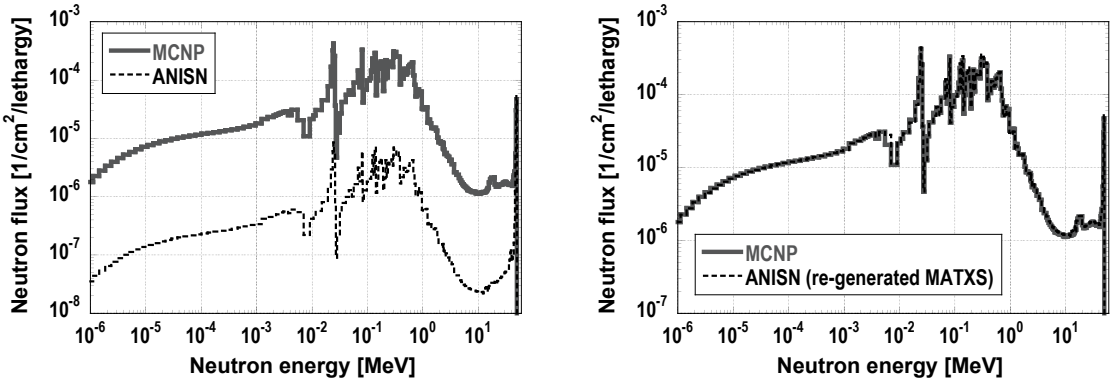

(a) Original MATXS files (b) Re-generated MATXS files

Fig. 3 Calculated neutron spectra at 40 cm from center of iron sphere.

4. Problem 3 : KERMA and DPA data included in the ACE and MATXS files

We compared KERMA and DPA data included in the ACE and MATXS files of FENDL-3.0 with those in JENDL-4.0 [11] and ENDF/B-VII.1 [12]. As a result, the following problems were found out.

i) ^{1}H : No increase with the decreasing neutron energy in low neutron energy as shown in Fig. 4. This is due to a NJOY bug, which is the same issue reported at International Conference on Nuclear Data for Science and Technology in 2013 [13] because the ^{1}H data in FENDL-3.0 are those in ENDF/B-VII.1.

ii) ^{13}C, ^{15}N, ^{18}O, ^{31}P, ^{34}S, ^{36}S, ^{41}K, ^{50}Cr, ^{52}Cr, ^{53}Cr, ^{54}Cr, ^{58}Fe, ^{70}Ge, ^{72}Ge, ^{73}Ge, ^{74}Ge, ^{76}Ge, ^{138}La, ^{139}La, ^{175}Lu, ^{176}Lu, ^{185}Re, ^{187}Re, ^{195}Pt, ^{196}Pt, ^{198}Pt, ^{204}Pb, ^{206}Pb, ^{207}Pb : No increase with the decreasing neutron energy in low neutron energy as shown in Fig. 5. This is due to the older version (99.364) of NJOY used for processing FENDL-3.0, except for ^{15}N, reasons

for which are not specified yet. These data should be re-processed with the latest version of NJOY, NJOY99.396 or NJOY2012.8 [14].

iii) ^{32}S, ^{33}S, ^{39}K, ^{40}K, ^{209}Bi : Drastically large KERMA and DPA data (only KERMA data for ^{39}K and ^{40}K) in low neutron energy as shown in Fig. 6. This is due to much larger helium production cross section data in low neutron energy than those in the other nuclear data

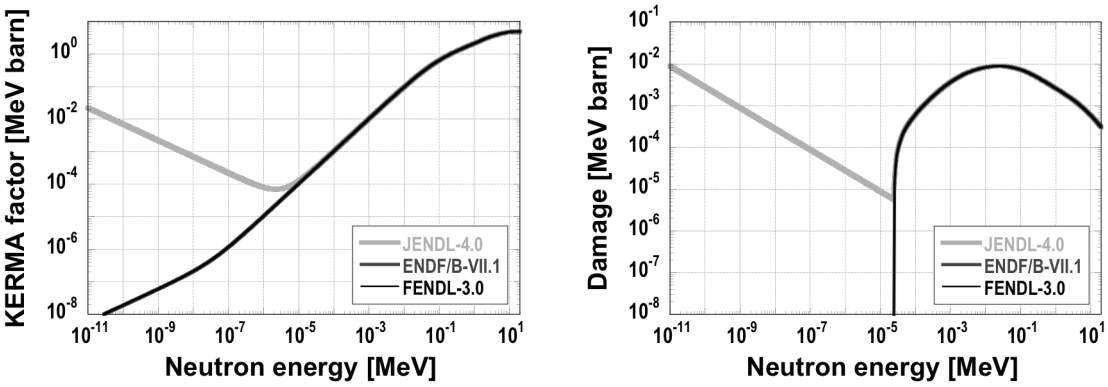

(a) KERMA factor (b) DPA cross section

Fig. 4 KERMA factor and DPA cross section of ^{1}H.

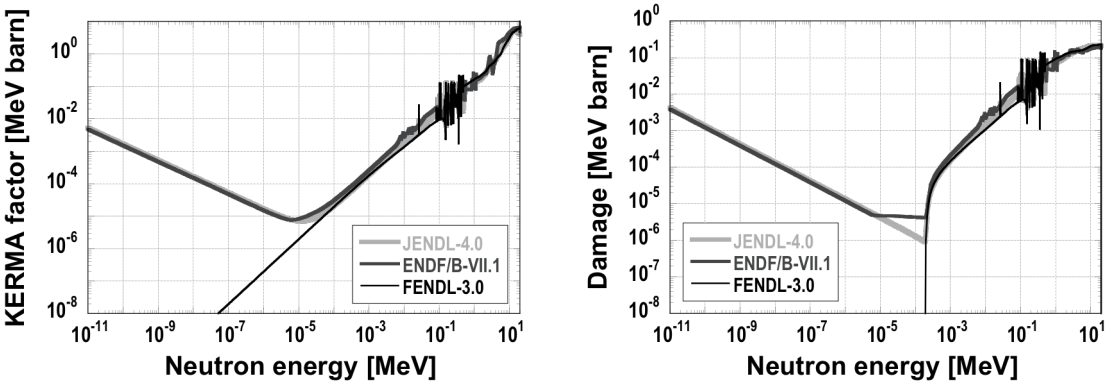

(a) KERMA factor (b) DPA cross section

Fig. 5 KERMA factor and DPA cross section of ^{31}P.

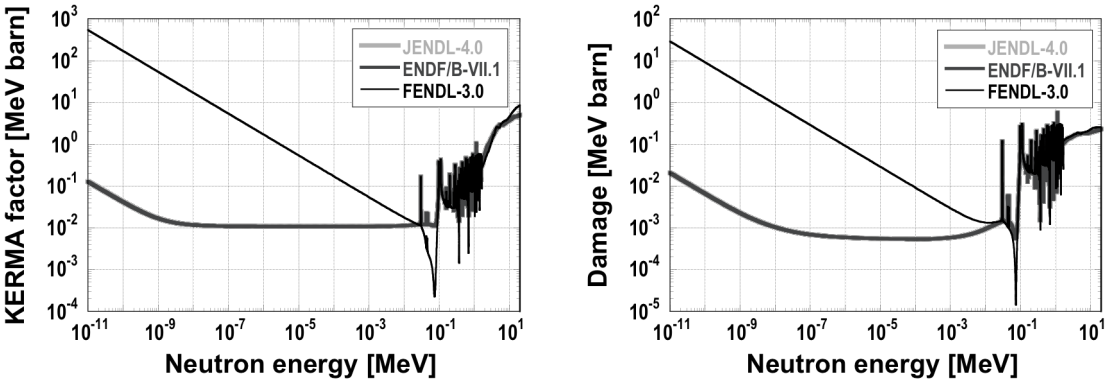

(a) KERMA factor (b) DPA cross section

Fig. 6 KERMA factor and DPA cross section of ^{32}S.

libraries as shown in Fig. 7. It is required to check if the huge helium production cross section data in low neutron energy are correct. If necessary, the helium production data for these nuclei in FENDL-3.0 should be revised.

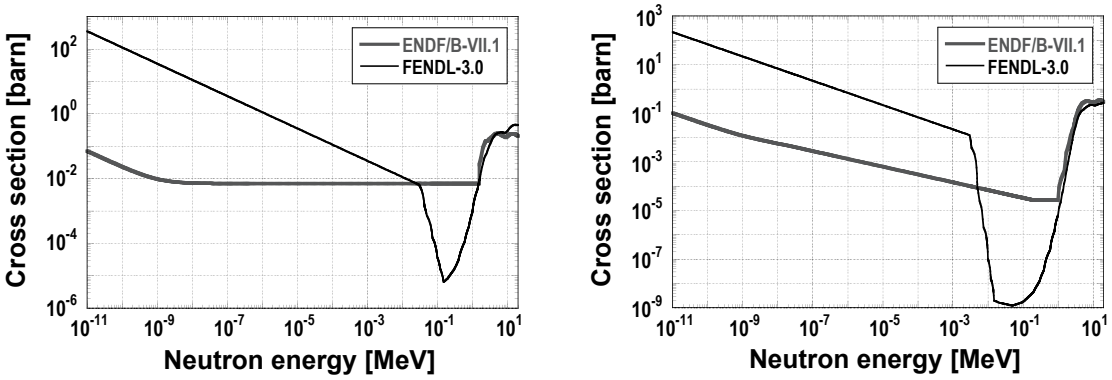

(a) ^{32}S (b) ^{39}K

Fig. 7 Helium production cross section data.

5. Summary

We found out the following problems in FENDL-3.0 through the validation study for FENDL-3.0.

1) The ^{16}O data above 20 MeV in FENDL-3.0 should be replaced with those in JENDL/HE-2007.
2) The most MATXS files in FENDL-3.0 have no energy-angular distribution data for the non-elastic scattering reaction. They should be re-generated with NJOY.
3) Several KERMA and DPA data included in the ACE and MATXS files of FENDL-3.0 are not correct. They should be revised.

These problems have been reported to IAEA. We hope that IAEA will revise them.

References

[1] Forrest RA, Capote N, Otsuka N, Kawano T, Koning AJ, Kunieda S, Sublet J-Ch, Watanabe Y. FENDL-3 Library – Summary documentation. INDC(NDS)-0628. Austria: International Atomic Energy Agency; 2012.

[2] Kato Y, Takakura K, Ohta M, Ochiai K, Sato S, Konno C. Benchmark test of JENDL-4.0 with TOF experiments at Osaka Univ./OKTAVIAN. Prog. Nucl. Sci. Technol. 2014; 4 : 596-600.

[3] Konno C, Ohta M, Asahara H, Ochiai K, Sato S. FENDL-3.0 benchmark test with shielding experiments at JAEA/TIARA. Proceedings of the 2014 Symposium on Nuclear Data. Published to JAERI-Conf.

[4] Konno C, Ochiai K, Sato S, Ohta M. Analyses of iron and concrete shielding experiments at JAEA/TIARA with JENDL/HE-2007, ENDF/B-VII.1 and FENDL-3.0. Published to

Fusion Eng. Design.

[5] Nakane Y, Hayashi K, Sakamoto Y, Yoshizawa N, Nakao N, Ban S, Hirayama H, Uwamino Y, Shin K, Nakamura T. Neutron transmission benchmark problems for iron and concrete shields in low, intermediate and high energy proton accelerator facilities. JAERI-Data/Code 96-029 , 1996.

[6] Aldama DL, Noy RC. FENDL-3 : Processing the evaluated nuclear data library for fusion applications. INDC(NDS)-0611. Austria: International Atomic Energy Agency; 2011.

[7] RSICC. DOORS3.2a: One, two- and three-dimensional discrete ordinates neutron/photon transport code system. CODE PACKAGE CCC-650. USA: Oak Ridge National Laboratory; 2007.

[8] MacFarlane RE. TRANSX 2: a code for interfacing MATXS cross-section libraries to nuclear transport codes. LA-12312-MS. USA : 1993.

[9] X-5 Monte Carlo Team. MCNP - A General Monte Carlo N-Particle Transport Code, Version 5. LA-UR-03-1987. USA: 2005.

[10] MacFarlane RE, Muir DW. The NJOY Nuclear Data Processing System, Version 91. LA-12740-M. USA: 1994.

[11] Shibata K, Iwamoto O, Nakagawa T, Iwamoto N, Ichihara A, Kunieda S, Chiba S, Furutaka K, Otuka N, Ohsawa T, Murata T, Matsunobu H, Zukeran A, Kamada S, Katakura J. JENDL-4.0: a new library for nuclear science and engineering. J Nucl Sci Technol. 2011; 48: 1–30.

[12] Chadwick MB, Herman M, Oblozinsky P, Dunn ME, Danon Y, Kahler AC, Smith DL, Pritychenko B, Arbanas G, Arcilla R, Brewer R, Brown DA, Capote R, Carlson AD, Cho YS, Derrien H, Guber K, Hale GM, Hoblit S, Holloway S, Johnson TD, Kawano T, Kiedrowski BC, Kim H, Kunieda S, Larson NM, Leal L, Lestone JP, Little RC, McCutchan EA, MacFarlane RE, MacInnes M, Mattoon CM, McKnight RD, Mughabghab SF, Nobre GPA, Palmiotti G, Palumbo A, Pigni MT, Pronyaev VG, Sayer RO, Sonzogni AA, Summers NC, Talou P, Thompson IJ, Trkov A, Vogt RL, van der Marck SC, Wallner A, White MC, Wiarda D, Young PG. ENDF/B-VII.1 Nuclear Data for Science and Technology: Cross Sections, Covariances, Fission Product Yields and Decay Data. Nucl Data Sheets. 2011; 112: 2887–2996.

[13] Konno C, Ochiai K, Takakura K, Sato S. Remarks on KERMA Factors in ACE files. Nuclear Data Sheets. 2014; 118: 450–452.

[14] MacFarlane RE, Kahler AC. Methods for Processing ENDF/B-VII with NJOY. Nuclear Data Sheets. 2010; 111: 2739–2890.

25 New Nuclear Data Group Constant Sets for Fusion Reactor Nuclear Analyses based on FENDL-2.1

Chikara Konno, Masayuki Ohta, Saerom Kwon, Kentaro Ochiai, and Satoshi Sato

Sector of Fusion Research and Development, Japan Atomic Energy Agency
Tokai-mura, Naka-gun, Ibaraki-ken 319-1195 Japan
e-mail : konno.chikara@jaea.go.jp

Japanese fusion research community has widely used the nuclear group constant sets, FUSION-J3 (neutron : 175 groups, gamma : 42 groups, P5 approximation) and FUSION-40 (neutron : 42 groups, gamma : 21 groups, P5 approximation), produced from the old Japanese Evaluated Nuclear Data Library, JENDL-3, in 1991 for parametttric studies and outline calculations of fusion reactor nuclear analysis. However FENDL-2.1 is widely used worldwide. Thus we have produced new nuclear group constant sets, FUSION-F21-175 and FUSION-F21-42, similar to FUSION-J3 and FUSION-40 from the official and our MATXS files of FENDL-2.1 with the TRANSX code. Several test calculations with a simple model were carried out in order to validate these nuclear group constant sets. They suggested that these group constant sets had no problem. Response data (KERMA factors, DPA and gas production cross-section data) were also prepared. It was also confirmed that these data had no problem.

1. Introduction

The nuclear group constant sets for 40 materials (^{1}H, ^{2}H, ^{3}He, ^{4}He, ^{6}Li, ^{7}Li, ^{9}Be, ^{10}B, ^{11}B, ^{12}C, ^{14}N, ^{16}O, ^{19}F, ^{23}Na, ^{nat}Mg, ^{27}Al, ^{nat}Si, ^{31}P, ^{nat}S, ^{nat}K, ^{nat}Ca, ^{nat}Ti, ^{51}V, ^{nat}Cr, ^{55}Mn, ^{nat}Fe, ^{nat}Co, ^{nat}Ni, ^{nat}Cu, ^{nat}Zr, ^{93}Nb, ^{nat}Mo, ^{nat}Cd, ^{nat}W, ^{nat}Pb, ^{209}Bi, ^{232}Th, ^{235}U, ^{238}U and ^{239}Pu), FUSION-J3 [1] (neutron : 125 groups, gamma : 40 groups, P5 approximation) and FUSION-40 [1] (neutron : 42 groups, gamma : 21 groups, P5 approximation), were generated from the old Japanese Evaluated Nuclear Data Library, JENDL-3 [2], in 1991 and they are still used for parametric studies and outline calculations of fusion reactor nuclear analysis in Japan because of no additional treatment in Sn calculations. However the Fusion Evaluated Nuclear Data Library, FENDL-2.1 [3], is widely used in the world. Thus we have produced new nuclear group constant sets similar to FUSION-J3 from FENDL-2.1 for 40 materials.

2. Method

The FUSION-J3 type nuclear group constant set of FENDL-2.1, FUSION-F21-175 (neutron : 175 groups, gamma : 42 groups, P5 approximation), was produced from the official MATXS file of FENDL-2.1, FENDL/MG-2.1 [3], with the TRANSX [4] code. The FUSION-40 type nuclear group constant set of FENDL-2.1, FUSION-F21-42 (neutron :42 groups, gamma : 21 groups, P5 approximation), was produced from our MATXS file, which was generated from FENDL-2.1 with the NJOY [5] code, with TRANSX. They were produced for 40 nuclides in Table 1, where nuclides of no. 37 - no. 40 were different from FUSION-J3 and FUSION40. The Cd data were taken from JENDL-3.3 [6], which were processed with NJOY and TRANSX, because FENDL-2.1 had no Cd data. It is noted that self-shielding for neutron resonance peaks is not corrected in these libraries. KERMA, DPA and gas production libraries were also prepared from FENDL/MG-2.1 and our MATXS file with TRANSX because they had been prepared for FUSION-J3 and FUSION-40. Kinematic maximum KERMA factors were adopted as KERMA factors because KERMA factors with

Table 1 Material list in FUSION-F21-175 and FUSION-F21-42.

No.	Nuclide	Matt. No. (P0-P5)	No.	Nuclide	Mat. No. (P0-P5)	No.	Nuclide	Mat. No. (P0-P5)	No.	Nuclide	Mat. No. (P0-P5)
1	^{1}H	1 - 6	11	^{14}N	61 - 66	21	^{nat}Ca	121 - 126	31	^{93}Nb	181 - 186
2	^{2}H	7 - 12	12	^{16}O	67 - 72	22	^{nat}Ti	127 - 132	32	^{nat}Mo	187 - 192
3	^{3}He	13 - 18	13	^{19}F	73 - 78	23	^{51}V	133 - 138	33	^{nat}Cd	193 - 198
4	^{4}He	19 - 24	14	^{23}Na	79 - 84	24	^{nat}Cr	139 - 144	34	^{nat}W	199 -204
5	^{6}Li	25 - 30	15	^{nat}Mg	85 - 90	25	^{55}Mn	145 - 150	35	^{nat}Pb	205 - 210
6	^{7}Li	31 - 36	16	^{27}Al	91 - 96	26	^{nat}Fe	151 - 156	36	^{209}Bi	211 - 216
7	^{9}Be	37 - 42	17	^{nat}Si	97 - 102	27	^{nat}Co	157 - 162	37	^{nat}Cl	217 - 222
8	^{10}B	43 - 48	18	^{31}P	103 - 108	28	^{nat}Ni	163 - 168	38	^{181}Ta	223 - 228
9	^{11}B	49 - 54	19	^{nat}S	109 - 114	29	^{nat}Cu	169 - 174	39	^{nat}Sn	229 - 234
10	^{12}C	55 - 60	20	^{nat}K	115 - 120	30	^{nat}Zr	175 - 180	40	^{nat}Ga	235 - 240

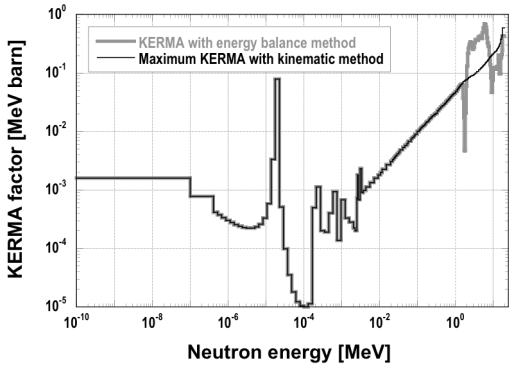

Fig. 1 KERMA factor of ^{186}W in FENDL/MG-2.1.

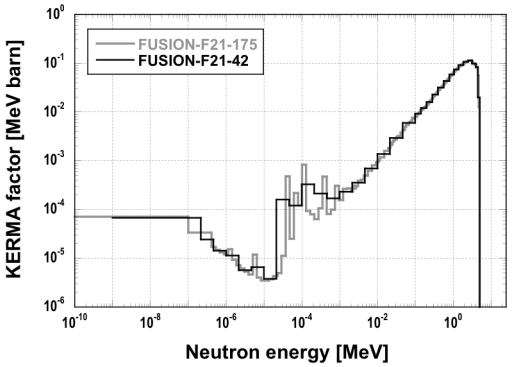

Fig. 2 KERMA factor of ^{nat}Sn.

the energy balance method were not always correct in cases, where energy balance in the nuclear data was not kept, as shown in Fig. 1. The KERMA factor and DPA cross-section data of natural Sn in FUSION-F21-175 and FUSION-F21-42 were omitted because they had inadequate data as shown in Figs. 2 and 3.

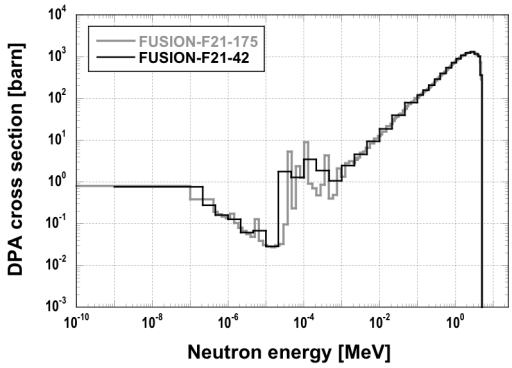

Fig. 3 DPA cross section data of ^{nat}Sn.

3. Tests of FUSION-F21 and FUSION-J40

3.1 Test with simple model

In order to validate FUSION-F21-175 and FUSION-F21-42 we carried out radiation transport calculations with a simple model. Neutron spectra inside a sphere of 1 m in radius for materials in Table 1 with 20 MeV neutrons in the center with the one-dimensional Sn code ANISN [7] and the following multigroup libraries (no self-shielding correction).

1) FUSION-F21-175
2) FUSION-F21-42
3) Mutigroup library from FENDL/MG-2.1 with TRANSX
4) Mutigroup library from our MATXS file (neutron :42 groups, gamma : 21 groups) with TRANSX

Figures 4 and 5 shows typical results for an iron sphere. Neutron spectra inside the iron sphere with FUSION-F21-175 and FUSION-F21-42 are the same as those with FENDL/MG-2.1 and our MATXS file, respectively. It is confirmed that FUSION-F21-175 and FUSION-F21-42 have no problem from this simple test.

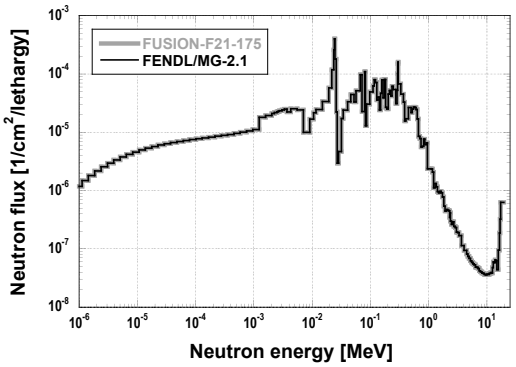

Fig. 4 Neutron spectra at 50cm from iron sphere center calculated with FUSION-F21-175 and FENDL/MG-2.1.

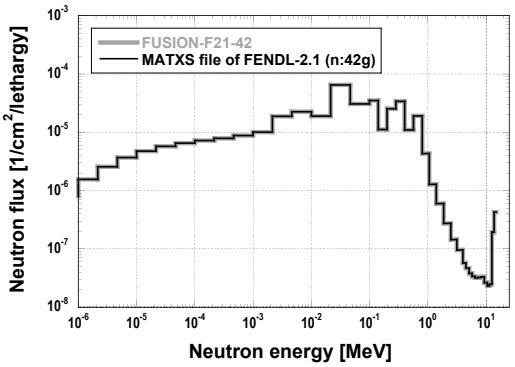

Fig. 5 Neutron spectra at 50cm from iron sphere center calculated with FUSION-F21-42 and our MATXS.

3.2 KERMA, DPA and gas production libraries

We also compared KERMA factors, DPA and gas production cross-section data between FUSION-F21-175 and FUSION-F21-42. Figure 6 compares the KERMA factors of ^{nat}W. The both KERMA factors are almost the same. It is comfirmed that KERMA factors, DPA and gas production cross-section data in FUSION-F21-175 and FUSION-F21-42 have no problem.

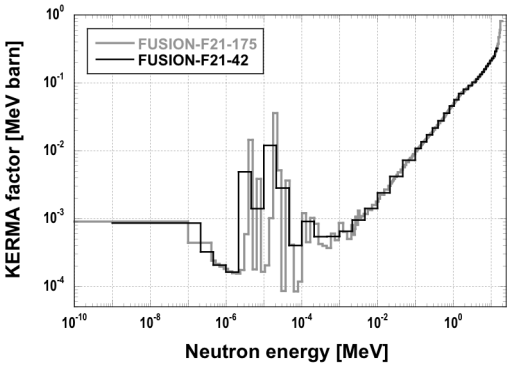

Fig. 6 KERMA factor of ^{nat}W.

4. Conclusion

We prepared FUSION-J3 type group constant sets, FUSION-F21-175 and FUSION-F21-42, from the official and our MATXS files of FENDL-2.1 with the TRANSX code for parametric studies and outline calculations in fusion reactor nuclear analyses. Several test calculations with a simple model were carried out in order to validate these nuclear group constant sets. They suggested that these group constant sets had no problem. Response data (KERMA factors, DPA and gas production cross-section data) were also prepared. It was also confirmed that these data had no problem.

References

[1] Maki K, Kosako K, Seki Y, Kawasaki H. Nuclear Group Constant Set FUSION-J3 for Fusion Reactor Nuclear Calculations Based on JENDL-3. JAERI-M 91-072. , 1991. [in Japanese]

[2] Shibata K, Nakagawa T, Asamai T, Fukahori T, Narita T, Chiba S, Mizumoto M, Hasegawa A, Kikuchi Y, Nakajima Y, Igarashi S. Japanese Evaluated Nuclear Data Library, Version-3 – JENDL-3 –. JAERI 1319 , 1990, 516p.

[3] Aldama DL, Trokov A. FENDL-2.1 Update of an evaluated nuclear data library for fusion applications. INDC(NDS)-467. Austria: International Atomic Energy Agency; 2004.

[4] MacFarlane RE. TRANSX 2: a code for interfacing MATXS cross-section libraries to nuclear transport codes. LA-12312-MS. USA: Los Alamos National Laboratory; 1993.

[5] MacFarlane RE, Muir DW. The NJOY Nuclear Data Processing System, Version 91. LA-12740-M. USA: 1994.

[6] Shibata K, Kawano T, Nakagawa T , Iwamoto O, Katakura J, Fukahori T, Chiba S, Hasegawa A, Murata T, Matsunobu T, Ohsawa T, Nakajima Y, Yoshida T, Zukeran A,

Kawai M, Baba M, Ishikawa M, Asami T, Watanabe T, Watanabe Y, Igashira M, Yamamuro N, KitazawaH, Yamano N, Takano H. Japanese Evaluated Nuclear Data Library Version 3 Revision-3: JENDL-3.3. J Nucl Sci Technol. 2002; 39: 1125-1136.

[7] RSICC. DOORS3.2a: One, two- and three-dimensional discrete ordinates neutron/photon transport code system. CODE PACKAGE CCC-650. USA: 2007.

This is a blank page.

26 Measurements of gamma-ray emission probabilities of minor actinides

K. Terada[1], S. Nakamura[1], A. Kimura[1], T. Nakao[1], H. Harada[1], T. Katabuchi[2], M. Igashira[2], J. Hori[3]

[1]*Nuclear Data Center, Japan Atomic Energy Agency, 2-4 Shirakata, Tokai-mura, Naka-gun, Ibaraki 319-1195, Japan*

[2]*Research Laboratory for Nuclear Reactors, Tokyo Institute of Technology, 2-12-1 Ookayama, Meguro-ku, Tokyo 152-8550*

[3]*Research Reactor Institute, Kyoto University, 2, Asashiro-nishi, Kumatori-cho, Sennan-gun, Osaka 590-0494, Japan*

E-mail: terada.kazushi@jaea.go.jp

Abstract

The measurements of the gamma-ray emission probabilities (Iγ) of ^{243}Am-^{239}Np have been performed at Kyoto University Research Reactor Institute. Gamma- and alpha-ray spectroscopic methods were applied with a high purity Ge and a Si detector, respectively.

1 Introduction

Measurements of neutron capture cross sections of Minor Actinides (MA) have been performed with the Accurate Neutron Nucleus Reaction Measurement Instrument (ANNRI) of the Materials and Life science experimental Facility (MLF) in the Japan Proton Accelerator Research Complex (J-PARC). Although recent studies have given capture cross sections of MA with good energy dependence, uncertainty corresponding to the normalization still remains[1–3]. The research project entitled "Research and development for Accuracy Improvement of neutron nuclear data on Minor ACtinides (AIMAC)" has been started to improve the reliability of the neutron cross section date for the R&D of innovative nuclear systems and environmental load reduction from the disposal of nuclear wastes. In order to obtain accurate cross section data, it is indispensable to determine the amount of MA sample accurately and non-destructively. Since, amount of the sample has a more direct influence on the absolute value of cross section data. However, the uncertainty concerning the amount of sample is not assured in some cases. Measurements of decay gamma-rays from the MA sample is expected to determine the amount of sample, uncertainty of the gamma-ray emission probabilities should be improved. Therefore, as a part of the AIMAC project, this study is aimed to development the technique for accurate determination of the amount of ^{237}Np and ^{241,243}Am sample with gamma- and alpha-ray spectroscopic methods, and to provide gamma-ray emission probability with high precision. We measured the gamma-ray emission probabilities of ^{243}Am and ^{239}Np.

2 Experimental Procedure and Results

Measurements of the gamma-ray emission probabilities of ^{243}Am and ^{239}Np were performed preliminarily at Kyoto University Research Reactor Institute. Americium-243 is alpha decay nuclide with a half life of 7370 years. Neptunium-239 is daughter nuclide of ^{243}Am with a half life of 2.35 days by beta minus decay, which is radioactive equilibrium with ^{243}Am.

An Americium-243 source sample was prepared as the standard solution (AmN_3O_9) supplied by Japan Radioisotope Association. The ^{243}Am solution of 2μl was dropped on a high purity quartz plate, and dried by an infrared lamp. Three measuring samples were prepared by similar method. Their diameters and radioactivities were approximate 3 mm and 2 kBq. The amount of the samples were determined by counting alpha particles with a Si detector (BU-016-300-100) having a diameter of 19.5 mm. **Figure 1** indicates the alpha-ray pulse height spectra from the ^{243}Am samples. A sharp peak located at 2500 ch is due to the alpha particles from the decay of ^{243}Am. The distance between the samples and the Si detector was 32 mm. The absolute detection efficiency of the Si detector was obtained by using an ^{241}Am standard source whose diameter was 15 mm. Corrections for solid angle between the ^{243}Am samples and the ^{241}Am source were made analytical.

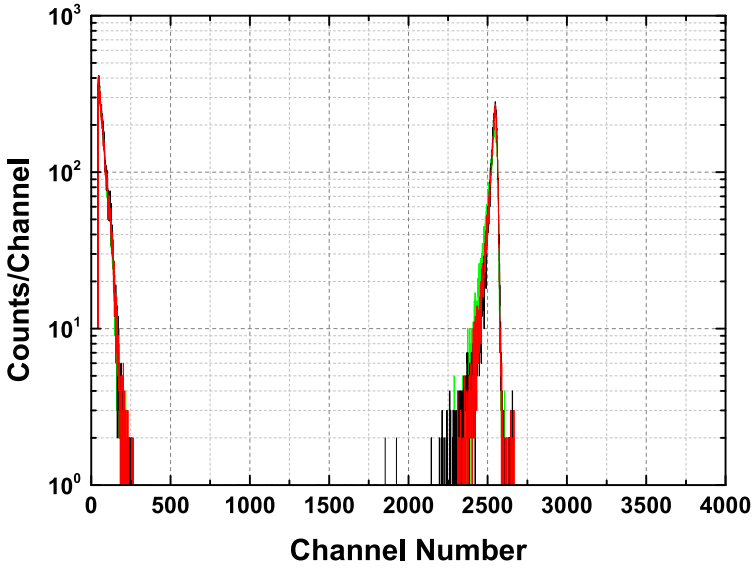

Figure 1: Alpha-ray spectra from the decay of ^{243}Am measured with the Si detector.

The gamma rays emitted from the ^{243}Am samples were measured by 90 minutes respectively with a low energy photon spectrometer (ORTEC 70450-30-PS) having dimensions of 70 mmϕ x 30 mmt. The distance from the samples to the surface of Ge detector was 65 mm. **Figure 2** shows the gamma-ray pulse height spectra from the ^{243}Am samples. Two strong gamma-rays with the energy of 43.5 keV and 74.6 keV were measured in the decay of ^{243}Am. Above 100 eV, several decay gamma-rays were observed corresponding to the gamma-ray emissions from ^{239}Np. Around 100 keV, Pu K X-rays were measured. The absolute detection efficiencies of Ge detector were derived from a measurement with a standard mixed source (^{241}Am, ^{109}Cd, ^{57}Co, ^{139}Ce, ^{203}Hg, ^{113}Sn, ^{85}Sr, ^{137}Cs, ^{60}Co, ^{88}Y). The gamma-ray emission probabilities were obtained by dividing the gamma ray yield by the activity. Corrections were made for conversion electrons, cascade sum effects of gamma rays and attenuation of gamma rays due to the sample cover. **Figure 3** shows the gamma-ray emission probabilities of ^{243}Am at 75 keV with previous results

and date from Table of Isotopes. There are 4 previous measurements for the last 30 years: those of Ahmad [4], Vaninbroukx *et al* [5], Sardari*et al* [6] and Wood *et al* [7]. By comparing the previous results with the present results, their measurements are in good agreement with the present results. The value from the Table of Isotopes [8], which was derived from limited relative statistical weight method, was also in accord with the present results.

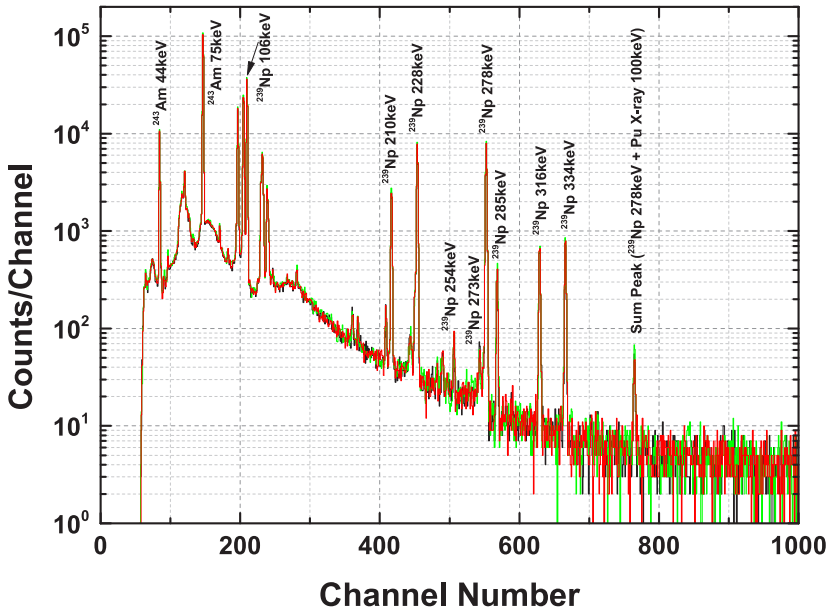

Figure 2: Gamma-ray spectra from the decay of ^{243}Am and ^{243}Np measured with the Ge spectrometer.

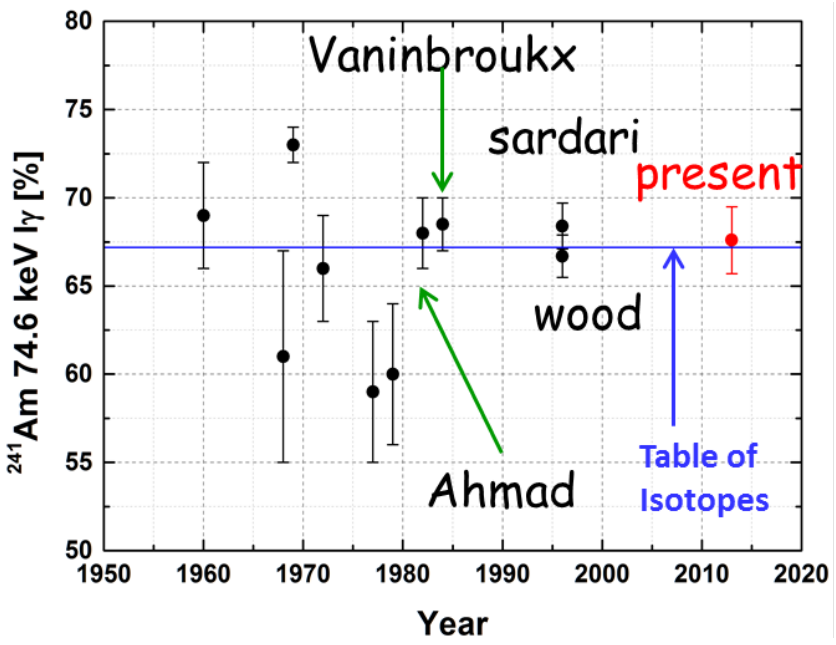

Figure 3: Comparison of the gamma-ray emission probabilities of ^{243}Am at 74.6 keV.

3 Summary

The AIMAC project has been started to improve the accuracy of the neutron cross section date. As a part of the project, we have measured the gamma-ray emission probabilities of ^{243}Am and ^{239}Np in order to develop the technique for accurate determination of the amount of MA samples.

Acknowledgments

Present study includes the result of "Research and Development for accuracy improvement of neutron nuclear data on minor actinides" entrusted to the Japan Atomic Energy Agency by the Ministry of Education, Culture, Sports, Science and Technology of Japan (MEXT).

References

1) H. Harada *et al*, Study of Neutron Capture Reactions Using the 4π Ge Spectrometer, Journal of Korean Physical Society **59**, 1547-1552 (2011).

2) A. Kimura *et al*, Neutron-Capture Cross-Sections of ^{244}Cm and ^{246}Cm Measured with an Array of Large Germanium Detectors in the ANNRI at J-PARC/MLF, Journal of Nuclear Science and Technology, **49**, 708-724 (2011).

3) K. Hirose *et al*, Cross-Section Measurement of ^{237}Np(n,γ) from 10 meV to 1 keV at Japan Proton Accelerator Research Complex, Journal of Nuclear Science and Technology, **50**, 188-200 (2013).

4) I. Ahmad, ALPHA-EMITTING NUCLIDES AS ABSOLUTE EFFICIENCY CALIBRATION SOURCE FOR GERMANIUM DETECTORS, Nuclear Instruments and Method, **193**, 9-13 (1982).

5) R. Vaninbroukx *et al*, Alpha-Particle-Emission Probabilities in the Decay of ^{243}U and Photon-Emission Probabilities in the Decays of ^{243}U, ^{239}Np and ^{243}Am, International Journal of Radiation Applications and Instrumentation, **35**, 1081-1087 (1984).

6) D. Sardari *et al*, ^{239}U and ^{243}Am decay data, Nuclear Instruments and Methods in Physics Research A, **369**, 486-490 (1996).

7) S. A. Woods *et al*, Standardisation and measurement of the decay scheme data of ^{243}Am and ^{239}Np, Nuclear Instruments and Methods in Physics Research , **369**, 472-476 (1996).

8) R. B. Firestone *et al*, Table of Isotopes, Eighth Edition, John Wiley and Sons, Inc., New York, (1999).

27 Compilation for Chart of the Nuclides 2014: A comprehensive decay data

Hiroyuki Koura
Advanced Science Research Center, Sector of Nuclear Science Research, Japan Atomic Energy Agency, Tokai, Ibaraki 319-1195, Japan
Jun-ichi Katakura
Department of Nuclear System Safety Engineering, Nagaoka University of Technology
Kamitomioka-machi 1603-1, Nagaoka, Niigata 940-2188, Japan
Takahiro Tachibana
Research Institute for Science and Engineering, Waseda University
Okubo 3-4-1, Shinjuku-ku, Tokyo 169-8555, Japan
Futoshi Minato
Nuclear Data Center, Nuclear Science and Engineering Center, Japan Atomic Energy Agency
Shirakata-shirane 2-4, Tokai-mura, Ibaraki 319-1195, Japan
e-mail: koura.hiroyuki@jaea.go.jp

Abstract:

A 2014 version chart of the nuclides is now under preparation to be published by the Japan Atomic Energy Agency (JAEA). This will be the latest successive version of the chart since 1977, and continues from 1980, 1984, 1988 1992, 1996, 2000, 2004 and 2010. This chart includes decay data for isotopes as half-lives, decay modes, isotopic abundance, and isomeric states with certain long half-lives. In addition, the periodic table of the elements, fundamental physical constants, characteristic X-rays, thermal neutron capture and fission cross sections are listed and tabulated.

The latest version is now compiled with recent experimental data up until the end of June in 2014, with some additional improvements. The number of experimentally identified nuclides totals 3,150, which includes 2,916 half-life-measured nuclides. With regard to theoretical predictions, five decay modes are considered; alpha decay, beta decay, spontaneous fission, and one- and two-proton emission. In addition, experimental proton and neutron drip lines are included.

1. Introduction

A comprehensive evaluated nuclear decay data set termed the Chart of the Nuclides 2014 is constructed by the Japan Atomic Energy Agency (JAEA). This is a successive version of the nuclear chart on nuclear decay. The first version was published in 1977, and publication was continued in 1980, 1984, 1988 1992, 1996, 2000, 2004 and 2010. The first eight series were published from the Japan Atomic Energy Research Institute, and last one from JAEA, which is the institute subsequently formed by joining with the Japan Nuclear Cycle Development Institute. These charts include nuclear decay data for isotopes as half-lives, decay modes, isotopic abundance, and isomeric states with certain long half-lives. In addition, the periodic table of the elements, fundamental physical constants, characteristic X-rays, and thermal neutron capture cross sections are listed and tabulated.

In the current process of constructing a revision of the Chart of the Nuclides, it was determined that some points required improvement. Consequently, a total of 16 sheets comprising the chart were prepared, 4 sheets more than the previous version in 2010. In this paper, we present current results for the chart prior to finalization.

2. Main nuclear chart

The following points were modified in part of the main nuclear chart.

(1) Experimental data

The main points of revision in the experimental data are as follows:

i. Lighter mass region: Neutron- or proton-emitting unstable nuclides are adopted. These nuclides have been well studied in the lighter nuclear mass region, and many of the resonance states were reported in recent years. Subsequently, 32 nuclei have been added.

ii. Border of unstable nuclides against particle nucleon emission: From this version, neutron and proton drip lines are newly drawn. The lines are defined as the borders of neutron or proton separation energies. The 2012 Atomic Mass Evaluation [1] is adopted to obtain the ground-state masses of nuclides.

iii. Adopted experimental data: Experimental decay data were adopted from both the 2014 April version of Evaluated Nuclear Structure Data File (ENSDF) and Nuclear Data Sheets. In addition, recent experimental results from published peer-review papers are adopted. The cutoff date for Nuclear Data Sheets and journal papers is set as **June 30, 2014**.

(2) Theoretical data

The main points of revision in theoretical predictions are as follows:

i. Extension of decay modes: In the previous version, three decay modes were adopted in the theoretical prediction; beta-decay, alpha decay (since 2000), and spontaneous fission (2010). When users applied this to the neutron-deficient region, they found only beta-decay and (sometimes) alpha-decay. However, if outside of the proton drip line, then nuclide may decay with proton emission and its half-life will probably be quite short. Therefore, one-proton and two-proton emissions are adopted to avoid such inconsistencies. In total, five partial half-lives are adopted. These partial half-lives are listed for the first-three shortest ones. However, the values are given only for half-lives within 10^6 times longer than the shortest half-life. These partial half-lives are ordered as p, 2p, f, β, and α. See References [2-7] for actual calculations.

Figure 1 shows an overview of the 2104 chart. The rectangular area corresponds to the actual region of the main chart in the sheet. The number of nuclides experimentally identified is 3,150 in total, which includes 2,916 half-life-measured nuclides.

The transition of the number of nuclides since 1977 obtained from the previous charts is shown in Figure 2. In 1977, the number of identified nuclides was less than 2,000. The number of nuclides has increased and reached 3,000 in the current version of the chart, as shown in Figure 2.

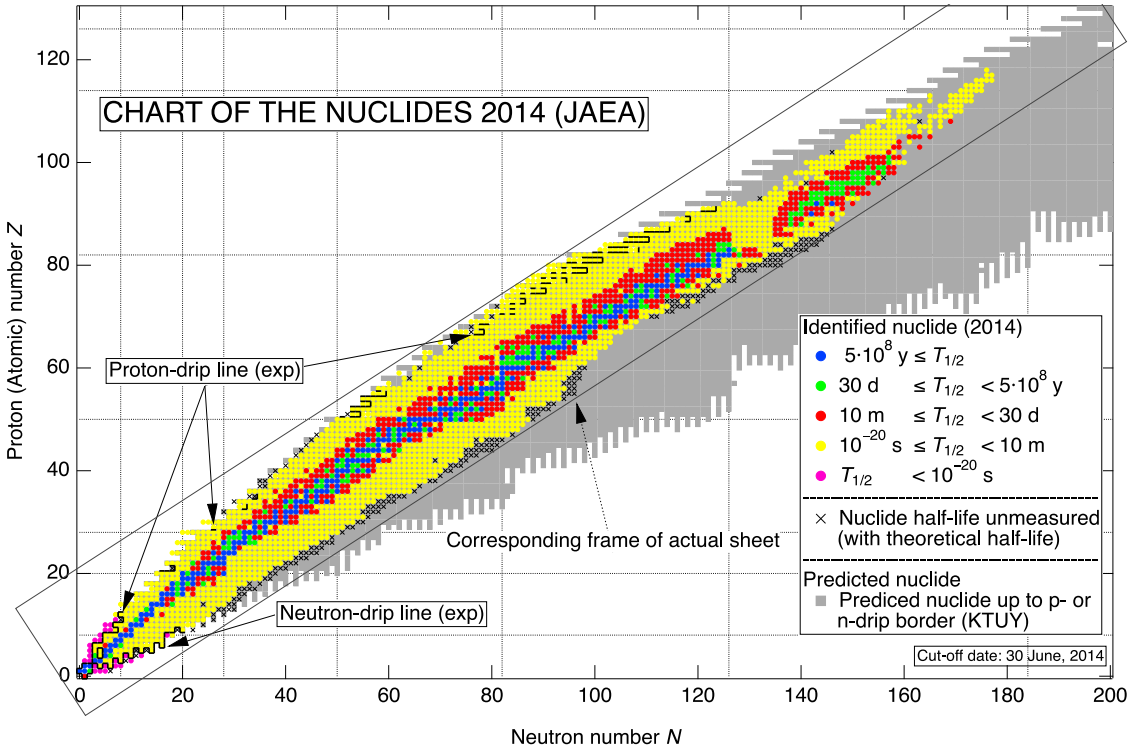

Figure 1: Overview of the 2014 chart.

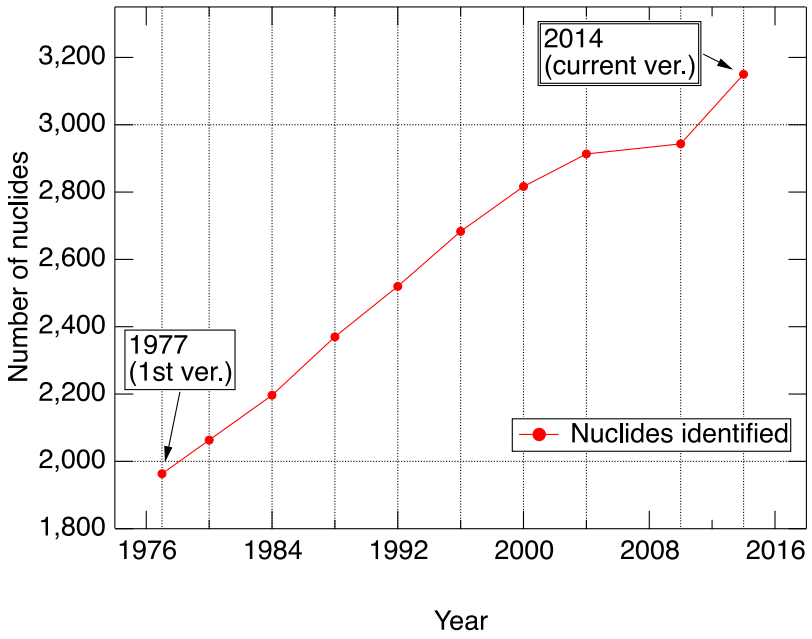

Figure 2: Transition of the number of nuclides identified in the JAEA (JEARI) chart of the nuclides since 1977.

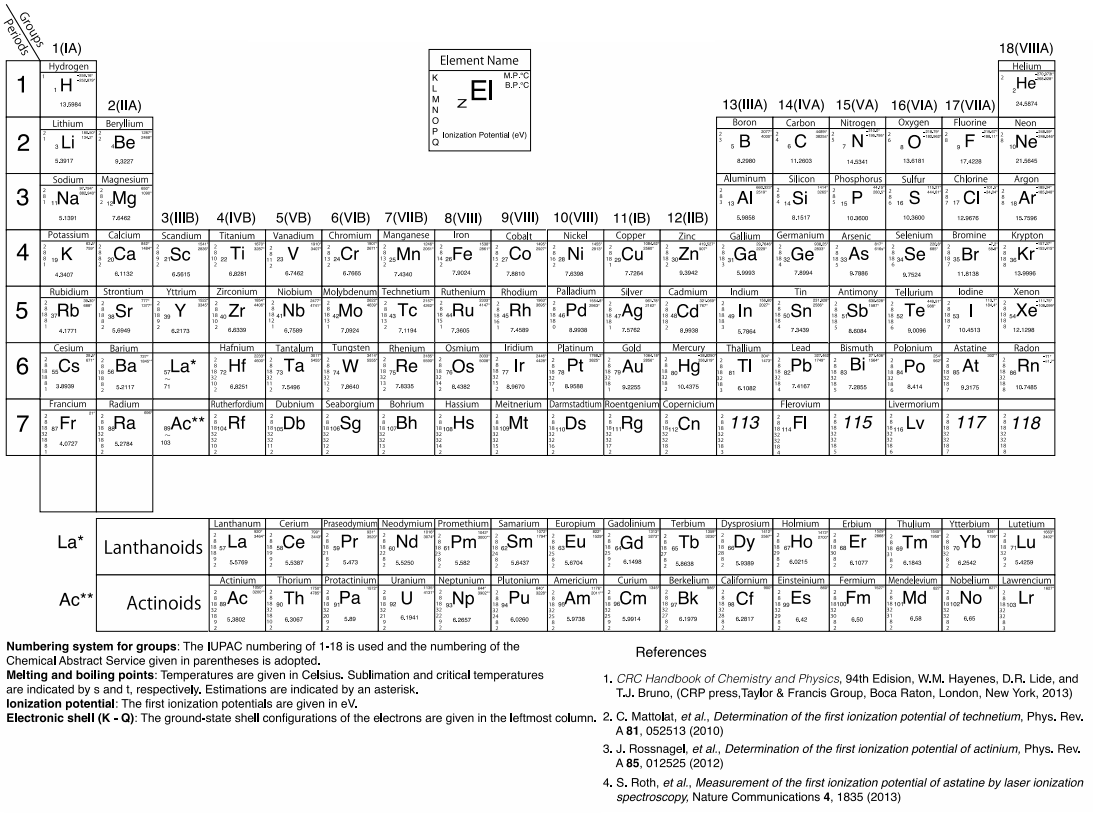

Figure 3: Periodic table of the elements.

3. Periodic table of the elements

Figure 3 shows a summary of the periodic table of the elements. The previous periodic tables used data until 1996. We have remade the table using the 2013 Handbook of Chemistry and Physics [8]. In addition, recent experimental results for the first ionization potentials are adopted for Technetium, Astatine, and Actinium. [9-11]

4. Thermal neutron capture and fission cross section

The thermal neutron capture cross section for U-235 was adopted in the sheets. In the previous sheets, only a table-based list was presented. However, when the neutron reaction process is considered for a reactor, for example, a successive reaction view is helpful in order to understand the process. **Figure 4** shows thermal neutron capture cross sections as a nuclear chart in the actinide region. The fission cross sections are also presented in the region. Data are taken from JENLD-4.0 [12].

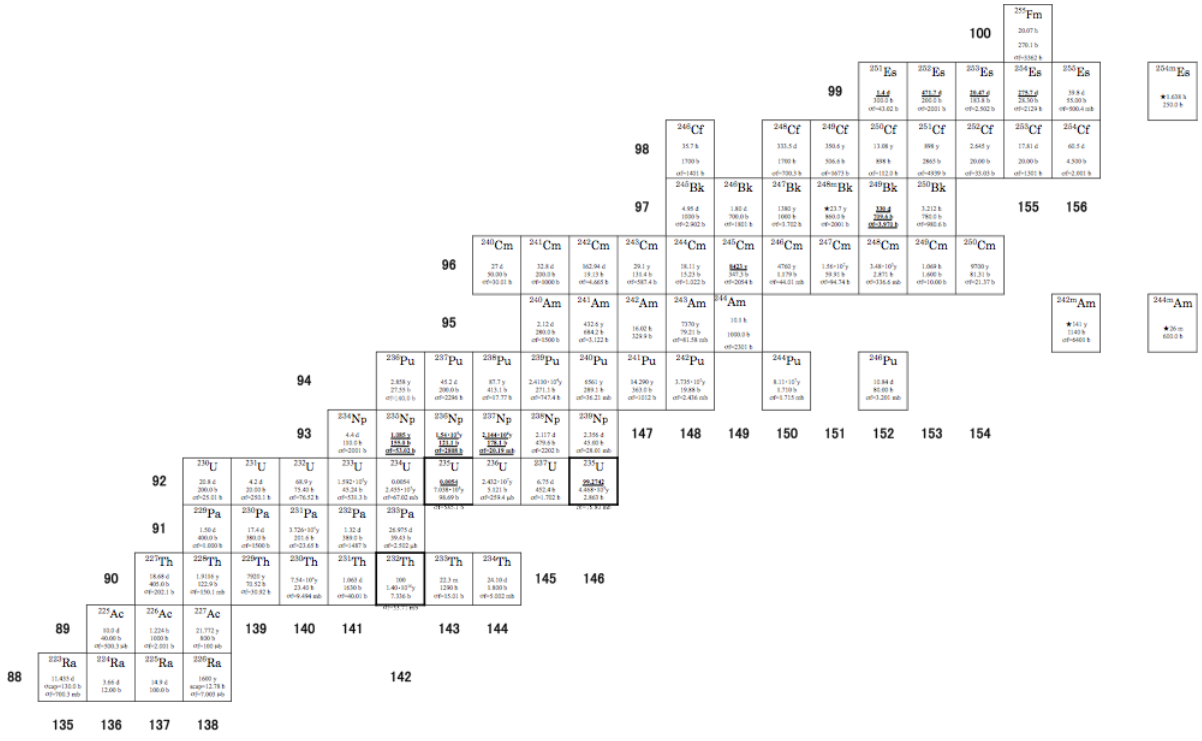

Figure 4: Nuclear chart for thermal neutron capture and fission cross section.

Acknowledgement

We thank Dr. H. Harada for valuable comments on the design of the neutron capture cross section.

References

[1] M. Wang, G. Audi, A.H. Wapstra, F.G. Kondev, M. MacCormic, X. Xu and B. Pfeiffer, *The AME2012 atomic mass evaluation (II), Tables, graphs and references*, Chinese Physics C **36**, 1603-2014 (2012)

[3] H. Koura, T. Tachibana, M. Uno and M. Yamada, *Nuclidic mass formula on a spherical basis with an improved even-odd term*, Prog. Theor. Phys. **113**, 305-325 (2005)

[4] H. Koura, *Phenomenological formula for alpha-decay half-lives*, J. Nucl. Sci. Technol., **49**, 816-823 (2012)

[5] T. Tachibana, M. Yamada, Proc. Int. Conf. on exotic nuclei and atomic masses, Arles, 1995, *eds.* M. de Saint Simon and O. Sorlin (Editions Frontueres, Gif-sur-Yvette, 1995) p. 763.

[6] H. Koura, *Ground-state properties of heavy and superheavy nuclei predicted by nuclear mass models*, Tours symposium on nuclear physics V (AIP Conf. **704**, Melville, New York, 2004) p. 60-69

[7] H. Koura and T. Tachibana, *How far does the area of superheavy element extend? – Decay modes of heavy and superheavy nuclei predicted by a mass formula*, BUTSURI (Bulletin of the Physical Society of Japan) 60, p. 717-724 (2005) (in Japanese)

[8] *CRC Handbook of Chemistry and Physics*, 94th Edision, W.M. Hayenes, D.R. Lide, and T.J. Bruno, (CRP press, Taylor & Francis Group, Boca Raton, London, New York, 2013)

[9] C. Mattolat, *et al.*, *Determination of the first ionization potential of technetium*, Phys. Rev. A **81**, 052513 (2010)

[10] J. Rossnagel, *et al.*, *Determination of the first ionization potential of actinium,* Phys. Rev. A **85**, 012525 (2012)

[11] S. Roth, *et al.*, *Measurement of the first ionization potential of astatine by laser ionization spectroscopy,* Nature Communications **4**, 1835 (2013)

[12] K. Shibata, O. Iwamoto, T. Nakagawa, N. Iwamoto, A. Ichihara, S. Kunieda, S. Chiba, K. Furutaka, N. Otuka, T. Ohsawa, T. Murata, H. Matsunobu, A. Zukeran, S. Kamada, and J. Katakura: "JENDL-4.0: A New Library for Nuclear Science and Engineering," J. Nucl. Sci. Technol. 48(1), 1-30 (2011).

28 Sensitivity of Delayed Neutron to Fission Yields and Beta-Decay Half-Lives

Futoshi MINATO
Nuclear Data Center, Japan Atomic Energy Agency
Tokai-mura, Naka-gun, Ibaraki-ken 319-1195 Japan
e-mail: minato.futoshi@jaea.go.jp

Sensitivity analyses of delayed neutron yields of U-235, 238, and Pu-239 to fission yields and delayed neutron emission probabilities were carried out. The analysis is performed by the aggregate calculation with the JENDL FP Decay Data File 2011 and JENDL FP Fission Yields Data File 2011. It is found that sensitivities of U-235 and Pu-239 to fission yields and delayed neutron emission probabilities are almost same in case of both thermal and fast neutron fissions. However, there are some nuclei which play an important role in either U-235 or Pu-239. Sensitivities of U-238 are slightly different from U-235 and Pu-239. The present result not only gives a priority list of precursors to be measured experimentally in future but also will be useful for compiling next fission yields and decay data files.

1. Introduction

It is well known that the delayed neutron plays a crucial role for stable operation of nuclear reactors. JENDL-4.0 general purpose file [1] evaluates it, based on several experimental data, and the values are benchmarked by reactor simulation calculations.

On the other hand, as JENDL Special Purpose Files, JENDL FP decay data file (JENDL/FPD-2011) and fission yields data files (JENDL/FPY-2011) were released in 2011 [2]. JENDL/FPD-2011 reflects new experimental data, for instance TAGS (Total Absorption Gamma-ray Spectroscopy), since its last update of JENDL/FPD-2000, and several modifications are also performed in JENDL/FPY-2011 to be consistent with JENDL/FPD-2011. An aggregate calculation with JENDL/FPD-2011 and JENDL/FPY-2011 files reproduce experimentally measured decay heats of fission products [2]. However, delayed neutron yields calculated with JENDL/FPD-2011 and

JENDL/FPY-2011 are not reproduced well as compared to the decay heat. The discrepancy between the decay heat and delayed neutron must be attributed from accuracy and incompleteness of fission yield and delayed neutron emission probability. Needless to say, it is more favorable to reproduce the delayed neutron and decay heat consistently with same decay and yield data files.

The purpose of this study is to make a new decay and yield data files reproducing consistently not only the decay heat but also the delayed neutron. However, it is difficult to identify where problematic data of fission products come from because the delayed neutron involves a number of nuclides. To tackle this problem, a sensitivity analysis is performed. This approach is useful when a lot of input data are involved like the reactor physics [3]. In this work, the sensitivity to fission yields and delayed neutron emission probabilities of fission products of U-235, Pu-239 and U-238 are analyzed. Sec.2 gives our calculation method, and Sec.3 shows the results. In Sec.4, we discuss our result and conclude this paper.

2. Calculation

Our calculation is performed by a code developed by Oyamatsu [4]. It is simply based on the Bateman equation [5] assuming a certain decay chain, given by

$$\begin{cases} \dfrac{dn_1(t)}{dt} = -\lambda_1 n_1(t) \\ \dfrac{dn_k(t)}{dt} = -\lambda_k n_k(t) + \lambda_{k-1} n_{k-1}(t) \quad (2 \le k). \end{cases}$$

The function $n_k(t)$ is the number of nuclide labeled by k at time t. The initial condition is $n_1(0) = y_i,\ n_k(0) = 0\ (2 \le k)$, where y_i is the yield of a fission product labeled by i at $t = 0$. The indices $k(\geq 2)$ represent nuclides being downstream from the fission product. The solution can be obtained analytically as

$$n_k(t) = y_i \sum_{j=1}^{k} d_j e^{-\lambda_j t}, \qquad d_1 = 1,\ d_j = \frac{\prod_l^{i-1} \lambda_l}{\prod_{l=1, l\neq j}^{j} (\lambda_l - \lambda_j)}\ (2 \le j \le k)$$

The actual abundance can be obtained by summing $n_k(t)$ for all the decay chains and the fission products. Delayed neutron is derived from the following aggregate calculation,

$$\nu_d(t) = \sum_k P_n(k) \lambda_\beta(k) n_k(t), \qquad \nu_{tot} = \int \nu_d(t)\, dt,$$

where $P_n(k)$ and $\lambda_\beta(k)$ are delayed neutron emission probabilities and beta-decay rates of nuclei labeled by k. Sensitivity of fission yields and delayed neutron emission probabilities are defined as

$$S_{y_i} = \frac{\Delta \nu_{tot}/\nu_{tot}}{\Delta y_i / y_i}, \qquad S_{P_n(i)} = \frac{\Delta \nu_{tot}/\nu_{tot}}{\Delta P_n(i)/P_n(i)},$$

respectively. In this work, we fix $\Delta y_i/y_i$ and $\Delta P_n(i)/P_n(i)$ to be 0.1, namely the

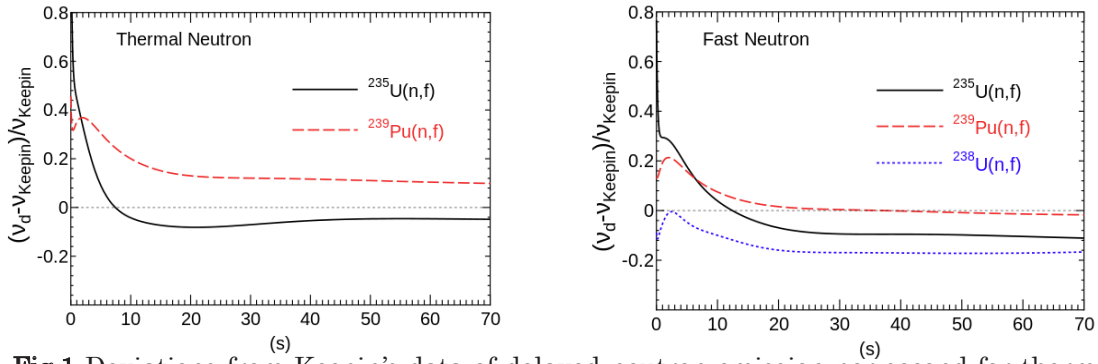

Fig.1 Deviations from Keepin's data of delayed neutron emission per second for thermal neutron fission (the left panel) and fast neutron fission (the right panel).

sensitivities are obtained when we increase fission yields or delayed neutron emission probabilities of nuclide i by 10%.

3. Result

Difference of the theoretical calculation from experimentally measured delayed neutron of the actinides induced by thermal and fast neutrons are shown in **Fig.1**. The experimental one is taken from Keepin's data [6]. The vertical line is the deviation defined as $(\nu_d - \nu_{Keepin})/\nu_{Keepin}$ and the horizontal line is the time after instantaneous radiation of neutron. In case of thermal neutron shown in the left panel, large deviations appear up to first 10 seconds. It becomes close to zero for U-235 after 10 seconds, but the finite deviation continues. In case of fast neutron shown in the right panel, large deviations appear until first 20 seconds, and it becomes almost zero for Pu-239 after 20 seconds. For U-235 and 238, the aggregate calculations of JENDL/FPY-2011 and JENDL/FPD-2011 underestimate Keepin's data. This result indicates there exist some inaccurate data of fission yields or delayed neutron emission probabilities, especially those of fission product with half-life shorter than 10 to 20 seconds.

Figure 2 shows sensitivities for thermal neutron fission of U-235 and Pu-239. The left and right panels are the results for S_{y_i} and $S_{P_n(i)}$, respectively. The overall trends are

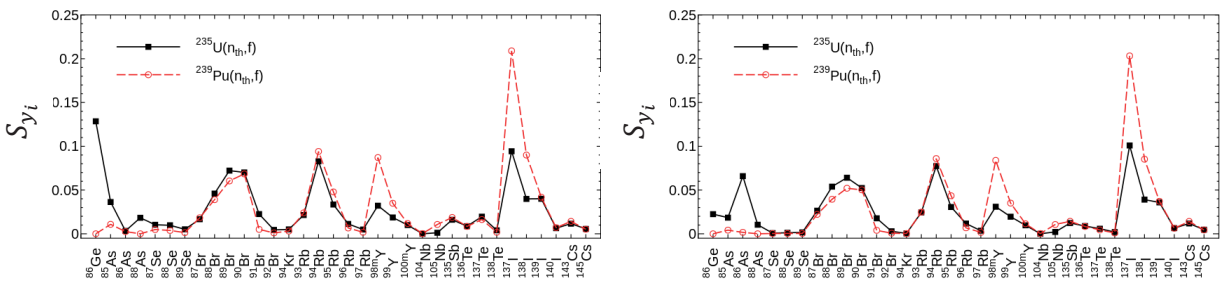

Fig.2 Sensitivity of aggregate delayed neutron for thermal neutron fission. The left and right panels are the results for S_{y_i} and $S_{P_n(i)}$, respectively.

similar between U-235 and Pu-239. For S_{y_i}, the strong sensitivities are obtained for Ge-86, Br-89, 90, and 91, Rb-94, Y-98m, I-137, and I-138. U-235 shows the different sensitivities to Ge-86, Y-98m, I-137 and 138 from Pu-239. The result for $S_{P_n(i)}$ is similar to S_{y_i} both for U-235 and Pu-239, however, less sensitivity to Ge-86 and higher one to As-86 are obtained for U-235.

Figure 3 shows sensitivities for fast neutron fission of U-235, Pu-239 and U-238. The whole structures are similar to the results of thermal fission. However, we can see that sensitivities to light nuclides such as Ge-86 and As isotopes are different from thermal neutron. For U-238, S_{y_i} show different sensitivities from U-235 and Pu-239, in particular, around A~137, while $S_{P_n(i)}$ have the similar dependence on them.

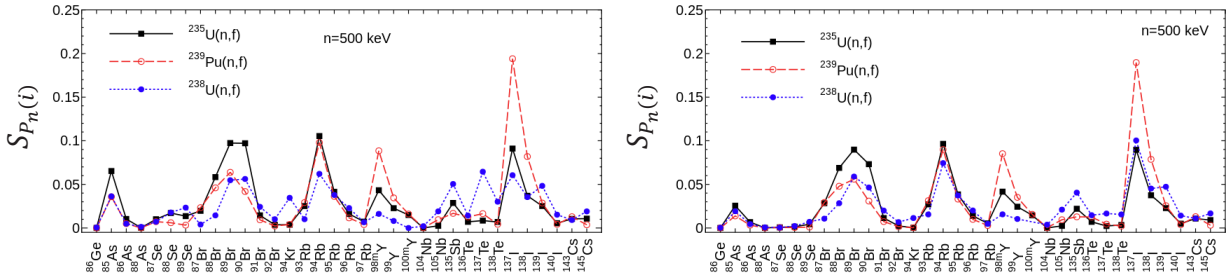

Fig.3 Same as Fig.2, but for fast neutron fission.

4. Conclusion

We have shown the important nuclei for delayed neutron by analyzing sensitivities. The sensitivities between U-235 and Pu-239 are similar. However, some differences appear which gives some clues for improved fission yield and decay data files. The present work also showed that large differences are attributed to nuclei with half-life shorter than 10-20 seconds. We plan for the next work to improve this time region at the first time, then to make modifications to nuclei with longer half-lives. We did not discuss the decay heat in this study, however, we plan to analysis it together with delayed neutron in the next work.

Acknowledgements: Author thanks Prof. K. Oyamatsu at Aichi Schukutoku Univ.

References

[1] K. Shibata *et al.*: J. Nucl. Sci. Tech. 48, 1 (2011).
[2] J. Katakura: JAEA-Data/Code 2011-025 (2011),73p.
[3] G. Chiba, K. Okumura, A. Oizumi, and M. Saito:J. Nucl. Sci. Tech. 47, 652 (2010).
[4] K. Oyamatsu: Proc. 1998 Symposium on Nuclear Data, Nov. 1998, JAERI, Tokai, Japan, JAERI-Conf 99-002, pp.234-239.
[5] K. Tasaka: JAERI-M 8727 (1980).
[6] G.R. Keepin, T.F. Wimett, and R.K. Zeigler: Phys. Rev. 107, 1044 (1957).

This is a blank page.

29 Measurement of γ-ray production cross sections and yields from carbon induced by 500 MeV/u iron beam

Youichi IMAHAYASHI[1], Yutaro ITASHIKI[1], Nobuhiro SHIGYO[1], Yusuke UOZUMI[1], Daiki SATOH[2], Tsuyoshi KAJIMOTO[3], Toshiya SANAMI[4], Yusuke KOBA[5], Naruhiro MATSUFUJI[5] and LEE Cheol-Woo[6]

[1] *Kyushu University, Fukuoka, 819-0395, Japan*

[2] *Japan Atomic Energy Agency (JAEA), Tokai, 319-1195, Japan*

[3] *Hiroshima University, Higashi-Hiroshima, 739-8527, Japan*

[4] *High Energy Accelerator Research Organization (KEK), Tsukuba, 305-0801, Japan*

[5] *National Institute of Radiological Sciences (NIRS), Chiba, 263-8555, Japan*

[6] *Korea Atomic Energy Research Institute (KAERI), Daejeon, 305-353, Korea*

e-mail: youichi@kune2a.nucl.kyushu-u.ac.jp

γ-ray production double differential cross sections (DDXs) and thick target γ-ray yields (TTYs) on incidence of 500 MeV/u iron to a carbon target were measured. In order to obtain neutron production DDXs and TTYs by means of time-of-flight (TOF) method in parallel, NE213 detectors were employed for this measurement. The γ-ray experimental results were compared with calculations using Monte Carlo simulation codes.

1. Introduction

Heavy ion accelerator facilities are planed to be build focusing on heavy ion cancer therapy or nuclear physics of spallation reactions including experiments about production of unknown neutron-rich nuclei, anti-matters and so on. Various kinds of secondary particles are emitted from a target material irradiated by heavy ion beams. Such facilities should be designed to shield these particles by considering dose levels of workers, equipments and areas. In particular, neutron and γ-ray have a large impact on the radiation level due to their long mean free path.

Some particle transport codes using Monte Carlo simulation are developed to be employed on shielding designs of accelerator facilities. They are able to simulate secondary particle production, decay, moderation in materials and streaming in a duct. For the validation of such codes, measurements of neutron production double differential cross sections (DDXs) and thick target yields (TTYs) from a target irradiated by heavy ions had already been performed, for exapmle, by D. Satoh, et al.[1]. However, the validation of γ-ray production from heavy ion incident reactions is not enough because existent experimental data are deficient. For example, secondary γ-ray yields from PMMA targets induced by carbon ion beams were measured and compared with results of Monte Carlo simulations as the previous studies about prompt γ-ray imaging in heavy ion therapy[2, 3]. The experimental data, however, of γ-ray yields are at only 90 degrees. In order to estimate accurate γ-ray doses in heavy ion accelerator facilities by means of Monte Carlo codes, experimental γ-ray production DDXs and TTYs on a wide angle and of more various incident particles and targets should be measured and compared with simulation results. Such validations are important to improve these codes and optimize shielding designs of facilities.

In this study, γ-ray production DDXs and TTYs from a carbon target irradiated by 500 MeV/u iron beam were measured. The beam and target are planned to be employed at the

heavy ion accelerator of Korea, "RAON" in future. Monte Carlo simulations using three codes, PHITS-2.67[4], FLUKA-2011.2b[5] and GEANT4-10.01[6] were also done. The experimental results were compared with calculated results to validate accuracy of these codes.

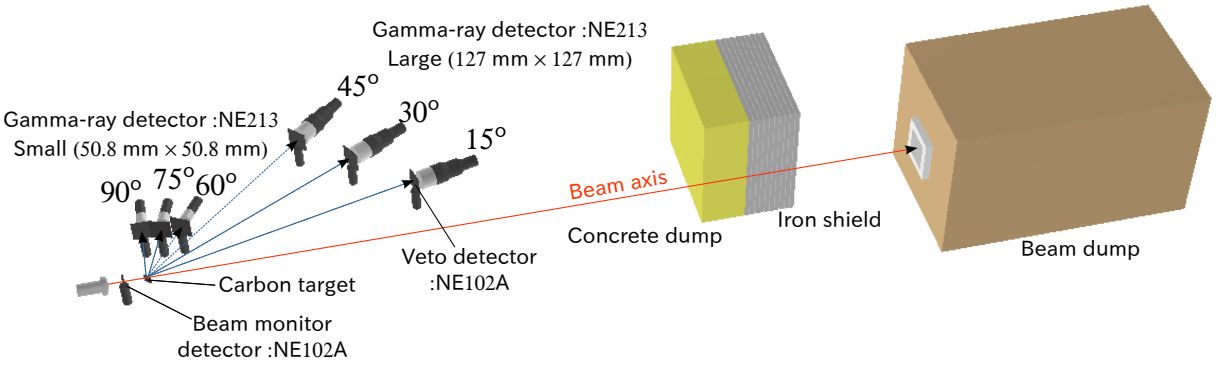

Figure 1: Experimental setup

2. Experiment

The experiment was performed at PH2 beam line of HIMAC at the NIRS. The experimental setup is shown at **Figure 1**. ^{56}Fe ions were accelerated to 500 MeV/u by the synchrotron. Average beam intensity was $2-4\times10^5$ ions/3.3 sec, and the beam spot diameter was less than 10 mm.

Table 1: Flight path length at each angle

	Flight path length (m)	
Angle (deg.)	Large	Small
15	3.9	1.7
30	3.4	1.7
45	3.4	1.7
60	1.8	1.2
75	1.8	1.1
90	1.9	1.1

Two thicknesses of graphite targets were used in this experiment, $50\times50\times10$ mm^3 (thin target) and $50\times50\times80$ mm^3 (thick target). They were employed for the DDXs measurement and the TTYs measurement respectively. The thin target was placed on the beam axis and rotated with 45° according to the axis, therefore the effective thickness was 14 mm. This was because thin target thickness should have been kept almost same to all measurement directions. The incident ^{56}Fe ions lost 15 % of the energy in the thin target. The thickness of the thick target was longer than the range of the iron beam in carbon.

The iron ions were passed through a beam monitor detector and irradiated the carbon target. The beam monitor detector was a NE102A plastic scintillator of which thickness was 0.5 mm, and counted the number of incident ions. In this experiment, measurements of neutron production DDXs and TTYs were also performed using the time-of-flight (TOF) method with γ-ray measurement simultaneously, and NE213 liquid organic scintillators were applied for neutron and γ-ray detectors from the aspect of the time resolution. γ-rays emitted from the target were detected by the six NE213 scintillators arranged from 15° to 90° to obtain the angle distribution. Two sizes of NE213 detectors were employed for neutron and γ-ray measurements in a wide energy region. The smaller detectors had 50.8 mm diameter and thickness, and were tuned to measure below 4 MeV of γ-ray. The diameter and thickness of the larger detectors were 127 mm, and the detectors covered above 2.5 MeV of γ-ray. The distances between the carbon target and each NE213 detector, i.e. flight path lengths, were determined as shown in **Table 1**. Measurements with some γ-ray sources were also performed to calibrate light output of the NE213 detectors. ^{241}Am, ^{133}Ba, ^{22}Na and ^{60}Co were used for the smaller detectors, and ^{60}Co and ^{241}Am-Be were used for the larger detectors. In order to discriminate between events of

charged and non-charged particles, a 2 mm thick NE102A plastic scintillator was installed in front of each NE213 detector.

The concrete dump and iron shields were placed as drawn in **Figure 1** to reduce neutron and γ-ray background events from the beam dump. The thickness of concrete and iron were 50 and 63 cm, respectively.

Data of light output of each detector and TOF were measured by a NIM and CAMAC electronic circuit. A gate of TOF measurement was triggered by a signal of the NE213 detector which was produced by a secondary particle from the target, and closed by a signal of the beam monitor detector which was produced by a iron ion and delayed in the circuit.

3. Data Analysis

In order to obtain energy spectra of prompt γ-ray, experimental data were analyzed with three processes; (i) discrimination of prompt γ-ray events, (ii) calibration of γ-ray light output and (iii) unfolding calculation.

(i) Discrimination of prompt γ-ray events

Non-Charged particle events were distinguished from charged particle events by use of veto detector. A example of light output spectrum of a veto detector is shown in **Figure 2**. Non-charged particles, i.e. neutrons and γ-rays, deposit less energy than charged particles in the veto detector. A sharp peak by neutrons and γ-rays is shown in the low light output region in **Figure 2**.

In a NE213 scintillator, γ-rays were detected as electrons which obtained energy from interactions with γ-rays, which were Compton Scattering, photo electron effect and pair production. On the other hand, neutrons were mainly detected as recoiled protons. Because decay time of the pulse caused by electron event was shorter than that of proton, it was possible to separate events of γ-ray and neutron by two integration gate method. **Figure 3** indicates two dimensional histogram of light output integrated in two different widths of the gate. The γ-ray events were picked up in the figure. After this discrimination of γ-rays and neutrons, the prompt γ-ray events were separated for analysis using TOF spectra to treat only γ-rays produced from the C(Fe, nγ) reaction.

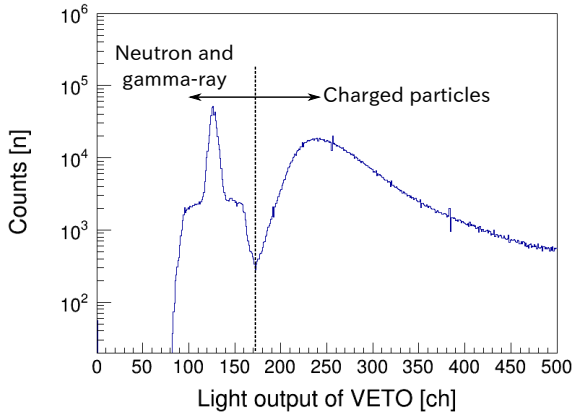

Figure 2: Light output spectrum of the veto detector at 15°

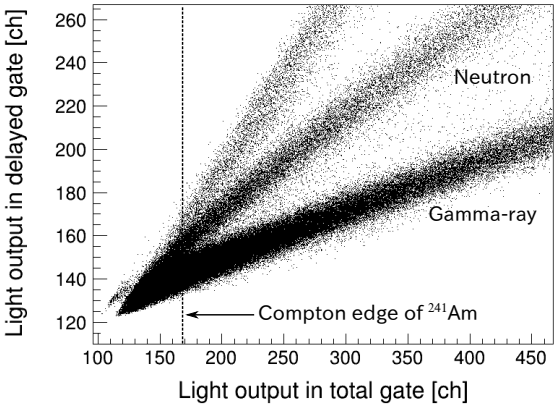

Figure 3: Discrimination of γ-ray and neutron events at 15°

(ii) Calibration of γ-ray light output

The light outputs of proton events in larger NE213 detector were related with the TOFs as shown in the left histogram of **Figure 4**. The deposition energies of proton were obtained by TOF method, considering the proton energy loss during their flight via the target, air, the

veto detector and the aluminum case of the NE213 detector. The calculation of the energy loss was performed with PHITS code. On the other hand, neutron events were detected as recoiled protons in the NE213 detector, and the maximum energy which protons were obtained by mono-energetic neutrons was indicated as recoil protons edge in light output spectrum. The recoil proton edges were obtained as the curve shown in the right histogram of **Figure 4**, and the deposition energies of the recoil protons were calculated with neutron TOF method. The deposition energies of protons and recoil protons were converted to the electron equivalent light unit by use of the following formula[7],

$$E_e = 0.81E_p - 2.8\{1.0 - \exp(-0.20E_p)\}$$

where E_e [MeVee] and E_p [MeV] are energy of electron and proton, respectively. The light outputs of larger detectors were calibrated by fitting plots obtained with the Compton edges of γ-ray source and the experimental correlation between proton deposition energy and light output. On the other hand, only the standard sources were employed for the calibration of the smaller detectors.

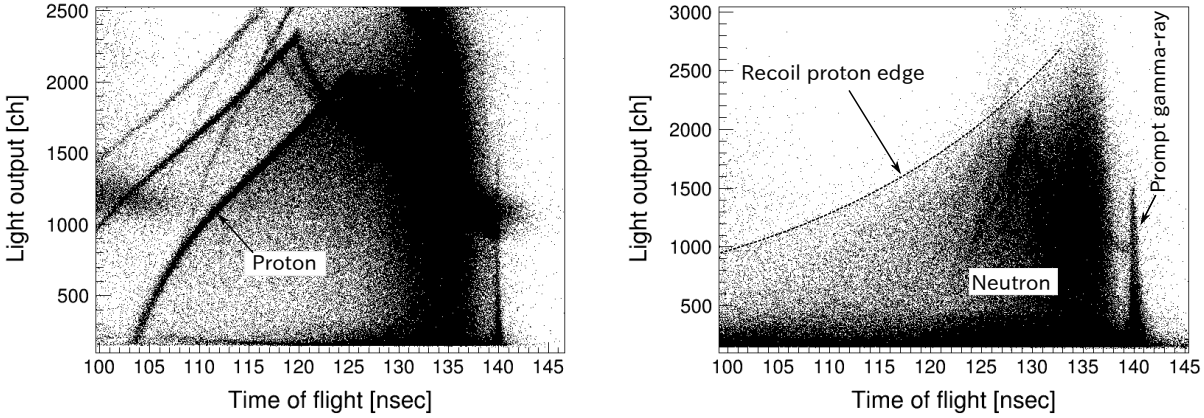

Figure 4: TOF vs. light output histogram of charged(left) and non-charged(right) particles in larger NE213 detector at 15°

(iii) Unfolding calculation

The γ-ray response functions of smaller and larger NE213 detectors were calculated with EGS5 code[8]. In order to reproduce the actual response, the simulated response functions were folded by Gaussian function using light output resolution of the detectors. The resolutions on Compton edges made by the γ-rays of standard source were obtained with fitting the experimental responses of the standard source measurements. **Figure 5** indicates the example of the resolution estimation on Compton edge made by γ-ray from ^{60}Co source. The resolution on full light output R [-] was approximately achieved by means of the following formula[9],

$$R = \Delta E_e/E_e = \sqrt{A^2 + B^2/E_e + C^2/E_e^2}$$

with the light output E_e [MeVee]. A, B and C are resolution parameters, and were determined by fitting the resolutions of standard sources (**Figure 6**).

The experimental light output spectra of prompt γ-ray were unfolded using the response function. For the unfolding calculation, MXD_MC33 and IQU_MC33 codes in UMG package were employed[10], in which the maximum entropy technique was used.

Prompt γ-ray DDXs $d^2\sigma/dEd\Omega$ [mb/sr/MeV] were gained from the following equation,

$$\frac{d^2\sigma}{dEd\Omega} = \frac{f(E)F}{N_{ion}\rho\Delta\Omega}$$

where $f(E)$ [n/MeV] is the γ-ray spectrum obtained by using MXD_MC33 code, N_{ion} [n] is the number of the incident iron ion, ρ [n/cm^2] is the surface density of the carbon target, $\Delta\Omega$ [sr] is the solid angle of each γ-ray detector and F is the factor which contains the correction of multiple iron ion incidence to the beam monitor detector and detection dead time.

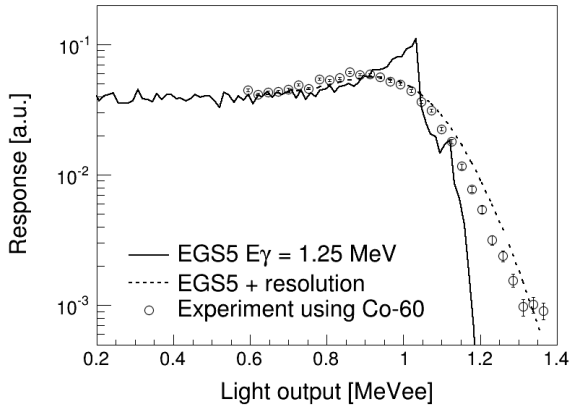

Figure 5: EGS5 response (solid line) and experimental light output (points) at 15° of the smaller detector. The 23 % of resolution was applied to the folded line (dashed line).

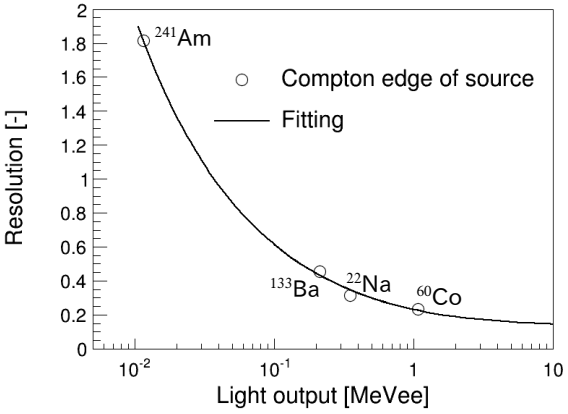

Figure 6: The light output resolution curve estimated by fitting on smaller detector at 15°

4. Results

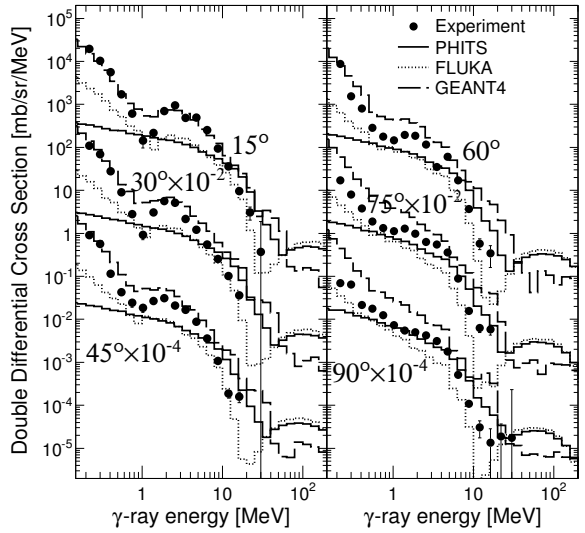

Figure 7: Prompt γ-ray production DDXs induced from 500 MeV/u ^{56}Fe + Carbon

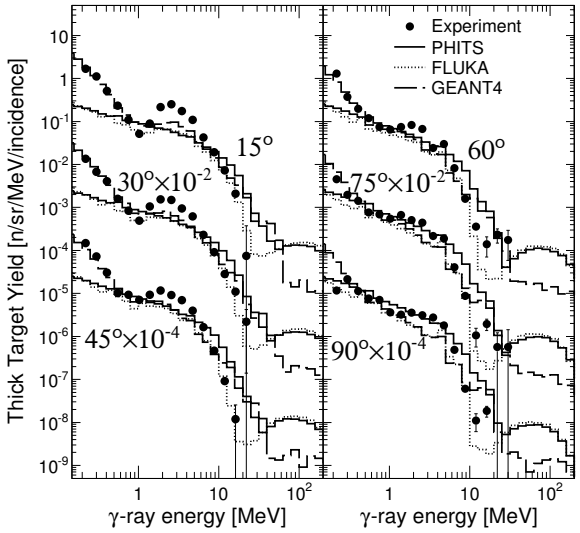

Figure 8: Prompt γ-ray TTYs induced from 500 MeV/u ^{56}Fe + Carbon

The γ-ray production simulations using PHITS-2.67, FLUKA-2011.2b and GEANT4-10.01 were performed. JAERI-QMD (Quantum Molecular Dynamics) and GEM (Generalized Evaporation Model) were used for simulation of hadronic interaction caused by heavy ion in PHITS and GEANT4. On the other hand, BME (Boltzmann Master Equation) or Relativistic QMD, and FLUKA evaporation models were employed for heavy ion interaction in FLUKA. For default setting, "HADROTHErapy" and "Electromagnetic Standard option 3"[11] were employed in FLUKA and GEANT4 calculations, respectively.

The experimental DDXs and TTYs were obtained in wide energy range from 0.2 to 20-30 MeV at from 15° to 90°. The experimental and calculated DDXs are presented in **Figure 7**. The errors were estimated with IQU_MC33 code. The γ-ray spectra have peak which strongly depend on emission angle around 2-3 MeV. In three Monte Carlo codes, GEANT4 results have best agreement with the peak and the increasing below 1 MeV in lower angle. However, GEANT4 largely overestimate the experimental DDXs in higher angle. In the FLUKA calculation, the results of DDXs underestimate the experimental DDXs at all angles. On the other hand, the PHITS results of DDXs differ substantially with the experimental ones on the shape of spectra and the value. The TTYs' results of the experiment and simulation are shown in **Figure 8**. Along with the DDXs, the experimental results have peak around 2-3 MeV, GEANT4 results, however, have lower peak than experimental results. It is possible to say that GEANT4 underestimate γ-ray yields produced by lower incident energy of iron ions. GEANT4 underestimate the experimental spectra in higher angles unlike in the case of the DDXs.

5. Conclusion

In order to validate Monte Carlo simulation codes, prompt γ-ray production DDXs and TTYs from carbon target induced 500 MeV/u iron beam were measured. NE213 scintillators were employed for the measurement to get the neutron DDXs and TTYs using TOF method, simultaneously. The experimental γ-ray DDXs and TTYs were obtained in wide energy region from 0.2 to 20-30 MeV. The DDXs and TTYs have peak which strongly depend on emission angle, and only GEANT4 is able to reproduce the peak of DDXs at low angles.

Acknowledgment

This work was performed as a Research Project with Heavy Ions at NIRS-HIMAC.

References

[1] D. Satoh, et al., Measurement of neutron-production double-differential cross-sections on carbon bombarded with 290-MeV/nucleon carbon and oxygen ions, Nucl. Inst. Meth. A644 (2011), 59-67.

[2] G. Dedes, et al., Monte Carlo nuclear models evaluation and improvements for real-time prompt gamma ray monitoring in proton and carbon therapy, IEEE NSS/MIC (2012).

[3] C. Robert, et al., Distributions of secondary particles in proton and carbon-ion therapy: a comparison between GATE/Geant4 and FLUKA Monte Carlo codes, Phys. Med. Biol. 58 (2013), 2879-2899.

[4] T. Sato, et al., Particle and Heavy Ion Transport Code System PHITS, Version 2.52, J. Nucl. Sci. Tech. 50:9 (2013), 913-923.

[5] G. Battistoni, et al., Proceedings of the Hadronic Shower Simulation Workshop 2006, Fermilab 6–8 September 2006, M. Albrow, R. Raja eds., AIP Conference Proceeding 896 (2007), 31-49.

[6] S. Agostinelli, et al., Geant4 a simulation toolkit, Nucl. Inst. Meth. A506 (2003), 250-303.

[7] N. Nakao, et al., Measurement of response function of organic liquid scintillator for neutron energy range up to 135 MeV, Nucl. Inst. Meth. A362 (1995), 454-465.

[8] H. Hirayama, et al., The EGS5 Code System, SLAC-R-730 (2005) and KEK Report 2005-8 (2005).

[9] G. Dietze and H. Klein, Gamma-calibration of NE213 scintillation counters, Nucl. Inst. Meth. 193 (1982), 549-556.

[10] M. Reginatto and PTB, The 'Multi-Channel' Unfolding Programs in the UMG Package: MXD_MC33, GRV_MC33 and IQU_MC33, (2004).

[11] V. Ivanchenko, et al., Recent Improvement in Geant4 Electromagnetic Physics Models and Interfaces, Nucl. Sci. Tech. vol.2 (2011), 898-903.

30 Measurements of Cross Sections for Production of Light Nuclides by 120 GeV Proton Bombardment of Au

S. Okumura[1], S. Sekimoto[1], H. Yashima[1], Y. Matsushi[2], H. Matsuzaki[3], H. Matsumura[4], A. Toyoda[4], K. Oishi[5], N. Matsuda[6], Y. Kasugai[6], Y. Sakamoto[7], H. Nakashima[6], D. Boehnlein[8], R. Coleman[8], G. Lauten[8], A. Leveling[8], N. Mokhov[8], E. Ramberg[8], A. Soha[8], K. Vaziri[8], K. Ninomiya[9], T. Shima[10], N. Takahashi[9], A. Shinohara[9], M. W. Caffee[11, 12], K. Nishiizumi[13], S. Shibata[14], T. Ohtsuki[1]

[1] Research Reactor Institute, Kyoto University, Kumatori, Osaka, 590-0494, Japan

[2] Disaster Prevention Research Institute, Kyoto University, Uji, Kyoto, 611-0011, Japan

[3] Department of Nuclear Engineering and Management, School of Engineering, University of Tokyo, Bunkyo, Tokyo, 113-0032, Japan

[4] High Energy Accelerator Research Organization, Tsukuba, Ibaraki, 305-0801, Japan

[5] Shimizu Corporation, Ecchujima, Tokyo, 135-8530, Japan

[6] Japan Atomic Energy Agency, Tokai-mura, Naka-gun, Ibaraki, 319-1195, Japan

[7] ATOX Co., Ltd., Kashiwa, Chiba, 277-0861, Japan

[8] Fermi National Accelerator Laboratory, Batavia, IL 60510 , USA

[9] Graduate School of Science, Osaka University, Toyonaka, Osaka, 560-0043, Japan

[10] Research Center for Nuclear Physics, Osaka University, Suita, Osaka, 567-0047, Japan

[11] Department of Physics and Astronomy, Purdue University, West Lafayette, IN 47907, USA

[12] Department of Earth, Atmospheric, and Planetary Sciences, Purdue University, West Lafayette, IN 47907, USA

[13] Space Sciences Laboratory, University of California, Berkeley, CA 94720-7450, USA

[14] RIKEN Nishina Center for Accelerator-Based Science, Wako, Saitama 351-0198, Japan

e-mail : sekimoto@rri.kyoto-u.ac.jp

The production cross sections of ^{10}Be and ^{26}Al produced from Au target irradiated with 120 GeV protons were measured by accelerator mass spectrometry. Those of ^{10}Be and ^{26}Al obtained in this work are compared to the literature data, which are production cross sections of corresponding light nuclides produced from various target elements irradiated with 50 MeV-12 GeV protons. From the comparison, induced energy- and target mass number-dependence of production cross sections of light nuclides were discussed and then, it was found that dependence of production cross sections of light nuclides on the target mass number is affected by the binding energy.

1. Introduction

In high-energy nuclear reactions, fragmentation process as well as spallation and fission is important. Fragmentation process is normally defined as high-energy process in which nuclides with masses between 10

and 30 are split off from a heavier target nucleus. Fragmentation has quite different process from the mechanism for spallation and fission [1-3]. To further study fragmentation process it is necessary to measure production cross sections of light nuclides, such as ^{10}Be and ^{26}Al. Those cross section data also have a very practical benefit for health and safety; they serve as a comprehensive nuclear database that can be used to estimate residual radioactivities in accelerator facilities. Finally, ^{10}Be and ^{26}Al, which are cosmic-ray produced long-lived nuclides, can be observed in terrestrial and extraterrestrial materials. Those cosmogenic radionuclides provide an opportunity to the deciphering of fossil records stored in those materials and allow investigations of their irradiation history by solar and galactic cosmic radiation. To obtain reliable scientific information based on the amounts of those cosmogenic radionuclides for the terrestrial and extraterrestrial materials, accurate information concerning their production cross sections are indispensable and a detailed investigation of induced energy- and target mass number-dependence of those production cross section values is required. For the target mass number with over 60, however, few measurements of production cross sections for those cosmogenic radionuclides have been made and published. The maximum energy is 12 GeV for protons with which production cross sections for those cosmogenic radionuclides were reported [1]. In this work, we measured ^{10}Be and ^{26}Al production cross sections for 120 GeV protons on Au. The concentration of ^{10}Be and ^{26}Al were measured using AMS techniques at MALT (Micro Analysis Laboratory, Tandem accelerator), University of Tokyo. The results obtained in this work are compared to the production cross sections of corresponding light nuclides produced from various target elements for 50 MeV-12 GeV protons [1-2, 4-16]. Based on that comparison, induced energy- and target mass number-dependence of production cross sections of light nuclides were discussed.

2. Experimental procedure

The proton irradiation at 120 GeV was performed at Fermi National Accelerator Laboratory (FNAL). In the proton irradiation at 120 GeV, the target stacks including the Au foil with a thickness of 57.9 mg cm^{-2} was installed into the proton beamline at M01 in FNAL. The target was arranged so that the center of the proton beam would penetrate the center of the Au foil, and was irradiated for 3.583 h. The average intensity of the 120 GeV proton beam at M01 in FNAL was measured using a secondary-emission monitor to be 1.11×10^9 protons/s. The beam current obtained by this method is consistent with the beam current determined from the ^{27}Al(p,3pn)^{24}Na monitor reaction. After the irradiation the target samples were prepared chemically for AMS measurements. The irradiated Au foil was dissolved in acua regia after adding 200 μg of Be and 500 μg Al carriers. Gold was first removed from the solution by anion exchange using 1M HCl. The Be and Al were separated by cation exchange using 1M HCl and 1.5M HCl, respectively. The $Be(OH)_2$ and $Al(OH)_3$ were individually precipitated with aqueous ammonia and rinsed with H_2O. The Be and Al hydroxides were converted to BeO and Al_2O_3, respectively. The isotopic ratios of ^{10}Be/^{9}Be and ^{26}Al/^{27}Al in the Au target foil were determined by AMS at MALT [17]. The isotopic ratios of AMS measurements

Table 1 Estimated production cross sections of ^{10}Be and ^{26}Al with results of AMS measurements.

Target / (E_p)	Au (E_p=120 GeV)
^{10}Be (atom) ($\times 10^8$)	1.387 ± 0.092
σ (^{10}Be) (mb)	54.7 ± 3.6
^{26}Al (atom) ($\times 10^6$)	4.27 ± 1.18
σ (^{26}Al) (mb)	1.68 ± 0.47

were normalized using the same ^{10}Be and ^{26}Al AMS standards [18, 19].

3. Results and discussion

The results of the AMS measurements and the production cross sections for Au obtained in this work are summarized in Table 1; The uncertainties (± 1σ) quoted in the cross sections are quadratically added from the AMS measurements and proton fluence measurements (± 5 %).

The production cross sections of ^{10}Be and ^{26}Al from Au (A=197) produced by 120 GeV protons, measured by this work, are shown in Figs. 1 and 2, respectively. In these figures those cross sections are compared with the corresponding light nuclides from various target elements produced by protons with some kinds of energy (50 MeV-120 GeV) [1-2, 4-15]. When the proton energy is over a few GeV, production cross sections of ^{10}Be simply increase with increasing target mass number, not depending on E_p values. This trend implies that those cross section values at E_p > a few GeV depend on diameter of atomic nuclei for target. When the proton energy is below 800 MeV, production cross sections of ^{10}Be decrease according to E_p values as target mass number increases from carbon to nickel. On the other hand, this trend does not continue from yttrium. Our previous results about production cross sections of ^{10}Be at E_p = 400 MeV [15] suggest that those cross sections increase as target mass number increases from yttrium through terbium; this trend is supported by those cross sections for yttrium and bithmuth at $E_p \approx$ 300 MeV obtained by Schumann et al.[4]

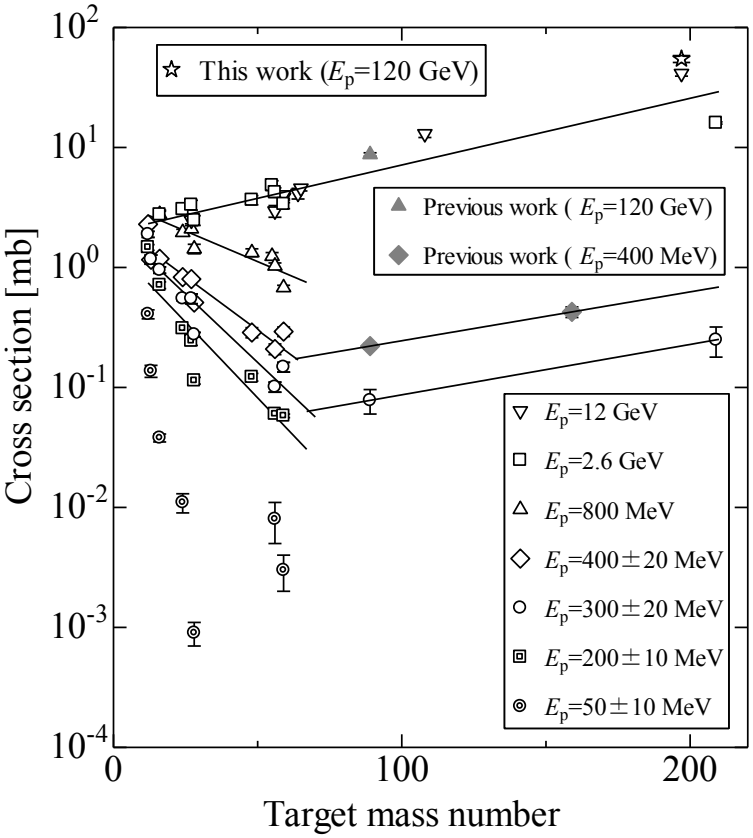

Fig. 1 Target mass number-dependence of the production cross sections for ^{10}Be at E_p = 50 MeV-120 GeV.
The open star (E_p=120 GeV) is the experimental cross section obtained in this work. The solid triangle (E_p=120 GeV) and diamonds (E_p=400 MeV) are obtained in our previous work [15]. The inverted open triangles (E_p=12 GeV), the open squares (E_p=2.6 GeV), the open triangles (E_p=800 MeV), the open diamons (E_p=400 ±20 MeV), the open circles (E_p=300±20 MeV), the double squares (E_p=200±10 MeV) and the double circles (E_p=50±10 MeV) are taken from Ref. [1], Ref. [2, 4], Ref. [2, 7, 12, 16], Ref. [7, 9, 11, 13, 14], Ref. [4, 7, 10, 11, 13, 14], Ref. [7, 9, 11, 13], and Ref. [7, 9, 11, 12], respectively.

Due to Fig. 2, when the proton energy is over a few tens of GeV and even 120 GeV, production cross sections of ^{26}Al do not always increase with increasing target mass number like the case in ^{10}Be. Although there are few

production cross section data for ^{26}Al shown in Fig. 2, those cross sections decrease as the target mass number increases from aluminum to zinc, and from yttrium those do not decrease but increase. This decreasing trend between aluminum to zinc is supported by those cross sections obtained by Shibata et al. [1] for aluminum, iron, cobalt, nickel, copper and zinc at E_p = 12 GeV, those by Michel et al. [5] for silicon, iron and nickel at E_p = 600 MeV, those by Regnier et al. [6] for silicon and iron at E_p = 24 GeV, and those by Sisterson et al. [7-8] for aluminum and silicon at E_p = 300 MeV. This increasing trend between yttrium and bithmuth is supported by the cross section measured in this work for gold at E_p = 120 GeV, that measured in our previous work for yttrium at E_p = 120 GeV, those obtained by Shibata et al. [1] for silver and gold at E_p = 12 GeV and those obtained by Sisterson et al. [9] for bithmuth and by our previous work [10] for yttrium at $E_p \approx$ 300 MeV. This decreasing and increasing trend for ^{26}Al shown in Fig. 2 is similar to the trend for ^{10}Be at E_p = 300 and 400 MeV. The decreasing trend changes to the increasing trend between the target mass number of nickel (A=58-64) and that of yttrium (A=89). This change implies that the production cross sections of ^{10}Be and ^{26}Al have minimum values in the range of the target mass numbers described above. The mass numbers in which the decreasing trend changes to the increasing one overlap the mass numbers where the binding energy per a nucleon has maximum values. Presumably, the production cross sections of ^{10}Be and ^{26}Al are minimum in the target with the maximum binding energy, except for the case in ^{10}Be at E_p > a few GeV. This suggests that dependence of production cross sections of light nuclides on the target mass number is affected by the binding energy of the target at E_p < 800 MeV for ^{10}Be and even at E_p > a few GeV for ^{26}Al. It may be noted, however, that the target mass number-dependence cannot be explained by only the binding energy of the target, and further that investigating the target mass number-dependence of production cross sections of light nuclides in detail requires measurements from various target elements, especially target mass number with over 100, induced by protons with various kinds of energy.

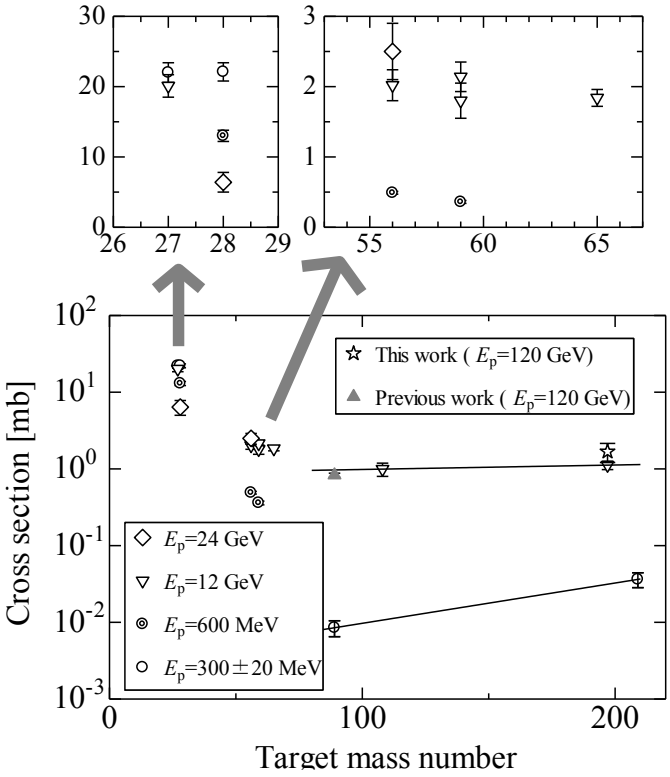

Fig. 2 Target mass number-dependence of the production cross sections for ^{26}Al at E_p = 300 MeV – 120 GeV. The open star (E_p=120 GeV) is the experimental cross section obtained in this work. The solid triangle (E_p=120 GeV) is our previous work. The open diamonds (E_p=24 GeV), the inverted open triangles (E_p=12 GeV), the double circles (E_p=600 MeV) and the open circles (E_p=300±20 MeV) are taken from Ref. [6], Ref. [1], Ref. [5], and Ref. [7, 8, 9, 10], respectively.

4. Conclusion

The production cross sections of the long-lived nuclides ^{10}Be and ^{26}Al were measured by AMS using Au target irradiated by 120 GeV protons. A comparison of those cross sections obtained in this work with the literature data in which the corresponding light nuclides were measured in various target elements produced by protons with some kinds of energy (50 MeV-120 GeV) revealed the followings about induced energy- and target mass number-dependence of production cross sections. When the proton energy is over a few GeV, production cross sections of ^{10}Be simply increase with increasing the target mass number, not depending on E_p values. This trend implies that those cross section values at E_p > a few GeV depend on diameters of atomic nuclei for target. When the proton energy is over a few tens of GeV and even 120 GeV, production cross sections of ^{26}Al do not always increase with increasing the target mass number. The production cross sections for ^{26}Al decrease as the target mass number increases from aluminum to zinc, and from yttrium those do not decrease but increase. It was suggested that dependence of production cross sections of light nuclides on the target mass number is affected by the binding energy of the target at E_p < 800 MeV for ^{10}Be and even at E_p > a few GeV for ^{26}Al.

Acknowledgments

The authors express their gratitude to the RCNP for their generous supports in this experiment (RCNP-E298). This work was supported by a grant-in-aid from the Ministry of Education, Science and Culture (KAKENHI 19360432, 21360473, 23656589, 25790081) in Japan, embryonic research project support in Kyoto University Global COE Program “International Center for integrated Research and Advanced Education in Materials Science”, Kansai Research Foundation for technology promotion for SS, National Science Foundation (NSF) and National Aeronautics and Space Administration (NASA) for KN and MWC. Fermilab is a US Department of Energy Laboratory operated under Contract E-AC02-07CH11359 by the Fermi Research Alliance, LLC.

Reference

[1] Shibata S, Imamura M, Nagai H, Kobayashi K, Sakamoto K, Furukawa M, and Fujiwara I. Measurements of ^{10}Be, ^{26}Al production cross sections with 12 GeV protons by accelerator mass spectrometry. Phys. Rev. C. 1993 Dec; 48: 2617-2624.

[2] Michel R, Gloris M, Lange H.-J, Leya I, Lüpke M, Herpers U, Dittrich-Hannen B, Röse1 R, Schiekel Th, Filges D, Dragovitsch P, Suter M, Hofmann H.-J, Wölfli W, Kubik P.W, Baur H, and Wieler R. Nuclide production by proton-induced reactions on elements($6 \leq Z \leq 29$) in the energy range from 800 to 2600 MeV. Nucl. Instr. Meth. B. 1995 Oct; 103: 183-222.

[3] Shibata S, Imamura M, Sakamoto K, Okizaki S, Shibutani S, Matsumura H, Furukawa M, Fujiwara I, Nagai H and Kobayashi K. Yield Measurements of ^{7}Be and ^{10}Be Produced by Photonuclear Reactions at Intermediate Energies: Intercomparison of Fragmentation Processes between Photon- and Proton-Induced Reactions. Radiochim. Acta. 1998 Apr; 80: 181-188.

[4] Schumann D, Neuhausen J, Michel R, Alfimov V, Synal H.-A, David J.-C, and Wallner A. Excitation functions for the production of long-lived residue nuclides in the reaction ^{nat}Bi(p;xn,yp)Z. J. Phys. G: Nucl. Part. Phys. 2011 May; 38: 065103.

[5] Michel R, Dittrich B, Herpers U, Peiffer F, Schiffmann T, Cloth P, Dragovitsch P, and Filges D. Proton-induced spallation at 600 MeV. Analyst. 1989 Mar; 114: 287-293.

[6] Regnier S, Lagarde M, Simonoff G. N, and Yokoyama Y, PRODUCTION DE ^{26}A1 DANS Fe ET Si PAR PROTONS DE 0.6 ET 24 GeV. Earth Planet. Sci. Letters. 1973 Feb; 18: 9-12.

[7] Sisterson J. M, Kim K, Beverding A, Englert P. A. J, Caffee M, Jull A. J. T, Donahue D. J, McHargue L, Castaneda C, Vincent J, and Reedy R. C. Measurement of proton production cross sections of ^{10}Be and ^{26}A1 from elements found in lunar rocks. Nucl. Instr. Meth. B. 1997 Mar; 123: 324-329.

[8] Sisterson J. M, Kim K, Beverding A, Englert P. A. J, Caffee M. W, Vincent J, Castaneda C, Reedy R. C. Measuring excitation functions needed to interpret cosmogenic nuclide production in lunar rocks. AIP Conf. Proc. 1997; 392: 811-814.

[9] Sisterson J. M, Kim K, Beverding A, Englert P. A. J, Caffee M. W, Vincent J, Castaneda C, and Reedy R. C. Measuring excitation functions needed to interpret cosmogenic nuclide production in lunar rocks. Conf.on Appl.of Accel.in Res.and Ind; 1996; USA. p.811.

[10] Sekimoto S, Omoto T, Joto H, Utsunomiya T, Yashima H, Ninomiya K, Welten K. C, Caffee M. W, Matsushi Y, Matsuzaki H, Nakagaki R, Shima T, Takahashi N, Shinohara A, Matsumura H, Satoh D, Iwamoto Y, Hagiwara M, Nishiizumi K, and Shibata S. Measurements of cross sections for production of light nuclides by 300 MeV proton bombardment of Cu and Y. Nucl. Instr. Meth. B. 2013 Jan; 294: 475-478.

[11] Michel R, Bodemann R, Busemann H, Daunke R, Gloris M, Lange H.-J, Klug B, Krins A, Leya I, Lüpke M, Neumann S, Reinhardt H, Schnatz-Büttgen M, Herpers U, Schiekel Th, Sudbrock F, Holmqvist B, Condé H, Malmborg P, Suter M, Dittrich-Hannen B, Kubik P.-W, Synal H.-A, and Filges D. Cross sections for the production of residual nuclides by low- and medium-energy protons from the target elements C, N, O, Mg, Al, Si, Ca, Ti, V, Mn, Fe, Co, Ni, Cu, Sr, Y, Zr, Nb, Ba and Au. Nucl. Instr. Meth. B. 1997 July; 129: 153-193.

[12] Dittrich B, Herpers U, Hofmann H. J, Wölfli W, Bodemann R, Lüpke M, Michel R, Dragovitsch P, and Filges D. AMS measurements of thin-target cross sections for the production of ^{10}Be and ^{26} Al by high-energy protons. Nucl. Instr. Meth. B. 1990 Dec; 52: 588-594.

[13] Kim K. J, Sisterson J. M, Englert P. A. J, Caffee M. W, Reedy R. C, Vincent J, and Castaneda C. Experimental cross-sections for the production of ^{10}Be from natural carbon targets with 40.6 to 500 MeV protons. Nucl. Instr. Meth. B. 2002 Nov; 196: 239-244.

[14] Schiekel Th, Sudbrock F, Herpers U, Gloris M, Lange H.-J, Leya I, Michel R, Dittrich-Hannen B, Synal H.-A, Suter M, Kubik P. W, Blann M, and Filges D. Nuclide production by proton-induced reactions on elements ($6 \leq Z \leq 29$) in the energy range from 200 MeV to 400 MeV. Nucl. Instr. Meth. B. 1996 Jun; 114: 91-119.

[15] Sekimoto S, Okumura S, Yashima H, Matsushi Y, Matsuzaki H, Matsumura H, Toyoda A, Oishi K, Matsuda N, Kasugai Y, Sakamoto Y, Nakashima H, Boehnlein D, Coleman R, Lauten G, Leveling A, Mokhov N, Ramberg E, Soha A, Vaziri K, Ninomiya K, Shima T, Takahashi N, Shinohara A, Caffee M. W, Nishiizumi K, Shibata S, Ohtsuki T. Measurements of cross sections for production of light nuclides by 120 GeV and 400 MeV proton bombardment of Y and Tb. Nucl. Instr. Meth. B.2015 Oct; 361: 685-688.

[16] Dittrich B, Herpers U, Bodemann R, Lüpke M, Michel R, Signer P, Wieler R, Hofmann H.J, and Wölfli W. Integral Excitation Functions For the Production of Long-Lived Be-10 and Al-26 by Proton-Induced Reactions. France: CEC-Countries and CEC to NEANDC; 1990, Vol.U, No.312, p.51.

[17] Matsuzaki H, Nakano C, Tsuchiya Y. S, Kato K, Maejima Y, Miyairi Y, Wakasa S, and Aze T. Multi-nuclide AMS performances at MALT. Nucl. Instr. Meth. B. 2007 Jun; 259: 36-40.

[18] Nishiizumi K, Imamura M, Caffee M. W, Southon J. R, Finkel R. C, McAninch J. Absolute calibration of ^{10}Be AMS standards. Nucl. Instr. Meth. B. 2007 May; 258: 403-413.

[19] Nishiizumi K. Preparation of ^{26}Al AMS standards. Nucl. Instr. Meth. B. 2004 Aug; 223: 388-392.

This is a blank page.

31 Supplemental Integral Experiment for Benchmarking Nuclear Data Libraries on Copper with D-T Neutron Source at JAEA/FNS

Saerom Kwon*, Masayuki Ohta, Kentaro Ochiai, Satoshi Sato, Chikara Konno
Japan Atomic Energy Agency
Tokai-mura, Naka-gun, Ibaraki-ken 319-1195 Japan
**e-mail: kwon.saerom@jaea.go.jp*

An integral experiment by using a copper assembly newly covered with Li_2O blocks has been carried out to investigate the underestimation of the measured data related to lower energy neutrons in the previous copper integral experiment. Reaction rates were measured inside the assembly with five kinds of activation foils (Nb, Al, In, Au and W). In addition, we measured fission rates of ^{235}U and ^{238}U with two micro fission chambers (MFCs). The Monte Carlo neutron transport code, MCNP5-1.40 and recent nuclear data libraries, ENDF/B-VII.1 (ENDF/B-VII.0, FENDL-3.0), JEFF-3.2 and JENDL-4.0 were used for the analysis. Although the underestimation in the reaction rate of the $^{197}Au(n, \gamma)^{198}Au$ reaction was improved compared to the previous experiment result, the underestimation tendency for the reaction rates sensitive to lower energy neutrons still appeared in this experiment. It is considered that the nuclear data on copper have some problems.

1. Introduction

Copper is used as a winding material with D-shaped superconducting coils in common magnet confinement fusion devices and as a part of blanket shield with stainless steel in ITER blanket. A benchmark experiment on copper with D-T neutrons was performed two decades ago at JAEA/FNS [1]. In the experiment the calculated results tended to underestimate the measured data related to lower energy neutrons below a few keV in the experiment, which suggested that the measured data might be affected by neutrons scattered in the concrete wall of the experiment room or other surroundings. Therefore, we have carried out an additional integral experiment on copper, where a copper assembly was covered with Li_2O blocks to reduce neutrons scattered in the concrete wall.

2. Preliminary Analysis

Before the experiment, we analyzed several cases for selection of a proper experimental assembly with MCNP5-1.40 [2] as a neutron transport code and JENDL-4.0 [3] as a nuclear data library. Figure 1 shows a common calculation model, where Li_2O layers

cover the copper assembly of 315 mm in radius and 608 mm in thickness in order to reduce background neutrons scattered in the concrete wall. The concrete wall was set from 5 m in distance from the copper assembly. We changed the Li_2O layer thicknesses shown in Fig. 1.

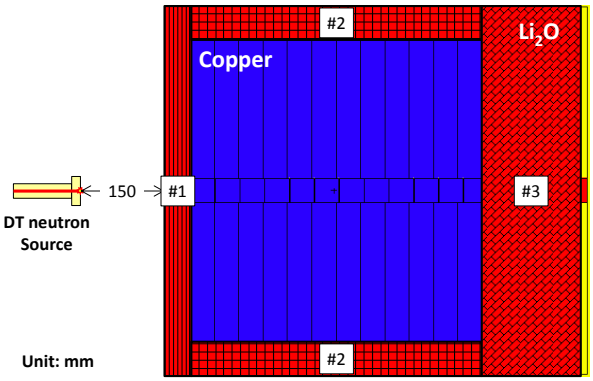

Figure 1. Common calculation model.

The # with a number of the Li_2O regions in Fig. 1 represents the position of Li_2O blocks around the copper assembly; #1 is the front part of the copper assembly, #2 is the side part of the copper assembly and #3 is the back part of the copper assembly. Four types of calculation conditions are selected as follows; (a) w/o Li_2O: only the copper assembly without Li_2O regions (#1/#2/#3 = 0/0/0 in unit of centimeter), (b) Li_2O TA: the copper assembly with 5 cm of Thin All Li_2O layers (5/5/5), (c) Li_2O TS: the copper assembly with 5 cm of Li_2O at #1, Thick Side 20 cm Li_2O at #2 and #3 (5/20/20), (d) Li_2O MC: the copper assembly with Multiple Combination of Li_2O layers (5/5/20).

Figure 2 shows typical results of reaction rate ratios of NO WALL to WALL, where NO WALL and WALL mean calculation results without and with the concrete wall, respectively.

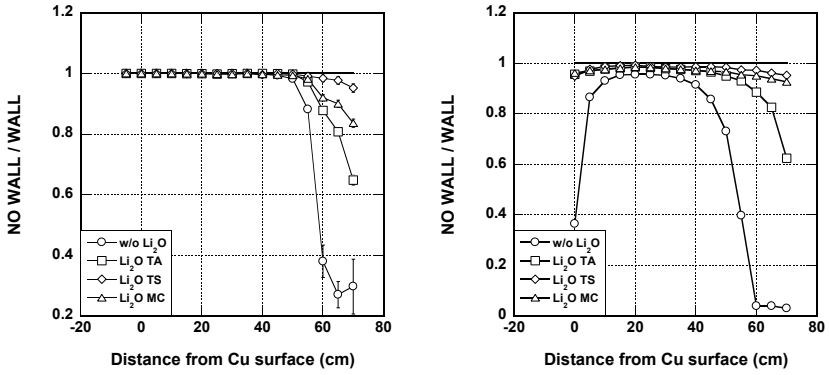

(a) $^{93}Nb(n, 2n)^{92m}Nb$ (b) $^{197}Au(n, \gamma)^{198}Au$

Figure 2. Reaction rate ratios (No wall / Wall) of $^{93}Nb(n, 2n)^{92m}Nb$ and $^{197}Au(n, \gamma)^{198}Au$ reactions.

The Li_2O cover is effective for reducing background neutrons scattered in the concrete wall of the experimental room. Although the result of Li_2O TS is better than any others, we selected the copper assembly with Li_2O MC due to space limitation. However, there is almost no discrepancy between reaction rates without and with concrete for Li_2O MC at 50 cm depth. Namely Li_2O MC we selected is enough to reduce neutrons scattered in the concrete wall.

3. Experiment

A quasi-cylindrically shaped natural copper assembly of 630 mm in diameter and 608 mm in thickness was the same as that in the previous experiment, which was covered with Li_2O blocks to reduce background neutrons scattered in the experiment room. The atomic densities of the copper and Li_2O blocks were 8.46×10^{22} atoms/cm^3 and 8.65×10^{22} atoms/cm^3, respectively.

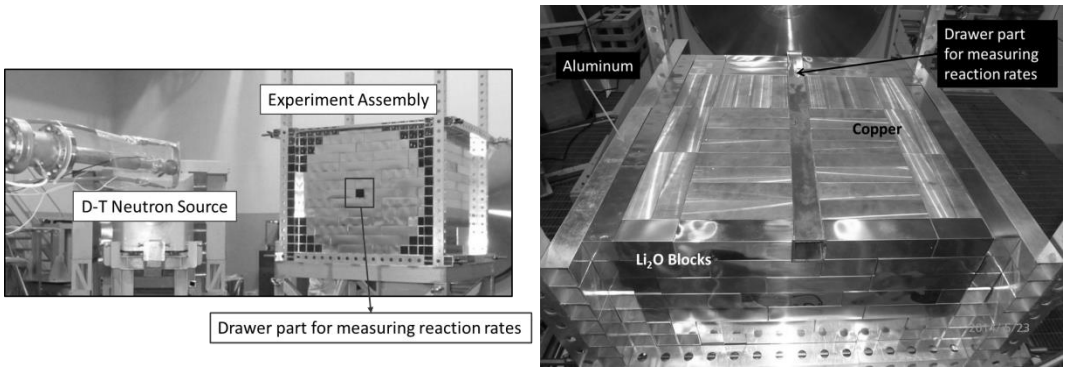

Figure 3. Photograph of experiment assembly, (a) whole view and (b) cross sectional view.

Figure 3 shows (a) the whole experiment assembly and (b) the transverse sectional view of the assembly configuration. The experiment assembly was set at the distance of 149 mm from the D-T neutron source. The reaction rates of the $^{93}Nb(n, 2n)^{92m}Nb$, $^{27}Al(n, \alpha)^{24}Na$, $^{115}In(n, n')^{115m}In$, $^{197}Au(n, \gamma)^{198}Au$ and $^{186}W(n, \gamma)^{187}W$ reactions were measured every 5 cm inside the center region in Fig. 4 by using the activation foils in Table 1. The average D-T neutron yield was 1.32×10^{11} n/s and the irradiation time for the activation foils was 6 hours.

Table 1. Activation foils

Element (Symbol)	Configuration, Size	Thickness (mm)
Niobium (Nb)	Disc, 10 mm in diameter	1.00
Aluminum (Al)	Disc, 10 mm in diameter	1.00
Indium (In)	Square, 10 mm ×10 mm	1.00
Gold (Au)	Square, 10 mm ×10 mm	0.05
Tungsten (W)	Square, 10 mm ×10 mm	0.10

In addition, we measured the fission rates of ^{235}U and ^{238}U with ^{235}U and ^{238}U micro fission chambers (MFCs) of 6.25 mm in outer diameter and 25.4 mm in active length. The measured fission rates of ^{235}U and ^{238}U were corrected with appropriate contents of uranium in each micro fission chamber (7% ^{238}U in the ^{235}U MFC, 0.044% ^{235}U in the ^{238}U MFC).

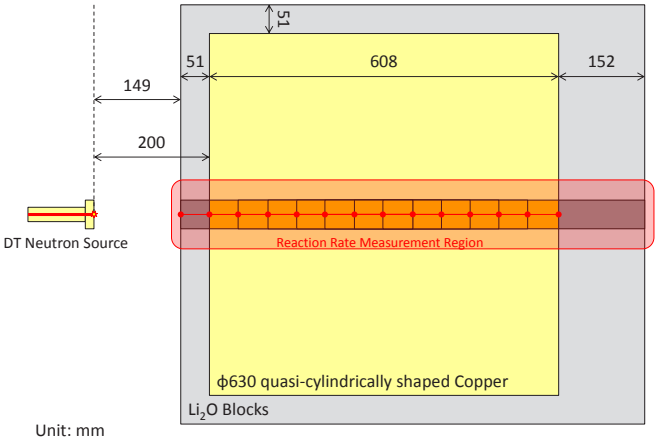

Figure 4. Schematic cross sectional view of the experiment assembly.

4. Analysis

We used the Monte Carlo neutron transport code, MCNP5-1.40 and the recent nuclear data libraries, ENDF/B-VII.1 [4] (ENDF/B-VII.0, FENDL-3.0 [5]), JEFF-3.2 [6] and JENDL-4.0 for the experiment analysis. JENDL Dosimetry File 99 (JENDL/D-99) [7] was used as dosimetry cross section data. We modeled only the copper assembly with the Li_2O blocks. The track length tally (F4) function was used to calculate reaction rates of activation foil and MFC cells. The actual sizes, thicknesses and materials of the activation foils as shown in Table 1 were applied to the cells for F4 in order to consider the self-shielding effect.

5. Results and Discussion

Figure 5 shows the ratios of calculated values to experimental reaction rate data (C/E) in this study with those with JENDL-4.0 in the previous study. The calculated reaction rates of the $^{93}Nb(n,2n)^{92m}Nb$ reaction sensitive to neutrons above 10 MeV with all the nuclear data libraries show a comparatively reasonable agreement with the measured one. The calculated reaction rates of the $^{197}Au(n,\gamma)^{198}Au$ and $^{186}W(n,\gamma)^{187}W$ reactions sensitive to lower energy neutrons with all the nuclear data libraries still underestimate the measured data, although the underestimation is improved compared to the previous experiment result.

Figure 6 shows the C/Es of the fission rates. The calculated fission rates of ^{235}U with all the nuclear data libraries underestimate the measured one depending on the depth of the

copper assembly, which is almost the same tendency as the results of the reaction rates of the $^{197}Au(n,\gamma)^{198}Au$ and $^{186}W(n,\gamma)^{187}W$ reactions. The C/Es of ^{238}U are slightly over 1.0 at the front of the copper assembly, but they become smaller than 1.0 at the deeper positions of the assembly.

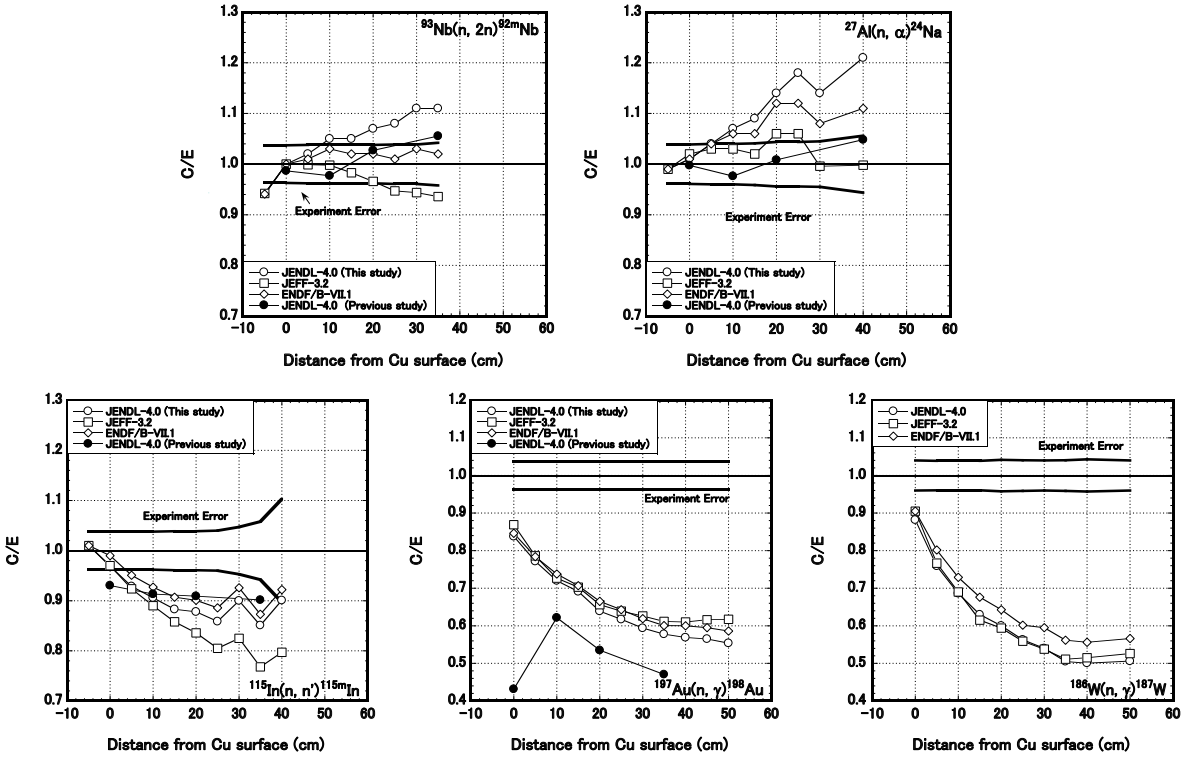

Figure 5. C/Es of reaction rates.

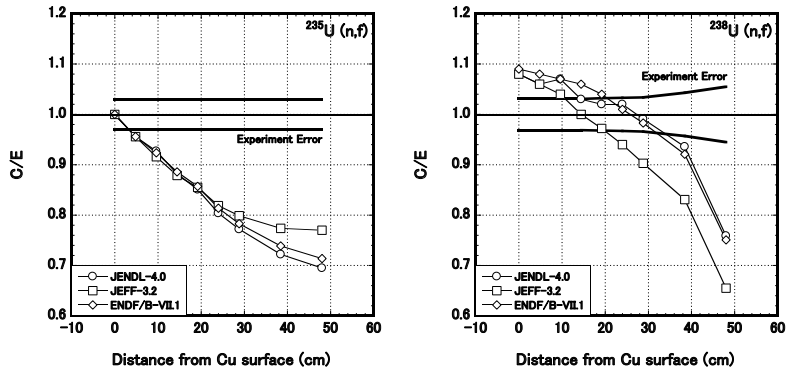

Figure 6. C/Es of fission rates.

We reduced background neutrons in the present study, but the underestimation tendency for the reaction rates sensitive to lower energy neutrons still appeared, which indicates that the underestimation comes from nuclear data libraries. We will study this issue in detail by modifying nuclear data libraries.

6. Conclusion

We carried out a supplemental integral experiment on copper with D-T neutron source at JAEA/FNS since agreement between the measured and calculated data had not be good in the 1990's benchmark experiment on copper. The copper assembly was covered with Li_2O blocks to reduce neutrons scattered in the concrete wall of the experiment room. The C/E results were improved compared to the previous experiment results, for the reaction rate of the $^{197}Au(n,\gamma)^{198}Au$ reaction in particular. However, the underestimation tendency for the reaction rates sensitive to lower energy neutrons was not solved in this experiment. It is considered that the nuclear data on copper have some problems. We will investigate the copper data in nuclear data libraries in detail to solve this underestimation problem.

Acknowledgements

We are grateful to the following FNS accelerator group members for their proficient operation: Messrs. Y. Abe, S. Tanaka, S. Kakizaki, Y. Oginuma and S. Urai.

References

[1] F. Maekawa, et al., "Benchmark Experiment on a Copper Slab Assembly Bombarded by D-T Neutrons," JAERI-M 94-038 (1994) , 77p.

[2] X-5 Monte Carlo Team, "MCNP – A General Monte Carlo N-Particle Transport Code, Version 5," LA-UR-03-1987 (2003).

[3] K. Shibata, et al., "JENDL-4.0: A New Library for Nuclear Science and Engineering," J. Nucl. Sci. Technol., 48(1), 1 (2011).

[4] M. B. Chadwick, et al., "ENDF/B-VII. 1 nuclear data for science and technology: cross sections, covariances, fission product yields and decay data," Nuclear Data Sheets, 112, 2887 (2011).

[5] R.A. Forrest, et al., "FENDL 3 Library-Summary Documentation," INDC (NDS)-628 (2012).

[6] O. Cabellos, "Processing of the new JEFF-3.2T4 Cross Section Library with the NJOY Code System into Various Formats for Testing Purposes," NEA Report (2014).

[7] K. Kobayashi, et al., "JENDL Dosimetry File 99 (JENDL/D-99)," JAERI 1344 (2002), 133p.

32 Integral Test of JENDL Dosimetry File 99 with a Graphite Experiment at JAEA/FNS

Masayuki OHTA*, Saerom KWON, Kentaro OCHIAI, Satoshi SATO, Chikara KONNO
Japan Atomic Energy Agency, Tokai-mura, Naka-gun, Ibaraki-ken, Japan
*e-mail: ohta.masayuki@jaea.go.jp

We use an integral experiment with a graphite pseudo-cylindrical assembly and a DT neutron source at JAEA/FNS in order to validate JENDL Dosimetry File 99 (JENDL/D-99). The size of the graphite assembly used in the experiment is 31.4 cm in equivalent radius and 61.0 cm in thickness. The assembly is placed at a distance of 20.3 cm from the DT neutron source. Reaction rates for dosimetry reactions in JENDL/D-99 are measured at the depth positions of 9.6 and 29.3 cm along the central axis of the assembly. This experiment is analyzed by using the Monte Carlo neutron transport code MCNP5-1.40 with the nuclear data library ENDF/B-VII.1. The reaction rates calculated with JENDL/D-99 are generally in agreement with the experimental ones as well as International Reactor Dosimetry and Fusion File release 1.0 (IRDFF 1.0) except for the reaction rates for the ^{60}Ni(n,p)^{60}Co and ^{63}Cu(n,α)^{60}Co reactions. The cross section data of the ^{60}Ni(n,p)^{60}Co and ^{63}Cu(n,α)^{60}Co reactions in JENDL/D-99 should be revised.

1. Introduction

JENDL Dosimetry File 99 (JENDL/D-99)[1] is used as the standard dosimetry file in Japan. It has not been updated for a long term since it was released in 1999. Recently, the International Atomic Energy Agency (IAEA) released a new dosimetry cross section library, International Reactor Dosimetry and Fusion File release 1.0 (IRDFF 1.0)[2], in order to meet the demand for fusion applications in addition to reactor dosimetry. Although the main feature of IRDFF 1.0 was an extension of the energy limit of the cross section data to at least 60 MeV from 20 MeV in the former International Reactor Dosimetry File 2002 (IRDF-2002)[3], about a half of the reaction data in IRDFF 1.0 were newly evaluated or revised from IRDF-2002 for cross section data below 20 MeV. IAEA initiated a new Co-ordinated Research Project (CRP) in order to validate and test IRDFF 1.0. We performed an integral experiment with a graphite pseudo-cylindrical assembly and the DT neutron source at JAEA/FNS under the CRP[4]. We use the experimental data for the validation of JENDL/D-99 in this study. We clarify the problems of JENDL/D-99 by comparison with the results with IRDFF-v1.03.

2. Experiment Overview

We adopt the graphite assembly used in the previous experiment[5] because it is confirmed that neutron fluxes from DT neutrons to thermal neutrons inside the assembly are specified well. The size of the graphite assembly used in the experiment is 31.4 cm in equivalent radius and 61.0 cm in thickness as shown in Fig. 1. The assembly is supported with thin aluminum frames. A lot of foils for the reaction rate measurement of the dosimetry reactions are inserted into small spaces between the graphite blocks at two depth positions of 9.6 and 29.3 cm along the center axis of the assembly. Niobium, indium and gold foils are placed at four depth positions of 9.6, 19.3, 29.3 and 39.5 cm in order to confirm the reproducibility of the neutron flux inside the assembly. The assembly is placed at a distance of 20.3 cm from the DT neutron source and is irradiated for 5 hours at the DT neutron intensity of 1.74×10^{11} sec^{-1}. After the DT neutron irradiation, reaction rates for the dosimetry reactions are deduced by measuring the decay gamma-rays with high purity germanium (HPGe) detectors.

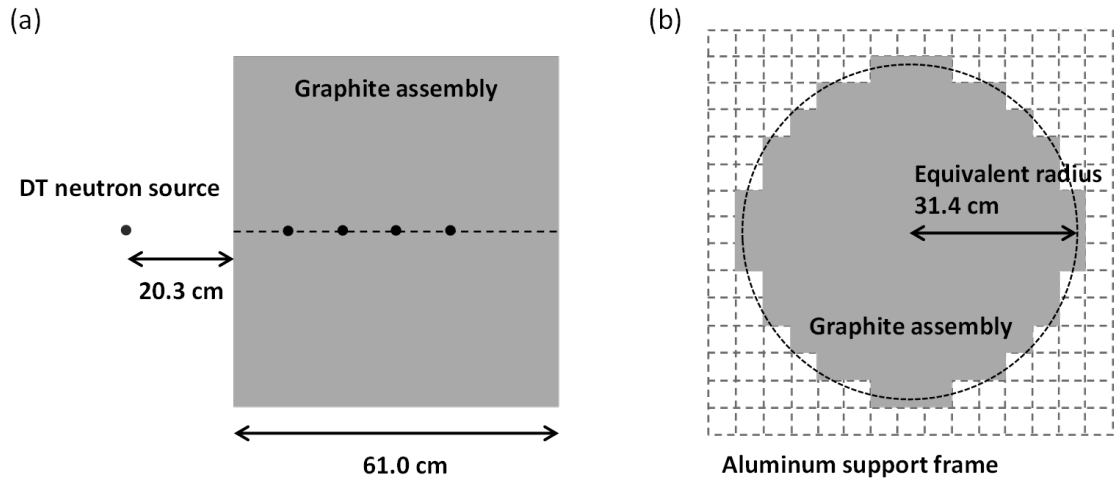

Fig. 1 Experimental configuration: (a) layout and (b) cross-sectional view.

3. Analysis

This experiment is analyzed by using the Monte Carlo transport code MCNP5-1.40[6] with the nuclear data library ENDF/B-VII.1[7] including the thermal neutron scattering law data S(α,β). The experimental configuration is modeled in the analysis. The dosimetry reaction rates are calculated by using the cell flux (F4) tally for capture reactions with thick foils and the surface flux (F2) tally for the others, where JENDL/D-99 is adopted as the response functions for the dosimetry reactions. The reaction rates are also calculated with IRDFF-v1.03 for comparison.

4. Results and Discussion

Figure 2 shows the ratios of calculated reaction rates to experimental ones (C/Es) for the ^{93}Nb(n,2n)^{92m}Nb, ^{115}In(n,n′)^{115m}In and ^{197}Au(n,γ)^{198}Au reactions, which are dosimetry reactions used as the standard. The C/E results for these dosimetry reactions are from 0.9 to 1.1. It means that the calculation can represent neutron spectra at the measurement points inside the graphite assembly well. The calculated neutron spectra are shown in Fig. 3. The spectrum at 9.6 cm has more higher energy neutron component than that at 29.3 cm. Both spectra have low energy neutrons moderated in the graphite sufficiently to test the cross section data of the (n,γ) dosimetry reactions.

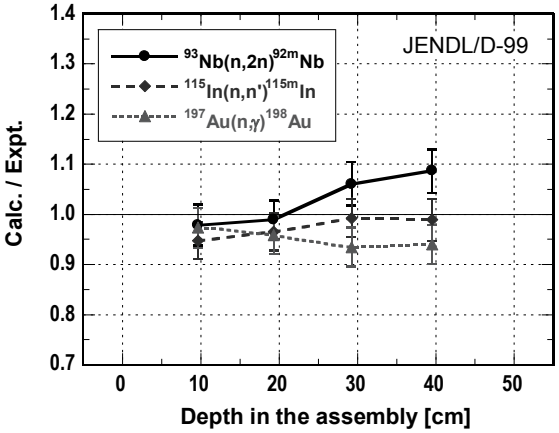

Fig. 2 C/Es of reaction rates for ^{93}Nb(n,2n)^{92m}Nb, ^{115}In(n,n′)^{115m}In and ^{197}Au(n,γ)^{198}Au reactions.

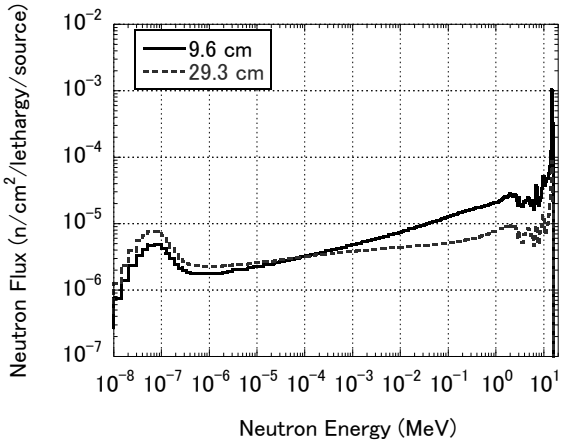

Fig. 3 Calculated neutron spectra inside the graphite assembly.

Figure 4 shows the C/E results for the dosimetry reactions in JENDL/D-99. Thirty-five reactions out of sixty-seven ones in JENDL/D-99 are investigated in this experiment. The upper results in the column shown by closed circles are for the depth position of 9.6 cm and the lower ones shown by closed triangles are for 29.3 cm. The ^{46}Ti(n,p)^{46}Sc and ^{47}Ti(n,x)^{46}Sc reactions produce the same radioactive nucleus. The contributions from these reactions cannot be distinguished in the foil activation method. That goes for the ^{47}Ti(n,p)^{47}Sc and ^{48}Ti(n,x)^{47}Sc, ^{48}Ti(n,p)^{48}Sc and ^{49}Ti(n,x)^{48}Sc, and ^{63}Cu(n,γ)^{64}Cu and ^{65}Cu(n,2n)^{64}Cu reactions. The reaction cross section data for natural titanium are also included in JENDL/D-99: ^{nat}Ti(n,x)^{46}Sc, ^{nat}Ti(n,x)^{47}Sc and ^{nat}Ti(n,x)^{48}Sc. The C/E results calculated with these data give the same as those with the sum of ^{46}Ti(n,p)^{46}Sc and ^{47}Ti(n,x)^{46}Sc, that of ^{47}Ti(n,p)^{47}Sc and ^{48}Ti(n,x)^{47}Sc, and that of ^{48}Ti(n,p)^{48}Sc and ^{49}Ti(n,x)^{48}Sc, respectively. The C/E results of these reactions for natural titanium are omitted in Fig. 4.

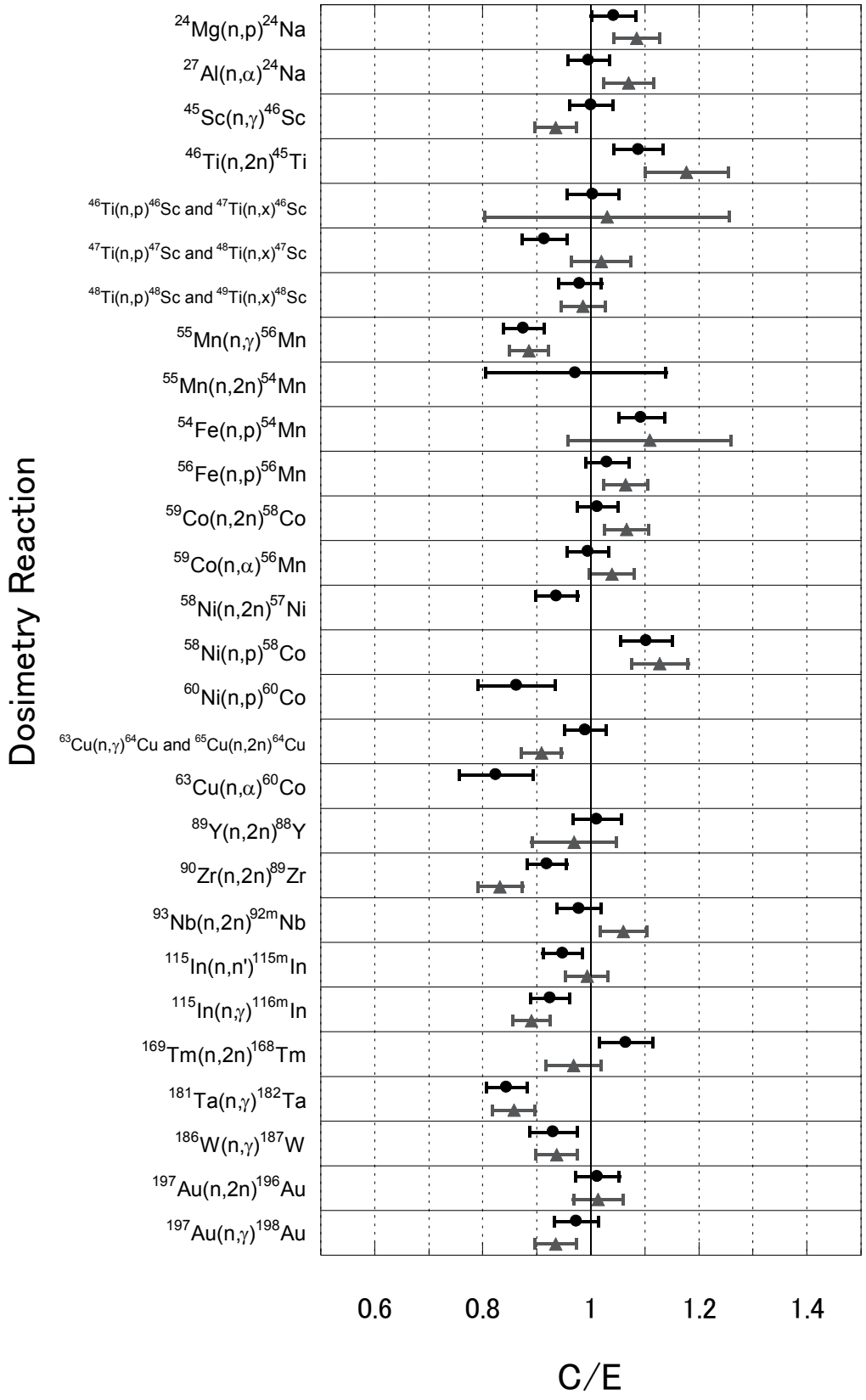

Fig. 4 C/E of dosimetry reaction rates with JENDL/D-99 (Closed circles are for depth position of 9.6 cm and closed triangles are for that of 29.3 cm).

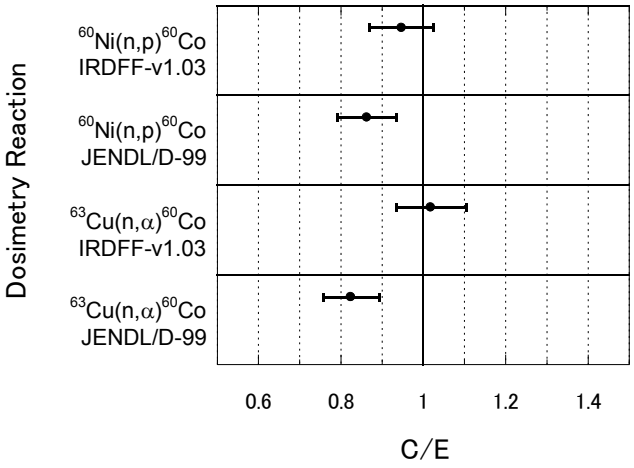

Fig. 5 Comparison between C/Es with JENDL/D-99 and IRDFF-v1.03 for ^{60}Ni(n,p)^{60}Co and ^{63}Cu(n,α)^{60}Co reactions.

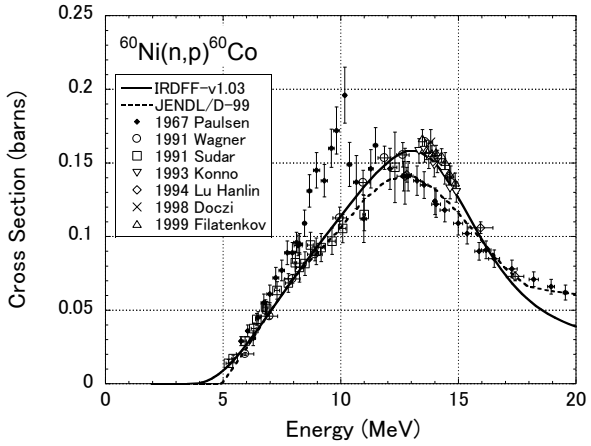

Fig. 6 Comparison for ^{60}Ni(n,p)^{60}Co reaction cross section data.

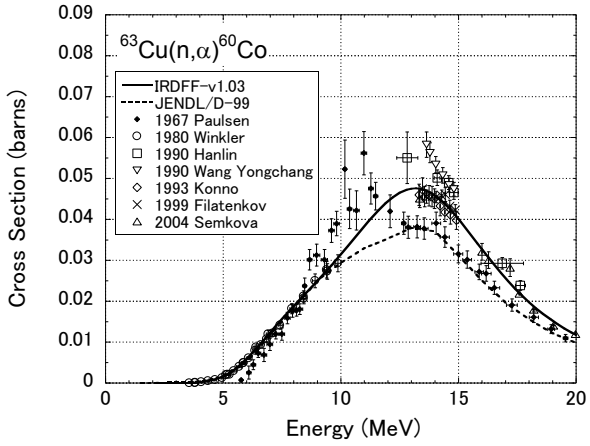

Fig. 7 Comparison for ^{63}Cu(n,α)^{60}Co reaction cross section data.

The reaction rates calculated with JENDL/D-99 generally show agreements with the experimental ones as well as IRDFF-v1.03. The C/E results are from 0.9 to 1.0 for most dosimetry reactions and from 0.8 to 1.2 for the others. The results for IRDFF-v1.03 were reported in the other paper in detail[4]. There are discrepancies between the C/E results with JENDL/D-99 and IRDFF-v1.03 for the ^{60}Ni(n,p)^{60}Co and ^{63}Cu(n,α)^{60}Co reactions as shown in Fig. 5, although the C/E results with JENDL/D-99 for these reactions are not so bad.

Figures 6 and 7 show comparisons for the evaluated ^{60}Ni(n,p)^{60}Co and ^{63}Cu(n,α)^{60}Co reaction cross section data with measured ones[8], respectively. The cross section data for these reactions in JENDL/D-99 would be evaluated based on the older measured cross section data. These cross section data in JENDL/D-99 seem to be slightly small judging from not only the measured data but also the C/E results in Fig. 5. The cross section data of the

^{60}Ni(n,p)^{60}Co and ^{63}Cu(n,α)^{60}Co reactions in JENDL/D-99 should be revised.

5. Conclusion

An integral test with a graphite pseudo-cylindrical assembly and the DT neutron source at JAEA/FNS was used in order to validate JENDL/D-99. Thirty-five dosimetry reactions out of sixty-seven ones in JENDL/D-99 were verified with the measured reaction data. This experiment was analyzed by using MCNP5-1.40 and ENDF/B-VII.1. The reaction rates were calculated with JENDL/D-99 as the response functions for the dosimetry reaction. For comparison, the reaction rates were also calculated with IRDFF-v1.03. Most of the C/E results with JENDL/D-99 were from 0.9 to 1.1 and the others were from 0.8-1.2. Although these results generally showed good agreements with the measured ones, there were discrepancies between the C/Es calculated with JENDL/D-99 and with IRDFF-v1.03 for the ^{60}Ni(n,p)^{60}Co and ^{63}Cu(n,α)^{60}Co reactions. The results in this experiment and the recent measured cross section data supported IRDFF-v1.03 rather than JENDL/D-99. The cross section data of the ^{60}Ni(n,p)^{60}Co and ^{63}Cu(n,α)^{60}Co reactions in JENDL/D-99 should be revised.

References

[1] K. Kobayashi, T. Iguchi, S. Iwasaki, T. Aoyama, S. Shimakawa, et al.: "JENDL Dosimetry File 99 (JENDL/D-99)," JAERI 1344 (2002), 133p.

[2] E.M. Zsolnay, R. Capote, H.K. Nolthenius and A. Trkov: "Summary Description of the New International Reactor Dosimetry and Fusion File (IRDFF release 1.0)," INDC(NDS)-0616, IAEA (2012).

[3] O. Bersillon, L.R. Greenwood, P.J. Griffin, W. Mannhart, H.T. Nolthenius, et al.: International Reactor Dosimetry File 2002 (IRDF-2002), IAEA Technical Reports Series No. 452 (2006).

[4] M. Ohta, S. Sato, K. Ochiai and C. Konno: "Integral Test of International Reactor Dosimetry and Fusion File on Graphite Assembly with DT Neutron at JAEA/FNS," Fus. Eng. Design (Proc. the 28th Symposium on Fusion Technology) , 98, pp.1847-1850(2015).

[5] H. Maekawa, Y. Ikeda, Y. Oyama, S, Yamaguchi, K. Tsuda, et al.: "Benchmark Experiments on a 60 cm-Thick Graphite Cylindrical Assembly," JAERI-M 88-034 (1988), 65p.

[6] X-5 Monte Carlo Team: "MCNP-A General Monte Carlo N-Particle Transport Code, Version 5 - Volume I: Overview and Theory," LA-UR-03-1987 (2003).

[7] M.B. Chadwick, M. Herman, P. Obložinský, M.E. Dunn, Y. Danon, et al.: "ENDF/B-VII.1 Nuclear Data for Science and Technology: Cross Sections, Covariances, Fission Product Yields and Decay Data," Nucl. Data Sheets, 112, 2887 (2011).

[8] Available from IAEA (https://www-nds.iaea.org/exfor/exfor.htm).

33 Integral Experiment on Molybdenum with DT Neutrons at JAEA/FNS

Masayuki Ohta*, Saerom Kwon, Kentaro Ochiai, Satoshi Sato, Chikara Konno
Japan Atomic Energy Agency, Tokai-mura, Naka-gun, Ibaraki-ken, Japan
*e-mail: ohta.masayuki@jaea.go.jp

We perform an integral experiment with a molybdenum assembly and a DT neutron source at JAEA/FNS to validate the recent nuclear data of Mo. A rectangular Mo assembly, the size of which is 253 mm × 253 mm × 354 mm, is placed at a distance of 201 mm from the DT neutron source and is covered with 51, 202 and 253 mm thick Li_2O blocks around the front, side and back surfaces in order to eliminate background neutrons at the measuring points in the Mo assembly, respectively. Several dosimetry reaction rates and fission rates measured in the assembly are compared to those calculated with the Monte Carlo neutron transport code MCNP5-1.40 and the recent nuclear data libraries of ENDF/B-VII.1, JEFF-3.2 and JENDL-4.0 (FENDL-3.0). The ratios of the calculated reaction rates to the experimental ones generally decrease with the increasing distance from the front surface of the assembly. We will investigate reasons of the underestimation as a future task.

1. Introduction

Type 316 stainless steel (SS316) is a main shielding material in ITER. The SS316 is composed of type 304 stainless steel (SS304) adding a few percent of molybdenum in order to improve corrosion resistance. It has been pointed out that the nuclear data of Mo may have some problems for low energy neutrons and the effect of Mo may not be so small in a benchmark experiment on the SS316 [1]. Accurate nuclear data of Mo are needed in nuclear design and analysis of ITER as one of the composition elements of SS316. Integral experiments are required in order to validate the nuclear data, but few experiments for benchmarking nuclear data on Mo have been carried out so far. In this study, we perform an integral experiment with a Mo assembly and the DT neutron source at JAEA/FNS to validate the recent nuclear data of Mo.

2. Experiment

Figure 1 shows the experimental configuration for the reaction rate measurement. A

rectangular Mo assembly, the size of which is 253 × 253 × 354 mm^3, is built with Mo blocks of 10.2 g/cm^3 in density. Molybdenum has seven stable isotopes: ^{92}Mo (14.53 %), ^{94}Mo (9.15 %), ^{95}Mo (15.84 %), ^{96}Mo (16.67 %), ^{97}Mo (9.60 %), ^{98}Mo (24.39 %) and ^{100}Mo (9.82 %). The assembly is placed at a distance of 201 mm from the DT neutron source and is covered with 51, 202 and 253 mm thick Li_2O blocks around the front, side and back surfaces in order to reduce background neutrons at the measuring points in the Mo assembly, respectively. The advantage of Li_2O has been shown in the titanium benchmark experiment [2]. Foils of niobium, aluminum, indium, gold, tungsten and molybdenum are inserted into small spaces between the Mo blocks along the central axis of the assembly for the dosimetry reaction rate measurement. After the DT neutron irradiation for 6 hours at the intensity of 1.27 × 10^{11} sec^{-1}, the dosimetry reaction rates of the ^{93}Nb(n,2n)^{92m}Nb, ^{27}Al(n,α)^{24}Na, ^{115}In(n,n′)^{115m}In, ^{197}Au(n,γ)^{198}Au, ^{186}W(n,γ)^{187}W, ^{92}Mo(n,p)^{92m}Nb reactions and sum of the ^{98}Mo(n,γ)^{99}Mo and ^{100}Mo(n,2n)^{99}Mo reactions are deduced by measuring the decay gammas from the foils with high purity germanium (HPGe) detectors. The fission rates of ^{235}U and ^{238}U are also measured by using ^{235}U and ^{238}U micro fission chambers (MFCs) of 6.25 mm in outer diameter and 25.4 mm in active length inside the assembly with almost the same experimental configuration as the foil experiment except for blocks with a hole of 21 mm in diameter for installing the MFCs. The MFCs are inserted from the back of the assembly through the hole. The blocks ahead of the measuring point are replaced with the usual blocks without a hole.

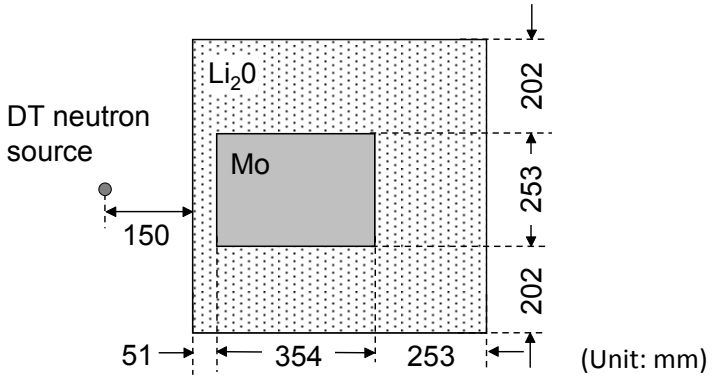

Fig 1. Experimental configuration for the reaction rate measurement.

3. Analysis

The experiment is modeled precisely and the dosimetry reaction rates are calculated by using the cell flux (F4) tally in the Monte Carlo neutron transport code MCNP5-1.40 [3] and the recent nuclear data libraries of ENDF/B-VII.1 [4], JEFF-3.2 [5] and JENDL-4.0 [6]. The Mo data below 20 MeV in FENDL-3.0 [7] are the same as those in JENDL-4.0. The JENDL Dosimetry File 99 (JENDL/D-99) [8] is used as the response functions for the dosimetry reactions except for the ^{92}Mo(n,p)^{92m}Nb, ^{98}Mo(n,γ)^{99}Mo and ^{100}Mo(n,2n)^{99}Mo

reactions. The reaction rate of the ^{92}Mo(n,p)^{92m}Nb reaction is calculated with the International Reactor Dosimetry and Fusion File release 1.0 (IRDFF-v1.02) [9]. The summed reaction rate of the ^{98}Mo(n,γ)^{99}Mo and ^{100}Mo(n,2n)^{99}Mo reactions is calculated with the reaction cross section data in the general purpose files which are used in the neutron transport calculations. The calculated reaction rates are compared to the measured ones.

4. Results and Discussion

Figures 2–8 show the ratios of the calculated reaction rates to the experimental ones (C/Es) for the ^{93}Nb(n,2n)^{92m}Nb, ^{27}Al(n,α)^{24}Na, ^{115}In(n,n′)^{115m}In, ^{197}Au(n,γ)^{198}Au, ^{186}W(n,γ)^{187}W, ^{92}Mo(n,p)^{92m}Nb reactions and sum of the ^{98}Mo(n,γ)^{99}Mo and ^{100}Mo(n,2n)^{99}Mo reactions, respectively. The ^{93}Nb(n,2n)^{92m}Nb, ^{100}Mo(n,2n)^{99}Mo, ^{27}Al(n,α)^{24}Na and ^{115}In(n,n′)^{115m}In reactions are sensitive to neutrons above 8.9 MeV, 8.4 MeV, 3.2 MeV and 0.34 MeV, respectively. The ^{92}Mo(n,p)^{92m}Nb reaction is mainly sensitive to neutrons in MeV energy region. The ^{197}Au(n,γ)^{198}Au, ^{186}W(n,γ)^{187}W and ^{98}Mo(n,γ)^{99}Mo reactions are sensitive to lower energy neutrons. The zero point in the horizontal axis shows the boundary between Li_2O and Mo at the front region. Figures 9 and 10 show the C/Es of the fission rates of ^{235}U and ^{238}U.

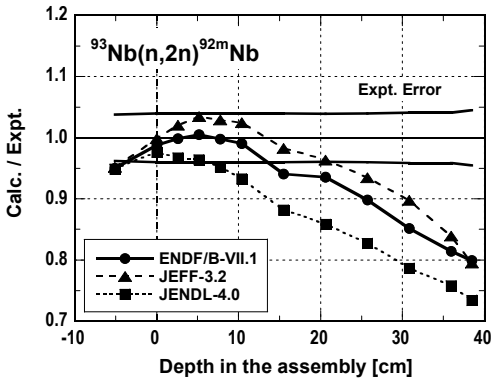

Fig. 2 C/E of reaction rate for ^{93}Nb(n,2n)^{92m}Nb.

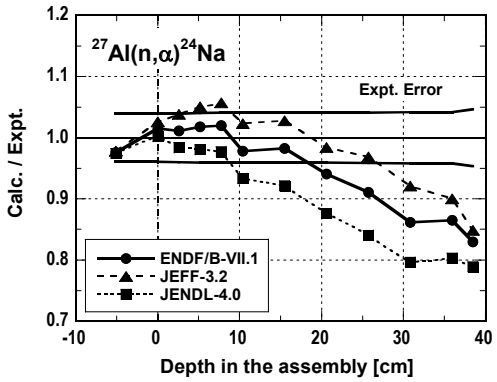

Fig. 3 C/E of reaction rate for ^{27}Al(n,α)^{24}Na.

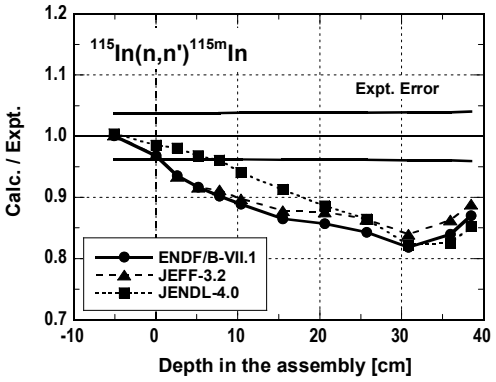

Fig. 4 C/E of reaction rate for ^{115}In(n,n′)^{115m}In.

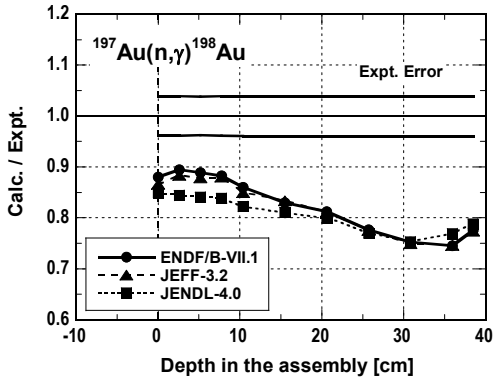

Fig. 5 C/E of reaction rate for ^{197}Au(n,γ)^{198}Au.

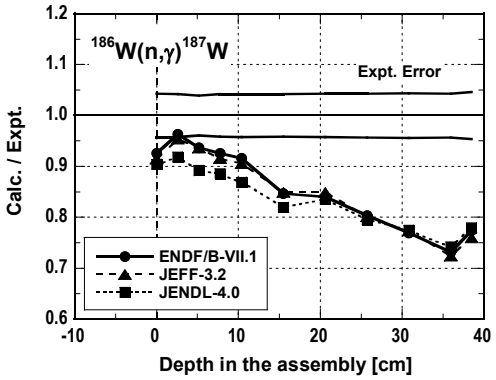

Fig. 6 C/E of reaction rate for ^{186}W(n,γ)^{187}W.

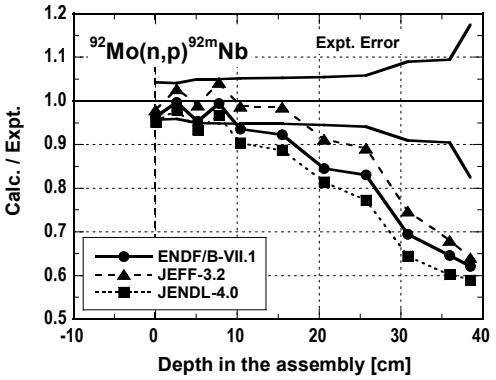

Fig. 7 C/E of reaction rate for ^{92}Mo(n,p)^{92m}Nb.

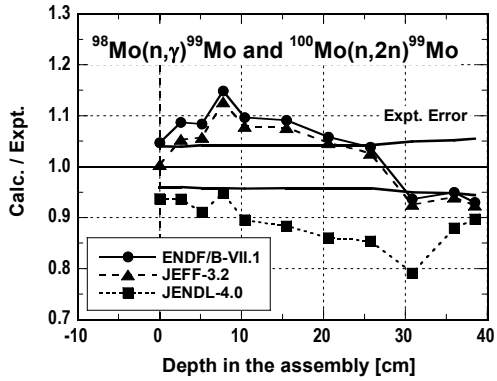

Fig. 8 C/E of reaction rate for sum of ^{98}Mo(n,γ)^{99}Mo and ^{100}Mo(n,2n)^{99}Mo.

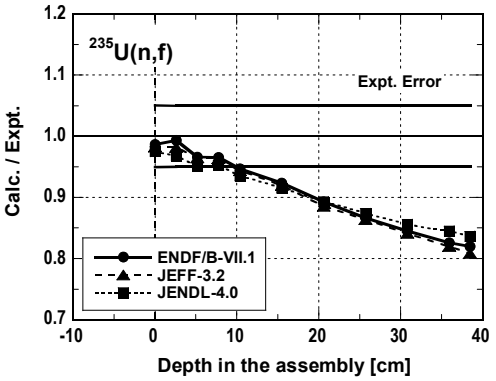

Fig. 9 C/E of fission rate for ^{235}U.

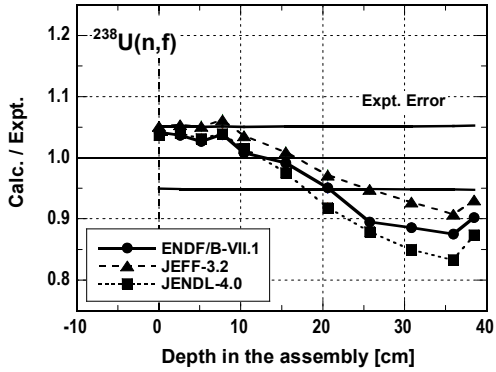

Fig. 10 C/E of fission rate for ^{238}U.

The C/Es generally decrease with the increasing distance from the front surface of the assembly, although the degree of the decrease is different depending on the dosimetry reactions and nuclear data libraries. There are discrepancies among the C/Es with ENDF/B-VII.1, JEFF-3.2 and JENDL-4.0 for the dosimetry reactions which are sensitive to higher energy neutrons. Several reaction cross sections are shown in Figs. 11–14 as examples which are very different among the nuclear data libraries and may cause the

underestimations and discrepancies of C/Es: the (n,2n) reaction cross section of ^{95}Mo, inelastic scattering cross section of ^{100}Mo, elastic scattering cross section of ^{95}Mo and (n,γ) reaction cross section of ^{94}Mo, respectively. The differences of the (n,2n) reaction, elastic and inelastic scattering cross sections are considered to affect the C/Es of the reaction rates which are sensitive to higher energy neutrons, especially.

We will investigate which reaction cross section in the molybdenum isotopes causes the underestimation as a future task. A temporarily modified nuclear data file is produced by replacing specified reaction cross sections in an original nuclear data file with those in other nuclear data files. An ACE file of the modified nuclear data file is produced with the NJOY99 code [10]. The C/Es of the dosimetry reaction rates are calculated with the modified nuclear data file in order to check the degree of improvement of the C/Es. Through this analysis, we will clarify problems of the nuclear data of molybdenum in detail.

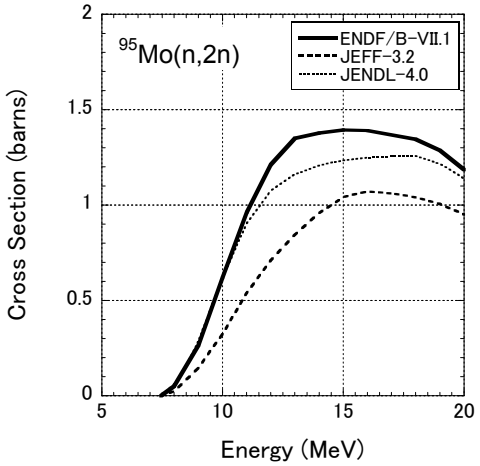

Fig. 11 (n,2n) cross section of ^{95}Mo.

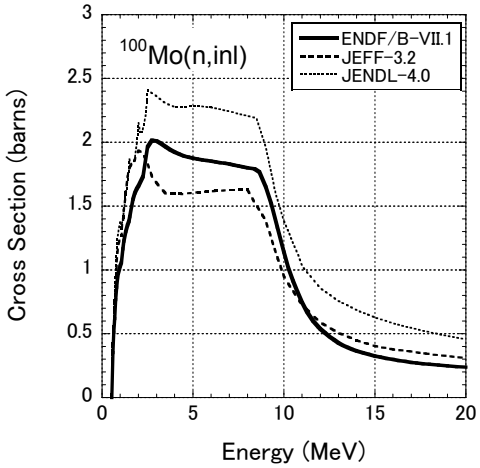

Fig. 12 Inelastic scattering cross section of ^{100}Mo.

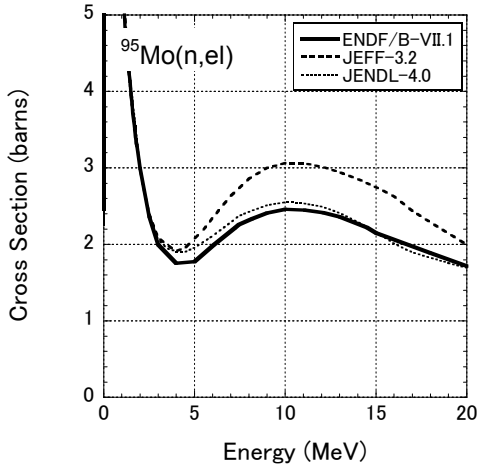

Fig. 13 Elastic scattering cross section of ^{95}Mo.

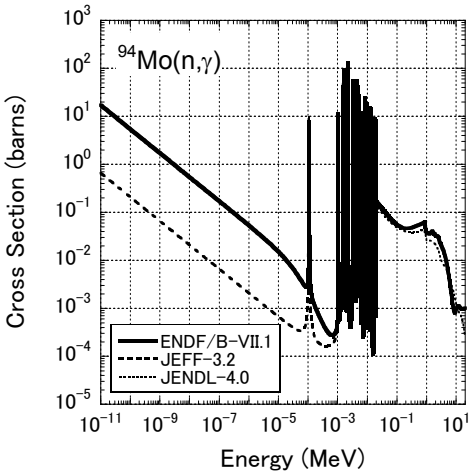

Fig. 14 (n,γ) cross section of ^{94}Mo.

5. Conclusion

An integral experiment on molybdenum is performed with the DT neutron source at JAEA/FNS. The Mo assembly is covered with the Li_2O blocks in order to reduce background neutrons. The dosimetry reaction rates of the $^{93}Nb(n,2n)^{92m}Nb$, $^{27}Al(n,\alpha)^{24}Na$, $^{115}In(n,n')^{115m}In$, $^{197}Au(n,\gamma)^{198}Au$, $^{186}W(n,\gamma)^{187}W$, $^{92}Mo(n,p)^{92m}Nb$, $^{98}Mo(n,\gamma)^{99}Mo$ and $^{100}Mo(n,2n)^{99}Mo$ reactions are measured at several points inside the Mo assembly. The C/Es of the dosimetry reaction rates generally decrease with the increasing distance from the front surface of the assembly. We will investigate reasons of the underestimation as a future task.

References

[1] C. Konno, K. Ochiai, M. Wada and S. Sato, "Analysis of fusion integral benchmark experiments at JAEA/FNS with FENDL-2.1 and other recent nuclear data libraries," Fus. Eng. Design, 83, 1774 (2008).

[2] M. Ohta, K. Takakura, K. Ochiai, S. Sato and C. Konno, "Benchmark experiment on titanium with DT neutron at JAEA/FNS," Fus. Eng. Design, 89, 2164 (2014).

[3] X-5 Monte Carlo Team, "MCNP-A General Monte Carlo N-Particle Transport Code, Version 5 - Volume I: Overview and Theory," LA-UR-03-1987 (2003).

[4] M.B. Chadwick, M. Herman, P. Obložinský, M.E. Dunn, Y. Danon, et al., "ENDF/B-VII.1 Nuclear Data for Science and Technology: Cross Sections, Covariances, Fission Product Yields and Decay Data," Nucl. Data Sheets, 112, 2887 (2011).

[5] O. Cabellos, "Processing of the new JEFF-3.2T4 Cross Section Library with the NJOY Code System into Various Formats for Testing Purposes," JEF/DOC-1562 (2014).

[6] K. Shibata, O. Iwamoto, T. Nakagawa, N. Iwamoto, A. Ichihara, et al., "JENDL-4.0: A New Library for Nuclear Science and Engineering," J. Nucl. Sci. Technol., 48, 1 (2011).

[7] R.A. Forrest, R. Capote, N. Otsuka, T. Kawano, A.J. Koning, et al., "FENDL-3 Library – Summary documentation," INDC(NDS)-0628 (2012).

[8] K. Kobayashi, T. Iguchi, S. Iwasaki, T. Aoyama, S. Shimakawa, et al., "JENDL Dosimetry File 99 (JENDL/D-99)," JAERI 1344 (2002), 133p.

[9] E.M. Zsolnay, R. Capote, H.K. Nolthenius and A. Trkov, "Summary Description of the New International Reactor Dosimetry and Fusion File (IRDFF release 1.0)," INDC(NDS)-0616, IAEA (2012).

[10] R.E. MacFarlane and D.W. Muir, "The NJOY Nuclear Data Processing System Version 91," LA-12740-M (1994).

34 Nuclear data evaluation of the ^{7}Li(p,xn) reaction for incident energies up to 200MeV

Yuiki Matsumoto[1], Yukinobu Watanabe[1]*, Satoshi Kunieda[2], Osamu Iwamoto[2]

[1]Department of Advanced Energy Engineering Science, Kyushu University, Japan
[2]Nuclear Science and Engineering Center, Japan Atomic Energy Agency, Japan
*watanabe@aees.kyushu-u.ac.jp

Double-differential neutron production cross sections (DDXs) for proton-induced reactions on ^{7}Li are evaluated for incident energies from 7 to 200 MeV on the basis of experimental data and theoretical model calculation. The differential cross sections corresponding to the ground and first excited states of ^{7}Be are derived by interpolation based on the Legendre fitting of existing experimental data up to 45 MeV and DWBA calculations for incident energies above 45 MeV. Preequilibrium and evaporation components are calculated using the statistical model code CCONE. The evaluated DDXs are used to calculation of double differential neutron production yields, and satisfactory agreement with the measured data is obtained.

1. Introduction

In recent years, nuclear data of the ^{7}Li(p,n)^{7}Be reaction are required in the design of accelerator-based neutron sources for various applications such as boron neutron capture therapy (BNCT) and calibration of neutron detectors. However, available evaluated nuclear data are very limited. There is no evaluated cross section data for ^{7}Li in JENDL High Energy File (JENDL/HE-2007) [1], and FENDL-3 (Fusion Evaluated Nuclear Data Library) [2] includes the cross section data only in the low incident energy region below 10 MeV. Previously, Mashinik et al. developed a ^{7}Li(p,n) nuclear data library up to 150MeV for MCNPX [3], and Liskin et al. reported their evaluated cross section data for energies up to 7 MeV [4]. On the other hand, many experimental data of differential cross sections for transition to the ground and the first states are available and there are several measurements of double differential neutron production cross sections (DDXs) at incident energies above 7 MeV.

In the present work, we evaluate the DDXs for incident energies from 7 to 200 MeV using experimental data and theoretical model calculations.

2. Method of cross section evaluation

Neutron emission from the ^{7}Li(p,xn) reaction can be divided into two components: a discrete component for the transition to the ground state ($3/2^{-}$) and the first excited state ($1/2^{-}$, 0.478 MeV) and a continuum component formed by ^{7}Li breakup processes. For the former, we have obtained the differential cross sections by interpolation based on Legendre fitting of available experimental data up to 45 MeV and calculations with DWBA above 45 MeV. Next, we have applied the statistical model code CCONE [5] to

DDX calculations of the continuum component, and adjusted pre-equilibrium model parameters to reproduce experimental data well. Finally, both the results are merged and then the evaluated DDX data are completed. The detail of each evaluation method is described below.

2.1 Legendre fitting of experimental differential cross section

We have performed the Legendre fitting to angular distributions of all available experimental data from 7 up to 45 MeV. Some examples of the fitting for the transition to the ground state are shown in Fig.1. Differential cross sections in the incident energy range where there is no experimental data were estimated using interpolation and extrapolation of the Legendre polynomial coefficients derived by the fitting.

2.2 DWBA calculation

The DWBA calculation was applied to evaluation of differential cross sections for the transition to both the ground and first excited states in the incident energy region higher than 45MeV, because of insufficient experimental data. The DWBA calculation was done using the DWUCK4 code [6] with the optical potential parameters of Ye et al. [7] We assumed that both the transitions to the ground and the first excited states correspond to the IAS and GT transitions with L=0 transfer, respectively, and are caused by charge-exchange process through a central two-body interaction. A microscopic effective interaction of a simple Yukawa type with 1.0fm range was used. In addition, we assumed that both initial and final states can be described as $0p_{3/2}$ single-particle states. The depth of the interaction potential was determined by fitting to available experimental data [9]. The incident energy dependence of the depth parameters was found to be weak.

The results for incident energies from 80 to 200 MeV are shown in Fig.2. The DWBA calculations are in fairly good agreement with experimental data [10] at forward angles.

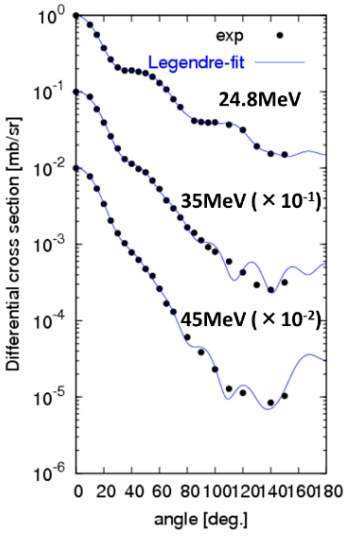

Fig. 1. Example of Legendre fitting of differential cross sections of the ^{7}Li(p,n)^{7}Be$_{g.s.}$

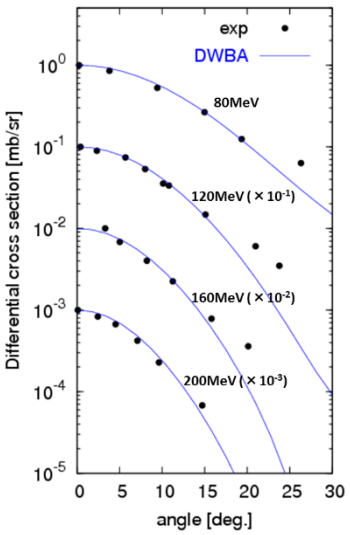

Fig. 2. Comparison of DWBA calculations with measured differential cross sections of the ^{7}Li(p,n)^{7}Be$_{g.s.+1st}$

2.3 Calculation of double-differential cross sections with CCONE

The CCONE code [5] was applied to DDX calculations of the continuum component. The total cross section of the ^{7}Li(p,n)^{7}Be$_{g.s+1st}$ reaction evaluated in the preceding subsection was subtracted from the total reaction cross section in the CCONE calculation. The preliminary CCONE calculation with default parameters was not able to reproduce experimental data satisfactorily. We have attempted to adjust input parameters and found that the parameters related to the preequilibrium exciton model are sensitive to the continuum part of DDX.

The sensitive parameters are included in an empirical expression of the transition matrix:

$$M^2 = \frac{M_0}{A^3}\left[6.8M_1 + \frac{4.2\times10^5 M_2}{\left(\frac{E}{n}+10.7M_3\right)^3}\right], \quad (1)$$

where A is the target mass number, E is the excitation energy of the composite system, and n is the exciton number, and M_i (i=0 to 3) are adjustable parameters. The parameters M_i were determined so that the calculated DDX reproduces experimental data over a wide range of incident energy. The optimum parameter sets were found to be M_0=8.0, M_1=M_2=0.01, and M_3=-0.3 .

Additionally, the potential V in the surface effect correction contains the sensitive parameters:

$$V = C_0 + C_1\frac{E_p^4}{E_p^4+\left(\frac{C_2}{A^{1/3}}\right)^4}, \quad (2)$$

where E_p is the incident energy and A is the target mass. The adjustable parameters in Eq. (2), C_0, C_1, and C_2, were chosen to be 3.0, 36.0, and 50.0, respectively.

Furthermore, the value of E_{t1} used in the formula of the Kalbach systematics [8] was changed to 100MeV from 130MeV so that experimental DDXs are reproduced well at high incident energies.

In Fig.3, the DDXs calculated with default and adjusted parameters are shown by the dashed and the solid lines, respectively. The calculation result with the adjusted parameters is in better agreement with experimental data than that with the default parameter, especially in the intermediate emission energy region between 20 to 70 MeV.

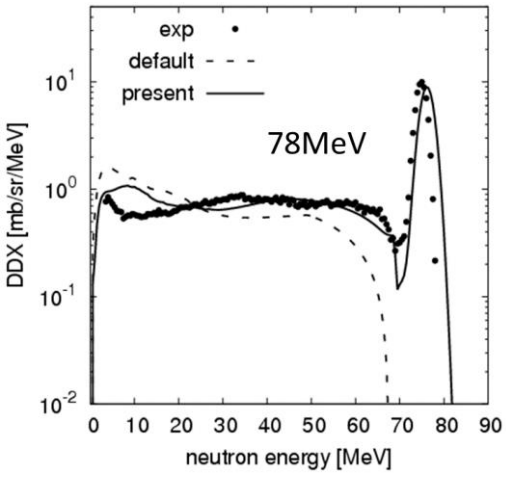

Fig.3. Comparison between experimental and calculated DDX at the incident energy 78 MeV and emission angle of 0 degree.

3. Calculation of neutron production yields from ^{7}Li(p,xn) reaction

There exist some measured neutron yields from thick Li target. The double-differential neutron production yield is estimated from the evaluated DDX data using the following expression:

$$\frac{d^2Y}{dE_n d\Omega_n} = N \int_{E_0-\Delta E}^{E_0} \left[\frac{d^2\sigma}{dE_n d\Omega_n}\right]_{(E_p,\theta_n)} \left[\frac{dE_p}{dx}\right]^{-1} \times \exp\left(-\int_{E_p}^{E_0} \Sigma_{non}(E') \left[\frac{dE'}{dx}\right]^{-1} dE'\right) dE_p , \quad (3)$$

where N is the atomic density in a Li target, E_0 is the incident proton energy, ΔE is the energy loss in the target, $d^2\sigma/dE_n d\Omega_n$ is the neutron emission DDX, dE/dx is the stopping power of the incident proton in Li, and the $\Sigma_{non}(E')$ is the macroscopic reaction cross sections at the proton energy E'. It should be noted that the scattering of secondary neutrons in the target is not considered in the calculation.

4. Results and discussion

Figure 4 shows comparisons between the calculated DDXs of the ^{7}Li(p,xn) reaction at the emission angle of 0 degree and the measured ones for incident energies of 53, 100, and 150MeV [11,12]. The calculated DDXs reproduce the experimental data satisfactorily, although the position of the peak observed at high-energy end is slightly different between the calculation and the experimental data at 100 and 150 MeV. This energy shift may be seen because the energy loss of incident protons in the Li target is not considered in the present calculation.

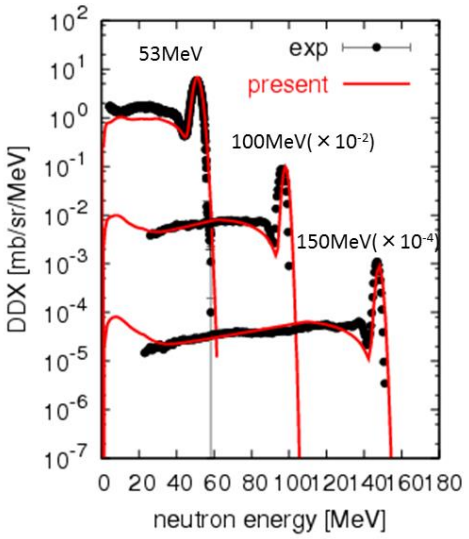

Fig. 4. Comparison of calculated and experimental DDX at 0 degree.

Next, the calculated DDXs are compared with measured DDXs at 137 MeV[13] in Fig.5. Solid and dashed lines denote the present evaluation and the calculation by the INCL+GEM model in the PHITS code [14], respectively. In the high energy end, the present DWBA calculation shows underestimation with increasing emission angle. The same trend is seen in Fig.2. The present evaluation overestimates the measured data in the low emission energy region where evaporation process is predominant, whereas the INCL+GEM calculation provides better agreement with the measurement than the present evaluation. In the intermediate region where preequilibrium process is predominant, the present evaluation improves remarkable underestimation seen in the INCL+GEM calculation at 0 and 15 degrees. However, it is found that the preequilibrium exciton model in CCONE cannot describe the quasi-free scattering component corresponding to a broad peak in the INCL+GEM calculation.

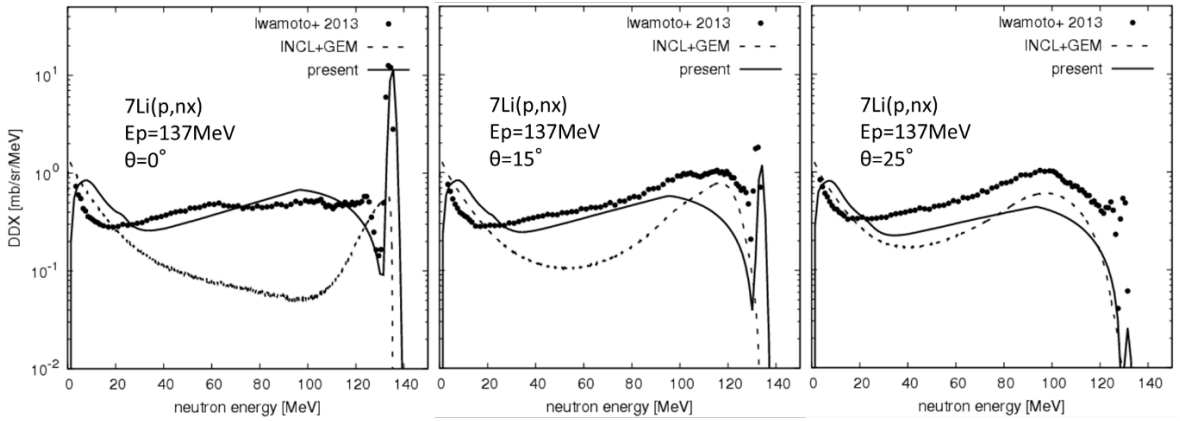

Fig. 5. Double differential cross sections of neutron production from proton-induced reaction on ^{7}Li for the incident energy of 137 MeV and three emission angles of 0, 15, and 25 degrees.

Figure 6 shows comparisons between calculated neutron production yields and experimental data [11,15] at 43 and 150 MeV. The energy loss ΔE in the Li target is denoted in the figure. The histogram represents the calculation result by a new version of PHITS (ver.2.70), in which the DWBA calculation [16] is included. The PHITS calculation underestimates the measurement remarkably in the continuum region at 150 MeV as expected from Fig.5. On the other hand, the calculation with Eq.(3) denoted by the solid line reproduces the measured neutron spectra over a wide range of emission energy fairly well.

5. Conclusions and outlook

The cross section evaluation of the ^{7}Li(p,n)^{7}Be reaction was performed for incident energies from 7 to 200 MeV using experimental data and theoretical model calculations. The differential cross sections corresponding to the ground and first excited states of ^{7}Be were evaluated by interpolation based on the Legendre fitting of available experimental data up to 45 MeV and the DWBA calculation with the microscopic form factor at incident energies above 45 MeV. The double differential neutron production cross sections (DDXs) corresponding to preequilibrium and evaporation components were calculated using the CCONE code. The evaluated DDXs were used for calculation of neutron production yields. The result showed relatively good agreement with experimental data.

In the future, we plan to extend the present evaluation to lower incident energies and other reaction channels in order to make a complete set of nuclear data on ^{7}Li. Since some resonance peaks are observed in the ^{7}Li(p,n)^{7}Be cross section in the incident energy region lower than 7 MeV, we will need to apply the R-matrix theory [17] to the resonance region. In addition, it will be necessary to consider the breakup channel of ^{7}Li into triton and alpha properly. The CDCC approach [18] will be effective for cross section calculations including the breakup channel.

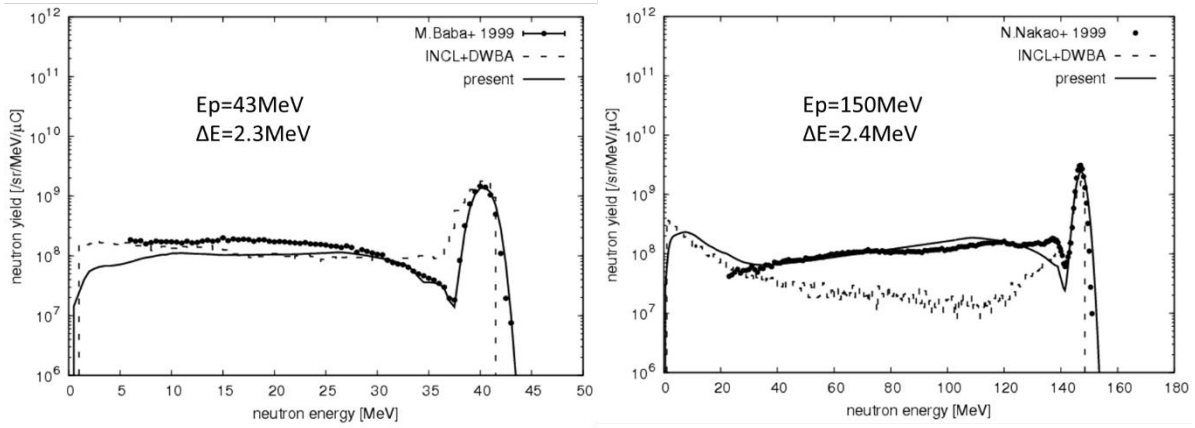

Fig. 6. Production yields of neutrons from thick lithium target bombarded by 43 and 150 MeV protons at 0 degree. The solid line and the dashed line denote the neutron yields calculated with Eq.(3)and those with PHITS, respectively.

References

[1] S.G. Mashnik et al., LANL Report LA-UR-00-1067, Los Alamos 2000, http://mcnp.lanl.gov/.

[2] Y. Watanabe et al., J. Korean Physical Society,59,2,1040-1045 (2011).

[3] FENDL-3, http://www-nds.iaea.org/fendl3/

[4] H.Liskien et al., J. AND. 15, 57–84 (1975).

[5] O.Iwamoto, J. Nucl. Sci. Technol. 44, 687 (2007).

[6] P.D. Kunz, Computational Nuclear Physics 2 88 (1993).

[7] T.Ye, el al., Phys. Rev. C 78 024611 (2008).

[8] C. Kalbach, Phys. Rev. C 37, 2350 (1988).

[9] S. Schery, el al., Nucl. Instr. Meth. Phys. Res. 147, 399 (1977).

[10] T. N. Taddeucci, el al., Phys. Rev. C 41, 2548 (1990).

[11] N. Nakao, el al., Nucl. Instr. Meth. Phys. Res. A 420, 218 (1999).

[12] T. Nakamura, el al., Nucl.Data for Sci.and Techn., Trieste 1997, 2, 1508 (1997).

[13] Y.Iwamoto, el al., Nucl. Instr. Meth. Phys. Res. A 629, 43 (2011).

[14] T.Sato, el al., J. Nucl. Sci. Technol. 50, 913 (2013).

[15] M. Baba, el al., Nucl.Data for Sci.and Techn.,Gatlinburg 1994, Vol.1, p.90 (1994).

[16] S. Hashimoto et al., Nuclear Data Sheets 118, 258–261 (2014)

[17] S. Kunieda, JAEA-Conf 2015-003 (2015).

[18] H. Guo et al., Nuclear Data Sheets 118, 254-257 (2014).

35 Investigation of Variable Neutron Field for Accurate Determination of Thermal Neutron Capture Cross Section at KURRI-LINAC

Takahiro YAGI[a,*], Jun-ichi HORI[a], Tadafumi SANO[a], Hiroshi YASHIMA[a],
Yoshiyuki TAKAHASHI[a], Cheol Ho PYEON[a], Hideo HARADA[b]

[a]*Kyoto University Research Reactor Institute, Asashiro-Nishi, Kumatori-cho, Sennan-gun, Osaka 590-0494, Japan*
[*]*e-mail: takahiro@rri.kyoto-u.ac.jp*
[b]*Japan Atomic Energy Agency, 2-4 Shirane, Shirakata, Tokai-mura, Nakagun, Ibaraki 319-1195, Japan*

To supply independent and accurate thermal capture cross sections, we have developed a method of independent and accurate thermal capture cross section measurement at the KURRI-LINAC. In this study, we proposed the thermal capture cross section measurement methods using variable neutron fields, developed the variable neutron fields using the light water activated boric-acid solution, and investigated neutron spectra in these fields using the TOF and activation methods.

MA, thermal capture cross section, KURRI-LINAC, TOF

1. Introduction

In order to reduce radioactive toxicity, feasibility for nuclear transmutation of minor actinides (MAs) and long-lived fission products (LLFPs) by utilizing innovative nuclear system (i.e. fast breeder reactors and accelerator-driven systems) has been investigated. The report on OECD/NEA No.6410 [1] indicates that the accuracy of neutron nuclear data of MAs and LLFPs are lower than that of required accuracy. Although high precision measurements of relative neutron capture cross sections of MAs and LLFPs are conducted with time-of-flight (TOF) method using high-intensity–pulsed neutrons generated by spallation reaction, accurate normalization of TOF data is still an important issue, and unrecognized bias effect needs to be eliminated as much as possible. To meet accuracy needs, the project entitled as “Research and development for Accuracy Improvement of neutron nuclear data on Minor ACtinides (AIMAC)” has been started as one of the “Innovative Nuclear Research and Development Program” in Japan at October 2013 [2].To investigate the nuclear data, it is necessary to conduct integral experiments using reactors. Several integral experiments for fission and capture reaction rates of ^{237}Np and ^{241}Am had been previously conducted at the Kyoto University Critical Assembly (KUCA) [3-5]. In this program, the differential TOF data is cross-checked with an integral data for validation of ^{237}Np, ^{241}Am, and ^{243}Am. To supply independent and accurate thermal capture cross sections, we have developed a method of independent and accurate thermal capture cross section measurement at the Kyoto University Research Reactor Institute - LINear ACcelerator (KURRI-LINAC) [6], and planned integral experiments in the various neutron spectra at the KUCA [7]. In this study, we proposed the thermal capture cross section measurement methods using variable neutron fields, developed variable neutron fields in the KURRI-LINAC, and investigated neutron

spectra in these fields using TOF and activation methods.

2. Method of thermal capture cross section measurements

The effective cross section $\hat{\sigma}$ is expressed as

$$\hat{\boldsymbol{\sigma}} = \frac{\boldsymbol{R}}{\Phi}, \quad (1)$$

where R is the reaction rate and Φ is the total neutron flux. When the effective cross section is not obeys the 1/v law, it is expressed as the following equation by Westcott's convention [8].

$$\hat{\sigma} = \sigma_0 \left(g(T_n) + r\sqrt{\frac{T_n}{T_0}}\, s_0 \right), \quad (2)$$

where σ_0 is the thermal capture cross section for 2200 m/sec, $r\sqrt{T_n/T_0}$ is the epithermal index that denotes the ratio of the epithermal neutron flux to the thermal neutron flux, T_n and T_0 are neutron temperature and 293.59 K, $g(T_n)$ is Westcott's factor. The s_0 is defined by

$$s_0 = \frac{2}{\sqrt{\pi}} \frac{I_0'}{\sigma_0}, \quad (3)$$

where I_0' is the reduced resonance integral above Cd cut-off after subtracting the 1/v component, and expressed as [9,10].

$$I_0' = I_0 - 2g(T_n)\sigma_0\sqrt{\frac{E_0}{E_c}} \cong I_0 - 0.45\,\sigma_0\,, \quad (4)$$

where E_0 is 0.0253 eV of the thermal neutron energy, E_c is 0.5 eV of the Cd cut-off energy, and I_0 is the resonance integral. The effective cross section can be deduced by Equations (2), (3), and (4) as follows:

$$\hat{\sigma} = \left(g(T_n) - 0.45\, r\sqrt{\frac{T_n}{T_0}}\,\frac{2}{\sqrt{\pi}} \right)\sigma_0 + r\sqrt{\frac{T_n}{T_0}}\,\frac{2}{\sqrt{\pi}}\, I_0, \quad (5)$$

where $g(T_n)$ and $r\sqrt{T_n/T_0}$ are obtained with the TOF and the activation foil method. The $\hat{\sigma}$ of Equation (5) is obtained as the following equation:

$$\hat{\sigma} = \frac{R}{A\int C(E)dE}, \quad (6)$$

where A is constant coefficient and $\int C(E)dE$ is integral counts obtained from the TOF measurement. Various measurement data of R, $\int C(E)dE$, $g(T_n)$, and $r\sqrt{T_n/T_0}$ are obtained from the variable neutron fields. Then the A, σ_0 and I_0 can be deduced with simultaneous equations of the Equation (5).

3. Experiments

All of experiments were carried out using a photo-neutron source in the KURRI-LINAC[7]. A water–cooled tantalum (Ta) was used to the photo-neutron target. The arrangements of the light water moderator and Ta target are shown in **Figure 1**. Four types of variable neutron fields were set with the light water activated boric-acid solution, as listed in **Table 1**. Neutron spectra of these fields were measured with the TOF method. The experimental setup of the TOF method and Au foil irradiation measurements are shown in **Figure 2**. The Au foils was set at the -135 degree and 1.3 m distance from the target. The samples

for TOF method was set at the 135 degree and 12.7 m distance from the target. Neutron spectrum measurements were obtained from capture reaction rate of ^{10}B and dummy samples [11]. The γ-ray detector composed of 12 bricks (5 × 5 × 7.5 cm^3) BGO scintillators were used for measuring a total energy absorption γ-ray. Reaction rates were measured with an activation foil method using Au foils (10 × 10 × 0.05 mm^3) covered with/without Cd-sheets of 0.8 mm thickness. The conditions of the accelerator were as follows: average beam current was 18 μA; frequency was 50 Hz; and pulse width was 100 ns.

Figure 1. Experimental setup of the Ta target and the light water moderator activated boric-acid solution

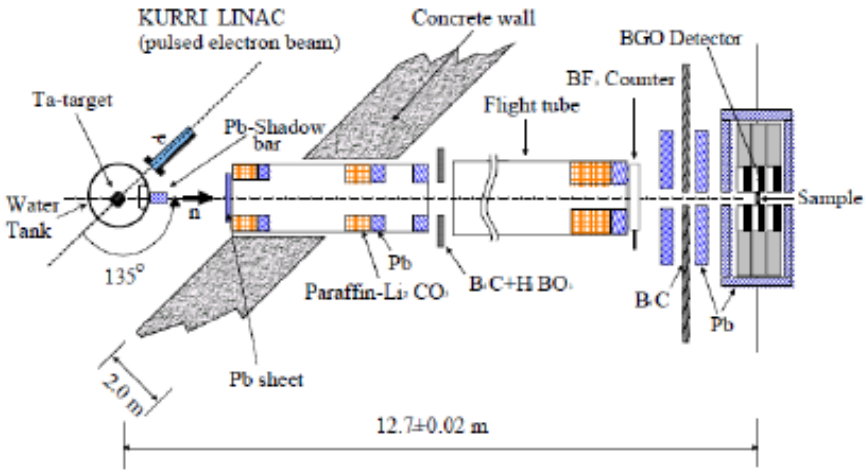

Figure 2. Image of experimental arrangement of the TOF method at the KURRI-LINAC

Table 1. Boric-acid concentration of the light water moderator

Case	Concentration [ppm]
Case 1	0
Case 2	318
Case 3	1404
Case 4	2946

4. Results and discussion

Measured results of TOF spectrum using ^{10}B and dummy samples in case of the 0 ppm concentration are shown in **Figure 3**. The TOF spectrum of 0 ppm was subtracted from the results of dummy sample. The time of flight t is converted to the neutron energy E using the following equation:

$$E = \frac{1}{2} m_n v_n^2 = \frac{m_n}{2} \left(\frac{L}{t}\right)^2, \qquad (7)$$

where m_n is the neutron mass, v_n is the neutron velocity, L is 12.7 m of the flight path, and t is the time of flight. Neutron energy spectra in four cases are shown in **Figure 4**. These neutron spectra are different in thermal region. Then, neutron temperatures were obtained with the Maxwell distribution equation:

$$\emptyset_M = B \frac{E}{(kT_n)^2} \exp\left\{-\frac{E}{kT_n}\right\}, \qquad (8)$$

where B is constant coefficient and k is Boltzmann's constant. The measured results of neutron spectra in thermal neutrons were fitted to Equation (8) using the least squares method. The results of neutron temperature are listed in **Table 2**, which show neutron temperature varied from 319.5 to 430.8 K.

Experimental reaction rates of ^{197}Au(n,γ)^{198}Au were obtained with activation foil method using a HPGe detector. The results are listed in **Table 3**. To compare the neutron spectrum of position of Au foil measurements with that of TOF measurements, reaction rates at the positon of TOF measurements were estimated. The reaction rates can be approximated to the Equation (9) because the reaction rates were mainly caused by the thermal neutrons. The reaction rates of $\int_0^{1keV} \emptyset(E)\sigma(E)dE$ were calculated with the measured neutron flux $\emptyset(E)$ and the microscopic cross section $\sigma(E)$ of JENDL-4.0 data. The calculated results of four cases are listed in Table 3, which means neutron capture reaction rates of Au were measured within 2 % compared to calculation results. Then neutron spectrum measurements using the TOF method can be effective for that of the activation foil method.

$$\int_0^\infty \boldsymbol{R(E)dE} = \boldsymbol{N} \int_0^\infty \boldsymbol{\emptyset(E)\sigma(E)dE} \cong \boldsymbol{N} \int_0^{\boldsymbol{1keV}} \boldsymbol{\emptyset(E)\sigma(E)dE} \qquad (9)$$

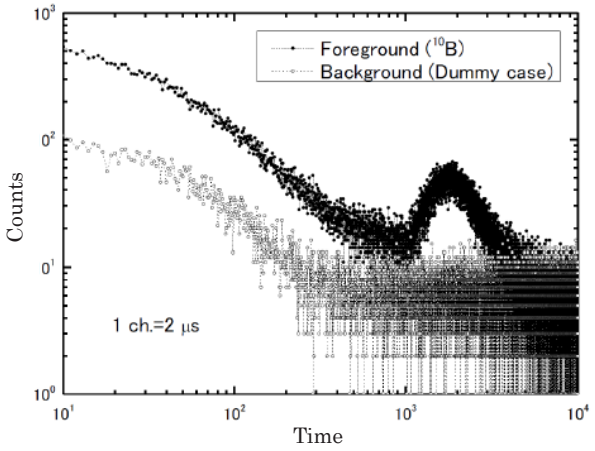

Figure 3. Comparison between TOF spectra with ^{10}B and dummy case

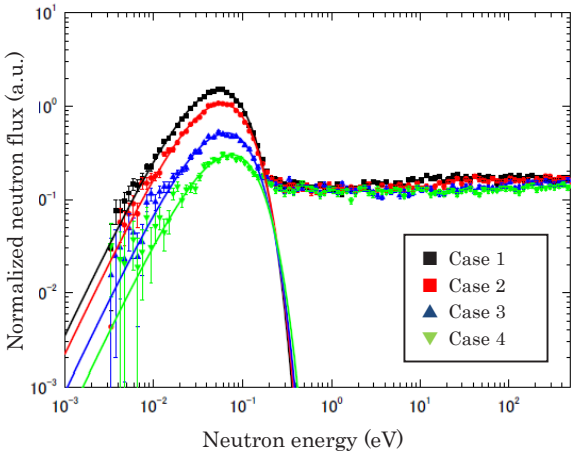

Figure 4. Measured neutron spectra of four types of neutron fields

Table 2. Result of neutron temperature in four cases

Case	kT (eV)	T (K)
Case 1	2.75	319.5
Case 2	2.95	341.8
Case 3	3.26	378.8
Case 4	3.71	430.8

Table 3. Results of normalized reaction rates of ^{197}Au(n,γ)^{198}Au

Case	Experiments	Calculation
Case 1	1.858 ± 0.040	1.874
Case 2	1.535 ± 0.032	1.577
Case 3	1.152 ± 0.022	1.141
Case 4	1.000	1.000

5. Conclusions

In this study, we proposed the method of σ_0 measurement using variable neutron fields, and developed variable neutron fields of effective neutron temperature varied from 319.5 to 430.8 K. Additionally, the TOF method is considered to be effective for neutron spectrum measurements of variable neutron fields close to the target.

Acknowledgements

Present study includes the result of "Research and Development for accuracy improvement of neutron nuclear data on minor actinides" entrusted to the Japan Atomic Energy Agency by the Ministry of Education, Culture, Sports, Science and Technology of Japan (MEXT).

References

[1] Salvatores M et al. Uncertainty and Target Accuracy Assessment for Innovative Systems Using Recent Covariance Data Evaluations. OECD/NEA; 2008, No. 6410.

[2] Harada H, Iwamoto O, Iwamoto N, Kimura A, Terada K, Nakao T, Nakamura S, Mizuyama K, Igashira M, Katabuchi T, Sano T, Takahashi Y, Takamiya K, Pyeon CH, Fukutani S, Fujii T, Hori J, Yagi T, Yashima H. Accuracy Improvement of Neutron Nuclear Data on Minor Actinides. Fifteenth International Symposium on Capture Gamma-Ray Spectroscopy and Related Topics (CGS15); 2014 Aug 25-29; Dresden (Germany).

[3] Unesaki H, Iwasaki T, Kitada T, Kohashi A, Fujiwara D, Kuroda M, Kato T, Ikeuchi Y, Shiroya S. Measurement of ^{237}Np Fission Rate Ratio Relative to ^{235}U Fission Rate in Cores with Various Thermal Neutron Spectrum at the Kyoto University Critical Assembly. J. Nucl. Sci. Tehcnol. 2000 Aug;37:627-635.

[4] Unesaki H, Iwasaki T, Kitada T, Ikeuchi Y, Shiroya S. Measurement and Analysis ^{241}Am Fission Rate Ratio Relative to ^{235}U Fission Rate in Thermal Neutron Systems Using Kyoto University Critical

Assembly. J. Nucl. Sci. Tehcnol. 2001 Aug;38:600-606.

[5] Iwasaki T, Horiuchi T, Fujiwara D, Unesaki H, Shiroya S, Hayashi M, Nakamura H, Kitada T, Shinohara N. Measurement and Analysis of Capture Reaction Rate of ^{237}Np in Various Thermal Neutron Fields by Critical Assembly and Heavy Water Thermal Neutron Facility of Kyoto University. Nucl. Sci. Eng. 2000 Apr;136:321-339.

[6] Kobayashi K, Jin G, Yamamoto S, Takami K, Kimura Y, Kozuka T, Fujita Y. KURRI-Linac as a Neutron Source for Irradiation. Annu. Rep. Res. Reactor Inst. Kyoto Univ. 1989; 22:142-153.

[7] Pyeon CH. Experimental Benchmarks for Accelerator-Driven System (ADS) at Kyoto University Critical Assembly. Japan: Kyoto University Research Reactor Institute; 2012, KURRI-TR-444.

[8] Westcoot CH, Walker WH, Alexander TK. Effective Cross Sections and Cadmium Ratios for the Neutron Spectra of Thermal Reactors. Proc. 2nd Int. Conf. on the Peaceful Uses of Atomic Energy, 1958 Sep 1-13; Geneva (Switzerland).

[9] Gryntakis EM, Kim JI. A Compilation of Resonance Integrals Part I, Z = 1-52 (Hydrogen - Tellurium). J. Radioanal. Chem. 1976 Mar; 29:175-224.

[10] Gryntakis EM, Kim JI. A Compilation of Resonance Integrals Part II, Z = 53-100 (Iodine - Fermium). J. Radioanal. Chem. 1978 Mar; 42:181-278.

[11] Yamamoto S, Kobayashi K, Fujita Y. Application of BGO Scintillators to Absolute Measurement of Neutron Capture Cross Sections between 0.01 eV and 10 eV. J. Nucl. Sci. Technol. 1996 Nov; 33:815-820.

36 Composite Source System to Measure a Neutron and X-ray Imaging at Hokkaido University

Kaoru Y. HARA, Hisao TAIRA#, Hirotaka SATO, and Takashi KAMIYAMA
Faculty of Engineering, Hokkaido University
Kita 13 Nishi 8, Kita-ku, Sapporo 060-8628, Japan
e-mail: hara.kaoru@eng.hokudai.ac.jp

#Present address:
Faculty of Science, Tokyo University of Science, 1-3 Kagurazaka, Shinjuku-ku, Tokyo 162-8601

A composite source system has been newly installed to measure neutron and X-ray images in the 45-MeV electron linear accelerator facility at Hokkaido University. Using the PHITS code, we performed the simulations for the energy distributions of the neutron and X-ray beams, which were provided from the source system.

1. Introduction

A complex utilization of neutron and X-ray beams for an imaging experiment is an important application. By taking advantage of the different penetrating ability of the beams in materials, the images measured with each beam are expected to provide mutually complementary information about material elements and structures. The X-ray interacts with electrons of atoms in the material such as scattering and absorbing whereas the neutron interacts with atomic nuclei. For the neutron and X-ray imaging experiments, an accelerator-based neutron and X-ray source system has been installed at Hokkaido University. In this paper, the configuration of the source system and the simulated energy distributions of the both beams are reported.

2. Hokkaido University Neutron and X-ray Source

The composite source system is located on a so-called “CENTER” beam course in the electron linear accelerator facility. The schematic view of the source system is shown in Fig. 1. The source system which contains two production targets allows us to selectively use both neutron and X-ray beams without change of sample and detector positions. The produced beam is chosen by moving the positions of the targets up and down with respect to the electron beam axis. The switching time is several minutes.

To obtain the X-ray beam of a few hundred keV, a bremsstrahlung photon is generated by hitting a copper plate with the electron beam. The cross-sectional view of the X-ray production

target is shown in Fig. 2(a). The copper plate is tilted at a 60 degrees angle with respect to the electron beam axis. The bremsstrahlung photons which are emitted in a direction perpendicular to the electron beam axis are extracted at an exit window as the X-ray beam. Here, the 9-MeV electron beam is used for the production of X-ray beam. Because the neutron separation energies of ^{63}Cu (10.9 MeV) and ^{65}Cu (9.9 MeV) are higher than the energy of electron beam, background neutrons due to the $^{63, 65}$Cu(γ,n) reactions are not caused.

On the other hand, the higher energy electron beam (34 MeV) is required for the production of neutron beam since the bremsstrahlung photon which is generated by hitting a tungsten disc with the electron beam is applied to induce the photonuclear reaction of lead, where the separation energy and resonance energy for the photonuclear reaction of lead isotopes are 7-8 MeV and ~15 MeV, respectively. In addition, the produced neutrons are thermalized with a polyethylene moderator. The cross-sectional view of the neutron production target is shown in Fig. 2(b). The polyethylene moderator is located on the downstream of the target and surrounded with graphite reflectors. The thermal neutrons are extracted at an exit window as a neutron beam in a direction perpendicular to the electron beam axis. As shown in Fig. 2(b), thick lead blocks are mounted in the graphite reflectors in order to prevent the bremsstrahlung photons from entering the neutron beam course.

3. Simulations for the energy distribution of the X-ray and neutron beam

We performed simulations to obtain the energy distributions of the X-ray and neutron beams using the Monte-Carlo simulation code PHITS [1]. The nuclear data library JENDL4 [2] was applied to all materials that the transported particles pass through.

For the X-ray beam simulation, the pencil-like electron beam with a diameter of 1 cm and the energy of 9 MeV was defined as an initial source. The incident electron induced the bremsstrahlung photon in the copper plate. The energy distribution of the bremsstrahlung photons which were transported to the exit window was counted at a 10 × 10-cm tally surface, where the distance L between the electron beam axis and the tally surface is 30 cm. Although the sample for an imaging experiment is placed on further downstream (about 600 cm), we set the tally position at L = 30 cm to obtain the adequate statistics in this simulation. The simulation for L = 600 cm is in progress. As shown in Fig. 3, the result shows the energy distribution of the X-ray beam with the peak energy of 100 keV.

For the neutron beam simulation, a point neutron source with the Maxwell-Boltzmann distribution of kT = 1.3 MeV was defined at the neutron production target as an initial source. In fact, the high-energy electron beam is needed to induce the photonuclear reaction with the bremsstrahlung photon as described in the previous section. In this simulation, however, the particle transportation was approximately initiated from the neutron source because it took too much time to simulate the photon production and the successive photonuclear reaction. The

energy distribution of the neutrons which were thermalized with the polyethylene moderator and transported to the exit window was counted in the similar manner of the X-ray beam simulation. As shown in Fig. 4, the result shows the energy distribution of the thermal neutron beam with the peak energy of 0.03 eV in the energy range of 0.01 eV - 10 MeV.

4. Conclusion

We have installed the composite source system to measure neutron and X-ray images in the 45-MeV electron linear accelerator facility at Hokkaido University. The system consists of the accelerator-based neutron and X-ray sources, moderators, reflectors, and shields. As a first step to obtain the beam profiles of the source system, the simulations for the energy distributions of the X-ray and neutron beams were performed using the PHITS code. The energy distributions of the X-ray and neutron beams at the exit windows were presented.

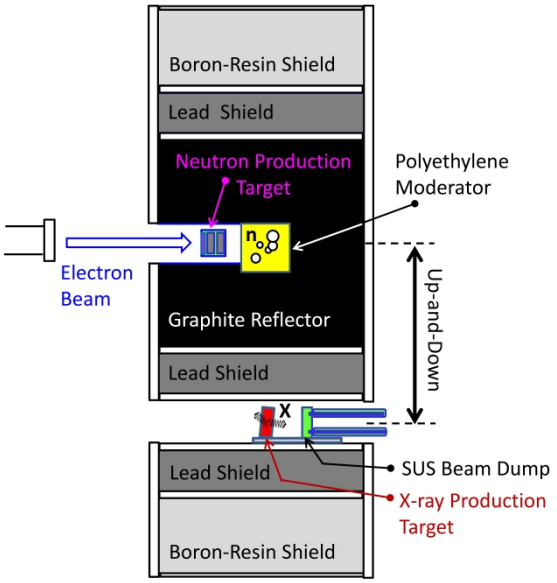

Figure 1: Hokkaido University neutron and X-ray source system

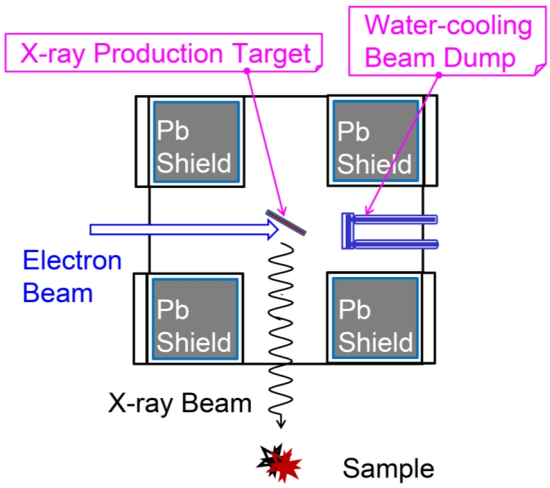

Figure 2(a): Production of X-ray beam

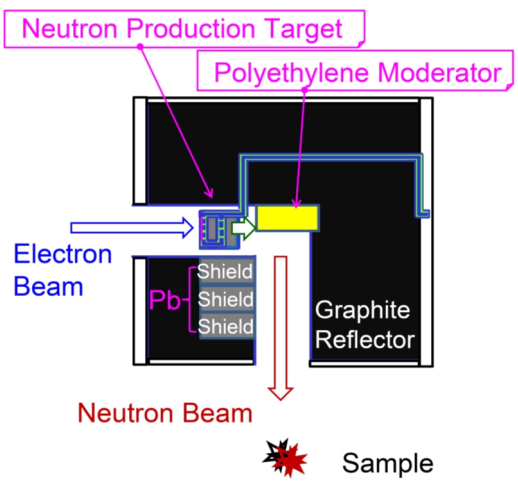

Figure 2(b): Production of neutron beam

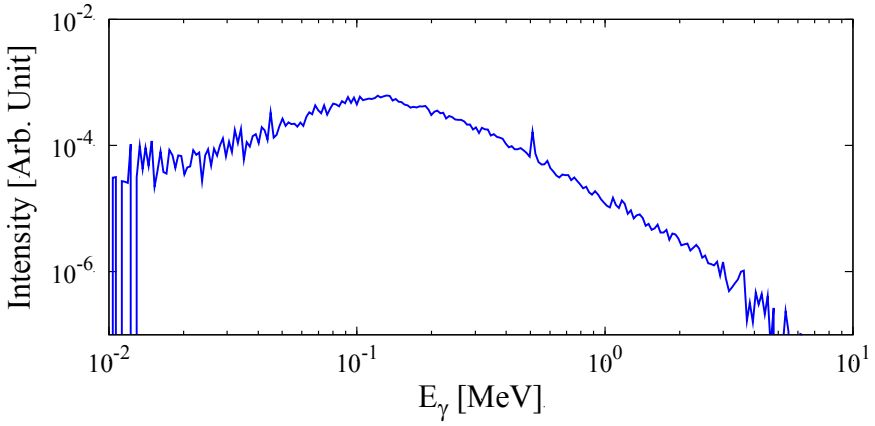

Figure 3: Energy distribution of the X-ray beam calculated with the PHITS code

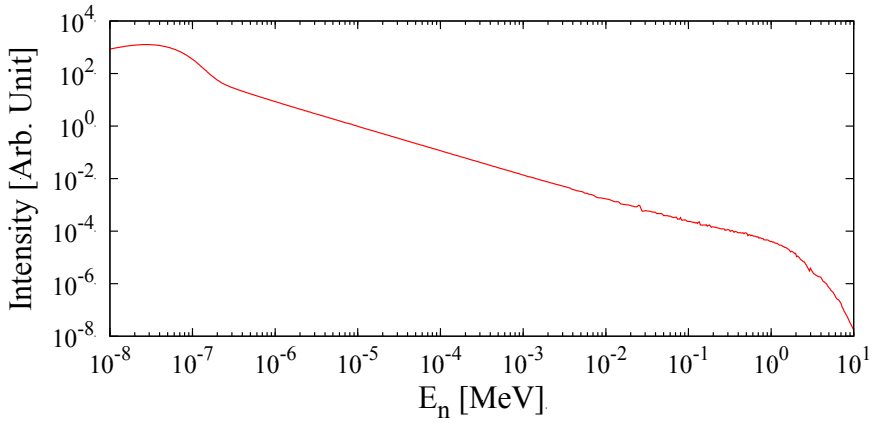

Figure 4: Energy distribution of the thermal neutron beam calculated with the PHITS code

Acknowledgements

The research is supported under the Photon and Quantum Basic Research Coordinated Development Program by the Ministry of Education, Culture, Sports, Sicence, and Technology (MEXT), Japan.

References

[1] Sato T, Niita K, Matsuda N, Hashimoto S, Iwamoto Y, Noda S, Ogawa T, Iwase H, Nakashima H, Fukahori T, Okumura K, Kai T, Chiba S, Furuta T and Sihver L, Particle and Heavy Ion Transport Code System PHITS, Version 2.52. J. Nucl. Sci. Technol. 2013;50:913-923.

[2] Shibata K, Iwamoto O, Nakagawa T, Iwamoto N, Ichihara A, Kunieda S, Chiba S, Furutaka K, Otuka N, Ohsawa T, Murata T, Matsunobu H, Zukeran A, Kamada S, Katakura J. JENDL-4.0: a new library for nuclear science and engineering. J Nucl Sci Technol. 2011;48:1-30.

37 Neutron Intensity Monitor with Isomer Production Reaction for p-Li Neutrons for BNCT

Y. Otani[1], F. Sato, I. Murata[1]
[1]*Graduate School of Engineering, Osaka University, Yamada-oka 2-1, Suita, Osaka 565-0871, Japan*
email: yotani@eei.eng.osaka-u.ac.jp

Abstract

Proton-lithium (p-Li) reaction is being examined as a candidate nuclear production reaction for accelerator based neutron source (ABNS) for BNCT. Several research groups are now developing a new ABNS with this reaction for BNCT. It is well known that the number of neutrons produced by p-Li reaction can be confirmed by measuring radioactivity of the target after irradiation by means of gamma-ray spectrometry. However, in an actual BNCT, it is not so easy to retrieve the target after irradiation. In the present study, it was investigated how to monitor the absolute neutron intensity of the p-Li neutron source easily. For a simple measurement in the real BNCT scene, we are examining activation foils suitable for measuring neutrons produced by p-Li reaction, which are around several hundreds keV. This kind of foil is not known so far. In the present study, for keV region neutrons we investigate possibilities of isomer production reaction via inelastic scattering. Isomer production reactions having low threshold energies of up to around several hundreds keV were examined by calculating their reaction rates taking into consideration their activation cross sections and the emission angle-dependent spectrum of neutrons emitted via p-Li reaction. As a result, it was found that ^{115}In, ^{107}Ag, and ^{189}Os would be feasible. These nuclides have different feartures with each other, so that we would be able to measure neutron intensity of every emission angle from the beam line. In the next step, validity of these foils will be examined experimentally using a p-Li neutron source.

1. Introducion

Boron Neutron Capture Therapy (BNCT) is a newly developing therapy for low permeation cancer, which can kill only tumors suppressing damage to normal tissues. So far, only reactor based neutron sources were available for BNCT and their size and safety are considered as critical difficulty to construct the source in medical facilities. To solve this problem, development of accelerator based neutron source (ABNS) is on the drawing board recent years. In Osaka University p-Li neutron source development is underway to realize BNCT in hospitals.[1] However, to achieve ABNS for clinical use, there are several problems to be cleared. One of them is establishment of a simple method to measure the accurate neutron source intensity for checking and normalization of the source in the accelerator room.

For this purpose, activation foil method is the most convenient and feasible. The activation foil method is well known as an easy way to measure neutron intensity. Activation foils are commonly made of metals which would emit gamma-rays after short-time neutron irradiation. Measuring the emitted gamma-rays enables us to know the neutron intensity. However, available nuclides have not been known so far especially for several hundred keV neutrons, which are normally produced in a p-Li base ABNS for BNCT.

The aims of the present study are investigation of available activation nuclides for measuring several hundreds keV neutrons and examination of their feasibility for practical use.

2. Selection of foils

2.1 Principles for foil selection

Neutrons for BNCT we are interested in are produced by p-Li reaction shown below.

$$\mathbf{p + {}^{7}Li \rightarrow n + {}^{7}Be - 1.88MeV}$$

Typical neutron spectra for several emission angles for incident proton energy of 2.5 MeV are shown in Fig. 1. Conventional activation foil method can deal with only fast and thermal neutrons by using threshold and neutron capture reactions, respectively. For epi-thermal neutrons very few activation foils are known. Especially for several hundred keV neutrons in the epi-thermal energy region, i.e., p-Li neutrons, no available activation foils have not been reported ever.

Investigating the problem in mind by examining nuclear data files, Table of Isotopes[2] and so on, we came to focus on isomer production reaction via (n,n') reaction, because the threshold energy is sometimes smaller than 1 MeV.

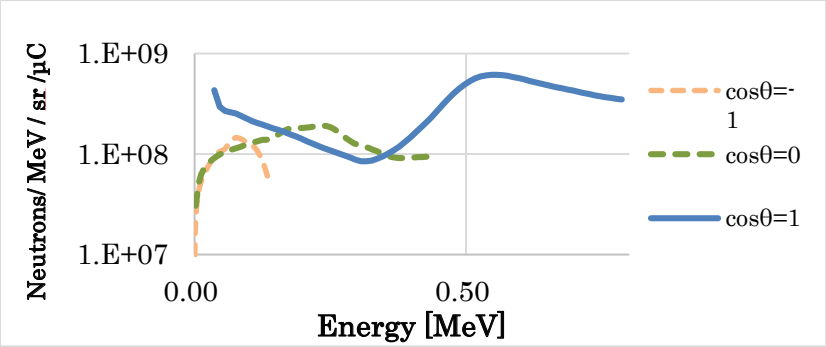

Fig. 1 Angle dependent neutron flux for p-Li reaction from DROSG2000[3].

2.2 Selection of foils

(1) First stage –Isomer Production Reaction via (n,n')-

We examined all the available activation materials and selected 24 isotopes listed below, which can be activated by p-Li neutrons (below 600 keV). It means, if they are an isomer production reaction via inelastic scattering, it can be expected that the activated foils can emit measurably low energy

γ-rays, because the reaction threshold energy is more-or-less the same as the nuclear level gap energy and the incident neutron energy.

First stage selection list:

^{60}Co, ^{77}Se, ^{79}Se, ^{87}Sr, ^{94}Nb, ^{96}Tc, ^{99}Tc,^{101}Rh, ^{107}Pb, ^{107}Ag, ^{111}Cd, ^{113}In, ^{115}In, ^{117}Sn, ^{133}Ba, ^{134}Cs, ^{135}Ba, ^{154}Eu, ^{158}Tb,^{163}Ho, ^{167}Er, ^{183}W, ^{189}Os, ^{193}Pt

(2) Second stage –Half-life and Cross Section-

From these 24 isotopes, we selected isotopes listed below considering the following conditions.

i) Half-lives of activated isotopes

We rejected isotopes whose half-lives are less than 30 seconds, because it is difficult to complete measurement with acceptably good statistical accuracy, if the half-life is too short.

ii) Cross section of (n, n') reaction

From databases of JENDL-Activation Files[4] and EXFOR[5], we selected available isotopes by examining their threshold energies, absolute cross sections and energy dependence precisely.

Second stage selection list:

^{87}Sr, ^{107}Ag, ^{111}Cd, ^{113}In, ^{115}In, ^{117}Sn, ^{135}Ba, ^{189}Os

(3) Third stage –Final Selection-

About the isotopes listed in the second stage selection, we divided two groups of them, one of which are ^{189}Os,^{107}Ag,^{87}Sr,^{117}Sn,^{111}Cd and the other of which are ^{113}In^{115}In,^{135}Ba. Then, we examined them by drawing their energy dependent cross sections according to the data from JENDL activation file.

- ^{189}Os,^{107}Ag,^{87}Sr,^{117}Sn,^{111}Cd

As shown in Fig. 2, ^{87}Sr, ^{117}Sn and ^{111}Cd are found to be unavailable because of their high threshold energy and low cross section. Cross sections of ^{107}Ag, ^{189}Os are large enough for measuring low energy neutrons. We finally considered these two isotopes are suitable for the present activation foils.

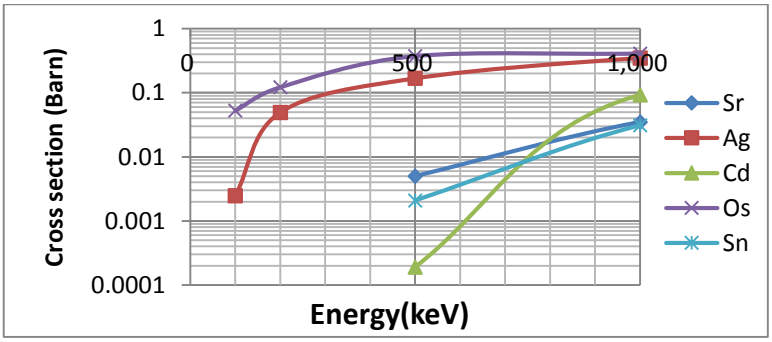

Fig. 2 Energy dependence of cross sections for ^{189}Os,^{107}Ag,^{87}Sr,^{117}Sn,^{111}Cd.

・^{113}In^{115}In,^{135}Ba

These 3 isotopes have fairly large cross sections which are around between those of ^{189}Os,^{107}Ag and ^{87}Sr,^{117}Sn,^{111}Cd. And they have quite similar energy dependence for their cross sections as shown in Fig. 3. We therefore compared their half-lives and abundance ratio as shown in Table 1 and chose ^{115}In because of its appropriate half-life and high abundance ratio showing the largest radiaoctivity.

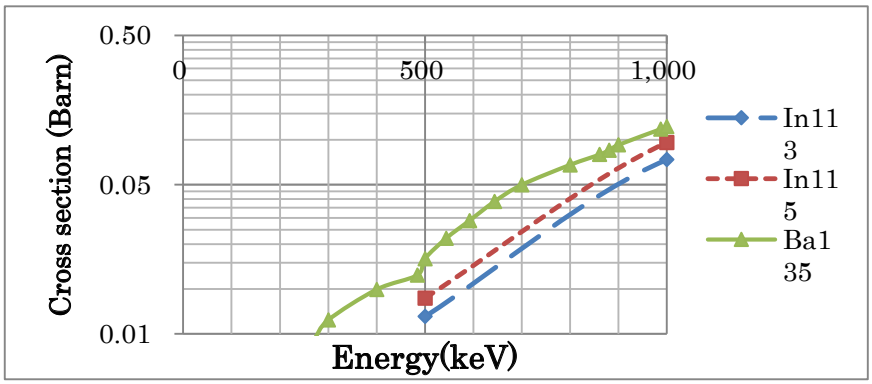

Fig. 3 Energy dependence of cross sections for ^{113}In, ^{115}In, ^{135}Ba.

Table 1 Half-lives and abundance ratios of ^{113}In,^{115}In,^{135}Ba.

	Half-lives	Abundance ratio(%)
^{113}In	1.16582h	4.29
^{115}In	4.480h	95.71
^{135}Ba	28.7h	6.592

As a result of these steps, we finally sellected three isotopes as below. The isometric transition schemes and cross sections of these isotopes are shown in Figs. 4 and 5, respectively.

Final stage selection list:

^{107}Ag, ^{115}In, ^{189}Os

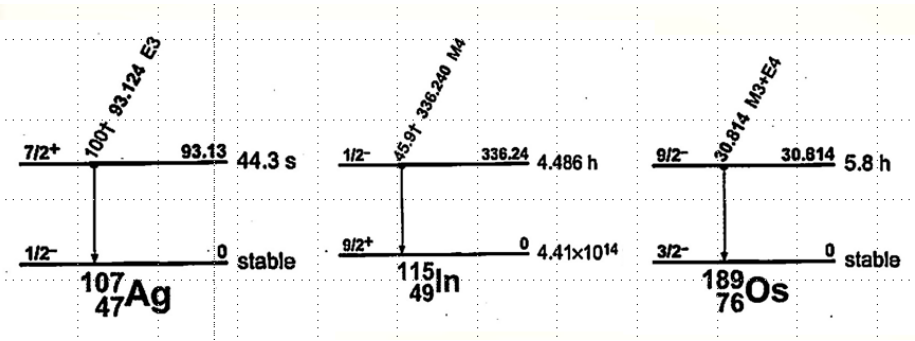

Fig. 4 Isometric transition of ^{107}Ag, ^{115}In, ^{189}Os.

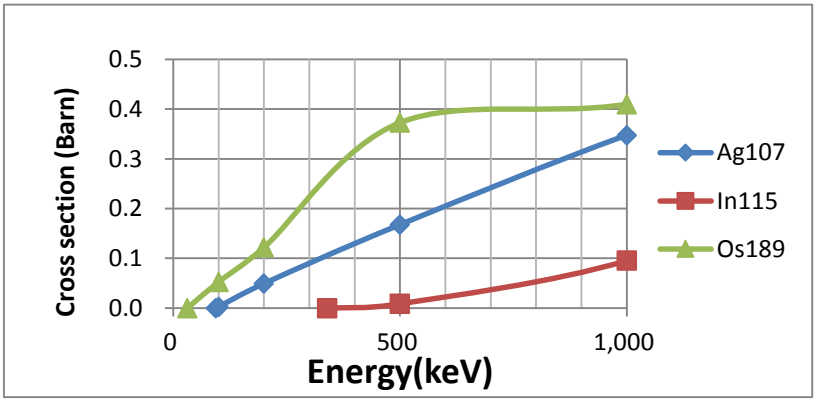

Fig. 5 Cross sections of ^{107}Ag,^{115}In, ^{189}Os.

3. Results and Discussion

It was found from the numerical analysis that the selected three foils of ^{107}Ag,^{115}In, ^{189}Os could be used for p-Li source neutron monitor. In addition, they have their own half-life and energy dependence of cross section. It means it can be used depending on measuring purposes in the real scene of BNCT as in the following.

(1) ^{107}Ag

^{107}Ag foil seems to be the most convenient among the three for an actual BNCT, because it has a short half-life and enough large reaction rate, meaning short measuring time with an acceptably high accuracy.

(2) ^{115}In

^{115}In enables us to measure flux intensity in the highest accuracy because it has a longer half-life and the emitted gamma-ray energy is higher. However, the cross section becomes small in the lower energy region. It means it is difficult to measure neutrons emitted in backward angles with this foil.

(3) ^{189}Os

Because of the largest cross section in the lower energy region, ^{189}Os is only available for measuring neutrons emitted in backward angles. However, it would be difficult to prepare an Os foil because the emitted γ-ray energy is very low and osmium tetroxide is quite harmful to human health.

4. Future works

We are planning to test these three foils by using a p-Li source at Tohoku-Univ., Japan, in order to examine their activation reaction cross sections. In order to perform this experiment, we are now trying to make Os foil safely. At the same time, accuracy of the cross sections of these isotopes has

to be checked. We should also carefully examine contribution of room return neutrons, which may misread the absolute source intensity in the actual measuring situation.

5. Conclusion

For p-Li reaction based ABNS for BNCT, a simple technique to monitor the absolute neutron intensity was examined with foil activation method. Since several handreds keV neutrons should be measured in the p-Li reaction, we focused on the isomer production reaction via inelastic scattering, because the threshold energy is sometimes less than 1 MeV. As a result of numerical analysis, we have finally found that ^{107}Ag, ^{115}In and ^{189}Os foils are available for measuring the neutron source intensity. These three foils have different features with each other as follows:

^{107}Ag: ^{107}Ag foil seems to be the most convenient because of the short half-life and enough large reaction rate.

^{115}In: ^{115}In enables us to measure the flux intensity in the highest accuracy because it has a longer half-life and the emitted gamma-ray energy is higher.

^{189}Os: Because of the largest cross section in the lower energy region, ^{189}Os is only available for measuring neutrons emitted in backward angles.

In the next step, we are planning to test these three foils experimentally by using a p-Li source at Tohoku-Univ., Japan, in order to examine their activation reaction cross sections.

6.References

[1] http://www.sumitomocorp.co.jp/news/detail/id=27107

[2] http://www.wiley-vch.de/books/info/0-471-35633-6/toi99/toi99cd.pdf

[3] https://www-nds.iaea.org/drosg2000.html

[4]Y. Nakajima, JNDC WG on Activation Cross Section Data: “JENDL Activation Cross Section File,” Proc. the 1990 Symposium on Nuclear Data, *JAERI-M 91-032*, p. 43 (1991).

[5] http://www.nndc.bnl.gov/exfor/exfor.htm

38 Systematic study of fission modes by a dynamical model based on Langevin equation

D. Hosoda, Y. Aritomo and S. Chiba

Research Laboratory for Nuclear Reactors, Tokyo Institute of Technology, 2-12-1 Ookayama, Meguro-ku, Tokyo 152-8550,Japan
email : hosoda.d.aa@m.titech.ac.jp

A dynamical model based on multi-dimensional Langevin equation was applied to calculate systematic trends of the mass distributions and average total kinetic energy of fission fragments in a wide mass region of fissioning nuclei. It was found that our calculation could reproduce experimentally-known trends of mean mass numbers of heavy and light fission fragments and averate values of total kinetic energy (TKE) for a region of ^{236}U to ^{246}Cm, while heavier, nuetron-rich nuclei led to single-peaked mass distributions with TKE values slightly higher than systematics. Furthermore, it was found that deformation of fission fragments affected mechanisms of nuclear fission such as structure of mass and TKE distributions noticeably.

1 Introduction

Inspite of intensive studies over many decades, mechanisms of nuclear fission have not been understood well yet since it proceeds as a complicated large-amplitude collective motion of many-nucleon systems. For example, it is still a mystery that structure of mass distribution of fission fragments greately changes when mass number of fissioning system is different only by one or two unit[1] in the region of Fm and No isotopes. Therefore it is worthwhile to study such a fission phenomenon using a dynamical model based on Langevin equation including quantum effects to assess how dynamics is important to understand the basic mechanisms of nuclar fission.

However, it is not comprehended enough how this dynamical model can repdocue important exprimental properties such as asymmetric or symmetric mass distributions systematically. For this reason, reproducibility of calculations were investigated by comparing results of Langevin calculation with experimental data having been already obtained and summarized in Ref.[2]. Here, two kinds of experimental data were used. One is weighted mean peak position of light and heavy asymmetric peaks. The other is average total kinetic energy (TKE) vs.($Z^2/A^{1/3}$) of fissioning nuclei for spontaneous fission. According to Ohtsuki *et al.*[2], the mean mass number of heavy fission fragments stays constant, while that of light fission fragments increases as a function of mass number of the fissioning nuclei. Furthermore, the TKE value of the fission fragments grows large when the coulomb energy of the fissioning systems increases, with some exceptionally high values for a couple of nuclei.

2 Method

A dynamical model based on the multi-dimensional Langevin equation has been successfully applied to nuclear reactions as fission[3, 4]. In this study, we apply this model to investigate

systematically mass distribution and TKE of fission fragments in a region from ^{236}U to ^{264}Fm at excitation energy E^*= 20MeV. The nuclear shape is defined by the two center parametrization, that is z, δ and α. First, z is the normalized distance between two centers of (pre)fragments, and defined as $z = z_0/(R_{CN}B)$, where z_0 means the distance of two (pre)fragments' center. R_{CN} is the radius of a spherical comound nucleus and B is defined as $B = (3+\delta)/(3\text{-}2\delta)$. Second, δ denotes the deformation of each fragments, and is defined as $\delta = 3(a-b)/2a+b$, where a is the length of abscissa axes of two fragments, and b is the length of vertical axes of those in fission process. Third, α is the mass asymmetry of two fragments, and defined as $\alpha = (A_1 - A_2)/A_{CN}$. Here, A_1 and A_2 denote the mass numbers of fragments, and A_{CN} denotes the mass number of compound nucleus.

The multi-dimensional Langevin equations are given as

$$\frac{dq_i}{dt} = (m^{-1})_{ij}p_j, \tag{1}$$

$$\frac{dp_i}{dt} = \frac{\partial V}{\partial q_i} - \frac{\partial}{\partial q_i}(m^{-1})_{jk}p_jp_k - \gamma_{ij}(m^{-1})_{jk}p_k + g_{ij}R_j(t), \tag{2}$$

where $\{q_i\} = \{z,\delta,\alpha\}$ and p_i is a momentum conjugate to coordinate q_i. In the Langevin equation, m_{ij} and γ_{ij} are hydrodynamical mass and friction tensors, respectively. The normalized random force R_j(t) is assumed to be property of white noise, that is $\langle R_i(\mathrm{t})\rangle = 0$ and $\langle R_i(t_1)R_j(t_2)\rangle = 2\delta_{ij}\delta(t_1-t_2)$. The strength of random force g_{ij} is given by inputting γ_{ij} into Einstein relation $\gamma_{ij}T = \sum_k g_{ik}g_{jk}$. This T is temperature of compound nucleus, related with the excitation energy of composite system as $E_{int} = aT^2$ where a is the level density parameter. Intrinsic energy E_{int} is given as

$$E_{int} = E^* - \frac{1}{2}(m^{-1})_{ij}p_ip_j - V(q,l,T=0). \tag{3}$$

where E^* denotes the excitation energy.

The potential V is defined as a sum of Liquid drop energy based on a Liquid drop model (LDM) V_{LDM}, rotation energy and quantum correction energy V_{QC}:

$$V(q,l,T) = V_{LDM}(q) + \frac{\hbar^2 l(l+1)}{2I(q)} + V_{QC}(q,T), \tag{4}$$

$$V_{LDM}(q) = E_s(q) + E_C(q), \tag{5}$$

$$V_{QC} = V_{SH} + V_{Pair}, \tag{6}$$

$$V_{SH}(q,T) = E^0_{Shell}(q)\Phi(T), \tag{7}$$

$$\Phi(T) = \exp\left(-\frac{aT^2}{E_d}\right). \tag{8}$$

Here, V_{LDM} is given as a sum of the nuclear surface energy E_s and the Coulomb energy E_C. The second term on the right-hand side of Eq.(4) is the rotational energy for an angular momentum l with a moment of inertia at q, $I(q)$. V_{QC} consists of the shell correction energy V_{SH} evaluated by two center shell model based on Strutinski method and the pairing correction energy V_{Pair} [4]. The shell correction energy V_{SH} is expressed as a product of shell correction energy E^0_{shell} at the zero temperature ($T = 0$) and temperature dependence factor $\Phi(T)$, and has a temperature dependence. Normally, we take shell damping energy E_d to be 20 MeV,but we calculated mass and TKE distributions as $\Phi(T) = 1$ in this work.

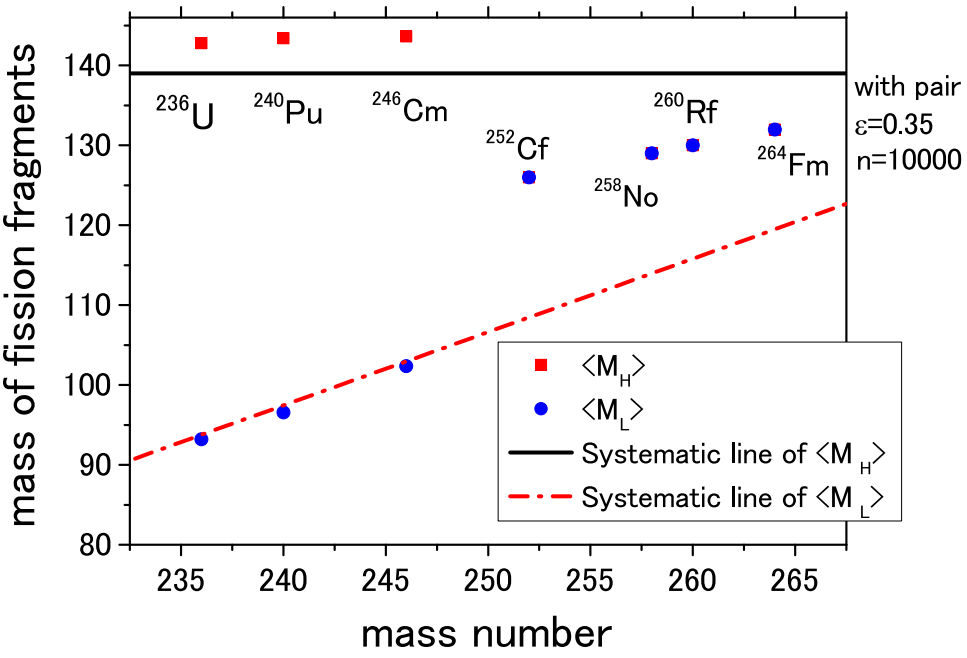

Figure 1: Mean mass numbers of heavy($< M_H >$)and light($< M_L >$) fission fragments

3 Results and discussion

3.1 Tendency of mean mass number in the region of ^{236}U∼^{264}Fm

Figure 1 shows the mean mass numbers of heavy $< M_H >$ and light $< M_L >$ fission fragments calculated by using dynamical model. The closed squares and circles correspond to $< M_H >$ and $< M_L >$, respectively. The two lines denote systematic trend given by Ohtsuki *et.al.*[2]. In the region of ^{236}U∼^{246}Cm, calculated value reproduced the trends that the mean mass number of heavy fission fragments stays constant, while that of light fission fragments increases systematically.

3.2 Relation of deformation parameter δ and mass distribution of ^{236}U

Figure 2 shows how mass distrobutions of ^{236}U depend on δ at step of 0.1 from -0.2 to 0.1. Firstly, we notice that the distributions greately change by the δ value. Secondly, peak position changes into more asymmetry component when δ changes from negative to positive value. Thirdly, it is found that fission proceeds predominantly when δ is from -0.20 to 0.10. From above result, we can conclude that mass distribution of fission fragments depend on how the fission fragments are deformed at scission.

3.3 Relation of deformation parameter δ and structure of mass distribution

From the result of Fig.1, the distribution shows two peaks in the region from ^{236}U to ^{246}Cm. However, in the region from ^{252}Cf to ^{264}Fm, it seems to show single peak. To consider difference of two kinds of the distributions, they were investigated by calculating δ distribution.

Figure 3 exhibits average value of δ for each fissioning systems. From this figure, the average values of δ changes between in the region from ^{236}U to ^{246}Cm and that from ^{252}Cf to ^{264}Fm.

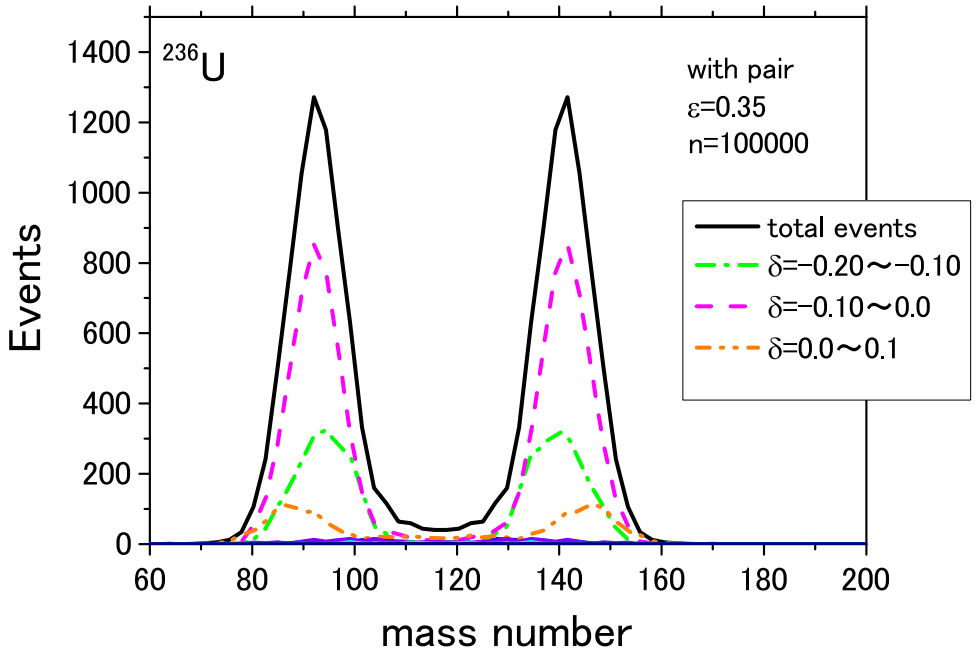

Figure 2: Calculation chart of mass distribution of ^{236}U

Therefore, there is a strong correlation between structure of mass distribution and δ distribution.

3.4 The influence of δ on TKE

Figure 4 shows a comparison of average value of TKE distribution calculated by a dynamical model filled squares and systematic trends given by Viola[5] and Unik*et.al.*[6]. From this result, the calculated value reproduces a systematic chart of average value of TKE. In the region from ^{252}Cf to ^{264}Fm, these TKE values, however, are larger than systematical lines. The fact that TKE values are larger than systematical lines for ^{252}Cf to ^{264}Fm is understood using Fig.5.

4 Conclusion

We investigated mass and TKE distributions of fission fragments by using multi-dimensional Langevin equation in the region from ^{236}U to ^{264}Fm at exciatation energy of 20MeV. Firstly, this dynamical model reproduced roughly systematic trends of the mean mass number and TKE of fission fragments. Secondly, it is found that there were substantial correlation between structure of mass distribution and deformation parameter δ. Thirdly, the parameter δ also gives substantial influence on TKE. Therefore, from these results, it was found that deformation parameter δ of fission fragments at scission is very important to understand mechanism of nuclear fission.

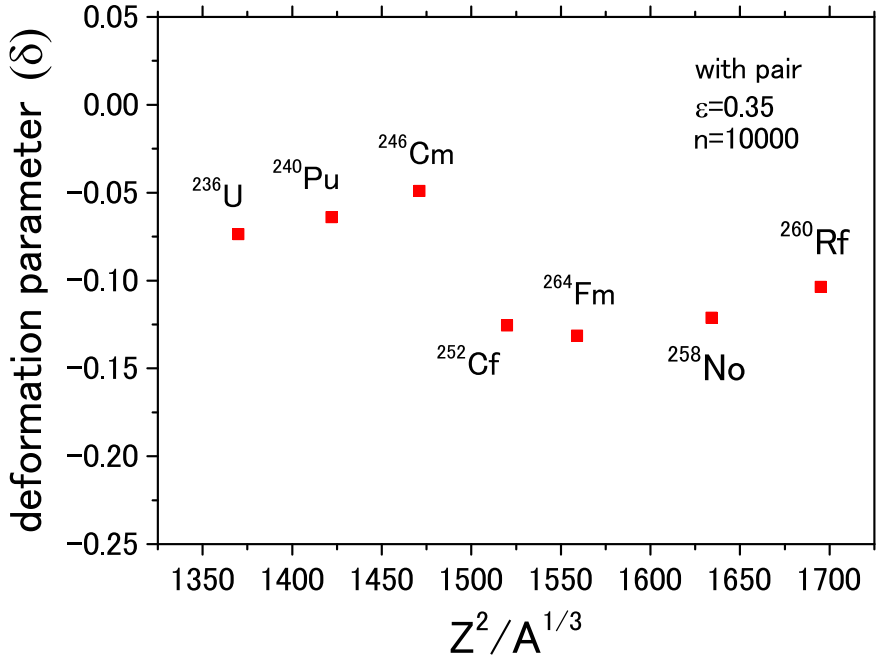

Figure 3: Relation of δ and structure of mass distribution

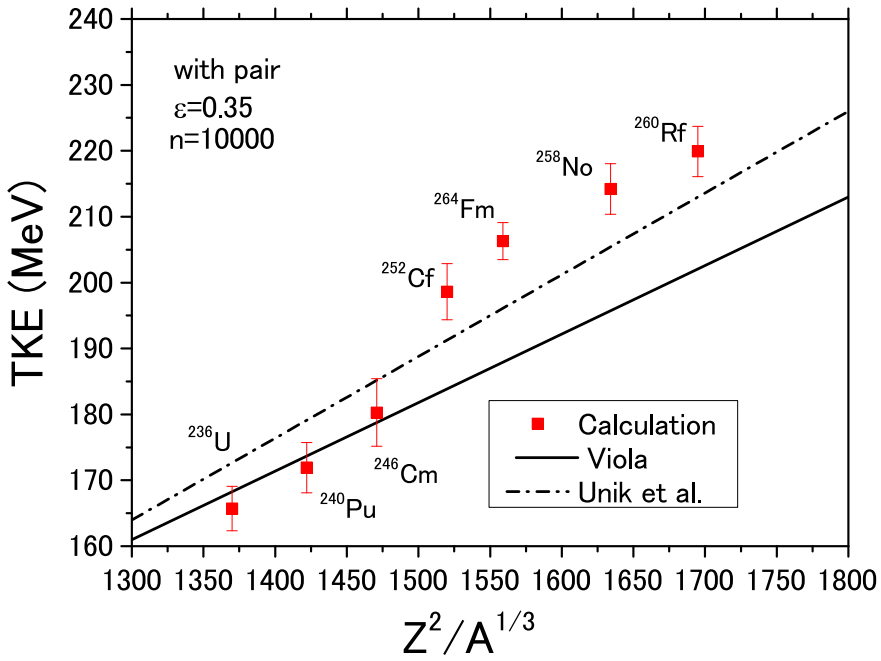

Figure 4: Comparison of average value of TKE

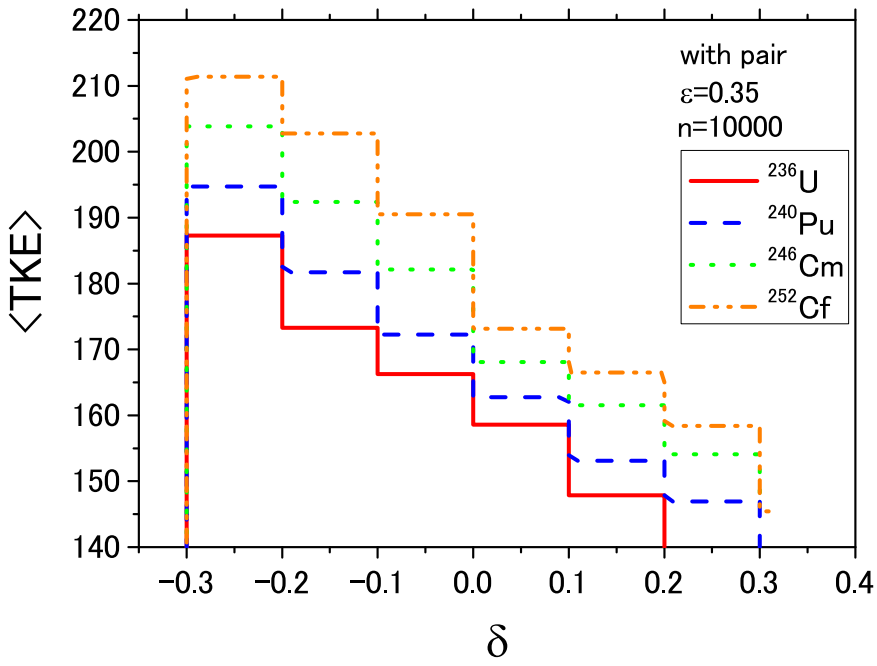

Figure 5: Dependence of average value of TKE on δ

References

[1] T.M.Hamilton et al, Phys. Rev. C46(1992)187

[2] T. Ohtsuki, Y. Nagame, H. Nakahara Heavy Elem. Relat. Phenom. 1, (1998),p. 507-535

[3] Y. Aritomo, S. Chiba, Phys. Rev. C88(2013) 044614

[4] Y. Aritomo, S. Chiba, and F. Ivanyuk Phys. Rev. C90(2014) 054609

[5] V.E. Viola, K. Kwiatkowski and M. Walker, Phys. Rev. C31(1985)1550

[6] J.P. Unik, J.E. Gindler, L.E. Glendenin, K.F. Flynn, A. Gorski, R.K. Sjoblom, in *ProceedingsoftheThirdIAEASymposiumonthePhysicsandChemistryofFission*, *Rochester*, 1973 (IAEA, Viena, 1974), Vol.2, p. 19

39 Simple phase-space-population control method for Monte-Carlo particle transport calculation

Shingo TAMAKI, Fuminobu SATO, Isao MURATA
Graduate School of Engineering, Osaka University
2-1 Yamadaoka, Suita, Osaka 565-0871 Japan
e-mail:stamaki@ef.eie.eng.osaka-u.ac.jp

In this study, we derived the relationship between the WW parameter and particle population for each phase space. And an automatic WW parameter generating system was developed to enable users to easily set and/or modify the WW parameter by themselves, to control the particle population in the calculation model as they desire. We confirmed availability of the system numerically by calculating the convergence efficiency of WW parameters by WWG for several tallies.

1. Introduction

For Monte-Carlo particle transport calculation code such as MCNP-5 [1], variance reduction techniques are quite important to reduce the computation time to obtain results with sufficient accuracy. There are some kinds of variance reduction techniques provided in MCNP. Weight Window (WW) is one of the Population Control Method, which splits and Russian roulette particles to control the particle weight for each phase space (energy and 3-dimensional space). WW is very effective if used appropriately, however, it is generally difficult for users to utilize WW properly because it is required to prepare a lot of parameters. Although MCNP provides a useful option, Weight Window Generator (WWG), that automatically generates WW parameters depending on the phase space importance to the specific tally, i.e., importance functions. However, it sometimes generates parameters different from what a user desires, and then the user should modify the WW parameter appropriately by himself, in spite of its difficulty shown above.

In this study, we derived the relationship between the WW parameter and particle population for each phase space, and developed an automatic WW parameter generating system to make particle population to be desired, and to enable users to finalize the WW parameters. In the paper, we confirmed its availability by making uniform population distribution in all phase spaces.

2. Theory

Particle flux per history in particular phase space $\mathrm{C}(\mathbf{r},\mathrm{E})$ can be obtained from Eq. (1) in MCNP.

$$\Phi(\mathbf{r},\mathrm{E}) = \sum_{i}^{m(\boldsymbol{r},E)} \frac{w_i(\boldsymbol{r},E)\cdot s_i(\boldsymbol{r},E)}{V(\boldsymbol{r})} \times \frac{1}{n} \quad (1) \tag{1}$$

Here, $\Phi(\mathbf{r},\mathrm{E})$ is particle flux, $m(\boldsymbol{r},E)$ is the number of sampled particles in $\mathrm{C}(\mathbf{r},\mathrm{E})$, $s_i(\boldsymbol{r},E)$ is i^{th} particle track length in $\mathrm{C}(\mathbf{r},\mathrm{E})$, $V(r)$ is volume of $\mathrm{C}(\mathbf{r},\mathrm{E})$, n is the total particle weight emitted from the source and $w_i(\boldsymbol{r},E)$ is i^{th} particle weight in $\mathrm{C}(\mathbf{r},\mathrm{E})$. From the physical viewpoint, n means the number of emitted particle from the source. To utilize WW, we assume $w_i(\boldsymbol{r},E) \approx \overline{w_s(\boldsymbol{r},E)}$, particle survival weight that can be set by users freely. And ideally $\overline{w_s(\boldsymbol{r},E)}$, is constant.

Then the flux is expressed as Eq. (2),

$$\Phi(\boldsymbol{r},E) = \frac{1}{n} \times \frac{\overline{w_s(\boldsymbol{r},E)}}{V(\boldsymbol{r})} \cdot \sum_{i}^{m(\boldsymbol{r},E)} s_i(\boldsymbol{r},E) = \frac{1}{n} \times \frac{\overline{w_s(\boldsymbol{r},E)}}{V(\boldsymbol{r})} \cdot m(\boldsymbol{r},E) \cdot \overline{s(\boldsymbol{r},E)} \tag{2}$$

$$\therefore m(\boldsymbol{r},E) = n \times V(\boldsymbol{r}) \times \frac{\Phi(\boldsymbol{r},E)}{\overline{s(\boldsymbol{r},E)}} \times \frac{1}{\overline{w_s(\boldsymbol{r},E)}} \tag{3}$$

$\overline{s(\boldsymbol{r},E)}$ is average particle track length in $\mathrm{C}(\mathbf{r},\mathrm{E})$, given in Eq. (4).

$$\overline{s(\boldsymbol{r},E)} = \frac{1}{m(\boldsymbol{r},E)} \sum_{i}^{m(\boldsymbol{r},E)} s_i(\boldsymbol{r},E) \tag{4}$$

The aim of this study is to control population distribution $m(\boldsymbol{r},E)$ with Eq. (3). For that, we introduce $I(\boldsymbol{r},E)$ function defined as Eq. (5), and population distribution $m(\boldsymbol{r},E)$ can be obtained by MCNP as in Eq. (6), while WW lower bound is given in Eq. (7).

$$I(\boldsymbol{r},E) = \frac{\Phi(\boldsymbol{r},E)}{\overline{s(\boldsymbol{r},E)}} \times \frac{1}{\overline{w_s(\boldsymbol{r},E)}} \tag{5}$$

$$m(\boldsymbol{r},E) = n \times V(\boldsymbol{r}) \times I(\boldsymbol{r},E) \tag{6}$$

$$WW_{lower\ bound} = k \times \overline{w_s(\boldsymbol{r},E)} = k \times \frac{1}{I(\boldsymbol{r},E)} \times \frac{\Phi(\mathbf{r},\mathrm{E})}{\overline{s(\boldsymbol{r},E)}} \tag{7}$$

$\boldsymbol{k}$ is a ratio between WW lower bound and Survival weight in MCNP. Here, $I(\boldsymbol{r},E)$ is regarded as user defined 3-d distribution of population per volume per history. For example, if $I(\boldsymbol{r},E)$ is set to be a constant value in all phase spaces, the obtained population distribution, $m(\boldsymbol{r},E)$, becomes uniform in the calculation model.

3. Numerical Test

3.1. Test procedure

The practical test procedure of the developed WW parameter generating system consists of the following steps. At first, particle flux and average track length were calculated by MCNP-5 for each concerned phase space. After that, these values were substituted to variables in Eq. (5) to obtain the suitable survival weight for given $I(\boldsymbol{r}, E)$ by a user. Finally, WW lower bounds were set from the survival weight according to Eq. (7). These steps were repeated until the WW parameters were converged.

3.2. Performance test to control the population

Numerical test calculation was performed to confirm the availability of this method. Calculation model in the test is shown in Figure 1. This is a neutron transmission experiment with 10 % boron doped HDPE blocks. Neutron source was assumed as ^{241}Am-Be, and $I(\boldsymbol{r}, E)$ were set to be 0.1 for all phase space.

In this study, we calculated the average track length in two ways, one was computed by using tallyx subroutine in MCNP, and another was obtained by processing all the event log data, obtained by PTRAC option in MCNP.

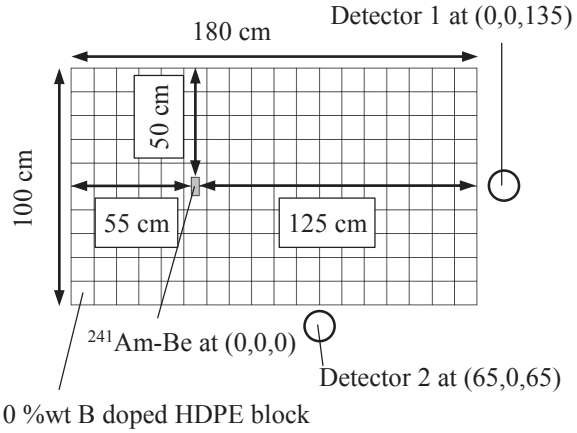

Fig. 1. Test calculation model. Calculation area was divided into 21600 phase spaces, i.e., 10 meshes in x-axis, 10 meshes in y-axis, 18 meshes in z-axis and 12 meshes in energy.

3.3. Examination of WWG convergence efficiency

The availability was examined by checking the parameter converge performance of WWG according to the following steps. At first, importance function for the specified tally was calculated in two ways. The first way is to use WWG with the WW parameter obtained in section 3.2 to make a uniform population distribution, called post-processing result (calc. A). As a post-processing, average track lengths were calculated by using tallyx subroutine. The second is to use WWG with no importance function at first, and apply the obtained WW parameter to the following calculations iteratively, until the parameters were converged (calc. B). These results were compared to evaluate WWG convergence efficiency with the uniform population distribution. This examination was performed for the several different detectors shown in Fig. 1.

4. Results and Discussion

4.1. Result of performance test

Figures 2 and 3 show the number of phase spaces for particle population representing the value $m(\boldsymbol{r}, E)$ in chapter 2. The result with tallyx subroutine is in Fig 2 and that with PTRAC option in Fig. 3. Prescribed population, obtained average population and mode population are summarized in Table 1. It was found that the population was roughly controlled by this method, however, the result of population distribution with tallyx was about 40 % smaller than the prescribed population, while the result with PTRAC agreed with the prescribed population. This was maybe caused by the algorithm to calculate average track length with tallyx subroutine that generated lather mean free path than average track length, because of large cell size, and as a result it led the incorrect solution. On the other hand, the result with PTRAC seems to have led the correct result, however, the PTRAC output becomes a very large file, finally about 17 GB for 10000 history, and therefore it was unreal to increase the history, number of source particles in the calculation. These problems could be avoided by mounting the algorithm into MCNP to calculate the average track length from the PTRAC output in the code.

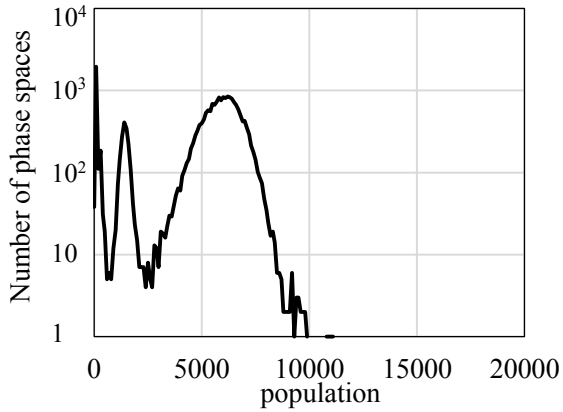

Fig. 2. Result of performance test for the system with tallyx subroutine. Prescribed population was 10000.

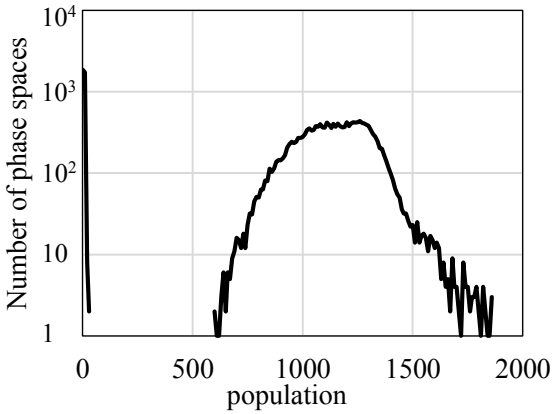

Fig. 3. Result of performance test for the system with PTRAC option. Prescribed population was 1000.

Table 1. Summary of performance test result

	Source particles	**Prescribed population**	**Average population**	**Mode population**
With tallyx	100000	10000	4950	6266
With PTRAC	10000	1000	949.9	1264

4.2. Result of WWG convergence efficiency examination

Tables 2 and 3 show the result of average flux, relative error, and FOM for detectors 1 and 2, respectively. It was found that WW parameters generated by WWG were immediately converged in calc. A, irrespective of the detector's position, while 4 times repetitions were required in calc. B. It means, once the converged WW solution was obtained for the uniform population distribution, in the next calculation, the WW parameters for a certain tally could be obtained by WWG option, no matter where the tally is located.

Table 2. Calculation result for Detector 1

	Repetition of WWG	**Average flux [n/cm^2/s]**	**Relative error**	**FOM**
Calc. A	0 (Initial calc.)	3.68E-12	0.0939	11
	1	**3.61E-12**	**0.0228**	**192**
Calc. B	0 (Initial calc.)	5.25E-13	0.3022	1.1
	1	3.05E-12	0.1905	2.8
	2	3.50E-12	0.0355	79
	3	3.54E-12	0.0266	141
	4	**3.43E-12**	**0.0239**	**175**

Table 3. Calculation result for Detector 2

	Repetition of WWG	**Average flux [n/cm^2/s]**	**Relative error**	**FOM**
Calc. A	0 (Initial calc.)	5.38E-09	0.0329	92
	1	**5.24E-09**	**0.0063**	**2517**
Calc. B	0 (Initial calc.)	5.48E-09	0.0824	15
	1	5.21E-09	0.0134	556
	2	5.22E-09	0.0075	1763
	3	5.24E-09	0.0069	2117
	4	**5.25E-09**	**0.0067**	**2234**

5. Conclusion

In this study, we derived the relationship between the population and weight window parameter as Eq. (3). And when the WW lower bound was given in Eq. (7), the population becomes proportional only to the number of particle histories, cell volume and user defined control factor $I(\boldsymbol{r}, E)$, as represented in Eq. (6). It was confirmed that phase space population could be roughly controlled in the transport calculation by the present automatic WW parameter generating system. We found that just one time WWG calculation is enough to obtain the converged WW parameters regardless of the tally position by the presently proposed

system. On the other hand, more than 4 times iterations were required to reach convergence by a common procedure with WWG.

In the next step, we will develop a new code system to generate WW parameters for several tallies at the same time. In future, we will apply this system to the neutronics and shielding design calculation of the accelerator based neutron source for BNCT.

Reference

[1] X-5 Monte Carlo Team. MCNP –A General Monte Carlo N-Particle Transport Code, Version 5, Volume I: Overview and Theory, LA-UR-03-1987. USA: Los Alamos National Laboratory; 2003.

40 Thick-target yields on radioactive targets estimated by inverse kinematics

Shotaro Imai[1], Masayuki Aikawa[2], and Shuichiro Ebata[1]
[1]Meme Media Laboratory, Hokkaido University
Sapporo, Hokkaido 060-8628, Japan
[2]Faculty of Science, Hokkaido University
Sapporo, Hokkaido 060-0810, Japan
E-mail: imai@nucl.sci.hokudai.ac.jp

We suggest a method to evaluate the thick-target yields (TTY) on a radioactive lump. The method is based on the inverse kinematics on the projectile and target nuclei, in which the energy of projectile inside target is calculated by a stopping power. The stopping powers reflected with matter properties, are evaluated with using SRIM2008 code. To show the procedure of our method and the availability, we apply it to the specific examples ($^{\rm nat}$Cu(^{12}C,X)^{24}Na and ^{137}Cs(^{12}C,X)X). Indeed, we obtained the TTYs on $^{\rm nat}$Cu(^{12}C,X)^{24}Na and ^{12}C(^{63,65}Cu,X)^{24}Na using the experimental reaction cross section, and estimated the TTYs relation in the inverse kinematics on ^{137}Cs(^{12}C,X)X reaction.

1 Introduction

Disposing and/or reducing way of nuclear wastes produced in nuclear power plants is strongly required in nuclear technology. Nuclear transmutation is considered as an effective technique, especially for long-lived fission products (LLFP) [1]. Nuclear data, such as cross sections, related to the transmutation is unavoidable for the technology. Indeed, a recent project measures neutron capture cross sections of LLFP and minor actinides [2], although experiments of such radioactive targets remain limited due to high radioactivity of the targets.

One candidate method to obtain the data is to utilize the experimental values measured in inverse kinematics. Radioactive isotopes, including LLFP, are available as a beam in accelerators to obtain nuclear data. For instance, an experiment has been performed at RIBF to obtain cross section data relating to ^{90}Sr and ^{137}Cs. It is also applied to obtain cross sections deduced from the thick-target method of elastic scattering (e.g., Ref. [3]).

In addition to such cross section data, an essential quantity for the transmutation is thick-target yields (TTY) [4]. If we require information pertaining to transmutation of LLFP lumps, the TTY plays a key role. However, the TTY to reduce LLFP are nearly impossible to obtain directly in accelerators since the preparation of LLFP lumps as a target is miserable due to high radioactivity. We therefore suggest an estimation method for the TTY of a radioactive material based on inverse kinematics without the experiment using the radioactive target. The inverse kinematics with RI beam suggests that the exchange the role between radioactive target matter and incident particle, and we may obtain the TTY of radioactive matter theoretically. Since real nuclear wastes are composed of a lot of radioactive nuclei, the data of TTY of such matter would give a fundamental knowledge for the transmutation of the wastes.

2 Theoretical Evaluation of Thick-Target Yields

The reaction probability Y is defined as

$$Y = \frac{N_{\rm r}}{N_{\rm i}}, \tag{1}$$

using the initial particle number $N_{\rm i}$ and the reacted particle number $N_{\rm r}$. The thick-target yields (TTY) is the probability in the case of a thick-target matter. To evaluate TTY theoretically, we consider a reaction system

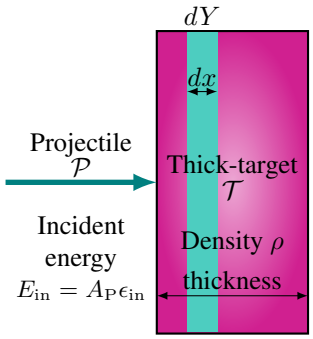

Figure 1: The schematic picture of the reaction system. The projectile particle $\mathcal{P}$ comes in the target $\mathcal{T}$ with incident energy $E_{\rm in} = A_{\rm P}\epsilon_{\rm in}$ [MeV], where $A_{\rm P}$ is the mass number of the projectile particle and $\epsilon_{\rm in}$ [MeV/A] is the energy per nucleon. The differential reaction probability dY is defined at infinitesimal length dx [cm].

that the thick-target matter $\mathcal{T}$ and the projectile $\mathcal{P}$ (see Fig. 1). The differential reaction probability dY at an infinitesimal length dx [cm] in the matter is described as:

$$dY = \sigma \frac{\rho N_{\mathcal{A}}}{A_T} dx, \tag{2}$$

where the cross section σ [cm^2], the Avogadro constant $N_{\mathcal{A}}$ [mol^{-1}], the mass number of the target A_T [g·mol^{-1}] and the density ρ [g·cm^{-3}]. Since the projectile particles come in with the incident energy $E_{\rm in}$ [MeV] and the energy is decreasing inside the target, the dY may be described as a function of the energy rather than the infinitesimal length. Such a decreasing effect is expressed by the stopping power:

$$S(E) = -\frac{dE}{d(\rho x)} \quad [\text{MeV}\cdot\text{g}^{-1}\cdot\text{cm}^2], \tag{3}$$

with the energy at a certain point x inside the target. Under the condition that the all projectile particles are stopped inside the target, the TTY is obtained by integrating over the energy from incident energy to zero:

$$Y(\epsilon_{\rm in}) = \frac{N_{\mathcal{A}} A_P}{A_T} \int_0^{\epsilon_{\rm in}} \sigma(\epsilon) \frac{1}{S(\epsilon)} d\epsilon, \tag{4}$$

which leads to:

$$\frac{dY(\epsilon)}{d\epsilon} = \frac{N_{\mathcal{A}} A_P}{A_T} \sigma(\epsilon) \frac{1}{S(\epsilon)}, \tag{5}$$

where we have used the energy per nucleon $\epsilon = E/A_{\rm P}$ [MeV/A] with the mass number of the projectile $A_{\rm P}$ and its incident energy $\epsilon_{\rm in}$ [MeV/A].

In this paper, we define the projectile $\mathcal{P}$ induced reaction on a target $\mathcal{T}$ as "forward system" and its inverse kinematics as "inverse system" (see Fig. 2). Those TTYs which are evaluated from Eq. (4) are denoted $Y_{\rm for}$ and $Y_{\rm inv}$, and Eq. (5) leads to the ratio $R(\epsilon)$ between differential yields at the same energy ϵ:

$$R(\epsilon) \equiv \frac{dY_{\rm for}(\epsilon)}{dY_{\rm inv}(\epsilon)} = \frac{A_P^2}{A_T^2} \frac{S_{\rm inv}(\epsilon)}{S_{\rm for}(\epsilon)}, \tag{6}$$

$$dY_{\rm for}(\epsilon) = R(\epsilon) dY_{\rm inv}(\epsilon). \tag{7}$$

This relation suggests that we can evaluate the $Y_{\rm for}(\epsilon)$ without the direct experiment of the forward system reaction in cases where the $Y_{\rm inv}(\epsilon)$ and the $R(\epsilon)$ are known. It is obviously that the cross sections of both systems are same and removed in the ratio due to the inverse kinematics and therefore it is an unnecessary information in the evaluation. It is well known that the stopping power is dominated by the coulomb force in high energy where nuclear transmutation is occurred, which means that Eq. (7) is essentially determined by only electronic interaction, while we discuss nuclear physics. Since the stopping power is proportional to the square of the projectile atomic number Z_P^2 and the target atomic number Z_T in the high energy region, the heavier projectile is more easily stopped inside the target.

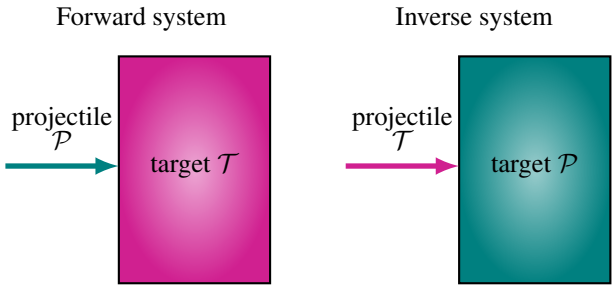

Figure 2: The forward and inverse systems defined in this paper. Due to the inverse kinematics, the cross sections in both systems are same but the stopping powers have a difference.

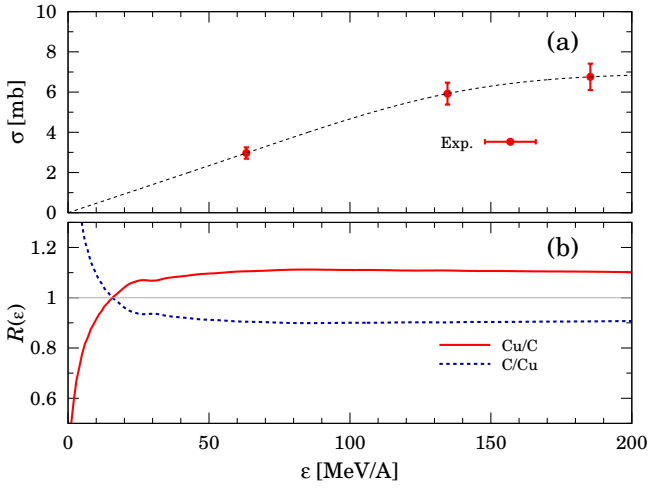

Figure 3: (a) Cross section with respect to $\epsilon = E/A_P$ of the $^{\mathrm{nat}}$Cu(^{12}C,X)^{24}Na with experimental data [5], and (b) the evaluated ratio $R(\epsilon)$ by SRIM2008 [6].

3 An Example of the Procedure

To explain the procedure, as well as its availability, we show the example of $^{\mathrm{nat}}$Cu(^{12}C,X)^{24}Na [5]. We find the relation between the forward system, $^{\mathrm{nat}}$Cu(^{12}C,X)^{24}Na, and the inverse system, ^{12}C(^{63,65}Cu,X)^{24}Na. In order to calculate the Y_{for} and Y_{inv}, the cross section $\sigma(\epsilon)$ and stopping power $S(\epsilon)$ are necessary. The $\sigma(\epsilon)$ as a function of ϵ is prepared by the spline fitting of experimental data [5], while the $S(\epsilon)$ is computed using the SRIM2008 code [6]. The $\sigma(\epsilon)$ and $R(\epsilon)$ which is calculated from Eq. (6) are shown in Fig. 3 (a) and (b). The Y_{for} with $A_T(^{\mathrm{nat}}\mathrm{Cu})$ = 63.546 at the incident energies $\epsilon = 40$ and 100 MeV/A and the Y_{inv} with the same energies are evaluated by Eq. (4). The result is shown in Table 1. As we mentioned in previous section, since the heavier projectile which is ^{63,65}Cu in this case is easier stopped inside the target, the TTY of inverse system Y_{inv} is smaller than the forward system.

We now evaluate Y_{for} using Eq. (7) with considering the dY_{inv} as a given data. Here, we find that the $R(\epsilon)$ converges on a constant value at the high energy over 50 MeV/A. The cross section of $^{\mathrm{nat}}$Cu(^{12}C,X)^{24}Na is

Table 1: The thick-target yields of forward and inverse system with two incident energies evaluated from Eq. (4).

	40 MeV	100 MeV
Froward system Y_{for}	0.91×10^{-5}	0.114×10^{-3}
Inverse system Y_{inv}	0.86×10^{-5}	0.103×10^{-3}

Table 2: The thick-target yields of forward system $Y_{\rm for}$ with two incident energies evaluated from Eq. (8) taking $R \simeq 1.1$ and the $Y_{\rm for}$s evaluated from Eq. (4) are also listed for comparison.

	40 MeV	100 MeV
From Eq. (8)	0.94×10^{-5}	0.113×10^{-3}
From Eq. (4)	0.91×10^{-5}	0.114×10^{-3}

negligible in the low energy region since such fragmentation reaction requires a large amount of energy, which means the both of $dY_{\rm for}$ and $dY_{\rm inv}$ in the low energy region can be considered to be zero. This simple behavior of $R(\epsilon)$ in Eq. (7) and the small $\sigma(\epsilon)$ allows us to utilize a more convenient conversion method as:

$$Y_{\rm for}(\epsilon_{\rm in}) \simeq \tilde{R}\, Y_{\rm inv}(\epsilon_{\rm in}), \tag{8}$$

where $\tilde{R}$ is a constant value of $R(\epsilon)$ at the high energy over 50 MeV/A. We can estimate $Y_{\rm for}$ from $Y_{\rm inv}$ and $\tilde{R}_{\rm Cu/C} \simeq 1.1$ and obtain $Y_{\rm for}(40) = 0.94 \times 10^{-5}$ and $Y_{\rm for}(100) = 0.113 \times 10^{-3}$. Indeed, these are in good agreement with values derived from Eq. (4) (see Table 2). This conversion method is practically justified using the SRIM2008 code and a negligible cross section at the low energy. If the TTY of ^{12}C(^{63}Cu,X)^{24}Na and ^{12}C(^{65}Cu,X)^{24}Na can be measured experimentally, we can confirm the method. The lower incident energy case, $\epsilon = 40$ [MeV], is less agreement than $\epsilon = 100$ [MeV], although the nuclear spallation reaction may be occurred at such high energy. This fact suggests that 40 MeV is regarded as a lower limit of Eq. (8) in this reaction system, and the lower limit of the conversion method should be determined depending on a reaction system in generally.

4 Evaluation of Thick-Target Yields for Radioactive Material

Finally, we consider the transmutation reaction of ^{137}Cs induced by ^{12}C as the forward system. The transmutation reaction consists of any channels with the exception of the ^{137}Cs(^{12}C,X)^{137}Cs reaction. This reaction is a considerable one for the radioactive waste disposal. The projectile ^{12}C is one of examples for the transmutation and a better reaction which has large cross section and stable residual particles may exist. The inverse system has the ^{12}C target which is easily set up experimentally and the radioactive ^{137}Cs projectile. The $Y^{\rm tr}$ to transmute the incident particles bombarding the thick-target is described as:

$$Y^{\rm tr} = \frac{N_{\rm tr}}{N_{\rm i}} = \frac{N_{\rm i} - N_{\rm u}}{N_{\rm i}}, \tag{9}$$

where $N_{\rm tr}$, $N_{\rm i}$, and $N_{\rm u}$ are the number of transmuted, incident, and un-transmuted particles, respectively. $N_{\rm i}$ is a countable number experimentally, and $N_{\rm u}$ can also be observed through detection of the specific gamma-rays if the projectile is radioactive and can be identified by gamma decay modes. The $Y^{\rm tr}$ of a radioactive projectile is therefore obtainable.

In order to evaluate the $Y^{\rm tr}_{\rm for}$ for the transmutation reaction of ^{137}Cs, we calculate the $R(\epsilon)$ with Eq. (6) using the SRIM2008 code. The $R(\epsilon)$ of the reaction of ^{137}Cs beam on the ^{12}C target (Cs/C) is shown in Fig. 4. The plateau and convergence of $R(\epsilon)$ can be seen in the high energy region as is the case with the previous example. In these system, the convenient conversion method shown in Eq. (7) will also be available. In the figure, we also plot two other examples, gold with carbon target (Au/C) and copper with nickel target (Cu/Ni), which have similar tendencies. Such convergence behavior seems to be an ordinal property at least these example. An interesting difference appears for the case of Cu/Ni that the ratio seems to be constant in whole range of the energy. This difference would relate to the difference of the atomic number of projectile and target. Copper and nickel are listed in the next on the periodic table and thus, the behavior of the stopping power would be similar.

We expect that the reactions at below 20 MeV/A will contribute little to the transmutation TTY since elastic and inelastic reactions govern at the lower energy region. We roughly estimate the range of $R(\epsilon)$, 1.0 ± 0.12, and note that the value of ratio itself should depend on a system as we can see in Fig. 4. The transmutation TTY of the reaction with ^{12}C beam on the ^{137}Cs lump target can be obtained at approximately 10% uncertainty while accuracy will be improved in more high energy regions.

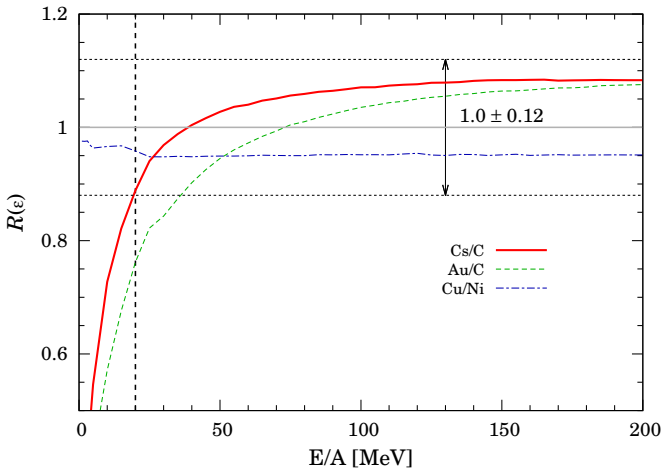

Figure 4: Ratio of differential yields between cesium and carbon (Cs/C) in comparison with two other samples, gold with carbon target (Au/C) and copper with nickel target (Cu/Ni).

5 Summary

We have suggested a new method to estimate the thick-target yields of a radioactive material using inverse kinematics. One of important points of this method is that the cross section of a projectile and a radioactive target is unnecessary information, if the TTY of the inverse system would be measured by the experiment. To explain detail of our method, we have discussed $^{\mathrm{nat}}\mathrm{Cu}(^{12}\mathrm{C},\mathrm{X})^{24}\mathrm{Na}$ reaction. The both of forward and inverse system of TTYs may be a possible reaction to measure experimentally and our method would be tested. Furthermore, the TTY of carbon-induced reaction on the cesium lump has been estimated from the cesium-induced reaction on a carbon target as an example of radioactive material case. A better projectile which has large probability and stable residual particles would exist and be searched in the future.

References

[1] W. S. Yang, Y. Kim, R. N. Hill, T. A. Taiwo and H. S. Khalil, Nucl. Sci. Eng. 146, 291 (2004).

[2] M. Igashira, T. Katabuchi, H. Harada, S. Nakamura, A. Kimura, N. Iwamoto and J. Hori, Y. Kiyanagi, Nucl. Data Sheets 118, 72 (2014).

[3] H. S. Jung, , C. S. Lee, Y. K. Kwon, J. Y. Moon, J. H. Lee, C. C. Yun, M. J. Kim, T. Hashimoto, H. Yamaguchi, D. Kahl, S. Kubono, Y. Wakabayashi, Y. Togano, S. Choi, Y. H. Kim, Y. K. Kim, J. S. Park, E. J. Kim, C.-B. Moon, T. Teranishi, N. Iwasa, T. Yamada, S. Kato, S. Cherubini, S. Hayakawa and G. C. Rapisarda, Phys. Rev. **C90**, 035805 (2014).

[4] N. Otuka and S. Takács, Radiochim. Acta, 103, pp.1-6 (2015).

[5] H. Yashima, , Y. Uwamino, H. Sugita, T. Nakamura, S. Ito and A. Fukumura, Phys. Rev. **C66**, 044607 (2002).

[6] J. F. Ziegler, J. P. Biersack and M. D. Ziegler, SRIM: the Stopping and Range of Ions in Matter, http://www.srim.org.

This is a blank page.

41 Measurement of Neutron-Capture Cross Section of ^{120}Sn with the array of Ge Spectrometer at the J-PARC/MLF/ANNRI

A.Kimura[1)], H.Harada[1)], S.Nakamura[1)], Y.Toh[1)], M.Igashira[2)], T.Katabuchi[2)], M.Mizumoto[2)], J.Hori[3)], K.Kino[4)]

1) Japan Atomic Energy Agency
Nuclear Science and Engineering Center, Japan Atomic Energy Agency
2-4 Shirakata Shirane, Tokai, Naka, Ibaraki 319-1195, Japan
2) Research Laboratory for Nuclear Reactors, Tokyo Institute of Technology
3) Research Reactor Institute, Kyoto University
4) Faculty of Engineering, Hokkaido University
e-mail: kimura.atsushi04@jaea.go.jp

The neutron-capture cross section of ^{120}Sn was measured in the energy range from 10 meV to 2 keV with an array of germanium detectors in ANNRI at J-PARC. The preliminary result of the neutron-capture cross section was obtained by normalizing the relative cross sections to the data in JENDL 4.0 at the 3rd and 4th resonances. Two miss assigned resonances were found on ENDF/B VII.1.

1. Introduction

In the study of transmutation of radioactive waste, accurate data of the neutron-capture cross section for long-lived fission products (LLFPs) are required. ^{126}Sn, which is included in spent-fuels of light water reactors with relatively large yields, is one of the most important LLFPs. However, for ^{126}Sn, there is only one experimental data at the thermal energy[1]. Accurate cross-section measurements for ^{126}Sn are required.

A ^{126}Sn sample for a nuclear data experiment contains a large amount of tin stable isotopes, $^{115, 117\text{-}120, 122, 124}$Sn, because they also have fission yields and the sample is normally prepared only through a chemical process from spent-fuels. These isotopes have large effects on neutron-capture cross-section measurements for ^{126}Sn. Therefore, to obtain accurate cross-section data for ^{126}Sn, a series of neutron-capture cross-section measurements for all the tin stable isotopes have been started with Accurate Neutron-Nucleus Reaction measurement Instrument (ANNRI) of Materials and Life science experimental Facility (MLF) in Japan Proton Accelerator Research Complex (J-PARC). The preliminary results of the neutron-capture cross sections for ^{112}Sn and ^{118}Sn have been reported in ND2013[2]. In this

presentation, preliminary result of the neutron-capture cross-section for ^{120}Sn is reported in the neutron energy range from 10 meV to 2 keV.

2. Experimental Procedure

The measurement was performed with an array of Ge spectrometer in ANNRI. The spectrometer is located on the flight length of 21.5-m and composed of two cluster-Ge detectors, eight coaxial-Ge detectors and anti-coincidence shields around each Ge detector.[3] In the measurements, two cluster Ge detectors were used, but the coaxial Ge detectors were not used because they suffered from severe electrical noise. The pulsed neutron beam was collimated to a 7mm at the sample position. J-PARC was operated with a proton beam power of 270kW and at a repetition rate of 25 Hz in the “double-bunch mode", in which each proton pulse consists of two bunches (each with a width of 100 ns) at intervals of 600 ns.

The ^{120}Sn Sample was isotopically enriched metallic tin with a diameter of 5 mm. The weight of the sample was 68.7 mg. The isotopic enrichment for the sample was 98.8mole% with 0.12, 0.1, 0.3, 0.4, 0.15 and 0.1 mole% isotopic contaminations of $^{116, 117, 118, 119, 122, 124}$Sn. The sample was chemically contaminated with 60, 400, 500 and 600 ppm of Sb, Al, Fe and Si on the certification sheet. The sample was put in a bag of fluorinated ethylene propylene (FEP) films and attached to a sample holder. The sample holders were made of polytetrafluoroethylene (PTFE) and shaped into a 50 mm × 70 mm rectangular frame, which was made much larger than the size of the collimated neutrons (7 mm) to avoid background production by neutron beam. To deduce the background, measurements for a ^{208}Pb sample with a diameter of 5 mm, a weight of 159.7 mg, and an isotopic enrichment of 99.60 mole% and a sample holder with an empty FEP film were also carried out. The total measuring time was about 63 hours for the ^{120}Sn sample, about 22 hours for the blank sample and 16 hours for the ^{208}Pb sample.

3. Data analysis

The dead time of the data acquisition system was corrected using the random timing pulses [4]. The frame-overlap backgrounds were deduced and subtracted in almost the same manner as that described in Ref. [5]. The time-of-flight dependent backgrounds were estimated using the capture γ-ray yields for the ^{208}Pb sample and the blank sample. Correction factors for neutron self-shielding and multiple scattering were calculated with the Monte Carlo simulation code. The neutron spectrum was measured by detecting the 478-keV γ rays emitted from the ^{10}B(n,αγ)^{7}Li reaction. The energy dependence of the relative cross-section, for ^{120}Sn were deduced by dividing the obtained capture yield by the neutron spectrum. At last, The preliminary result of the neutron-capture cross section was obtained by normalizing the relative cross sections to the data in JENDL 4.0 at the 3rd and 4th resonances.

4. Preliminary result

The obtained neutron-capture cross section for ^{120}Sn is shown in **Figure 1** together with values of JENDL-4.0 for T = 300 K (broadened with the resolution function **[6]**) and those of the other impurities. The 67.32- and 150-eV resonances were not observed although they were listed on ENDF/B VII.1.

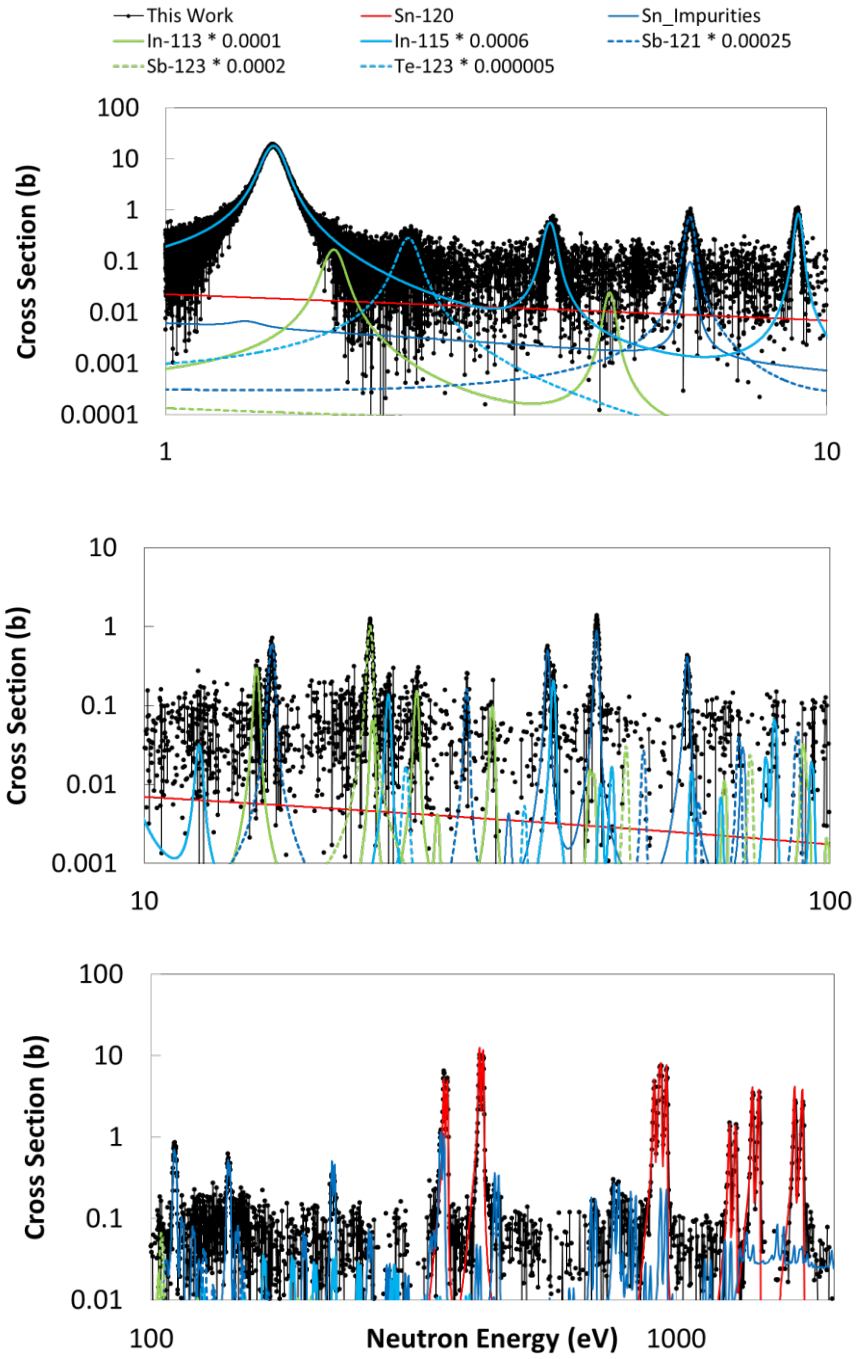

Fig.1 Preliminary results of the neutron-capture cross-sections for ^{120}Sn together with values of JENDL-4.0 for T = 300 K (broadened with the resolution function **[6]**) and those of the other impurities.

5. Summary

The neutron-capture cross section of ^{120}Sn was measured in the energy range from 10 meV to 2 keV with an array of germanium detectors in ANNRI at J-PARC. The preliminary result of the neutron-capture cross section was obtained by normalizing the relative cross sections to the data in JENDL 4.0 at the 3rd and 4th resonances. Two miss assigned resonances were found on ENDF/B VII.1.

This work is supported by JSPS KAKENHI (22226016).

References

[1] S. Zhang, *et al.*, *Radiochimica Acta* **94**, 385, (2006)

[2] A. Kimura, *et al.*, *Nuclear Data Sheets.*, **119**, 150, (2014).

[3] T. Kin, *et al.*, *the 2009 NSS-MIC Conf. Rec.*, Orland USA, Oct. 25-31, 2009 (2009),

[4] A. Kimura, *et al.*, *Int. Conf. on ND 2004*, Santa Fe, USA, Sept. 27 - Oct. 1 2004, *AIP Conference Proceedings*, **769** (2005), pp. 792-795.

[5] K. Hirose, *et al.*, *J. Nucl. Sci. Technol.*, **50**, (2013) 188.

[6] K. Kino *et al.*, *Nucl. Instrum. Methods. Phys. Res. A* **736,** 66 (2014).

42 ^{243}Am neutron-induced capture cross section measurement with a large coverage HPGe detector at ANNRI/J-PARC

Leong Lou Sai, Kimura Atsushi, Nakamura Shoji, Iwamoto Osamu, Harada Hideo

Japan Atomic Energy Agency, Tokai-mura, Ibaraki 319-1195, Japan

Neutron-induced cross sections of Minor Actinides (MAs) are needed data for neutron-based applications like nuclear reactors, where thermal and epithermal fluxes are among the most applied channels.

ANNRI is an outstanding neutron facility, which uses neutrons produced by spallation at the MLF/J-PARC. The neutron spectrum of ANNRI spans from thermal to intermediate energies. In addition, due to the high power (280 kW), it achieves the highest flux of this spectrum compared to other facilities. Therefore, it is a well-suited facility for neutron cross section measurements. Besides, as the MLF delivers a pulsed neutron beam, it allows measuring the energy dependence of the cross section by using a time of flight (TOF) method.

^{243}Am is considered as a high-level waste because of its long half-life. This nuclide is produced in reactors primarily by the successive neutron capture in plutonium isotopes. Neutron capture in ^{243}Am followed by β- decay lead to ^{244}Cm, which has an intense spontaneous fission rate and hence a very high activity. Therefore, an accurate knowledge of the neutron capture cross section of ^{243}Am is required. Currently, few data exist below 250 eV, except for data from measurements at thermal energy (0.0025eV)[1][2]. These data are very discrepant.

^{243}Am (n,γ) cross section was measured at ANNRI using the TOF method. In this experiment, we used HPGe detectors that covered a substantial fraction of the solid angle. Ge detectors can achieve a very high energy resolution. It permits to obtain efficiently the mass of sample impurities by identify the intensity (I_γ) of gamma decay. In this work, we focused the analysis on the capture rate to extract the corresponding cross section. We will show how the dead time correction, and the background estimation were estimated to derive the capture yield.

Ackowledgement
This work is supported by JSPS KAKENHI (22226016).

[1] Masayuki OHTA, et al. J. Nuclear Sciene and Technology
Vol. 43, No. 12, p. 1441–1445 (2006)
[2] Mughabghab,S.F. and Dunford,C.L., Proc.Int.Conf. on Phys
of Nuclear Sciene and Technology, Long Island, New York p. 784.

This is a blank page.

43 Evaluation of Delayed Neutron Data of the Photo-Fission

T. Murata*[1], N. Iwamoto[2] and K. Kosako[3]
1) High Energy Nuclear Data Evaluation WG, JENDL Committee
2) Nuclear Data Center, JAEA,
3) Institute of Technology, Shimizu Corporation
*E-mail : t.murata.phd@kdt.biglobe.ne.jp

Abstract

The delayed neutron data of the photo-fission were evaluated tentatively, utilizing the data of neutron induced fission of the same compound nucleus. The existent methods of P_n calculation were tested and a new formula for P_n estimation is presented.

1. Introduction

Development of non-destructive assay technic of nuclear materials is required for the nuclear safeguard and nuclear security, especially for high level radioactive wastes such as vitrified solids. For these objects, irradiation of high transparent gamma rays and detection of fission responses with high discrimination with irradiation rays are required and will be attained with high energy photon irradiation and delayed neutron detections.

To study the feasibility of the methods and to design the apparatus, the delayed neutron data are requested. So, the present status of evaluation method of the data was studied. The existent methods of delayed neutron emission probability P_n of the precursor nuclides are summarized shortly and a new method of P_n estimation is presented.

2. Tentative evaluation of the delayed neutron data

The data will be obtained approximately by utilizing neutron induced fission delayed neutron data of JENDL-4.0[(1)] or by M. C. Brady and T. R. England [(2)] for the same fissioning compound nucleus as the photo-fission. The results are summarized in **Table 1**.

In the case of same compound nucleus whose data were not available, group delayed neutron intensities (such as, six groups or so) will be calculated with the method given by M. C. Brady and T. R. England [(2)] with the cumulative fission yields systematics given by A. C. Wahl [(3)]. To prepare the evaluation method for the delayed neutron data of the photo-fission, neutron induced fission data were analyzed with two existing methods of delayed neutron emission probability P_n calculation, one developed by Kratz-Herrmann[4] and another by McCutchan et al.[5] recently.

Table 1. Tentative results of delayed neutrons of photo-fission

A: six-group delayed neutron amplitudes (relative), λ: decay constant (1/sec)

Target	j	1	2	3	4	5	6	En	Eg(MeV)	ν_d
U233	A	0.1360	0.2745	0.1509	0.3052	0.1007	0.0326	(T)	5.743	0.52+/-0.08
(U232+n)	λ	0.0128	0.0350	0.1073	0.2557	0.6620	2.0254			
U235	A	0.0550	0.1964	0.1803	0.3877	0.1324	0.0482	(F)	En+5.298	1.29+/-0.15
(U234+n)	λ	0.0131	0.0337	0.2110	0.2952	0.8136	2.5721			
	A	0.0808	0.1880	0.1791	0.3888	0.1212	0.0420	(H)	En+5.298	0.77+/-0.11
	λ	0.0128	0.0364	0.1256	0.2981	0.8475	2.5696			
U238	A	0.0178	0.1477	0.1445	0.3864	0.2095	0.0941	(F)	En+5.298	3.50+/-0.28
(U237+n)	λ	0.0138	0.0316	0.1211	0.3162	0.9073	3.0368			
Pu239	A	0.0377	0.2390	0.1577	0.3562	0.1590	0.0504	(F)	En+5.647	0.79+/-0.09
(Pu238+n)	λ	0.0133	0.0312	0.1162	0.2888	0.8561	2.7138			
Pu240	A	0.0306	0.2623	0.1828	0.3283	0.1482	0.0479	(T)	6.533	0.76/-0.04
(Pu239+n)	λ	0.0133	0.0301	0.1135	0.2953	0.8537	2.6224			
	A	0.0363	0.2364	0.1789	0.3267	0.1702	0.0515	(F)	En+6.533	0.68+/-0.08
	λ	0.0133	0.0309	0.1134	0.2925	0.8575	2.7297			
	A	0.0678	0.1847	0.1553	0.3685	0.1750	0.0487	(H)	En+6.533	0.38+/-0.06
	λ	0.0129	0.0353	0.1215	0.2885	0.8486	2.5587			

3. Existent methods of P_n calculation

(Kratz-Herrmann)

Delayed neutron emission probability P_{ni} of the precursor i is given by

$$Pn = a\left[\frac{Eb - Ens}{Eb - K}\right]_i^b , \qquad (1)$$

where E_b is the Q-value of the beta decay of precursor nuclide, and E_{ns} is the neutron separation energy of the daughter nuclide, K depends on the even-odd of the precursor nuclide (K=0 for even-even, K=13/$\sqrt{A}$ for odd A and K=26/$\sqrt{A}$ for odd-odd nuclides), constant b was determined to be 3.44+/-0.51.

(McCutchan et al.)

$$\mathrm{Pn} = \frac{\int_{\mathrm{Ens}}^{\mathrm{Ebx}} \mathrm{Sb(Eb)dEb}}{\int_{0}^{\mathrm{Ebx}} \mathrm{Sb(Eb)dEb}} \ , \qquad (2)$$

where $Sb(E_b)$ is the beta ray energy spectrum, E_{bx} is the maximum energy of beta rays and E_{ns} neutron separation energy of the daughter nuclide.

Presently, beta ray energy spectra were calculated approximately with allowed transition spectra[6]. Exactly, the spectra include beta decay strength function, which has nuclear structure dependence caused by the isobaric spin of daughter nucleus levels and may have structures caused by neutron emission strength related with the compound nuclear formation cross section of the final nucleus plus a neutron. The latter structure is shown quantitatively in section 5.

4. Delayed neutron yields calculation

Delayed neutron yields were given by summing up for all precursors

$$\nu_d = \sum_i \mathrm{Yc}_i P_{ni} \ , \qquad (3)$$

where Y_{Ci} is the cumulative fission yield of precursor i.

Time dependence of the delayed neutron density after fission was given by summing up for all precursors (presently 86 nuclides, including 6 metastable nuclides):

$$n_d(t) = \sum_{i=1}^{i=max} A_i e^{-\lambda_i t} \ . \qquad (4)$$

Usual six-group sum of exponential decay is

$$n_d(t) = \sum_{j=1}^{j=6} A_j e^{-\lambda_j t} \ . \qquad (5)$$

Results are shown in **Figs.1-4** for the ^{235}U and ^{239}Pu thermal neutron fission.

The discrepancy between sum of the present precursors calculation (shown by circles) and six-group data based on the experiments by G. R. Keepin referred in the reference (2) may be originated from the insufficiency of the precursors or the P_n model. Further studies should be made.

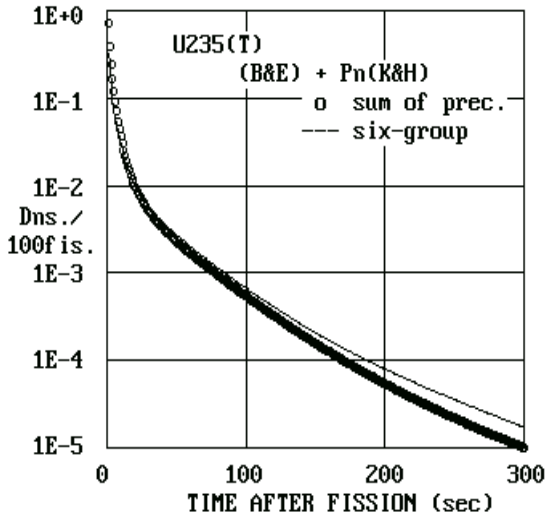

Fig.1 Brady & England 6-group parameters with Pn (Kratz-Herrmann) and J-4 FP-yields of JENDL-4.0

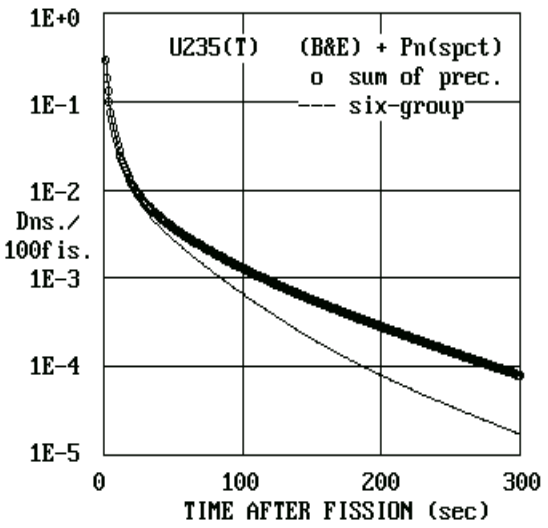

Fig.2 Brady & England 6-group parameters with Pn (spct) and J-4 FP-yields of JENDL-4.0, where Pn (spct) was calculated with the method by McCuthan et al.

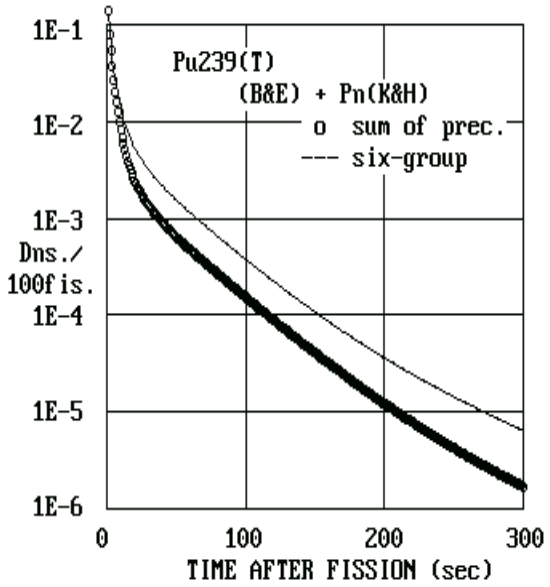

Fig.3 Brady & England 6-group parameters with Pn (Kratz-Herrmann) and FP-yields of JENDL-4.0

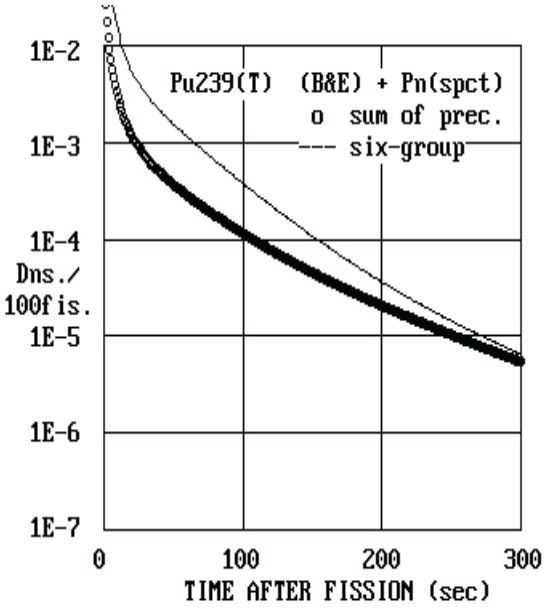

Fig.4 Brady & England 6-group parameters with Pn (spct) and FP-yields of JENDL-4.0, where Pn (spct) was calculated with the method by McCuthan et al.

5. New model of the delayed neutron emission probability P_n

Though the above mentioned P_n models depend on the final state only on the neutron separation energy E_{ns}, it depends on the intensity of single neutron structure of the final states which is given by optical model reaction cross sections of neutron incident. Energy scheme of the delayed neutron emission of the precursor I-137 is shown in **Fig.5**, as an example.

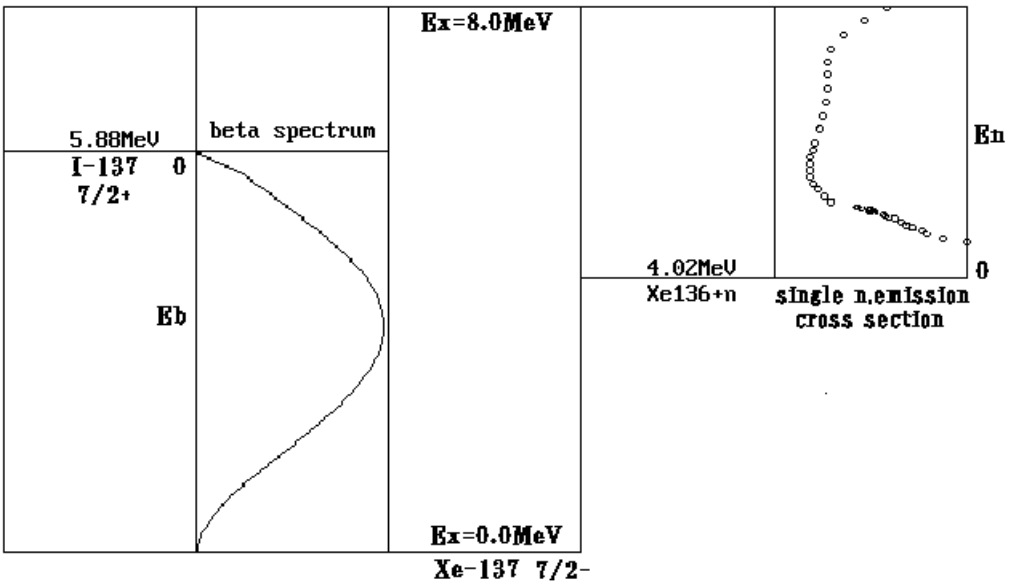

Fig.5 Energy scheme of I-137 beta decay and delayed neutron emission.

From the left side of Fig.5, I-137 ground state, beta ray energy spectrum, Xe-137 excitation energy (the lowest is the ground state of Xe-137), Xe-136 +n state and cross section of Xe-136+1n reaction (circles show JENDL4.0; MF=3, MT=4). Initial state density of the delayed neutron emission process corresponds to the beta ray spectrum and the final state density corresponds to the single neutron emission cross section. For some other nuclides, the relevant cross sections are shown in **Fig.6**.

So, the present P_n is described as

$$Pn = \frac{\int_{Ens}^{Ebx} Sb(Ex) \int_0^{Ex-Ens} \sigma(En)dEn \cdot dEx}{\int_0^{Ebx} Sb(Ex) \int_0^{Ebx-Ens} \sigma(En)dEn \cdot dEx} \quad , \qquad (6)$$

where σ is the single neutron emission cross section at $E_n=E_x-S_n$ and is shown in Fig.6. Below the (n,2n) reaction threshold energy, the cross section nearly equals to the compound nucleus formation cross section, which is obtained easily with the deformed potential optical model, and decreases rapidly with neutron energy above the (n,2n) reaction threshold energy. Numerical calculation of the present P_n was not yet completed.

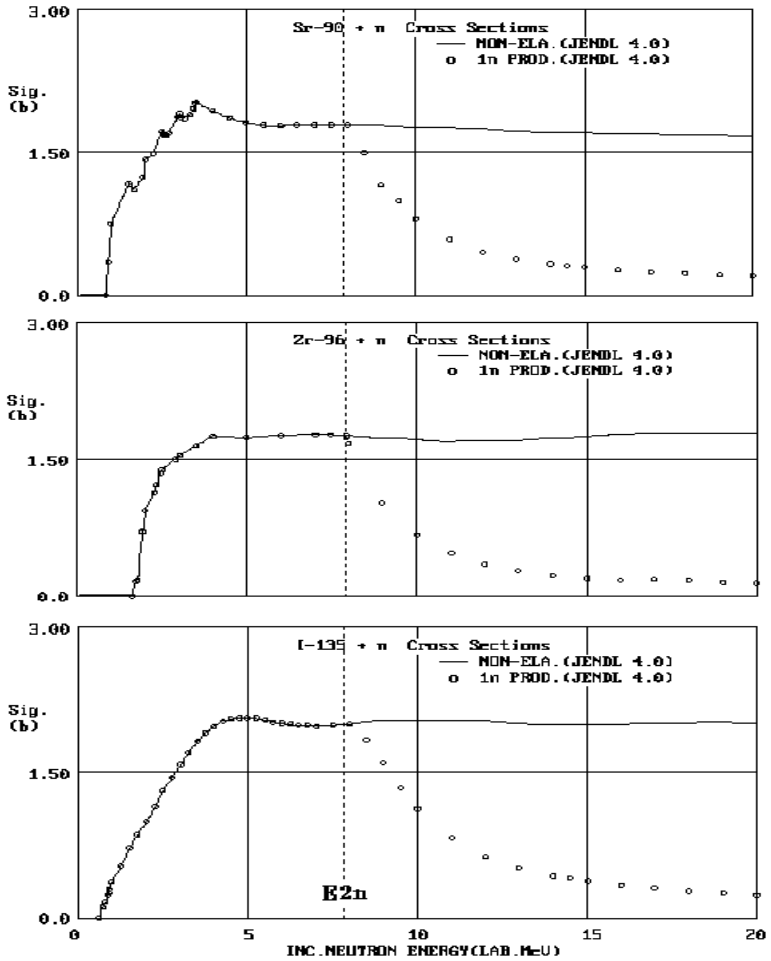

Fig.6 Examples of single neutron emission cross sections (shown by circles) and compound nucleus formation cross sections (shown by solid line). Dashed lines show threshold energy of the (n,2n) reactions.

REFERENCES

(1) K. Shibata et al., J. Nucl. Sci. Technol., **48**, 1 (2011).
(2) M. C. Brady and T. R. England, Nucl. Sci. Eng., **103**, 129 (1989).
(3) A. C. Wahl, IAEA-STI/PUB/1286, p.117 (2008).
(4) K. -L. Kratz and G. Herrmann, Z. Phys, **263**,435 (1973).
(5) E. A. McCutchan et al., Nucl. Data Sheets, **120**, 62 (2014).
(6) M. A. Preston, Physics of the Nucleus, p.424 (1962), Addison-Wesley Pub. Inc.

44 Nuclear data for shielding design on International Linear Collider

Toshiya Sanami
High energy accelerator research organization

The international linear collider (ILC) is an electron-positron collider with energies up to 500 GeV for elementary physics studies. The collider, the detail of which is published as a technical design report (TDR) on 2013, is under design phase with considering a model site located in Japan. To complete the design process, the shielding design is indispensable for mitigating leakage of radiation and induced activities cased by beam losses of high energy intense electron/positron. In this presentation nuclear data required for the shielding design on ILC is discussed with overview of ILC accelerators and it's beam losses.

This is a blank page.

45 Verification of the Cd-ratio method in ^{241}Am using JENDL-4.0

Kazuhito Mizuyama, Nobuyuki Iwamoto, and Osamu Iwamoto
Nuclear Science and Engineering Center, Japan Atomic Energy Agency
Tokai-mura, Naka-gun, Ibaraki-ken 319-1195, Japan
e-mail: mizuyama.kazuhito@jaea.go.jp

The Cd-ratio method has been widely used for the determination of the thermal neutron capture cross section σ_0. However, there is large discrepancy among the previous measurements for minor actinides (MAs). Especially, the Cd-ratio method tends to provide the larger values than the TOF measurements of ^{241}Am. This may be due to the contribution of the 1st resonance of ^{241}Am which appears below the cut-off energy ($\sim$ 0.5 eV). By reviewing the Westcott's formulation and verifying the Cd-ratio method by using the JENDL-4.0, we found out the way to correct the Cd-ratio method by taking account the contribution of the 1st resonance. We applied the present correction method to the analysis of Shinohara *et al.*, then $\sigma_0 = 689$ b was obtained.

1 Introduction

The minor actinides (MAs) are very important in the nuclear waste problem because of their long term radiotoxicity. One of the most important MAs is ^{241}Am, because it is abundant in the spent nuclear fuel. The high precision of the neutron capture cross section of ^{241}Am is required in order to measure the total amount of the ^{241}Am in the nuclear waste. Nevertheless, the thermal neutron capture cross section of ^{241}Am has large uncertainty (see **Table 1**). In addition, the cross section measured by the activation method has a trend to provide larger values than the time-of-flight (TOF) method. The activation technique requires the Westcott's conventional representation for the reaction rate [1]. The Cd-ratio method is one of the well-known methods to deduce the value of the thermal cross section σ_0 and the resonance integral I_0. Rather reasonable results have been obtained in many isotopes successively, so far.

The Cd-ratio method is used in the experiments [2–5] listed in Table 1, in which thermal capture cross sections of ^{241}Am are summarized. Especially, the results of Ref. [3–6] are much larger values by around 20 % than those of TOF method. The reason of the overestimation has been roughly understood [7]. It would be due to the special structure of the resonances in ^{241}Am. ^{241}Am has huge resonances at neutron energies of 0.308 and 0.573 eV. In the Cd-ratio method, normally the cut-off energy of 0.5 eV has been adopted. The Cd-cover can not filter the contribution of the 1st resonance of ^{241}Am. The contribution of the 1st resonance to the reaction rate would give the overestimation in the results. The correction of the low-lying resonances was taken into account by using the Monte Carlo simulation in Ref. [2], but the detailed correction method was not explained. In order to correct the results of the previous measurements, it is necessary to make clear the quantitative contribution of the 1st resonance in the Cd-ratio method.

Therefore the purpose of this study is to quantitatively make clear the contribution of the 1st resonance in ^{241}Am by verifying the Cd-ratio method with use of the JENDL-4.0 [8]. Firstly, we shall review the Westcott's formulation and the Cd-ratio method, and introduce the correction term of the s-factor δs_0 which contains the contribution of the lower resonances than the cut-off energy in Sec. 2.

Then, in Sec. 3, we verify the Cd-ratio method by using the JENDL-4.0, and show the quantitative contribution of the 1st resonance of ^{241}Am by the correction δs_0. We apply the correction by δs_0 to the analysis of Shinohara *et al.* [3].

Table 1. Experimental data for the thermal capture cross section of ^{241}Am.

Author(Year)	Method	σ_0[b]	Ref.
Fraval+(2014)	TOF	678±68	[9]
Jandel+(2008)	TOF	665±33	[10]
Bringer+(2007)	Activation, Av.CS*	705±23	[11]
Fioni+(2001)	Activation, Av.CS*	696±48	[12]
Maidana+(2001)	Activation, Cd-ratio**	602±9	[2]
Shinohara+(1997)	Activation, Cd-ratio	854±58	[3]
		689 (This work)	
Gavrilov+(1976)	Activation, Cd-ratio	853±52	[4]
Bak+(1967)	Activation, Cd-ratio	740±60	[5]
Harbour+(1973)	Activation, Rel. ^{59}Co***	832±20	[6]
JENDL-4.0	Evaluation	684	[8]

* The averaged cross section was used for the determination of the thermal cross section.

** The contribution of the 1st resonance was corrected by using the Monte Carlo simulation.

*** The neutron capture cross section was measured relative to ^{59}Co.

2 Westcott's convention and Cd-ratio method

The original definition of the reaction rate is given by

$$R(T_1, T_2) = \frac{1}{m}\int_0^\infty dE n(E, T_1)\sigma(E, T_2), \tag{1}$$

where $\sigma(E, T_2)$ is the neutron capture cross section, E is the neutron energy, T_1 and T_2 are the temperature of the neutron flux and the temperature of the target under the condition of the irradiation in the reactor respectively, and m is the mass of the neutron.

The neutron flux distribution $n(E, T)$ is given by

$$n(E, T) = n_0(1-f)\rho_m(E, T) + n_0 f\rho_e(E, T), \tag{2}$$

where n_0 is the neutron density, f is the parameter of the neutron flux to determine the fraction of the thermal and epithermal components. The Maxwellian and epithermal density distribution functions ρ_m and ρ_e are defined by

$$\rho_m(E, T) = \frac{4}{\pi^{\frac{1}{2}} v_0}\sqrt{\frac{T_0}{T}}\frac{E}{kT}e^{-\frac{E}{kT}}, \tag{3}$$

$$\rho_e(E, T) = \frac{\mu^{\frac{1}{2}}}{2} m v_0 \sqrt{\frac{T}{T_0}}\frac{\Delta(E)}{E}, \tag{4}$$

$$\Delta(E) = \theta(E - \mu kT) \sim \frac{1}{1 + (\mu kT/E)^{16}}, \tag{5}$$

where k is the Bolzmann's constant, $v_0 = 2200$ m/s, $T_0 = 293.6$ K. $\Delta(E)$ is a step function with a lower energy limit of μkT.

By inserting the neutron distribution function Eq. (2) into the definition of the reaction rate R Eq. (1), the Westcott's conventional representation of the reaction rate is derived straightforwardly as,

$$R(T_1,T_2) = \left(g(T_1,T_2)\phi_1 + \phi_2(T_1)s_0(T_1,T_2)\right)\sigma_0, \tag{6}$$

$$g(T_1,T_2) = \sqrt{\frac{T_1}{T_0}}\frac{2}{\pi^{\frac{1}{2}}\sigma_0}\frac{\int_0^\infty dE\frac{E}{kT_1}e^{-\frac{E}{kT_1}}\sigma(E,T_2)}{\int_0^\infty dE\frac{E}{kT_1}e^{-\frac{E}{kT_1}}}, \tag{7}$$

$$\phi_1 = n_0 v_0, \qquad \phi_2(T_1) = n_0 v_0 \frac{f\mu^{\frac{1}{2}}\pi^{\frac{1}{2}}}{4}\sqrt{\frac{T_1}{T_0}}, \tag{8}$$

$$s_0(T_1,T_2) = \frac{2}{\pi^{\frac{1}{2}}\sigma_0}\int_{\mu kT_1}^\infty \frac{dE}{E}\left(\sigma(E,T_2) - \sqrt{\frac{E_0}{E}}g(T_1,T_2)\sigma_0\right), \tag{9}$$

where E_0 is the thermal neutron energy.

The Cd-covered reaction rate R' is defined by

$$R'(T_1,T_2) = \frac{1}{m}\int_0^\infty dE\Delta_F(E,h)n(E,T_1)\sigma(E,T_2). \tag{10}$$

The neutron transmission through the Cd-cover $\Delta_F(E,h)$ is given by

$$\Delta_F(E,h) = \exp(-\sigma_{Cd}(E)\rho_{Cd}h), \tag{11}$$

where $\sigma_{Cd}(E)$, ρ_{Cd} and h are the absorption cross section, the density of the Cadmium and the thickness of the Cd-cover, respectively. $\Delta_F(E,h)$ is shown as a function of the neutron energy in **Figure 1**.

The Westcott's conventional representation with the Cd-cover is also derived as

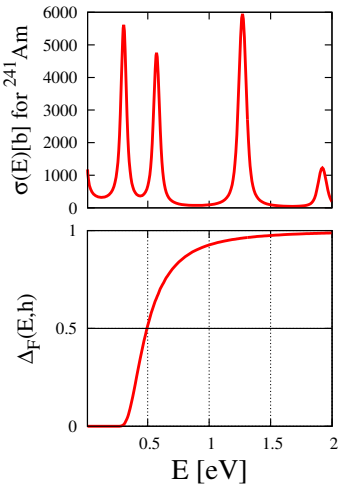

Figure 1. The capture cross section of ^{241}Am at low-energy region (upper panel), and the neutron transmission $\Delta_F(E,h)$ (Eq.(11)) through the Cd-cover with the thickness $h = 0.1$ cm (lower panel) respectively. For each panel, the JENDL-4.0 was used.

$$R'(T_1,T_2) = \left(g(T_1,T_2)\phi_1'(T_1) + \phi_2'(T_1)s_0^C(T_1,T_2)\right)\sigma_0, \tag{12}$$

$$\phi_1'(T_1) \approx n_0 v_0 \frac{f\mu^{\frac{1}{2}}\pi^{\frac{1}{2}}}{4}\sqrt{\frac{T_1}{T_0}}\frac{1}{K}, \tag{13}$$

$$\phi_2'(T_1) = n_0 v_0 \frac{f\mu^{\frac{1}{2}}\pi^{\frac{1}{2}}}{4}\sqrt{\frac{T_1}{T_0}}, \tag{14}$$

$$s_0^C(T_1,T_2) = \frac{2}{\pi^{\frac{1}{2}}\sigma_0}\int_{\mu kT_1}^\infty \frac{dE}{E}\Delta_F(E,h)\left(\sigma(E,T_2) - \sqrt{\frac{E_0}{E}}g(T_1,T_2)\sigma_0\right), \tag{15}$$

$$\frac{1}{K} = \frac{2}{\pi^{\frac{1}{2}}}\int_{\mu kT_1}^\infty \frac{dE}{E}\Delta_F(E,h)\sqrt{\frac{E_0}{E}}. \tag{16}$$

$s_0^C(T_1,T_2)$ is approximately represented by

$$s_0^C(T_1,T_2) \approx \frac{2}{\pi^{\frac{1}{2}}\sigma_0}\int_{E_C}^{\infty}\frac{dE}{E}\left(\sigma(E,T_2)-\sqrt{\frac{E_0}{E}}g(T_1,T_2)\sigma_0\right) \tag{17}$$

with use of the cut-off energy E_C defined by

$$\Delta_F(E_C,h) \equiv \frac{1}{2}. \tag{18}$$

By using the difference between s_0 and s_0^C, δs_0 is defined by

$$\begin{aligned}\delta s_0(T_1,T_2) &\equiv s_0(T_1,T_2)-s_0^C(T_1,T_2)\\ &= \frac{2}{\pi^{\frac{1}{2}}\sigma_0}\int_{\mu kT_1}^{E_C}\frac{dE}{E}\left(\sigma(E,T_2)-\sqrt{\frac{E_0}{E}}g(T_1,T_2)\sigma_0\right).\end{aligned} \tag{19}$$

Note that this δs_0 expresses the contribution from the resonances after subtracting $1/v$ contribution within the energy range $\mu kT_1 \le E \le E_C$, and does not depend on the absolute values of $\sigma(E)$ by definition. Just only the shape of $\sigma(E)$ is necessary to deduce δs_0.

By using δs_0, the reaction rate without Cd-cover Eq.(6) can be represented by

$$R(T_1,T_2) = \Big(g(T_1,T_2)\phi_1+\phi_2(T_1)s_0^C(T_1,T_2)+\phi_2(T_1)\delta s_0(T_1,T_2)\Big)\sigma_0. \tag{20}$$

When the Cd-ratio method is used, the reaction rate R and R' for the target are measured from the experiment. The values of $\phi_1^{(')}$ and $\phi_2^{(')}$ are determined from the flux monitors (two sets of ^{59}Co and ^{197}Au wires). If one assumes $\delta s_0 = 0$, Eqs. (12) and (20) can be solved by using the values $R^{(')}$, $\phi_1^{(')}$ and $\phi_2^{(')}$, and then $s_0^C(T_1,T_2)$ and σ_0 are obtained as follows:

$$s_0^C(T_1,T_2) = -\frac{g(T_1,T_2)\left(\phi_1-\phi_1'(T_1)R(T_1,T_2)/R'(T_1,T_2)\right)}{\phi_2(T_1)-\phi_2'(T_1)(R(T_1,T_2)/R'(T_1,T_2))}, \tag{21}$$

$$\sigma_0=\sigma_{0,W} \equiv \frac{R(T_1,T_2)}{g(T_1,T_2)\phi_1+\phi_2(T_1)s_0^C(T_1,T_2)}. \tag{22}$$

Here we define $\sigma_{0,W}$ as a solution of the Eqs. (12) and (20) in order to distinguish the "true" $\sigma_0=\sigma(E_0)$.

In case of the ^{241}Am, one can not ignore the contribution of δs_0 because the 1st resonance exists at 0.308 eV ($< E_C = 0.5$ eV). Eqs. (21) and (22) should be modified by taking into account of the contribution of δs_0 as follows:

$$s_0^C(T_1,T_2) = -\frac{g(T_1,T_2)\left(\phi_1-\phi_1'(T_1)R(T_1,T_2)/R'(T_1,T_2)\right)+\phi_2(T_1)\delta s_0(T_1,T_2)}{\phi_2(T_1)-\phi_2'(T_1)(R(T_1,T_2)/R'(T_1,T_2))}, \tag{23}$$

$$\sigma_0=\sigma_{0,W} \equiv \frac{R(T_1,T_2)}{g(T_1,T_2)\phi_1+\phi_2(T_1)s_0^C(T_1,T_2)+\phi_2(T_1)\delta s_0(T_1,T_2)}. \tag{24}$$

3 Verification of the Cd-ratio method

In this section, we verify the Cd-ratio method by the quantity $(\sigma_{0,W}-\sigma(E_0))/\sigma(E_0)$, where $\sigma_{0,W}$ is obtained using the Cd-ratio R/R' from $\sigma(E)$ of JENDL-4.0, and $\sigma(E_0)$ is the thermal capture cross section originally given by the JENDL-4.0.

Firstly we calculate the reaction rate $R^{(')}$ for ^{241}Am, and then we obtain s_0^C and $\sigma_{0,W}$ from Eqs. (23) and (24) (or Eqs. (21) and (22)), respectively, for the results with (or without) δs_0 correction. The values of $\phi_1^{(')}$ and $\phi_2^{(')}$ are also fixed by using the reaction rate with the JENDL-4.0 for ^{59}Co and ^{197}Au.

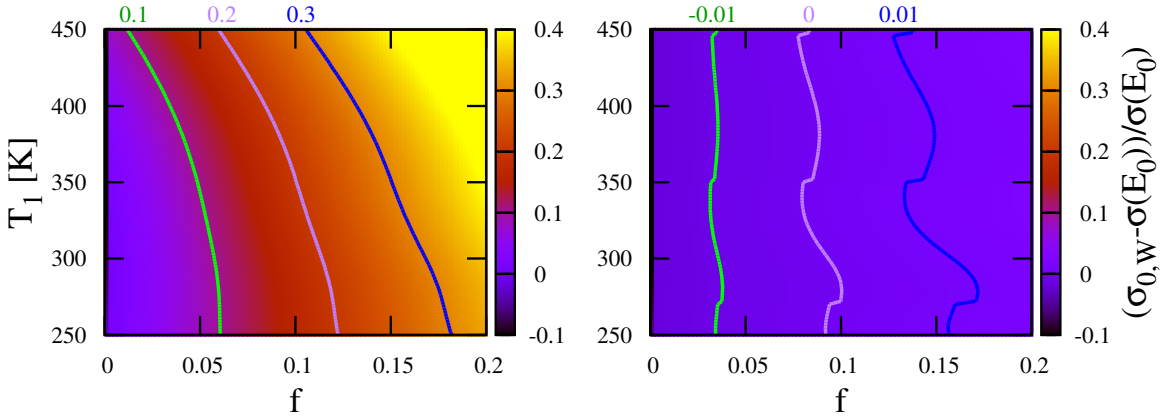

Figure 2. The contour graph of the quantity $(\sigma_{0,W} - \sigma(E_0))/\sigma(E_0)$ as a function of f and T_1 for ^{241}Am with the JENDL-4.0 The left (right) panel is the result without (with) δs_0 correction. In the left panel, g-factor is taken as 1 from the analysis [3], but in the right panel, the g-factor is calculated as a function of T_1 by using JENDL-4.0.

In **Figure 2**, we show the quantity $(\sigma_{0,W} - \sigma(E_0))/\sigma(E_0)$ as a function of f and T_1 under the condition of $\mu = 2.5$ and $T_2 = 410$ K[*1]. As seen from the left panel of Figure 2, $\sigma_{0,W}$ without the correction can be overestimated from the original value $\sigma(E_0)$ by maximally 40 %. For example, by looking at $f \sim 0.09$ and $T_1 \sim 313$ K which correspond to the experimental condition of Shinohara *et al.* [3] guessed from the values of the flux monitor, the overestimation would be 18 %. As shown in the right panel of Figure 2, the Cd-ratio method with the δs_0 correction reproduces the original value of JENDL-4.0 within a few percent. The correction by δs_0 reduces this overestimation. If one adopts $g(T_1, T_2) = 1$ in the right panel, the quantity increases by roughly 2 %, but the contribution of the g-factor is much smaller than δs_0.

By applying the δs_0 correction and the g-factor obtained from the JENDL-4.0, we obtain the corrected value $\sigma_{0,W} = 689$ b for the experimental data of Shinohara *et al.* [3]. This value is in good agreement with that of JENDL-4.0 and the measurements of the TOF method.

4 Summary

By reviewing the Westcott's convention and the Cd-ratio method, we found the correction term of s-factor δs_0 which contains the contribution of the lower resonances than the cut-off energy. In order to estimate their contributions quantitatively, we verified the Cd-ratio method by using the JENDL-4.0. Then we found that the contribution of the 1st resonance of ^{241}Am causes the overestimation by maximally 40% in this survey. Also we confirmed that the Cd-ratio method reproduces the original value of the JENDL-4.0 within a few percent by taking account of δs_0. We applied the present correction to the analysis of Shinohara *et al.* [3], then $\sigma_{0,W} = 689$ b was obtained.

Acknowledgement

The authors are grateful for the financial support of "Research and development for Accuracy Improvement of neutron nuclear data on Minor ACtinides (AIMAC)" project entrusted to Japan Atomic Energy Agency by Ministry of Education, Culture, Sport, Science and Technology of Japan (MEXT).

[*1] The deduced temperature of the target under the long-time neutron irradiation condition of JMTR [13].

References

[1] Westcott CH, Walker WH, Alexander TK. Effective cross sections and cadmium ratios for the neutron spectra of thermal reactors. In: Proc. 2nd Geneva Conf. 1958;16:70.

[2] Maidana NL, Mauro SD, Koskinas MF. Measurement of the thermal neutron capture cross section and resonance integral of ^{241}Am. Radiochim Acta. 2001;89:419-423.

[3] Shinohara N, Hatsukawa Y, Hata K, Kohno N. Radiochemical Determination of Neutron Capture Cross sections of ^{241}Am. J Nucl Sci Technol. 1997;34:613-621.

[4] Gavrilov VD, Goncharov VA, Ivanenko VV, Kustov VN, Smirnov VP. Thermal cross sections and resonance integrals of fission and capture of ^{241}Am,^{243}Am,^{249}Bk, and ^{249}Cf. Sov At Energy. 1976;41:808.

[5] Bak MA, Krivokhatskii AS, Petrzhak KA, Petrov YG, Romanov YF, Shlyamin EA. Cross sections and resonance integrals for capture and fission in long-lived americium isotopes. Sov At Energy. 1967;23:1059.

[6] Harbour RM, MacMurdo KW, McCrosson FJ. Thermalneutron capture across sections and capture resonance integrals of americium-241. Nucl Sci Eng.1967;50:1059.

[7] Nakamura S, Ohta M, Harada H, Fujii T, Yamana H. Thermal-Neutron Capture Cross Section and Resonance Integral of Americium-241. J Nucl Sci Technol. 2007;44:1500-1508.

[8] Shibata K, Iwamoto O, Nakagawa T, Iwamoto N, Ichihara A, Kunieda S, Chiba S, Furutaka K, Otuka N, Ohsawa T, Murata T, Matsunobu H, Zukeran A, Kamada S, Katakura J. JENDL-4.0: A New Library for Nuclear Science and Engineering. . J Nucl Sci Technol. 2011;48(1):1-30. .

[9] Fraval K, et al.(n_TOF Collaboration). Measurement and analysis of the ^{241}Am(n,γ) cross section with liquid scintillator detectors using time-of-flight spectroscopy at the n_TOF facility at CERN. Phys Rev C. 2014;89:044609.

[10] Jandel M, Bredeweg TA, Bond EM,Cahdwick MB, Clement RR, Couture A, O'Donnell JM, Haight RC, Kawano T, Reifarth R, Rundberg RS, Ullmann JL, Vieira DJ, Wilhelmy JB, Wouters JM, Agvaanluvsan U, Parker WE, Wu CY, Becker JA. Neutron capture cross section of ^{241}Am. Phys Rev C.2008;78:034609.

[11] Bringer O, AIMahamid I, Chabot A, Chartier F, Dupont F, Letourneau A, Mutti P, Oriol L, Panebianco S, Veyssière C. Measurement of thermal fission and capture cross sections of minor actinides within the Mini-INCA project. In: Proceedings of the International Conference on Nuclear Data for Science and Technology 2007;DOI: 10.1051/ndata:07612.

[12] Fioni G, Cribier M, Marie F, et al. Incineration of ^{241}Am induced by thermal neutrons. Nucl Phys A. 2001;693:546.

[13] N. Shinohara. private comminication.

46 A Burnup Calculation for Creation of Palladium by Nuclear Transmutation

Atsunori TERASHIMA[1] and Masaki OZAWA[2]
[1] Department of Nuclear Engineering, Graduate School of Science and Engineering,
Tokyo Institute of Technology, 2-12-1-N1-21 Ookayama, Meguro-ku, Tokyo 152-8550, Japan
[2] Research Laboratory for Nuclear Reactors, Tokyo Institute of Technology,
2-12-1-N1-21 Ookayama, Meguro-ku, Tokyo 152-8550, Japan
e-mail: terashima.a.aa@m.titech.ac.jp

The purpose of this study is creation of palladium with low radioactivity which can be considered as resources by nuclear transmutation of rhodium in fission products. Assuming to create palladium in a PWR by neutron capture reaction and beta decay of rhodium target which was separated and recovered from spent nuclear fuels of PWRs, a burnup calculation was performed by using 3-dimensional Monte Carlo simulation code; MVP-BURN.

1. Introduction

Recently, many rare elements are needed in various fields, and there are supply risks of these elements in Japan. Otherwise, spent nuclear fuels include rare earth, platinum group metals (PGM), and other useful elements. But, most of these elements have very strong radioactivity or long half-life that cannot be considered as resources. Thus, our research aims at creating highly-valuable elements with low radioactivity by nuclear transmutation of another element in fission products (FPs).

In this paper, the target of research was focused on the creation of palladium (Pd) by transmutation of rhodium (Rh). Comparison of Rh (irradiated element) and Pd (created element) is shown in Table 1. Price and demand were the data in 2013[1], and yield and cooling period were calculated by using ORLIBJ40 package[2]. Both Rh and Pd are PGM elements mainly used as catalyst for removing exhaust gas in automobiles. Although price of Pd is lower than Rh, demand of Pd is ten times larger than that of Rh. Otherwise, spent nuclear fuels include both Rh and Pd. However, when they were recovered and used as resources, they need long-cooling period because of their strong radioactivity. In addition, Pd in FPs includes ^{107}Pd which is very long half-life (3.3×10^{7} years), so this Pd could not be recycled unless isotope separation would be performed. Therefore, it is considered to be meaningful to transmute Rh in FPs into Pd with non-radioactivity.

2. Calculation Method

2.1 Condition of Calculation

In this study, assuming to use 1100MW class PWR reactor and irradiate neutron 1 year (360 days), assembly calculation was performed by using Monte Carlo simulation code; MVP-BURN[3] and neutron cross section library; JENDL-4.0[4]. Main reactor parameters of PWR are shown in Table 2. Then, in the burnup calculation, the number of steps, histories, and batches were 12, 5000/step, and 100/step (burnup step period is 30 days/step).

Figure 1 is design of PWR assembly in this simulation. Assuming to replace inner region of control rod guide thimble from water to Rh target pin, form and smeared density of target Rh were changed as parameters (Table 3).

Table 1: Comparison of Rh and Pd [1,2]

	Rhodium	**Palladium**
Average price (2013) [1]	39 $/g	26 $/g
World demand (2013) [1]	28.7 t/year	273 t/year
Yield in fission products [2] (UO_2 fuel : 4.5GWd/tHM)	600 g/tHM	1800 g/tHM
Required cooling period [2] (to below the exemption level)	70 years	3.3×10^7 years

Table 2: Main reactor parameters of PWR

Parameters		**Data**
Reactor	Reactor type	PWR
	Reactor thermal power	3423 MWt
	Coolant	H_2O
	The number of assemblies	193
Assembly	The number of pin cells	17×17 pin /assembly
	Pitch of pin cell	12.6 mm
	Height of fuel assembly	390 cm
	The number of "UO_2 fuel" pins	248 pin /assembly
	The number of "Gd fuel" pins (UO_2+Gd_2O_3)	16 pin /assembly
	The number of control rod guide thimbles	24 pin /assembly
	The number of measurement guide thimbles	1 pin /assembly
Pin	Diameter of fuel pin	8.19 mm
	Enrichment of U-235 in "UO_2 fuel" pin	3.4 wt%
	Density of "UO_2 fuel" pin	90 %
	Enrichment of U-235 in "Gd fuel" pin	3.2 wt%
	Concentration of Gd_2O_3 in "Gd fuel" pin	10 wt%
	Density of "Gd fuel" pin	90 %
	Diameter of absorber ("Rh target")	8.70 mm

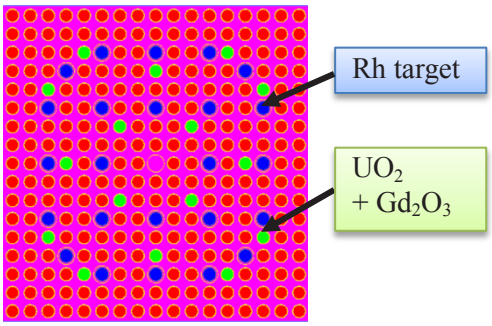

Figure 1: PWR assembly including Rh target

Table 3: Form and smeared density of Rh target

Form of Rh target	**Smeared density of target**
Metal (Rh)	0.1 % ~ 100 %
Oxide (Rh_2O_3)	100 % (Equivalent to 53.6 % of the metal)
Solution ($Rh+H_2O$)	1000 ppm, 10000 ppm (Equivalent to 0.008 %, 0.08 % of the metal)

2.2 Burnup Chain from Rh to Pd

Burnup chain around Rh (Figure 2[2]) is complicated because there are many isomer of Rh. Although there are isotopes of ^{101}Rh, ^{102}Rh, and ^{103}Rh in FPs[5], cross section data of radioactive Rh such as ^{102}Rh is not enough. However, ^{103}Rh is enough larger amounts than other isotopes in FPs[5]. Therefore, main reaction is ^{103}Rh captures a neutron, beta-decays, and then becomes ^{104}Pd.

Thus, in this simulation, default burnup chain for MVP-BURN code (Figure 3[2,3]) was used. Namely, only stable isotope ^{103}Rh was loaded as target pin. Then, in terms of radioactivity, that of generated ^{107}Pd with long half-life had been evaluated in this paper.

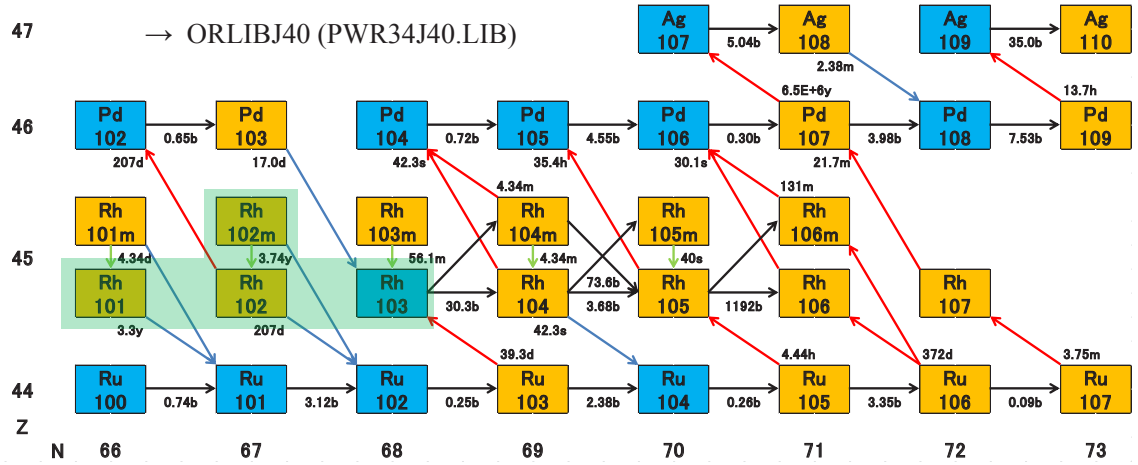

Figure 2: Burnup chain around Rh[2]

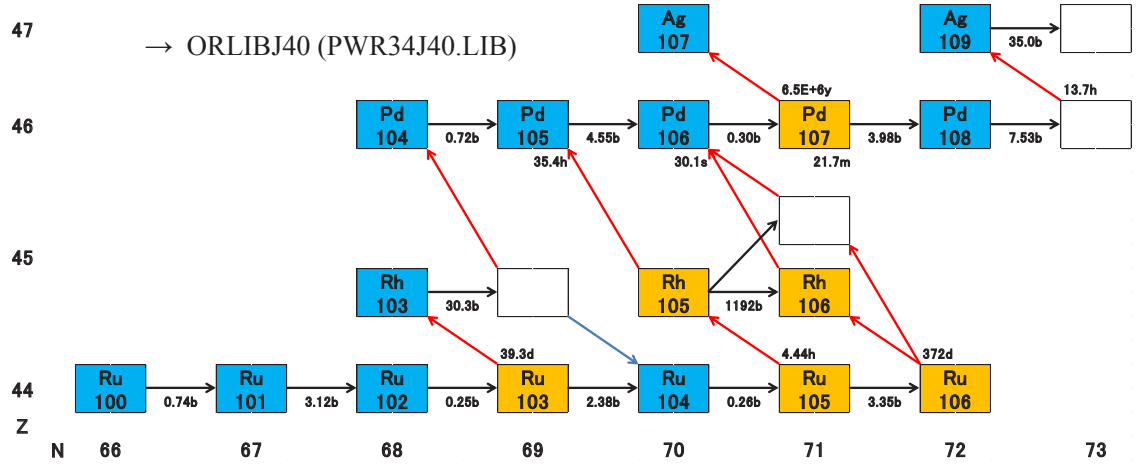

Figure 3: Burnup chain in this simulation[2,3]

3. Result and Discussion

3.1 Creation Rate of Pd and Weight of Created Pd

Firstly, in order to discuss transmutation efficiency quantitatively, "creation rate (CR) of Pd" was defined as equation (1)[5], and calculated in each condition (Table 3).

$$\left(\begin{matrix}\text{Creation rate}\\ \text{of Pd}\end{matrix}\right)[\%/\text{year}] = \frac{\left(\begin{matrix}\text{Amount of}\\ \text{created Pd}\end{matrix}\right)[\text{n/cm}^3]}{\left(\begin{matrix}\text{Initial amount of}\\ \text{loaded Rh}\end{matrix}\right)[\text{n/cm}^3]} \times \frac{100}{\left(\begin{matrix}\text{Irradiation}\\ \text{period}\end{matrix}\right)[\text{year}]} \quad (1)$$

Then, all results of the CR of Pd and the weight of created Pd per assembly are shown in Figure 4. It turned out that high CRs of Pd were obtained at solution conditions (33%/year), but yields of Pd were very small because amounts of loaded Rh were extremely small. In terms of the weight of created Pd, it was the greatest at 100% smeared density (SD) of Rh. However, at more than SD = 1%, these CRs were decreased significantly. It turned out this effect depended on not the form of Rh but the SD of Rh because of comparison between solution (SD=0.08%) and metal (SD=0.1%) and between oxide (SD=53.6%) and metal (SD=50%, 60%). Therefore, this effect was considered to be "self-shielding effect" depending on SD of Rh, and it was presumed that the CR of Pd became lower when SD of Rh was higher than 1% because a lot of around Rh prevented own transmutation.

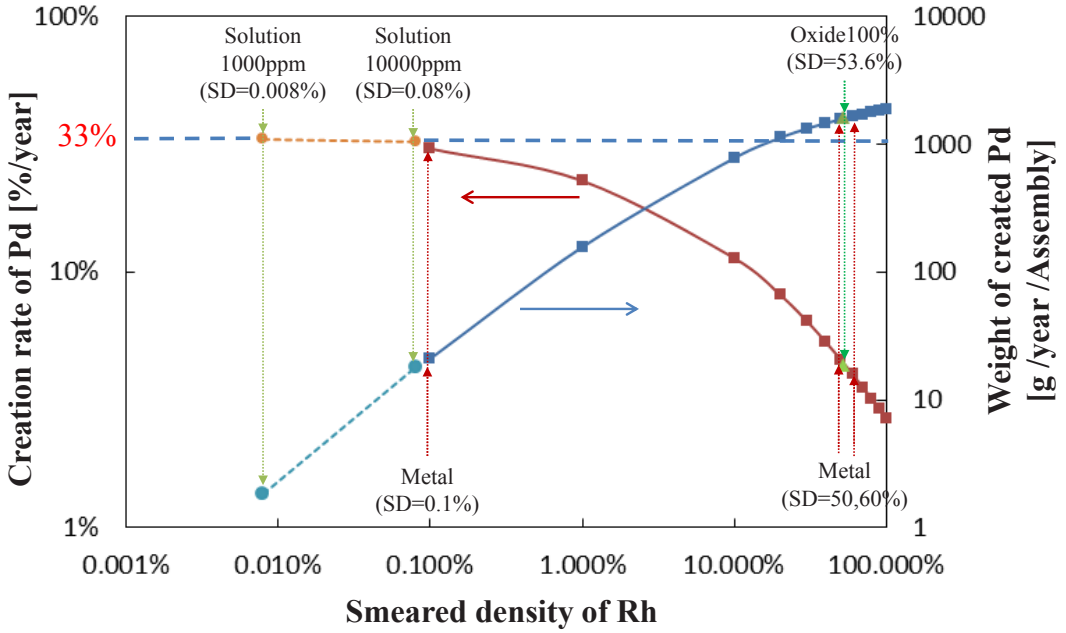

Figure 4: Smeared density dependence of creation rate of Pd and weight of created Pd per assembly

3.2 Infinite Multiplication Factor of Assembly

Secondly, in order to discuss the feasibility in terms of operating the reactor, simulation results of infinite multiplication factor of assembly (k_{inf}) are shown in Figure 5. It was clear that k_{inf} in solution conditions were almost the same as the reference case (not Rh but water), but k_{inf} in solid conditions did not reached 1.00. Therefore, when the irradiation in the case of solid condition is considered, it was necessary to decrease the number of loaded Rh pins per assembly or to adjust fuel enrichment of surrounding assemblies.

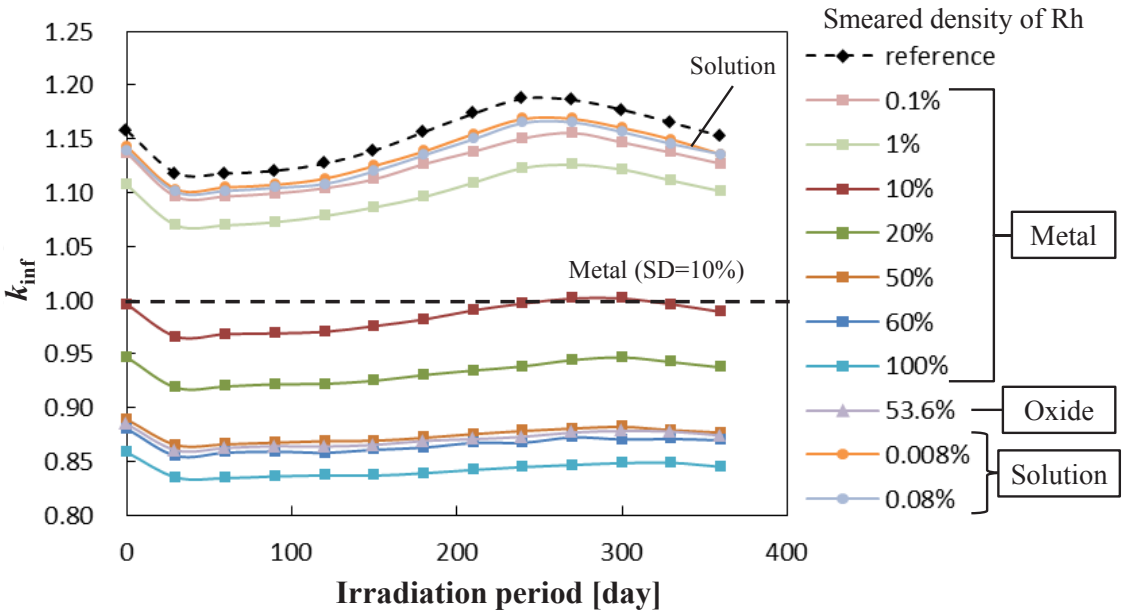

Figure 5: Time dependence of infinite multiplication factor of assembly (k_{inf})

3.3 Radioactivity of Generated ^{107}Pd

Finally, in order to discuss radioactivity of products, calculation results of radioactivity concentration of created Pd, in the case of assuming isolation of Pd after irradiation, are shown in Figure 6. Thus, radioactivity concentration of ^{107}Pd in FP Pd[2] was higher than the exemption level defined by IAEA[6]. On the other hand, in the case of created Pd by transmutation of Rh, it had only 1Bq/g. Therefore, the generation of ^{107}Pd was enough suppressed below the exemption level that it can be considered as resources.

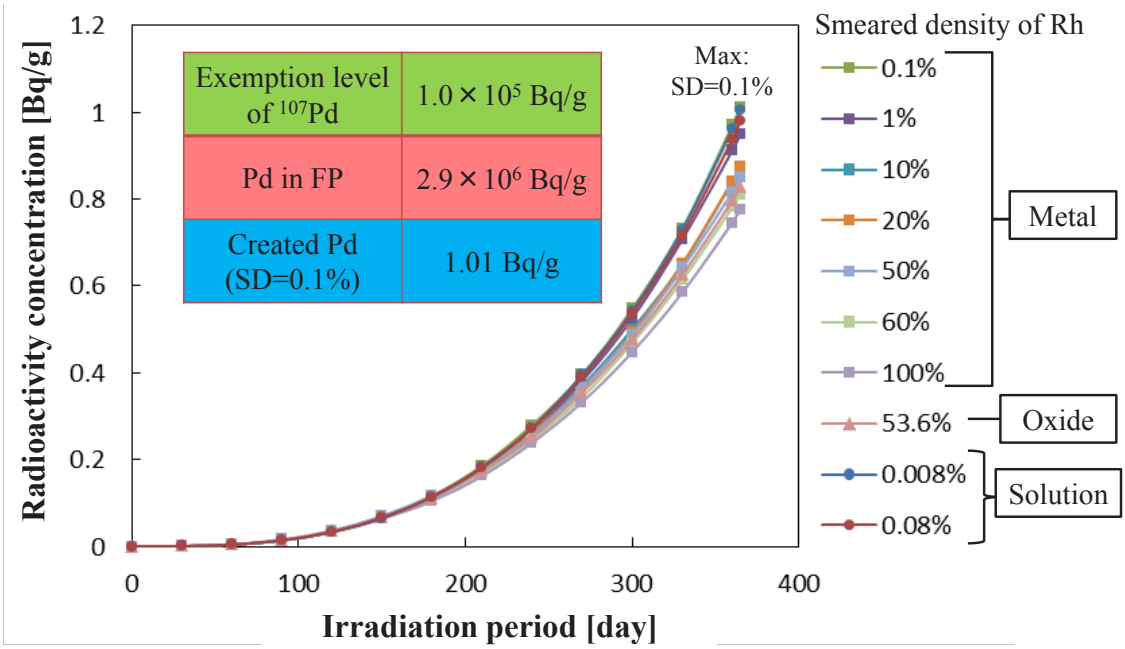

Figure 6: Time dependence of radioactivity concentration of created Pd

4. Conclusion

Creation of Pd by using PWR reactor was simulated. High creation rates of Pd were obtained at Rh solution condition. However, at more than 1% smeared density of target Rh, these creation rates of Pd were decreased by the self-shielding effect. In cases of solution, k_{inf} were hardly affected. On the other hand, k_{inf} in solid conditions did not reached 1.00 when 24 target Rh pins were loaded per assembly. In the case of 1 year irradiation, the generation of ^{107}Pd was enough suppressed in all conditions that the Pd created by transmutation of Rh can be considered as resources.

References

[1] "Platinum 2013 Interim Review," Johnson Matthey Public Limited Company (2013).
[2] K. Okumura, K. Sugino, K. Kojima, *et al*.: "A Set of ORIGEN2 cross section libraries based on JENDL-4.0: ORLIBJ40," JAEA-Data/Code 2012-032 (2012).
[3] K. Okumura, T. Mori, M. Nakagawa, and K. Kaneko: *J. Nucl. Sci. Technol.* **37**(2), pp.128-138 (2000).
[4] K. Shibata, O. Iwamoto, T. Nakagawa, *et al*.: *J. Nucl. Sci. Technol.* **48**(1), pp.1-30 (2011).
[5] A. Terashima and M. Ozawa: *Nucl. Sci. Tech.* **26**, S010311 (2015).
[6] "Radiation Protection and Safety of Radiation Sources: International Basic Safety Standards," IAEA Safety Standards Series No. GSR Part 3, IAEA (2014).

This is a blank page.

47 Cross Talk Experiment of Array-type CdTe Detector for BNCT-SPECT -Experimental design-

Masanobu Manabe*, Fuminobu Sato, Isao Murata
Division of Sustainable Energy and Environmental Engineering,
Graduate School of Engineering, Osaka University
Yamada-oka 2-1, Suita, Osaka, 565-0871 Japan
*E-mail: manabe@qr.see.eng.osaka-u.ac.jp

BNCT is a new radiation therapy which can destroy only tumor cells and will not damage healthy cells. This therapy is not yet established as a usually utilized treatment at present, because it has some very serious unsolved problems. One of them is that the treatment effect cannot be known during BNCT in real time. We are now developing a SPECT system to measure it, named BNCT-SPECT, with a cadmium telluride (CdTe) semiconductor detector. BNCT-SPECT can obtain a three-dimensional image for the BNCT treatment effect by measuring 478keV gamma-rays emitted from the excited state of 7Li nucleus created by 10B(n,α) reaction.

In the previous study, we investigated the feasibility of the BNCT-SPECT system. As a result, the estimated count rate of 478 keV gamma-rays was sufficiently large being more than the target value of over 1000 counts/hour. However, the ancillary target value of S/N ratio did not meet the target value (S/N >1). We then tried to improve the S/N ratio, because we confirmed that deterioration of the S/N ratio was caused by the influence of Compton scattering especially due to capture gamma-rays of hydrogen. To solve this problem, we produced an arrayed detector with two CdTe crystals to test anti-coincidence detection technique. We then carried out anti-coincidence measurement with a standard gamma-ray source and confirmed possibility of reduction of noises formed by Compton continuum. However, it was difficult to discuss the result appropriately, because agreement was not sufficient between experiment and analysis. For more precise analysis for the anti-coincidence detection, we designed and made a collimator having a similar performance to the real BNCT-SPECT. The collimator size was designed to be 14cm at maximum and the hole diameter is 2mmφ. Now we are carrying out experiments with the collimator to precisely examine the effect of cross talk of scattering gamma-rays between CdTe elements.

1. Introduction

Recently, boron neutron capture therapy (BNCT) attracts medical field as a new radiation therapy. BNCT can destroy tumor cells by alpha particles(α) and lithium nuclei (^{7}Li) emitted by the reaction of thermal neutron or epithermal neutron with boron (^{10}B). Ranges of emitted α and ^{7}Li particles are as long as the same size as a human body cell. Hence, if ^{10}B would be accumulated only in tumor cells, it would be expected that only the tumor cells would be killed. Also, BNCT has an advantage that drugs containing boron compounds have already been developed, with which 10B could be accumulated only in the tumor cells.

However, this therapy was not yet established as a usually utilized therapy at the present time. The reason is that there are some very serious problems unsolved. One of them is that the treatment effect cannot be known during BNCT in real time. In the present study, we have been developing BNCT with a SPECT technology, named BNCT-SPECT, as a gamma-ray measuring device in real time in order to solve the problem mentioned above. The BNCT treatment effect can be estimated by measuring 478keV gamma-rays emitted from the exited state of ^{7}Li nucleus created by ^{10}B(n,α)^{7}Li reaction by the SPECT technology. However, it is known to be very difficult to measure 478keV gamma-rays, because capture gamma-rays of 2.22MeV produced by ^{1}H(n,γ)^{2}H reaction and annihilation gamma-rays of 511keV to be detected just adjacent to 478keV gamma-rays become a large and critical background.

In the previous study, we investigated the feasibility of the BNCT-SPECT system considering the arrangement of CdTe crystals and collimators. As a result, the estimated count rate of 478 keV gamma-rays was sufficiently large being more than the target value of over 1000 counts/hour. However, the ancillary target value of S/N ratio did not meet the target value (S/N >1). Next, we started to improve the S/N ratio

because we confirmed that deterioration of the S/N ratio was caused by the influence of Compton scattering especially due to capture gamma-rays of hydrogen. To solve this problem, we focused on anti-coincidence detection by arrayed detector in the BNCT-SPECT [1].

In this present study, we produce an arrayed detector with two CdTe crystals to test anti-coincidence detection by the adjacent two elements. We then carry out anti-coincidence measurement with a standard gamma-ray source to confirm possibility of reduction of noises formed by Compton continuum. At the same time, we design and make a collimator having a similar performance to the real BNCT-SPECT to precisely examine the effect of cross talk of scattering gamma-rays between CdTe elements.

2. BNCT-SPECT

At first, the principle of BNCT–SPECT is given in this chapter. $^{10}B(n,\alpha)^{7}Li$ reaction is expressed by the next two nuclear reactions:

$$^{10}B + n \rightarrow \alpha + {}^{7}Li + 2.79\ MeV\ (6.1\%)$$
$$\rightarrow \alpha + {}^{7}Li^{*} + 2.31MeV + \gamma(478keV)(93.9\%) \quad (1)$$

94 % of ^{7}Li is in the first excited state, i.e., $^{7}Li^{*}$. $^{7}Li^{*}$decays in its half-life of 10^{-14} sec to emit a 478keV gamma-ray via transition from the first excited state to the ground state. If the intensity distribution of 478keV gamma-rays could be measured three-dimensionally, we could obtain the distribution of $^{10}B(n,\alpha)^{7}Li$ reaction rate in the tumor. Also, the attenuation coefficient of this photon in tissues is about 0.1 cm^{-1}. The 478keV gamma-rays can escape from a human body to a large extent. The result of the measurement can be regarded as the treatment effect of BNCT. A schematic figure of BNCT-SPECT is shown in Fig.1

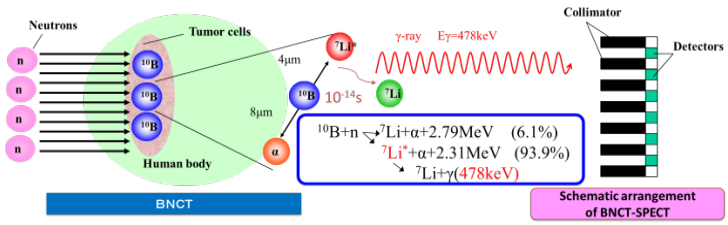

Fig.1 Principle of BNCT–SPECT.

BNCT-SPECT is composed of a collimator and a multiple γ-ray detector (arrayed γ-ray detector). Emitted 478keV gamma-rays are collimated by this collimator, and measured by this array detector. The BNCT treatment effect (local tumor dose) can be estimated from an obtained three dimensional image of the gamma-rays.

However, the 478keV gamma-rays must be measured in a very high neutron field. The point is that many secondary neutrons and gamma-rays created by primary neutrons form a very high background field. It is thus quite difficult to accurately measure only 478keV gamma-rays out of such various unwanted radiations.

3. Design requirements for BNCT-SPECT

As mentioned in the previous chapter, BNCT-SPECT should be so designed that 478keV gamma-rays have to be measured in a very high background field. Also, actual medical conditions, i.e., protocol, irradiation site and so on, must be considered. Taking into account the above situation, we set four design conditions as follows.

① The spatial resolution should be about several mm in the obtained SPECT image from the viewpoint of medical treatment.
② It is necessary to complete a measurement in about 60 minutes, because the treatment time of BNCT is normally less than one hour.
③ The number of counts per unit detector should be more than 1000 counts so that the statistical accuracy

can be kept to be less than several percent.

④ The energy resolution, full width at half maximum (FWHM), should be less than 33keV (511keV－478keV) so as to measure annihilation gamma-rays and 478keV prompt gamma-rays separately.

To meet requirement ①, an elemental gamma-ray detector should be downsized to be as large as the spatial resolution. However, to meet requirement ② and ③, contrary to requirement ①, a gamma-ray detector having an enough high counting efficiency for 478keV gamma-rays should be selected. In addition, the detector should have a good energy resolution for requirement ④. Finally, we decided using a CdTe device with the following reasons [2]: a CdTe crystal is not necessarily enclosed with a casing, so that the area of radiation incidence can be kept to be small enough to easily improve the spatial resolution. Recently, a larger wafer can be produced and a high counting efficiency can be obtained so as to clear requirements ② and ③. Also, a Schottky type CdTe crystal was introduced. The energy resolution can thus be improved in order to meet requirement ④.

In the previous study, we have conducted basic researches theoretically and experimentally for one-element CdTe detector [3～5]. The S/N ratio obtained showed less than unity. However, the final goal is an array-type detector. It means, with the array-type detector, coincidence measurement could be expected to improve the S/N ratio.

4. Development of the two-element CdTe detector

Figure 2 shows a one-element CdTe detector and two-element CdTe detector produced in this series study. The two-element CdTe detector was made by various original ideas though photos (a) and (b) were hardly distinguishable except the number of BNC connectors. As shown Fig. 3, we used two CdTe crystals. One crystal has 8 pixels horizontally. One CdTe element consists of 8 pixels, in which 4 are in an upper crystal and another 4 are in a lower one to form one CdTe detector. This complex structure is for development of the array-type CdTe detector with so-called ASIC. And this structure helps to carry out andante-coincidence detection inherently. As for the bonding of the two crystals, Au wires were placed as GND lines between them.

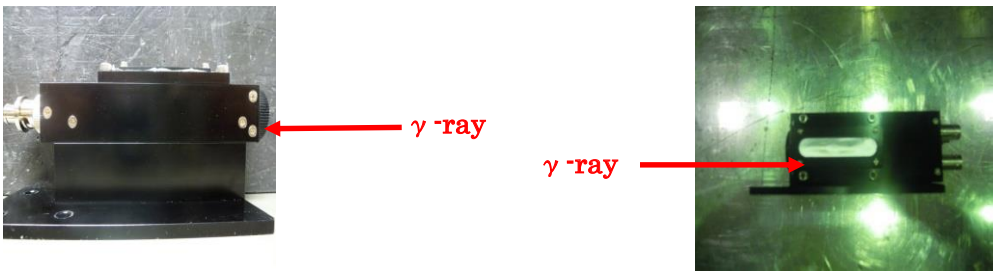

(a) One-element CdTe detector. (b) Two-element CdTe detector.

Fig. 2 Produced trial CdTe elemental detector.

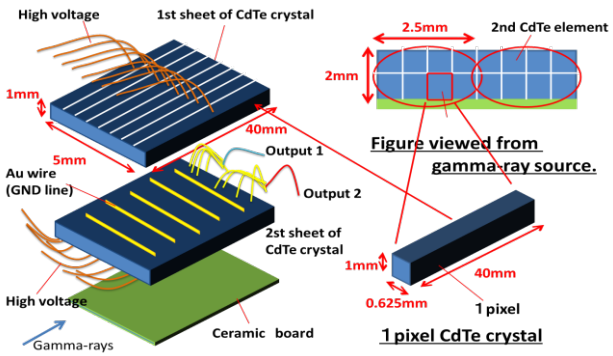

Fig. 3 Structure of the two-element CdTe detector.

5. Experiments and Results

5.1 Basic property measurement

As the most important detector property, detection efficiency and energy resolution were measured for the two-element CdTe detector to confirm requirements ②～④.

(1) Intrinsic efficiency

We measured the intrinsic efficiency of the two-element CdTe detector with four standard gamma ray sources (such as ^{137}Cs (Eγ=662keV)) by the experimental scheme in Fig.4. Applied voltage was set to 1000V and the sharping time of amplifier is set to 3μsec.

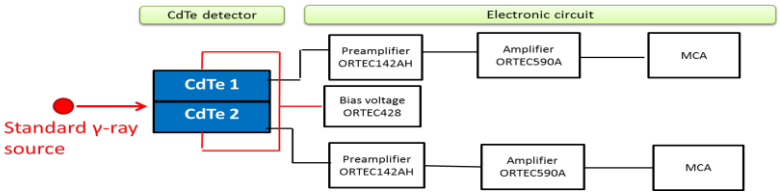

Fig. 4 Experimental scheme of intrinsic efficiency and energy resolution measurement with two-element CdTe detector.

Figure 5 shows the measured intrinsic efficiency together with the result for one-element CdTe detector obtained previously [6]. The interpolated efficiency at 478 keV is 0.21 and is more-or-less the same as that of the one-element CdTe detector. We thus confirmed the two-element CdTe detector can detect gamma-rays of 478keV more than 1000 counts per 1 hour.

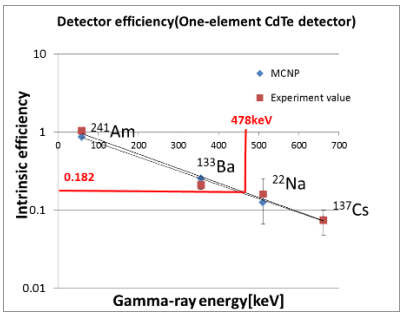

(a) One-element CdTe detector.

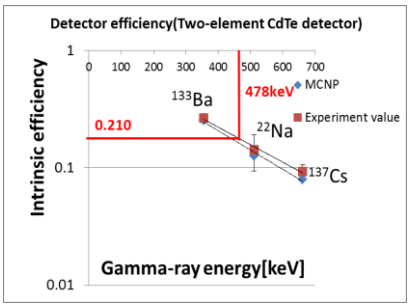

(b) Two-element CdTe detector.

Fig.5 Intrinsic efficiency of one- and two-element CdTe detectors.

(2) Energy resolution

Figure 6 shows the energy resolution for both CdTe detectors measured with the same experimental arrangement in Fig. 4 using standard gamma-ray sources. The measured FWHMs of 478keV were 17.7keV and 16.8keV for one- and two-element CdTe detector, respectively. As a result, we confirmed discrimination possibility of 478keV and 511keV gamma-rays, because both values are smaller than 33 keV (=511 keV – 478 keV).

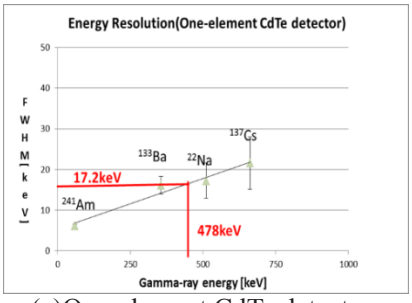

(a)One-element CdTe detector.

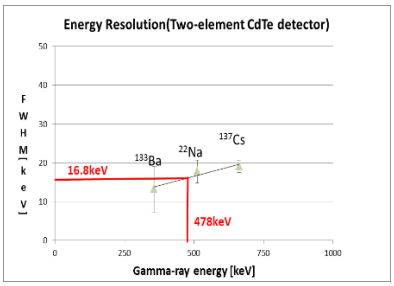

(b)Two-element CdTe detector.

Fig.6 Energy resolution at 478keV for one- and two-element CdTe detectors.

5.2 Coincidence rate measurement via cross talk events

We examined the cross talk event between two CdTe elements by measuring coincidence signals of the two to confirm improvement of the S/N ratio. Figure 7 shows the experimental arrangement. In the experiment ^{137}Cs gamma-ray source was used. In the figure, upside MCA measured ^{137}Cs spectrum from one of the two CdTe detectors. And downside MCA measured the coincidence spectrum, meaning two signals are detected in both detectors at the same time. Other experimental conditions are as follows: Applied voltage is set to 1000 V, sharping time of amplifier is set to 3μsec and gate width of linear gate is set to 10μsec.

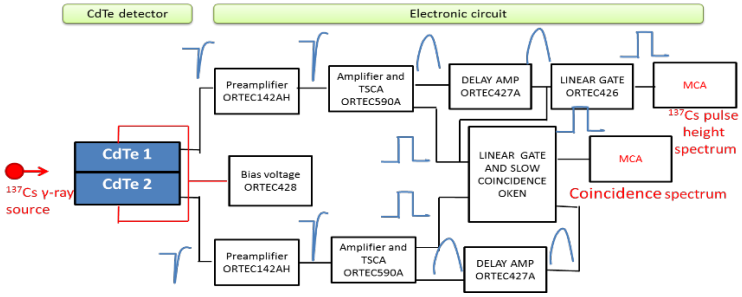

Fig. 7 Experimental arrangement of coincidence measurement.

Figure 8 shows the experimental results, in which left-hand side is pulse height spectrum (PHS) of ^{137}Cs measured by CdTe 1 in Fig. 7. Right-hand side is the coincidently measured PHS. The total counts of Fig. 8(a) and 8(b) are 79529 and 4007, respectively. Therefore the coincidence rate = 4007/79529 = 0.05. As a result, we confirmed possibility of anti-coincidence detection using two-element CdTe detector experimentally in order possibly to improve the S/N ratio.

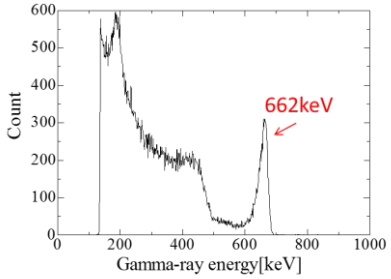

(a) Measured raw ^{137}Cs PHS.

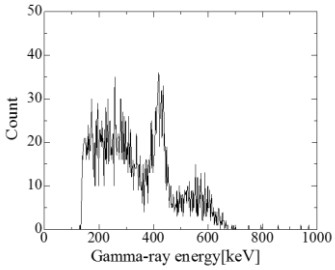

(b) Measured coincidence PHS.

Fig. 8 Measured pulse height spectra of ^{137}Cs and coincidence events.

Next, we carried out numerical simulation of coincidence events with MCNP5. Calculated PHS of ^{137}Cs with one detector and that of coincidence events are shown in Fig. 9(a) and 9(b), respectively. The total count of Fig. 9(a) and (b) are 1520 and 34900, respectively. Therefore the coincidence rate = 1520/34900 = 0.08. Comparing the result with the experiment, the calculation

shows smaller, that is, 0.08 (Cal.) > 0.05 (Exp.). The reason is not clear now, however, it ispresumed that this may be due to treatment of leaking electrons from the CdTe detector in MCNP5.

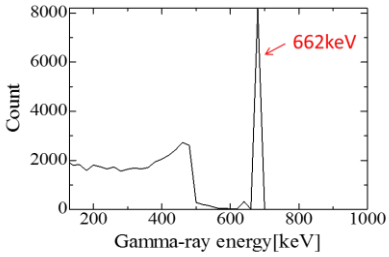

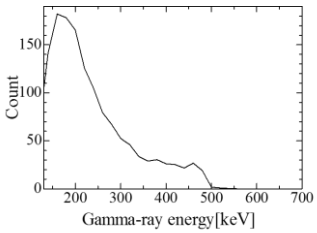

(a) Calculated raw ^{137}Cs PHS. (b) Calculated coincidence PHS.

Fig.9 Calculated pulse height spectrum (PHS) of ^{137}Cs and Coincidence.

6. Future Work

Cross talk event was confirmed experimentally. However, discrepancy is still existing between experiment and numerical calculation. We are thus planning to carry out experiment of the two-element CdTe detector with a collimator we will use in a real case. At first, we have designed and produced a variable-length collimator having two small holes for the two-element CdTe detector as shown in Fig. 10(a). With this collimator, the cross talk event can be restricted such that gamma-rays are incident only to one CdTe element. Fig. 10(b) shows the experimental system for the planned experiment. Now, we are carrying out experiments with the collimator.

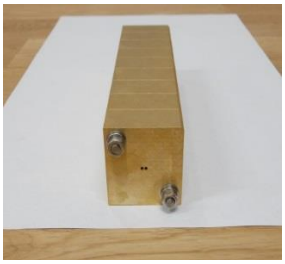

(a) Photo of the collimator. (b)Experimental arrangement of the coincidence measurement.

Fig.10 Photos of designed cross talk Experiment.

7. Conclusion

We produced two-element CdTe detector for BNCT-SPECT development. The CdTe detector met the design requirements for the basic property (intrinsic efficiency and energy resolution). Also, we measured coincidence rate for the two-element CdTe detector. As a result, the measured coincidence rate was 0.05, while the calculated rate was 0.08. The simulation obtained showed a little larger value than the experiment. In the next step, more precise analysis will be done with the real collimator finally to extrapolate the performance to the real array-type CdTe detector.

References

[1] M.Manabe, S.Nakamura, I.Murata, “Study on Measuring Device Arrangement of Array-type CdTe Detector for BNCT-SPECT”, presented in 7th Young Researchers’ Boron Neutron Capture Therapy (7YBNCT), Sep.22-26,Granada, Spain (2013).

[2] I. Murata, T. Mukai, M. Ito, H. Miyamaru, S.Yoshida, “Feasibility study on BNCT-SPECT using a CdTe detector”, Progress in Nucl. Sci. Technol.1, pp. 267-270 (2011).

[3] M.Manabe, S.Nakamura, I.Murata, “Present Status of BNCT-SPECT Development with CdTe Detector”,presented in the 2013 Symposium on Nuclear Data, Nov.14-15,Fukui, Japan(2013).

[4]M.Manabe, S.Nakamura, I.Murata, “Separate measurement of 478keV and annihilation gamma-rays by

CdTe detector for BNCT-SPECT" presented in 7th International Symposium on Radiation Safety and Detection Technology(ISORD-7),Jun.15-18,2013,Sanya,China(2013): JAEA-Conf 2014-002, pp.198-203.
[5]I.Murata, S.Nakamura, M.Manabe,H.Miyamaru, I. Kato" Characterization Measurement of A Thick CdTe Detector for BNCT-SPECT - Detection Efficiency and Energy Resolution -" Appl. Radiat. Isotopes,88, pp. 129-133 (2014).
[6] M.Manabe, F.Sato, I.Murata," Basic property of array-type CdTe detector for BNCT-SPECT" presented in 16th International Congress on Neutron Capture Therapy(ICNCT-16),June14-19, Helsinki, Finland (2014).

This is a blank page.

48 Measurement of double differential cross sections of light-ions emission in interaction of 430 MeV/u carbon-ions with a carbon

Tsuyoshi KAJIMOTO[1], Yutaro ITASHIKI[2], Youichi IMAHAYASHI[2],
Hidearu YONESHIGE[2], Taro HASHIGUCHI[2], Nobuhiro SHIGYO[2], Daiki SATOH[3],
Yusuke UOZUMI[2], Kenichi TANAKA[1], Satoru ENDO[1]

Hiroshima University, 1-4-1 Kagamiyama, Higashi-Hiroshima 739-8527, Japan
Kyushu University, Motooka, Nishi-ku, Fukuoka 819-0395, Japan
Japan Atomic Energy Agency, Tokai, Ibaraki 319-1195, Japan

E-mail: kajimoto@hiroshima-u.ac.jp

Double differential cross sections of proton, deuteron, triton, ^{3}He, and alpha-particle emissions from 430 MeV/nucleon carbon-ions on a carbon target were measured at the Heavy-Ion Medical Accelerator in Chiba of the National Institute of Radiological Sciences. Measured double differential cross sections were compared with calculations by PHITS and FLUKA codes. Large discrepancies were found between measured and calculated data except for protons.

1. Introduction

Carbin-ion beam is one of the great candidates for the cancer treatment due to the high dose-concentration around the Bragg peak and the high biological effect in the cancer tissue. For patients, carbon-ion radiotherapy also has advantages which reduces physical damages and remains better quality of life after the treatment. For those reasons, the number of patients receiving carbon-ion radiotherapy has increased. However, the patients have a concern which is the risk of secondary cancer. Studies for the risk have been performed [1, 2], however, further studies are required to elucidate the risk [3].

In order to estimate the risk, three-dimensional dose distribution is needed in the treatment. The dose includes the exposure by not only carbon-ions but also secondary particles produced by nuclear reactions in the body. Particle transport Monte-Carlo simulation with PHITS [4], FLUKA [5], and GEANT4 [6] is an effective tool to obtain the dose distribution. However, experimental data is needed for accuracy verification of the simulation.

Neutron production double differential cross sections (DDXs) for carbon ion incidence have been measured by Satoh et al. [7] and Shigyo et al. [8]. The experimental DDXs have been compared with calculations of PHITS, and differences between experimental and calculated data were found at the neutron emission energy region below 10 MeV. For further accuracy verification of the code, experimental DDXs are needed not only for neutron production but also the others particle production.

In this work, we reported measured double differential cross sections (DDXs) for protons, deuterons, tritons, ^{3}He, and alpha-particles produced by incident 430 MeV/u carbon-ions on a carbon target. The light-ions production DDXs were derived from data obtained for the neutron production DDX measurement. Measured DDXs were compared with calculations by PHITS and FLUKA codes.

2. Experiment

The experiment was carried out at the Heavy-Ion Medical Accelerator in Chiba (HIMAC) of the National Institute of Radiological Sciences (NIRS). Since the light-ions production DDXs were

derived from data obtained for neutron production DDX measurement, the experimental set up and data acquisition system were similar to those reported by Satoh et al. [7].

A schematic of the experimental arrangement is shown in Fig. 1. For neutron measurement, this experiment was performed in the atmosphere, therefore, the experimental set up could not be optimized for charged particle measurement. The 430 MeV/u carbon beam pulsed at 2×10^5 s^{-1} was delivered into PH2 course. A 50 × 50 × 10 mm^3 graphite target was set to be 14.1 mm long on beam line by rotating the target at 45 degrees to the beam axis. A beam detector which consisted of a 0.5 mm thick plastic scintillator was placed upstream of the target. Particles emitted from the target were detected by three particle detectors with Φ127 × 127 mm^3 NE213 scintillator. The particle detectors were located at 15, 30, and 45 degrees as a forward angle measurement, and 60, 75, and 90 degrees as a backward angle measurement. A 2 mm thick plastic scintillator was set in front of each particle detector as the veto detector.

Values from analog to digital converters (ADC), a time to digital converter (TDC), and an identifier of fired NE213 scintillator were acquired event by event. ADC values were whole and slow components of the signal from each NE213 scintillator, the signal from each veto detector, and the signal from beam detector. The TDC value was the time difference between signals from the fired NE213 scintillator and the beam detector. Apart from these data, the number of carbon-ions was recorded by a NIM scaler in the measurement. The electronics circuit for data acquisition consisted of NIM and CAMAC modules.

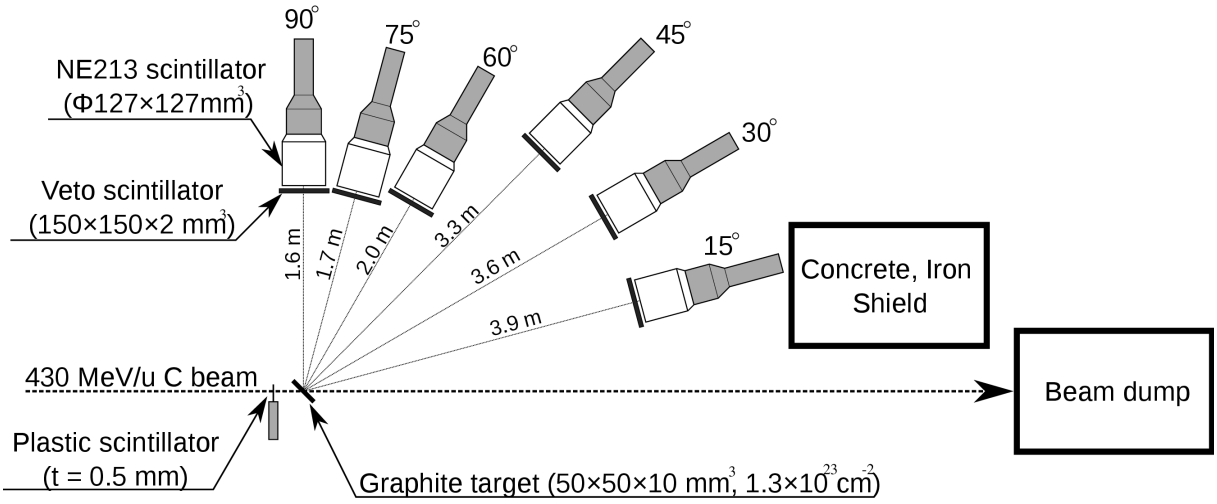

Fig. 1 A schematic of the experimental arrangement.

3. Analysis

Protons, deuterons, tritons, ^{3}He, and alpha-particles emission DDXs ($d\sigma^2/dEd\Omega$) in energy bin width of dE, centered at an energy of E, into a solid angle $d\Omega$ was

$$\frac{d^2\sigma}{dE\,d\Omega} = \frac{C(E)\,f}{\epsilon(E)\,\rho_A\,N\,\Delta E\,\Delta\Omega} \quad ,$$

where $C(E)$ is energy histogram of protons, deuterons, tritons, ^{3}He, or alpha-particles, and obtained through analysis for particle identification and energy determination. f is correction factor of counting loss, $\varepsilon(E)$ is peak detection efficiency of each particle, ρ_A is area density of the target, N is incident particle counts, ΔE is the energy bin width of the histogram, and $\Delta\Omega$ is the solid angle at the front surface of the NE213 scintillator.

The energy histograms of each particle was obtained from analyzing event by event data.

Charged particle events were extracted from ADC value distribution of the veto detector. Events of atomic number Z=1 and 2 in charged particle events were discriminated using pulse shape discrimination with ADC values of whole and slow component of NE213 scintillator. The isotope identification was performed with a scatter plot of the TDC value and the whole component ADC values of NE213 scintillator. As an example, Fig. 2 shows the scatter plot. The particle energy was determined with the time-of-flight technique by considering energy attenuation in flight. The energy attenuation were calculated with values of stopping power by SRIM code [9].

Calculated values were adopted to the peak detection efficiency. Deposition energy distribution in the NE213 scintillator to each particles and each energy were calculated with PHITS. The efficiency were obtained from the only peak part on the energy deposition distribution.

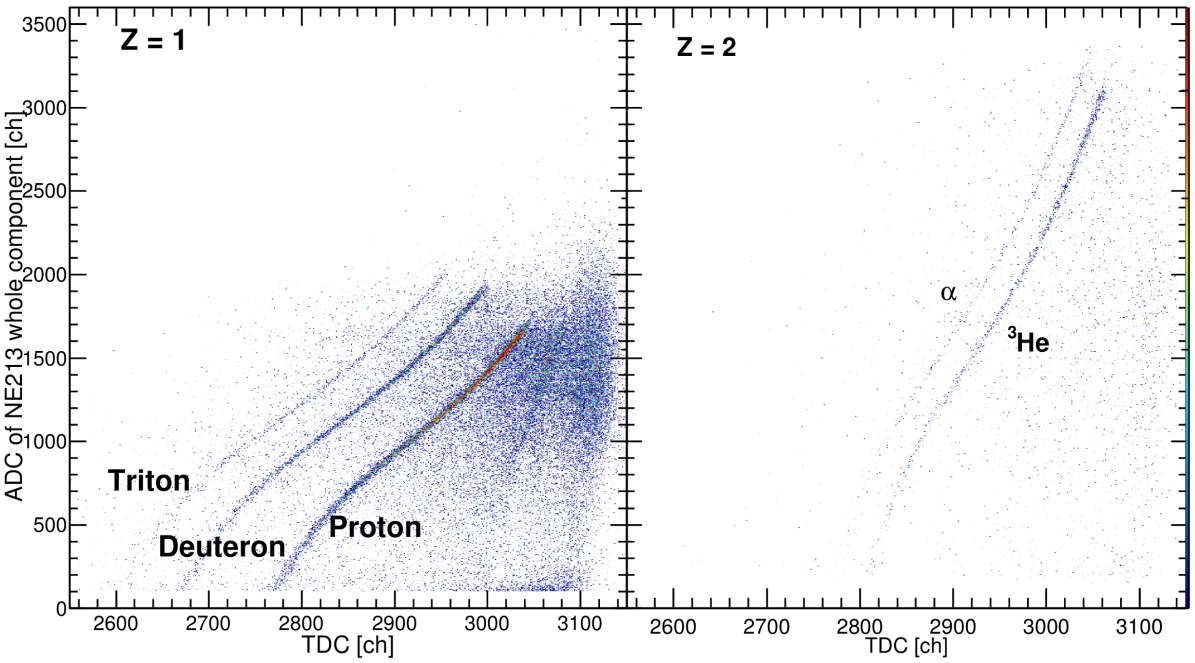

Fig. 2 Scatter plots of the TDC values and the whole component ADC values from NE213 scintillator at 30 degrees. Left and right plots show events extracted as atomic number 1 and 2 in pulse shape discrimination, respectively.

4. Monte Carlo simulation

DDXs of proton, deuteron, triton, ^{3}He, and alpha-particle emissions in the interaction of 430 MeV/u carbon-ions on a carbon target were calculated with PHITS and FLUKA. Each version was PHITS264 and FLUKA2011.2c.0, respectively. In the PHITS calculation, SMM [10] and EBITEM [11] modes were on. The FLUKA calculation with "PRECISIO" mode [12] was performed by activating the coalescence mechanism and the new evaporation model with heavy fragment evaporation.

The same geometry was constructed for both codes. A Φ0.002 × 1.0 mm^3 carbon target was irradiated with 430 MeV/u carbon pencil beam. The areal density of the target was 1.0×10^{22} cm^{-2}). A Φ2.0 m sphere was set centered in the target. The sphere excluding the target was filled with ideal vacuum. The position and kinetic energy of light-ions passing through the surface of the sphere were dumped.

DDXs of each particle were derived

$$\frac{d^2\sigma}{dE\,d\Omega} = \frac{h(E)}{\rho_A\, N\, \Delta E\, \Delta\Omega} \quad ,$$

where *h(E)* is energy histogram of each particle within an angle width. The angle of outgoing particles was determined from the position of dumped data. The angle width was set at ±0.5 degrees of the aimed angle. The symbol ρ_A is area density of the target, N is incident particle number, ΔE is the energy bin width of the histogram, and $\Delta\Omega$ is the solid angle which was calculated from the angle width.

5. Results and discussion

Figures 3 and 4 show DDXs of proton, deuteron, triton, ^{3}He, and alpha-particle emissions in the interaction of 430 MeV/u carbon-ions on a carbon target. The energy range of the DDXs is restricted due to the limitation of the particle identification. Since enough statistic could not be obtained for ^{3}He and alpha at 60, 75, and 90 degrees, the DDXs could not be derived.

Values calculated with PHITS and FLUKA are also shown in Figs. 4 Discrepancies of the shape of DDXs except for proton emission are found between calculations due to the difference of pre-equilibrium process. For evaporation process, there is a trend that particle emissions are larger for FLUKA calculation than for PHITS calculation.

Experimental proton DDXs give good agreement with calculations of both codes. However, large difference is found between measured and calculated data except for protons. Since experimental DDXs become smaller with the increase of the angle, we believe that the underestimation of light ion emissions occurs in the pre-equilibrium model of codes.

6. Conclusion

DDXs of proton, deuteron, triton, ^{3}He, and alpha-particle emissions in the interaction of 430 MeV/u carbon-ions on a carbon target were measured at the Heavy-Ion Medical Accelerator in Chiba of the National Institute of Radiological Sciences. Experimental DDXs were compared with values calculated with PHITS and FLUKA. Large difference was shown between experimental and calculated values except for protons. The improvement for the model of light-ion production for heavy ion incidence is necessary.

Acknowledgments

We thank members of the Accelerator Engineering Corporation (AEC) for technical assistance. This experiment was performed as a part of Research Project with Heavy Ion at NIRS-HIMAC.

References

[1] D. J. Brenner, E. J. Hall, Radiother. Oncol. 86 (2008) 165-170.
[2] U. Schneider, A. Lomax, B. Timmermann, Radiother. Oncol. 89 (2008) 135-140.
[3] E. Fokas, G. Kraft, H. An, et al., Biochimica et Biophysica Acta 1796 (2009) 216-229.
[4] T. Sato, K. Niita, N. Matsuda, et al., J. Nucl. Sci. Technol. 50 (2013) 913-923.
[5] T. T. Bohlen, F. Cerutti, M. P. W. Chin, et al., Nucl. Data Sheets, 120 (2014) 211-214.
[6] S. Agostinelli, J. Allison, K. Amako, et al., Nucl. Instrum. Methods A 506 (2003) 250-303.
[7] D. Satoh, D. Moriguchi, T. Kajimoto, et al., Nucl. Instrum. Methods A 644 (2011) 59-67.
[8] N. Shigyo, U. Uozumi, H. Uehara, et al., Nucl. Data Sheets 119 (2014) 303-306.
[9] J. F. Ziegler, M. D. Ziegler, J. P. Biersack, Nucl. Instrum. Methods B 268 (2010) 1818-1823.
[10] T. Ogawa, S. Hashimoto, T. Sato, et al., Nucl. Instrum. Methods A 723 (2013) 36-46.
[11] T. Ogawa, S. Hashimoto, T. Sato, et al., Nucl. Instrum. Methods B 325 (2014) 35-42.
[12] http://www.fluka.org/content/manuals/fluka2011.manual

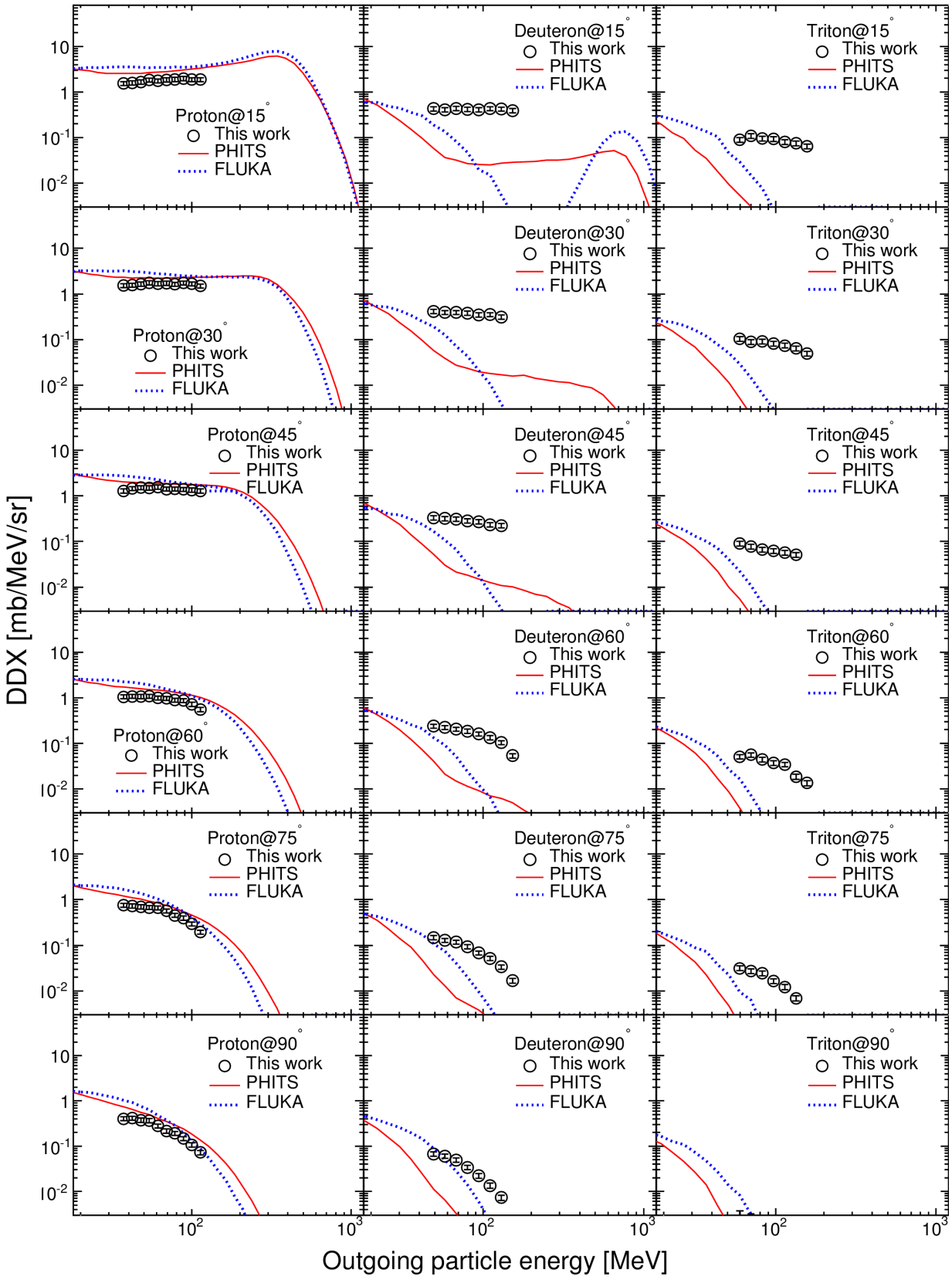

Fig. 3 DDXs of proton, deuteron, and triton emissions in the interaction of 430 MeV/u carbon-ions on the carbon target.

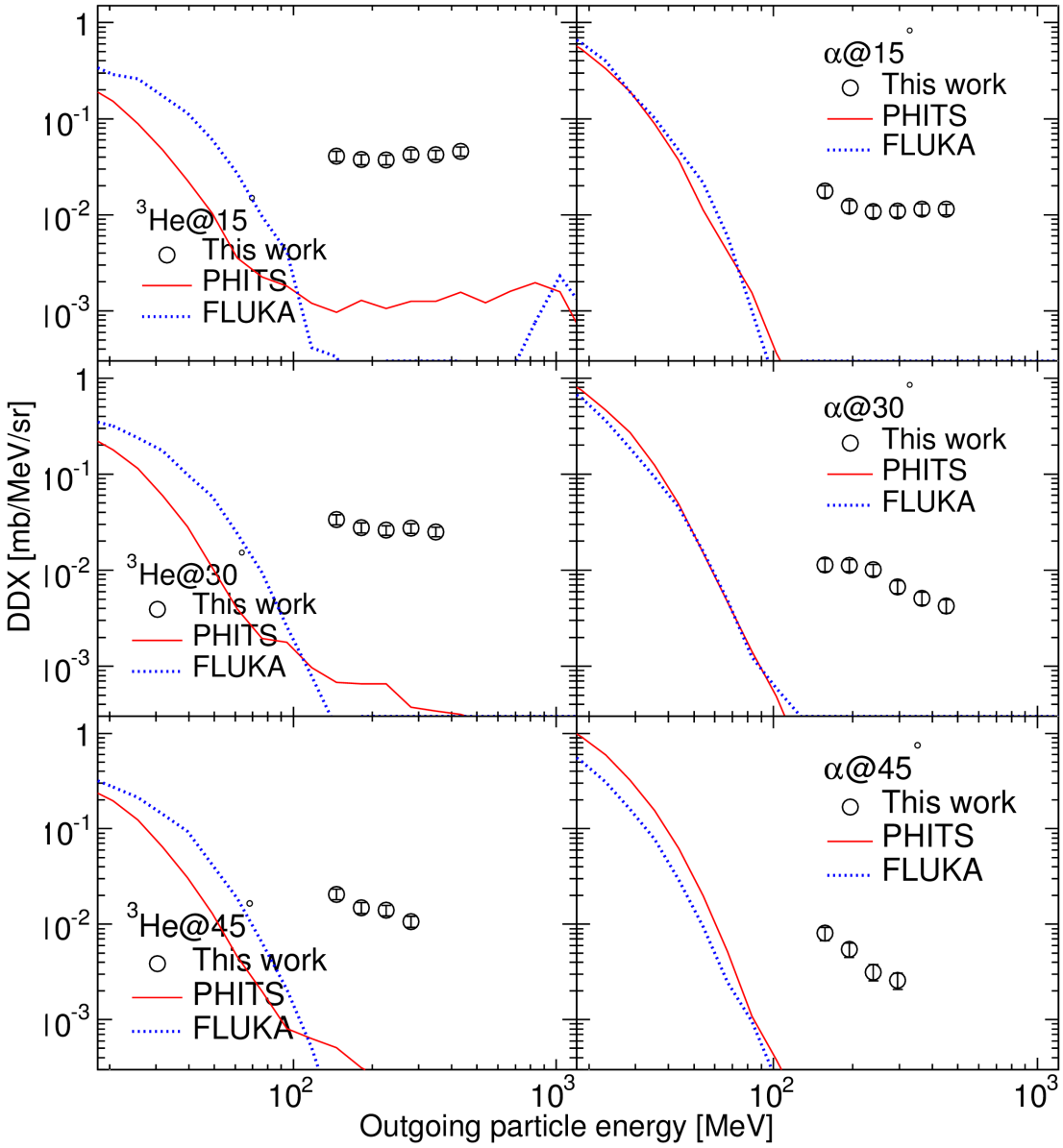

Fig. 4 DDXs of ^{3}He and alpha-particle emissions in the interaction of 430 MeV/u carbon-ions on the carbon target.

49 The container picture with two-alpha correlation for the ground state of ^{12}C

Bo Zhou[1,2,3], Yasuro Funaki[4], Akihiro Tohsaki[5], Hisashi Horiuchi[5,6], and Zhongzhou Ren [1,7]

[1]Department of Physics, Nanjing University, Nanjing 210093, China
[2]Yukawa Institute for Theoretical Physics, Kyoto University, 606-8502 Kyoto, Japan
[3]Meme Media Laboratory, Hokkaido University, Sapporo 060-8628, Japan
[4]Nishina Center for Accelerator-Based Science, The institute of Physical and Chemical Research (RIKEN), Wako 351-0198, Japan
[5]Research Center for Nuclear Physics (RCNP), Osaka University, Osaka 567-0047, Japan
[6]International Institute for Advanced Studies, Kizugawa 619-0225, Japan
[7]Center of Theoretical Nuclear Physics, National Laboratory of Heavy-Ion Accelerator, Lanzhou 730000, China

E-mail: bo@nucl.sci.hokudai.ac.jp; funaki@riken.jp

It is found that, by incorporating the 2α correlation, the single 0^+ 2α+α THSR (Tohsaki-Horiuchi-Schuck-Röpke) wave function is almost completely equivalent to the 3α wave function obtained as the full solution of the 3α cluster model. Their squared overlap is as high as 98% while it is at most 93% if the 2α correlation is not included. This result implies that in the container picture, the 2α correlation is very important in the ground state of ^{12}C.

In nuclear cluster physics, ^{12}C can be seen as the most important and interesting nucleus due to its very typical 3α cluster structures [1–8]. Since 1970, the traditional microscopic cluster models have been used for exploring the rich cluster characters of ^{12}C, e.g., OCM (orthogonality condition model) calculation by Horiuchi [9], the full microscopic 3α cluster calculations by Uegaki et al, [10] and Kamimura et al. [11]. As for the famous Hoyle state (0_2^+) of ^{12}C, it has been proved to have a weakly coupled 3α structure in relative S waves by using these cluster models. Different from the gas-like Hoyle state, the ground state of ^{12}C below the 3α threshold by 7.27 MeV is considered to have a very compact 3α cluster configuration.

The proposed THSR wave function in 2001 [12] has been very successful for the description of the gas-like cluster states, e.g., as for ^{12}C, Funaki et al. [13] showed that the squared overlap between the single 3α THSR wave function and the RGM (resonating group method)/GCM (generator coordinate method) wave function was almost 100% for the Hoyle state. While in the case of the ground state of ^{12}C the squared overlap became at most 93%. Quite recently, it was found that the ^{16}O + α Brink-GCM wave functions of the inversion-doublet band states of ^{20}Ne are almost 100% equivalent to single ^{16}O + α THSR wave functions [14, 15], e.g., as for the compact ground state of ^{20}Ne, the squared overlap is 99.3%. These results show that the THSR wave function can not only describe the gas-like cluster states with low density but also the cluster states with the normal density very well. This discovery urged us to introduce the container picture of cluster dynamics underlying the THSR wave function [16]. In the container picture, the clusters make nonlocalized motion occupying the lowest orbit of the cluster mean-field potential characterized by the size parameter. The high-percentage description of the compact ground state of ^{20}Ne by the single THSR wave function which is one of the important motivations to reconsider the squared overlap 93% between the single 3α THSR wave function of the ground state of ^{12}C and the corresponding RGM/GCM wave function. Thus, we expect to generalize the original THSR to study whether the compact ground state of ^{12}C can also be described well by a single THSR wave function or not in the container picture. As for this work, see details in Ref. [17].

The constructed 2α+α THSR wave function can be written as follows [17],

$$\Phi(\boldsymbol{\beta}_1, \boldsymbol{\beta}_2) = \int d^3R_1 d^3R_2 \exp[-\sum_{i=1}^{2}(\frac{R_{ix}^2}{\beta_{ix}^2} + \frac{R_{iy}^2}{\beta_{iy}^2} + \frac{R_{iz}^2}{\beta_{iz}^2})]\Phi^B(\boldsymbol{R}_1, \boldsymbol{R}_2) \quad (1)$$

$$\propto \phi_G \mathcal{A}\{\exp[-\sum_{i=1}^{2}(\frac{r_{ix}^2}{B_{ix}^2} + \frac{r_{iy}^2}{B_{iy}^2} + \frac{r_{iz}^2}{B_{iz}^2})]\phi(\alpha_1)\phi(\alpha_2)\phi(\alpha_3)\}, \quad (2)$$

and $\Phi^B(\boldsymbol{R}_1, \boldsymbol{R}_2)$ is the Brink wave function of ^{12}C [18],

$$\Phi^B(\boldsymbol{R}_1, \boldsymbol{R}_2) \propto \phi_G \mathcal{A}\{\exp[-\frac{(\boldsymbol{r}_1 - \boldsymbol{R}_1)^2}{b^2} - \frac{(\boldsymbol{r}_2 - \boldsymbol{R}_2)^2}{\frac{3}{4}b^2}]\phi(\alpha_1)\phi(\alpha_2)\phi(\alpha_3)\}, \quad (3)$$

$B_{1k}^2 = b^2 + \beta_{1k}^2$, $B_{2k}^2 = \frac{3}{4}b^2 + \beta_{2k}^2$, and $\boldsymbol{\beta}_i \equiv (\beta_{ix}, \beta_{iy}, \beta_{iz})$ and b is the size parameter of the harmonic-oscillator wave function. $\phi(\alpha_i)$ is the α-cluster intrinsic wave function and $\boldsymbol{X}_i$ is the corresponding center-of-mass coordinate. $\boldsymbol{r}_1 = \boldsymbol{X}_2 - \boldsymbol{X}_1$, $\boldsymbol{r}_2 = \boldsymbol{X}_3 - (\boldsymbol{X}_1 + \boldsymbol{X}_2)/2$. $\boldsymbol{R}_1$ and $\boldsymbol{R}_2$ are the inter-cluster distance generator coordinates in the Brink wave function. ϕ_G is the center-of-mass wave function of ^{12}C, which can be written as $\exp(-6X_G^2/b^2)$.

In the 2α+α THSR wave function in Eq. (1), two deformed size parameters $\boldsymbol{\beta}$ ($\boldsymbol{\beta}_1$ and $\boldsymbol{\beta}_2$) are introduced. In this 3α cluster system of ^{12}C, 2α clusters make the motion in a container confined by the size parameter $\boldsymbol{\beta}_1$ and this ^{8}Be(2α) cluster and the third α cluster can be considered to move in the other $\boldsymbol{\beta}_2$-size container. Thus, the 2α correlation has been included in the constructed 2α+α THSR wave function. If we make the replacement, $\boldsymbol{\beta}_1 \to \sqrt{2}\boldsymbol{\beta}_0$ and $\boldsymbol{\beta}_2 \to \sqrt{3/2}\boldsymbol{\beta}_0$ in Eq. (1), this 2α+α THSR wave function becomes the 3α THSR wave function with single $\boldsymbol{\beta}_0$ parameter used by Funaki et al. in Ref [13].

In the practical calculations, we assume the axial symmetry of the 2α+α system, namely, $\boldsymbol{\beta}_i \equiv (\beta_{ix} = \beta_{iy}, \beta_{iz})$ (i=1, 2). Thus, the projected 0^+ THSR wave function can be obtained by making the angular momentum projection on the intrinsic 2α+α THSR wave function. To compare with the full solution results of the 3α cluster models, two kinds of potential parameters are adopted. Force 1 in Table 1 represents the parameters, Volkov No.1 with Majorana parameter M=0.575 and b=1.41 fm, which is used by Uegaki et al. for 3α Brink-GCM calculation [10]. Force 2 represents the parameters, Volkov No.2 (modified version) with Majorana parameter M=0.59 and b=1.35 fm, which is used by Kamimura et al. for 3α RGM calculation [11].

Firstly, we make the variation calculations using the projected 0^+ THSR wave function in the deformed four-parameter space $\beta_{1x} = \beta_{1y}$, β_{1z} , $\beta_{2x} = \beta_{2y}$, and β_{2z}. Adopting Force 1 potential parameter, we can find the minimum energy $E_{\min}$= −87.28 MeV at the position $\beta_{1x} = \beta_{1y} = 1.5$, $\beta_{1z} = 0.1$, $\beta_{2x} = \beta_{2y} = 0.1$, $\beta_{2z} = 3.2$ fm, which is about 1.2 MeV deeper than the obtained minimum energy, -86.09 MeV by using the one-deformed-$\boldsymbol{\beta}$ THSR wave function. As for the Force 2 case, the minimum energy $E_{\min}$= −89.05 MeV appears at the position $\beta_{1x} = \beta_{1y} = 0.1$, $\beta_{1z} = 2.3$, $\beta_{2x} = \beta_{2y} = 2.8$, $\beta_{2z} = 0.1$ fm, which is about 1.4 MeV deeper than the obtained minimum energy -87.68 MeV by using the one-deformed-$\boldsymbol{\beta}$ THSR wave function. These obtained deeper energies indicate that the 2α correlation cannot be neglected in the compact ground state of ^{12}C.

Table 1: For the ground state of ^{12}C, $E_{\min}(\boldsymbol{\beta}_0)$ are the obtained minimum energies by using one deformed parameter $\boldsymbol{\beta}_0$ in the 3α THSR wave function and $E_{\mathrm{GCM}}(\boldsymbol{\beta}_0)$ are the corresponding GCM energy [13]. $E_{\min}(\boldsymbol{\beta}_1, \boldsymbol{\beta}_2)$ are the obtained minimum energies by using two deformed parameters $(\boldsymbol{\beta}_1, \boldsymbol{\beta}_2)$ in the 2α+α THSR wave function and $E_{\mathrm{GCM}}(\boldsymbol{\beta}_1, \boldsymbol{\beta}_2)$ are the corresponding GCM energy. The squared overlaps between $\hat{\Phi}_{\mathrm{GCM}}(\boldsymbol{\beta}_1, \boldsymbol{\beta}_2)$ and the single normalized 2α+α THSR wave functions corresponding to their minimum energies are also listed [17]. Here, SO= $|\langle\hat{\Phi}_{\min}(\boldsymbol{\beta}_1, \boldsymbol{\beta}_2)|\hat{\Phi}_{\mathrm{GCM}}(\boldsymbol{\beta}_1, \boldsymbol{\beta}_2)\rangle|^2$. Units of energies are MeV.

Potential	$E_{\min}(\boldsymbol{\beta}_0)$ [13]	$E_{\min}(\boldsymbol{\beta}_1, \boldsymbol{\beta}_2)$	Full 3α calculations	$E_{\mathrm{GCM}}(\boldsymbol{\beta}_0)$ [13]	$E_{\mathrm{GCM}}(\boldsymbol{\beta}_1, \boldsymbol{\beta}_2)$	SO
Force 1	−86.09	−87.28	−87.92 [10]	−87.81	−87.98	0.975
Force 2	−87.68	−89.05	−89.4 [11]	−89.52	−89.65	0.978

Next, we solve the Hill-Wheeler equation and obtain the converged eigenvalues for the ground state of ^{12}C, -87.98 MeV and -89.65 MeV for the Force 1 and Force 2 effective interactions, respectively.

The square overlaps between these obtained THSR-GCM wave functions $\hat{\Phi}_{\rm GCM}(\boldsymbol{\beta}_1, \boldsymbol{\beta}_2)$ and the single normalized 2α+α THSR wave functions corresponding to their minimum energies are also obtained. The related results are listed in Table 1.

It can be seen that the present 2α+α THSR wave function with 2α correlation has improved much the description of the ground state of ^{12}C compared with the result from the one-$\boldsymbol{\beta}$ case. The obtained ground state energy from the single optimum 2α+α THSR wave function is more than 1 MeV deeper than 3α THSR case for the two effective potential parameters. It is surprising to find that there is still so large room for improvement for the compact ground state of ^{12}C in the container picture. Even in the THSR-GCM calculations, the energies also have some slighter improvement if the 2α correlation is included. This shows that in the container picture the 2α correlation plays an important role in the ground state of ^{12}C.

In Table 1, we can find that the calculated squared overlaps $|\langle\hat{\Phi}_{\rm min}(\boldsymbol{\beta}_1, \boldsymbol{\beta}_2)|\hat{\Phi}_{\rm GCM}(\boldsymbol{\beta}_1, \boldsymbol{\beta}_2)\rangle|^2$ are as high as 98% by using two kinds of potentials. It is not surprising that the wave function can be improved by increasing the number of variational parameters. However, the obtained squared overlap 98% is surprising since this simple improved single THSR wave function is now almost 100% equivalent to the full solution of 3α cluster model. Since almost all the observed quantities including those related to the ground state are reproduced very well by the RGM/RGM wave functions [10, 11], this means that our container wave function is also well supported by experiments. Furthermore, while the previous THSR calculations for ^{12}C show that the squared overlap between the single 3α THSR wave function and the THSR-GCM wave function for the ground state is at most 93%, by introducing the 2α correlation, the corresponding squared overlap increases to 98%. This provides a strong support for the existence of the 2α correlation in the ground state of ^{12}C.

As we know, the Hoyle state has a gas-like cluster structure and 2α correlation is very weak in contrast to the ground state of ^{12}C. This character is reflected in the fact that the single 3α THSR wave function without the 2α correlation is almost 100% equivalent to the corresponding RGM/GCM wave function [13]. On the other hand, the 0_3^+ and 0_4^+ states of ^{12}C are possible to have a strong 2α correlation according to theoretical studies including the AMD (antisymmetrized molecular dynamics) calculations [7] and also to recent experimental studies [19]. Quite recently, the performed calculations for the excited 0^+ states of ^{12}C using this 2α+α THSR wave function have been done by Funaki [20].

In summary, we extended the original 3α THSR wave function to 2α+α THSR wave function by introducing the 2α correlation for describing the ground state of ^{12}C. It is found that the compact cluster structure of the ground state can be described well in the container picture and the squared overlap between this single THSR wave function and the THSR-GCM wave function is as high as 98%. While the corresponding squared overlap is at most 93% if we use the 3α THSR wave function without 2α correlation, we further conclude that the 2α correlation is very important in the ground state of ^{12}C.

Acknowledgement

The authors would like to thank Prof. Gerd Röpke, Prof. Peter Schuck, Prof. Taiichi Yamada, and Prof. Chang Xu for helpful discussions. B.Z. wishes to acknowledge discussions with Prof. Naoyuki Itagaki, Prof. Eiji Uegaki, and Dr. Tadahiro Suhara. This work is supported by the National Natural Science Foundation of China (Grants No. 11035001, No. 10975072, No. 10735010, No. 11375086, No. 11175085, No. 11235001, and No. 11120101005), by the 973 Program of China (Grants No. 2010CB327803 and No. 2013CB834400), and by the Project Funded by the Priority Academic Program Development of Jiangsu Higher Education Institutions (PAPD).

References

[1] Yukawa T, Yoshida S. An alpha-cluster model calculation of ^{12}C. Phys. Lett. B. 1970;33(5):334–6.

[2] Takigawa N, Arima A. Structure of ^{12}C. Nucl. Phys. A. 1971;168(3):593–624.

[3] Fujiwara Y, Horiuchi H, Ikeda K, Kamimura M, Katō K, Suzuki Y, et al. Chapter II. Comprehensive Study of Alpha-Nuclei. Prog. Theor. Phys. Supple. 1980;68:29–192.

[4] von Oertzen W, Freer M, Kanada-En'yo Y. Nuclear clusters and nuclear molecules. Phys. Rep. 2006;432(2):43–113.

[5] Chernykh M, Feldmeier H, Neff T, von Neumann-Cosel P, Richter A. Structure of the Hoyle State in ^{12}C. Phys. Rev. Lett. 2007;98(3):032501.

[6] Freer M. The clustered nucleus—cluster structures in stable and unstable nuclei. Rep. Prog. Phys. 2007 Dec 1;70(12):2149.

[7] Kanada-En'yo Y. The Structure of Ground and Excited States of ^{12}C. Prog. Theor. Phys. 2007;117(4):655–80.

[8] Horiuchi H, Ikeda K, Katō K. Recent Developments in Nuclear Cluster Physics. Prog. Theor. Phys. Supple. 2012;192:1–238.

[9] Horiuchi H. Many-Cluster Problem by the Orthogonality Condition Model General Discussion and ^{12}C Problem. Prog. Theor. Phys. 1975 Jan 2;53(2):447–60.

[10] Uegaki E, Okabe S, Abe Y, Tanaka H. Structure of the Excited States in ^{12}C. I. Prog. Theor. Phys. 1977;57(4):1262–76; On the Positive-Parity States with Anomalous α-Decay Properties in ^{12}C. Prog. Theor. Phys. 1978 Jan 3;59(3):1031–3; Structure of the Excited States in ^{12}C. II. Prog. Theor. Phys. 1979;62(6):1621–40.

[11] Y. Fukushima and M. Kamimura, Proceedings of the International Conference on Nuclear Structure, Tokyo, 1977, edited by T. Marumori (Suppl. J. Phys. Soc. Jpn. 44, 1978), p. 225

[12] Tohsaki A, Horiuchi H, Schuck P, Röpke G. Alpha Cluster Condensation in ^{12}C and ^{16}O. Phys. Rev. Lett. 2001 Oct 17;87(19):192501.

[13] Funaki Y, Tohsaki A, Horiuchi H, Schuck P, Röpke G. Analysis of previous microscopic calculations for the second 0^+ state in ^{12}C in terms of 3-α particle Bose-condensed state. Phys. Rev. C. 2003 May 30;67(5):051306.

[14] Zhou B, Ren Z, Xu C, Funaki Y, Yamada T, Tohsaki A, et al. New concept for the ground-state band in ^{20}Ne within a microscopic cluster model. Phys. Rev. C. 2012 Jul 3;86(1):014301.

[15] Zhou B, Funaki Y, Horiuchi H, Ren Z, Röpke G, Schuck P, et al. Nonlocalized Clustering: A New Concept in Nuclear Cluster Structure Physics. Phys. Rev. Lett. 2013;110(26):262501.

[16] Zhou B, Funaki Y, Horiuchi H, Ren Z, Röpke G, Schuck P, et al. Nonlocalized cluster dynamics and nuclear molecular structure. Phys. Rev. C. 2014;89(3):034319.

[17] Zhou B, Funaki Y, Tohsaki A, Horiuchi H, Ren Z. The container picture with two-alpha correlation for the ground state of ^{12}C. Prog. Theor. Exp. Phys. 2014 Jan 10;2014(10):101D01.

[18] D. M. Brink, *Proc. Intern. School of Physics "Enrico Fermi", course 36* (Academic Press, 1966).

[19] M. Itoh et al., Journal of Physics: Conference Series 436, 012006 (2013).

[20] Funaki Y. Hoyle band and α condensation in ^{12}C. Phys. Rev. C. 2015;92(2):021302.

50 Prediction Calculation of Criticality at KUCA Solid Moderator Core for Integral Validation of MA nuclear data

Tadafumi SANO[a], Takahiro YAGI[a], Jun-ichi HORI[a], Yoshiyuki TAKAHASHI[a], Hiroshi YASHIMA[a], Koichi TAKAMIYA[a], Cheol Ho PYEON[a], Hideo HARADA[b]

[a]Kyoto University Research Reactor Institute, [b]Japan Atomic Energy Agency

t-sano@rri.kyoto-u.ac.jp

In 2013, polyethylene solid moderators of KUCA have been renewed. Criticalities with new polyethylene moderator have been different from the criticalities of the old core. Therefore, prediction calculations of criticalities of KUCA core to measure reaction rate ratios with Back-to-Back fission chamber are performed. The calculations are performed by MVP2.0 with JENDL-4.0. As the results, it is predicted that the inventory of enriched uranium plates in hard neutron spectrum core is 3600 plates and the multiplication factor (k_{eff}) is 1.00454±0.0139%. On the other hand, in the case of the soft spectrum core, the k_{eff} is 1.00433±0.0144% with 864 enriched uranium plates. In addition, preliminary calculations of the fission rate ratios (^{241}Am/^{235}U) with JENDL-4.0 are 0.0441±1.46% in soft spectrum core and 0.0149±0.95% in hard spectrum core.

1. Introduction

In order to improve accuracy of minor actinides (MAs) and long life fission products (LLFPs), the project entitled as “Research and development for Accuracy Improvement of neutron nuclear data on Minor Actinides (AIMAC)” has been started as one of the “Innovative Nuclear Research and Development Program” in Japan at October 2013. In this project, differential experiments of MAs and LLFPs nuclear data with pulsed neutron source are carried out. In addition, measurements of reaction rate ratio as integral validation are performed using Kyoto University Critical Assembly (KUCA) to be cross-checked with differential data. The target nuclides are ^{241}Am and ^{237}Np and so on.

The ^{241}Am and ^{237}Np fission rate ratios relative to ^{235}U and the neutron capture rate ratio between ^{237}Np and ^{197}Au have been measured [1]. The relative experimental errors were 2.6% to 2.8%. In those errors, the largest contribution was numbers of target nuclei. Thus, we have planned to reduce the uncertainties of the numbers and to perform follow-up critical experiment. On the other hand, because the polyethylene solid moderators have been renewed at September 2013 [2], it is predicted that the criticalities with new polyethylene moderator are different from the criticalities of the old core.

In this study, prediction calculations of criticalities of KUCA core to measure the reaction rate ratio are performed. The calculations are performed by MVP2.0 [3] with JENDL-4.0 [4]. . In addition, preliminary calculations of the fission rate ratios (^{241}Am/^{235}U) with JENDL-4.0, JENDL-3.3 [5] and ENDF/B-VII.0 [6].

2. Irradiation conditions at KUCA soiled moderated core

KUCA solid moderator core is able to consist of enriched uranium fuel plate and various moderator plates (i.e. polyethylene and graphite). Figure 1 shows the schematic view of KUCA solid moderator core. In order to vary the neutron spectrum of the irradiation field, the H/^{235}U nuclide ratio in the unit cell is varied by the combination of the U-Al alloy fuel plates and the polyethylene moderator plates. The enrichment of the uranium is about 93 wt %. The width of the plates have 2 inch square. The thickness of the fuel plates has 1/16 inch and the polyethylene plate is 1/8 inch.

In this study, the E3 core and the EE1 core are employed. The unit cell in E3 core consists of the 1 fuel plate and the 2 polyethylene plates. The EE1 unit cell has the 2 fuel plates and the 1 polyethylene plates. When a MA foil and a ^{235}U foil are simultaneously irradiated in the neutron spectrums, we can measure energy dependency of a fission rate ratio.

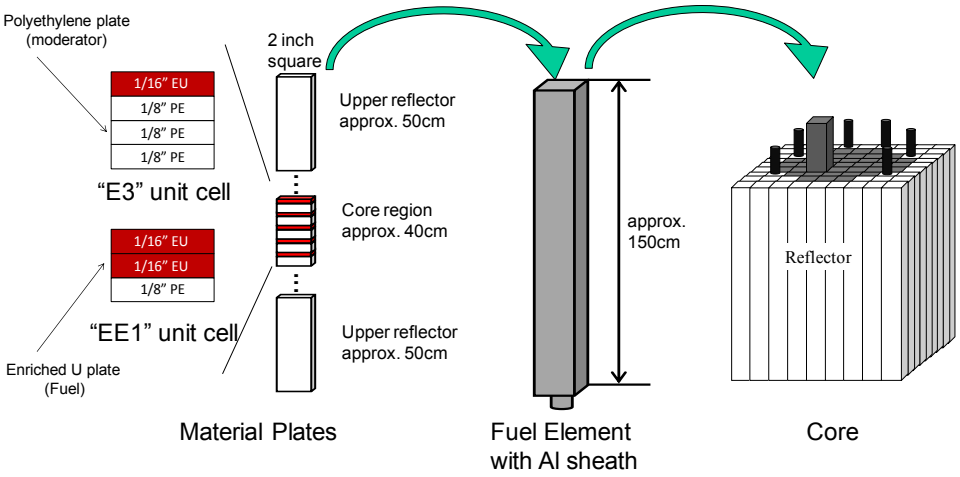

Fig.1 Schematic view of KUCA solid moderator core

3 Numerical calculations and results

3.1 Numerical conditions

In this study, the one of object is to predict calculation of criticalities for the experimental cores with new polyethylene moderators. The core has a void region in the center of core and the BTB fission chamber is inserted into the void region. The criticality of the core to measure a reaction rate ratio is calculated by changing the number of the loaded fuel elements or the unit cells in the fuel element. The prediction calculations are performed by the continuous energy Monte-Carlo code MVP2.0 with the JENDL-4.0. In the MVP calculations for the criticality, 500M neutron histories are

generated to suppress the statistical error of keff to less than 0.03% (1σ) because the typical experimental error for the keff is estimated to be about 0.03%.

On the other hand, the preliminary calculations of the reaction rate ration are performed by MVP2.0 with JENDL-4.0. In the calculations, 1G neutron histories are generated to suppress the statistical error of reaction rate ratio to less than 2.0% (1σ) because the typical experimental error for the keff is estimated to be about 2.3 to 2.0% [1]. In addition, the sensitivity analysis is performed by generalized perturbation code SAGEP [7].

3.2 Criticality

The numerical results of the criticalities and the control rods worth are shown in table 1. The core configurations of EE1 core (hard neutron spectrum) and E3 core (soft neutron spectrum) are shown in Fig.2 and the neutron spectra in the cores are shown in Fig.3. In order to insert a BTB fission chamber, the core has a void region in the center of core. As the results, it is predicted that the inventory of enriched uranium plates in hard neutron spectrum core (EE1 core) is 3600 plates and the multiplication factor (k_{eff}) is 1.00454±0.0139%. On the other hand, in the case of the soft spectrum core (E3 core), the k_{eff} is 1.00433±0.0144% with 864 enriched uranium plates.

Table 1 Numerical results of criticality and control rod worth

	EE1 core	E3 core
k_{eff}	1.00454±0.0139%	1.00433±0.0144%
C1 rod worth (%dk/k)	1.033±0.020%	1.214±0.020%
C1 rod worth (%dk/k)	0.679±0.020%	0.545±0.020%
C1 rod worth (%dk/k)	1.036±0.020%	0.935±0.020%
Center core worth (%dk/k)	11.614±0.021%	9.997±0.020%

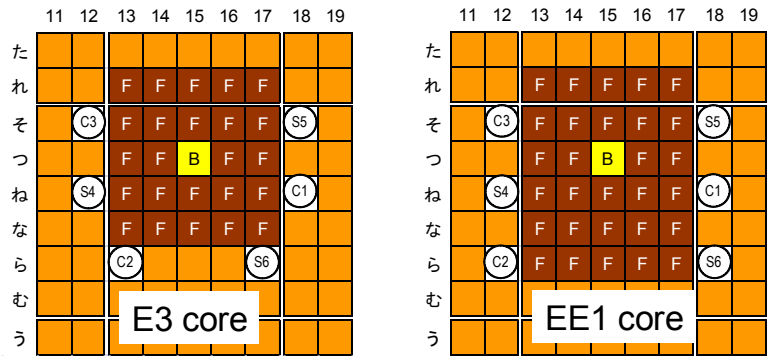

Fig.2 Core configuration to measure fission rate ratio

F:Fuel element, B:Void region with BTB chamber, C and S: Control rod

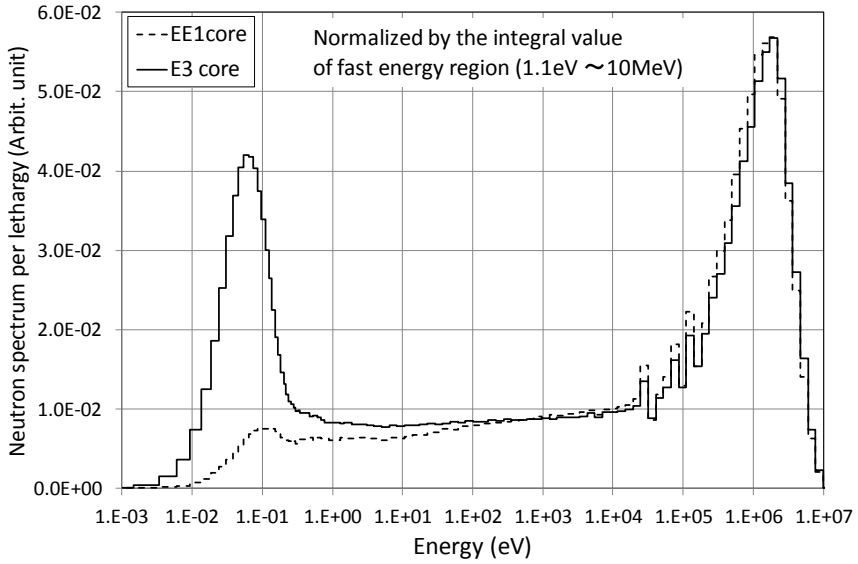

Fig.3 Neutron spectrum in BTB fission chamber

3.3 Fission rate ratio

The MA foil and the ^{235}U foil are inserted into a back-to-back (BTB) fission chamber shown in Fig.4. In the prediction calculations of fission rate ration, the amounts of ^{241}Am and ^{235}U are set to a same condition as reference [1] shown in table 2.

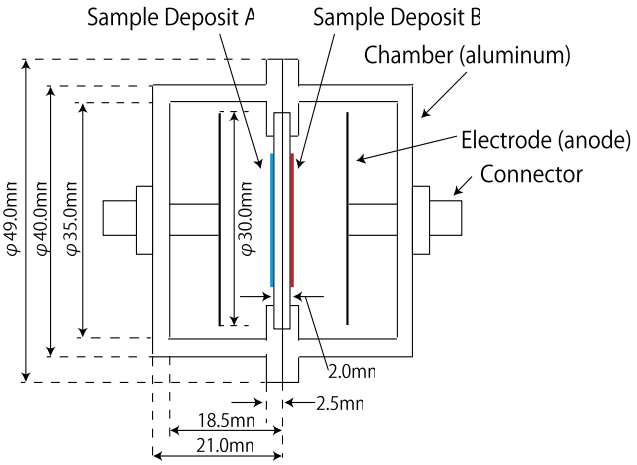

Fig.4 BTB fission chamber

As the preliminary calculation results with JENDL-4.0, JENDL-3.3 and ENDF/B-VII.0, the fission rate ratios 0.0435±1.50% to 0.0448±1.46% in the EE1 core and 0.0149±1.02% to 0.0151±0.95% shown in table 3. Where, the ^{235}U cross section from JENDL-4.0 is used for all cases. The results of reaction rate ratio among each library are agree within the statistical error. Figure 5 shows sensitivity coefficients of ^{241}Am/^{235}U fission rate ratio respect for ^{241}Am fission cross section. The sensitivity coefficients have large value in the energy range of thermal region to resonance region and the sensitivity coefficient of the EE1 core is sifted to high energy by the hard neutron spectrum. Especially, the sensitivity coefficient in the 79'th group which includes the first resonance (E=0.305eV) has large difference between EE1 core and E3 core. Thus, researchers can obtain integral data of ^{241}Am fission cross section with above sensitivities via the critical experiments at the EE1 core and E3 core.

Table 2 Number of target nuclide

^{241}Am	(1.73±0.02) ×10^{16}
^{235}U	(1.49±0.02) ×10^{16}

Table 3 Numerical results of the fission rate ratio

	EE1	E3
JENDL-4.0	0.0441±1.46%	0.0149±0.95%
JENDL-3.3	0.0448±1.46%	0.0151±0.95%
ENDF/B-VII.0	0.0435±1.46%	0.0149±1.02%

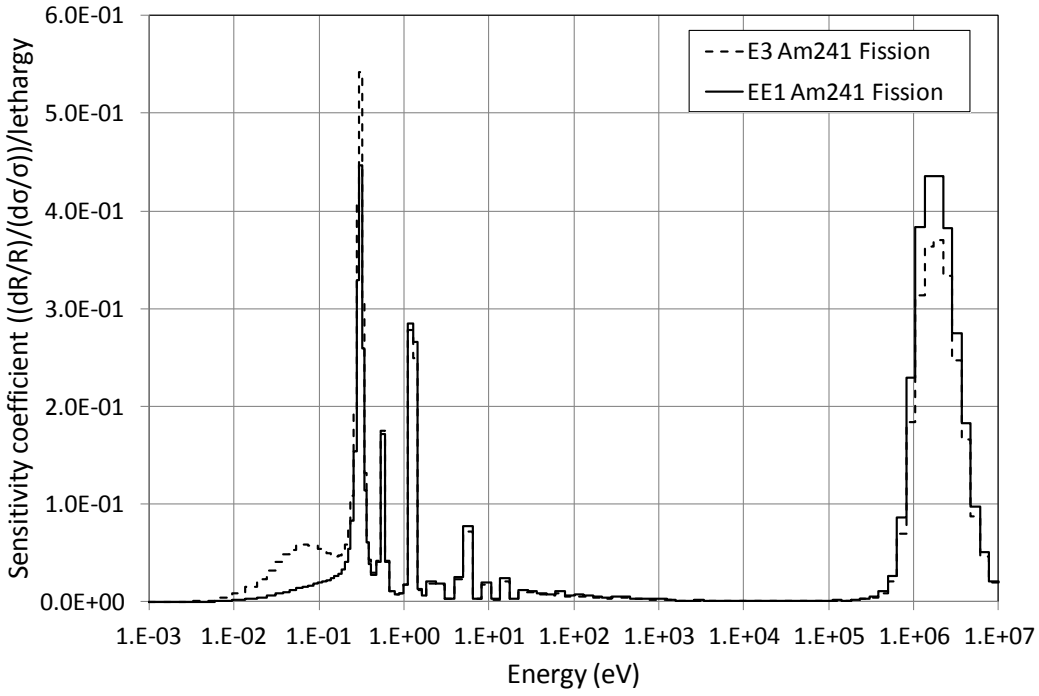

Fig.5 Sensitivity coefficient of ^{241}Am/^{235}U fission rate ratio respect for ^{241}Am fission cross section

4. Conclusion

In this study, prediction calculations of criticalities of KUCA core to measure the reaction rate ratio are performed. The calculations are performed by MVP2.0 with JENDL-4.0. As the results, it is predicted that the inventory of enriched uranium plates in EE1 core is 3600 plates and the k_{eff} is 1.00454±0.0139%. On the other hand, the k_{eff} of E3 core is 1.00433±0.0144% with 864 enriched uranium plates. In addition, preliminary calculations of sensitivity coefficients for the fission reaction rate (Am241/U235) are carried out. In the preliminary calculations, the results showed that the reaction rate ratios among each library are agreement within the range of the statistical error.

Acknowledgment

Present study includes the result of “Research and Development for accuracy improvement of neutron nuclear data on minor actinides” entrusted to the Japan Atomic Energy Agency by the Ministry of Education, Culture, Sports, Science and Technology of Japan (MEXT).

References

[1] Unesaki H. Study on Verification of Nuclear Data for Nuclear Design of Next Generation Thermal Reactors [dissertation]. [Kyoto]: Kyoto University; 2001. 126p.

[2] Sano T, Pheon C H, Yagi T, Takahashi Y, Shiga H, Unesaki H, Misawa T, Nakajima K. Impact of new polyethylene moderator and reflector for criticality in KUCA solid core [abstract]. AESJ Fall Meeting; 2014 Sep 8-10; Kyoto, Japan; [CD-ROM]. Japanese.

[3] Nagaya Y, Okumura K,Mori T. MVP/GMVP II: General Purpose Monte Carlo Codes for Neutron and Photon Transport Calculations based on Continuous Energy and Multigroup Methods. JAERI 1348, 2005.

[4] Shibata K, Iwamoto O, Nakagawa T, N. Iwamoto N, A. Ichihara A, S. Kunieda S, S. Chiba S, Furutaka K, Otuka N, Ohsawa T, Murata T, Matsunobu H, Zukeran A, Kamada S, Katakura J. JENDL-4.0: A New Library for Nuclear Science and Engineering. J Nucl Sci Technol. 2011; 48(1):1-30.

[5] Shibata K, Kawano T, Nakagawa T, Iwamoto O, Katakura J, Fukahori T, Chiba S, Hasegawa A, Murata T, Matsunobu H, Ohsawa T, Nakajima Y, Yoshida T, Zukeran A, Kawai M, Baba M, Ishikawa M, Asami T, Watanabe T, Watanabe Y, Igashira M, Yamamuro N, Kitazawa H, Yamano N Takano H. Japanese Evaluated Nuclear Data Library Version 3 Revision-3: JENDL-3.3. J Nucl Sci Technol. 2002; 39(11):1125-1136.

[6] Chadwick MB, Obložinský P, Herman M, Greene NM, McKnight RD, Smith DL, Young PG, MacFarlane RE, Hale GM, Frankle SC, Kahler AC, Kawano T, Little RC, Madland DG, Moller P, Mosteller RD, Page PR, Talou P, Trellue H, White MC, Wilson WB, Arcilla R, Dunford CL, Mughabghab SF, Pritychenko B, Rochman D, Sonzogni AA, Lubitz CR, Trumbull TH, Weinman JP, Brown DA, Cullen DE, Heinrichs DP, McNabb DP, Derrien H, Dunn ME, Larson NM, Leal LC, Carlson AD, Block RC, Briggs JB, Cheng ET, Huria HC, Zerkle ML, Kozier KS, Courcelle A, Pronyaev V, Marck SC. ENDF/B-VII.0: Next Generation Evaluated Nuclear Data Library for Nuclear Science and Technology. Nucl. Data Sheets. 2006;107(12):2931-3060.

[7] Hara A, Takeda T, Kikuchi Y. SAGEP: Two-Dimensional Sensitivity Analysis Code Based on Generalized Perturbation Theory. JAERI-M 84-027, 1984. [Japanese]

51 A new EXFOR editor system: Java version of HENDEL

A. Sarsembayeva[1,2*], S. Imai[1,2], S. Ebata[1,2], M. Chiba[3], K. Katō[1], N. Otuka[4], M. Aikawa[1]

[1]Nuclear Reaction Data Centre, Faculty of Science, Hokkaido University, Sapporo 060-0810, Japan

[2]Meme Media Laboratory, Hokkaido University, Sapporo 060-8628, Japan

[3]Sapporo-Gakuin University, Ebetsu, 069-8555, Japan

[4]Nuclear Data Section, International Atomic Energy Agency, A-1400 Wien, Austria

[*] E-mail: aiganym@nucl.sci.hokudai.ac.jp, Phone: 011-706-3518

Compiled nuclear reaction data have widely been used in many fields of technological researches such as design and operation of nuclear power plants, medical isotopes, radiotherapy, etc. as well as fundamental researches. To keep the nuclear reaction database high quality for such users, an editor to compile the data plays an important role. In this report, we present a new EXFOR editor system based on the Java programming language. At the current stage we design input forms of the new system.

The International Network of the Nuclear Reaction Data Centers (NRDC) [1] is a world-wide network of nuclear data centers organized under the auspices of the International Atomic Energy Agency (IAEA). It has been established to coordinate collection, compilation, and dissemination of nuclear data on an international scale. Nuclear data have been utilized in the following many areas: nuclear physics, astrophysics, nuclear engineering, medicine, etc. Since the early 80s the Nuclear Reaction Data Centre of Hokkaido University (JCPRG, formerly Japan Charged-Particle Nuclear Reaction Data Group) [2] has been extensively active as a member of the network.

Under the NRDC network, experimental nuclear reaction data are compiled and stored in the EXFOR library [3] in a unified format EXFOR (Exchange Format), which defines full details of the experimental and bibliographical information.

In order to simplify EXFOR compilation, various editor systems have been developed within the NRDC community. ANDEX [4] developed by IAEA-NDS (Vienna) and ERES by CNDC (Beijing) [5] are such systems developed in 1990s. An EXFOR editor developed by CNPD (Sarov) in 2000s is currently used by many EXFOR compilers. In JCPRG, a web-based nuclear data input system HENDEL (Hyper Editor for Nuclear Data Exchange Libraries) was developed for compilation of experimental nuclear reaction data in NRDF and EXFOR formats [6], and it has been used as a standard compilation editor system at JCPRG since 2001 [7]. For beginners of EXFOR compilation, the HENDEL system is very useful because it requires very limited knowledge on EXFOR, and it is now also used by new EXFOR

compilers in Kazakhstan and Mongolia. While the current HENDEL system is well designed to create outputs in both NRDF and EXFOR format, some extra input forms for creation of NRDF outputs could be rather confusing for foreign compilers who do not create NRDF outputs. Therefore a clone of HENDEL specialized for EXFOR outputs is of our interest. Recently, we have started to develop a new HENDEL system using the Java programming language for a standalone application type (GUI). Java is platform independent and an object-oriented programming language. Note that EXFOR compilers emphasized in a recent EXFOR compilation workshop (6-10 Oct. 2014, Vienna) that it is important to develop an OS independent EXFOR editor system [8]. We adopt Java Swing API for building GUI (graphical user interface) application.

A main page of the new HENDEL editor under development is shown in Fig.1. Contents of the editor will be organized in a Tree format. The contents of editor consist: Bibliography, information commonly applied to all data sets of the EXFOR entry (Subentry 001), and information applied to each data set of the EXFOR entry independently (Subentry 002, 003,..). The Bibliography section consists of Title, Author, Affiliation and Reference. One of the new improvements in this editor is that Affiliation and Reference part in the Bibliographic section can be multiplied by "+" button as shown in Fig. 1.

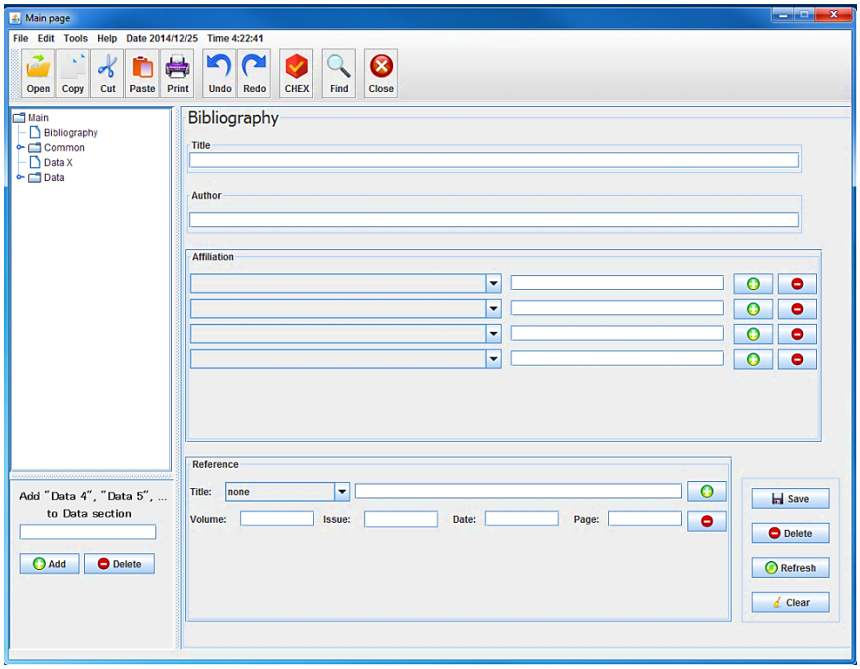

Figure 1: Main page of Java based Hendel system (under development)

Such a new HENDEL system is expected to be very useful for compilation not only in JCPRG but also in foreign countries .

We plan to develop the new HENDEL system by the following steps:

- Design of the user interface;
- Coding for realization of desired functions;

- Inclusion of utilities (e.g., checking tools);
- Data output in EXFOR format.

References

[1] N. Otuka (ed.), Report INDC(NDS)-0401 Rev.6, International Atomic Energy Agency (2014).

[2] http://www.jcprg.org/

[3] N. Otuka et al., Nucl. Data Sheets **120**(2014)272.

[4] V. Osolio, Report IAEA-NDS-0101, International Atomic Energy Agency (1991).

[5] Li Shubing, Liang Qichang, Liu Tingin, Report IAEA-NDS-0151, International Atomic Energy Agency (1994).

[6] http://www.jcprg.org/hendel/

[7] N. Otuka, H. Noto, A. Ohnishi, K. Kato, Report INDC(NDS)-0434, p.144, International Atomic Energy Agency (2002).

[8] V. Semkova, B. Pritychenko (eds.), Report INDC(NDS)-0672, International Atomic Energy Agency (2015).

This is a blank page.

52 Calculation of the scattering cross section for ^{6}Li+n reactions

D. Ichinkhorloo [1], M. Aikawa [2], S. Chiba [3], Y.Hirabayashi [4], and K. Katō [2]

[1]*Meme Media Laboratory, Hokkaido University, Sapporo 060-8628, Japan*
[2]*Nuclear Reaction Data Centre, Faculty of Science, Hokkaido University, Sapporo 060-0810, Japan*
[3]*Research Laboratory for Nuclear Reactors, Tokyo Institute of Technology, Tokyo 152-8550, Japan*
[4]*Information Initiative Center, Hokkaido University, Sapporo 060-0811, Japan*

Abstracts

We study the integrated elastic and inelastic scattering cross sections of ^{6}Li + *n* using an (α + *d*) + *n* cluster model and the continuum-discretized coupled-channel framework. The cluster folding potential of the α-*n* and *d*-*n* optical model potentials is applied to the low-energy scattering for the incident neutron energies below 10 MeV, while the microscopic single-folding potential is used for the neutron energies above 10 MeV. The calculated elastic and inelastic scattering cross sections with observed incident energies are good agreement with experimental and evaluated data.

1. Introduction

The Li + *n* reactions are important not only from the basic interest but also from the application point of view. Lithium isotopes will be used as a tritium-breeding material in *d*-*t* fusion reactors. Therefore accurate nuclear data are required for n- and p-induced reactions.

In the previous works [1-3], we have successfully studied cross sections for the ^{6,7}Li + *n* elastic and inelastic scattering angular distributions and neutron spectra applying the continuum-discretized coupled-channel method (CDCC) method [4] with α + *d* + *n* and α + *t* + *n* model. It was found that the calculated cross sections data for incident energies from 7.47 to 24 MeV can be reproduced by the present cluster model with one normalization parameter for the imaginary part of the Jeukenne-Lejeune-Mahaux effective nucleon-nucleon (JLM) [5] interaction. More recently, H. Guo et al [6] have analyzed both neutron and proton scattering from ^{6,7}Li in wide incident energy up to 150 MeV, and demonstrated the applicability of CDCC to nucleon scattering from ^{6,7}Li. They analyzed neutron total cross sections, proton reaction cross sections and differential cross sections for nucleon elastic and inelastic scatterings. However, it is still difficult to reproduce low energy data below 10 MeV in the frameworks due to the applicable limit of the JLM potential.

In this work, we extended the CDCC analysis to the integrated elastic and inelastic scattering cross sections for ^{6}Li at incident neutron energies below 10 MeV by using optical model potential (OMP) [7,8] and above 10 MeV by using JLM. We adjust the normalization constants for the OMP, because the agreement of the calculated cross sections data at very low incident energies of the neutron is insufficient without any adjustments. The energy dependent normalization constants, real part λ_{v} and imaginary part λ_{w}, of the OMP and JLM are determined explicitly from integrated elastic cross section data, respectively. Comparing the results of calculations and experimental data, we discuss

the present CDCC calculations, which reproduce the experimental data observed in incident energies higher than 10 MeV with the single folding potential of the JLM and in lower energies with introducing the normalization factors for the cluster folding potential of the OMP.

2. The Method and Model

We prepare the wave functions of the bound and α-d scattering states of ^{6}Li in the similar way as previous work [1-2] in the CDCC method. The binding energy of the 1^+ ground state is observed as 1.47 MeV with respect to the $^6\mathrm{Li} \rightarrow \alpha + d$ threshold, and the low-energy part of the α-d scattering phase shifts in the S-wave (ℓ =0) and D-wave (ℓ =2) have been obtained experimentally. The excited 3^+, 2^+ and 1^+ states of ^{6}Li are observed at 2.18, 4.31, and 5.68 MeV, respectively, which are considered to be the triplet resonance state in the α-d, D-wave. According to the cluster model, the wave functions for the ground state (1^+) and the exited states are written as

$$\phi_{\ell I}(^6Li;k) = A\left\{\varphi(\alpha)[\varphi_I(d)\otimes u_\ell(k,\ r)]_I\right\}, \tag{1}$$

where $\varphi(\alpha)$ and $\varphi_I(d)$ stand for the internal wave functions of the alpha and deuteron clusters, respectively.

The interaction between α and d has central and spin-orbit parts, which are parametrized by a two-range Gaussian form and by a two-range Gaussian-derivative form, respectively;

$$\begin{aligned} V^{CE}{}_\ell(r) &= \upsilon_{1,\ell}e^{-(r/r_{1,\ell})^2} + \upsilon_{2,\ell}e^{-(r/r_{2,\ell})^2} + V_{CL}(r) \\ V_\ell^{SO}(r) &= \upsilon_{1,\ell}^{SO} r e^{-(r/r_{1,\ell})^2} + \upsilon_{2,\ell}^{SO} r e^{-(r/r_{2,\ell})^2} \\ V_{CL}(r) &= \begin{cases} Z_1Z_2e^2/r, & r \ge R_{CL} \\ \left(Z_1Z_2e^2/(2R_{CL})\right)\left(3 - r^2/R_{CL}{}^2\right), & r < R_{CL}. \end{cases} \end{aligned} \tag{2}$$

They are chosen ℓ-dependently so as to reproduce well the energies of the ground and excited states and the α-d scattering phase shifts. The parameter values are listed in Table 1.

Table 1. The parameters of the effective central and spin orbit potentials between α and d for ℓ =0 and 2

Parameters	$r_{1,\ell}$ (fm)	$r_{2,\ell}$ (fm)	$\upsilon_{1,\ell}$ (MeV)	$\upsilon_{2,\ell}$ (MeV)	$\upsilon_{1,\ell}^{(SO)}$ (MeV)	$\upsilon_{2,\ell}^{(SO)}$ (MeV)	R_{CL} (fm)
$\ell = 0$	2.191	1.607	-105.85	46.22	--	--	3.00
$\ell = 2$	2.377	1.852	-82.00	26.00	-2.31	1.42	3.00

The Schrödinger equation of the ^{6}Li + n scattering system, which is described by using the $n + \alpha + d$ three body model, is written as

$$\left[K_R + K_r + V_{d\alpha}(r) + U_{dn}(r_{dn} + U_{\alpha n}(r_{\alpha n}) - E\right]\Psi_{JM}^{CDCC} = 0\,, \tag{3}$$

where E is the energy of the total system, vector $\vec{r}$ is the relative coordinate between α and d, $\vec{R}$ the one between the center of mass of the d-α pair and n, and $\vec{r}_{dn}$ $(\vec{r}_{\alpha n})$ denotes the

relative coordinate between two particles $d(\alpha)$ and n. Operators K_r and K_R are kinetic energies associated with $\vec{r}$ and $\vec{R}$, respectively, and $V_{d\alpha}(\vec{r})$ is the interaction between d and α. The total wave function Ψ_{JM} with the total angular momentum J and its projection M on z-axis is expanded in terms of the orthonormal set of eigenstates $\phi_{\ell I}$ of $H(^6\mathrm{Li})$ for the α-d system;

$$\Psi_{JM}^{CDCC}(\vec{r},\vec{R}) = \sum_{L} Y_{JM}^{\ell_0 I_0 L}\phi_0(r)\hat{\chi}_{\gamma_0}(P_0,R)/R + \sum_{i=1}^{N}\sum_{\ell=0}^{\ell_{\max}}\sum_{I}\sum_{L} Y_{JM}^{\ell I L}\hat{\phi}_{i\ell I}(r)\hat{\chi}_{\gamma}(\hat{P},R)/R, \quad (4)$$

where the spin and angular parts are described as

$$Y_{JM}^{\ell I L} = \left[[i^{\ell}Y_{\ell}(\Omega_r)\otimes\eta_d]\otimes i^{\ell}Y_L(\Omega_R)\right]_{JM}\varphi(\alpha)\varphi(d), \quad (5)$$

with

$$\hat{\chi}_{\gamma_0}(P_0,R) = \chi_{\gamma_0}(P_0/R), \quad \gamma_0 = (0,\ell_0,I_0,L,J)$$
$$\hat{\chi}_{\gamma}(\hat{P}_{\gamma},R) = W_{\gamma}\chi_{\gamma}(\hat{P}_{\gamma}/R), \quad \gamma = (i,\ell,I,L,J) \quad (6)$$

On the right hand side of Eq.(4), the first term presents the elastic channel denoted by γ_0 and the second one corresponds to the discretized breakup channels, each denoted by γ. The expansion-coefficient χ_{γ} in Eq.(6) represents the relative motion between n and ^{6}Li, and L is the orbital angular momentum regarding $\vec{R}$.

The interaction U_{dn} ($U_{\alpha n}$) between d (α) and n is taken to be the optical potential for d+n (α+n) scattering. In Table 2, the parameters are shown explicitly. For simplicity, the spin dependence of the interaction is neglected. In this study, we adopt $p + \alpha$ scattering at 31MeV [7] instead of n-α interactions. For $n + d$ scattering, we used a neutron potential parameter set presented by Wilmore et al. [8] at lower incident energies. However, these optical potentials cannot reproduce the calculated cross section of the $n + {}^6$Li scattering. We introduce normalization parameters for real and imaginary parts of the cluster folding potential. We also use the JLM interaction based on a single folding model in the incident neutron energy region above 10 MeV. In the previous works [1-3], we reported the CDCC calculation with JLM interaction.

Table 2. Parameters of the optical potentials for d+n and α+n at half the neutron incident energy.

System	V_0(MeV)	r_0(fm)	a_0(fm)	W_D(MeV)	r_{WD}(fm)	a_{WD}(fm)
$d + n$	65.8	1.574	0.501	4.59	1.511	0.517
$\alpha + n$	47.0	2.098	0.660	9.52	2.009	0.280

3. Results and discussion

In this calculation, we analyze the integrated elastic and inelastic scattering cross sections of the ^{6}Li+n collision at incident neutron energies below 10 MeV by using optical model potential (OMP) and above 10 MeV by using JLM for the ^{6}Li-n folding potential. For the JLM single-folding potential, we take the normalization factors λ_v=1.0 and λ_w=0.2 for the real and imaginary parts, respectively. These values indicate that the small imaginary potential is needed while the real part has no any adjustment parameter. This is consistent with the previous studies [1-3]. However, because the JLM potential has not been constructed for incident neutron energies lower than about 10 MeV [5], we cannot

use the JLM single-folding potential for these energies. Instead of the microscopic JLM single-folding potential, we employ a more phenomenological cluster folding potential in lower energies.

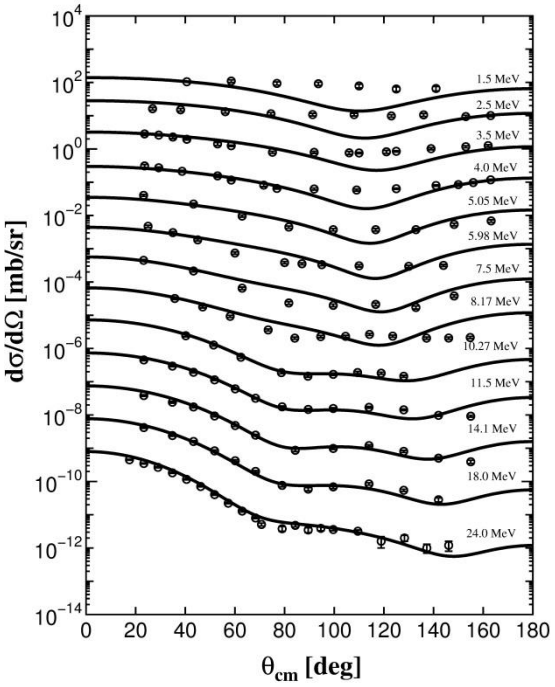

Figure 1. Elastic angular distribution of the differential cross sections for the ^{6}Li + *n* scattering for incident energies between 1.5 and 24.0 MeV. The solid lines and open circles correspond to the calculated data and experimental data. The data are subsequently shifted downward by a factor of 10^{-1}-10^{-12} from 2.5 MeV to 24.0 MeV, respectively.

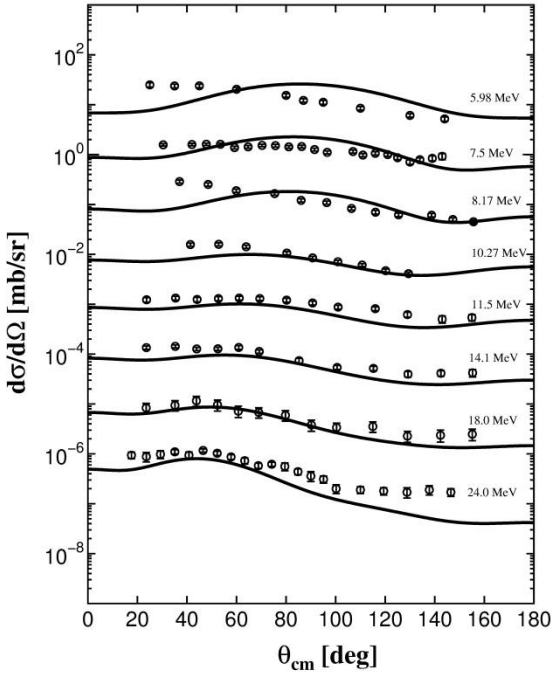

Figure 2. Neutron inelastic scattering angular distribution for the 3^{+} resonance state 0.71 MeV above the *d*-*α* threshold. The solid lines and open circles correspond to the calculated data and experimental data. The data are subsequently shifted downward by a factor of 10^{-1}-10^{-7} from 7.5 MeV to 24.0 MeV, respectively.

We determine normalization factors, real part λ_{v} and imaginary part λ_{w}, of the cluster folding ^{6}Li-n potential using α-*n* and *d*-*n* OMPs from measured integrated elastic cross section data. The obtained factors are expressed as the following linearly energy dependent form:

$$\lambda_{\mathrm{V}}(E) = 1.23 - 0.04\mathrm{E}$$

$$\lambda_{W}(E) = \begin{cases} 0.07\mathrm{E} - 0.4 & (6\,\mathrm{MeV} \le \mathrm{E} \le 10\mathrm{MeV}) \\ 0 & (\mathrm{E} \le 6\mathrm{MeV}) \end{cases} \qquad (6)$$

Figure 1 shows the differential cross sections of the ^{6}Li + *n* elastic scattering with incident energies between 1.5 and 24.0 MeV. One can see that the results of the CDCC calculation represented with solid lines are in good agreement with the experimental data.

For inelastic scattering, Fig.2 shows the angular distributions to the 3^{+} resonance state of ^{6}Li for E_n=5.98, 7.5, 8.17, 10.27, 14.1, 18.0 and 24.0 MeV. The calculated differential cross sections are obtained by integrating the breakup cross section to several discretized 3^{+} solutions obtained around the resonance energy region. We can see that the CDCC calculation can also reproduce the inelastic observed cross sections together with the elastic ones.

We also calculate the integrated elastic and inelastic cross sections between 1.5 and 24.0 MeV. The integrated elastic cross sections for ^{6}Li agree with the evaluated data (JENDL-3.3) and other measurements within the experimental uncertainties, as shown in

Fig. 3. In Fig.4, the integrated inelastic cross-section values for the 2.186-MeV state of ^{6}Li are almost in good agreement with the evaluation data of JENDL-3.3 and the experimental data.

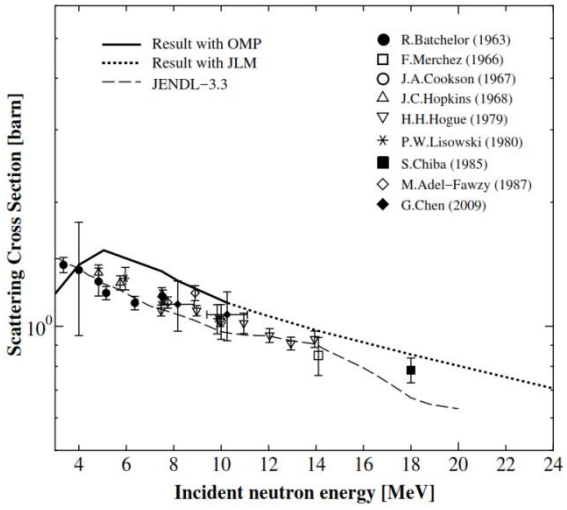

Figure 3. The integrated elastic scattering cross sections of ^{6}Li, in comparison with the evaluated data and experimental data.

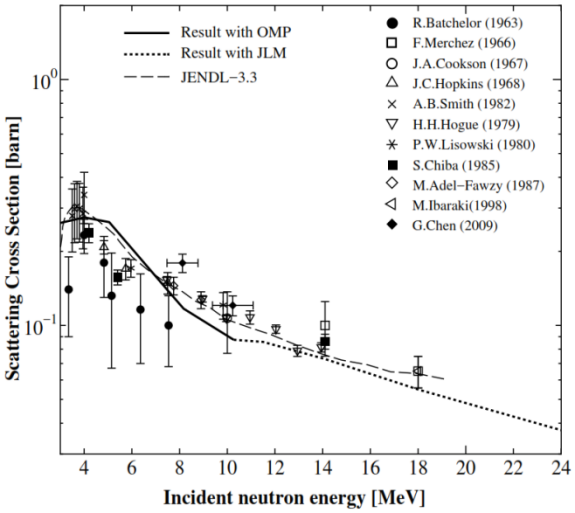

Figure 4. The integrated inelastic scattering cross sections for the 3^{+} state of ^{6}Li, in comparison with the evaluated data and experimental data.

4. Summary

Using the CDCC framework of the (α+*d*)+*n* model, we investigated the integrated elastic and inelastic scattering cross sections for ^{6}Li at incident neutron energies below 10 MeV using the cluster-folding of the optical model potentials and above 10 MeV using the JLM single-folding potential. Energy dependence of the normalization factors, λ_{v} and λ_{w}, of the cluster folding potential is introduced and determined from measured integrated elastic cross sections. The CDCC calculation gives a satisfactorily good agreement with the experimental data.

References

[1] Matsumoto T, Ichinkhorloo D, Hirabayashi Y, Katō K, Chiba S. Systematic description of the ^{6}Li(n,n')^{6}Li$*$ → d+α reactions with the microscopic coupled-channels method. Phys. Rev. C. 2011;83:064611.

[2] Ichinkhorloo D, Matsumoto T, Hirabayashi Y, Katō K, Chiba S. ^{6}Li + n reactions in the continuum discretized coupled channels method. J. Nucl. Sci. Technol. 2011 Sep; 48:1357-1460.

[3] Ichinkhorloo D, Hirabayashi Y, Katō K, Aikawa M, Matsumoto T, Chiba S. Analysis of ^{7}Li(n,n')^{7}Li$*$ reactions using the continuum-discretized coupled-channels method Phys. Rev. C. 2012;86:064604.

[4] Kamimura M, Yahiro M, Iseri Y, Sakuragi M, Kameyama H, Kawai M. Coupled-channels theory of breakup processes in nuclear reactions. Prog. Theor. Phys. Suppl. 1986; 89.

[5] Jeukenne J.-P, Lejeune A, Mahaux C. Optical-model potential in finite nuclei from Reid's hard core interaction. Phys. Rev. C. 1977;16:80.

[6] Guo H, Watanabe Y, Matsumoto T, Ogata K, Yahir M. Systematic analysis of nucleon scattering from ^{6,7}Li with the continuum discretized coupled channels method. Phys. Rev. C. 2013;87:024610.
[7] Burger S. J, Heymann G. Alpha-particle and proton scattering from even mass molybdenum isotopes. Nucl. Phys. A. 1974;243-461.
[8] Wilmore D, Hodgson P.E. The calculation of neutron cross-sections from optical potentials. Nucl. Phys. 1964;55:673.
[9] Chen G, Ruan X, Zhou Z, Zhang J, Qi B, Li X, Huang H, Tang H, Zhong O, Jiang J, Xin B, Bao J, Chen L. Double-differential neutron emission cross-section measurement of ^{6}Li and ^{7}Li at incident energies of 8.17 abd 10.27 MeV. Nuclear Science and Engineering. 2009;163:272–284.
[10] Smith A.B. Neutron total and scattering cross sections of Li-6 in the low MeV region. J. Nucl. Phys. A. 1982; 375:8201.
[11] Hogue H.H. Elastic and inelastic scattering of 7- to 14-MeV neutrons from Lithium-6 and Lithium-7. J. Nucl. Sci. Eng.1976;69:22.
[12] Lisowski P.W. Cross sections for neutron induced, neutron producing reactions in Li-6 and Li-7 at 5.96 and 9.83 MeV. LA-8342, Los Alamos Scientific Laboratory. 1980.
[13] Cookson J.A. Scattering of 10 MeV neutrons by Li-6 and Li-7. J. Nucl. Phys. A. 1967;91:273.
[14] Adel-Fawzy M. Elastic and inelastic scattering of neutrons in the energy range 7 to 12 MeV on 6-Li, 7-Li, 12-C, 32-S, 93-Nb and 209-Bi. Nucl. Instrum. Methods. 1980;169:533.
[15] Batchelor R. The interactions of neutron with Li-6 and Li-7 between 1.5 and 7.5MeV. J. Nucl. Phys. 1963;47:385.
[16] Hopkins J.C. Elastic and inelastic scattering of fast neutron from Li-6 and Li-7. J.Nucl. Phys. A. 1968;107:139.
[17] Merchez F. J. Study of the elastic and inelastic scattering of neutrons on the nuclei of Li-6 and Li-7 and Be-9. Physique Colloque. 1966;27:61.
[18] Chiba S. Double-differential neutron emission cross sections of Li-6 and Li-7 at incident neutron energies of 4.2, 5.4, 6.0 and 14.2 MeV. J. Nucl. Sci. Technol. 1985;25:210.
[19] Ibaraki M. Li-6, Li-7 and Be-9 neutron emission cross sections at 11.5 - 18 MeV neutron energy. J. Nucl. Sci. Technol. 1998;35:843.

53 Nuclear data sensitivity analysis for isotopic generation using JEFF-3.1.1 and -3.2

Yosuke Kawamoto, Go Chiba, Masashi Tsuji and Tadashi Narabayashi

Nuclear Reactor Engineering Laboratory,
Division of Energy and Environmental Systems,
Hokkaido University, Sapporo, Hokkaido, Japan
e-mail: y_kawamoto@eng.hokudai.ac.jp

Abstract

In burn-up calculations, accuracy of isotopic generation prediction strongly depends on the nuclear data. In this study, we perform burn-up calculations using neutron cross section data from JEFF-3.1.1 and -3.2, and compare the calculation results with PIE (Post Irradiation Examination) data. We also perform burn-up sensitivity analysis based on the generalized perturbation theory to clarify the cause of differences on the isotopic generations between the libraries. As a result, except some nuclides, there have not been so large discrepancies generally between JEFF-3.1.1 and -3.2. Furthermore, we clarify the causes of the discrepancies which are over 5%. Cross sections of some nuclides have large differences between JEFF-3.1.1 and -3.2, and they have given relatively large impacts on specific isotopic generation predictions.

1 INTRODUCTION

Accurate isotopic generation predictions are important for the evaluations of decay heat, nuclear waste inventory, severe accident source term and others.

In burn-up calculations, neutron transport and fuel depletion calculations are done alternately for whole cycle, and neutron reaction cross sections, fission yields and decay constants of each nuclide are used. Thus the accuracy of isotopic generations obtained by the burn-up calculations depends on the employed nuclear data strongly. As shown in Refs. [1] and [2],it is well known that there are non-negligible differences on the isotopic generations among the nuclear data libraries.

Ideally, nuclear data given in different libraries should converge to the unique true value. Thus, in nuclear data improvement, it is quite important to see the difference between libraries on isotopic generations and clarify its cause on the nuclear data in detail, for each nuclide and energy range.

In the present study, we focus on the difference of JEFF-3.1.1 [4] and -3.2 [5], the newest version of JEFF library, which was released on March 2014. We perform burn-up calculations with the neutron cross section data from the two libraries, and compare the results to the PIE (Post Irradiation Examination) data, which are the chemical isotopic analysis data of the spent fuel composition. Then we evaluate the impacts of the nuclear data differences on the isotopic generation predictions.

In order to clarify the causes of these differences, we also perform burn-up sensitivity analysis. By multiplying sensitivity coefficients by nuclear data differences between the libraries, we can evaluate the influences of nuclear data differences on the isotopic generation predictions quantitatively.

2 CALCULATION

2.1 PIE data

We use the PIE data of UO_2 and MOX fuels reported in Refs. [1] and [2] to compare with calculation results.

For the UO_2 fuel, there are measured data of 17 actinides and 38 FP (Fission Products) for four samples. For the MOX fuel, there are 40 FP and U-238 data for two samples. For both the fuels, the measurement uncertainties for all the nuclides are reported in the references. The details of the measurement methods used for the samples are described in Ref. [6].

The UO_2 and MOX fuels were irradiated at the different European commercial PWR, respectively, and each sample was in the same cycles but at different positions in the core. Thus their burn-ups and moderator temperatures are different from each other. References [1] and [2] provide information of these temperatures and burn-ups obtained from chemical isotopic analysis for each sample.

2.2 Burn-up calculation by CBZ code system

In this study, we perform burn-up calculations to simulate the UO_2 and MOX fuel irradiation described in Refs. [1] and [2]. It is done by CBZ[7], a multi-purpose reactor physics calculation code system which is being developed at Hokkaido University. In the burn-up calculation, self-shielding, neutron transport and depletion calculations are done alternately for whole cycle.

The resonance self-shielding calculation is based on the equivalence theory. The neutron transport calculation is done with the collision probability method for two-dimensional square pin-cell model. 107-group cross section is used for the transport calculation. The depletion calculation is done by the matrix exponential method with the Chebyshev rational approximation method[8]. The burn-up chain which we use includes 197 FP and 21 actinide nuclides. Concerning this chain, except four nuclides (Sb-125, Cs-134, Sm-149, Gd-154), it is same as the SRAC2006 detailed burn-up chain[9].

To simulate the UO_2 and MOX fuel irradiation in Refs. [1] and [2] properly, we adopt physical conditions consistent with these references. The conditions which are not described in the references are quoted from Ref. [10] or [11] as general cases.

In Refs. [1] and [2], the unit of measured data is number density per one gram solution of spent fuel. Thus, to compare between calculated and measured values, we normalize these values by U-238 inventories.

To evaluate impacts of nuclear data differences on isotopic generation predictions, we use JEFF-3.1.1 and -3.2 for neutron reaction cross sections. For fission yields and decay constants, we use the JEFF-3.1.1 data in both the cases because only neutron cross section data were revised between JEFF-3.1.1 and -3.2.

The CBZ code system has a burn-up sensitivity calculation function based on the generalized perturbation theory. We use this function to obtain sensitivity coefficients, and then clarify the cause of the difference on the isotopic generation prediction between the libraries by the sensitivity coefficients.

3 RESULTS

3.1 Isotopic generations

Relative differences of calculation values to experimental ones (C/E-1) are shown in Figures 1 and 2 for the UO_2 and MOX fuels, respectively. They are averaged values among the samples. The results with the same calculation condition using JENDL-4.0 [3] are also shown for a reference.

Generally, the discrepancies between JEFF-3.1.1 and -3.2 are not so large. In Table 1, the discrepancies of JEFF-3.2 compared with JEFF-3.1.1 which are over 1% are shown. Ones of only Cm-245 and Gd-158 generations in UO_2 fuel are over 5%.

3.2 Sensitivity analysis

For the Cm-245 and Gd-158 generation discrepancies in UO_2 fuel which are over 5% mentioned in Section 3.1, we perform the sensitivity analysis to investigate the causes of the discrepancies.

The Gd-158 generation discrepancy is almost from Eu-156 capture cross section difference between JEFF-3.1.1 and -3.2. Figure 3 shows an energy-wise contribution of Eu-156 capture cross section difference on the Gd-158 generation discrepancy. The difference around 0.1eV mainly affects the discrepancy. It is because of the thermal neutron peak.

The Cm-245 generation discrepancy is mainly ($\sim$60%) from Cm-244 capture cross section difference, and partially ($\sim$40%) from Cm-245 fission cross section difference between JEFF-3.1.1 and -3.2. Figure 4 shows an energy-wise contribution of Cm-244 capture cross section difference on the Cm-245 generation

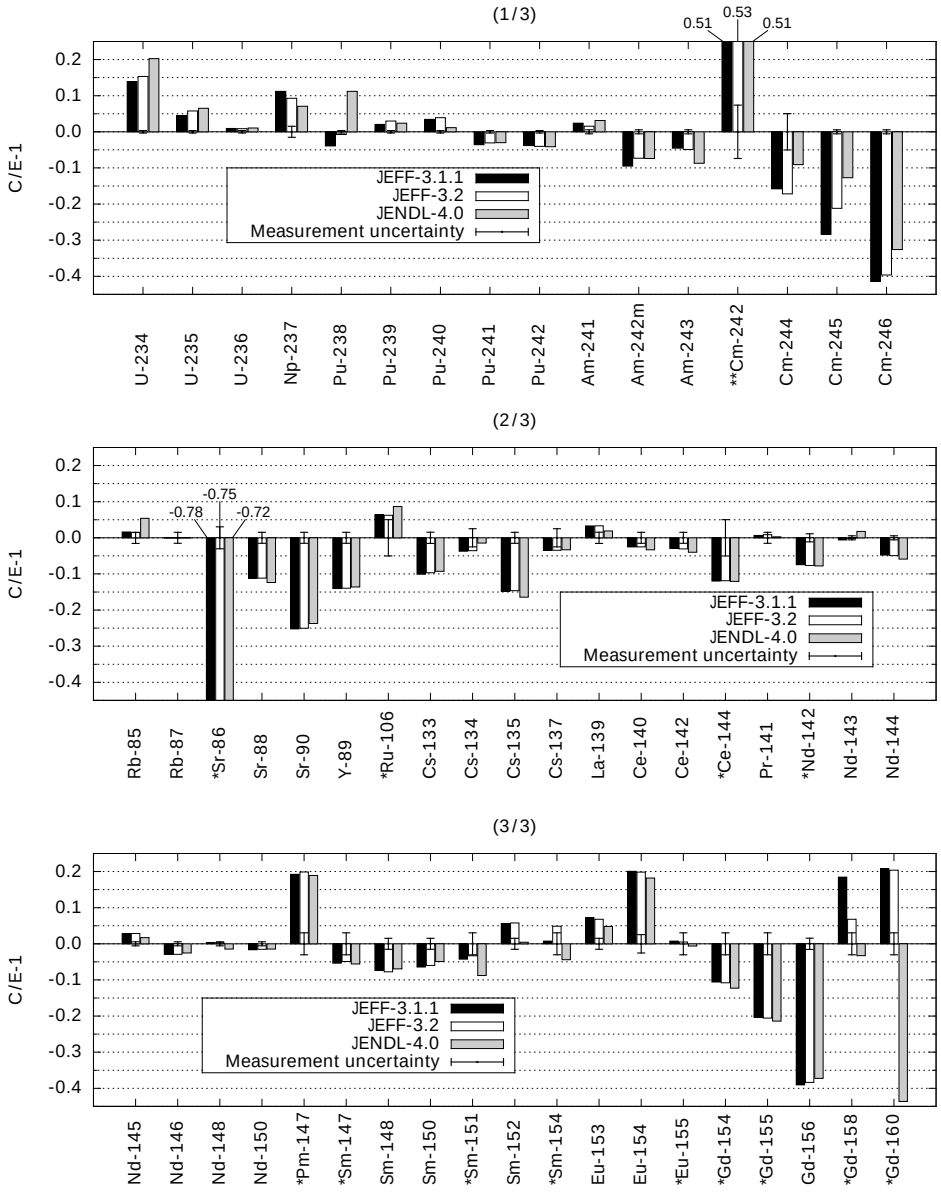

Figure 1: Relative differences of calculated nuclide number densities to experimental measured ones in the UO_2 fuel. There is only one sample (*) or three samples (**) for some nuclides, while four samples are provided for other nuclides.

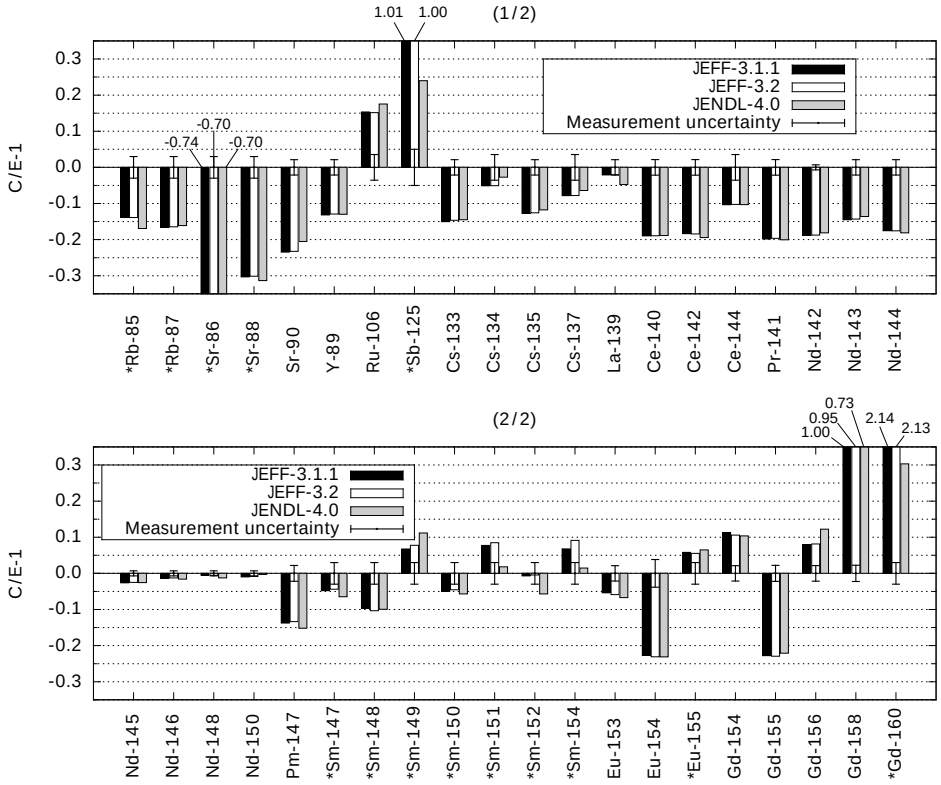

Figure 2: Relative differences of calculated nuclide number densities to experimental measured ones in the MOX fuel. There is only one sample (*) or three samples (**) for some nuclides, while four samples are provided for other nuclides.

Table 1: Differences of isotopic generations of JEFF-3.2 compared with JEF-3.1.1 in the UO_2 and MOX fuels. Ones which are over 1% are only listed.

Fuel	Nuclide	Difference [%]
UO_2	U-234	1.4
	U-235	1.3
	Np-237	-1.9
	Pu-238	3.2
	Am-242m	2.2
	Cm-242	2.6
	Cm-244	-1.4
	Cm-245	7.2
	Cm-246	1.8
	Sr-86	3.2
	Sm-154	4.2
	Gd-158	-11.7
MOX	Sr-86	3.8
	Sm-149	1.0
	Sm-154	2.4
	Gd-158	-4.2
	Gd-160	-1.1

discrepancy. The resonance peak difference at 7.67eV almost affects the discrepancy. Figure 5 shows an energy-wise contribution of Cm-245 fission cross section difference on the Cm-245 generation discrepancy. The difference around 0.1eV mainly affects the discrepancy. It is same as the above Eu-156 capture cross section case.

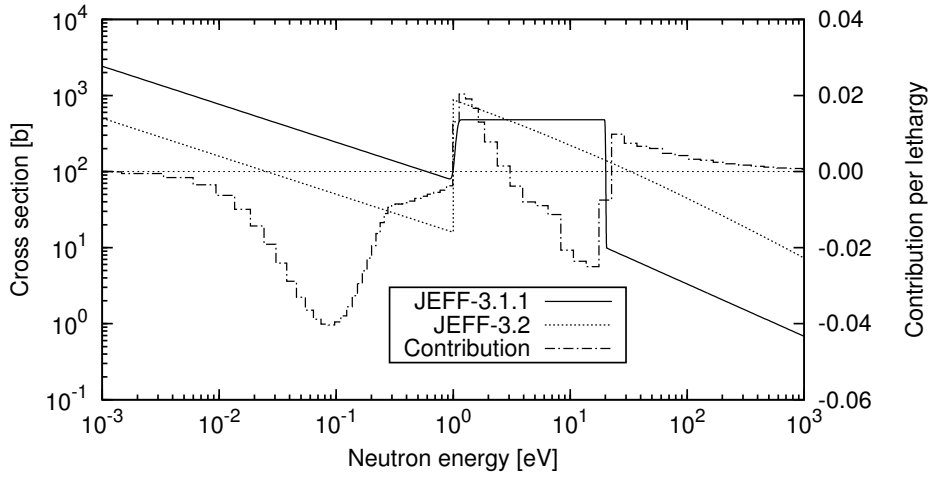

Figure 3: Capture cross sections of Eu-156 from JEFF-3.1.1 and -3.2, and contribution of the difference between both to the Gd-158 generation difference between the libraries in the UO_2 fuel.

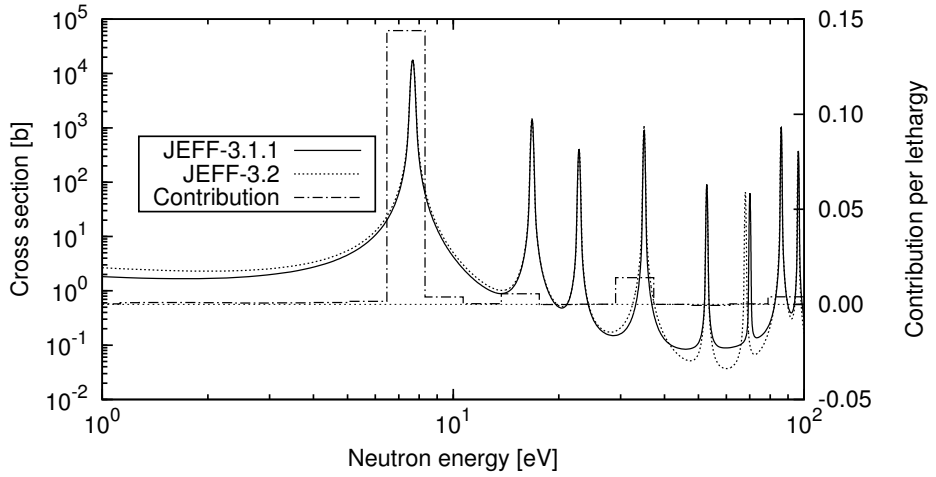

Figure 4: Capture cross sections of Cm-244 from JEFF-3.1.1 and -3.2, and contribution of the difference between both to the Cm-245 generation difference between the libraries in the UO_2 fuel.

4 CONCLUSION

On the UO_2 PIE results, only two nuclides, Gd-158 and Cm-244, have had isotopic generation differences over 5% between JEFF-3.1.1 and -3.2. In the MOX case, there have been no nuclides whose difference are over 5%. Generally, the impacts of cross section differences between JEFF-3.1.1 and -3.2 have been relatively small compared to the other nuclear data library analysis cases [1][2].

By means of the burn-up sensitivity calculation, we have clarified the cause of the discrepancies of the above Gd-158 and Cm-245 generations in detail.

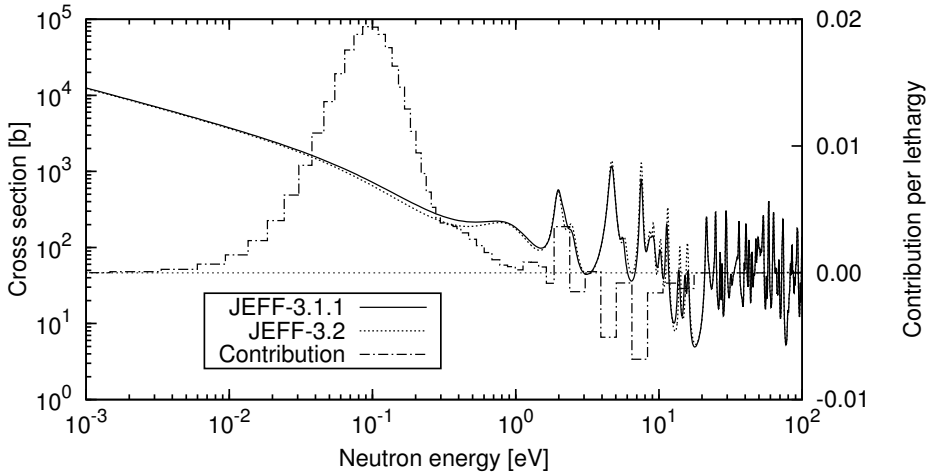

Figure 5: Fission cross sections of Cm-245 from JEFF-3.1.1 and -3.2, and contribution of the difference between both to the Cm-245 generation difference between the libraries in the UO_2 fuel.

References

[1] A. Sasahara, et al.: *J. Nucl. Sci. Technol.*, **45**[4], 313 (2008).

[2] A. Sasahara, et al.: *J. Nucl. Sci. Technol.*, **45**[5], 390 (2008).

[3] K. Shibata, et al.: *J. Nucl. Sci. Technol.*, **48**[1], 1 (2011).

[4] A. Santamarina, D. Bernard, Y. Rugama: "The JEFF-3.1.1 Nuclear Data Library," JEFF Report 22 (2009).

[5] The JEFF team: "JEFF-3.2: Evaluated nuclear data library," URL: `http://www.oecd-nea.org/dbdata/jeff`, (2014).

[6] A. Sasahara, et al.: "Post Irradiation Examinations and the Validity of Computational Analysis for High Burn-up UO2 and MOX Spent Fuels," CRIEPI report T95012 (1996).[in Japanese]

[7] Y. Kawamoto, et al.: "Validation of CBZ Code System for Post Irradiation Examination Analysis and Sensitivity Analysis of (n,γ) Branching Ratio," JAEA-Conf 2006-009, p.113 (2006).

[8] M. Pusa: *Nucl. Sci. Eng.*, **169**, 155(2011).

[9] K. Okumura, et al.: "SRAC2006 : A Comprehensive Neutronics Calculation Code System," JAEA-Data/Code 2007-004 (2007) , 313p.

[10] A. Sasahara: private communication (2013).

[11] J. Katakura, et al.: "A Set of ORIGEN2 Cross Section Libraries Based on JENDL-3.3 Library: ORLIBJ33," JAEA-Data/Code 2004-015 (2004) , 115p.

54 Measurement of neutron yield by multiple-foil activation unfolding method for medical radioisotopes production using accelerator neutrons

Takaya KAWAGOE, Tadahiro KIN, Shouhei ARAKI, Yukinobu WATANABE
Department of Advanced Energy Engineering Science, Kyushu University, Kasuga, Fukuoka 816-8580, Japan
e-mail: kin@aees.kyushu-u.ac.jp

Accelerator neutrons have been proposed to produce medical radioisotopes. The C(*d*,*n*) reaction is one of the candidates to produce neutrons. The data of thick target neutron yields (TTNYs) is needed for reliable prediction of the amount of production. We measured the angle-differential TTNYs of the C(*d*,*n*) reaction at E_d = 12 MeV using multiple-foil activation unfolding method. The spectral shape was in good agreement with previous experimental data. This demonstrates that the experimental method is applicable to prediction of the amount of medical radioisotopes produced with accelerator neutrons.

1. Introduction

Medical radioisotopes (RIs) have been widely used for in vivo diagnosis, in vitro diagnosis, therapy of tumor, and so on. These RIs are usually produced by nuclear reactors or by small-sized accelerators installed in or near hospitals. However, some problems are addressed in terms of stable supply, management of radioactive materials, and production cost. To reduce risks associated with the above problems, a method of RI production using accelerator neutrons has recently been proposed and attracts much attention.

Technetium-99m is one of representative medical RIs. ^{99m}Tc is most-used in diagnosis in the world, and it is produced as ^{99}Mo, the parent nuclide of ^{99m}Tc. ^{99}Mo is produced by nuclear reactors with highly-enriched uranium as starting material. Only a few aged reactors can be used for the purpose in the present status. Such unstable supply system has recently caused some troubles. For instance, the National Research Universal (NRU) reactor and the High Flux Reactor (HFR) were stopped due to repairing and failure, respectively. Since they had produced more than 60% of world demands, so-called technetium-crisis happened at that time. Accordingly, a new production method via the ^{100}Mo(n,2n)^{99}Mo reaction using accelerator neutrons have been proposed to improve the supply system[1].

We pay attention to the supply system of RIs for Positron Emission Tomography (PET) as a typical example. Fluorine-18, which is most-used for PET, is produced by accelerators installed in or near hospitals because of the short half-life (1.8 h). Also the management of radioactivity induced by accelerated particles is troublesome matter for hospitals. Recently, ^{64}Cu has been proposed as a new RI with longer half-life (13 h) for PET. Since the longer half-life makes it possible to produce ^{64}Cu in a dedicated facility outside hospitals, we would realize an ideal supply system to deliver ^{64}Cu to

hospitals on demands. Furthermore, ^{64}Cu has a potential for molecular imaging by PET because of the longer half-life. ^{64}Cu can be produced via the ^{64}Zn(n,p) reaction using accelerator neutrons[2].

Until now, two types of deuteron-induced reactions have been considered as neutron sources for production of ^{64}Cu: one is the DT reaction and the other is the C(d,n) or the Be(d,n) reaction. In the present work, we paid attention to the ^{64}Cu production. Fig. 1 shows neutron excitation functions of ^{64}Zn contained in JENDL-4.0 [3]. Below E_n = 12 MeV, cross section of the (n,p) is large compared with other reactions. Briefly, ^{64}Cu can be made with small amount of by-products. Thus, we focus on the C(d,n) or the Be(d,n) reaction by the deuterons accelerated up to a few ~ 12 MeV.

For reliable prediction of medical RIs with accelerator neutrons, thick target neutron yields (TTNYs) are very important data. However, experimental data of TTNYs are not sufficient in quantity and quality. Although some theoretical models can calculate the TTNYs, the reproducibility is not good enough. To overcome the situation, we have measured the angle-differential TTNYs of the C(d,n) reaction at E_d = 12 MeV using a multiple-foil activation unfolding method.

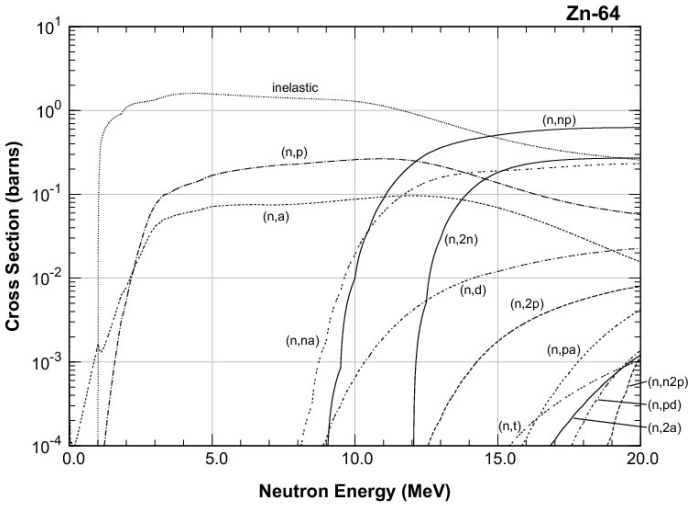

Fig 1. Neutron excitation functions of ^{64}Zncontained in JENDL-4.0 [3]. The (n,p) reaction produces ^{64}Cu.

2. Experiment

2.1 Irradiation

The experiment was carried out at the 1st room in the Kyushu University Tandem Accelerator Laboratory. The experimental setup is illustrated in Fig. 2, and the schematic view of the irradiation is shown in Fig. 3.

Deuterons were accelerated up to 12 MeV and delivered to a neutron converter target made of carbon. The target thickness of 1 mm was chosen so that incident deuterons stop completely in the target. The target was insulated from other experimental apparatus and connected only with a current integrator to acquire the deuteron beam current.

The neutrons passed through a 1mm thick window made of Al, and irradiated activation foils located at 123 mm downstream from the target. The foils were arranged from 0 to 90 degrees in steps of 10 degrees in the laboratory system. Materials of the foils were ^{197}Au (10×10×0.3 mm^3), ^{59}Co (10×10×0.1 mm^3), ^{27}Al (21×20×0.5 mm^3), ^{93}Nb (21×20×0.1 mm^3), ^{nat}Fe (21×20×0.5 mm^3), and ^{nat}Ni(21×20×0.3 mm^3).

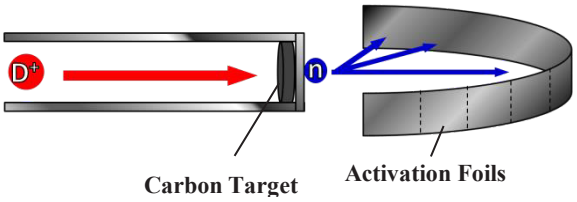

Fig. 2. Outline of the experimental set up.

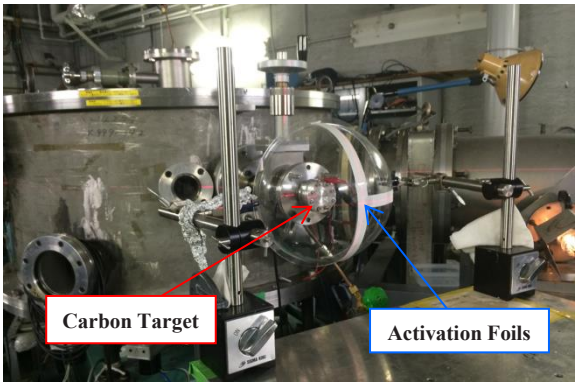

Fig. 3. Schematic view of the irradiation.

2.2 Measurement

We measured gamma rays from the activated foils by HP-Ge detector (GEM30P4-70 Ortec, USA) with relative efficiency of 35%. To reduce background gamma rays, the detector was shielded by lead blocks (50×100×200 mm^3) as shown in Fig.4. The foils were set at the top of the HP-Ge detector. Gamma rays from a ^{152}Eu standard source were measured at the same point to determine the photo peak efficiency and energy calibration function.

Table 1. Reactions identified by observed gamma rays in the spectra.

Reaction	E_{thresh} [MeV]	$T_{1/2}$
$^{27}Al(n,\alpha)^{24}Na$	3.25	15.0 hours
$^{93}Nb(n,2n)^{92m}Nb$	9.06	10.2 days
$^{197}Au(n,\gamma)^{198}Au$	0.00	2.70 days
$^{197}Au(n,2n)^{198}Au$	8.11	6.18 days
$^{59}Co(n,\alpha)^{56}Mn$	0.00	2.58 hours
$^{nat}Fe(n,x)^{56}Mn$	0.00	2.58 hours
$^{nat}Na(n,x)^{58}Co$	0.50	70.9 days

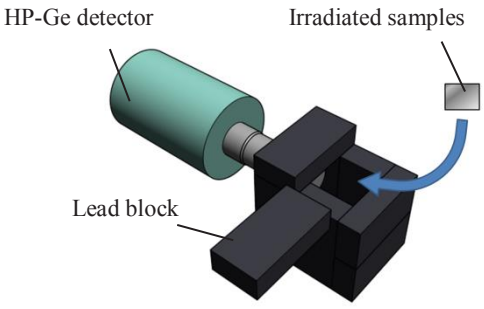

Fig. 4. Schematic view of the HP-Ge detector and the lead shield blocks of the measurement

3. Analysis

3.1 Production yield calculation

Based on the peak energies of gamma rays observed in the measured spectra, radioactive nuclides and production reactions were identified as listed in Table 1. The production yield of a nuclide (N_{yield}) was calculated from a counting rate of a full energy peak of gamma-ray (S_γ) as the following equation:

$$N_{yield} = \frac{\lambda S_\gamma}{\varepsilon_\gamma I_\gamma (1-e^{-\lambda t_i}) e^{-\lambda t_c} (1-e^{-\lambda t_m})} \eta_{sum}, \quad (1)$$

where λ is the decay constant, ε_γ is the peak detection efficiency, I_γ is the intensity per decay, t_i is the irradiation time, t_m is the real time of the spectroscopic measurement, and η_{sum} is the correction factor for cascade sum.

3.2 Unfolding thick target neutron yields

The production yields, N_k, for nuclide k=x,y,… are calculated as follows;

$$\begin{pmatrix} N_x \\ N_y \\ \vdots \end{pmatrix} = \begin{pmatrix} R_{x,E1} & R_{x,E2} & \cdots \\ R_{y,E1} & \ddots & \\ \vdots & & \end{pmatrix} \begin{pmatrix} \Phi_{E1} \\ \Phi_{E2} \\ \vdots \end{pmatrix}, \quad (2)$$

where $R_{k,Ei}$ is the response function for production of nuclide $k = x, y, \ldots$ at neutron energy $E_i (i = 1,2,\ldots)$, and Φ_{Ei} is the number of neutrons at E_i. The response function is calculated as the following equation:

$$R_{x,Ei} = \sigma_{Ei} N_x l I_x \frac{N_A}{M_x} \eta_{irr}, \quad (3)$$

where σ_{Ei} is the cross section obtained from JENDL-4.0, N_x is the foils density, l is the foil thickness, I_x is the relative isotopic abundance, η_{irr} is the correction factor for beam fluctuation.

We have derived the TTNYs by means of unfolding with the GRAVEL code based on the Maximum-likelihood method [4]. TTNYs calculated by the PHITS code [5] were used as initial guess TTNYs.

4. Results and discussion

The unfolded TTNYs are shown in Figs. 5 and 6. At backward angles larger than 60 degrees, we could not derive TTNYs successfully due to low induced activity.

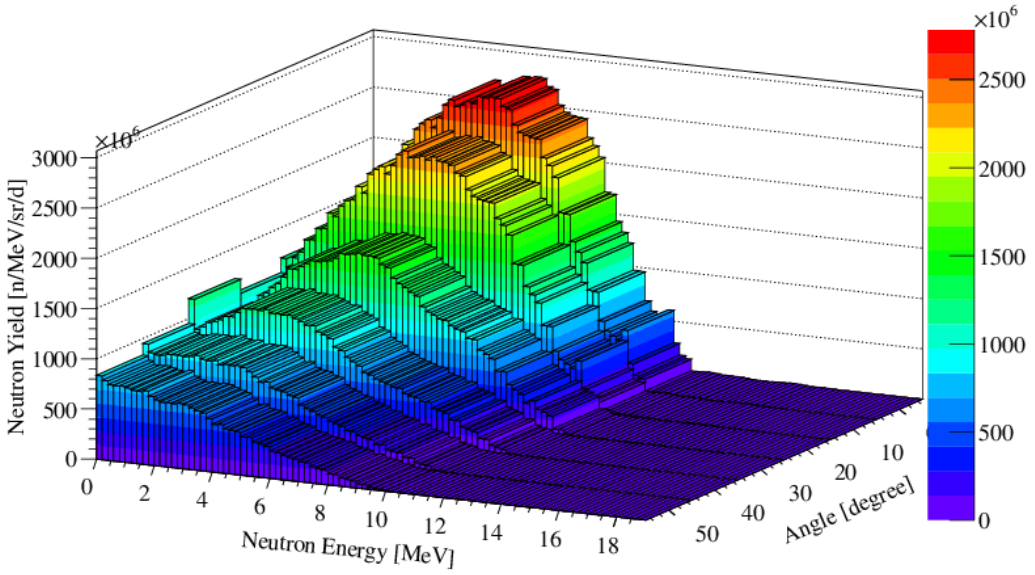

Fig. 5. Unfolded TTNYs of the C(*d*,*n*) reaction at E_d = 12 MeV (linear scale)

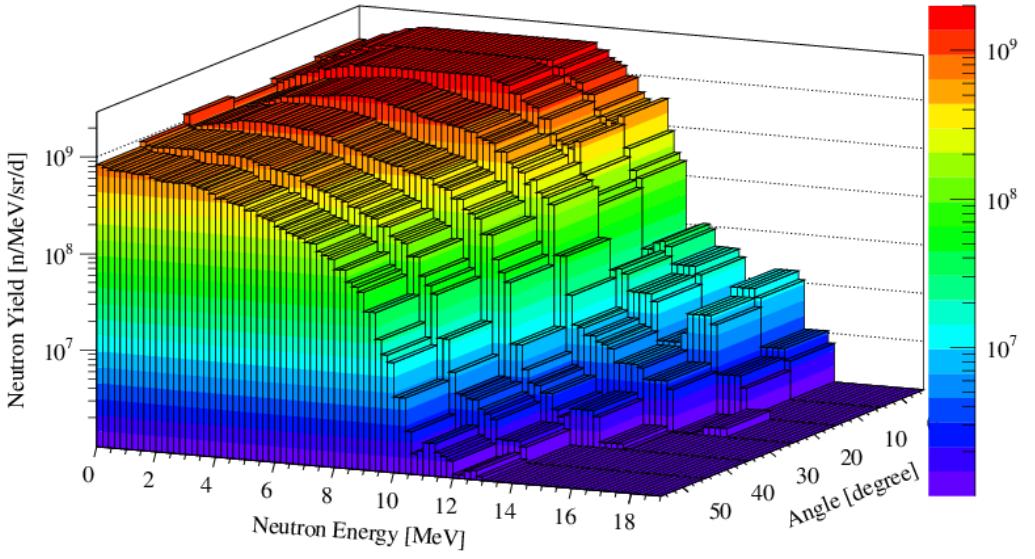

Fig. 6. Unfolded TTNYs of the C(*d*,*n*) reaction at E_d = 12 MeV (logarithm scale)

Figure 7 shows a comparison of the unfolded TTNY at 0 degree with previous experimental data measured at 3.5 degrees [6]. The PHITS result used as the initial guess TTNY in the GRAVEL calculation is also shown. The initial guess TTNY provided underestimation in the energy range below 8 MeV. On the other hand, the shape of the unfolded TTNY was in generally good agreement with the previous data.

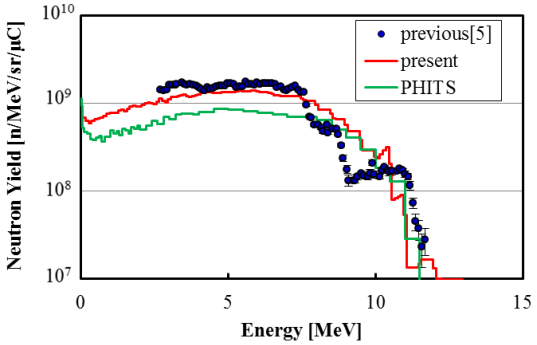

Fig. 7. Comparison with the previous data [6], PHITS calculation, and unfolded the TTNY.

For validation of the results, we calculated the yields of produced nuclides using the unfolded TTNY and compared with the experimental yields. The corresponding C/E ratios are shown in Fig. 8. The statistical and systematic uncertainty of gamma-ray spectroscopy (0.7 ~ 4.9 % and 3.8 %, respectively), systematic uncertainty of the irradiation position (5.2 %) were included. For ^{58}Co, the uncertainty of population ratio between the ground state and metastable state (6.0 %) was also considered. The calculated RI yields were consistent with measured ones within the experimental error. Consequently, it was found that the present TTNYs can be used for prediction of the amount of medical RIs with accelerator neutrons produced by the C(d,n) reaction.

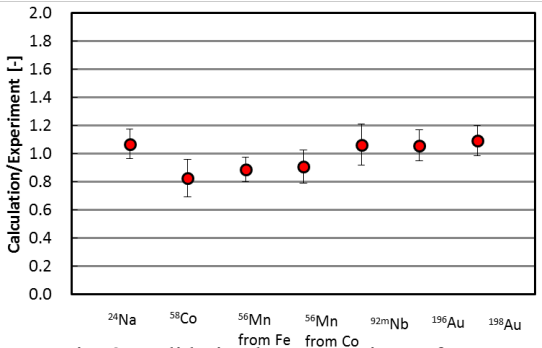

Fig. 8. Validation by comparison of calculated and experimental yields

5. Conclusion

We measured the angle-differential thick target neutron yields (TTNYs) of the C(d,n) reaction at E_d = 12 MeV using the multiple-foil activation unfolding method. The TTNYs were obtained from 0 to 50 degrees in steps of 10 degrees. The spectral shape of the TTNY at 0 degree was in good agreement with the previous data measured at 3.5 degrees [6]. Thus, we found that the measured TTNYs can be used for prediction of the amount of medical RIs. In the future, they will be also available for designing optimum irradiation geometry.

Acknowledgement

We would like to thank Kenshi Sagara for operation of the KUTL accelerator and fabrication of the neutron converter. This work was supported by JSPS KAKENHI Grant Number 23000005.

References

[1] Y. Nagai and Y. Hatsukawa, J. Phys. Soc. Jpn. 78, 033201(2009)
[2] T. Kin, Y. Nagai, N. Iwamoto, et al., J. Phys. Soc. Jpn. 82,034201 (2013)
[3] K. Shibata, O. Iwamoto, T. Nakagawa, et al., J. Nucl. Sci. Technol., 48, 1 (2011)
[4] M. Reginatto and P. Goldhagen, Health Phys. 77, 579 (1999)
[5] T. Sato, K. Niita, N. Matsuda, et al., J. Nucl. Sci. Technol. 50:9, 913-923 (2013)
[6] K. A. Weaver, J. D. Anderson, H. H. Barschall, et al., Nucl. Sci. Eng. 52, 35 (1973)

55 R&D of the heat measurement method for accurate determination of amount of minor actinides samples for accuracy improvement of neutron nuclear data

Taro NAKAO[1], Shoji NAKAMURA[1], Kazushi TERADA[1], Atsushi KIMURA[1], Hideo HARADA[1]
Masayuki IGASHIRA[2], Tatsuya KATABUSHI[2],
Junichi HORI[3]
[1]*Japan Atomic Energy Agency, Tokai-mura, Naka-gun, Ibaraki-ken 319-1195 Japan*
[2]*Tokyo Institute of Technology, Research Laboratory for Nuclear Reactors, 2-12-1 Ookayama, Meguro-ku Tokyo 152-8550 JAPAN*
[3]*Kyoto University Research Reactor Institute, 2, Asashiro-Nishi, Kumatori-cho, Sennan-gun, Osaka 590-0494 JAPAN*
e-mail: nakao.taro@jaea.go.jp

1. Introduction

The reaction cross-section is one of the most fundamental information in nuclear and particle physics. For the precise determination of reaction cross-section, the precise information of the total amounts of target samples is required. However, to obtain precise values of total amounts of target samples is sometimes very hard. One reason is that many experimental situations require for radioactive samples to be packed in order not to contaminate. Therefore, it is necessary to determine the absolute amount of samples accurately non-destructively. In this report, a plan about heat deposit measurements from radioactive samples using micro-calorimeter is reported, in order to determine the absolute amounts of samples precisely.

Total heat deposit is written as

$$E = N \cdot R \cdot Q.$$

Here, N is the total number of particles, Q is heat deposit from one heat loss event and R means the heat loss event rate. If three of the four unknown values are determined precisely, the last one value can be determined. In case of radioactive samples, precise decision of Q-value, $T_{1/2}$ and total heat deposit allows us to decide the total amount of sample particles. The systematic error is propagated not only from total

heat deposit accuracy but also both Q-value and $T_{1/2}$ accuracy. For example in case of ^{241}Am minor actinide sample, Q-value and $T_{1/2}$ are decided as 5637.82(12) keV and 432.6(6) year with determination accuracies 0.0021% and 0.13% in turn. As a 1 GBq sample of ^{241}Am has 903μW, 1μW precision of heat measurement allows deciding sample amounts with order of 0.1% accuracy.

2. Review for TAM III micro-calorimeter1

In order to measure total heat deposit from minor actinides samples by 1μW precision, TAM III micro-calorimeter manufactured by the TA Instrument Company was reviewed. According to the spec sheet of TAM III, micro-calorimeter has an ability of 100nW precision and 200nW/day baseline drift. To reviewing about TAM III, 370kBq(～300nW) ^{241}Am standard γ-source was used. As a reference of baseline position, blank cell measurement was also performed. Measurements were performed in Japanese office of TA Instrument Company.

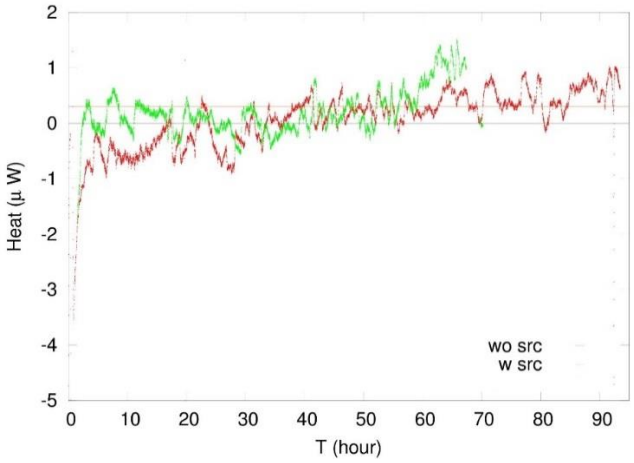

Figure 1: Test measurement result by TAM III. A green line shows heat deposit of ^{241}Am standard source. A red line means blank measurement.

Figure 1 shows heat deposit difference between ^{241}Am standard source and blank cell. A green line shows heat deposit of ^{241}Am standard source. A red line means the blank measurement. In spite of the expected heat deposit (300nW) was comparable of catalog spec baseline drift (200nW/day), TAM III can distinguish existence of heat source compared with the blank measurement.

3. Estimation of radiation shielding effect

Measurement value of heat deposit is associated to total heat loss only inside the measuring volume of calorimeter. Differs from chemical heat reaction, radioactive decay has possibilities to escape heat from the measuring volume by penetrating radiation

which can be cause of a systematic error. In order to reduce heat escape, radioactive shielding effects for minor actinides ^{241,243}Am and ^{239}Np were estimated by Monte-Carlo simulation code GEANT4.[2] ^{239}Np is not a long lived minor actinide but a daughter nucleus of alpha decay nucleus ^{243}Am which become radioactive equilibrium.

Minor actinides samples are supposed to have 0.5mm thickness 10mm diameter distribution in the center of 2mm thickness 22mm diameter Al plate. Shielding materials have same diameter with Al plate, 10mm thickness Pb plates at both sides of sample plate. A stainless sample cell tube which has 1mm thickness wall, 24mm diameter and 70mm length is also taken into the simulation geometry.

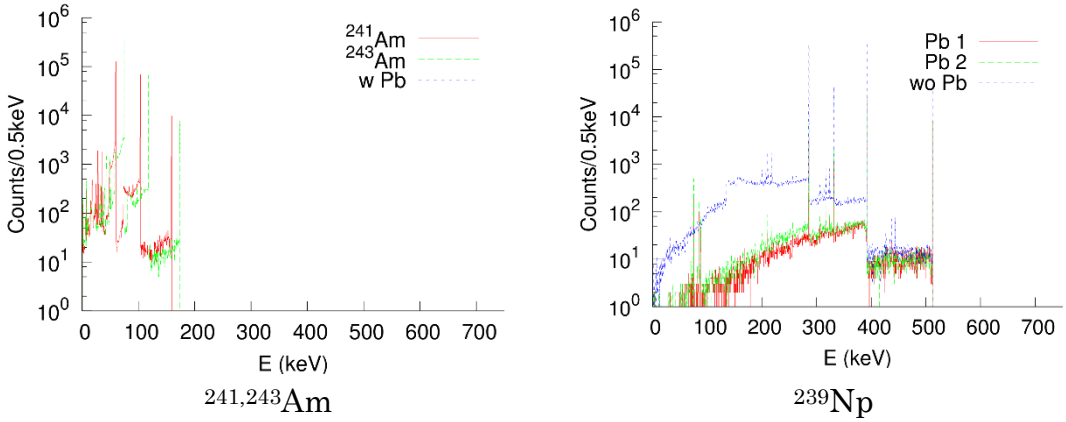

Figure 2: γray shielding effects for ^{241,243}Am and ^{239}Np by 10mm thickness Pb plate.

Figure 2 shows the result of the simulation for ^{241,243}Am and ^{239}Np. In case of ^{241}Am and ^{243}Am, shielding is perfect. Differs from Am, ^{239}Np have remaining γray components. Penetrating heat loss by shielding plates was order of 0.3% compared to the total Q-value from ^{243}Am to ^{239}Pu. For determination of ^{243}Am sample amount, order of 0.3% systematic error must be taken into account.

4. Summary

In this report, total heat deposit measurement method for determination of total amounts of radioactive samples was overviewed. Heat measurement precision requirement was discussed as 1 μW. As a good candidate of 1 μW precision heat measurement, TAM III micro-calorimeter was investigated. GEANT4 Monte-Carlo simulation was also performed to estimate amounts of heat losses from measuring sample cell area because of the radioactive particle penetration.

Acknowledgement

Present study includes the result of "Research and Development for accuracy improvement of neutron nuclear data on minor actinides" entrusted to the Japan Atomic Energy Agency by the Ministry of Education, Culture, Sports, Science and Technology of Japan (MEXT)

References

[1] http://www.tainstruments.co.jp/

[2] https://geant4.web.cern.ch/geant4/

56 Evaluation of the photoabsorption cross section of three-nucleon systems

Rie Sekine[1] and Wataru Horiuchi
Department of physics, Hokkaido University, Sapporo 060-0810, Japan
E-mail: sekine@nucl.sci.hokudai.ac.jp[1]

Phoroabsorption cross section is one of the fundamental nuclear data. We employ the time-dependent method to calculate it theoretically. A time-dependent Schödinger equation is solved by a basis expansion method using correlated Gaussian functions. In this contribution, we calculate the photoabsorption cross sections of ^{3}H and ^{3}He and compare with the experimental data.

1 Introduction

We can know information on nuclear structures and excited states by studying photoabsorption cross section. For its importance, it has been approached both experimentally and theoretically. In the photoabsorption process, the electric dipole ($E1$) field excites nuclei to some discretized states or the continuum states. However, it is difficult to treat many-body continuum states theoretically. Therefore, some method avoiding the difficulty have been developed, for example, Complex Scaling Method [1], Lorentz Integral Transform method [2], and time-dependent method [3]. We employ the time-dependent method in which we solve a time-dependent Schrödinger equation to obtain the photoabsorption cross section. The wave function is expanded by complex-range correlated Gaussians. The correlated Gaussians basis functions [4, 5] describe many-body correlations explicitly. By extending it to complex-range, the oscillation in a large distance can be expressed more efficiently than real-range one. We calculate the photoabsorption cross sections of three-nucleon systems, ^{3}H and ^{3}He to evaluate the experimental data.

In Sec.2, we introduce the Hamiltonian, how to calculate the photoabsorption cross section with the time-dependent method using complex-range correlated Gaussians basis functions. In Sec.3, we show the results obtained with real- and complex-range basis functions. The calculated photoabsorption cross sections are compared with the experimental data. Summary is given in Sec.4.

2 Method

2.1 Model

We consider the three-nucleon systems, in which the protons and neutrons are assumed to be identical particles. The total Hamiltonian of the system is

$$\hat{H} = \sum_{i=1}^{3} \frac{\boldsymbol{p}_i^2}{2m} - T_{CM} + \sum_{j>i}^{3} V_{NN}(|\boldsymbol{r}_i - \boldsymbol{r}_j|) + \sum_{j>i}^{3} V_{coul}(|\boldsymbol{r}_i - \boldsymbol{r}_j|), \tag{1}$$

where $\boldsymbol{r}_i$ is the single particle coordinate of the i-th particle, T_{CM} is the kinetic energy of the center of mass, and V_{NN} and V_{coul} are nucleon-nucleon interaction and Coulomb interaction, respectively. The Minnesota potential [6] is employed as V_{NN}. As time passes, some artificial reflection waves appear from

the model space boundaries. In order to exclude them, we add an imaginary potential to the Hamiltonian in order to absorb the reflected waves [7].

$$\hat{H} \rightarrow \hat{H} + i\sum_{i=1}^{3} W\left(|\boldsymbol{r}_i - \boldsymbol{x}_3|\right) \tag{2}$$

$$W\left(r\right) = W_0\theta(|\boldsymbol{r}| - R)\left(|\boldsymbol{r}| - R\right)^2, \tag{3}$$

where $\boldsymbol{x}_3$ is a position vector of the center of mass, and θ is the step function. The absorbing potential has two parameters, the one is the strength of the potential W_0, and the other is the potential starting position R. We decide these parameters to minimize the oscillations in the time evolution of the overlap between the wave function and the initial state.

2.2 Photoabsorption cross section

The photoabsorption cross section is obtained by the formula[9]

$$\sigma_\gamma(E_\gamma) = \frac{4\pi^2}{\hbar c} E_\gamma S(E_\gamma), \tag{4}$$

where E_γ is the photon energy, and $S(E_\gamma)$ is the $E1$ response function,

$$S(E_\gamma) \equiv \int d^3\boldsymbol{k} \left|\langle\phi_{\boldsymbol{k}}|\hat{D}_{10}|\phi_0\rangle\right|^2 \delta(E_{\boldsymbol{k}} - E_0 - E_\gamma), \tag{5}$$

where $\phi_{\boldsymbol{k}}$ and $E_{\boldsymbol{k}}$ are the eigenstate of the Hamiltonian and its energy.

We assume the ground state nucleus is excited by the electric dipole ($E1$) field at time $t = 0$ and dissociate. The initial state is constructed by multiplying the $E1$ operator $\hat{D}_{10}$ to the ground state wave function ϕ_0 as

$$\psi(0) = \hat{D}_{10}\phi_0, \tag{6}$$

$\hat{D}_{10}$ is defined as

$$\hat{D}_{10} = \sum_{i=1}^{3} e\sqrt{\frac{4\pi}{3}}\mathcal{Y}_{10}(\hat{\boldsymbol{r}}_i)\left(\frac{1}{2} - \frac{\hat{\tau}_{zi}}{2}\right), \tag{7}$$

where $\hat{\tau}_{zi}/2$ is the z component of the isospin of the i-th particle, and

$$\mathcal{Y}_{LM}(\boldsymbol{r}) = r^L \mathrm{Y}_{LM}(\hat{\boldsymbol{r}}), \tag{8}$$

where Y_{LM} is spherical harmonics.

2.3 Time-dependent method

From the time-dependent Schrödinger equation

$$i\hbar\frac{\partial}{\partial t}\psi(\boldsymbol{r}, t) = \hat{H}\psi(\boldsymbol{r}, t), \tag{9}$$

the wave function at t is expressed by time evolution operator and the initial state,

$$\psi(\boldsymbol{r}, t) = \mathrm{e}^{-\frac{i\hat{H}}{\hbar}t}\psi(\boldsymbol{r}, 0). \tag{10}$$

We divide the time variation into short time steps Δt, and approximate the time evolution operator for Δt,

$$\mathrm{e}^{-\frac{i\hat{H}}{\hbar}t} = \left(\mathrm{e}^{-\frac{i\hat{H}}{\hbar}\Delta t}\right)^n, \tag{11}$$

$$\mathrm{e}^{-\frac{i\hat{H}}{\hbar}\Delta t} \simeq \frac{1-\frac{i\hat{H}}{2\hbar}\Delta t}{1+\frac{i\hat{H}}{2\hbar}\Delta t}. \tag{12}$$

$E1$ response function $S(E_\gamma)$ can be written the time-dependent form

$$S(E_\gamma) = \frac{1}{\pi}\mathrm{Re}\int_0^\infty d\left(\frac{t}{\hbar}\right)\mathrm{e}^{\frac{i(E_\gamma+E_0+i\varepsilon)t}{\hbar}}\left\langle\psi(0)|\psi(t)\right\rangle, \tag{13}$$

where ε is the smoothing factor needed to stop time-evolution at a finite time, which is a small value about 0.05 MeV in our calculation. We only need to calculate the time evolution of the overlap of the wave function with the initial state to obtain the photoabsorption cross section.

2.4 Basis expansion

We expand the time-dependent wave function $\psi(t)$ by time-independent basis functions $\varphi_i(\boldsymbol{x})$. The time evolution of the wave function is expressed by the time-dependent coefficients $c_i(t)$,

$$\psi(t,\boldsymbol{x}) = \sum_{i=1}^{N} c_i(t)\varphi_i(\boldsymbol{x}), \tag{14}$$

N is the number of basis functions. The time evolution is described by Δt by solving the liner equations,

$$\left(B+\frac{iH}{2\hbar}\Delta t\right)\boldsymbol{c}(t+\Delta t) = \left(B-\frac{iH}{2\hbar}\Delta t\right)\boldsymbol{c}(t), \tag{15}$$

where B and H are $N\times N$ matrix, and their elements are $\langle\varphi_i|\varphi_j\rangle$ and $\langle\varphi_i|\hat{H}|\varphi_j\rangle$, and $\boldsymbol{c}(t)$ is N-dimensional vector that consists of $c_i(t)$.

The basis function is

$$\varphi_i(\boldsymbol{x}) = \mathcal{A}\left\{\mathrm{e}^{-\frac{1}{2}\tilde{\boldsymbol{x}}A_i\boldsymbol{x}}\left[\mathcal{Y}_L(\tilde{u}\boldsymbol{x})\chi_S\right]_{JM_J}\eta_{M_T}\right\}, \tag{16}$$

where $\mathcal{A}$ is the antisymmetrizer, $\tilde{}$ means transpose of vectors, u is a 2-dimensional vector by the $E1$ operator, χ_S and η are spin and isospin wave function, and S, J, M_J, and M_T are total spin, total angular momentum, z component of J, and that of isospin, respectively. The spacial part is called correlated Gaussian, in which A_i is a positivedefinite 2×2 symmetric matrix. $\boldsymbol{x}$ denotes a vector

$$\boldsymbol{x} = (\boldsymbol{x}_1,\boldsymbol{x}_2,\boldsymbol{x}_3), \tag{17}$$

where the Jacobi coordinate is taken as $\boldsymbol{x}_i$

$$\boldsymbol{x}_1 = \boldsymbol{r}_1-\boldsymbol{r}_2 \tag{18}$$

$$\boldsymbol{x}_2 = \frac{\boldsymbol{r}_1+\boldsymbol{r}_2}{2}-\boldsymbol{r}_3 \tag{19}$$

$$\boldsymbol{x}_3 = \frac{\boldsymbol{r}_1+\boldsymbol{r}_2+\boldsymbol{r}_3}{3}. \tag{20}$$

$\tilde{\boldsymbol{x}}A\boldsymbol{x}$ is a quadratic form for $\boldsymbol{x}$,

$$\tilde{\boldsymbol{x}}A\boldsymbol{x} = A_{11}\boldsymbol{x}_1^2+2A_{12}\boldsymbol{x}_1\cdot\boldsymbol{x}_2+A_{22}\boldsymbol{x}_2^2. \tag{21}$$

The nondiagonal element A_{12} involves the correlation between the relative coordinates. A is usually taken as real numbers, we extend it to complex numbers [8]. This increases the flexibility of the set of basis functions to express oscillations in a large distance. We carry out calculations with both of the basis functions having real-A and complex-A to compare them.

3 Result

In this section, we call the result calculated with the basis functions having complex number A the "complex" result, and with the ones having real A the "real" result.

3.1 Overlap

Fig.1 shows the absolute value of the overlap, $|\langle\psi(0)|\psi(t)\rangle|$, for ^{3}He. Both of the "complex" and "real" result are shown. The result of ^{3}H is similar to that of ^{3}He. As time passing, the wave function comes to have no overlap with the initial state, which is consistent with ^{3}He dissociation by the $E1$ field. Only in the "real" results shows some oscillations due to a lack of flexibility of the model space.

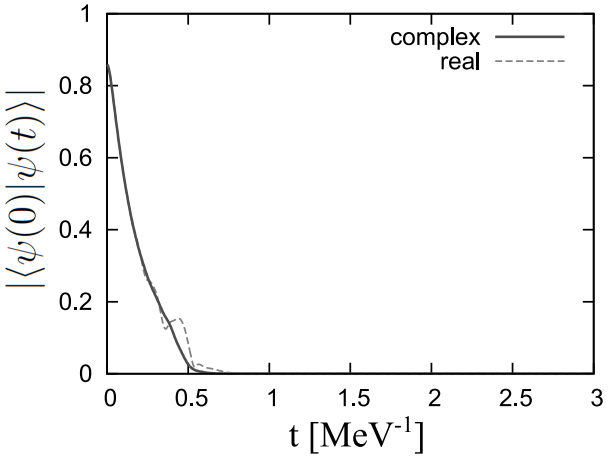

Figure 1: Overlap between the wave function and the initial state of ^{3}He calculated with complex- and real-range Gaussians.

3.2 Evaluation of the photoabsorption cross section

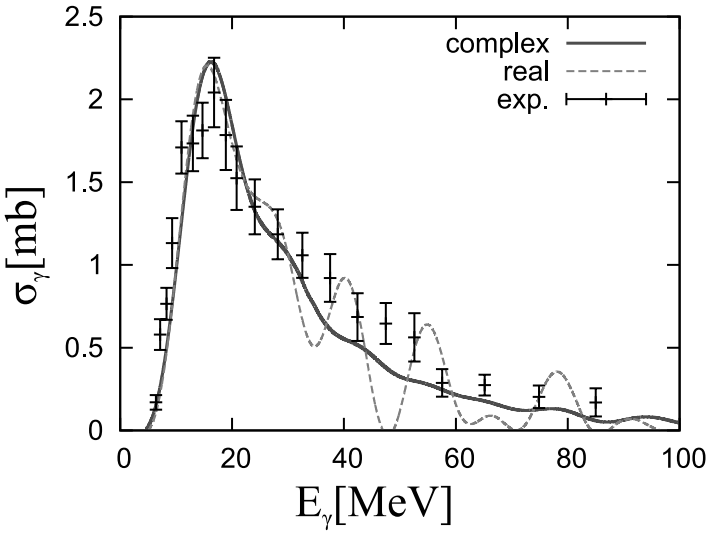

Figure 2: The calculated photoabsorption cross section of ^{3}He. The experimental data are taken from [10]

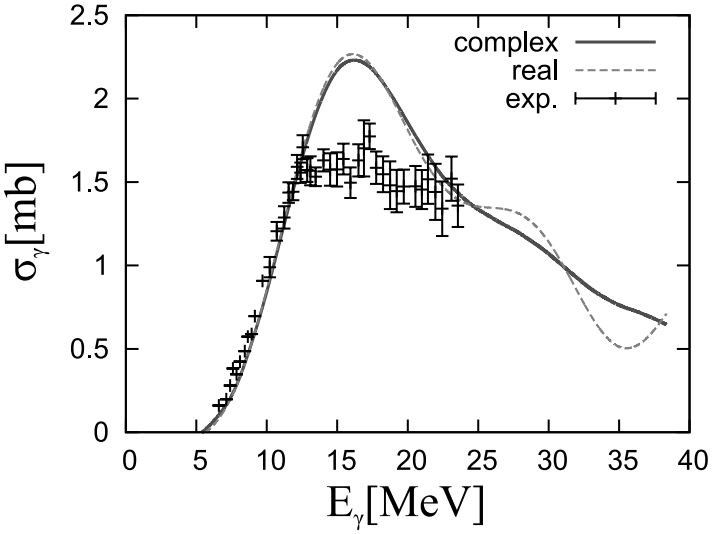

Figure 3: The same as Fig.2 but for ^{3}H. The experimental data are taken from [11]

We calculate the photoabsorption cross sections of ^{3}H and ^{3}He from the overlap using Eq. (5) and Eq. (13). The calculated cross sections of ^{3}H and ^{3}He are shown in Fig.2 and 3 with the experimental data. In ^{3}He case, "complex" result reproduces the experimental value up to high energy region about 80 MeV. On the other hand, in ^{3}H case, the calculated cross sections do not reproduce the experimental data at around 16 MeV. The further investigation is needed to resolve this discrepancy. In both of the "real" result, the calculated cross sections oscillate in the energy higher than 24 MeV due to the lack of the flexibility of the model space.

4 Summary

We develop a method to evaluate the photoabsorption cross section, in which we solve the time-dependent equation directly with basis expansion. We employ a complex-range correlated Gaussian basis function in order to treat many-body correlation explicitly. We apply the method to evaluate the photoabsorption cross sections of ^{3}H and ^{3}He. In the ^{3}He case, the experimental value is reproduced up to high energy region around 80 MeV. However, in the ^{3}H case, agreement between our calculation and the experimental data is not satisfactory. Further investigation is desired to resolve this problem. We also made a comparison with real- and complex-range correlated Gaussian basis functions, the complex ones are found to improve the calculation in the energy higher than 24 MeV.

References

[1] S. Aoyama, T. Myo, K. Katō, and K. Ikeda, Prog. Theor. Phys. 116, 1 (2006)

[2] V. G. Efros, W. Leidemann, G. Orlandini, and A. Barnea, J. Phys. G. 34, R459(2007)

[3] T. Kido, K. Yabana, and Y. Suzuki, Phys.Rev. C 53, 5 (1996)

[4] K. Varga, and Y. Suzuki, Phys. Rev. C 52, 2885 (1995)

[5] Y. Suzuki and K. Varga, *Stochastic Variational Approach to Quantum-Mechanical Few-body Problems*, Lecture Notes in Physics (Springer, Berlin, 1998), Vol. m54

[6] D. R. Thompson, M. Lemere, and Y. C. Tang, Nucl. Phys. A286, 53 (1977)

[7] T. Nakatsukasa, and K. Yabana, J. Chem. Phys. 114, 6(2001)

[8] S. Ohtsubo, Y. Fukushima, M. Kamimura, and E. Hiyama, Prog. Theor. Exp. Phys. 073D02 (2013)

[9] P. Ring and P. Shuck, *The Nuclear Many-Body Problem, Texts and Monographs in Physics* (Springer, New York, 1980)

[10] V. N. Fetisov, A. N. Gorbunov, and A. T. Varfolomeev, Nucl. Phys. A71, 305 (1965)

[11] D. D. Faul, B. L. Berman, P. Meyer, and D. L. Olson, Phys. Rev. C 24, 3 (1981)

57 Validation of CBZ Code System for Decay Heat Analysis

Takanori Kajihara, Yosuke Kawamoto, Go Chiba, Masashi Tsuji, and Tadashi Narabayashi

Division of Energy and Environmental Systems, Hokkaido University
Kita13 Nishi8, Kita-ku, Sapporo, Hokkaido, Japan
e-mail: kajihara@eng.hokudai.ac.jp

CBZ, a multi-purpose reactor physics calculation code system, is being developed at Hokkaido University. Verification and validation process is essential to guarantee the accuracy of simulated results. For this purpose, we simulate decay heat due to a pulse fission and that after a finite irradiation using JENDL/FPD-2011,FPY-2011, ENDF/B-VII.1, and JEFF-3.1.1, and its results are compared with some experimental data. There is a good agreement between CBZ numerical results and experimental data. These results contribute to the validation of CBZ for decay heat analysis.

1 Introduction

CBZ[1], which is a multi-purpose reactor physics calculation code system being developed at Hokkaido University, has various functionalities to perform neutron and photon transport, depletion of nuclides, uncertainty calculations, etc. There are many depletion calculation code systems in the world such as ORIGEN, FISPIN, and so on. CBZ also offers depletion calculation features in Burner and Cooler modules.

It is essential to validate a code system for the practical purposes. So far, CBZ has been evaluated in the PIE, and Sensitivity analyses[2] for the verification and validation process. In this study, we simulate the decay heat resulting from a pulse fission or a continuous fission in a irradiation period as a part of the verification and validation process of CBZ.

When we assume cooling time t, decay heat, $DH(t)$, is calculated by integrating the nuclide-wise decay heat like a following equation:

$$DH(t) = \sum_{i=1} \lambda_i N_i(t) E_i, \tag{1}$$

where λ_i is the decay constant, N_i is the number density, and E_i is the mean decay energy of nuclide i. It is consists of three components: alpha, beta, and gamma energy. We calculate number densities by a burn-up equation:

$$\frac{d\boldsymbol{N}(t)}{dt} = \boldsymbol{A}(t)\boldsymbol{N}(t), \tag{2}$$

where $\boldsymbol{A}$ and $\boldsymbol{N}$ are a burn-up matrix and a nuclide number density vector respectively.

2 Decay heat due to a pulse fission

We calculate decay heat due to beta, gamma, and total radiation energy by a single fission. Target fissile nuclides are U-235 and Pu-239. Regarding neutron energy, fast and thermal fissions are simulated for the nuclides above. We consider the difference of nuclear data evaluation by using yield and decay data from JENDL/FPD-2011,FPY-2011, ENDF/B-VII.1, and JEFF-3.1.1.

Regarding experimental data with uncertainties for the validation, We use YAYOI[3][4] experiments for the decay heat due to the fast system. For the thermal systems, we compare the Lowell[5], ORNL[6][7], and Tobias[8] experimental data with the numerical results.

Figure 1 through **3** show beta, gamma, and total decay heats due to the fast systems. Note that JENDL-2011 is a word that means JENDL-4.0 having the data of JENDL/FPD-2011 and FPY-2011. The results of CBZ match up accurately with all experimental data even though there are some differences depending on nuclear data evaluation.

Regarding the beta decay heat, fast U-235 and Pu-239 results are shown in Fig.1. Compared with the results using JENDL-2011 and ENDF/B-VII.1, the result using JEFF-3.1.1 shows larger values at most 7% in U-235 and 11% in Pu-239. In the U-235 case, all CBZ calculations are within the uncertainty bars of the YAYOI experimental data until 1×10^4 sec, while in the Pu-239 case, CBZ calculation by JEFF-3.1.1 overestimates the value beyond the range of experimental uncertainty.

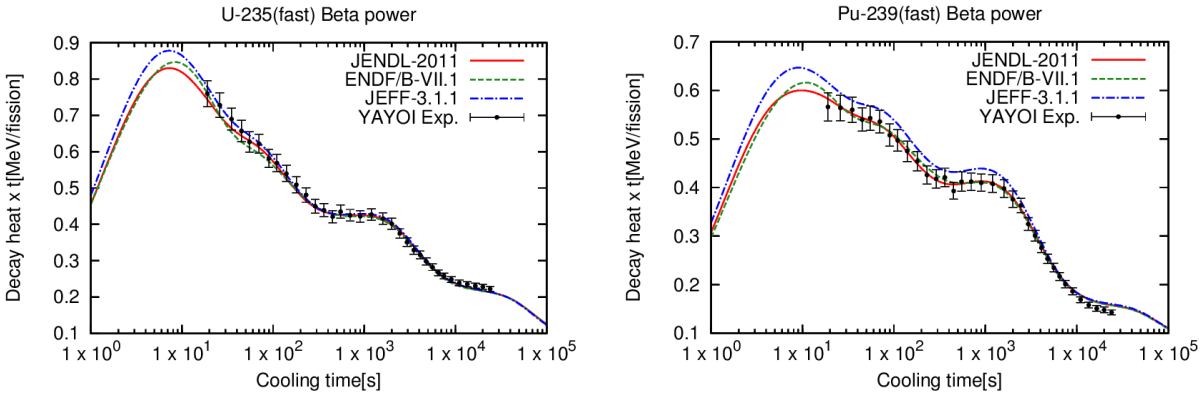

Figure 1: Beta decay heat by a fast fission on U-235 and Pu-239.

For the gamma decay heat component, as shown in Fig.2, CBZ results using JENDL-2011 and ENDF/B-VII.1 match well with the experimental data. On the other hand, the result using JEFF-3.1.1 underestimates the value, especially in the Pu-239 case. The difference between JENDL-2011 and JEFF-3.1.1 reaches around 14 % for Pu-239.

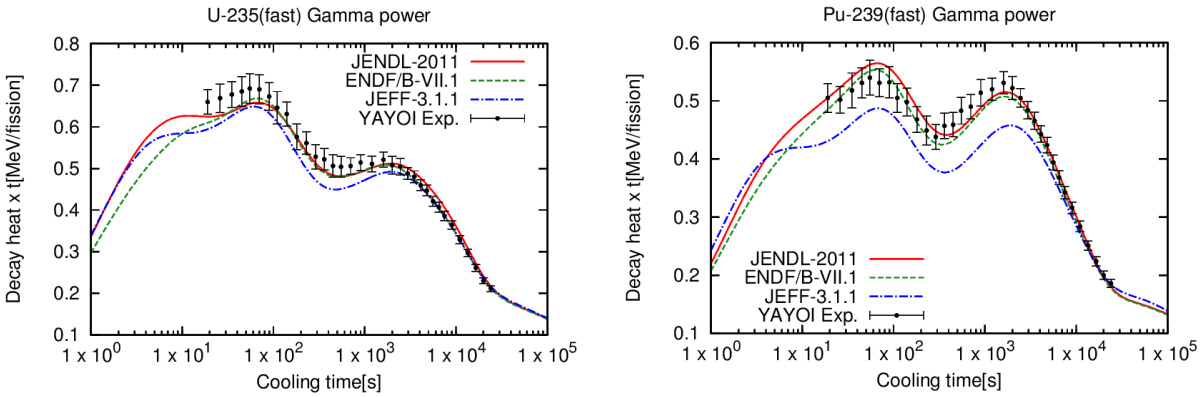

Figure 2: Gamma decay heat by a fast fission on U-235 and Pu-239.

Regarding total decay heat, Figure 3 shows the discrepancies between JEFF-3.1.1 and other nuclear evaluation data become small. In the Pu-239 case, JEFF-3.1.1 underestimates around 4 % relative to the others. Hence, CBZ numerical result using JENDL-2011 and ENDF/B-VII.1 can simulate the experimental data within the uncertainty bars except for the early part of the U-235 case.

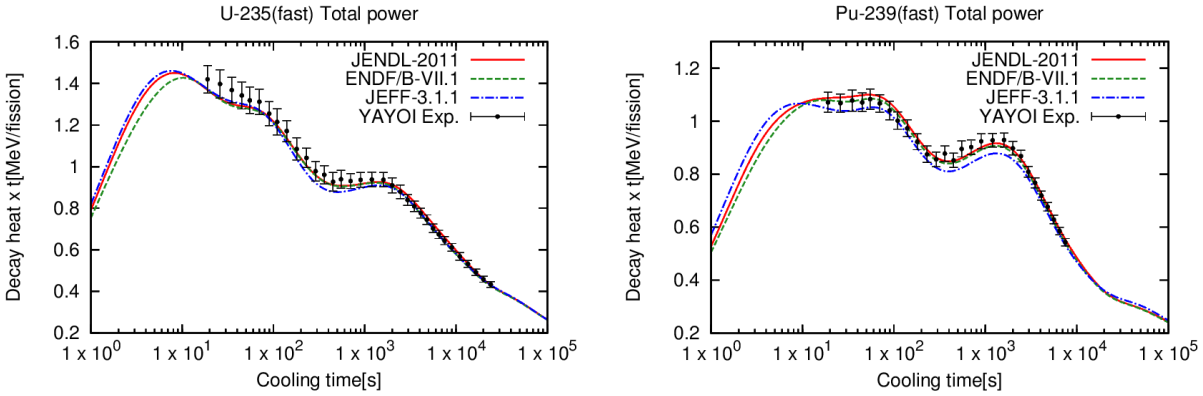

Figure 3: Total decay heat by a fast fission on U-235 and Pu-239.

Figure 4 through **6** show beta, gamma, and total decay heat due to thermal fission. In like manner, the results of CBZ reproduce well for all experimental data of the thermal neutron systems in whole.

The beta decay heat of thermal U-235 and Pu-239 results are shown as Fig.4. The data from JENDL-2011 and ENDF/B-VII.1 are plotted in a same shape except for around 1×10^1 sec. In contrast, JEFF-3.1.1 shows that the result stand at high level on a wide range. Compared with the results using JENDL-2011, the result using JEFF-3.1.1 shows larger values at most 11% in Pu-239. In the U-235 case, almost all CBZ outputs are in the uncertainty bars of the Lowell and ORNL experimental data, but the Tobias experimental data show a different curve around 1×10^1 sec.

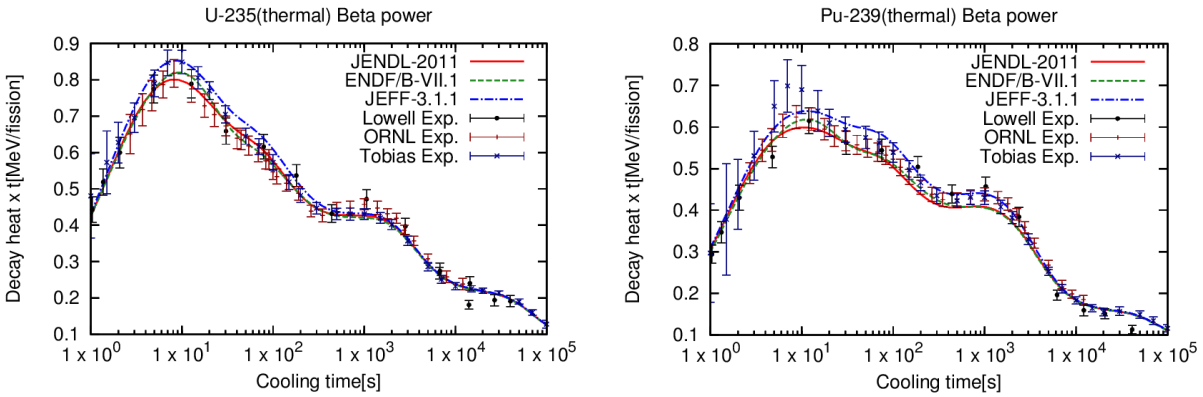

Figure 4: Beta decay heat by a thermal fission on U-235 and Pu-239.

In the case of gamma decay heat component, as shown in Fig.5, CBZ results using JENDL-2011 and ENDF/B-VII.1 match well with the experimental data of U-235 and Pu-239. In contrast, the result using JEFF-3.1.1 notably underestimates the value in the Pu-239. The gap between JENDL-2011 and JEFF-3.1.1 reaches up to 14 %.

Regarding total decay heat, Fig. 6 shows the difference derived from nuclear evaluation data becomes lower by the offset of overevaluation in the beta component and undersvaluation in the gamma component about JEFF-3.1.1 result. In the Pu-239 case, the difference between JEFF-

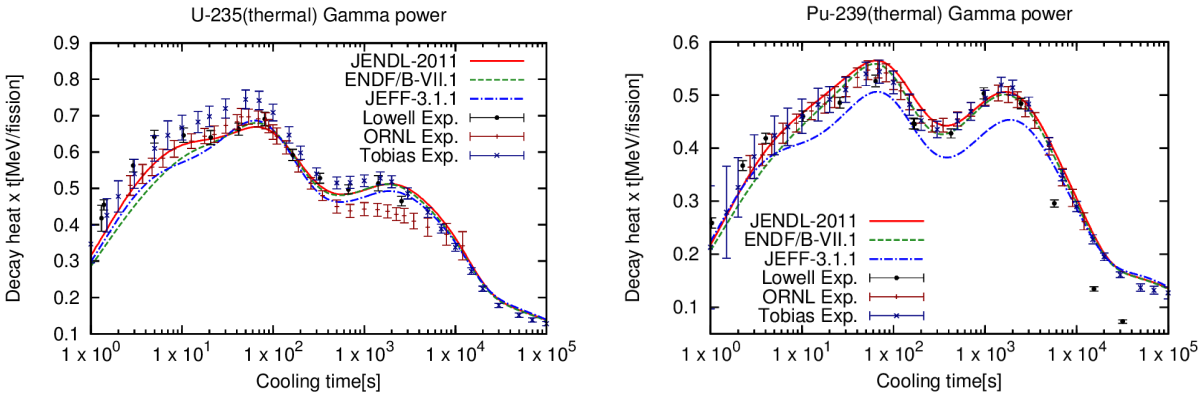

Figure 5: Gamma decay heat by a thermal fission on U-235 and Pu-239.

3.1.1 and others are at most 4 %. Except for the little difference around 1×10^3 sec, the results from JENDL-2011 and NEDF/B-VII.1 shape the similar curve within the uncertainty bars of experimental data through the cooling time. Hence, CBZ numerical result using JENDL-2011 and ENDF/B-VII.1 shows good reproduction for the experimental data.

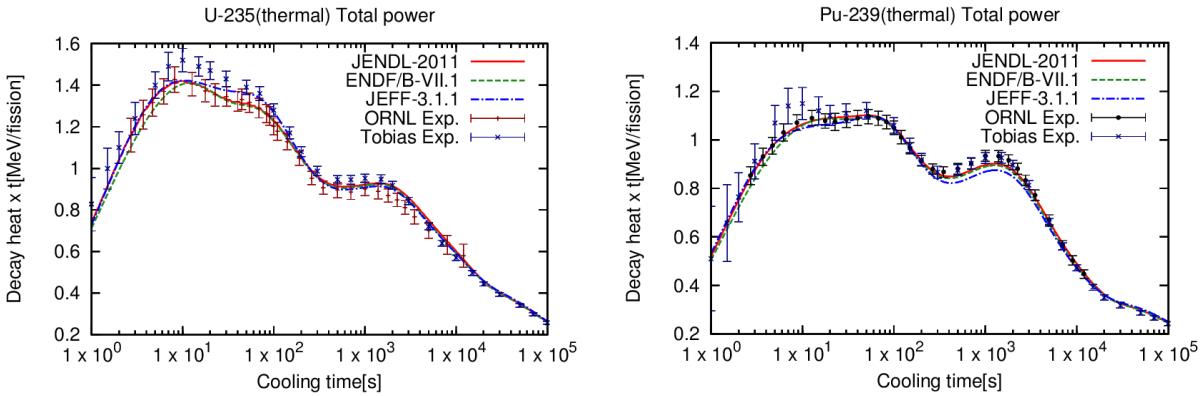

Figure 6: Total decay heat by a thermal fission on U-235 and Pu-239.

In terms of the simulation for the decay heat due to the pulse fission, other publications indicated similar plots.[9] [10]

3 Decay heat after an irradiation

In addition to the decay heat after fission burst, we also simulate the decay heat after a finite irradiation between 10 s and 10^5 s. The Tobias experimental data [8] include finite irradiation experiment at the fixed level of a fission per second for U-235 and Pu-239. CBZ numerical results from JENDL-2011, ENDF/B-VII.1, and JEFF-3.1.1 are compared with the Tobias experimental data for the thermal U-235 and Pu-239 systems.

Figures 7 and **8** show experimental data for total decay heat and CBZ numerical results from three nuclear evaluation data for U-235 and Pu-239 respectively. The Tobias experimental data and CBZ numerical calculations show similar results. Until 10^4 s cooling time in the case of 10^5 s irradiation, all uncertainty bars of experimental results overlap well. Overestimation occures in the cooling time around 1×10^5 s. In this case, the difference depending on nuclear data is reduced compared with the pulse fission. Regarding 10^4 s irradiation case of U-235, numerical values are in the uncertainty bars of experimental data till 1×10^3 s. On the other hand, in Pu-239, there is a difference between nuclear data evaluation, and at least one of the

numerical results is within the uncertainty bars through the cooling time. There is a good agreement betwen the numerical results of CBZ and experimental data. We can say that CBZ can simulate the decay heat after finite irradiation with good accuracy.

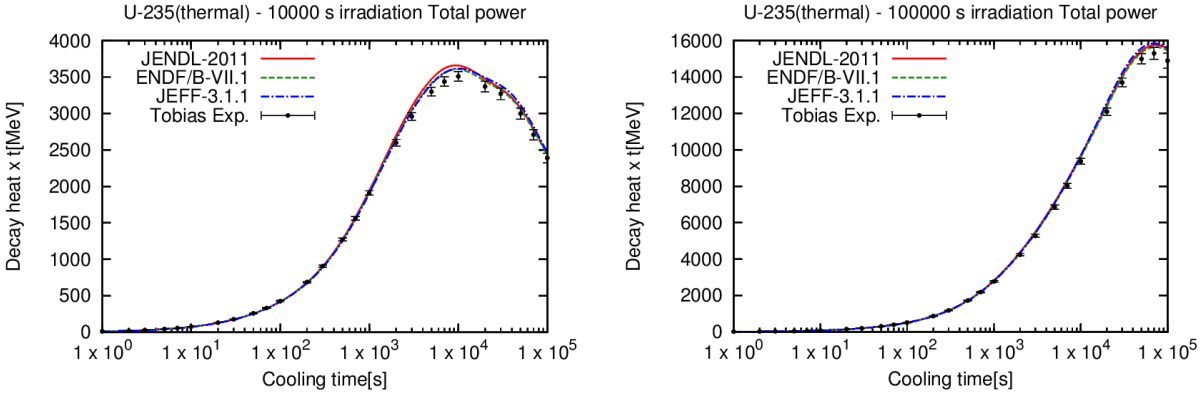

Figure 7: Total decay heat after 10^4 s and 10^5 s of pure fission of irradiation on thermal U-235.

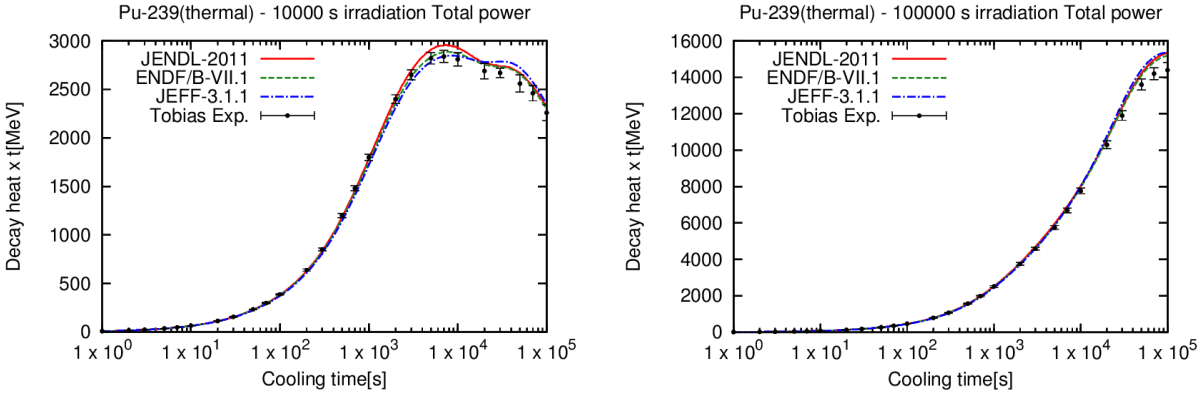

Figure 8: Total decay heat after 10^4 s and 10^5 s of pure fission of irradiation on thermal Pu-239.

4 Conclusion

In the decay heat analysis, discrepancy between numerical results of CBZ and experimental data is sufficiently small. The most of numerical results are inside experimental uncertainty when using JENDL-2011 or ENDF/B-VII.1. Hence the CBZ code system is validated regarding to the decay heat analysis.

References

[1] G. Chiba *et al.*, Uncertainty Quantification of Neutronic Parameters of Light Water Reactor Fuel Cells with JENDL-4.0 Covariance Data. J. Nucl. Sci. Technol. 2013 Jul; 50:751-760

[2] Y. Kawamoto *et al.*, Validation of CBZ Code System for Post Irradiation Examination Analysis and Sensitivity Analysis of (n,γ) Branching Ratio. Proc. of the 2012 Annual Symposium on Nuclear Data (NDS 2012); 2012 Nov.15-16; Ibaraki (Japan). pp.113-118

[3] M. Akiyama *et al.*, [Measurements of Beta-Ray Decay Heat of Fission Products for Fast Neutron Fission of ^{235}U,^{239}Pu, and ^{233}U]. Nihon-Genshiryoku-Gakkai Shi (J. At. Energy Soc. Jpn.). 1982; 24:803-816 [in Japanese].

[4] M. Akiyama *et al.*, [Measurements of Gamma-Ray Decay Heat of Fission Products for Fast Neutron Fission of ^{235}U,^{239}Pu, and ^{233}U]. Nihon-Genshiryoku-Gakkai Shi (J. At. Energy Soc. Jpn.). 1982; 24:709-722 [in Japanese].

[5] E.H. Seabury, *et al.*, Decay Heat Measurements Following Neutron Fission of ^{235}U and ^{239}Pu. Proc. Int. Conf. on Nucl. Data for Science and Technol.. 1997; Trieste (Italy). p.835

[6] J. Dickens *et al.*, Fission-Product Energy Release for Times Following Thermal-Neutron Fission of ^{235}U between 2 and 14,000 seconds. Nucl. Science and Eng.. 1980; 74:106

[7] J. Dickens *et al.*, Fission-Product Energy Release for Times Following Thermal-Neutron Fission of ^{239}Pu between 2 and 14,000 seconds. Nucl. Science and Eng.. 1981; 78:126

[8] A. Tobias *et al.*, Derivation of Decay Heat Benchmarks fr U235 and Pu239 by a Least Squares Fit to Measured Data; 1989.

[9] J. Katakura, Uncertainty Analysis of Decay Heat Summation Calculations Using JENDL, JEFF, and ENDF files. J. Nucl. Sci. Technol. 2013 Apr; 50:799-807

[10] S. Lahaye *et al.*, First Verification and Validation Steps of MENDEL release 1.0 Cycle Code System. Proc of the PHYSOR 2014; 2014 Sep.28-Oct.3; Kyoto(Japan).

58 Evaluation of neutron nuclear data on krypton isotopes

Md. Mamunur RASHID[1], Nobuhiro SHIGYO[1], Kenji ISHIBASHI[1]
Nobuyuki IWAMOTO[2], Osamu IWAMOTO[2]
[1] *Department of Applied Quantum Physics and Nuclear Engineering, Kyushu University*
744 Motooka, Nishi-ku, Fukuoka 819-0395, Japan
[2] *Nuclear Data Center, Nuclear Science and Engineering Center, Japan Atomic Energy Agency*
Tokai-mura, Ibaraki 319-1195, Japan
e-mail: M.Rashid@kune2a.nucl.kyushu-u.ac.jp

Neutron nuclear data on krypton isotopes have been evaluated in the incident neutron energy range from 1 keV to 20 MeV. The phenomenological optical model potential was employed, in order to calculate total cross section of natural krypton. This calculation was based on the coupled channel method. Optical potential parameters were obtained by best fitting the calculated result with experimental total cross section. The neutron transmission coefficients were calculated which were used for getting the cross sections of neutron emission from compound nucleus in statistical process. Compound, pre-equilibrium, and direct reaction processes were taken into consideration for cross section calculation. The present calculation results are compared with the experimental data and major evaluated nuclear data libraries. It is observed that the present evaluation can explain the experimental data reasonably well.

1. Introduction

Natural element of krypton with atomic number Z=36 consists of six stable isotopes of mass numbers A=78, 80, 82, 83, 84 and 86 with natural abundances 0.35%, 2.28%, 11.58%, 11.49%, 57% and 17.3% respectively. In fission reactors, unstable krypton isotopes are produced by neutron capture and fission reactions with long half-life 2.29×10^5 yr, for instance, of ^{81}Kr and 10.756 yr of ^{85}Kr. Therefore, evaluated neutron nuclear data on these isotopes are important in various fields of nuclear science applications.

The neutron nuclear data evaluation of ^{83,84,85,86}Kr isotopes was carried out first time in 1984 for JENDL-2 [1]. In this evaluation, the optical and statistical model code CASTHY [2] was used to calculate total, elastic and inelastic scattering, and capture cross sections. In 1990, the data of remaining isotopes of ^{78,80,82}Kr were evaluated and incorporated in JENDL-3.1 [3] where the pre-equilibrium and multi-step evaporation model code PEGASUS [4] was used for competing reactions. These data were eventually compiled into the subsequent versions of JENDL-3.2 [5] and JENDL-3.3 [6]. After that these data were re-evaluated in the latest JENDL-4.0 [7, 8] where total, elastic and inelastic scattering, capture cross sections as well as other competing reaction cross sections were calculated by nuclear reaction model code POD [9] and OPTMAN [10]. Obviously, re-evaluated data in JENDL-4.0 are better than those of previous evaluations due to the advancement of theoretical nuclear reaction models. Nevertheless, JENDL-4.0 still have inconsistency with measured data for some of reactions, and recent experimental data were not considered. It is to be noticed that the data evaluation of krypton isotopes has yet to be performed by using the CCONE [11] code which might predict cross sections well. The aim of this work is to get further improvements in nuclear data of krypton and, hence it is to be carried out by using CCONE code.

2. Evaluation Procedures

The calculation of neutron induced reaction cross sections was performed by theoretical nuclear reaction code, CCONE. In this evaluation all reactions, which emit neutrons, protons, deuterons, tritons, He-3, α-particles and γ-rays, were considered if the reaction channels were opened up to 20 MeV. The coupled-channels (CC) method [12], for instance, was to be employed for the calculation of total, shape elastic, direct inelastic scattering cross sections. Outgoing channels were delineated by other nuclear models. We included recently measured data in this evaluation.

2.1 Optical model

The interaction between the incident neutron and target nucleus as krypton was described by the phenomenological optical model with the CC method based on rigid rotor model. The functional form

of global optical model potential (OMP) was described by Kunieda et al. [13]. In this evaluation, the 0^+ (g.s.)- to 6^+-levels and $9/2^+$ (g.s.)- to $15/2^+$-levels in ground-state band were coupled for ^{78,80,82,84,86}Kr and ^{83}Kr, respectively. Total cross section was calculated by using the CC optical model with deformation parameters $\beta_2 = 0.352$, 0.265, 0.2021, 0.1563, 0.1489 and 0.145 for ^{78,80,82,83,84,86}Kr, respectively. The real volume V_R and imaginary surface W_D terms of OMPs are given by

$$V_R = \left(V_R^0 + V_R^1 + V_R^2 E^{\dagger 2} + V_R^3 E^{\dagger 3} + V_R^{DISP} e^{-\lambda_R E^\dagger}\right) \times \left[1 + \frac{1}{V_R^0 + V_R^{DISP}}(-1)^{Z'+1} C_{viso} \frac{N-Z}{A}\right] + C_{coul} \frac{ZZ'}{A^{1/3}} \varphi_{coul}(E^\dagger), \quad (1)$$

$$W_D = \left[W_D^{DISP} + (-1)^{Z'+1} C_{wiso} \frac{N-Z}{A}\right] e^{-\lambda_D E^\dagger} \times \frac{E^{\dagger 2}}{E^{\dagger 2} + WID_D^2}, \quad (2)$$

where Z, N, A and Z' are the number of protons, neutrons and nucleons in the target nucleus, and projectile charge number, respectively. $E^\dagger$ is the projectile energy relative to the Fermi one. $V_R^{(0-3)}$, V_R^{DISP}, W_D^{DISP}, WID_D, C_{viso}, C_{wiso}, $\lambda_{R,D}$, nuclear radius $R_{R,D}$ and diffuseness $a_{R,D}$ are the OMP parameters. In order to get better fitting to the experimental data, some OMP parameters were adjusted, while rest of the parameter values were kept same as Kunieda et al. [13]. The values of modified parameters are given in **Table 1**. By using this modified OMP, the total cross section was obtained from the calculation with CCOM code [14]. This code also calculated neutron transmission coefficients which were then applied to statistical model calculation. Several other OMPs were used for particle emission in the outgoing channels. The global OMP parameters for neutron and proton emissions were taken from Koning and Delaroche [15], Lohr and Haeberli [16] for deuteron, Becchetti and Greenlees [17] for triton and He-3, and Mcfadden and Satchler [18] for α-particle.

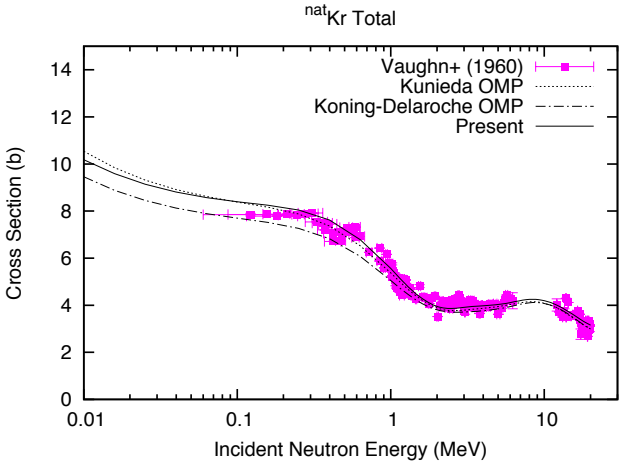

Fig. 1 Total Cross Section of Natural Kr.

Table 1 Values of modified and original OMP

Parameter	modified values	original values
V_R^0	-40.27 MeV	-34.40 MeV
V_R^{DISP}	99.83 MeV	94.88 MeV
W_D^{DISP}	12.5 MeV	11.08 MeV
WID_D	16.64 MeV	12.72 MeV
a_R	0.522 fm	0.49 fm

The present total cross section of natural krypton is compared with experimental data obtained by Vaughn et al. [19] as shown in **Figure 1**. The total cross sections calculated by using parameters of Kunieda OMP and Koning-Delaroche OMP are compared in this figure. It is observed that the present total cross section reproduces the experimental data better than those calculated with other parameters.

2.2 Pre-equilibrium model

The two component exciton model [20] was applied to describe the contributions of the pre-equilibrium process. The global exciton model parameters prescribed by Koning and Duijvestijn [21] were adopted in the calculation of cross section for pre-equilibrium components. In the framework of global parameterization, the single particle state densities are described by introducing the parameters C_ν for neutrons and C_π for protons as in the following equations

$$g_\nu = C_\nu \frac{N}{15} \quad \text{for neutrons,} \quad (3)$$

$$g_\pi = C_\pi \frac{Z}{15} \quad \text{for protons.} \tag{4}$$

In order to fit experimental data, these parameters were adjusted for target nuclei. The default value of these parameters is unity. The parameter values of C_ν for ^{82,84}Kr were chosen to be 1.22 and 1.5, respectively, whereas this value was set to 0.9 for ^{80}Kr. Moreover, C_π parameter value for ^{78}Kr was set to 0.83 in order to get best fitting with experimental data. In addition, the particle pickup and knockout processes were also considered in this evaluation.

2.3 Statistical model

The compound nuclear reaction cross sections were estimated on the basis of Hauser-Feshbach formalism [22] including width fluctuation correction. It is necessary to provide input of discrete levels and level density parameters. The discrete levels information was taken from the reference input parameters library, RIPL-3 [23]. The nuclear level density formulated by Gilbert and Cameron [24] was adopted in this evaluation. This prescription assumed the constant temperature model for lower excitation energies and the Fermi gas model for higher excitation energies in order to describe the level density above the adopted highest energy of discrete level. The level density parameter a, which characterizes the Fermi-gas part of level density, can be expressed by

$$a(U) = a^\star \left(1 + E_{sh} \frac{1 - e^{-\gamma U}}{U}\right), \tag{5}$$

where $a^\star$ is the asymptotic level density parameter, E_{sh} is the shell correction energy and γ is the damping factor. The level density parameters were determined by adjusting them so as to get the better agreement with average level spacing of s-wave neutron resonances which was derived from experiments. In this evaluation, in addition, the generalized Lorentzian form [25] was used for E1 γ-ray strength function.

3. Evaluated Results and Discussion

The experimental data were retrieved from EXFOR database [26]. The present results were not only compared with measured data but also, of course, visualized with the current available major evaluated nuclear data libraries (JENDL-4.0, ENDF/B-VII.1 [27], JEFF-3.2 [28]).

The capture cross sections of ^{78,80,82,83,84}Kr are illustrated in **Figs. 2-6**, respectively. The data of Walter et al. [29] are available up to 300 keV. It is found from the figures that the calculated results well reproduce the experimental data although there remain uncertainties above 300 keV. In Figure 2, the data of JENDL-4.0 and ENDF/B-VII.1 are almost identical except at around 100 keV where the latter data overestimated the measured ones.

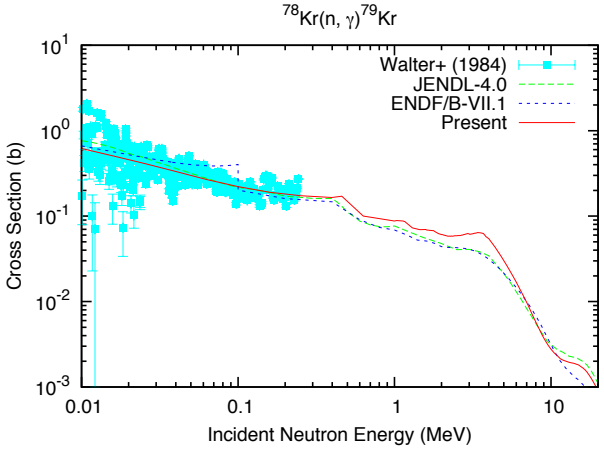

Fig. 2 ^{78}Kr(n,γ)^{79}Kr reaction cross section.

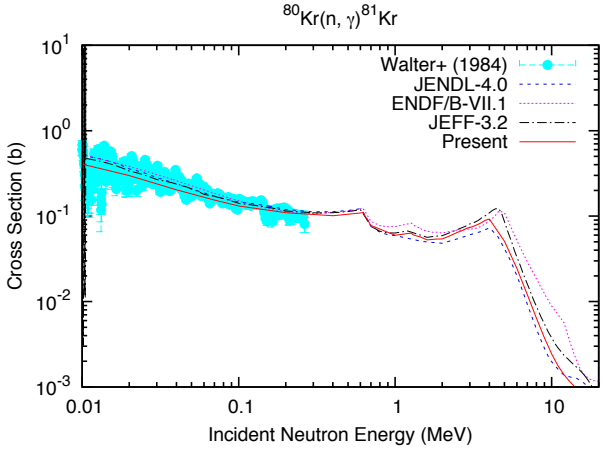

Fig. 3 ^{80}Kr(n,γ)^{81}Kr reaction cross section.

The calculated cross sections for $(n, 2n)$ reaction are compared with experimental data of Kondaiah et al. [30] and Bazan [31] which are shown in **Figs. 7** and **8** for ^{78}Kr and ^{80}Kr, respectively. The present evaluation for ^{78}Kr, indeed, explains well the Bazan's data while ENDF/B-VII.1 data agreed

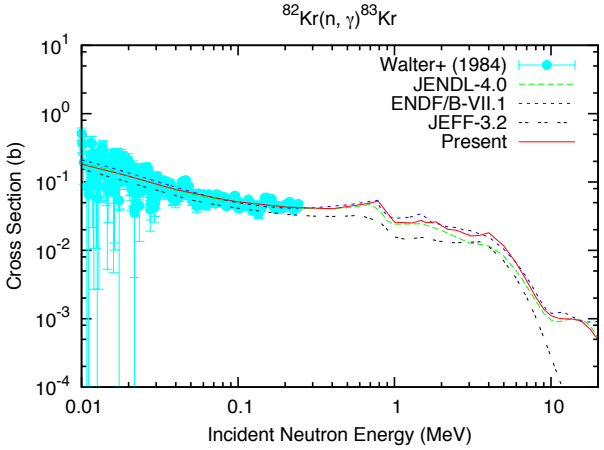

Fig. 4 ^{82}Kr(n, γ)^{83}Kr reaction cross section.

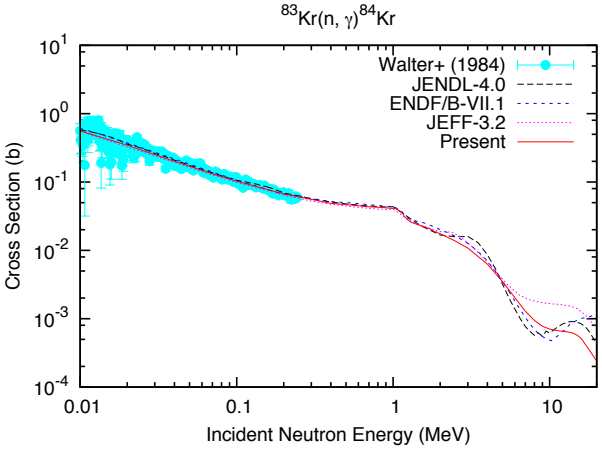

Fig. 5 ^{83}Kr(n, γ)^{84}Kr reaction cross section.

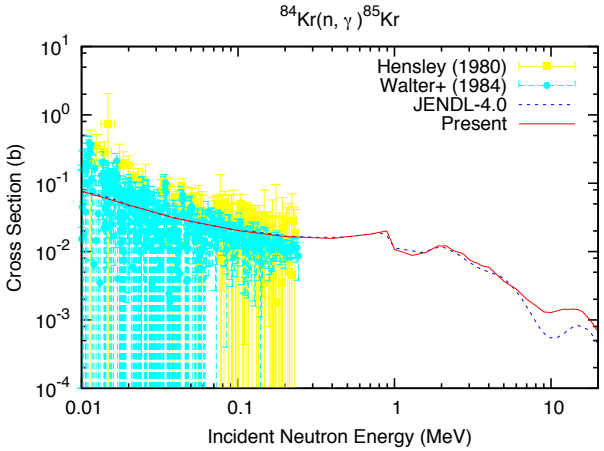

Fig. 6 ^{84}Kr(n, γ)^{85}Kr reaction cross section.

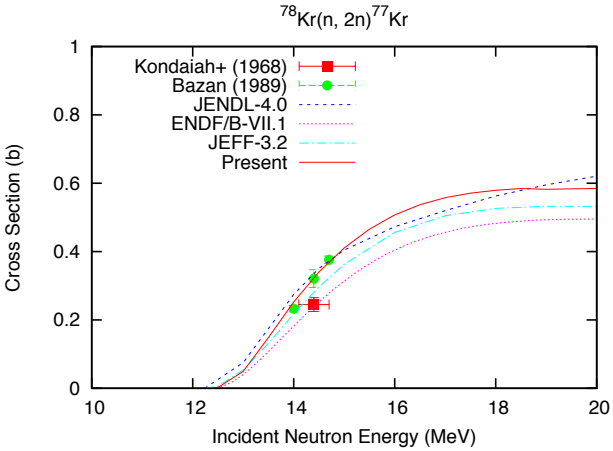

Fig. 7 ^{78}Kr(n, 2n)^{77}Kr reaction cross section.

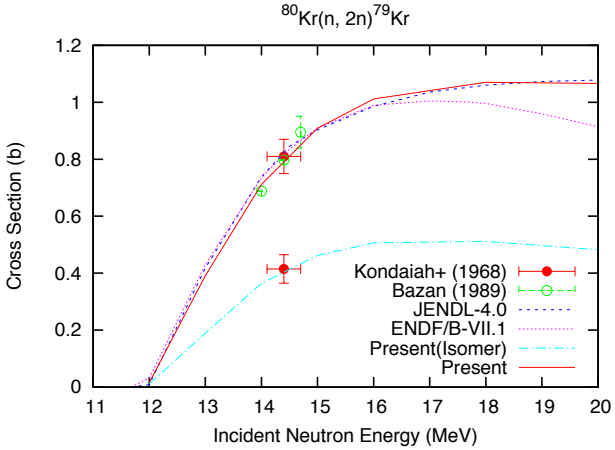

Fig. 8 ^{80}Kr(n, 2n)^{79}Kr reaction cross section.

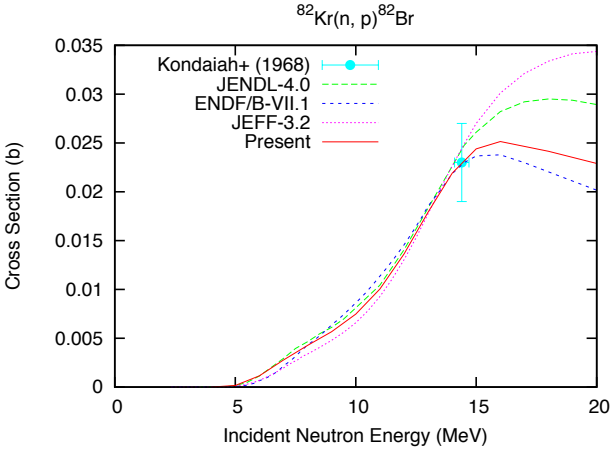

Fig. 9 ^{82}Kr(n, p)^{82}Br reaction cross section.

with Kondaiah's ones which provided smaller cross section than Bazan's. On the other hand, the present evaluation for ^{80}Kr not only shows a good fit to the Bazan's data, but also the Kondaiah's data. Moreover, calculated cross section of $(n, 2n)$ reaction for isomer production of ^{79}Kr describes well the Kondaiah's data.

Figs. 9 and **10** show the comparison of the present results for ^{82}Kr(n, p) and ^{84}Kr(n, p) reaction cross sections, respectively, with data of measurements and the evaluated libraries. It is observed that the calculated cross section for ^{82}Kr is in good agreement with the Kondaiah's data. Moreover, ENDF/B-

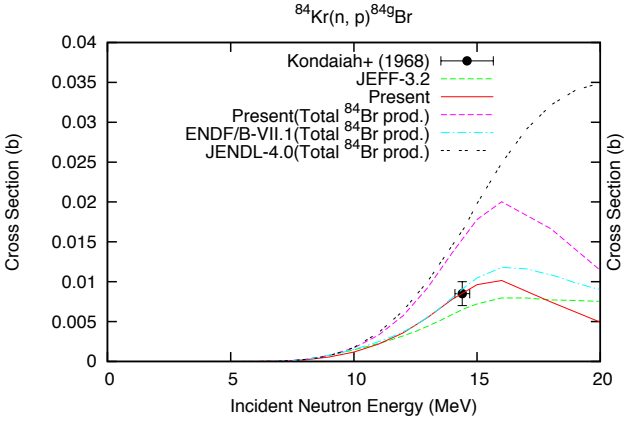

Fig. 10 ^{84}Kr(n, p)^{84g}Br reaction cross section.

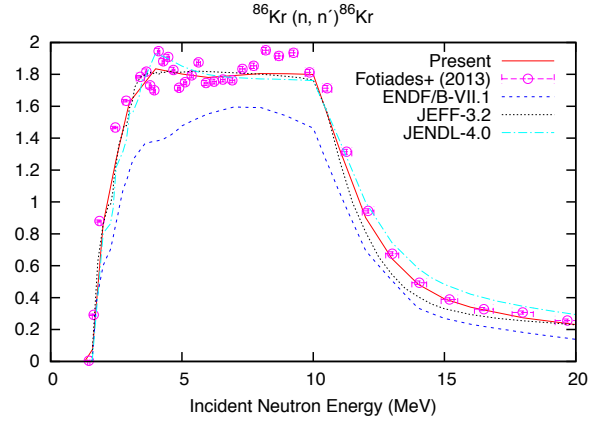

Fig. 11 ^{86}Kr(n, n′)^{86}Kr reaction cross section.

VII.1 reproduces the measured data at 14.4 MeV. In contrast, JENDL-4.0 and JEFF-3.2 evaluations made a slight deviation from the experimental data. On the other hand, JENDL-4.0 have a larger cross section than JEFF-3.2 and ENDF/B-VII.1 for ^{84}Kr. It should be noted that the activation measurement of Kondaiah for ^{84}Kr provided the production cross section of ground-state of ^{84}Br with half-life 31.76 min. The isomer-state of ^{84}Br decays directly to ^{84}Kr with half-life 6.0 min. So, the comparison of Kondaiah's data should be made with ^{84}Br ground-state production cross section. The present results for ^{84}Br ground-state production well reproduce the measured data. The data of other evaluated libraries might be underestimated.

A recent experimental data of ^{86}Kr(n, n') reaction cross section measured by Fotiades et al. [32] are compared with the data of present evaluation and evaluated libraries as illustrated in **Figure 11**. The present cross section shows good agreement with the experimental data. JENDL-4.0 and JEFF-3.2 evaluations also describe reasonably the experimental data, whereas ENDF/B-VII.1 data are underestimated above 1.8 MeV.

4. Conclusion

The neutron nuclear data on ^{78,80,82,83,84,86}Kr were evaluated in the incident neutron energy range from 1 keV to 20 MeV using the CC optical model and nuclear reaction model code, CCONE. The calculated results reproduce well the experimental data of cross sections for $(n, 2n)$, (n, p), (n, n'), and capture reactions as well as of the total cross section. The present data evaluation of krypton isotopes by using CCONE code are in no way inferior to JENDL-4.0, since latest measured data were also taken into account.

Acknowledgement

This work has been supported by JSPS KAKENHI Grant Number 23360429.

References

[1] Kikuchi Y, Nakagawa T, Asami T, Kawai M, Matsunobu H, Kanda Y. Second version of Japanese evaluated nuclear data library (JENDL-2). J Nucl Sci Technol. 1985;22:593-603.

[2] Igarasi S, Fukahori T. Program CASTHY - statistical model calculation for neutron cross sections and gamma ray spectrum - (JAERI 1321). Tokai: Japan Atomic Energy Research Institute; 1991.

[3] Asami T, Iijima S, Igarasi S, Ihara H, Kawai M, Kikuchi Y, Komuro Y, Shibata K, Takano H, Takeda T, Nakagawa T, Nakazawa M, Hasegawa A, Maekawa H, Mizumoto M, Yoshida T. [Japanese evaluated nuclear data library version 3, JENDL-3]. J At Energy Soc Jpn. 1989;31:1190-1217 [in Japanese].

[4] T. Nakagawa,S. Iijima, T. Sugi , T. Nishigori, PEGASUS: a preequilibrium and multi-step evaporation code for neutron cross section calculation JAERI-Data/Code 99- 031(1999), 78p.

[5] Nakagawa T, Shibata K, Chiba S, Fukahori T, Nakajima Y, Kikuchi Y, Kawano T, Kanda Y, Ohsawa T, Matsunobu H, Kawai M, Zukeran A, Watanabe T, Igarasi S, Kosako K, Asami T. Japanese evaluated nuclear data library version 3 revision-2: JENDL-3.2. J Nucl Sci Technol. 1995;32:1259-1271.

[6] Shibata K, Kawano T, Nakagawa T, Iwamoto O, Katakura J, Fukahori T, Chiba S, Hasegawa A, Murata T, Matsunobu H, Ohsawa T, Nakajima Y, Yoshida T, Zukeran A, Kawai M, Baba M, Ishikawa M, Asami T,

Watanabe T, Watanabe Y, Igashira M, Yamamuro N, Kitazawa H, Yamano N, Takano H. Japanese evaluated nuclear data library version 3 revision-3: JENDL-3.3. J Nucl Sci Technol. 2002;39:1125-1136.

[7] K. Shibata, O. Iwamoto, T. Nakagawa, N. Iwamoto, A. Ichihara, S. Kunieda, S. Chiba, K. Furutaka, N. Otuka, T. Ohsawa, T. Murata, H. Matsunobu, A. Zukeran, S. Kamada, and J. Katakura, JENDL-4.0: A new library for nuclear science and engineering. J. Nucl. Sci. Technol. 2011;48:1-30.

[8] K. Shibata, A. Ichihara, S. Kunieda, Evaluation of Neutron Nuclear Data on Bromine and Krypton Isotopes for JENDL-4.0, J. Nucl. Sci. Technol., 48(3), 429-439(2011).

[9] Ichihara A, Iwamoto O, Chiba S, Kunieda S, Shibata K. Program POD; a computer code to calculate cross sections for neutron-induced nuclear reactions (JAEA-Data/Code 2007-012). Tokai: JAEA; 2007.

[10] Soukhovitski ESh, Chiba S, Iwamoto O, Shibata K, Fukahori T, Morogovskij GB. Programs of OPTMAN and SHEMMAN version 8 (2004) JAERI-Data/Code 2005-002 . Tokai: 2005, 78p.

[11] O. Iwamoto, Development of a comprehensive code for nuclear data evaluation, CCONE, and validation using neutron induced cross sections for uranium isotopes. J. Nucl. Sci. Technol. 2007; 44(5): 687-697.

[12] T. Tamura, Analyses of the scattering of nuclear particles by collective nuclei in terms of the coupled-channel calculation. Rev. Mod. Phys. 1965; 37: 679-708.

[13] S. Kunieda, S. Chiba, K. Shibata, A. Ichihara, E. Sh. Sukhovitskii, Coupled-channels optical model analyses of nucleon-induced reactions for medium and heavy nuclei in the energy region from 1 keV to 200 MeV. J. Nucl. Sci. Technol. 2007; 44(6): 838-852.

[14] O. Iwamoto, Program CCOM—Coupled-channels Optical Model Calculation with Automatic Parameter Search. JAERI-Data/Code 2003-020 , 22p.

[15] A.J. Koning and J.P. Delaroche, Local and global nucleon optical models from 1 keV to 200 MeV. Nucl. Phys.A. 2003; 713: 231-310.

[16] J.M. Lohr and W. Haeberli, Elastic scattering of 9-13 MeV vector polarized deuterons. Nucl. Phys. A. 1974; 232: 381-397.

[17] F.D. Becchetti, Jr., and G.W. Greenlees, A General Set of ^{3}He and Triton Optical-Model Potentials for A>40, E<40 MeV, in Polarization Phenomena in Nuclear Reactions, H.H. Barshall and W. Haeberli, eds. University of Winsconsin Press, Madison. 1971: 682-683.

[18] L. McFadden and G.R. Satchler, Optical-model analysis of the scattering of 24.7 MeV alpha particles,. Nucl. Phys. 1966; 84: 177-200.

[19] F.J.Vaughn, W.L.Imhof, R.G.Johnson, M.Walt, Total neutron cross sections of helium, neon, argon, Krypton and Xenon. Phys. Rev. 1960; 118: 683-686.

[20] C. Kalbach, Two-component exciton model: Basic formalism away from shell closures. Phys. Rev. 1986; C33: 818.

[21] A. J. Koning, M. C. Duijvestijn, A global pre-equilibrium analysis from 7 to 200 MeV based on the optical model potential. Nucl. Phys. A. 2004; 744: 15-76.

[22] W. Hauser, H. Feshbach, The inelastic scattering of neutrons, Phys. Rev. 87, 366 (1952).

[23] R. Capote et al., RIPL—Reference Input Parameter Library for Calculation of Nuclear Reactions and Nuclear Data Evaluations. Nucl. Data Sheets. 110; 2009: 3107-3214.

[24] A. Gilbert and A.G.W. Cameron, A composite nuclear level density formula with shell corrections. Can. J. Phys. 1965; 43: 1446-1496.

[25] J. Kopecky, M. Uhl, Test of gamma-ray strength functions in nuclear reaction model calculations, Phys. Rev. 1990; C41: 1941-1955.

[26] Experimental Nuclear Reaction Data (EXFOR/CSISRS), available from: http://www.nndc.bnl.gov/exfor7/exfor00.htm.

[27] Chadwick MB et al., ENDF/B-VII.1 nuclear data for science and technology: cross sections, covariances, fission product yields and decay data. Nucl. Data Sheets. 2011; 112; 2887-2996.

[28] OECD Nuclear Energy Agency Data Bank. Available from: http://www.oecd-nea.org/dbforms/data/eva/evatapes/jeff_32/.

[29] G. Walter, B. Leugers, F. Kaeppeler, Z. Y. Bao, D. Erbe, G. Rupp, G. Reffo, F. Fabbri, Neutron capture cross sections of the krypton isotopes and the s-process branching at ^{79}Se, J. Nucl. Sci. Eng., 93(4), 357(1986).

[30] E.Kondaiah, N.Ranakumar, R.W.Fink, Neutron activation cross sections at 14.4 MeV for Kr and Xe isotopes. Nucl. Phys. A. 1968; 120 Issue 2: 337-341.

[31] F.Bazan, (n,2n) cross-section measurements of Krypton and Xenon isotopes. Prog.Rep.: U. C., Lawrence Rad. Lab. (Berkeley and Livermore); 1989, No.53929: 162.

[32] N. Fotiades, M. Devlin, R. O. Nelson, and T. Granier, Low-spin states in ^{86}Kr from the (n, n$'$) reaction, Phys. Rev. C 87(2013).

59 Dipole strength in ^{80}Se (γ, γ') below the neutron-separation energy

[1]*A. Makinaga, [2]R. Schwengner, [2]R. Massarczyk, [2]M. Anders, [2]M. Röder, [2]T.Al-Abdullah, [2]R. John, [2]S. Müller, [3]H. Otsu, [2]K. Schmidt, [2]R. Hannaske, [2]A. Wagner

[1]Faculty of Science, Hokkaido University, 060-0810, Sapporo, Japan

[2]Institute of Radiation Physics, Helmholtz-Zentrum Dresden-Rossendorf,, 01328 Dresden, Germany

[3]RIKEN Nishina Center, RIKEN, Hirosawa, Wako, Saitama 351-0918, Japan

*E-mail: makinaga@nucl.sci.hokudai.ac.jp

The photon strength of ^{80}Se is a key parameter to estimate the ^{79}Se(n,γ) cross section. ^{79}Se is important from the point of view of nuclear transmutation of the long-lived fission (LLFP) product ^{79}Se into the stable nucleus ^{80}Se. In previous work, photo neutron cross sections were measured for ^{80}Se directly above the neutron separation energy with LCS photon beams to experimentally constrain the E1 γ-ray strength function for ^{80}Se. The uncertainty of the predicted neutron capture cross sections for ^{79}Se (~a factor of 4) was still very large from the point of view of the transmutation of the nuclear waste ^{79}Se [1].

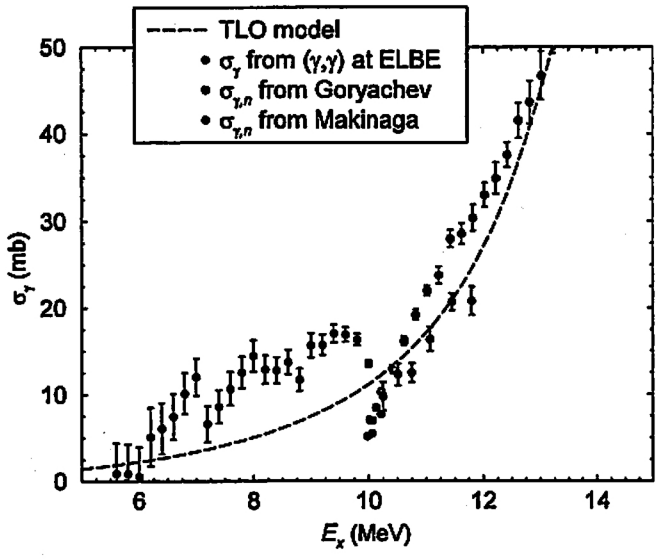

Figure 1 Photo absorption cross sections for Se-80

To test the model calculation, a photon scattering experiment on ^{80}Se up to the neutron separation energy was performed by using the bremsstrahlung facility of the superconducting electron accelerator ELBE at Helmholtz-Zentrum Dresden-Rossendorf [2]. We already reported the experimental situation of the ^{80}Se (γ, γ') in Symposium on Nuclear Data 2013 [3]. In this time, we report on the result of the photo-absorption cross sections for ^{80}Se.

[1] A. Makinaga et al., Phys. Rev. C **79**, 025801 (2009),

[2] R. Schwengner et al., Phys. Rev. C **87**, 024306 (2013).

[3] A. Makinaga et al., Proc. of Symposium on Nuclear Data 2013

*present address: ayanomakinaga@gmail.com

This is a blank page.

60 Photo-activation experiment on ^{197}Au

[1*]Ayano Makinaga, [2]Manwoo Lee,[3]Kwang-Soo Kim, [3]Muhammad Zaman, [3]Muhammad Shahid, [3]Guinyun Kim, [4]Sung-Gyun Shin and [4]Mooh-Hyun Cho

[1]Faculty of Science, Hokkaido University, 060-0810, Sapporo, Japan
[2]Research Center, Dongnam Institute of Radiological & Medical Sciences, Busan 619-953, Korea
[3]Center for High Energy Physics, Kyungpook National University, 702-701, Daegu, Korea
[4]Pohang University of Science and Technology, 790-784, Pohang, Korea
*E-mail: makinaga@nucl.sci.hokudai.ac.jp

Photo-nuclear reactions are well-studied around the energy of 25 MeV where the giant dipole resonance (GDR) exists. On the other hands, cross sections for the photo-nuclear reactions around the inter-mediate energy regions have still large uncertainties. The photon strength of ^{197}Au is often considered as one of the cross section standard. In this study, we performed the photo-activation experiment on ^{197}Au by using the bremsstrahlung facility of the electron accelerator at Pohang [1-4]. In this study, we used the bremsstrahlung end-point energies of 59, 61, 63 and 65 MeV. As a flux monitor, ^{27}Al (γ,2pn)^{24}Na reaction was used. After the 30 min irradiation, the γ-rays from an activated ^{197}Au samples were measured by using HPGe. The detailed experimental setup of the photo activation on ^{197}Au was already reported in Symposium on Nuclear Data 2013 [3]. In this time, we will report on the experimental result of the ^{197}Au (γ, n) ^{196}Au, ^{197}Au (γ, 3n) ^{194}Au, ^{197}Au (γ, 4n) ^{193}Au and ^{197}Au (γ, 5n) ^{192}Au reactions.

[1]G. N. Kim, et al.., Proceedings of the International Conference on Nuclear Data for Science and Technology 2007,07739 (2008).
[2]K. Devan, et al., Journal of the Korean Physical Society vol.49; no.1,p88-96(2006).
[3]G. N. Kim, et al., Nuclear Instruments and Methods in Physics Research A 485, 458-467(2002).
[4]Y. S. Lee, et al., Radiation Measurements 35, 321-326 (2002).
[5] A. Makinaga et al., Proc. of Symposium on Nuclear Data 2013

*present address: Graduate school of medicine, Hokkaido University

This is a blank page.

61 Development of Digitization Software GSYS for NRDF/EXFOR compilation

Ryusuke SUZUKI[1], Ayano MAKINAGA[2] and Masayuki AIKAWA[3]
[1]Department of Medical Physics, Hokkaido University Hospital, Sapporo, 060-8648, Japan
[2]Department of Medical Physics, Hokkaido University Graduate School of Medicine, Sapporo, 060-8638, Japan
[3]Nuclear Reaction Data Centre (JCPRG), Hokkaido University, Sapporo, 060-0810, Japan
e-mail: ryusuke@med.hokudai.ac.jp

We have been developed a digitizing software GSYS which is a Java based software to convert the graphical data on the paper into the numerical data for NRDF/EXFOR compilation. This system has some functions to reduce the operation for digitizing and improve the quality of digitized numerical values.

1 Introduction

For 30 years, Japan Charged-Particle Reaction Data Group (JCPRG) has been accumulating the charged-particle induced nuclear reaction data measured by accelerators in Japan for the Nuclear Reaction Data File (NRDF). Recently it becomes possible to obtain experimental data directly in cooperation with experimentalists. However, in case numerical data cannot be obtained from the experimentalist, it is necessary to convert the graphical data on the paper into numerical data by digitizing the graph. Practically, a quarter of the amount of the data in NRDF is obtained by the digitizing the graph [1]. In the EXFOR library, about 40% of all entries during the last decade contain digitized data [2]. Therefore, the digitization process plays an important role in the nuclear data compilation.

In the past, an input device called 'digitizer' was used for reading numerical data directly from printed matters. In 1984, JCPRG started to develop a system for this type of device. Then such a device was replaced by digitization software which digitizes numerical data from electric image files.

GSYS (shown in the left hand side of **Fig. 1**) is a Java based digitizing software, originally developed for NRDF compilation and available at the JCPRG website [4]. Nowadays, this system is also accepted for EXFOR compilation [5].

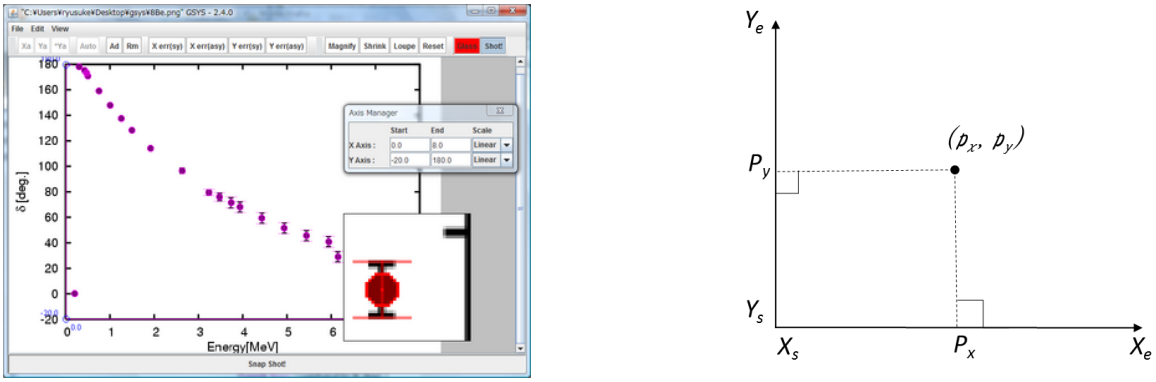

Fig.1. Screenshot of GSYS2.4 (left) and coordinate system used GSYS for digitization (right).

2 Features and functions.

The purpose of digitization used GSYS in the nuclear data activity is to read the coordinate of the data point (p_x, p_y) on the figure image and projection to the X and Y axis (P_x, P_y) of the graph as shown in the right hand side of Fig. 1. In addition to this basic function, GSYS has some functions to reduce the operation for numerical values:

- Feedback function: Feedback function is a function to load the numerical data from files and plot them directly on the graph image. This function enables us to reuse the data easily and check the data accuracy in greater detail. General numerical data as well as digitized data can be used for comparison and further digitization. (See Fig.2)

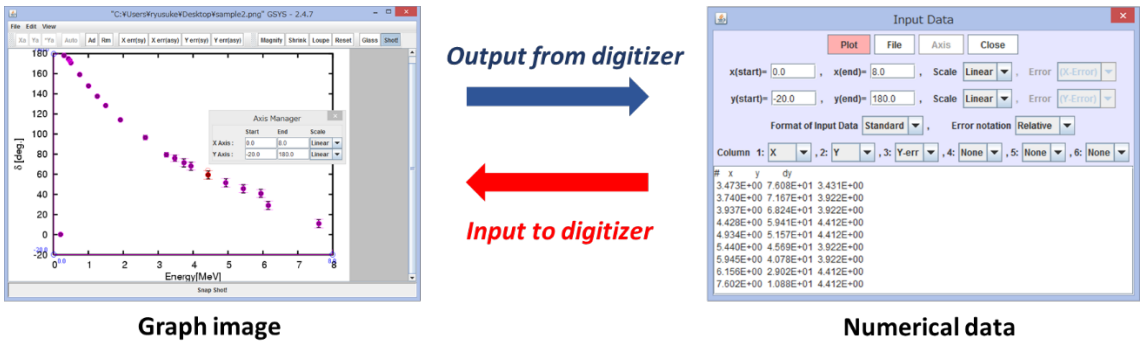

Fig.2. Data reading process and feedback function.

- Magnifying glass function: The glass windows magnify the local area of the figure to ease the fine adjustment. You can perform usual operation on this magnified figure.
- Automatic axis detection function: which automatically detects and sets the position of axis by easy operation. The aim of this function is to reduce operators' work and ambiguity of human judgment [6]. (See Fig.3)

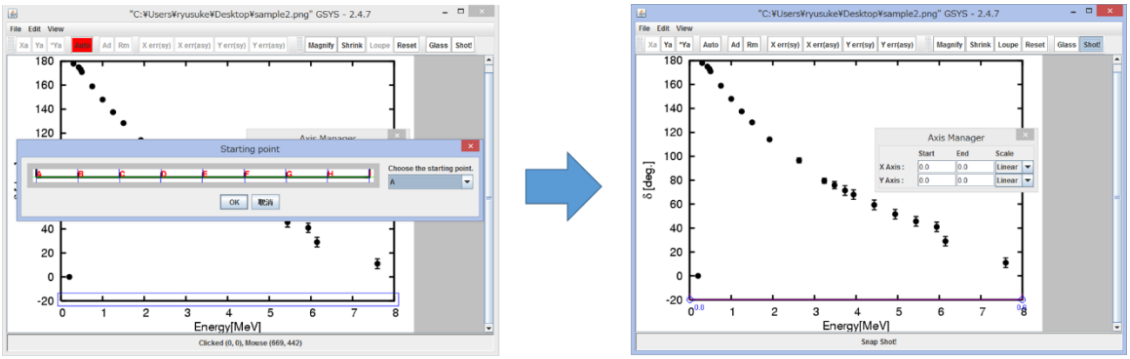

Fig. 3. Screenshot of Automatic axis detection function (left). After performing this function, axis is automatically set (right).

- Automatic point detection function: the maker on the figure is automatically recognized and position is automatically corrected as shown in Fig.4.

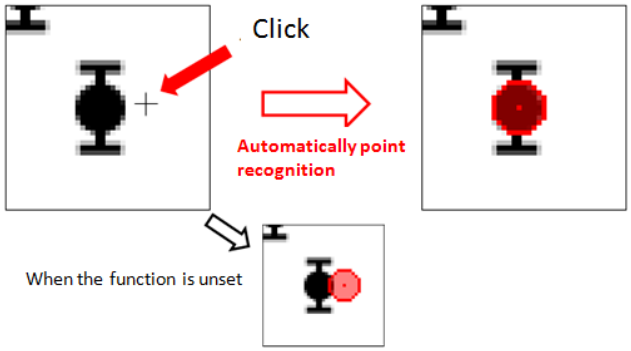

Fig.4. Automatic point recognition function. If you click the neighborhood of point as shown in left hand side, GSYS2.4 recognize and correct the point position, and add the point. If you do not use this function, data point is added at just the point where you click.

3 Discussion

GSYS is constantly developed to improve usability and simplicity and include some interesting features, for example, feedback function, magnifying glass function and automatically point recognition function. The quality of digitized numerical value is influenced with many kind of factors and sources. The authors believe that these features/functions implemented within GSYS improve the quality of digitized data. Digitizing software be able to further contribute to improve the quality of data, but it is difficult to take care of the factor especially come from human factor. In the initial work using the feedback function [7] and benchmark test [5, 8] shows the mistake of axes setting causes the big uncertainties. This kind of mistake easily happens, so each group should establish their own digitizing protocol to reduce this kind of error.

4 Conclusion

Nowadays, GSYS is widely used for NRDF/EXFOR compilation [5]. There is still room for improvement in this system.(See Fig.5) However the quality of digitization is not only determined by digitization software. Individual skill and experience are very important. Training, man power, QA and QC system for each compilation group are also important. The quality of figure image is another important factor which influences to the quality of digitized values. Though digitizing software can only take care of part of digitizing process, GSYS will be continually developed to improve the quality of digitized data.

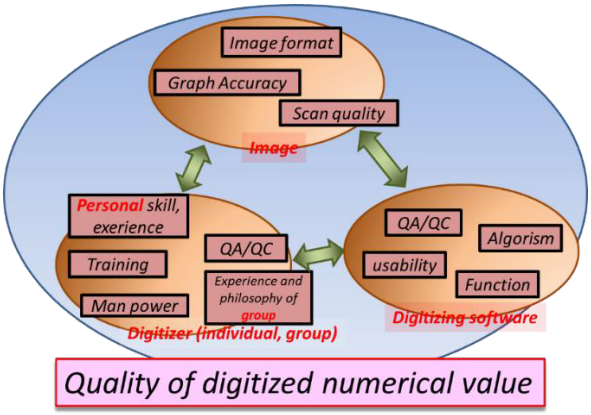

Fig.5. Factors and sources which influences the quality of digitized numerical value.

5 Future plan

Next major updated version of GSYS will be released in near future. Improvement of Automatic point recognition function, implementation of “Undo” “Redo” function and some new futures and improvements have been already performed into the GSYS source code.

References

[1] A. Minoguchi, K. Arai, N. Otuka and K. Naito, “GSYS：Development and usage of a software to read-in and digitize the graphical data”, INDC(JPN)-194/U, pp.19-22 (2005).

[2] N. Otsuka, V. Semkova, “Meeting summary”, Report INDC(NDS)-0629, pp. 3-6 (2013).

[3] R. Suzuki, “Introduction, Design and Implementation of Digitization Software GSYS “, Report INDC(NDS)-0629, pp.19-26 (2013).

[4] GSYS website, http://jcprg.hucc.hokudai.ac.jp/gsys/.

[5] V. Semkova, “Benchmarking of Digitization Software (Memo CP-D/761): Results and Discussions”, Report INDC(NDS)-0629, pp.42-57 (2013).

[6] S. Ito and R. Suzuki, “GSYS2.2 Manual”, NRDF Annual Report **20**, pp. 39-76 (2006).

[7] R. Suzuki, “GSYS2 Manual”, NRDF Annual Report **19**, pp. 10-44 (2005).

[8] N. Otuka and S. Dunaeva, “Quality and consistency of digitized data”, Report INDC(NDS)-0629, pp.63-69 (2013).

国際単位系（SI）

表１．SI 基本単位

基本量	SI 基本単位	
	名称	記号
長さ	メートル	m
質量	キログラム	kg
時間	秒	s
電流	アンペア	A
熱力学温度	ケルビン	K
物質量	モル	mol
光度	カンデラ	cd

表２．基本単位を用いて表されるSI組立単位の例

組立量	SI 組立単位	
	名称	記号
面積	平方メートル	m^2
体積	立方メートル	m^3
速さ，速度	メートル毎秒	m/s
加速度	メートル毎秒毎秒	m/s^2
波数	毎メートル	m^{-1}
密度，質量密度	キログラム毎立方メートル	kg/m^3
面積密度	キログラム毎平方メートル	kg/m^2
比体積	立方メートル毎キログラム	m^3/kg
電流密度	アンペア毎平方メートル	A/m^2
磁界の強さ	アンペア毎メートル	A/m
量濃度(a)，濃度	モル毎立方メートル	mol/m^3
質量濃度	キログラム毎立方メートル	kg/m^3
輝度	カンデラ毎平方メートル	cd/m^2
屈折率(b)	（数字の） 1	1
比透磁率(b)	（数字の） 1	1

(a) 量濃度（amount concentration）は臨床化学の分野では物質濃度（substance concentration）ともよばれる。
(b) これらは無次元量あるいは次元１をもつ量であるが、そのことを表す単位記号である数字の１は通常は表記しない。

表３．固有の名称と記号で表されるSI組立単位

組立量	SI 組立単位			
	名称	記号	他のSI単位による表し方	SI基本単位による表し方
平面角	ラジアン(b)	rad	1 (b)	m/m
立体角	ステラジアン(b)	sr(c)	1 (b)	m^2/m^2
周波数	ヘルツ(d)	Hz		s^{-1}
力	ニュートン	N		m kg s^{-2}
圧力，応力	パスカル	Pa	N/m^2	m^{-1} kg s^{-2}
エネルギー，仕事，熱量	ジュール	J	N m	m^2 kg s^{-2}
仕事率，工率，放射束	ワット	W	J/s	m^2 kg s^{-3}
電荷，電気量	クーロン	C		s A
電位差（電圧），起電力	ボルト	V	W/A	m^2 kg s^{-3} A^{-1}
静電容量	ファラド	F	C/V	m^{-2} kg^{-1} s^4 A^2
電気抵抗	オーム	Ω	V/A	m^2 kg s^{-3} A^{-2}
コンダクタンス	ジーメンス	S	A/V	m^{-2} kg^{-1} s^3 A^2
磁束	ウエーバ	Wb	Vs	m^2 kg s^{-2} A^{-1}
磁束密度	テスラ	T	Wb/m^2	kg s^{-2} A^{-1}
インダクタンス	ヘンリー	H	Wb/A	m^2 kg s^{-2} A^{-2}
セルシウス温度	セルシウス度(e)	℃		K
光束	ルーメン	lm	cd sr(c)	cd
照度	ルクス	lx	lm/m^2	m^{-2} cd
放射性核種の放射能(f)	ベクレル(d)	Bq		s^{-1}
吸収線量，比エネルギー分与，カーマ	グレイ	Gy	J/kg	m^2 s^{-2}
線量当量，周辺線量当量，方向性線量当量，個人線量当量	シーベルト(g)	Sv	J/kg	m^2 s^{-2}
酸素活性	カタール	kat		s^{-1} mol

(a)SI接頭語は固有の名称と記号を持つ組立単位と組み合わせても使用できる。しかし接頭語を付した単位はもはやコヒーレントではない。
(b)ラジアンとステラジアンは数字の１に対する単位の特別な名称で、量についての情報をつたえるために使われる。実際には、使用する時には記号radおよびsrが用いられるが、習慣として組立単位としての記号である数字の１は明示されない。
(c)測光学ではステラジアンという名称と記号srを単位の表し方の中に、そのまま維持している。
(d)ヘルツは周期現象についてのみ、ベクレルは放射性核種の統計的過程についてのみ使用される。
(e)セルシウス度はケルビンの特別な名称で、セルシウス温度を表すために使用される。セルシウス度とケルビンの単位の大きさは同一である。したがって、温度差や温度間隔を表す数値はどちらの単位で表しても同じである。
(f)放射性核種の放射能（activity referred to a radionuclide）は、しばしば誤った用語で"radioactivity"と記される。
(g)単位シーベルト（PV,2002,70,205）についてはCIPM勧告2（CI-2002）を参照。

表４．単位の中に固有の名称と記号を含むSI組立単位の例

組立量	SI 組立単位		
	名称	記号	SI 基本単位による表し方
粘度	パスカル秒	Pa s	m^{-1} kg s^{-1}
力のモーメント	ニュートンメートル	N m	m^2 kg s^{-2}
表面張力	ニュートン毎メートル	N/m	kg s^{-2}
角速度	ラジアン毎秒	rad/s	m m^{-1} s^{-1}=s^{-1}
角加速度	ラジアン毎秒毎秒	rad/s^2	m m^{-1} s^{-2}=s^{-2}
熱流密度，放射照度	ワット毎平方メートル	W/m^2	kg s^{-3}
熱容量，エントロピー	ジュール毎ケルビン	J/K	m^2 kg s^{-2} K^{-1}
比熱容量，比エントロピー	ジュール毎キログラム毎ケルビン	J/(kg K)	m^2 s^{-2} K^{-1}
比エネルギー	ジュール毎キログラム	J/kg	m^2 s^{-2}
熱伝導率	ワット毎メートル毎ケルビン	W/(m K)	m kg s^{-3} K^{-1}
体積エネルギー	ジュール毎立方メートル	J/m^3	m^{-1} kg s^{-2}
電界の強さ	ボルト毎メートル	V/m	m kg s^{-3} A^{-1}
電荷密度	クーロン毎立方メートル	C/m^3	m^{-3} s A
表面電荷	クーロン毎平方メートル	C/m^2	m^{-2} s A
電束密度，電気変位	クーロン毎平方メートル	C/m^2	m^{-2} s A
誘電率	ファラド毎メートル	F/m	m^{-3} kg^{-1} s^4 A^2
透磁率	ヘンリー毎メートル	H/m	m kg s^{-2} A^{-2}
モルエネルギー	ジュール毎モル	J/mol	m^2 kg s^{-2} mol^{-1}
モルエントロピー，モル熱容量	ジュール毎モル毎ケルビン	J/(mol K)	m^2 kg s^{-2} K^{-1} mol^{-1}
照射線量（X線及びγ線）	クーロン毎キログラム	C/kg	kg^{-1} s A
吸収線量率	グレイ毎秒	Gy/s	m^2 s^{-3}
放射強度	ワット毎ステラジアン	W/sr	m^4 m^{-2} kg s^{-3}=m^2 kg s^{-3}
放射輝度	ワット毎平方メートル毎ステラジアン	$W/(m^2$ sr)	m^2 m^{-2} kg s^{-3}=kg s^{-3}
酵素活性濃度	カタール毎立方メートル	kat/m^3	m^{-3} s^{-1} mol

表５．SI 接頭語

乗数	名称	記号	乗数	名称	記号
10^{24}	ヨタ	Y	10^{-1}	デシ	d
10^{21}	ゼタ	Z	10^{-2}	センチ	c
10^{18}	エクサ	E	10^{-3}	ミリ	m
10^{15}	ペタ	P	10^{-6}	マイクロ	μ
10^{12}	テラ	T	10^{-9}	ナノ	n
10^{9}	ギガ	G	10^{-12}	ピコ	p
10^{6}	メガ	M	10^{-15}	フェムト	f
10^{3}	キロ	k	10^{-18}	アト	a
10^{2}	ヘクト	h	10^{-21}	ゼプト	z
10^{1}	デカ	da	10^{-24}	ヨクト	y

表６．SIに属さないが、SIと併用される単位

名称	記号	SI 単位による値
分	min	1 min=60 s
時	h	1 h =60 min=3600 s
日	d	1 d=24 h=86 400 s
度	°	1°=(π/180) rad
分	’	1’=(1/60)°=(π/10 800) rad
秒	”	1”=(1/60)’=(π/648 000) rad
ヘクタール	ha	1 ha=1 hm^2=10^4m^2
リットル	L, l	1 L=1 l=1 dm^3=10^3cm^3=$10^{-3}m^3$
トン	t	1 t=10^3 kg

表７．SIに属さないが、SIと併用される単位で、SI単位で表される数値が実験的に得られるもの

名称	記号	SI 単位で表される数値
電子ボルト	eV	1 eV=1.602 176 53(14)×10^{-19}J
ダルトン	Da	1 Da=1.660 538 86(28)×10^{-27}kg
統一原子質量単位	u	1 u=1 Da
天文単位	ua	1 ua=1.495 978 706 91(6)×10^{11}m

表８．SIに属さないが、SIと併用されるその他の単位

名称	記号	SI 単位で表される数値
バール	bar	1 bar=0.1MPa=100 kPa=10^5Pa
水銀柱ミリメートル	mmHg	1 mmHg≈133.322Pa
オングストローム	Å	1 Å=0.1nm=100pm=10^{-10}m
海里	M	1 M=1852m
バーン	b	1 b=100fm^2=(10^{-12}cm)^2=$10^{-28}m^2$
ノット	kn	1 kn=(1852/3600)m/s
ネーパ	Np	SI単位との数値的な関係は、対数量の定義に依存。
ベル	B	
デシベル	dB	

表９．固有の名称をもつCGS組立単位

名称	記号	SI 単位で表される数値
エルグ	erg	1 erg=10^{-7} J
ダイン	dyn	1 dyn=10^{-5}N
ポアズ	P	1 P=1 dyn s cm^{-2}=0.1Pa s
ストークス	St	1 St =1cm^2 s^{-1}=$10^{-4}m^2$ s^{-1}
スチルブ	sb	1 sb =1cd cm^{-2}=10^4cd m^{-2}
フォト	ph	1 ph=1cd sr cm^{-2} =10^4lx
ガル	Gal	1 Gal =1cm s^{-2}=$10^{-2}ms^{-2}$
マクスウエル	Mx	1 Mx = 1G cm^2=10^{-8}Wb
ガウス	G	1 G =1Mx cm^{-2} =10^{-4}T
エルステッド(a)	Oe	1 Oe ≙ (10^3/4π)A m^{-1}

(a) ３元系のCGS単位系とSIでは直接比較できないため、等号「 ≙ 」は対応関係を示すものである。

表10．SIに属さないその他の単位の例

名称	記号	SI 単位で表される数値
キュリー	Ci	1 Ci=3.7×10^{10}Bq
レントゲン	R	1 R = 2.58×10^{-4}C/kg
ラド	rad	1 rad=1cGy=10^{-2}Gy
レム	rem	1 rem=1 cSv=10^{-2}Sv
ガンマ	γ	1 γ=1 nT=10^{-9}T
フェルミ		1 フェルミ=1 fm=10^{-15}m
メートル系カラット		1 メートル系カラット= 0.2 g = 2×10^{-4}kg
トル	Torr	1 Torr = (101 325/760) Pa
標準大気圧	atm	1 atm = 101 325 Pa
カロリー	cal	1 cal=4.1858J（「15℃」カロリー），4.1868J（「IT」カロリー），4.184J（「熱化学」カロリー）
ミクロン	μ	1 μ =1μm=10^{-6}m

（第8版，2006年）